LEABHARLANN CHOLÁISTE NA TRÍONÓIDE, BAILE ÁTHA CLIATH | TRINITY COLLEGE LIBRARY DUBLIN
Ollscoil Átha Cliath | The University of Dublin

Terms and Conditions of Use of Digitised Theses from Trinity College Library Dublin

Copyright statement

All material supplied by Trinity College Library is protected by copyright (under the Copyright and Related Rights Act, 2000 as amended) and other relevant Intellectual Property Rights. By accessing and using a Digitised Thesis from Trinity College Library you acknowledge that all Intellectual Property Rights in any Works supplied are the sole and exclusive property of the copyright and/or other IPR holder. Specific copyright holders may not be explicitly identified. Use of materials from other sources within a thesis should not be construed as a claim over them.

A non-exclusive, non-transferable licence is hereby granted to those using or reproducing, in whole or in part, the material for valid purposes, providing the copyright owners are acknowledged using the normal conventions. Where specific permission to use material is required, this is identified and such permission must be sought from the copyright holder or agency cited.

Liability statement

By using a Digitised Thesis, I accept that Trinity College Dublin bears no legal responsibility for the accuracy, legality or comprehensiveness of materials contained within the thesis, and that Trinity College Dublin accepts no liability for indirect, consequential, or incidental, damages or losses arising from use of the thesis for whatever reason. Information located in a thesis may be subject to specific use constraints, details of which may not be explicitly described. It is the responsibility of potential and actual users to be aware of such constraints and to abide by them. By making use of material from a digitised thesis, you accept these copyright and disclaimer provisions. Where it is brought to the attention of Trinity College Library that there may be a breach of copyright or other restraint, it is the policy to withdraw or take down access to a thesis while the issue is being resolved.

Access Agreement

By using a Digitised Thesis from Trinity College Library you are bound by the following Terms & Conditions. Please read them carefully.

I have read and I understand the following statement: All material supplied via a Digitised Thesis from Trinity College Library is protected by copyright and other intellectual property rights, and duplication or sale of all or part of any of a thesis is not permitted, except that material may be duplicated by you for your research use or for educational purposes in electronic or print form providing the copyright owners are acknowledged using the normal conventions. You must obtain permission for any other use. Electronic or print copies may not be offered, whether for sale or otherwise to anyone. This copy has been supplied on the understanding that it is copyright material and that no quotation from the thesis may be published without proper acknowledgement.

Constraining global Carboniferous climatic fluctuations using high resolution geochronology

Michael Pointon

2012

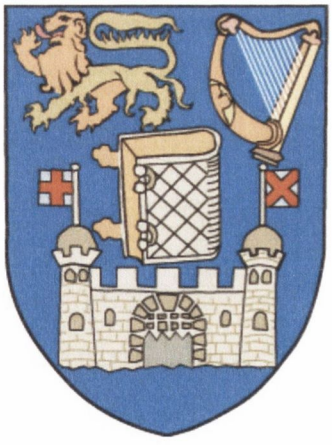

A dissertation submitted for the degree of Doctor of Philosophy to the University of Dublin, Trinity College

TRINITY COLLEGE
2 2 OCT 2012
LIBRARY DUBLIN

Thesis 9699

Declaration

I declare that this thesis has not been submitted as an exercise for a degree at this or any other university and it is entirely my own work.

I agree to deposit this thesis in the University's open access institutional repository or allow the library to do so on my behalf, subject to Irish Copyright Legislation and Trinity College Library conditions of use and acknowledgement.

M. Pointon

Michael Pointon

Summary

The Carboniferous Period was a time of substantial climatic change, during which occurred the transition from a greenhouse (ice-free) environment into major continental glaciation. The onset of major Carboniferous glaciation is reconstructed using two main stratigraphic records: the direct records of glacial sedimentary rocks preserved on the remnants of Gondwana and far-field, ice-distal proxy records from palaeo-equatorial regions. Neither of these records provides a perfect account of the onset of major glaciation and there are conflicts regarding the timing of the onset of glaciation, both between the direct and indirect records and also within the indirect proxy records themselves.

The aims of this project are three-fold: 1) to constrain better the timing of the onset of major Carboniferous glaciation as recorded by the indirect, far-field records of western Europe using high precision U-Pb geochronology; 2) to constrain the periodicity of western European cyclic sedimentation, which has been interpreted to reflect the waxing and waning of Carboniferous ice sheets on southern Gondwana (glacio-eustasy); 3) to provide additional high-precision age constraints for the improved calibration of the Carboniferous timescale.

Interbedded within the stratigraphy of western Europe are numerous diagenetically altered volcanic ash layers that are often termed tonsteins and bentonites. These horizons comprise predominantly clay minerals but also often contain a subordinate coarser fraction that includes euhedral zircon and apatite, biotite, sanidine and quartz, which are interpreted as original volcanic phenocrysts. Several of these phenocrysts are amenable to isotopic dating and the dating of these horizons can be employed to provide absolute age constraints on the stratigraphy. However, few of these altered ash horizons have been dated previously; most previous undertakings have employed the U-Pb SHRIMP method (mostly from the 1990s) and the $^{40}Ar/^{39}Ar$ method (mostly from the 1980s). These existing data have very large analytical uncertainties (typically >> 1 Myrs uncertainty) relative to the precision that is now attainable using modern high-precision U-Pb zircon chemical abrasion isotopic dilution thermal ionization mass spectrometry

(CA-ID-TIMS) analysis (< 0.1 % uncertainty on $^{206}Pb/^{238}U$ dates; equivalent to < 0.3 Myrs on a rock of Carboniferous age).

High-precision U-Pb zircon CA-ID-TIMS analysis was undertaken on several western European diagenetically altered volcanic ash layers of latest Tournaisian to Westphalian (Moscovian) age. Samples were collected from several sedimentary basins within western Europe: mid-to-upper Visean bentonites were sampled from the Namur-Dinant Basin, Belgium; Namurian bentonites were sampled from the Pennine Basin, northern England; and Westphalian samples were collected from the Campine and Ruhr basins (Belgium and Germany respectively). Eight of the investigated samples yielded statistically robust U-Pb zircon dates, which provide additional precise age constraints for the improved calibration of the Carboniferous timescale and offer substantial improvements in precision over the existing U-Pb SHRIMP and $^{40}Ar/^{39}Ar$ age determinations.

The appearance of glacio-eustatic sedimentary cyclicity has been suggested to signify the onset of major Gondwanan glaciation. However, in western Europe the appearance of sedimentary cyclicity is diachronous, appearing earlier in Belgium (Livian times; equivalent to the Holkerian) than in Britain and Ireland (Asbian times). The average cycle periodicities calculated for Livian sedimentary cycles do not lend support for these cycles being of glacio-eustatic origin. These cycles appear to be an isolated occurrence within western Europe and they may be of only local significance. In contrast to the Livian cycles, Belgian lower Warnantian cycles (equivalent to the Asbian) have comparable lateral equivalents in Britain and Ireland and yield periodicities that are compatible with the *c.* 100 kyrs Milankovitch 'short' eccentricity cycle, which is the dominant Milankovitch frequency observed within the recent (Pleistocene) glacial records. Thus, the periodicity estimates lend support to the hypothesis that these cycles are of glacio-eustatic origin. The available data support theories that the onset of major Carboniferous glaciation occurred close to the base of the Asbian Substage (correlated with the base of the Belgian Warnantian Substage). Furthermore, the new U-Pb zircon CA-ID-TIMS dates from Belgian Visean bentonite horizons constrain this event to between 336.22 ± 0.40 Ma and 335.59 ± 0.44 Ma (95% confidence; the cited uncertainties include systematic uncertainties in the calibration of the isotopic tracer solution and the U decay constants).

Acknowledgements

First and foremost I would like to thank my supervisor David Chew (Trinity College Dublin) for this opportunity and for all of the encouragement, patience and support throughout this project. My examiners, Quentin Crowley (Trinity College Dublin) and Colin Waters (British Geological Society), are gratefully acknowledged for a stimulating viva and thoughtful comments on this thesis.

I owe a debt of gratitude to Bernard Delcambre (Université Catholique de Louvain) for providing the Westphalian tonstein samples investigated during this project, for help during fieldwork, insights into the Lower Carboniferous geology of Belgium and access to unpublished literature. My thanks also for arranging access to the quarries at Awirs; the Carmeuse Corporation are acknowledged for allowing the sampling of limestones from Awirs West Quarry.

The high-precision U-Pb zircon CA-ID-TIMS elements of this project would not have been possible without the support of Urs Schaltegger and Maria Ovtcharova (University of Geneva). In particular, Maria Ovtcharova is thanked for the training that I have received in the CA-ID-TIMS method and for the sharing of unpublished U-Pb zircon CA-ID-TIMS data from some of the Belgian Visean bentonite horizons; the data from one horizon is reproduced in this thesis (bentonite L1 sampled from Lives-sur-Meuse). I would also like to thank Blair Schoene (Princeton University) for several stimulating discussions regarding the reduction of U-Pb zircon CA-ID-TIMS data.

Quentin Crowley (Trinity College Dublin) and Vanessa Pashley (NERC Isotope Geosciences Laboratory) are thanked for their assistance with the LA-MC-ICP-MS analyses performed at the NERC Isotope Geosciences Laboratory, Keyworth, UK. Gren Turner (British Geological Survey) is thanked for the imaging of zircon grains using scanning electron microscopy at the British Geological Survey, Keyworth, UK.

This project has benefited from the support and insights of George Sevastopulo (Trinity College Dublin). George is also acknowledged for initiating the dialogue with Paul

Henry (Boliden Tara Mines Ltd.), who provided the Irish upper Tournaisian bentonite sample (bentonite 300) investigated during this project.

The magnetic susceptibility aspects of the project would not have been possible without the help and co-operation of Brooks Ellwood (Louisiana State University). On a personal note, I would like to thank Brooks for making me feel very welcome during my research visit to Louisiana.

The help and support of Robbie Goodhue (Trinity College Dublin) with the XRD and stable isotopic analyses was greatly appreciated. The support of the technical staff within the Department of Geology at Trinity College Dublin (Neil, Frank, Maura and Noel), throughout this project, is gratefully acknowledged.

My colleagues in M7, Hudson, Maja and Sophie are thanked for a pleasant working environment. Thanks are also due to my dear Charlotte, for love, support and patience during what have been several difficult months. I am deeply grateful to my parents for encouragement and support throughout the past years.

This project would not have been possible without generous funding from Science Foundation Ireland, in the form of a Research Frontiers Programme grant (grant ID: 07/RFP/GEOF207) and a Short Term Travel Fellowship (grant ID: 07/RFP/GEOF207 STTF 08).

Table of Contents

1. Introduction **1**

1.1. Background: Carboniferous climate 1

1.2. Project approach and aims 4

1.3. Milankovitch cycles 6

1.4. The Carboniferous Timescale 7

1.5. Sample materials: western European diagenetically altered volcanic ash layers 11

1.5.1. Altered ash layer nomenclature 14

1.6. Structure of this thesis 16

2. Methodology **17**

2.1. Introduction 17

2.2. Zircon separation and concentration 17

2.3. U-Pb zircon dating 20

2.3.1. Overview of U-Pb zircon geochronology 20

2.3.2. Conventional (Wetherill) concordia diagrams 22

2.3.2.1. Lead loss 22

2.3.2.2. Inheritance 24

2.3.2.3. Protracted growth of zircon (antecrystic inheritance) 24

2.3.2.4. Common lead contamination 24

2.3.3. Defining the age of a diagenetically altered volcanic ash layer: weighted mean $^{206}Pb/^{238}U$ dates 25

2.3.4. Laser ablation (multi-collector) inductively coupled plasma mass spectrometry (LA-MC-ICP-MS) 26

2.3.4.1. Overview of the technique 26

2.3.4.2. Methodology 27

2.3.4.2.1. SEM imaging of grains 28

2.3.4.2.2. LA-MC-ICP-MS analysis 29

2.3.5. Chemical abrasion isotope dilution thermal ionization mass spectrometry (CA-ID-TIMS) 30

2.3.5.1. Overview of the technique 30

2.3.5.2. Methodology 31

2.3.5.2.1. Chemical abrasion 31
2.3.5.2.2. ID-TIMS analysis 31
2.3.5.2.3. CA-ID-TIMS data from bentonite L1 at Lives-sur-Meuse 36
2.3.5.2.4. U-Pb zircon data presentation 37
2.3.5.2.5. Weighted mean $^{206}Pb/^{238}U$ dates 37
2.3.5.3. Potential pre-eruptive zircon residence in magma chambers 39
2.4. Low-field magnetic susceptibility analysis of sedimentary rocks 40
2.4.1. Background 40
2.4.1.1. Mineral magnetism 41
2.4.2. MS analysis in marine carbonates 42
2.4.3. Methodology 43
2.5. Stable isotope analyses ($\delta^{13}C$ and $\delta^{18}O$) of limestones 44
2.5.1. Overview 44
2.5.2. Stable isotope analyses of carbonates 45
2.5.3. Delta notation 45
2.5.4. Carbon and oxygen isotopic variations in carbonate rocks 46
2.5.4.1. Environmental controls 47
2.5.4.2. Biological (vital) effects 47
2.5.4.3. Mineralogical controls 48
2.5.4.4. Secondary (diagenetic) alteration 48
2.5.5. Methodology 48
2.6. XRD analysis of the diagenetically altered volcanic ash layer samples 49
2.7. Whole-rock geochemistry of the diagenetically altered ash layer samples 50
2.8. Recalibration of legacy $^{40}Ar/^{39}Ar$ sanidine dates 52
2.9. Average periodicity calculations for sedimentary cycles 53
2.9.1. Assumptions 54

3. U-Pb zircon CA-ID-TIMS dates from Tournaisian and Visean western European diagenetically altered volcanic ash layers 55

3.1. Introduction 55
3.1.1. Palaeogeographic setting of western Europe during Mississippian times 57
3.2. Tournaisian Stage 57
3.2.1. Bentonite 300 57

3.3. Visean Stage 60
3.3.1. The Namur-Dinant Basin: an introduction 60
3.3.2. Mid-to-upper Visean stratigraphic framework of the Namur-Dinant Basin..63
3.3.2.1. Chronostratigraphy 63
3.3.2.2. Biostratigraphy 64
3.3.2.3. Lithostratigraphy 65
3.3.3. Diagenetically altered volcanic ash layers 66
3.3.3.1. Previous research 68
3.3.3.2. Horizons dated by U-Pb zircon CA-ID-TIMS and sampling localities..69
3.3.4. U-Pb zircon CA-ID-TIMS age constraints: Livian bentonite layers 72
3.3.4.1. Bentonite L1 (also known as the Banc d'Or de Bachant) 72
3.3.4.2. Bentonite L2 74
3.3.4.3. Bentonite L3 77
3.3.4.4. Bentonite W1 80
3.3.5. U-Pb zircon CA-ID-TIMS age constrains: Warnantian bentonite layers 82
3.3.5.1. Bentonite W8 82
3.3.5.2. Bentonites W12 and W13: introduction 85
3.3.5.2.1. Bentonite W12 86
3.3.5.2.2. Bentonite W13 88
3.4. Discussion 89
3.4.1. Mid-to-upper Visean cyclic sedimentation and the onset of major Gondwanan glaciation 90
3.4.1.1. Belgian mid-to-upper Visean carbonate cycles 95
3.4.1.2. Average periodicity estimates for Belgian Livian and Warnantian sedimentary cycles 98
3.4.1.2.1. Livian sedimentary cycles 98
3.4.1.2.2. Lower Warnantian cycles 100
3.4.1.2.2.1. Lower Warnantian cyclicity between bentonites W1 and W8 100
3.4.1.2.2.2. Periodicity of sedimentary cycles between bentonites W1 and W8 102
3.4.1.2.2.3. Lower Warnantian cyclicity between bentonites W8 and W13 103

3.4.1.2.2.4. Periodicity of sedimentary cycles between bentonites W8 and W13 104
3.4.1.2.3. Synthesis of periodicity calculations 104
3.4.2. Comparisons between the new U-Pb zircon CA-ID-TIMS data and existing age constraints 106
3.4.2.1. Trapp (2001) U-Pb zircon ID-TIMS dates (samples L168 and Bu 171) 108
3.4.2.1.1. Sample L168 (Lerbach) 108
3.4.2.1.2. Sample Bu 171 (Büchenberg) 110
3.4.2.2. U-Pb zircon SHRIMP dates 112
3.4.2.2.1. Martins Creek Ignimbrite (Roberts *et al.*, 1995a) 112
3.4.2.2.2. Paprotnia Beds bentonite (Kryza *et al.*, 2010) 112
3.4.2.2.3. Dainrode bentonite (Claoué-Long *et al.*, unpublished; discussed in Weyer & Menning, 2006) 113
3.4.3. Implications for timescale calibration 114
3.4.3.1. Base of the Livian Substage 115
3.4.3.2. Base of the Warnantian Substage 116
3.4.3.3. Base of the Upper Warnantian and the duration of the Early Warnantian 116
3.5. Conclusions 117

4. Irish Visean (Mississippian) clay partings 119
4.1. Introduction 119
4.2. Irish Asbian clay-rich horizons 120
4.2.1. SEM imaging of grains from Irish Asbian clay partings 122
4.2.2. U-Pb zircon LA-MC-ICP-MS dating 122
4.2.3. Potential for U-Pb zircon CA-ID-TIMS dating 125
4.3. Brigantian clay-rich horizons 126
4.3.1. SEM-CL imaging of grains from sample MAP 09/07/01 127
4.3.2. U-Pb zircon LA-MC-ICP-MS results 128
4.3.3. Potential for U-Pb zircon CA-ID-TIMS dating 130
4.4. Conclusions 131

5. U-Pb zircon dates from western European Namurian and Westphalian (Serpukhovian – Moscovian) diagenetically altered volcanic ash layers 132

5.1. Introduction 132

5.2. Namurian Stage 133

5.2.1. Namurian bentonite samples 135

5.2.2. Zircon populations from Namurian bentonites 137

5.2.2.1. Bentonite B1 137

5.2.2.2. Bentonite B7 138

5.2.2.3. Bentonites B8 and B9 138

5.2.3. U-Pb zircon LA-MC-ICP-MS dating of Namurian bentonites 138

5.2.3.1. Bentonite B1 139

5.2.3.2. Bentonite B7 140

5.2.3.3. Bentonite B9 141

5.2.3.4. Synthesis of LA-MC-ICP-MS data 142

5.2.4. U-Pb zircon CA-ID-TIMS dating of Namurian bentonites 142

5.2.4.1. Bentonite B1 142

5.2.4.2. Bentonite B9 144

5.2.4.2.1. Comparison to the B6 U-Pb CA-ID-TIMS date of Waters & Condon (2012) 146

5.3. Westphalian Stage 149

5.3.1. U-Pb zircon CA-ID-TIMS dating of Westphalian tonsteins 150

5.3.1.1. Tonstein T75 150

5.3.1.2. Tonstein Z1 152

5.3.1.2.1. Comparison to the Sub-High Main Tonstein U-Pb zircon CA-ID-TIMS date of Waters & Condon (2012) 154

5.3.1.3. Tonsteins T1Gb and T1P: introduction 156

5.3.1.3.1. Tonstein T1P 157

5.3.1.3.2. Tonstein T1Gb 158

5.4. Discussion 159

5.4.1. Upper Carboniferous cyclic sedimentation 160

5.4.1.1. Periodicity of upper Carboniferous marine bands 161

5.4.1.1.1. Arnsbergian to lower Langsettian cycles (bentonite B9 to tonstein T75) 164
5.4.1.1.2. Upper Langsettian to Duckmantian sedimentary cycles 167
5.4.2. Carboniferous timescale calibration and astronomical tuning 170
5.4.2.1. Base of the Namurian Stage 170
5.4.2.2. Mississippian – Pennsylvanian (Mid-Carboniferous) Boundary 173
5.4.2.3. Base of the Westphalian Regional Stage 175
5.4.2.4. Base of the Bolsovian Substage 176
5.4.2.5. Duration of Chokierian to Duckmantian substages 177
5.4.3. Correlation of the base of the Moscovian Stage with the regional stages of western Europe 178
5.5. Conclusions 179

6. Magnetic susceptibility and stable isotope ($\delta^{13}C$ and $\delta^{18}O$) data from Belgian Livian and Lower Warnantian carbonate cycles 182

6.1. Introduction 182
6.2. Samples and stratigraphy 183
6.3. Results 184
6.3.1. Overview 184
6.3.1.1. $\delta^{13}C$ data 186
6.3.1.2. $\delta^{18}O$ data 187
6.3.2. Lives-sur-Meuse (Livian Substage) 188
6.3.2.1. Haut-le-Wastia Member 188
6.3.2.1.1. Magnetic susceptibility data 188
6.3.2.1.2. Stable isotope ($\delta^{13}C$ and $\delta^{18}O$) data 190
6.3.2.2. Corphalie Member 191
6.3.2.2.1. Magnetic susceptibility data 191
6.3.2.2.2. Stable isotope ($\delta^{13}C$ and $\delta^{18}O$) data 193
6.3.2.3. Awirs Member 193
6.3.2.3.1. Magnetic susceptibility data 193
6.3.2.3.2. Stable isotope ($\delta^{13}C$ and $\delta^{18}O$) data 195
6.3.3. Awirs West Quarry (Livian Substage) 195
6.3.3.1. Awirs Member 195

6.3.3.1.1. Magnetic susceptibility data 195
6.3.3.1.2. Stable isotope ($\delta^{13}C$ and $\delta^{18}O$) data 196
6.3.3.2. Seilles Member 198
6.3.3.2.1. Magnetic susceptibility data 198
6.3.4. Anhée Nord (Lower Warnantian; Poilvache Member) 199
6.3.4.1. Magnetic susceptibility data 199
6.3.4.2. Stable isotope ($\delta^{13}C$ and $\delta^{18}O$) data 199
6.3.5. Anhée Sud (Lower Warnantian; Poilvache Member to Lower Member of the Anhée Formation) 201
6.3.5.1. Magnetic susceptibility data 201
6.4. Discussion 203
6.4.1. Correlation between MS and the sedimentary cycles 203
6.4.2. Magnetic susceptibility analysis as a correlation tool 206
6.4.3. Significance of the stable isotope ($\delta^{13}C$ and $\delta^{18}O$) analyses 207
6.5. Conclusions 208

7. Whole-rock geochemistry of western European diagenetically altered volcanic ash layers 210

7.1. Introduction 210
7.2. Samples 211
7.3. Whole-rock geochemistry 215
7.3.1. Belgian Visean samples 215
7.3.1.1. Vertical chemical structure of the bentonite horizons 219
7.3.1.2. Lateral variations in composition 221
7.3.2. Irish Asbian samples 222
7.3.3. Irish Brigantian samples 223
7.3.4. Namurian bentonite samples 224
7.3.5. Westphalian tonstein samples 225
7.4. Magma parentage of the altered ash layer samples 227
7.4.1. Trace element geochemistry: discrimination diagrams 228
7.4.1.1. Zr / TiO_2 – Nb / Y diagram (Winchester & Floyd, 1977) 228
7.4.1.2. Batchelor & Jeppsson (1999) ternary diagram 230
7.4.2. Rare-earth element geochemistry 231
7.4.2.1. CI-Chondrite normalised REE profiles 232

7.4.2.2. Shale-normalised REE profiles 236
7.4.2.3. Europium anomalies 240
7.5. Discussion: magmatic parentage of the original ash layers 242
7.5.1. Belgian Visean samples 242
7.5.2. Irish Asbian samples 243
7.5.3. Irish Brigantian samples 244
7.5.4. British Namurian samples 244
7.5.5. Westphalian tonstein samples 245
7.6. Conclusions 245

8. Conclusions 247

Bibliography 253

List of Figures

1.1 Global Mississippian palaeogeography 1
1.2 Published estimates for the onset of major Carboniferous glaciation 3
1.3 The Carboniferous Timescale (after Davydov *et al.*, 2004) 8
1.4 Stratigraphic distribution of recent U-Pb zircon dates 10
1.5 Simplified structural map of Europe 12
1.6 Stratigraphic column of the altered ash layer samples investigated 13

2.1 The Chas. W. Cooks and Sons magnetic separator used in this study 19
2.2 Explanatory U-Pb Wetherill concordia diagrams 23
2.3 Schematic diagram of the LA-MC-ICP-MS set-up used 27
2.4 Optical photomicrographs of chemically abraded zircon grains 32
2.5 Thermo Scientific Triton thermal ionization mass spectrometer 33
2.6 Acceptable MSWD values at the 95 % confidence level 39
2.7 Diagram illustrating the different types of magnetic behaviour 42
2.8 The custom-built magnetic susceptibility bridge used in this study 44
2.9 Main controls over the isotopic composition of carbonate rocks 46

3.1 Stratigraphic column of the samples discussed in chapter 3 56
3.2 Late Tournaisian palaeogeography of western Europe 57
3.3 Optical photomicrograph of zircon grains from bentonite 300 58
3.4 U-Pb concordia and weighted mean $^{206}Pb/^{238}U$ date diagrams of CA-ID-TIMS data from bentonite 300 59
3.5 Map of the Namur-Dinant Basin, southern Belgium 61
3.6 Lithostratigraphic framework for the Namur-Dinant Basin 62
3.7 Field photograph of bentonite M 67
3.8 Field photographs of bentonites L3 and L4 68
3.9. Map showing the sampling localities of the Livian and Warnantian bentonites dated using U-Pb zircon CA-ID-TIMS geochronology 71
3.10 U-Pb concordia and weighted mean $^{206}Pb/^{238}U$ date diagrams of CA-ID-TIMS data from bentonite L1 73
3.11 Field photograph of bentonite L2 at Lives-sur-Meuse 74

3.12 Sedimentary logs of the sections at Lives-sur-Meuse and Beez Quarry 75
3.13 Optical photomicrograph of zircon grains from bentonite L2 76
3.14 U-Pb concordia and weighted mean $^{206}Pb/^{238}U$ date diagrams of CA-ID-TIMS data from bentonite L2 77
3.15 Field photograph of bentonite L3 at Lives-sur-Meuse 78
3.16 U-Pb concordia and weighted mean $^{206}Pb/^{238}U$ date diagrams of CA-ID-TIMS data from bentonite L3 79
3.17 Sedimentary log of the Anhée Nord section 80
3.18 U-Pb concordia and weighted mean $^{206}Pb/^{238}U$ date diagrams of CA-ID-TIMS data from bentonite W1 81
3.19 U-Pb concordia and weighted mean $^{206}Pb/^{238}U$ date diagrams of CA-ID-TIMS data from bentonite W8 84
3.20 Field photograph of the Anhée Sud section 85
3.21 U-Pb concordia diagram of CA-ID-TIMS data from bentonite W12 87
3.22 U-Pb concordia and weighted mean $^{206}Pb/^{238}U$ date diagrams of CA-ID-TIMS data from bentonite W13 89
3.23 Mechanisms for driving sea-level change 93
3.24 Photographs of Belgian Livian bioclastic limestones 96
3.25 Field photograph of a palaoeosol horizon within the Corphalie Member 97
3.26 Stratigraphic positions of the bentonites used in the periodicity calculations 98
3.27 Composite record of Warnantian sedimentary cycles 101
3.28 Summary diagram of the periodicity calculations for the Belgian Visean sedimentary cycles 105
3.29 Stratigraphic column showing published Visean isotopic age data 107
3.30 U-Pb concordia diagram of data from sample L168 (Trapp, 2001) 109
3.31 U-Pb concordia diagrams of data from sample Bu 171 (Trapp, 2001) 111
3.32 Recent published timescales for the Visean Stage 114

4.1 Stratigraphic column of the samples discussed in chapter 4 119
4.2 Field photograph of the Ballyadams Quarry section 121
4.3 SEM-CL images of zircon grains from sample MAP 11/07/01 122

4.4 U-Pb concordia diagrams of LA-MC-ICP-MS data from samples MAP 11/07/01 and MAP 11/07/03 123
4.5 Field photograph of Altscraghy section, Cuilcagh Mountain 126
4.6 Optical photomicrographs of zircon grains from samples MAP 09/07/01 and MAP 09/07/05 127
4.7 SEM-CL images of grains from sample MAP 09/07/01 128
4.8 U-Pb concordia diagram of LA-MC-ICP-MS data from sample MAP 09/07/01 129

5.1 Stratigraphic column of the samples discussed in chapter 5 133
5.2 Map of the Pennine Basin 134
5.3 Field photographs of two Namurian bentonites 136
5.4 SEM-CL images of grains from bentonite B1 137
5.5 SEM-CL images of euhedral grains from bentonite B1 138
5.6 U-Pb concordia diagram of LA-MC-ICP-MS data from bentonite B1 139
5.7 U-Pb concordia diagram of LA-MC-ICP-MS data from bentonite B7 140
5.8 U-Pb concordia diagram of LA-MC-ICP-MS data from bentonite B9 141
5.9 U-Pb concordia diagram of CA-ID-TIMS data from bentonite B1 143
5.10 U-Pb concordia and weighted mean $^{206}Pb/^{238}U$ date diagrams of CA-ID-TIMS data from bentonite B9 145
5.11 U-Pb concordia diagram of LA-MC-ICP-MS and CA-ID-TIMS data from bentonite B9 146
5.12 U-Pb concordia diagram of CA-ID-TIMS data from bentonites B6 (redrawn from Waters & Condon, 2012) and B9 147
5.13 U-Pb concordia and weighted mean $^{206}Pb/^{238}U$ date diagrams of CA-ID-TIMS data from tonstein T75 151
5.14 U-Pb concordia and weighted mean $^{206}Pb/^{238}U$ date diagrams of CA-ID-TIMS data from tonstein Z1 153
5.15 Comparative diagram of the available isotopic age data from tonstein Z1 153
5.16 U-Pb concordia diagram of CA-ID-TIMS data from the Sub-High Main tonstein (redrawn from Waters & Condon, 2012) and tonstein Z1 155
5.17 U-Pb concordia diagram of CA-ID-TIMS data from tonstein T1P 157
5.18 U-Pb concordia diagram of CA-ID-TIMS data from tonstein T1Gb 159
5.19 Idealised faunal sequence in the Namurian sedimentary cycles 161

5.20 Namurian marine bands of the Pennine Basin 165
5.21 Westphalian faunal bands of the Pennine and Ruhr basins 166
5.22 Recent published timescales for the Namurian and Westphalian stages 172
5.23 Comparative diagram of isotopic age data from several Arnsbergian bentonites and tonsteins 174
5.24 Stratigraphic column showing different positions of the base of the Moscovian Stage within the western European stratigraphic framework 179

6.1 Stratigraphic distribution of the samples collected for MS analysis 183
6.2 Map of the Namur-Dinant Basin showing localities discussed in chapter 6 184
6.3 Cross plot of $\delta^{13}C$ and $\delta^{18}O$ data from Belgian Visean limestone samples 186
6.4 MS and stable isotope ($\delta^{13}C$ and $\delta^{18}O$) data from the Haut-le-Wastia Member at Lives-sur-Meuse 189
6.5 MS and stable isotope ($\delta^{13}C$ and $\delta^{18}O$) data from the Corphalie Member at Lives-sur-Meuse 192
6.6 MS and stable isotope ($\delta^{13}C$ and $\delta^{18}O$) data from the upper Corphalie Member and lower Awirs Member at Lives-sur-Meuse 194
6.7 MS and stable isotope ($\delta^{13}C$ and $\delta^{18}O$) data from the Awirs Member at Awirs West Quarry 197
6.8 MS data from the Seilles Member at Awirs West Quarry 198
6.9 MS and stable isotope ($\delta^{13}C$ and $\delta^{18}O$) data from the Anhée Nord section 200
6.10 MS data from the Anhée Sud section 202
6.11 Comparison of MS and stable isotope data from the Corphalie and Awirs members at Lives-sur-Meuse and Awirs West Quarry 204

7.1 Stratigraphic column of the samples discussed in chapter 7 212
7.2 Map of the Namur-Dinant Basin showing sampling localities 213
7.3 Major and trace element data from the Belgian Visean bentonites 216
7.4 Cross plots of major and trace element data from three Belgian bentonites (L4, L5 and W8) 220
7.5 X-ray diffraction data from bentonites L4 and L5 221
7.6 Major and trace element data from the Irish Asbian samples 223
7.7 Major and trace element data from the Irish Brigantian samples 224
7.8 Major and trace element data from the Namurian bentonite samples 225

7.9 Major and trace element data from the Westphalian tonstein samples 226
7.10 Zr / TiO_2 versus Nb / Y discrimination diagram (after Winchester & Floyd, 1977) 229
7.11 Ti / Th x 10 – Ce x 10 / Y – Zr / Nb ternary diagram (after Batchelor & Jeppsson, 1999) 230
7.12 CI-chondrite normalised REE sample data 233
7.13 Shale-normalised REE sample data 238
7.14 Sample europium anomalies 241

8.1 Stratigraphic column summarising the U-Pb zircon CA-ID-TIMS data acquired during this project 248
8.2 Summary diagram of the average periodicity estimates for western European Carboniferous sedimentary cycles 249

List of Tables

2.1 Composition of the Earthtime ^{202}Pb-^{205}Pb-^{233}U-^{235}U (ET2535) isotopic tracer used in this study 35

2.2 Magnitude of the increase in $^{206}Pb/^{238}U$ dates arising from the correction for initial ^{230}Th disequilibrium, assuming $(Th/U)_{magma}$ values of 3 to 5 36

2.3 Characteristic XRD peaks of some commonly occurring minerals in the samples investigated 50

2.4 Details of the limestone and shale (control) samples analysed for their whole-rock geochemistry 51

3.1 A summary of the new U-Pb zircon CA-ID-TIMS dates from the Tournaisian and Visean bentonites 90

3.2 Average cycle periodicity estimates for the Belgian Livian sedimentary cycles between bentonites L1 and W1 99

3.3 Average cycle periodicity estimates for the Lower Warnantian sedimentary cycles between bentonites W1 and W8 103

3.4 Average cycle periodicity estimates for the Lower Warnantian sedimentary cycles between bentonites W8 and W13 104

5.1 Sampling localities of the Namurian bentonites 136

5.2 Summary of the new U-Pb zircon CA-ID-TIMS dates from the Namurian bentonites and Westphalian tonsteins 159

5.3 Published periodicity estimates for Namurian and Westphalian sedimentary cycles 161

5.4 Average periodicity estimates for the sedimentary cycles between bentonite B9 and tonstein T75 164

5.5 Average periodicity estimates for the sedimentary cycles between tonsteins T75 and Z1 168

5.6 Average periodicity estimate for the sedimentary cycles between the base of the Namurian and bentonite B9 171

6.1 Summary statistics for the magnetic susceptibility and stable isotope ($\delta^{13}C$ and $\delta^{18}O$) data from Belgian Visean sedimentary cycles 185

7.1 Sampling localities of the Belgian Moliniacian and Livian bentonites 211

7.2 Sampling localities of the Westphalian tonsteins 214

Abbreviations and Symbols

A	Ampere (SI unit of electrical current)
a.m.u.	Atomic mass unit
CA-ID-TIMS	Chemical abrasion isotope dilution thermal ionization mass spectrometry
Cf	Carboniferous foraminifera zone / subzone (after Conil *et al.*, 1990). Zones are denoted by numbers (c.g. Cf6) and subzones are indicated by greek letters (e.g. Cf6α).
CF-IRMS	Continuous flow isotope ratio mass spectrometer
CSA	Condroz sedimentation area (of the Namur-Dinant Basin)
DSA	Dinant sedimentation area (of the Namur-Dinant Basin)
ID-TIMS	Isotope dilution thermal ionization mass spectrometry
ET2535	The Earthtime ^{202}Pb-^{205}Pb-^{233}U-^{235}Pb isotopic tracer solution
ET535	The Earthtime ^{205}Pb-^{233}U-^{235}Pb isotopic tracer solution
HREE	Heavy rare-earth elements (gadolinium to lutetium)
kyrs	1,000 years
LA-ICP-MS	Laser ablation inductively coupled plasma mass spectrometry
LA-MC-ICP-MS	Laser ablation multi-collector inductively coupled plasma mass spectrometry
LREE	Light rare-earth elements (lanthanum to europium)
ICCD	International Centre for Diffraction Data
ICP-OES	Inductively coupled plasma optical emission spectrometry
ICP-MS	Inductively coupled plasma mass spectrometry
M	Molar concentration (moles of solute / litres of solution)
Ma	1,000,000 years ago
MC-ICP-MS	Multi-collector inductively coupled plasma mass spectrometer
MFZ	Mississippian foraminifera zone (after Poty *et al.*, 2006)
MS	Magnetic susceptibility
MSWD	Mean square of weighted deviation
Myrs	1,000,000 years
$_N$	Denotes sample rare earth element concentrations that have been normalised to the CI-chondrite values of McDonough & Sun (1995)

NSA	Namur sedimentation area (of the Namur-Dinant Basin)
NIGL	National Environment Research Council (NERC) Isotope Geosciences Laboratory
P	Probability-of-fit
Pb	Lead
Pbc	Common (non-radiogenic) lead
Pb*	Radiogenic lead
REE	Rare-earth elements
SEM-CL	Scanning electron microscopy with cathodoluminescence imaging
SEM-EDS	Scanning electron microscope - energy dispersive X-ray spectroscopy
SHRIMP	Sensitive High Resolution Ion Microprobe
SI	Système International d'Unités (International System of Units)
Th	Thorium
$(Th/U)_{magma}$	Thorium / uranium ratio in the melt (magma)
$(Th/U)_{zircon}$	Thorium / uranium ratio of a sample zircon grain
U	Uranium
XRD	X-ray diffraction
V	Volt (SI unit of electrical potential)
V-PDB	Vienna Pee Dee Belemnite
WGS 84	World Geodetic System 84 datum (all latitude / longitude references given in this thesis are relative to this datum).

Å	Angstrom
σ	Sigma (confidence level)
θ	Angle of diffraction (degrees)
ρ	Density (g / cm^3)
Ω	Ohm (SI unit of electrical resistance)
ΣREE	Total concentration of rare earth elements (ppm)

Chapter 1

Introduction

1.1. Background: Carboniferous climate

The Carboniferous Period was a time of substantial climatic change, during which occurred the transition from a greenhouse (ice-free) environment into major continental glaciation. The onset of major Carboniferous glaciation is reconstructed using two main stratigraphic records: the direct records of glacial sedimentary rocks preserved on the remnants of Gondwana (Fig. 1.1; i.e. South America, Africa, Australia, Antarctica) and far-field (palaeo-equatorial), ice-distal proxy records from the margins of Laurussia (which includes western Europe; Fig. 1.1).

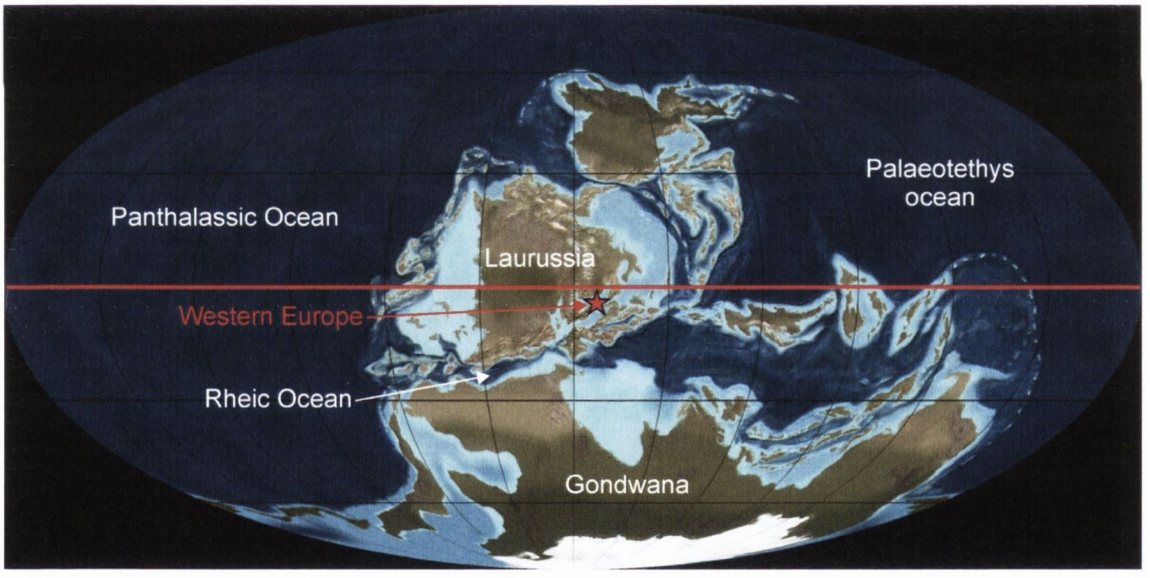

Figure 1.1. A global reconstruction of Mississippian palaeogeography (courtesy of Ron Blakey, Northern Arizona University). The red horizontal line denotes the palaeo-equator.

Neither the direct (austral) nor the far-field (palaeo-equatorial) sequences provide a perfect record of the onset of glaciation. The Gondwanan records of glacial sedimentary rocks preserve unambiguous evidence for glaciation, yet these strata are notoriously difficult to date and to correlate. This is because absolute age constraints from the glacial sequences are sparse and biostratigraphic correlations to palaeo-equatorial

latitudes (which have better temporal calibration) are not well constrained (Veevers & Powell, 1987; Frank *et al.*, 2008). Additionally, it is possible that early glacial deposits may have been reworked by subsequent glacial advance(s) (e.g. Veevers & Powell, 1987; Bishop *et al.*, 2009) and thus the direct glacial records may not preserve a complete record of the onset of glaciation. In contrast, the indirect palaeo-equatorial records are considered to be more continuous and to preserve an 'average' signal of the various glacial centres that were in existence on Gondwana (Bishop *et al.*, 2009). However, the expression of glaciation within the proxy records is complex and relies on identifying the indirect consequences of glaciation such as changes in ocean chemistry (e.g. oxygen isotopic excursions in marine carbonates as ^{16}O is sequestered preferentially into glacial ice) or the expression of high-frequency sea-level oscillations that arises from the periodic waxing and waning of ice sheets (glacio-eustatic cyclic sedimentation). The recognition of a glacial signature within the far-field proxy records is further complicated by local factors such as tectonism (which can obscure eustatic sea-level changes) and diagenesis (which can alter the isotopic composition of marine carbonates).

The current consensus derived from the direct glacial records on Gondwana is that widespread glacial deposits appear close to the base of the Namurian (early Serpukhovian; Fig. 1.2). There are instances of older Carboniferous glacial deposits (e.g. Glacial 1 of Isbell *et al.*, 2003 in Fig. 1.2), although these have generally been attributed to minor 'alpine' glacial centres (e.g. Isbell *et al.*, 2003). Within the far-field proxy records there is disagreement as to the precise timing of the onset of major Carboniferous glaciation (Fig. 1.2). However, these records are generally in agreement that the onset of major glaciation was somewhat earlier (late Visean) than is inferred from the direct glacial records (Fig. 1.2). The conflicts between the direct and indirect records and the internal disagreements within the far-field proxy records limit our understanding of when Carboniferous glaciation commenced. This project seeks to resolve some of the controversy surrounding the onset of this glaciation event by using high-precision geochronology to constrain both the onset of glaciation within the ice-distal proxy records of western Europe and the duration of Carboniferous glacial-interglacial cycles.

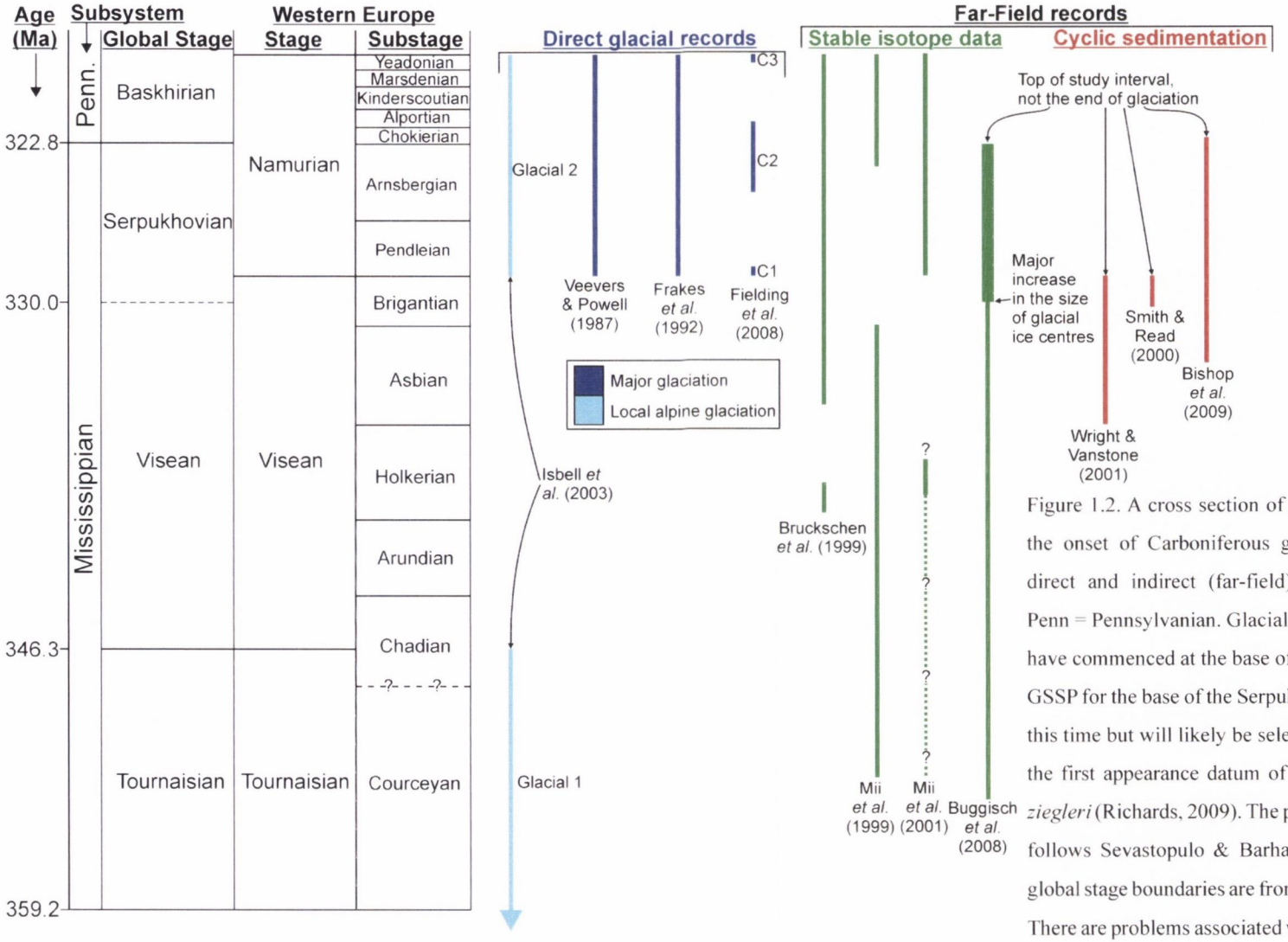

Figure 1.2. A cross section of published estimates for the onset of Carboniferous glaciation derived from direct and indirect (far-field) stratigraphic records. Penn = Pennsylvanian. Glacial episodes are inferred to have commenced at the base of the coloured lines. The GSSP for the base of the Serpukhovian is not ratified at this time but will likely be selected to correspond with the first appearance datum of the conodont *Lochriea ziegleri* (Richards, 2009). The position of this boundary follows Sevastopulo & Barham (2011). The ages of global stage boundaries are from Davydov *et al.* (2010). There are problems associated with the definition of the base of the Chadian (see Waters *et al.*, 2011).

1.2. Project approach and aims

The project uses three main analytical approaches, which are as follows:

1. High-precision U-Pb zircon geochronology to constrain the ages of several diagenetically altered ash layers that occur interbedded with western European Carboniferous sedimentary strata.
2. Whole-rock analysis of several (n = 52) diagenetically altered ash layers using ICP-OES/MS analysis to characterise sample elemental concentrations and XRD analysis to characterise sample mineralogies.
3. Stable isotope ($\delta^{13}C$ and $\delta^{18}O$) and magnetic susceptibility analyses of Belgian Livian and Warnantian (equivalent to Holkerian and Asbian; Fig. 1.2) carbonate shallowing-upwards cycles to determine if these cycles preserve evidence of glacio-eustasy.

The high-precision dates from several western European diagenetically altered ash layers serve three main purposes. Firstly, they provide a high-precision temporal framework for constraining the timing of the onset of glaciation. Secondly, they provide a basis for estimating the periodicity of western European sedimentary cycles. These cycles have been suggested to be of glacio-eustatic origin and their appearance within the stratigraphic record has been inferred to signal the onset of major glaciation (e.g. Wright & Vanstone, 2001). One of the arguments supporting the glacio-eustatic interpretation is that the cycles have periodicities that are compatible with Milankovitch cycles (explained in section 1.3), which have been shown to modulate recent Pleistocene glacial ice centres (e.g. Hays *et al.*, 1976). However, most of the existing periodicity estimates have relied upon published Carboniferous timescales for absolute age controls, and these timescales are not well calibrated (see section 1.4). The uncertainties in the timescale calibrations propagate through into the periodicity calculations, preventing a robust comparison of estimated cycle periodicities with contemporary Milankovitch cycles. By using high-precision U-Pb zircon CA-ID-TIMS geochronology to date several western European diagenetically altered volcanic ash layers that are interbedded within these sedimentary cycles, it is possible to generate periodicity estimates at an unprecedented level of precision. This enables a more robust comparison between the periodicities of sedimentary cycles and contemporary

Milankovitch cycles, and hence a better evaluation of the glacio-eustatic hypothesis. Lastly, the ash horizons dated in this study are biostratigraphically well constrained and provide additional age constraints for improved calibration of the Carboniferous timescale.

Whole-rock geochemical analyses were conducted on several western European Carboniferous diagenetically altered ash layer samples (n = 52), including all but one of the horizons that were dated using the U-Pb zircon CA-ID-TIMS method (the geochemistry of bentonite 300 was not determined because of insufficient sample material). These analyses were undertaken to elucidate the composition of the magma from which the altered volcanic ash layers were erupted. Such information can clarify why some bentonites contain abundant zircon (e.g. ashes that were derived from evolved, felsic magmas), whereas other horizons contain little or no zircon (e.g. ash layers that were sourced from silica-undersaturated magmas). Furthermore, by comparing the inferred magmatic compositions of the diagenetically altered ash layers to known coeval magmatic centres, it is possible to identify potential source magmatic centres. The XRD analyses were undertaken to provide constraints on the mineralogy of the ash layers. These analyses provide complementary data to that obtained from the whole-rock geochemical analyses; it is possible in several instances to link chemical variations between the studied samples (identified from the whole rock geochemical analyses) to differences in sample mineralogy (identified in the XRD data; e.g. see section 7.3).

The stable isotope ($\delta^{13}C$ and $\delta^{18}O$) and magnetic susceptibility analyses were undertaken on Belgian Livian and Warnantian (equivalent to Holkerian and Asbian; Fig. 1.2) carbonate shallowing-upwards carbonate cycles to determine if they preserve proxy evidence (in addition to cycle periodicities) that may support a glacio-eustatic origin. If the Belgian Livian cycles did yield such evidence, it would support a significantly earlier onset of glaciation than is currently suggested by the appearance of cyclic sedimentation within the British and Irish stratigraphic records (see Wright & Vanstone, 2001, in Fig. 1.2). Strontium isotope analyses, which can provide insights into continental weathering rates and the processes which control such rates (e.g. climate; Bruckschen *et al.*, 1995), were not undertaken. This is because the studied sedimentary cycles are of much shorter duration (< 500 kyrs / cycle; section 3.4.1.2.3)

than the residence time of strontium in the oceans (*c.* 2.7 Myrs; Richter & Turekian, 1993). Hence, any such variation in the strontium isotopic signature over the timescale of individual sedimentary cycles would have to be very large in order to be resolvable within the seawater strontium isotopic record. Short-term oscillations in strontium isotopic ratios of comparable duration to present glacial-interglacial cycles have been reported from recent geological records (e.g. Capo & DePaolo, 1990; Dia *et al.*, 1992). However, these variations have been argued to arise from local processes (Richter & Turekian, 1993) or to be the result of analytical artefacts (Henderson *et al.*, 1994) rather than global climatic processes. Thus, strontium isotopes may be of limited use in reconstructing the global environmental processes that operated during the deposition of the studied high-frequency sedimentary cycles.

The remainder of this chapter is structured so that a brief explanation of Milankovitch cycles is given in section 1.3. This is followed by an overview of the current state of the Carboniferous Timescale (section 1.4) and an introduction to the altered ash layer samples investigated in this project (section 1.5). The chapter concludes with an outline of the structure of this thesis (section 1.6).

1.3. Milankovitch cycles

Milankovitch cycles (named after the Serbian civil engineer and mathematician, Milutin Milanković) are quasi-periodic cycles in the Earth's orbit and tilt that drive seasonal and latitudinal variations in the amount of solar radiation received by the Earth (Hays *et al.*, 1976; Hinnov & Ogg, 2007). There are three main Milankovitch cycles, termed precession, obliquity and eccentricity. The precession cycle is caused by a gyroscopic wobble of the Earth's axis, which is often likened to the motion of a spinning top. In mathematical solutions of Milankovitch cycles, the precession cycle has four main periodicities, at 18.9 kyrs, 19.1 kyrs, 22.4 kyrs and 23.7 kyrs (Crucifix *et al.*, 2006). However, only two are resolved in the recent marine palaeoclimate record (19 kyrs and 23 kyrs; Hays *et al.*, 1976). The obliquity cycle arises from variations in the tilt angle of the Earth's axis (relative to the Earth's orbital plane), which varies between 22° and 25° with a periodicity of *c.* 41 kyrs (Crucifix *et al.*, 2006). The eccentricity cycle arises from cyclic variations in the shape of the Earth's orbit around the sun (from circular to mildly elliptical). The main eccentricity periodicities (in order of decreasing amplitude) are

c. 404 kyrs, 95 kyrs, 124 kyrs, 99 kyrs and 131 kyrs (Berger *et al.*, 1992; Schwarzacher, 1993; Crucifix *et al.*, 2006). The multiple periodicities within the 95 –131 kyrs band are not resolved within the recent (last 1 Myrs) palaeoclimatic record, which shows a single, strong peak at *c.* 100 kyrs (Hays *et al.*, 1976) that is often referred to as the '100 kyrs' eccentricity cycle. The *c.* 100 kyrs and *c.* 404 kyrs cycles are informally known as the 'short' and 'long' eccentricity cycles respectively.

The periodicities of precession and obliquity cycles vary through time (Berger *et al.*, 1992) and thus the present-day periodicities of these cycles are not necessarily representative of the same cycles during Carboniferous times. Mathematical solutions for the periodicities of Milankovitch cycles over geologic time have been computed (e.g. Berger *et al.*, 1992), although subsequent research by Laskar (1999) has cast doubt over the validity of extending the calculations back into the Palaeozoic. In contrast to the precession and obliquity cycles, the eccentricity cycles are thought to be relatively stable over geological timescales (Berger *et al.*, 1992; Laskar, 1999).

1.4. The Carboniferous Timescale

Until recently, Carboniferous timescales (e.g. Menning *et al.*, 2000; Dayvdov *et al.*, 2004) have primarily been constructed by fitting isotopic age data to composite standard (relative) stratigraphic scales (e.g. Fig. 1.3). This approach is necessary because the isotopic age data are usually derived from horizons that do not correspond exactly with stratigraphic boundaries and thus interpolation between the age data control points is required to derive the timings of stratigraphic boundaries. The construction of relative composite scales often requires assumptions (e.g. that stratigraphic thickness is linearly proportional to time duration or uniform rates of biological evolution) that impart uncertainties into the final timescale calibrations.

An alternative approach, which circumvents the need for a composite standard section, is astronomical tuning (Hinnov & Ogg, 2007). Where sedimentary strata contain evidence of cyclicity that can be demonstrated to correspond to a known Milankovitch orbital-forcing cycle (section 1.3), it is possible to tune the stratigraphic record to such a beat and interpolate the ages of stratigraphic boundaries against it. Such an approach has been applied to portions of the Carboniferous System (Davydov *et al.*, 2010;

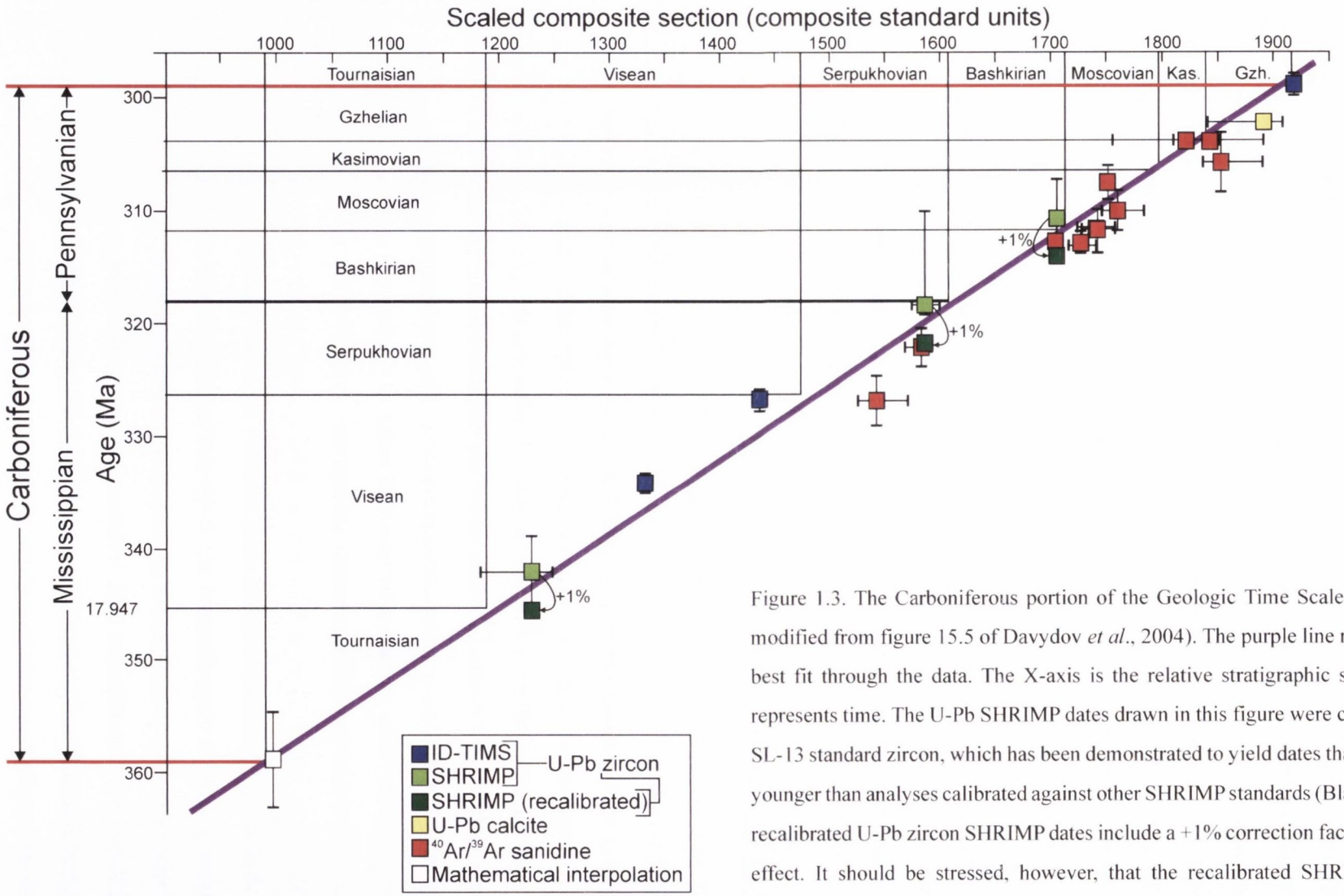

Figure 1.3. The Carboniferous portion of the Geologic Time Scale 2004 (redrawn and modified from figure 15.5 of Davydov *et al.*, 2004). The purple line represents the line of best fit through the data. The X-axis is the relative stratigraphic scale and the Y-axis represents time. The U-Pb SHRIMP dates drawn in this figure were calibrated against the SL-13 standard zircon, which has been demonstrated to yield dates that are on average 1% younger than analyses calibrated against other SHRIMP standards (Black *et al.*, 2003). The recalibrated U-Pb zircon SHRIMP dates include a +1% correction factor to counteract this effect. It should be stressed, however, that the recalibrated SHRIMP dates are only approximations and should not be considered as robust age estimates.

Peterson, 2011). However, this method requires assumptions about the constancy of cycle periodicities and is also dependent on the stratigraphic distribution of cyclic sedimentation.

When this PhD project was initiated in 2007, there was a dearth of Carboniferous high-precision U-Pb zircon dates. The Devonian – Carboniferous and Carboniferous – Permian boundaries were both relatively well constrained by precise U-Pb zircon ID-TIMS age constraints from interbedded altered ash horizons within auxiliary boundary stratotype sections by Trapp *et al.* (2004) and Ramezani *et al.* (2007) (the Hasselbachtal section, Germany and the Usolka section, southern Urals respectively). In contrast, the stratigraphic boundaries within the Carboniferous System were constrained by a less precise dataset: the *c.* 2007 dataset included several U-Pb zircon SHRIMP dates (e.g. Riley *et al.*, 1993; Claoué-Long *et al.*, 1995; Roberts *et al.*, 1995a, b), $^{40}Ar/^{39}Ar$ sanidine dates (e.g. Lippolt *et al.*, 1984; Hess & Lippolt, 1986), U-Pb dates from palaeosol calcite (Rasbury *et al.*, 1998) and only two U-Pb zircon ID-TIMS dates (Trapp, 2001). Several of these data are shown in Fig. 1.3 and most were derived from European diagenetically altered ash layers. It is important to note the heterogeneous distribution of these data, with most dates having been derived from Pennsylvanian altered volcanic ash horizons. These isotopic data typically carry substantial uncertainties (*c.* 0.3 to > 3 %, 2σ; equivalent to ± 0.9 – 10 Myrs for Carboniferous samples) that are much greater than the precision attainable using modern U-Pb zircon CA-ID-TIMS geochronology (< 0.1 %, 2σ uncertainty on a weighted mean $^{206}Pb/^{238}U$ date; e.g. Davydov *et al.*, 2010). Additionally, there are conflicts within the Carboniferous isotopic dataset. These have been discussed by Menning *et al.* (2000; p. 8 – 11) and include, for example, what appears to be a systematic bias between the existing U-Pb SHRIMP age determinations and the $^{40}Ar/^{39}Ar$ sanidine age determinations (this is visible in Fig. 1.3; the U-Pb SHRIMP dates mostly plot above the purple line-of-correlation, whereas the $^{40}Ar/^{39}Ar$ dates mostly plot below this line). Some of the discrepancy between the U-Pb SHRIMP and $^{40}Ar/^{39}Ar$ datasets may arise from standardisation problems with the U-Pb SHRIMP data. All of the U-Pb SHRIMP data drawn in Fig. 1.3 were calibrated against the same standard zircon (SL-13), which has been demonstrated to be heterogeneous on the spatial resolution of SHRIMP analyses and yield U-Pb dates that are on average 1 % younger than analyses calibrated against other SHRIMP standards (Black *et al.*, 2003). Whilst it is unrealistic to apply a

+1 % correction factor to individual SHRIMP data calibrated against the SL-13 zircon (because the SL-13 standard behaves heterogeneously), a correction of this magnitude would substantially reduce the visual offset between the U-Pb SHRIMP and $^{40}Ar/^{39}Ar$ datasets (as illustrated in Fig. 1.3).

Since 2007, there have been three notable publications that have provided further Carboniferous high-precision U-Pb zircon CA-ID-TIMS dates (Gastaldo *et al.*, 2009, Davydov *et al.*, 2010, Waters & Condon, 2012; totalling 16 additional isotopic dates). However, whilst these dates represent a step towards addressing the deficit of high-precision Carboniferous isotopic age data and facilitate improved calibration of the timescale, considerable work remains to be done. For example, there are still a number of stratigraphic substage boundaries that are not constrained by precise isotopic dates (Fig. 1.4) and are instead only constrained through considerable interpolation. Further isotopic dates from different palaeogeographic provinces (e.g. North America, Europe, Russia) would also improve correlations between these realms, supplementing existing biostratigraphic correlations. Thus, there is a clear need for more Carboniferous high-precision isotopic dates, particularly from horizons within the Mississippian Subsystem. In western and central Europe, there is considerable opportunity to acquire such isotopic dates.

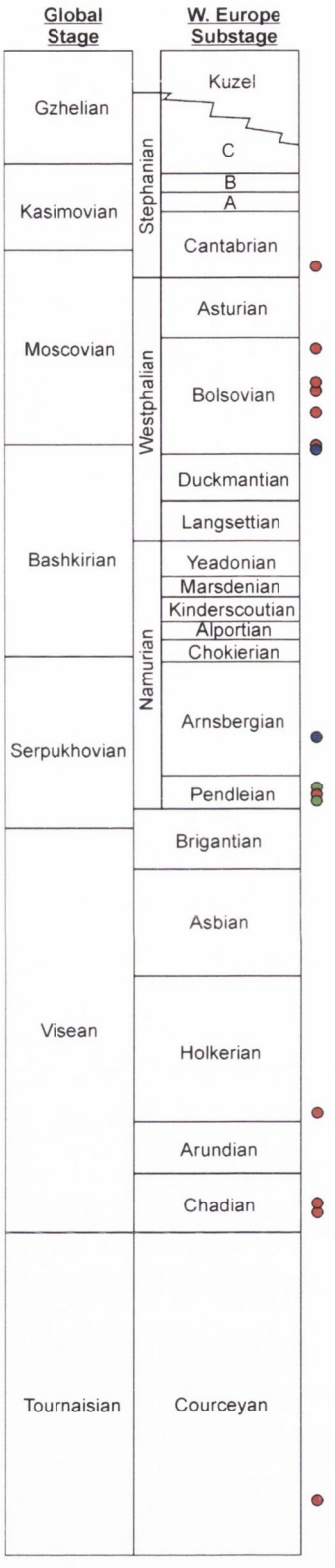

Figure 1.4. The stratigraphic distribution of recent isotopic dates from Davydov *et al.* (2010; red circles), Gastaldo *et al.* (2009; green circles) and Waters & Condon (2012; blue circles). The figure is redrawn from fig. 2 of Davydov *et al.* (2010).

1.5. Sample materials: western European diagenetically altered volcanic ash layers

Numerous diagenetically altered volcanic ash layers are interbedded with western European sedimentary strata. There are too many volcanic horizons to date within the time constraints of a single PhD project and therefore diagenetically altered volcanic ash layers were studied from four main geographical areas:

1. Visean bentonites (see section 1.5.1 for a definition of the term 'bentonite') from the Namur-Dinant Basin, Belgium (Fig. 1.5).

2. Irish Asbian and Brigantian clay-rich layers from the Carlow area and Cuilcagh Mountain respectively (Fig. 1.5), and an upper Tournaisian bentonite horizon that was sampled from a drillcore taken near to Claremorris, County Mayo (Fig. 1.5).

3. Namurian bentonites from the Pennine Basin, northern England (Fig. 1.5).

4. Westphalian tonstein horizons (see section 1.5.1 for a definition of the term 'tonstein') from the Campine Basin, Belgium, and the Ruhr Basin, Germany (Fig. 1.5).

The studied diagenetically altered volcanic horizons span the stratigraphic interval from the uppermost Tournaisian to Bolsovian (Fig. 1.6). These horizons typically comprise predominantly clay minerals but often also contain a small residual fraction of volcanic phenocrysts that can include euhedral zircon as well as apatite, sanidine and biotite, which are amenable to isotopic dating using the U-Pb (apatite, zircon) and K-Ar systems (biotite, sanidine).

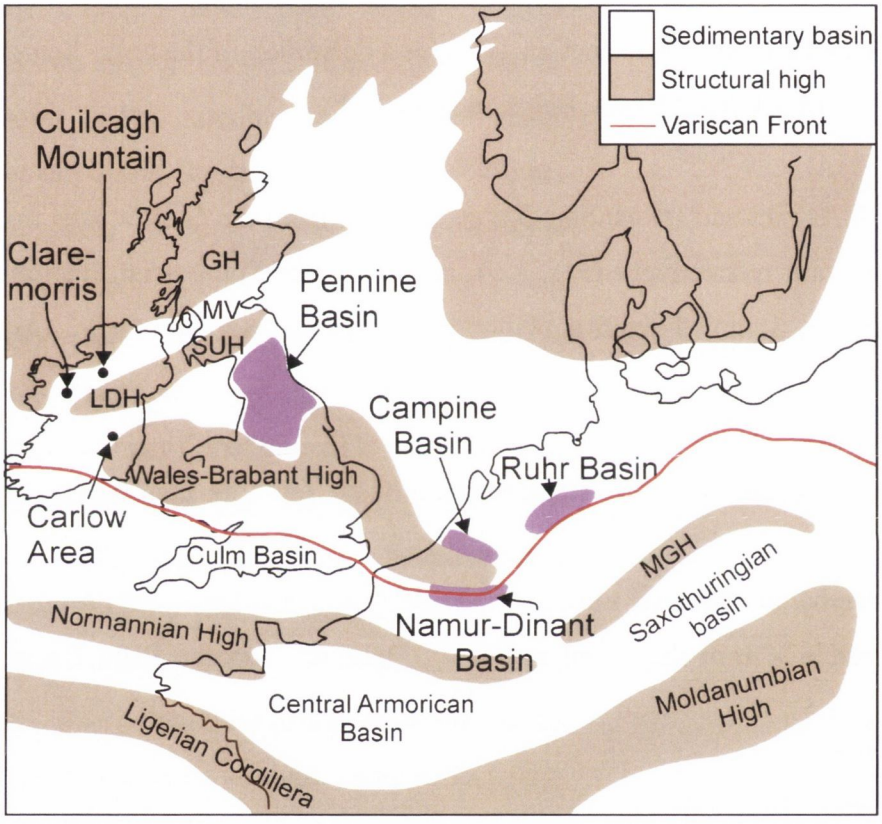

Figure 1.5. Simplified structural map of Europe. The locations of the sampled sedimentary basins are shown in purple. The figure is redrawn and simplified from Ziegler (1990). GH = Grampian Highlands; LDH = Longford-Down High; MGH = Mid-German High; MV = Midland Valley; SUH = Southern Uplands High.

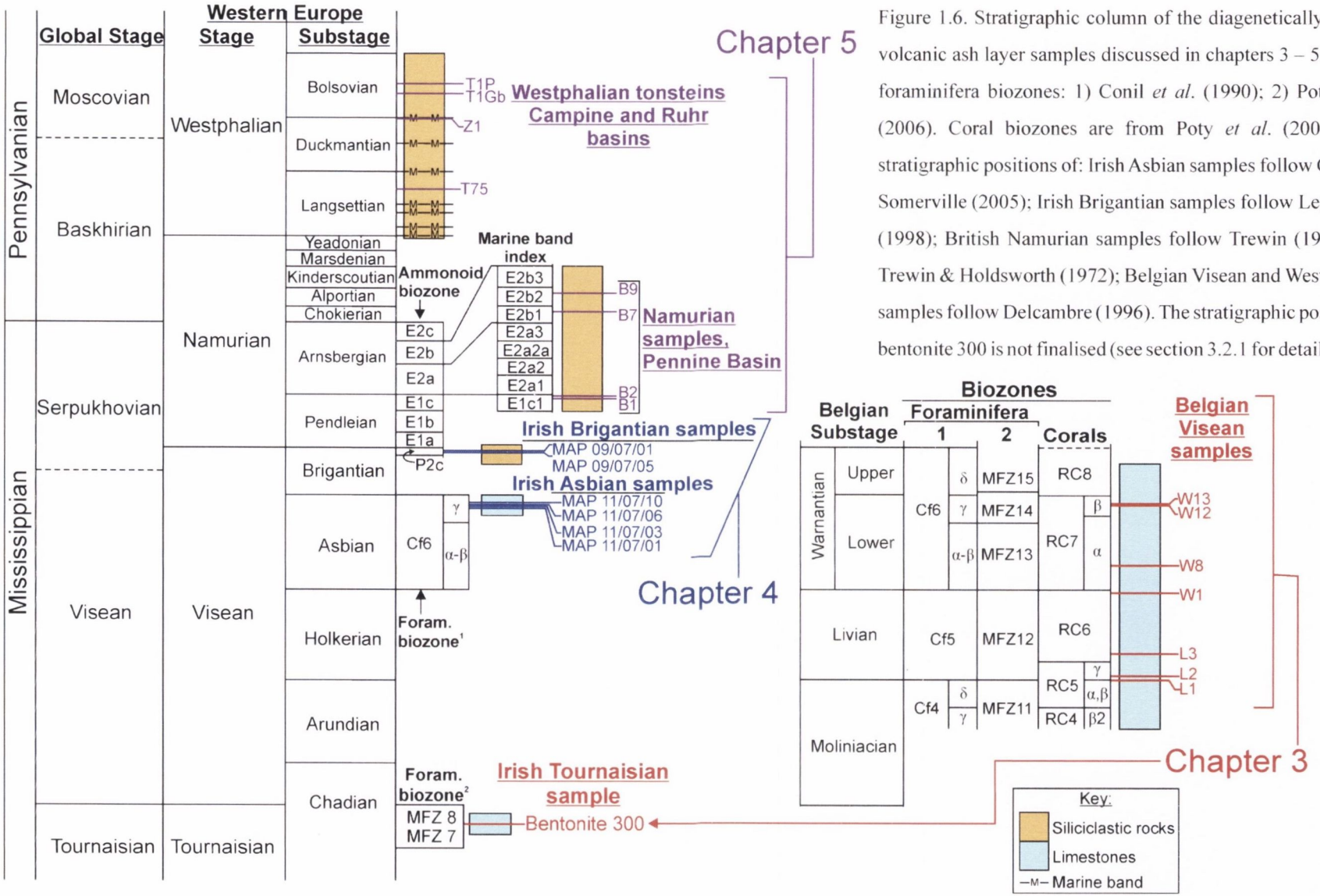

Figure 1.6. Stratigraphic column of the diagenetically altered volcanic ash layer samples discussed in chapters 3 – 5. Visean foraminifera biozones: 1) Conil *et al.* (1990); 2) Poty *et al.* (2006). Coral biozones are from Poty *et al.* (2006). The stratigraphic positions of: Irish Asbian samples follow Cózar & Somerville (2005); Irish Brigantian samples follow Legg *et al.* (1998); British Namurian samples follow Trewin (1968) and Trewin & Holdsworth (1972); Belgian Visean and Westphalian samples follow Delcambre (1996). The stratigraphic position of bentonite 300 is not finalised (see section 3.2.1 for details).

1.5.1. Altered ash layer nomenclature

Diagenetically altered volcanic ash layers have been described using several terms (e.g. ash, tuff, bentonite, K-bentonite, clay wayboard, tonstein). A brief review of these terms is given here, followed by the definitions of the terms used in this thesis.

The term 'ash' was used by Roen & Hosterman (1982) to describe a succession of Devonian clay-rich horizons of probable volcanic origin. Prior to the study of Roen & Hosterman (1982), these horizons had been described as K-bentonites. However, Roen & Hosterman (1982) argued that the horizons were mineralogically and physically distinct from industrial bentonite clays and thus merited a distinct name. The term 'ash' was accordingly selected to stress the inferred origin of these horizons (Roen & Hosterman, 1982). Huff (1983) subsequently suggested that the term 'ash' was inappropriate because the horizons had undergone substantial alteration and no longer retained the texture or mineralogy of unaltered ash layers. The same argument can be extended to the usage of the term 'tuff' (meaning a pyroclastic rock of > 75 % ash content; Le Maitre *et al.*, 2002).

The term bentonite is common within the literature (e.g. Huff, 1983; Spears *et al.*, 1999), although its meaning varies between studies. Spears *et al.* (1999) used the term in a general sense to describe a layer of volcanic ash that had since altered to clay, whereas Bohor & Triplehorn (1993) restricted the term 'bentonite' to mean clay-rich horizons of probable volcanic origin that were altered within a marine environment. Weaver (1953) used the term K-bentonite for some Ordovician clay-rich horizons (of volcanic origin) to emphasise their high potassium concentrations relative to Ca and Na montmorillonite bentonites. The potassium enrichment is thought to arise from the illitization of smectite clays during diagenesis and K-bentonites are frequently characterised by an abundance of mixed-layer illite / smectite clays (Huff, 1983).

The term 'tonstein' is of German origin and literally translated means 'clay stone' (Bohor & Triplehorn, 1993). The modern definition of tonstein carries genetic connotations, i.e. that the horizon is an altered volcanic ash horizon (Bohor & Triplehorn, 1993). Tonsteins occur predominantly in non-marine, coal-bearing sequences and are usually dominated by kaolinite clays (Bohor & Triplehorn, 1993),

which is thought to be a reflection of the acidic conditions of the coal-swamp environments wherein most of these altered ash layers were originally laid down (Bohor & Triplehorn, 1993; Spears, 2006). Some authors classify tonsteins as any altered ash layer within a non-marine sequence (Bohor & Triplehorn, 1993), whereas other authors prefer a definition based on an arbitrary percentage content of kaolinite; for example Lyons *et al.* (1994) used > 50 % kaolinite (by weight) as the threshold for describing a sample as a tonstein.

Less commonly encountered terms include cinerite and clay wayboard. The term cinerite has been used predominantly by Belgian researchers and means a horizon of volcanic origin (Bohor & Triplehorn, 1993). However, the term carries no information about the state of alteration, the clay mineralogy or the depositional environment (Bohor & Triplehorn, 1993). Clay wayboard is an old quarrying and mining term that was used by Walkden (1972) to describe several clay-rich horizons interbedded with upper Visean (Asbian – Brigantian) shelf limestones of the Derbyshire High (Fig. 5.1). The clay wayboards comprise predominantly mixed-layer illite / smectite, kaolinite and rarely chlorite, together with minor amounts of anatase, pyrite and quartz (Walkden, 1972). Walkden (1972) noted that the clay mineralogy of the wayboards is typical of K-bentonites and is similar to some altered pyroclastic rocks and basalts exposed in the surrounding areas of Derbyshire, leading Walkden (1972) to conclude that the wayboards represent altered volcanic ash horizons. The source of the wayboards has not been identified; however, it is probable that they originated from local basaltic volcanic activity (Spears, 2006).

In this thesis, the terms bentonite and tonstein are used to describe the studied samples. The term bentonite is used in the sense of Spears *et al.* (1999), i.e. a horizon of probable volcanic origin that has since been altered to a clay-rich layer. The term tonstein is retained to describe the Westphalian samples; its definition follows that of Bohor & Triplehorn (1993). As the Westphalian horizons have been traditionally termed tonsteins, there seems little need to change this practice.

1.6. Structure of this thesis

In Chapter 2, the techniques used during this PhD project are documented and detailed methodologies provided. In Chapter 3, new U-Pb zircon CA-ID-TIMS constraints from Tournaisian and Visean western European diagenetically altered volcanic ash layers (Fig. 1.6) are presented. These dates are used to estimate the periodicities of Belgian mid-to-upper Visean sedimentary cycles. Additionally, comparisons are made between the new isotopic dates and existing (published) isotopic age data. The implications that the new U-Pb dates have for calibration of the Mississippian timescale are also discussed. In Chapter 4, SEM-CL images and U-Pb zircon LA-ICP-MS data from several Irish Asbian and Brigantian samples (Fig. 1.6) are presented and discussed. In Chapter 5, U-Pb zircon LA-MC-ICP-MS and CA-ID-TIMS data from several Namurian bentonite and Westphalian tonstein samples (Fig. 1.6) are presented. The implications that these data have for the periodicity of western European Namurian and Westphalian cyclic sedimentation and the calibration of the Carboniferous timescale are also discussed. Stable isotope ($\delta^{13}C$ and $\delta^{18}O$) analyses and magnetic susceptibility analyses from Belgian mid-to-upper Visean carbonate shallowing-upwards cycles, which were undertaken to elucidate the origins of these carbonate cycles, are documented in Chapter 6. In Chapter 7, whole-rock geochemical data from several western European diagenetically altered volcanic ash horizons are presented and are used to infer the original magmatic source compositions of the studied altered volcanic horizons. Finally, conclusions to this thesis are presented in Chapter 8. The subsequent chapters were written to stand alone and thus there may be some slight repetition encountered.

Chapter 2

Methodology

2.1. Introduction

During this project several different analytical techniques were employed. An overview of each technique is given and is followed by a detailed methodology. The following techniques are discussed in subsequent sections:

2.2. Procedures for separating and concentrating zircon grains from the diagenetically altered ash layer samples.

2.3. U-Pb isotopic dating of zircon grains using the LA-MC-ICP-MS and CA-ID-TIMS methods. SEM imaging of grains prior to LA-MC-ICP-MS analysis is also discussed in this section (2.3.4.2.1).

2.4. Low-field magnetic susceptibility analysis of Carboniferous limestones.

2.5. Stable isotope analyses ($\delta^{13}C$ and $\delta^{18}O$) of Carboniferous limestones.

2.6. XRD analysis of the diagenetically altered volcanic ash layer samples.

2.7. Whole-rock geochemistry of the diagenetically altered volcanic ash layer samples determined by ICP-OES and ICP-MS.

2.8. Recalibration of legacy $^{40}Ar/^{39}Ar$ age data.

2.9. Average periodicity calculations for sedimentary cycles between two altered ash layers dated using the U-Pb zircon CA-ID-TIMS method.

2.2. Zircon separation and concentration

All zircon separation and concentration procedures were undertaken using the facilities at the Department of Geology, Trinity College Dublin. Bentonite samples collected from outcrops were typically 1 – 2 kg in weight (see section 1.5.1 for the definition of a bentonite). Samples were disaggregated using either a mechanical or chemical approach, depending on the nature of the sample. Well consolidated samples (several Belgian Visean bentonite samples) were crushed in a Retsch Jaw crusher equipped with

tungsten carbide plates. Poorly consolidated samples (e.g. the Arnsbergian bentonites from the Pennine Basin) required only a light grinding in a mortar and pestle. In both instances, samples were dried prior to disaggregation at 80 °C to prevent the 'caking' of the samples onto either the tungsten carbide plates or the mortar. Following disaggregation, samples were sieved at 300 μm and the < 300 μm fraction was subsequently processed for zircon. Samples were then washed several times in water to remove the clay fractions and were then dried in an oven. At this stage, samples were ready for heavy liquid separation.

Westphalian tonstein samples (see section 1.5.1 for the definition of a tonstein) were disaggregated chemically in a solution of 80 % dimethyl sulfoxide (DMSO) for about a week (method modified from Triplehorn *et al.*, 2002). During this time, the DMSO level was checked and topped up periodically to replace the DMSO absorbed by the kaolinite clay within the tonstein samples. When no further DMSO was absorbed, the samples were washed with distilled water and dried in an oven at 80 °C. This technique of disaggregation is very efficient but is only effective for samples containing kaolinite. Samples were then sieved with a 300 μm mesh sieve and zircons were concentrated from the < 300 μm fraction.

Zircons were concentrated using heavy liquid separation with methylene iodide (ρ = 3.32 g / cm^3). This technique is very effective at separating zircon (ρ = 4.6 – 4.7 g / cm^3) from the clay minerals that comprise the bulk of the samples investigated (e.g. kaolinite ρ = 2.6 g / cm^3; illite ρ = 2.6 – 2.9 g / cm^3). In several samples the heavy mineral separate contained abundant pyrite (ρ = 5.0 g / cm^3) which dominated the heavy mineral fraction, making the zircon grains difficult to observe. Pyrite was removed by submerging the heavy mineral separates in a 50:50 mixture of generic household bleach and distilled water overnight. Samples were subsequently washed several times in distilled water and dried. The pyrite, which was oxidised by the bleach, was removed by magnetic separation using a Chas. W. Cook & Sons magnetic separator (Fig. 2.1). The magnetic separator comprises two main parts: an electro-magnet and a brass chute with an attached vibration unit (Fig. 2.1). The brass chute is inclined forwards (termed forward slope) and to one side (termed side slope). Samples are introduced on to the upper portion of the chute (before the magnet; Fig. 2.1). Vibrations cause the sample grains to move down the inclined track, along the lower side of the chute (i.e. the 'A'

side of the chute in the inset cross section of Fig. 2.1). As the sample passes through the electromagnet, paramagnetic and weakly ferromagnetic (*sensu lato*; see section 2.4.1.1 for definitions) mineral grains are attracted towards the higher side of the chute (the 'B' side of the chute in the inset of Fig. 2.1), where the magnetic flux is strongest because the plates of the magnet are closer together (see the A – B cross section in Fig. 2.1). The chute is divided in two approximately halfway down its length, separating the magnetic and the non-magnetic fractions, which are collected at the lower end of the chute. The non-magnetic fraction was collected in a clean petri dish, whereas the volumetrically larger magnetic fraction was typically collected in a clean sample bucket.

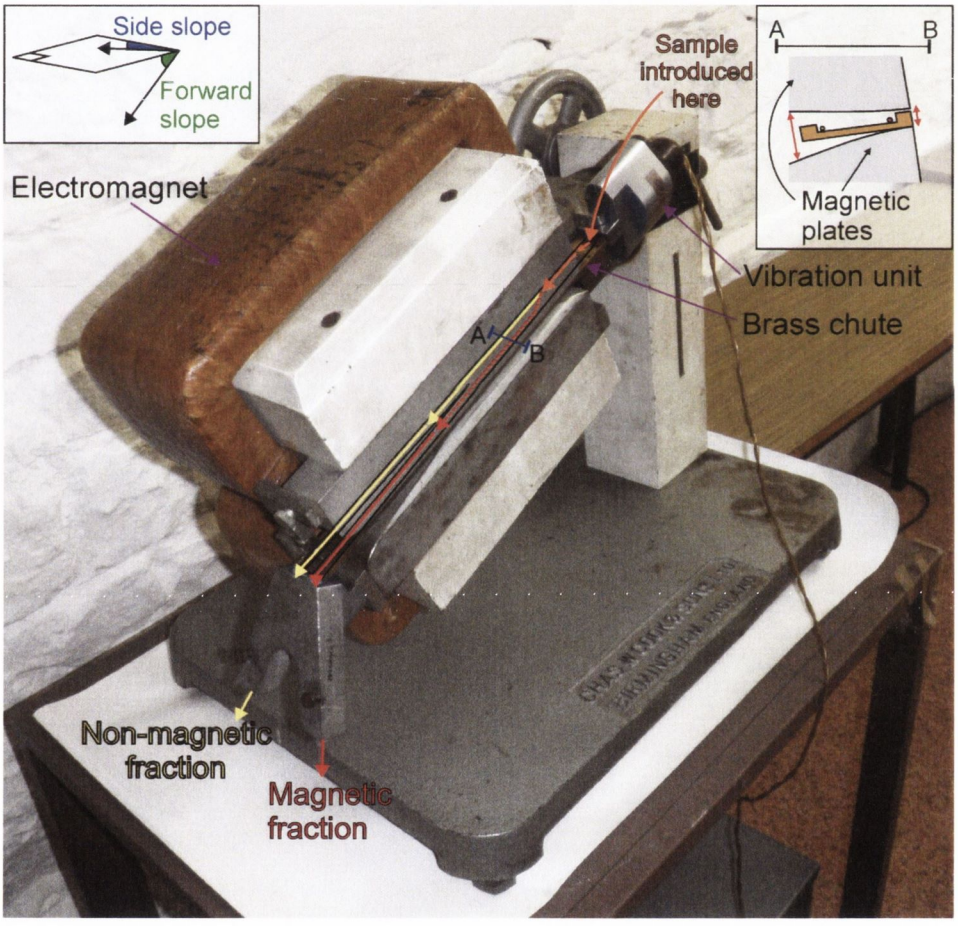

Figure 2.1. The Chas. W. Cooks and Sons magnetic separator used in this study.

Zircon ranges from diamagnetic to paramagnetic (Sircombe & Stern, 2002) and there is a well-established positive correlation between U-Pb age discordance (term defined in section 2.3.1), uranium concentration and magnetic susceptibility (Sircombe & Stern, 2002; references therein). For this reason, zircon from the least-magnetic fraction is routinely selected for analysis. Magnetic separation of zircon was conducted at full

magnetic field strength (*c.* 2.0 A) and at low side slope (*c.* $1 - 2^{\circ}$). Heavy mineral fractions that did not contain abundant pyrite were also subject to magnetic separation, using the same settings. Zircons from the non-magnetic fraction were subsequently hand-picked in alcohol at high magnification using a Nikon SMZ 1500 binocular microscope, using both transmitted and reflected light microscopy.

2.3. U-Pb zircon dating

2.3.1. Overview of U-Pb zircon geochronology

Zircon ($ZrSiO_4$) is the mineral of choice for U-Pb geochronology because:

1. It is physically robust and chemically stable. For example, it is commonly preserved intact in diagenetically altered ash layers even when other phenocrysts such as sanidine and biotite have undergone alteration.
2. It is represented in many crustal lithologies and is often cited as being ubiquitous, although it is less common in silica-undersaturated and peralkaline igneous lithologies (Watson, 1979; Hoskin & Schaltegger, 2003).
3. Its crystal structure incorporates uranium (parent element; substitutes for Zr^{4+}) whilst excluding lead (daughter product), generating high initial parent to daughter ratios and thus minimising the initial daughter product (common lead) correction.

Uranium has two long-lived radioactive isotopes which decay to isotopes of lead:

$$^{238}U \rightarrow {}^{206}Pb \quad \text{half life} = 4{,}468 \text{ Myrs}$$
$$^{235}U \rightarrow {}^{207}Pb \quad \text{half life} = 704 \text{ Myrs}$$

Half lives are based on the decay constants of Jaffey *et al.* (1971)

This dual-decay system of uranium allows three age determinations per sample analysis (two are independent and one is derived), which are calculated as follows:

$$^{206}Pb/^{238}U \text{ date} = \left(\frac{1}{\lambda^{238}}\right) \times \ln\left(\frac{^{206}Pb^{*}}{^{238}U} + 1\right)$$

$$^{207}\text{Pb}/^{235}\text{U date} = \left(\frac{1}{\lambda^{235}}\right) \times \ln\left(\frac{^{207}\text{Pb}^*}{^{235}\text{U}} + 1\right)$$

$$^{207}\text{Pb}^*/^{206}\text{Pb}^* = \left(\frac{1}{137.88}\right) \times \left(\frac{e^{\lambda 235 \times t76} - 1}{e^{\lambda 238 \times t76} - 1}\right)$$

where Pb* denotes radiogenic lead, λ^{235} and λ^{238} are the ^{235}U and ^{238}U decay constants respectively, 137.88 is the natural ^{238}U/^{235}U ratio and t76 is the ^{207}Pb/^{206}Pb date. The ^{207}Pb/^{206}Pb decay equation is solved iteratively. Typically, the ^{207}Pb/^{206}Pb and ^{206}Pb/^{238}U dates are measured while the ^{207}Pb/^{235}U dates are derived from those data. The above equations are from Schmitz & Schoene (2007).

The ability to derive two independent dates per U-Pb zircon analysis provides an internal consistency check; if a zircon has maintained a closed isotopic system since crystallisation then the two calculated dates should be equal (provided the uranium decay constants are accurate). In this instance, the data are described as concordant and the calculated dates are considered robust. If, however, the two decay systems yield different dates, it suggests that the zircon has experienced complexities (e.g. lead loss or it contains inherited material); these data are termed discordant. There are two types of discordance: normal and reverse. Normal discordance (where the ^{207}Pb/^{206}Pb dates are older than the ^{206}Pb/^{238}U dates) is more commonly encountered in zircon. Reverse discordance (where the ^{207}Pb/^{206}Pb dates are younger than the ^{206}Pb/^{238}U dates) in zircon is rare because it requires the preferential loss of the structurally-bound parent U or the incorporation of excess ^{206}Pb (Mattinson *et al.*, 1996). Excess ^{206}Pb is common in young, Th-rich minerals such as monazite because ^{230}Th, an intermediate daughter product of ^{238}U (which thus decays to ^{206}Pb), is preferentially incorporated during crystallisation (Schärer, 1984). However, in zircon ^{230}Th is preferentially excluded (relative to U) at the time of crystallisation, resulting in a small deficit of ^{206}Pb and slight normal discordance (Mattinson *et al.*, 1996; references therein). Most occurrences of reverse discordance in zircon have been attributed to analytical artefacts (e.g. Wiedenbeck, 1995), although models to generate it in nature have been proposed (e.g. Mattinson *et al.*, 1996).

2.3.2. Conventional (Wetherill) concordia diagrams

U-Pb data are normally presented on a concordia diagram (after Wetherill, 1956), which provides a visual representation of the concordance of data. The conventional (Wetherill) concordia represents the locus of points where the $^{207}Pb/^{235}U$ and $^{206}Pb/^{238}U$ systems yield the same age, as illustrated in Fig. 2.2.

Where the precision of analyses is high (e.g. for CA-ID-TIMS data), the concordia is often represented as a band whose thickness is a function of the U decay constant uncertainties (e.g. Fig 2.2c). Concordant analyses overlap with the concordia band, whereas reversely discordant and normally discordant analyses plot above and below the concordia band respectively (Fig. 2.2a).

The concordia plot is a powerful diagram that helps to distinguish the youngest magmatic (concordant) zircon population, which is used to constrain the age of an ash layer or bentonite, from analyses that exhibit complexities such as lead loss, common lead contamination, inheritance and / or protracted zircon growth. These complexities have predictable expressions on a concordia diagram (outlined below) and thus the concordia diagram can provide qualitative information about the origins of the complexities within sample data. There are, however, limitations to the concordia diagram; for example, it is often impossible to separate a magmatic zircon population from grains exhibiting subtle amounts of lead loss.

2.3.2.1. Lead loss

Lead loss involves the removal of radiogenic lead, which is not structurally bound in the zircon crystal lattice, from the zircon grain and is likely facilitated by radiation damage to the zircon crystal structure (Cherniak & Watson, 2001; Bowring *et al.*, 2006). The loss of lead results in measured $^{206}Pb/^{238}U$ and $^{207}Pb/^{235}U$ dates that are younger than the true age of the zircon grain. When plotted on the concordia diagram, analyses exhibiting lead loss typically plot below and to the right of the concordia curve, towards younger ages (Fig. 2.2b). Anomalously young and stratigraphically inconsistent dates are strong indicators of lead loss (e.g. in this study isotopic dates younger than the late Carboniferous).

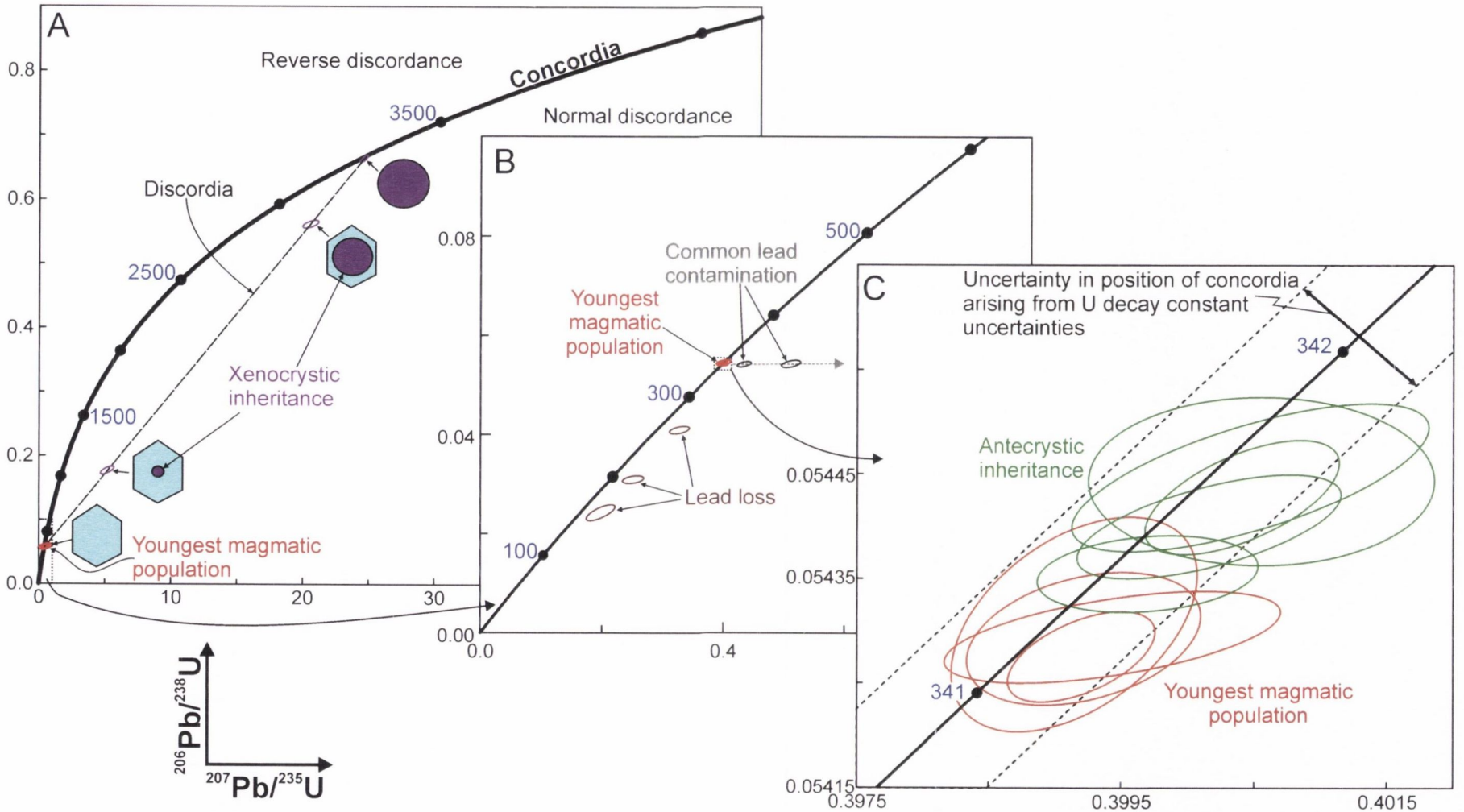

Figure 2.2. U-Pb concordia diagrams. Plots A to C are at a progressively finer scale of analysis. Blue numbers are concordant ages (Ma). The concordia separates the fields of normal and reverse discordance.

2.3.2.2. Inheritance

Inheritance arises from two main sources: detrital additions as a result of sedimentary reworking (detrital inheritance) and as intra-grain cores (xenocrystic inheritance). Detrital grains will yield dates older than the eruption age of the ash layer, that range from concordant to very discordant depending on the provenance and thermal history of the detrital zircons. Xenocrystic inheritance arises from the incomplete resorption of zircon material assimilated into the melt. New magmatic zircon crystallises around the relict cores, producing zircon grains that comprise multiple age domains. Isotopic dating of multiple age domains (e.g. by single grain TIMS analysis or poor positioning of laser ablation spots) yields an 'average' U-Pb date between that of the inherited core and the overgrowth (as shown in Fig. 2.2a). If only two age components are present in a sample then several analyses with varying proportions of core and overgrowth may form a linear array (a discordia) between the age of the core and overgrowth (Fig. 2.2a), provided that there are no additional complexities such as lead loss.

2.3.2.3. Protracted growth of zircon (antecrystic inheritance)

For CA-ID-TIMS analyses, the analytical precision is sufficient that multiple generations of zircon grains, crystallised over the lifetime of a single magma system (see section 2.3.5.3) and subsequently erupted together, may be resolved. The zircons that crystallised first in a magma system may be older (outside of analytical uncertainty) than the eruption age of the ash layer. This is a subtle form of inheritance that is often termed antecrystic inheritance (after Miller *et al.*, 2007). Its expression on the concordia diagram is illustrated in Fig. 2.2c.

2.3.2.4. Common lead contamination

Common lead contamination can also potentially complicate the interpretation of analyses. This is particularly problematic where the common lead abundance is not known (i.e. non-radiogenic ^{204}Pb is not measured, which is common in some LA-ICP-MS setups). Common lead contamination is expressed on the concordia diagram by analyses plotting on a sub-horizontal trend to the right of concordia (Fig. 2.2b).

The correction for common lead based on measurement of ^{204}Pb is not without uncertainty because assumptions about the source of the common lead (i.e.

anthropogenic versus common lead incorporated into the zircon at the time of crystallisation, which is often termed initial lead) and its isotopic composition have to be made. Anthropogenic common lead contributions (abundance and isotopic composition) can be estimated analytically, through repetition of blank measurements (e.g. using the same methodology as described in section 2.3.5.2.2 but without analysing a zircon grain). The isotopic composition of initial common lead can be estimated by analysing a co-magmatic, lead-bearing, uranium-poor mineral phase (e.g. potassium feldspar) where such mineral phases are present. When lead-bearing, uranium-poor mineral phases are not represented (or preserved) in a sample, which is a common scenario for the Carboniferous bentonites and tonsteins documented in this thesis, initial common lead can be estimated using terrestrial lead isotope evolution models such as that of Stacey & Kramers (1975). Presently, most high-precision U-Pb TIMS laboratories assume that all the common lead in zircon arises from the analytical blank (S. Bowring, pers. comm., 2011). This is because improvements in analytical blanks and the implementation of chemical abrasion (section 2.3.5) have demonstrated that zircon excludes lead during crystallisation and unless zircon grains contain common-lead bearing micro-inclusions, the measured common lead is instead introduced during analysis (Bowring *et al.*, 2006).

2.3.3. Defining the age of a diagenetically altered volcanic ash layer: weighted mean $^{206}Pb/^{238}U$ dates

Where the youngest magmatic population can be identified within a dataset, the weighted mean $^{206}Pb/^{238}U$ date of this population is used to define the eruption age of the altered ash layer. This is standard practice within the literature (e.g. Ramezani *et al.*, 2007; Davydov *et al.*, 2010; Gulbranson *et al.*, 2010). The $^{206}Pb/^{238}U$ system is used preferentially in this thesis because it yields the highest analytical precision for samples of Carboniferous age. In this thesis the suggestions of Bowring *et al.* (2006) are followed, whereby the term 'date' is reserved for the solution to the decay equations and the weighted mean calculations. The term 'age' is reserved for the interpretation of a date (e.g. the eruption age of an altered volcanic horizon).

2.3.4. Laser ablation (multi-collector) inductively coupled plasma mass spectrometry (LA-MC-ICP-MS)

2.3.4.1. Overview of the technique

A schematic diagram of the LA-MC-ICP-MS instrumental set-up used in this project is shown in Fig. 2.3. The LA-MC-ICP-MS technique involves focusing a laser beam onto the surface of a sample, which is held within an ablation cell (Fig. 2.3). Laser energy is absorbed by the sample and ablation (breaking of chemical bonds) occurs, releasing an aerosol of sample material that becomes entrained in the carrier gas (typically helium), which flows through the ablation cell continuously during analysis. A $^{203,\ 205}$Tl-^{235}U tracer aerosol (desolvated solution) is introduced into the sample aerosol – carrier gas mixture downstream of the sample cell. The isotopic ratios of the tracer (^{203}Tl/^{205}Tl, ^{205}Tl/^{235}U) provide an online correction of instrumental mass bias and plasma-induced inter-elemental effects. The sample – tracer – carrier gas mixture is then combined with the argon gas supply of the MC-ICP-MS upstream of the MC-ICP-MS (Fig. 2.3). Inside the MC-ICP-MS, the sample aerosol is vaporised, atomised and ionised by the high-temperature argon plasma source (Fig. 2.3). Sample ions then pass through a series of skimmer cones, which facilitate a change from atmospheric pressure to high vacuum, and are subsequently accelerated across a potential difference and collimated into a coherent ion beam by lenses. The ion beam passes through the mass analyser (a double focusing unit comprising an electrostatic analyser (ESA) and magnet; Fig. 2.3), which sorts the ion beam by kinetic energy and mass-to-charge ratio respectively (Košler & Sylvester, 2003). The zoom lens (Fig. 2.3) then focuses the mass spectrum onto the static collector array, which comprises Faraday cups and secondary electron multipliers.

LA-MC-ICP-MS is a rapid and relatively inexpensive analytical technique, but the precision of U-Pb zircon dates is limited to *c.* 0.5 – 3% (2σ), i.e. an order of magnitude poorer than ID-TIMS analysis. This technique was employed as a screening tool for detecting inheritance within samples and to rapidly characterise sample age populations.

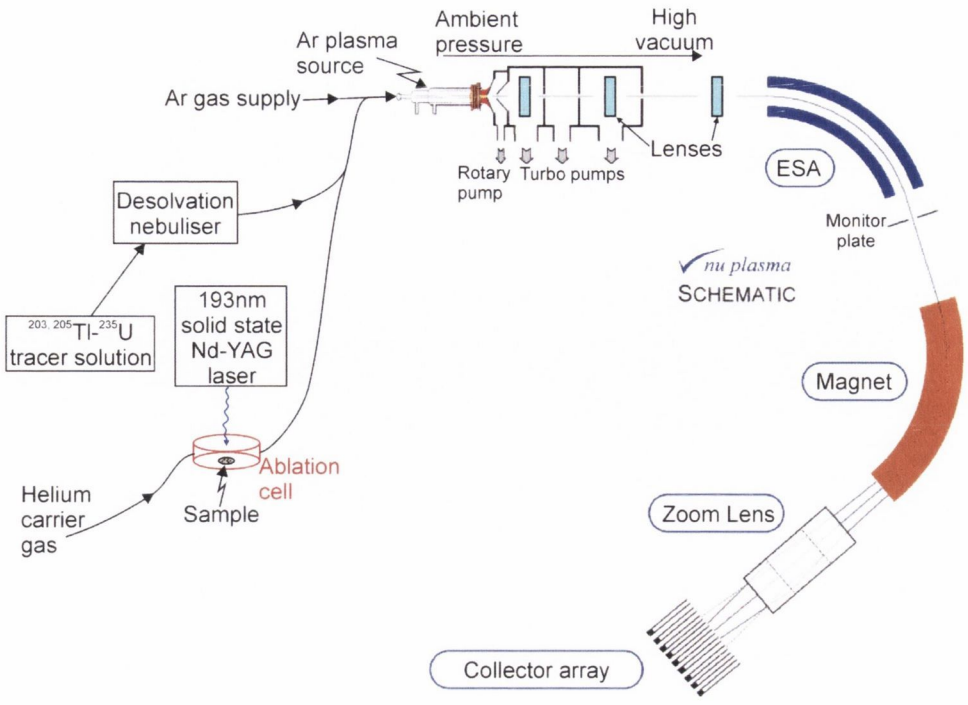

Figure 2.3. A schematic diagram of the LA-MC-ICP-MS instrumental set-up used at the NERC Isotope Geosciences Laboratory (NIGL), Keyworth, UK. All analyses were performed using a Nu-Plasma HR MC-ICP-MS coupled to a New Wave neodymium-doped yttrium aluminium garnet (Nd-YAG) 193nm laser. The MC-ICP-MS portion of the diagram is modified from the instrument manual.

2.3.4.2. Methodology

Small aliquots of the zircon separates were mounted in epoxy resin and polished to approximately half thickness. Unless stated otherwise, no attempt was made to hand pick grains prior to mounting, to avoid inadvertently fractionating the zircon population. Grain mounts were imaged under a scanning electron microscope (SEM) using backscattered-electron (BSE) and cathodoluminescence (CL) imaging prior to LA-MC-ICP-MS analysis. These images served as a guide for positioning laser spots during LA-MC-ICP-MS analysis.

2.3.4.2.1. SEM imaging of grains

Sample grains were imaged using BSE and CL techniques. These imaging techniques reveal subtle internal textures (linked to chemical variations) within zircon grains that are often invisible under a conventional petrographic microscope and which can provide qualitative information about both the origin (e.g. magmatic versus metamorphic) and the history of zircon grains.

BSE imaging maps variations in the average atomic mass within a zircon grain; the higher the average atomic number, the more electrons are reflected onto the BSE detector and the brighter the image appears (Hanchar & Miller, 1993; Corfu *et al.*, 2003). Cathodoluminescence occurs when incident electrons from the primary SEM beam excite sample electrons to a higher energy state (Marshall, 1988). After a short time, the excited electrons revert back to a lower energy state, releasing excess energy in the form of photons (Marshall, 1988). CL intensity in zircon is complex and is not well understood (Nasdala *et al.*, 2003). Trace element impurities in zircon are thought to be important CL emitters; however, CL intensity is not simply a function of REE concentrations (Poller *et al.*, 2001; Nasdala *et al.*, 2003). Crystallinity is also thought to be important; CL emissions decrease with reduced crystallinity (Nasdala *et al.*, 2003). U and Th concentrations indirectly affect CL emissions through radiation damage, which reduces crystallinity (Nasdala *et al.*, 2003). Thus, high U or Th zircons are typically dark under CL and low U – Th contents result in CL bright grains. A more detailed account of CL in zircon can be found in Nasdala *et al.* (2003).

SEM grain imaging was conducted at the British Geological Survey, Keyworth, UK, using a LEO (Zeiss) 435VP variable pressure scanning electron microscope equipped with secondary electron, BSE and CL detectors. All images were acquired using an accelerating voltage of 10 kV and a working distance of 19 mm. Samples were carbon coated prior to imaging.

2.3.4.2.2. LA-MC-ICP-MS analysis

Laser ablation analysis was conducted at the National Environment Research Council (NERC) Isotope Geosciences Laboratory (NIGL), Keyworth, UK. Analyses were performed using a Nu-Plasma HR MC-ICP-MS coupled to a solid state New Wave neodymium-doped yttrium aluminium garnet (Nd-YAG) 193 nm laser. The laser was configured to deliver 55 % power, a 25 μm spot diameter and 5 Hz repetition rate. Ablation was conducted in helium gas and 60 second sample ablations were conducted. Baselines were recalibrated every 10 measurements.

Mass fractionation and plasma-induced inter-element fractionation effects were corrected using a mixed $^{203,205}Tl$-^{235}U solution introduced to the MC-ICP-MS through a Cetac Technologies Aridus desolvating nebuliser. Laser-induced fractionation effects were corrected by bracketing sample analyses with analysis of the Plesovice standard zircon (Sláma *et al.*, 2008) and thereby deriving correction factors which were subsequently applied to sample analyses. Standard analyses were run every 30 analyses (roughly every hour). The accuracy of the sample analyses was determined by running the standard zircon 91500 as an unknown, interspersed with standard and sample analyses. 33 spot analyses of the 91500 zircon yielded a weighted mean $^{207}Pb/^{206}Pb$ date of 1060.6 ± 5.3 Ma (95 % conf., MSWD = 1.4, p = 0.085), which is within the uncertainty of the ID-TIMS $^{207}Pb/^{206}Pb$ age determination of Wiedenbeck *et al.* (1995; 1065.4 ± 0.3 Ma, 2σ).

Data were reduced using an in-house spreadsheet program and were corrected for baseline and fractionation. Unless stated otherwise, LA-MC-ICP-MS data were not corrected for common lead. Where a common lead correction is applied, the method of Horstwood *et al.* (2003) was used, which is a ^{204}Pb based correction, employing an ion counter to measure the ^{204}Pb peak. The correction for common lead was performed using the in-house data reduction spreadsheet program.

Data are presented as concordia diagrams and where the data are relatively simple i.e. where several analyses that overlap and are concordant within analytical uncertainties can be identified, the weighted mean $^{206}Pb/^{238}U$ date of these analyses is calculated. More details regarding the concordia diagrams and weighted mean calculations are given in section 2.3.5.2.4.

2.3.5. Chemical abrasion isotope dilution thermal ionization mass spectrometry (CA-ID-TIMS)

2.3.5.1. Overview of the technique

This analytical technique involves chemically abrading (*sensu* Mattinson, 2005) typically 40 – 100 zircon grains *en masse* in two steps (annealing and partial dissolution), followed by ID-TIMS analysis of single grains. Grains are annealed at high temperatures (typically 850 – 900 °C), although some studies have experimented with higher temperatures (e.g. Das & Davis, 2010). The annealing protocol serves to preserve sample material by annealing areas within zircon grains that have suffered some radiation damage but are not isotopically disturbed. This is followed by the partial dissolution of grains in concentrated hydrofluoric acid at elevated temperatures for several hours (typically 10 – 12 hours at 180 – 220 °C) to dissolve damaged and isotopically disturbed portions of the zircon grains. The chemical abrasion technique is a relatively new approach and has quickly replaced air abrasion (*sensu* Krogh, 1982) as the preferred method of removing sample lead loss in leading international U-Pb zircon TIMS laboratories.

Subsequent to chemical abrasion, ID-TIMS analysis is undertaken on single zircon grains. Grains are weighed (or photographed to calculate their dimensions) and loaded into Teflon bombs with concentrated hydrofluoric acid and a known amount of isotopic tracer solution. This tracer solution is used for concentration determinations, and also for the online determination of mass fractionation where double isotopic spikes are employed (e.g. $^{233}U - ^{235}U$). Sample grains are dissolved in Teflon bombs at elevated temperatures (*c.* 200 °C) over several days. Following dissolution, U and Pb are separated using anion chromatography, then loaded together onto rhenium filaments and analysed by thermal ionization mass spectrometry.

Several single grain aliquots are analysed per sample to ensure the youngest magmatic zircon population is represented in the results. CA-ID-TIMS analysis is time intensive and expensive, limiting the number of analyses undertaken per sample. However, these disadvantages are offset against the unrivalled precision of this method, which can readily generate U-Pb dates with uncertainties of < 0.1 % (2σ; $^{206}Pb/^{238}U$ dates; e.g.

Appendix 1 Table 1), which are necessary for high-precision applications such as timescale calibration.

2.3.5.2. Methodology

2.3.5.2.1. Chemical abrasion

40 – 60 grains were hand-picked from each sample in alcohol, under high magnification using a Nikon SMZ 1500 binocular microscope at the Department of Geology, Trinity College Dublin. Euhedral grains were preferentially selected. Grains were then transported to the Department of Mineralogy, University of Geneva, where U-Pb CA-ID-TIMS dating was undertaken over the course of three research visits in 2008, 2009 and 2010 (total of seven months analytical work). Grains were annealed in quartz crucibles at 900 °C for 48 hours and then transferred to pre-cleaned 3 ml Savillex containers in preparation for the partial dissolution step. Grains were partially dissolved in *c.* 120 µl 29 M HF and trace 7 M HNO_3 at 180 °C for *c.* 12 hours. Following the partial dissolution step, zircon grains were fluxed in 6 M HCl for 24 hours and then washed several times in ultrapure H_2O and acetone, with ultrasonic agitation employed between washes.

2.3.5.2.2. ID-TIMS analysis

Prior to the loading of grains into Teflon bombs for dissolution, the grains were characterised for their shape, aspect ratio, occurrence of fractures and opacity under a reflected light binocular microscope to determine if there are relationships between grain morphology and grain age. Prior to the final research visit to the University of Geneva in 2010, a high-powered binocular microscope was purchased in the Geneva laboratory and grains are now routinely imaged under transmitted light at high-magnification prior to loading. The impact of chemical abrasion on grain morphology is variable. Some grains appear relatively unchanged following chemical abrasion; e.g. grains 300/3, 300/6 in Fig. 2.4 retain crystal faces and remain relatively clear. Other grains show more extensive changes; e.g. grains T1Gb/1 and L2/8 in Fig. 2.4. However, no clear relationship between morphology and age was discernable.

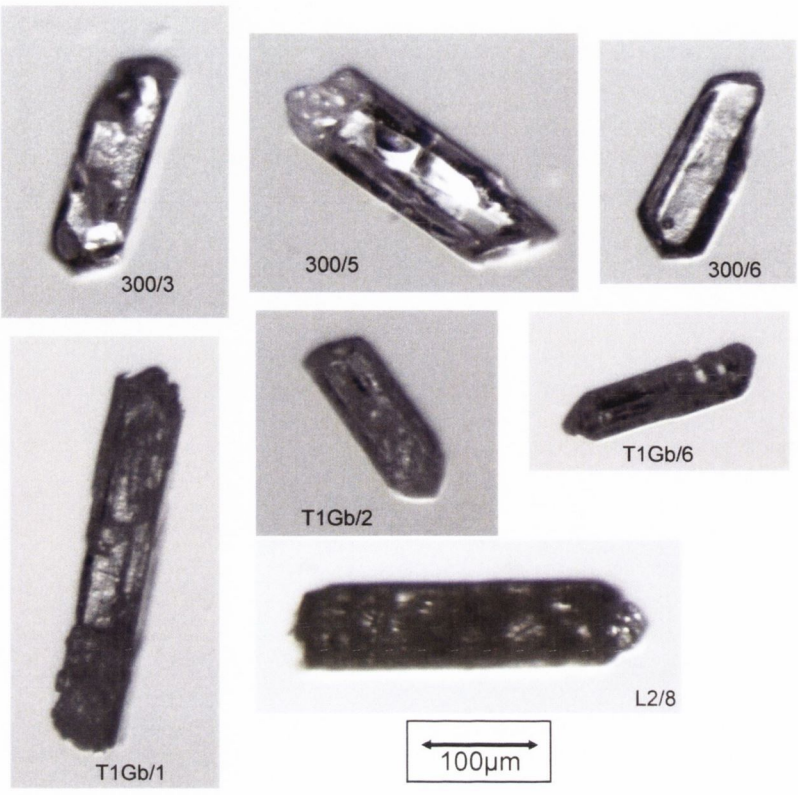

Figure 2.4. Photomicrographs of chemically abraded zircon grains. Photomicrographs are of the same scale.

Single chemically abraded grains were loaded into Teflon bombs in a solution of 63 µl 29 M HF and trace 7 M HNO_3. Analyses were spiked with *c.* 0.005 g (exact weight determined to ± 0.1 mg) of the Earthtime ^{202}Pb-^{205}Pb-^{233}U-^{235}U (ET2535) isotopic tracer and placed in an oven for 6 days at 206 °C. Following dissolution, samples were dried down and re-dissolved overnight in 36 µl 3 M HCl. Pb and U were separated sequentially using anion exchange chromatography (method modified from Krogh, 1973) and dried down together with 3 µl 0.05 M H_3PO_4. U and Pb were loaded together on single, outgassed rhenium filaments with 1 µl of silica gel, prepared according to Gerstenberger & Haase (1997).

The U and Pb isotopic compositions of samples were measured on a Thermo Scientific Triton thermal ionization mass spectrometer (TIMS) housed in the Department of Mineralogy, University of Geneva (Fig. 2.5).

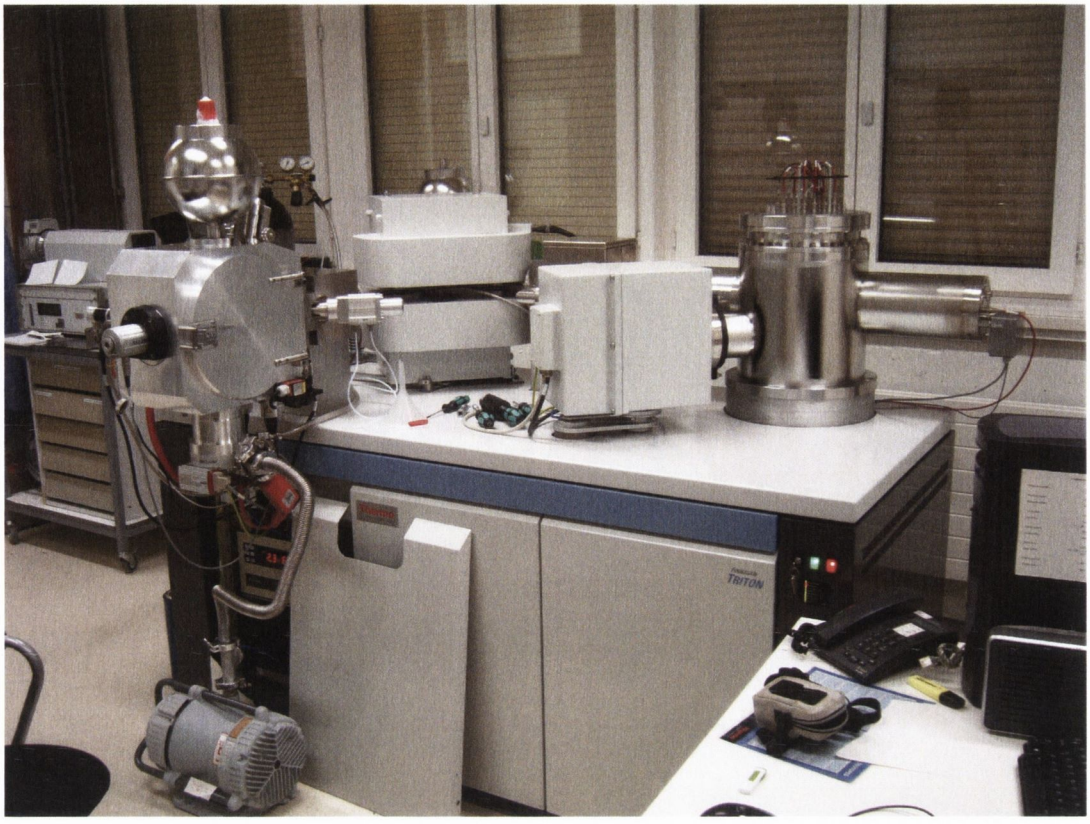

Figure 2.5. The Thermo Scientific Triton thermal ionization mass spectrometer housed at the Department of Mineralogy, University of Geneva.

Pb isotopes were measured first and in dynamic mode using the linear MasCom secondary electron multiplier. The linearity of the MasCom multiplier was calibrated using the standard reference solutions U500, Sr SRM987, and Pb SRM982 and SRM983 (M. Ovtcharova, pers. comm., 2008). Lead isotopic fractionation was corrected online using the $^{202}Pb/^{205}Pb$ ratio of the Earthtime spike (0.99989; Table 2.1). The online fractionation calculations were performed using the Triton's data acquisition software and applied on a line-by-line (point-wise) basis.

Uranium isotopes were measured following the lead isotopes and as UO_2. When U concentrations were sufficiently high, U measurements were acquired in static mode using the Triton's Faraday cup array coupled to amplifiers equipped with 10^{12} Ω resistors. For samples with modest U concentrations, U isotopes were measured in dynamic mode using the MasCom electron multiplier. Isobaric interference of $^{233}U^{18}O^{16}O$ on $^{235}U^{16}O^{16}O$ was corrected using an $^{18}O/^{16}O$ ratio of 0.00205 (as recommended by IUPAC; De Laeter *et al.*, 2003). U isotopic mass fractionation was

corrected using the $^{233}U/^{235}U$ ratio of the Earthtime isotopic spike (0.99464 ± 0.01 %, 2σ; Table 2.1) and assuming a natural $^{238}U/^{235}U$ ratio of 137.88 (as recommended by Steiger & Jäger, 1977). There have recent suggestions that a value of 137.88 for the natural uranium ratio is inaccurate (Condon *et al.*, 2010; Mattinson, 2010); however, a revised value has yet to be adopted by the international geological community. Thus, at this present time the internationally accepted value of 137.88 is retained. It is noteworthy that any future revisions to the value of the natural uranium ratio will have limited impact on the interpretations presented in subsequent chapters. This is because the natural uranium ratio is not used in the calculation of $^{206}Pb/^{238}U$ dates, which are the focus of subsequent interpretations (section 2.3.3).

Pb and U isotopic ratios were exported to the Tripoli program (v. 4.6.2.61; Bowring *et al.*, 2011), which was used to calculate initial statistics. Data were subsequently reduced following the algorithms of Schmitz & Schoene (2007) and Crowley *et al.* (2007). The propagated analytical uncertainties include non-systematic uncertainties arising from counting statistics, tracer subtraction and a common lead correction. All common lead was attributed to the analytical blank and was corrected for using the following isotopic compositions: $^{206}Pb/^{204}Pb = 18.30 \pm 0.26$, $^{207}Pb/^{204}Pb = 15.47 \pm 0.32$, $^{208}Pb/^{204}Pb = 37.60 \pm 0.74$ (all 2σ absolute). U blanks were < 0.1 pg and do not influence the degree of discordance at the age range of the studied samples, therefore a U blank value of 0.05 pg ± 50 % (2σ) was used in all data reduction.

At the time of writing this thesis, the compositions of the Earthtime spikes (ET2535 and ET535) are not finalised. This has resulted in several studies which have used the same Earthtime isotopic tracer solution employing different values for the $^{235}U/^{205}Pb$ tracer ratio. For example, using the ET535 tracer, Gastaldo *et al.* (2009) and Gulbranson *et al.* (2010) employed a $^{235}U/^{205}Pb$ ratio of 100.18 ± 0.05, whereas Schoene *et al.* (2010) used a value of 100.20 ± 0.1 and Davydov *et al.* (2010) employed a value of 100.206. Such variations will systematically affect the age calculations and are only important for inter-study data comparisons. The composition of the ET2535 spike used throughout is shown in Table 2.1 and follows that of Schoene *et al.* (2010) except for the uncertainty on the $^{235}U/^{205}Pb$ ratio, which follows a personal communication from B. Schoene (2011).

Isotope	Value	Unit
205Pb	9.882260145E-12	mol/g
235U	9.902024666E-10	mol/g
Isotopic ratio	**Value**	**Uncertainty (± 1σ %)**
202Pb/205Pb	9.998900000E-01	
206Pb/205Pb	2.989385290E-04	± 0.74
207Pb/205Pb	2.407104342E-04	± 0.10
204Pb/205Pb	8.875074984E-05	± 0.10
208Pb/205Pb	5.917328387E-04	± 0.10
207Pb/206Pb	8.052171630E-01	± 0.10
204Pb/206Pb	2.970280430E-01	± 0.10
238U/235U	3.087000000E-03	± 0.005
233U/235U	9.946400000E-01	± 0.005
238U/233U	3.103635486E-03	± 0.005
235U/205Pb	100.20	± 0.025

Table 2.1. The isotopic composition of the Earthtime ET2535 isotopic tracer used in this thesis.

Sample data are corrected for initial ^{230}Th disequilibrium, assuming a value of 4 for the initial Th/U ratio in the melt ($(Th/U)_{magma}$). This correction increases sample $^{206}Pb/^{238}U$ dates by *c.* 50 – 100 kyrs for model $(Th/U)_{zircon}$ ratios ranging between 0.187 – 1.862 (Table 2.2). The final (disequilibrium corrected) $^{206}Pb/^{238}U$ dates calculated for sample analyses are relatively insensitive to the value assumed for the $(Th/U)_{magma}$ ratio. As shown in Table 2.2, varying the assumed $(Th/U)_{magma}$ ratio by a factor of 1 (i.e. from 4 to 3 or from 4 to 5) has a minor effect on the disequilibrium corrected $^{206}Pb/^{238}U$ date, adjusting sample $^{206}Pb/^{238}U$ dates by only a few kyrs. The limited sensitivity of the data to the value assumed for the $(Th/U)_{magma}$ ratio arises because the magnitude of the initial thorium disequilibrium correction (*c.* 50 – 100 kyrs) is much smaller than the age of the studied sample materials (*c.* 310 – 350 Ma).

Analysis	$(Th/U)_{zircon}$	$^{206}Pb/^{238}U$ date* (Ma)	Increase in $^{206}Pb/^{238}U$ date arising from the correction for initial ^{230}Th disequilibrium, assuming $(Th/U)_{magma}$ = 3 – 5		
			$(Th/U)_{magma}$ = 3	$(Th/U)_{magma}$ = 4	$(Th/U)_{magma}$ = 5
B1/12	0.187	319.89	102 kyrs	103 kyrs	104 kyrs
B9/3	1.862	328.09	41 kyrs	58 kyrs	68 kyrs

Table 2.2. Increase in $^{206}Pb/^{238}U$ dates of sample analyses arising from the correction for initial ^{230}Th disequilibrium, assuming values of 3 – 5 for the $(Th/U)_{magma}$ ratio. * $^{206}Pb/^{238}U$ date corrected for initial ^{230}Th disequilibrium using a $(Th/U)_{magma}$ ratio of 4. Analyses B1/12 and B9/3 yielded the smallest and largest $(Th/U)_{zircon}$ ratios (respectively) of all sample analyses undertaken in this study (see Appendix 1 Table 1). The magnitude of the initial ^{230}Th disequilibrium correction is calculated from an equation presented in Schärer (1984; p. 200), using the model $(Th/U)_{zircon}$ ratios of sample analyses (Appendix 1 Table 1) and the following decay constant values: $^{238}U = 1.55125 \times 10^{-10}$ yrs^{-1} and $^{230}Th = 0.922 \times 10^{-5}$ yrs^{-1}.

The accuracy of the data was assessed by repeated analysis of the international standard zircon R33 (Black *et al.*, 2004), which was pre-treated by chemical abrasion and yielded an average $^{206}Pb/^{238}U$ date of 419.08 ± 0.19 Ma (95 % conf., n = 27; MSWD = 0.70; M. Ovtcharova, pers. comm., 2010). In addition, 100 Ma and 500 Ma synthetic NIGL solutions (Condon *et al.*, 2008) were measured and yielded an external reproducibility of $^{206}Pb/^{238}U$ dates of better than 0.1 % (M. Ovtcharova, pers. comm., 2010).

2.3.5.2.3. CA-ID-TIMS data from bentonite L1 at Lives-sur-Meuse

The U-Pb zircon CA-ID-TIMS data from the L1 bentonite (section 3.3.4.1) were acquired prior to this PhD project and used the Earthtime ^{205}Pb-^{233}U-^{235}U tracer solution (M. Ovtcharova, pers. comm., 2008). Sample data were reduced using the same tracer composition as shown in Table 2.1 for the ET2535 spike and following the same method as documented above (section 2.3.5.2). Lead isotopic fractionation on these data was corrected using a value of 0.11 ± 0.05 % / a.m.u. (2σ), which was determined by repeat measurements of the SRM 981 Pb standard (M. Ovtcharova, pers. comm., 2008).

2.3.5.2.4. U-Pb zircon data presentation

U-Pb zircon LA-MC-ICP-MS and CA-ID-TIMS data are presented as concordia diagrams and weighted average $^{206}Pb/^{238}U$ date diagrams. Both were drawn using Isoplot v. 3.0 (Ludwig, 2003a). Error ellipses (concordia diagrams) and error bars (weighted average date plots) are always drawn at the 2σ confidence level. In the concordia plots, the concordia is drawn using the decay constants of Jaffey *et al.* (1971), as recommended by Steiger & Jäger (1977). There are suggestions that one or both of the Jaffey *et al.* (1971) decay constants are inaccurate (e.g. Schoene *et al.*, 2006; Mattinson, 2010), as indicated by numerous high-precision, chemically-abraded analyses plotting consistently below and to the right of the concordia. Within this study, where the precision attained is sufficiently high (e.g. the CA-ID-TIMS data from samples L2 and Z1; sections 3.3.4.2 and 5.3.1.2 respectively), the data corroborate these suggestions. Concordance is assessed taking into consideration both analytical and decay constant uncertainties. This approach is probably the best that can be done until the decay constants are revised by international agreement, either by adopting the suggestions of Mattinson (2010) or through the re-determination of the U decay constants using direct counting methods.

2.3.5.2.5. Weighted mean $^{206}Pb/^{238}U$ dates

Where analyses are concordant and overlap within analytical uncertainty, the weighted mean $^{206}Pb/^{238}U$ date is calculated. Weighted mean $^{206}Pb/^{238}U$ dates were calculated before the addition of systematic uncertainties arising from the isotopic tracer calibration (0.05 %, 2σ; B. Schoene, pers. comm., 2011) and the ^{238}U decay constant (0.107 %, 2σ; Jaffey *et al.*, 1971). Uncertainties on weighted mean calculations are quoted at the 95 % confidence level (1.96σ). Unless stated otherwise, weighted mean uncertainties do not include systematic uncertainties arising from the calibration of the isotopic tracer solution and the U decay constants. Where the ± X/ Y/ Z uncertainty notation of Schoene *et al.* (2006) is used, the X uncertainty level refers to the internal error only, the Y uncertainty level is the internal error plus the uncertainty in the calibration of the isotopic tracer solution, and the Z uncertainty level includes the internal error, isotopic tracer calibration and decay constant uncertainties. Systematic uncertainties arising from the calibration of the isotopic tracer solution and the U decay constants were added in quadrature.

The mean square of weighted deviation (MSWD) and probability-of-fit (often shortened to probability or p) are calculated for each weighted mean calculation and provide a measure of the data scatter about the mean value. The two parameters are related; the probability-of-fit is derived from the MSWD, and can be calculated in Microsoft Excel as:

Probability-of-fit = CHIDIST (MSWD * degrees of freedom, degrees of freedom)

where CHIDIST is the Microsoft Excel function for a one-tailed probability of the chi-squared (χ^2) distribution (equation from Ludwig, 2003b).

An MSWD equal to 1 is optimal and suggests that all data scatter can be attributed to analytical uncertainties (Wendt & Carl, 1991; Horstwood, 2008). Critically, however, an MSWD of 1 does not preclude the presence of geological complexity; it simply indicates that if complexity is present, it is not resolvable within analytical uncertainties (Kalsbeek, 1992). However, for a given number of degrees of freedom and confidence level, there is a range of acceptable MSWD values (Wendt & Carl, 1991; Horstwood, 2008). MSWD values acceptable at the 95 % confidence level for 1 – 25 degrees of freedom (for a weighted average calculation, the degrees of freedom equals the number of data points minus one) are shown in Fig. 2.6 and are used throughout as a measure of quality control. MSWD values that exceed the upper 95 % confidence limit may indicate the underestimation of analytical uncertainties or the presence of geological complexities (Horstwood, 2008), whereas MSWD values smaller than the acceptable range may indicate the overestimation of analytical uncertainties (Horstwood, 2008). Where the MSWD exceeds the acceptable range of values at the 95 % confidence level (corresponding to a probability-of-fit of < 0.05), the weighted mean uncertainty is expanded by the square root of the MSWD multiplied by student's t factor for n-1 degrees of freedom, to take into consideration the observed excess data scatter. The square root of the MSWD parameter takes into account the actual scatter of the data, while the student's t factor takes into consideration that the data scatter is only estimated from a small number of data points (Ludwig, 2003a).

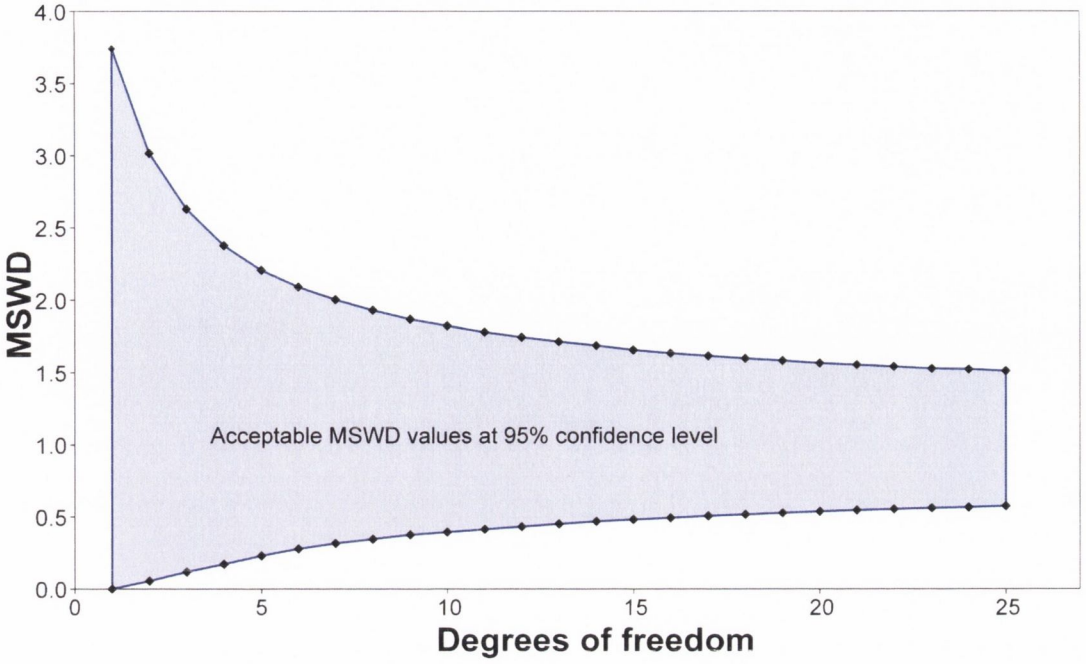

Figure 2.6. Acceptable MSWD values at the 95 % confidence level for a given number of degrees of freedom. The figure is redrawn from figure 3 of Wendt & Carl (1991). For a weighted mean calculation the degrees of freedom equals the number of data points minus one.

2.3.5.3. Potential pre-eruptive zircon residence in magma chambers

Several recent publications have presented evidence for the pre-eruptive residence of zircon in magmatic systems (e.g. Bachmann *et al.*, 2007; Miller *et al.*, 2007; Simon *et al.*, 2008; Schoene *et al.*, 2010). Thus, it is possible that the crystallisation ages recorded by zircon significantly pre-date ash layer eruptions. Whilst there is evidence for pre-eruptive residence of zircon, both its duration and how it varies between different ash layers are poorly quantified. Presently there is no sample-specific method for estimating the amount of residence present within a sample dataset (Simon *et al.*, 2008) and it is unclear how to treat potential pre-eruptive residence. Some studies have called for the indiscriminate expansion of U-Pb zircon age uncertainties (e.g. Peterson, 2011; Simon *et al.*, 2008). However, what value should be assigned to the residence uncertainty is equally unclear. For example, Simon *et al.* (2008) suggested an asymmetric uncertainty of +0 / -200 kyrs, whereas Peterson (2011) employed a range of residence uncertainties between ± 0 – 0.45 Myrs. The U-Pb zircon date uncertainties reported in subsequent chapters do not include an uncertainty for potential pre-eruptive residence, which is in-line with other contemporary studies (e.g. Davydov *et al.*, 2010). However, if it is subsequently proven necessary to include a residence uncertainty this can be added in quadrature to the reported U-Pb date uncertainties (e.g. Peterson, 2011).

2.4. Low-field magnetic susceptibility analysis of sedimentary rocks

2.4.1. Background

All minerals are susceptible to becoming magnetised when placed into a magnetic field (Ellwood, 2007; Ellwood *et al.*, 2000, 2007a); magnetic susceptibility (MS) analysis is a tool to measure this phenomenon. Low-field magnetic susceptibility is determined by introducing a sample of known mass or volume into a low-strength magnetic field (generated by a susceptibility bridge) and measuring the change in magnetic field strength. It is often expressed as the ratio of the induced magnetic moment relative to the strength of the applied field (Ellwood, 2007):

$$\chi = J / H \text{ (mass-normalised susceptibility)}$$

$$\kappa = J / H \text{ (volume-normalised susceptibility)}$$

where J is the induced moment, H is the applied field strength, χ and κ are magnetic susceptibilities measured relative to mass (units of m^3 / kg) and volume (dimensionless units) respectively. The equations are taken from Hunt *et al.* (1995).

Magnetic susceptibility is a rapid (minutes per analysis) and inexpensive technique that requires minimal sample preparation. The main drawback to MS analysis is that it exhibits anisotropy (e.g. Tarling & Hrouda, 1993), i.e. the measured MS varies as a function of sample orientation. Anisotropy arises from two main sources, which are termed magnetocrystalline anisotropy and shape anisotropy (Tarling & Hrouda, 1993). The former arises because magnetisation is more readily acquired along certain crystallographic axes within a mineral (Tarling & Hrouda, 1993). Shape anisotropy occurs in non-symmetric minerals (elongate grains) because magnetism is more readily acquired down the long axis of a grain (Tarling & Hrouda, 1993). Thus, any preferred alignment of elongate grains within a rock, which can arise through various sedimentary processes (e.g. flow alignment) or post-depositional processes (e.g. metamorphism), will generate some degree of anisotropy.

To quantify anisotropy on a sample-by-sample basis is time consuming and requires orientated samples (Ellwood *et al.*, 2007a). For these reasons, MS is often reported without consideration of anisotropy (e.g. Ellwood *et al.*, 2007a, 2007b, 2008b). However, the uncertainty in bulk MS analysis arising from anisotropy is very small for most samples (typically < 1 % for limestones; Ellwood *et al.*, 2007a) and is reduced by crushing samples to pebble-sized fragments prior to analysis.

2.4.1.1. Mineral magnetism

Minerals exhibit three main types of magnetic behaviour: diamagnetism, paramagnetism and ferromagnetism (*sensu lato*; Tarling & Hrouda, 1993). The magnetic behaviour of a mineral is controlled by its chemical composition (Rosenbaum & Brownfield, 1999). Diamagnetic minerals (e.g. calcite, quartz and gypsum) exhibit small negative susceptibilities, i.e. their acquired magnetism is in the opposite direction to the applied field (Fig. 2.7). Paramagnetic minerals (most iron-bearing sulphides, carbonates and silicates) exhibit positive susceptibilities, i.e. their acquired magnetism is of the same sense as the applied magnetic field. Paramagnetic effects are typically 10 – 100 times stronger than diamagnetic effects (Dunlop & Özdemir, 1997). Both diamagnetic and paramagnetic behaviours are temporary and disappear when the applied magnetic field is removed (Fig. 2.7). Ferromagnetic behaviour (*sensu lato*) is permanent and is superimposed on paramagnetic and diamagnetic effects (Tarling & Hrouda, 1993). It includes ferromagnetic (*sensu stricto)*, ferrimagnetic and antiferromagnetic behaviours (Fig. 2.7). Detailed descriptions of these types of behaviour are not discussed in this thesis but can be found in Dunlop & Özdemir (1997), Tarling & Hrouda (1993) and Harrison & Feinberg (2009). Ferromagnetic behaviour (*sensu stricto*) is generally restricted to metals and alloys (e.g. Harrison & Feinberg, 2009). Most minerals exhibit ferrimagnetic (e.g. magnetite, maghemite) or antiferromagnetic behaviours (e.g. ilmenite). Ferrimagnetic minerals exhibit very strong positive susceptibilities (Fig. 2.7), whereas antiferromagnetic substances exhibit weak positive magnetism in an applied field (Tarling & Hrouda, 1993).

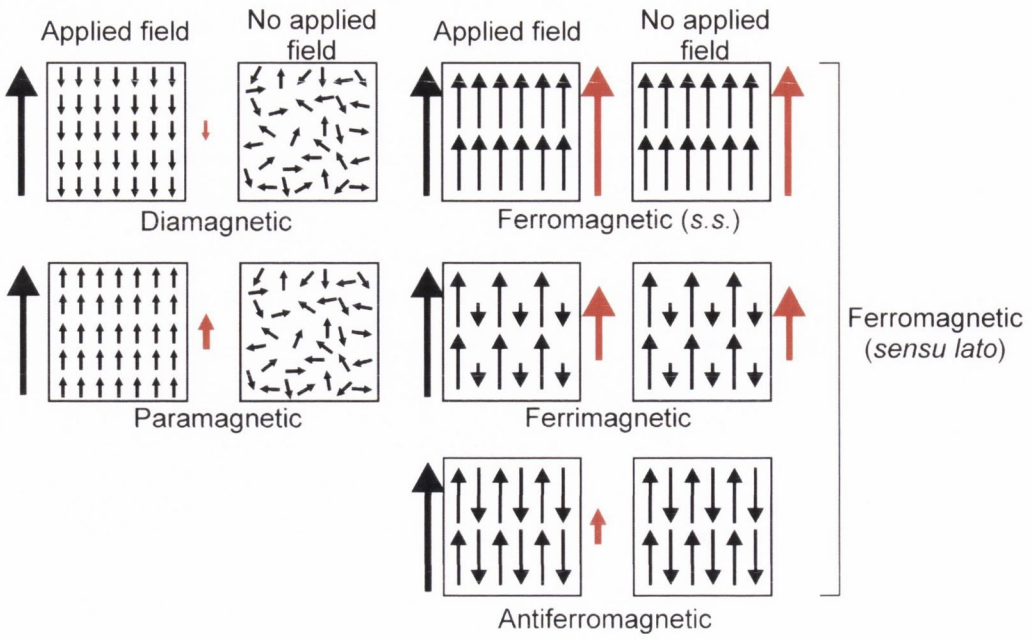

Fig. 2.7. The different types of magnetic behaviour (redrawn from figure 1.1 of Tarling & Hrouda, 1993). The vertical, thick, black arrows represent the magnitude and direction of the applied field. The red vertical arrows represent the net magnetic moment of a sample. The black arrows shown within the boxes (which symbolise sample materials) are schematic representations of the individual magnetic moments present within the sample materials. Ferromagnetism (*sensu lato*) includes ferromagnetic (s.s. = *sensu stricto*), ferrimagnetic and antiferromagnetic behaviours.

2.4.2. MS analysis in marine carbonates

The MS of sediments and sedimentary rocks in the low inducing magnetic fields applied during analysis is largely a function of the concentration and composition of grains, grain size and grain shape (Ellwood, 2007). In marine sediments two main components are thought to contribute to the measured MS signal: an exogenic (detrital / aeolian) contribution and a biogenic component formed *in situ* from calcareous and / or silicic organisms (Ellwood, 2007). The exogenic component can arise from multiple, different sources (see below) and can comprise a range of diamagnetic, paramagnetic and ferromagnetic (*sensu lato*) grains, whereas the *in situ* biogenic component is predominantly diamagnetic (Ellwood, 2007). In marine carbonates, the latter is volumetrically dominant but because it exhibits only a weak magnetic force it is easily swamped by small amounts of paramagnetic and ferromagnetic (*sensu lato*) detrital grains (Ellwood *et al.*, 2000, 2008a).

The origin of MS variations in lithified marine carbonates is an area of active research (da Silva *et al.*, 2009b). The prevailing hypothesis is that variations in MS primarily reflect variations in the flux of paramagnetic and ferromagnetic detrital grains into the marine realm (Crick *et al.*, 1997, 2001; Ellwood *et al.*, 2000, 2001; da Silva & Boulvain, 2006; da Silva *et al.*, 2009a, 2009b). A diverse range of processes including volcanism, extra-terrestrial impacts, climate, eustasy and tectonism can all contribute to this flux, over different timescales. In addition, variations in carbonate productivity will contribute to MS variability by diluting detrital inputs (Ellwood *et al.*, 2008b; da Silva *et al.*, 2009b). MS records are also potentially prone to post-depositional modification, although the effects of diagenesis on MS are not well understood (da Silva *et al.*, 2009a). Diagenetic processes can potentially create or destroy magnetic minerals (see da Silva *et al.*, 2009b for an overview). The MS of a sedimentary sequence is generally reduced through diagenesis, as lithified sedimentary rocks typically exhibit lower ranges of MS values than unlithified sediments (Ellwood *et al.*, 2001). Other potentially important post-depositional processes include weathering, metamorphism and the migration of fluids and hydrocarbons (Ellwood *et al.*, 2001; da Silva *et al.*, 2009b).

2.4.3. Methodology

Carbonate samples of *c.* 30 g were collected from outcrop sections in southern Belgium, employing a high sampling density (*c.* 5 – 30 cm intervals). Potential complicating factors in the sections such as calcite veins and macrofossils were avoided during sampling. Recent soil contamination and weathering rinds were removed from samples where necessary.

Samples were prepared and analysed for MS analysis at the Department of Geology and Geophysics, Louisiana State University (LSU) during September and October 2009. Sample preparation comprised reducing samples to pebble-sized fragments using a lump hammer (to reduce sample anisotropy) and weighing out approximately 10 g of sample for analysis.

Low-field MS measurements were acquired using a custom-built susceptibility bridge housed at the Department of Geology and Geophysics, LSU (Fig. 2.8), within a room designed to mitigate the effects of the Earth's magnetic field. The bridge was calibrated

using several standard magnetic salts and magnetite, and operates at a frequency of 5 kHz. The accuracy of the MS data was checked at the start of each day by analysing several in-house standard materials. Instrumental drift was monitored and corrected before every sample measurement using an internal reference count circuit within the susceptibility bridge. Data were reduced offline using an in-house data reduction software program and were corrected for blank contributions from the sample holder, which is diamagnetic. Three replicate measurements were made for each sample, which were then averaged and normalised to the sample mass (determined to ± 0.001 g using a Mettler Toledo PB303-S balance). All measurements are reported as mass-normalised susceptibilities.

Figure 2.8. The custom-built susceptibility bridge at LSU.

2.5. Stable isotope analyses ($\delta^{13}C$ and $\delta^{18}O$) of limestones

2.5.1. Overview

Carbon has two stable isotopes (^{12}C and ^{13}C) while oxygen has three (^{16}O, ^{17}O, ^{18}O). The small differences in mass between these isotopes subtly affect their chemical and physical properties, which leads to isotopic fractionation during chemical and physical processes (e.g. evaporation, condensation). This is the basis of stable isotope

geochemistry (Anderson & Arthur, 1983) and is why isotopic fractionation can be exploited to infer information about palaeoclimate (see section 2.5.4).

2.5.2. Stable isotope analyses of carbonates

All analyses were conducted using a Thermo Delta Plus continuous flow isotope ratio mass spectrometer (CF-IRMS) equipped with a Thermo GasBench II housed within the Department of Geology, Trinity College Dublin. The method entails samples being placed in sealed containers and reacted with concentrated phosphoric acid in an inert (helium) atmosphere, at a constant temperature (72 °C; section 2.5.5). The mixing of limestone sample and concentrated (100 %) phosphoric acid causes the following reaction:

$$CaCO_3\,(s) + H_3PO_4\,(l) \rightarrow HCaPO_4\,(s) + H_2O\,(l,g) + CO_2\,(g)$$

The equation is from Revesz *et al.* (2001).

The CO_2 and water vapour produced are entrained in a helium gas flow, which transfers the sample gases to the mass spectrometer. The water vapour is removed cryogenically, upstream of the mass spectrometer. Purified CO_2 passes into the mass spectrometer and is ionised by the source and sorted into a mass spectrum by the mass analyser (magnet). Masses 44 ($^{12}C^{16}O^{16}O$), 45 ($^{13}C^{16}O^{16}O$) and 46 ($^{12}C^{18}O^{16}O$) are measured simultaneously on the Faraday cup array, allowing sample ^{13}C / ^{12}C ratios (masses 45 / 44) and ^{18}O / ^{16}O ratios (masses 46 / 44) to be determined.

2.5.3. Delta notation

Stable isotope analyses are conventionally reported using the delta notation (δ) because it is easier to determine relative differences in isotopic ratios between two samples (an unknown and a standard) than the absolute isotopic ratio of an unknown sample (Sharp, 2007). Such relative differences provide sufficient information for palaeoclimatic applications. Sample isotopic ratios are hence measured and expressed relative to the corresponding isotopic ratios of a universal standard. Delta values for carbon and oxygen are defined as follows and have units of *per mille* (‰):

$$\delta^{13}C\,(‰) = \left[\frac{^{13}C/^{12}C_{sample}}{^{13}C/^{12}C_{standard}} - 1\right] \times 1000 \qquad \delta^{18}O\,(‰) = \left[\frac{^{18}O/^{16}O_{sample}}{^{18}O/^{16}O_{standard}} - 1\right] \times 1000$$

A positive δ value indicates that the sample isotopic ratio is greater ('heavier') than the corresponding ratio of the standard. The global reference standard for stable carbon and oxygen isotopic analyses of carbonates is the Vienna Pee Dee Belemnite (V-PDB) standard (Sharp, 2007). All δ values are thus cited with respect to the V-PDB value. Expressing analyses relative to this universal standard enables data from different samples and data determined in different laboratories to be compared against a common scale.

2.5.4. Carbon and oxygen isotopic variations in carbonate rocks

The measured isotopic composition of biogenic carbonate rocks represents the combination of primary environmental factors, biological (vital) effects, mineralogical considerations and post-depositional alteration processes such as diagenesis (Fig. 2.9). These factors are briefly discussed in subsequent sections. More exhaustive accounts of the processes controlling $\delta^{13}C$ and $\delta^{18}O$ variations in marine carbonates can be found in Anderson & Arthur (1983) and Marshall (1992).

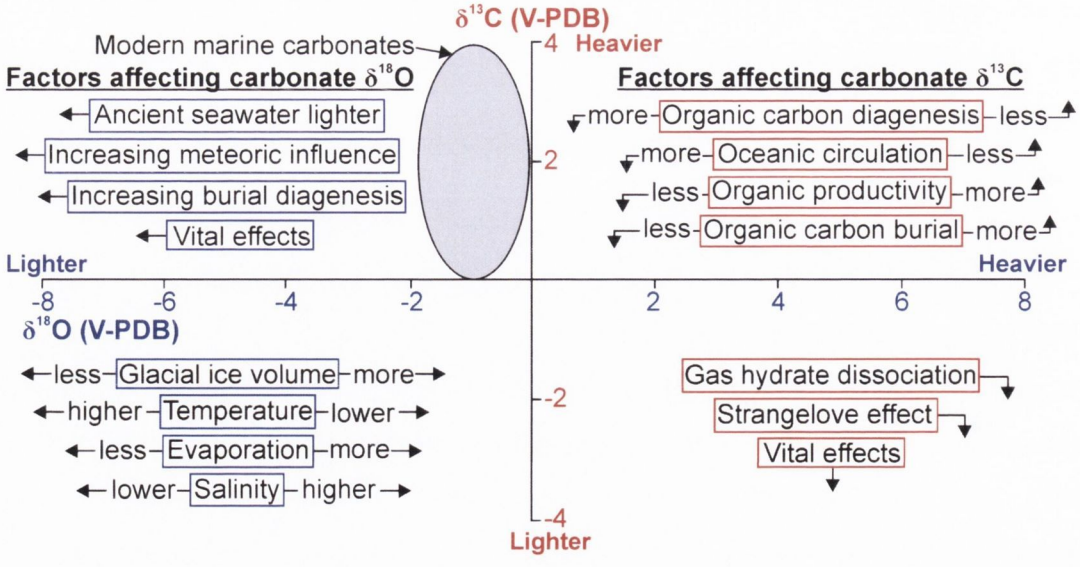

Figure 2.9. The main controls over the isotopic composition of carbonate rocks. The figure is redrawn and modified from Tucker *et al.* (2003). The Strangelove effect is the term given to shutdown of ocean productivity following a catastrophic event (e.g. bolide impact).

2.5.4.1. Environmental controls

The oxygen isotopic composition of marine carbonates reflects variations in sea water composition and temperature (Marshall, 1992). Variations in the $\delta^{18}O$ of ancient carbonates have been attributed to changing ice volume and temperature as well as local to regional hydrological factors (salinity, evaporation, meteoric runoff; Frank *et al.*, 2008). Published fractionation – temperature equations for calcite suggest $\delta^{18}O_{calcite}$ decreases by *c.* 1 ‰ for every 4 °C increase in sea water temperature (Marshall, 1992). Glacial ice preferentially sequesters ^{16}O, which consequently increases the $\delta^{18}O$ values of coexisting marine waters. It has been estimated that Pleistocene ice sheets at their maximum extent raised the $\delta^{18}O$ value of the oceans by 0.8 – 1.3 ‰ (Anderson & Arthur, 1983; references therein). It is difficult to isolate the effects of temperature from ice volume in carbonates precipitated during icehouse climates (such as the late Carboniferous) because decreasing temperatures and increasing ice volume generate $\delta^{18}O$ excursions of the same sense in marine carbonates.

In contrast to oxygen, carbon isotopic fractionation between dissolved inorganic carbon (DIC) and calcite is relatively insensitive to temperature (*c.* +0.035 ‰ per °C increase, based on Emrich *et al.*, 1970). The carbon isotopic composition of shallow water carbonates reflects the $\delta^{13}C$ of DIC in surface waters, which is a function of the rate of upwelling, rates of primary productivity, organic carbon burial and atmospheric CO_2 (Anderson & Arthur, 1983). Several processes have been suggested to generate short term (< 1 Myrs) $\delta^{13}C$ excursions within the geological record. For example, the oxidation of organic matter (Higgins & Schrag, 2006) and methane hydrate release (Dickens *et al.*, 1995) have both been suggested as possible causes of the rapid -2.5 ‰ $\delta^{13}C$ excursion in the marine carbon isotope record during the Palaeocene – Eocene Thermal Maximum (Higgins & Schrag, 2006).

2.5.4.2. Biological (vital) effects

Some organisms actively fractionate carbon and oxygen isotopes when secreting calcareous body parts, preferentially incorporating the light isotopes (^{12}C and ^{16}O), which is referred to as a vital effect (Wefer & Berger, 1991). Most extant species precipitate carbonates with oxygen isotopic compositions in or near equilibrium with

seawater, whereas disequilibrium precipitation is more common for carbon isotopes (Anderson & Arthur, 1983; Wefer & Berger, 1991).

2.5.4.3. Mineralogical controls

Different carbonate minerals exhibit slightly different relationships between temperature and oxygen isotopic fractionation (Wefer & Berger, 1991; Marshall, 1992). Additionally, different organisms precipitate different carbonate minerals which have varying resistance to diagenetic alteration, resulting in a preservation bias (Marshall, 1992).

2.5.4.4. Secondary (diagenetic) alteration

Diagenetic alteration occurs primarily through the dissolution of primary phases and precipitation of secondary phases in equilibrium with pore fluids (Sharp, 2007). The extent of diagenetic alteration is influenced by the composition of the carbonate sediments and pore fluids, water / rock ratios, the ambient temperature and the presence of organic matter (Algeo *et al.*, 1992; Marshall, 1992). Carbon isotopic compositions are generally considered to be more resistant to diagenetic alteration because of the greater mole fraction of carbon in a carbonate rock relative to pore fluids (Frank *et al.*, 2008) compared to oxygen, which occurs in roughly equal quantities in carbonate rocks and pore fluids (Frank *et al.*, 2008).

2.5.5. Methodology

Stable isotope analyses were performed on the same samples that were measured for their magnetic susceptibility characteristics. Carbonate powders were extracted from samples using a microdrill equipped with diamond-tipped drill bits, targeting homogeneous and micritic portions of the samples where possible.

All carbonate analyses were performed using the same instrumental set-up and methodology as reported by Chew *et al.* (2010), with one exception; eleven aliquots per sample were introduced to the continuous flow isotope ratio mass spectrometer (CF-IRMS) instead of the ten analysed by Chew *et al.* (2010). The following analytical protocol is summarised from Chew *et al.* (2010). Samples were analysed using a

Thermo Delta Plus CF-IRMS and a Thermo Gas Bench II equipped with a CTC Analytics CombiPal Autosampler, a thermostatic hot block and FMI acid pump, housed within the Department of Geology, Trinity College Dublin. Approximately 0.6 g of sample was weighed (absolute weight determined to ± 0.001 mg) into a clean, round-bottomed Exetainer® borosilicate glass vial that was subsequently capped with a new rubber septum and placed in the hot block. Samples were flush-filled with helium (100 ml / minute for 5 minutes) and then the double needle configuration of the autosampler was set up. Each sample was dosed with five drops of 100 % phosphoric acid by the acid needle and allowed to equilibrate for 91 minutes at 72 °C before the sample gas was siphoned off by the second (sample) needle. Eleven aliquots of CO_2 were introduced into the CF-IRMS. The first and last aliquots were discarded and results are averages of the remaining nine aliquots. The IAEA Co-1 marble standard was used to correct unknown sample analyses to primary standard (V-PBD) values. The accuracy of sample analyses and the stability of the CF-IRMS were checked by running repeat analyses of the in-house Cranford Dolomite standard interspersed with sample analyses; 52 analyses yielded $\delta^{13}C$ values (V-PDB) of -8.15 ± 0.11 ‰ (1σ) and $\delta^{18}O$ values (V-PDB) of -10.97 ± 0.08 ‰ (1σ).

2.6. XRD analysis of the diagenetically altered volcanic ash layer samples

XRD analysis was undertaken to characterise the bulk mineralogy of the bentonite and tonstein samples. The samples were dried prior to analysis at 80 °C and powdered by hand using an agate mortar and pestle. Approximately 0.5 g of sample material was loaded into a cavity mount and a glass slide was scraped across the surface of the mount twice to produce a flat surface suitable for analysis.

All XRD analyses were conducted using a Philips PW1720 X-ray generator coupled to a Philips PW1050/25 diffractometer, housed in the Department of Geology, Trinity College Dublin. Analyses were obtained using nickel filtered Cu kα radiation, a step size of 0.02 ° / second and operating conditions of 40 kV and 20 mA. Sample data were interpreted using the 'Traces' software program (from Hiltonbrooks Limited; http://www.xrays.u-net.com/Software.htm), which is equipped with the ICDD powder

diffraction database, and also using the 2θ diffraction data tables for common minerals of Chao (1969).

Within the XRD data it is possible to resolve several non-clay minerals, which are confirmed by the presence of multiple characteristic XRD peaks (Table 2.3). Only limited information about the clay mineralogy of these samples can be obtained from these analyses; it is possible to identify the presence of illite-mica, kaolinite and chlorite. In some analyses, the characteristic 10 Å peak for illite is notably shifted towards higher d-spacing values (*c.* 10 – 12 Å). This has been observed in other studies (e.g. Walkden, 1972) and attributed to the presence of mixed-layer clays (such as illite-smectite). It is not possible to definitely confirm the presence of mixed-layer clays from these XRD analyses and thus where the main illite-mica peak has noticeably shifted the probable occurrence of mixed-layer clays is noted.

Mineral	Characteristic peaks (degrees 2θ)
Calcite	23.0, 29.4, 36.0, 39.4, 43.2, 47.5†, 48.6, 57.4
Chlorite	6.3, 12.5, 18.7, 25.1
Illite-mica	8.8, 17.7, 26.6*
Kaolinite	12.3, 24.8
Quartz	20.8, 26.7*, 50.2
Pyrite	28.5, 33.0, 37.0, 40.8, 47.4†, 56.2

Table 2.3. Characteristic XRD peaks of minerals that commonly occur in the samples investigated. * peak overlap between illite-mica and quartz. † peak overlap between calcite and pyrite.

2.7. Whole-rock geochemistry of the diagenetically altered ash layer samples

52 diagenetically altered volcanic ash layer samples were analysed for their whole-rock geochemistry (major, trace and rare-earth elements). Additionally, three upper Visean limestone samples from the Namur-Dinant Basin, Belgium (Table 2.4) and two Namurian shale samples from the Pennine Basin, northern England (Table 2.4) were analysed for their whole-rock geochemistry, as control samples to provide geochemical constraints on the adjacent stratigraphy.

Sample	Lithology	Sampling locality	Elevation of sampling (m)
MAP 02-28	Bioclastic limestone	Lives-sur-Meuse, cliff section 2, Belgium (50.4686°N, 4.9285°E)	32.20 m (see Fig. 6.5)
MAP 03-02	Micritic limestone	Lives-sur-Meuse, cliff section 2, Belgium (50.4686°N, 4.9285°E)	38.00 m (see Fig. 6.5)
MAP 07-41	Bioclastic limestone	Anhée Sud, Belgium (50.2940°N, 4.8936°E)	15.85 m (see Fig. 6.10)
MAP 12/07/09	Shale	Vale of Edale, northern England (British Grid Ref: SK 1235 8595)	10 cm above bentonite B7
MAP 03/08/02	Shale	Vale of Edale, northern England (British Grid Ref: SK 1037 8512)	7 cm below bentonite B1

Table 2.4. Limestone and shale samples analysed for their whole-rock geochemistry.

Samples were crushed in a tungsten carbide jaw crusher to < 3 mm grain size and then dried at 105 °C overnight. Most samples (n = 42 bentonites and tonsteins; n = 3 limestones; n = 2 shales) were comminuted using a Resch planetary ball mill (model PM100) equipped with a 50 ml agate grinding jar. Some samples, including those containing significant pyrite, were ground to a powder using a TEMA tungsten carbide ring-and-puck mill to avoid unnecessary wear on the agate ball mill (n = 10). The use of a tungsten carbide mill and jaw crusher can potentially add small quantities of tungsten and cobalt to samples (e.g. Buhrke *et al.*, 1998). For this reason, tungsten concentrations are not discussed, while cobalt concentrations were not determined.

Whole-rock geochemical analyses (major, trace and rare-earth elements) were determined from 6 – 8 g of sample at OMAC laboratories, Loughrea, County Galway, using ICP-OES (for major elements) and ICP-MS (for trace and rare-earth elements). Samples were analysed following the OMAC laboratories BF ES/MS protocol, which involves fusing samples with lithium metaborate. The reproducibility of analyses was determined by duplicate sample analyses and was better than 10 % (2σ) except where analytes approached the limit-of-detection. The accuracy of the analyses and the stability of the ICP machines were monitored by analysis of in-house standard materials. Analytes below the limit of detection are arbitrarily assigned a value of half the limit of detection and are clearly labelled in the data table (Appendix 2 Table 1). Replicate analyses were averaged and these values are used in the interpretation.

2.8. Recalibration of legacy $^{40}Ar/^{39}Ar$ sanidine dates

Three Hess & Lippolt (1986) dates were recalibrated using the raw data presented in an earlier and more extensive paper (Lippolt *et al.*, 1984). Two dates are aliquots of a single tonstein horizon (tonstein 479; samples COT479/1 and COT479/2 in Hess & Lippolt, 1986), which are combined to produce an average date for tonstein 479. The third recalibrated date is from tonstein Z1 (sample COT-Z in Hess & Lippolt, 1986)

The recalibration process involves two steps: firstly, to recalibrate internal errors on the $^{40}Ar/^{39}Ar$ sanidine dates to make them comparable to U-Pb age uncertainties and secondly, to recalibrate the $^{40}Ar/^{39}Ar$ dates against recent estimates for the age of the monitor standard and the ^{40}K decay constant.

Recalculating the internal errors on the $^{40}Ar/^{39}Ar$ dates was undertaken to express them as the standard deviation of the weighted mean, which is how U-Pb internal errors are routinely expressed, rather than as the standard deviation of the population used by Lippolt *et al.* (1984) and Hess & Lippolt (1986), as discussed by Claoué-Long *et al.* (1995). This recalculation adjusts the date of sample COT479/1 to 319.4 ± 1.6 Ma (2σ). For sample COT479/2, the heating steps used by Hess & Lippolt (1986; steps 2 – 6) yield a plateau age with an unacceptably high MSWD (2.3) and a low probability-of-fit (< 0.05), and thus do not constitute a true plateau. Isoplot (Ludwig, 2003a) recommends the exclusion of step 2, which then yields a plateau age of 319.2 ± 1.2 Ma (2σ; MSWD = 0.76). This new plateau conforms to the definition criteria used by Isoplot (Ludwig, 2003a, p. 42), i.e. the plateau comprises more than 3 heating steps, includes more than 60 % of the total ^{39}Ar gas released, has no resolvable slope and yields a probability-of-fit greater than 0.05. Averaging the two aliquots of tonstein 479 yields a date of 319.3 ± 1.0 Ma (2σ). Recalculating the internal error on the tonstein Z1 date yields a date of 310.7 ± 1.6 Ma (2σ).

The procedure for recalibrating the $^{40}Ar/^{39}Ar$ sanidine dates against modern estimates for the age of the monitor standard and the ^{40}K decay constant is the same as that used by Gastaldo *et al.* (2009) and involves the recalculation of sample data against the astronomically-tuned Fish Canyon Tuff (FCT) sanidine standard (Kuiper *et al.*, 2008) via the McClure Mountain Hornblende (MMHb-1), which was the secondary standard

used by Hess & Lippolt (1986). Values for the absolute age of MMHb-1 and the intercalibration factor between MMHb-1 and FCT sanidine were derived from Renne *et al.* (1998). The astronomically-tuned FCT sanidine age of Kuiper *et al.* (2008) also incorporates the updated ^{40}K decay constant of Min *et al.* (2000), which is propagated into the recalibrated ages. Noah McLean's Microsoft Excel spreadsheet, downloaded from the Earthtime website (www.earth-time.org), was used to compute the recalibrated ages. The original age of MMHb-1 used is 519.2 Ma, which was determined by Hess & Lippolt (1986) against their primary standard (P-207 muscovite). Recalibrating the $^{40}Ar/^{39}Ar$ data in the manner described above yields a date of 323.7 ± 1.0 / 3.6 Ma (2σ; internal error / internal error plus standard and decay constant uncertainties) for tonstein 479 and 315.0 ± 1.6 / 3.7 Ma (2σ) for tonstein Z1.

2.9. Average periodicity calculations for sedimentary cycles

The periodicity calculations discussed in Chapters 3 and 5 were calculated using the method outlined below. The average periodicity of sedimentary cycles that occur between two bentonite horizons is calculated as:

$$\text{Average cycle periodicity (kyrs / cycle)} = \frac{\text{Time duration (kyrs)}}{\text{Number of cycles}}$$

The time duration between a pair of ash layers is:

$$\text{Time duration (Myrs)} = \text{Weighted mean } ^{206}Pb/^{238}U \text{ date of bentonite X (Ma)} - \text{Weighted mean } ^{206}Pb/^{238}U \text{ date of bentonite Y (Ma)}$$

The uncertainty of the calculated time duration is:

$$\text{Uncertainty } (\pm \text{ Myrs}) = \sqrt{\text{uncertainty on X date (Ma)}^2 + \text{uncertainty on Y date (Ma)}^2}$$

where date uncertainties are at the 95 % confidence level and exclude systematic uncertainties arising from isotopic tracer calibration and the ^{238}U decay constant (i.e. the ± X uncertainty level; section 2.3.5.2.5).

The uncertainty of the average cycle periodicity estimate arising from uncertainties in the time duration is calculated as:

$$\text{Uncertainty } (\pm \text{ kyrs}) = \left(\frac{1}{\text{no. of cycles}} \right) \times \text{uncertainty in time duration (kyrs)}$$

Between most of the bentonite pairs there is some ambiguity in the number of intervening sedimentary cycles. For the Belgian Visean calculations (section 3.4.1.2), there are some instances where cycles are locally subdivided into multiple cycles and it is not clear whether these localised 'extra' cycles represent regionally significant events that have not been recorded elsewhere or whether they are local phenomena. For the Namurian and Westphalian cycle calculations (sections 5.4.1.1.1 and 5.4.1.1.2), there is an uncertainty attached to the significance of several brackish faunal bands, which may or may not be of eustatic origin (further explained in section 5.4.1.1.1). The uncertainty in the number of cycles is factored into the calculations by calculating the average periodicity for a minimum and maximum number of cycles. Thus, for each stratigraphic interval, two periodicity estimates (each with uncertainty bounds arising from uncertainties in the time duration) are calculated. For convenience, these are then abbreviated to a single range of values.

2.9.1. Assumptions

There are a number of unavoidable assumptions within the periodicity calculations. Firstly, it is assumed that the CA-ID-TIMS dates approximate depositional ages for the altered ash layers (see section 2.3.5.3). Secondly, it is assumed that the time duration between two bentonite horizons resides entirely within the intervening stratigraphy, i.e. the bentonites are geologically instantaneous. It is also assumed that the sedimentary cycles between two bentonite horizons adhere to a common periodicity and that the record of cycles is complete.

Chapter 3

U-Pb zircon CA-ID-TIMS dates from Tournaisian and Visean western European diagenetically altered volcanic ash layers

3.1. Introduction

In this chapter, new U-Pb zircon CA-ID-TIMS dates from western European Tournaisian and Visean diagenetically altered volcanic ash layers (bentonites; defined in section 1.5.1) are presented. With the exception of one sample from an upper Tournaisian bentonite horizon in Ireland (sample 300; Fig. 3.1), all samples described in this chapter were collected from outcrop localities within the Namur-Dinant Basin of southern Belgium, where several bentonite layers occur interbedded with mid-to-upper Visean (Livian and Warnantian) shallow water, cyclically-bedded limestones. The U-Pb zircon CA-ID-TIMS data are presented in stratigraphic order (Fig. 3.1). In subsequent sections, the U-Pb zircon CA-ID-TIMS data are presented as concordia diagrams and weighted mean $^{206}Pb/^{238}U$ date plots. The sample data used in the construction of these diagrams can be found in Appendix 1 Table 1.

The new U-Pb zircon CA-ID-TIMS age constraints from the Belgian Visean bentonites are used to estimate the periodicity of sedimentary cycles that occur between the dated bentonite horizons (section 3.4.1.2). This is undertaken to establish whether these cycles yield periodicities compatible with Milankovitch cycles (see section 1.3), which have been shown to modulate recent Pleistocene glacial ice volume (Hays *et al.*, 1976), and thus evaluate whether there is evidence for these cycles being of glacio-eustatic origin. The new CA-ID-TIMS dates are also compared with existing, published Tournaisian and Visean isotopic age data (section 3.4.2). The implications that the new data have for the calibration of the Early Carboniferous (Mississippian) timescale are discussed in section 3.4.3.

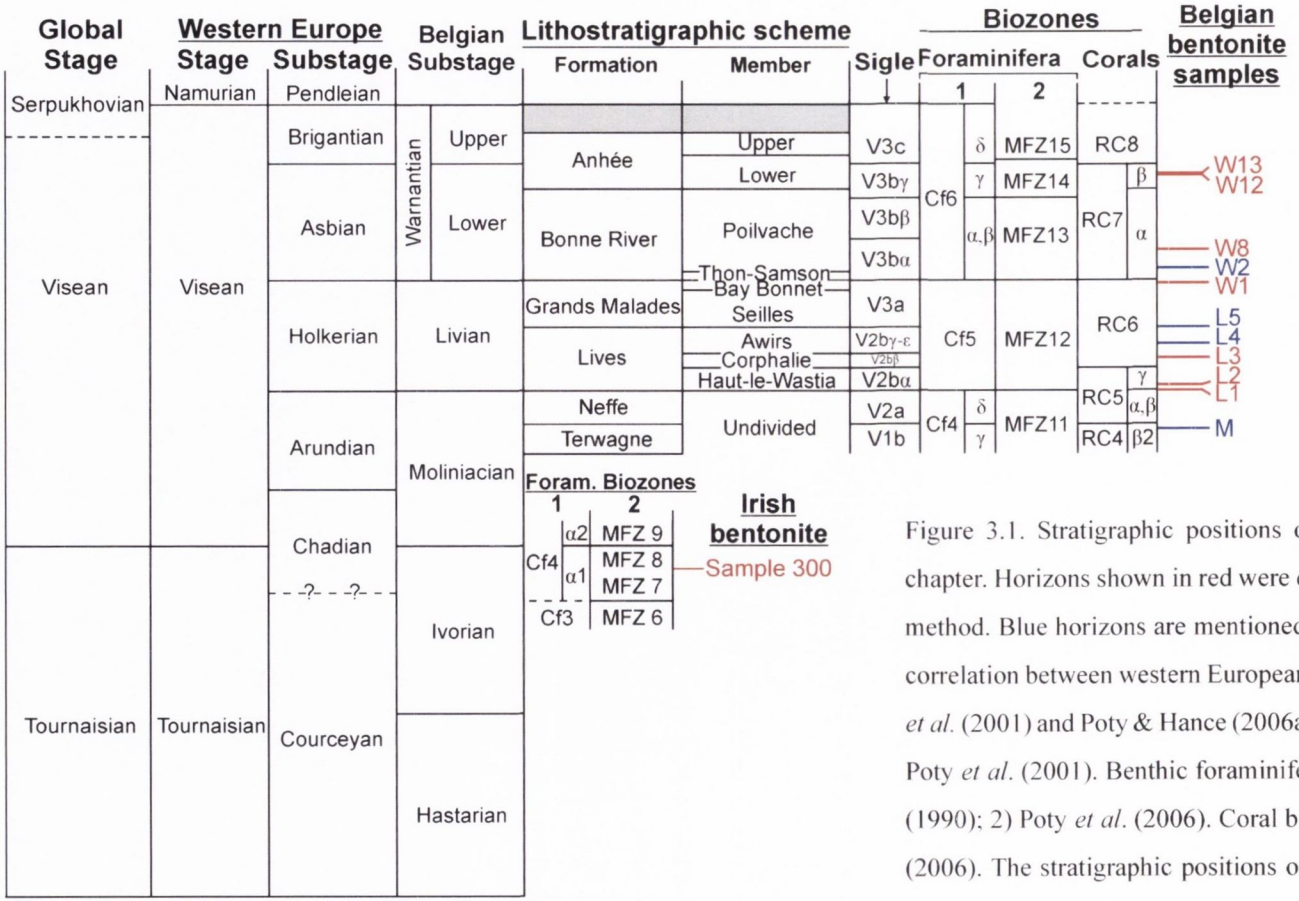

Figure 3.1. Stratigraphic positions of the bentonite layers discussed in this chapter. Horizons shown in red were dated using the U-Pb zircon CA-ID-TIMS method. Blue horizons are mentioned in the main text but were not dated. The correlation between western European and Belgian substages is based on Hance *et al.* (2001) and Poty & Hance (2006a, b). The lithostratigraphic scheme is from Poty *et al.* (2001). Benthic foraminifera biozones and subzones: 1) Conil *et al.* (1990); 2) Poty *et al.* (2006). Coral biozones and subzones are from Poty *et al.* (2006). The stratigraphic positions of Belgian bentonites are from Delcambre (1996) except L4, L5 (B. Delcambre, pers. comm., 2009) and W13 (personal observations). Sigles are the historical lithostratigraphic units (from Conil *et al.*, 1967). The grey area represents stratigraphic omission (see section 3.3.2.1).

3.1.1. Palaeogeographic setting of western Europe during Mississippian times

During Tournaisian and Visean times, western Europe lay at tropical latitudes, on the southern margin of Laurussia (see Fig.1.1). A regional palaeogeographic reconstruction for western Europe during early Carboniferous times is shown in Fig. 3.2. Belgium and Ireland are inferred to have lain in a narrow seaway, the remnants of which can be traced across western and central Europe, from Ireland to Germany. Also shown in Fig. 3.2 is the position of the Namur-Dinant Basin; most of the bentonites discussed in this chapter were sampled from this sedimentary basin.

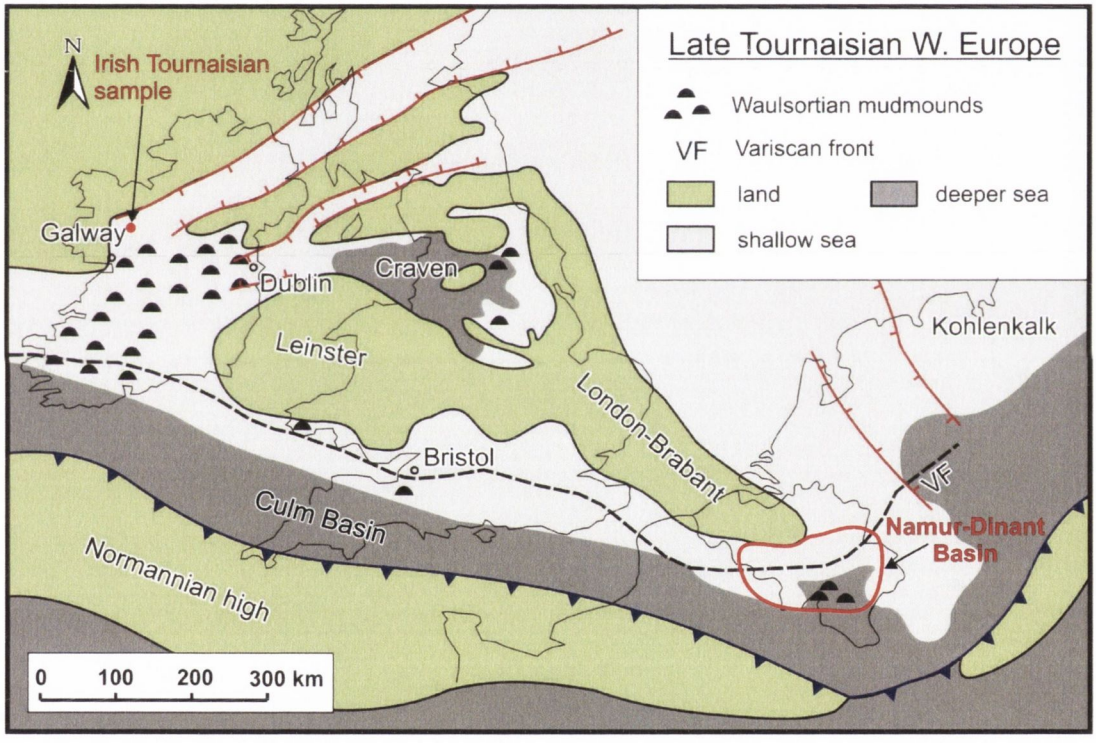

Figure 3.2. Palaeogeography of western Europe during the late Tournaisian. The Variscan Front is the present-day trace of the extent of Variscan deformation. The figure is reproduced from Devuyst *et al.* (2005).

3.2. Tournaisian Stage

3.2.1. Bentonite 300

A sample of this bentonite horizon was kindly provided by Paul Henry (Boliden Tara Mines Ltd.) and was obtained from an Irish drillcore (number 1680.2; drilled by

Boliden Tara Mines Ltd.) located near to Claremorris, County Mayo (Irish Grid Reference: M4763 6850). The bentonite horizon occurs at a depth of 300.90 – 300.95 m within the core and is interbedded with cherty limestones and shales that are considered to be laterally equivalent to the Waulsortian limestones (P. Henry, pers. comm., 2010). The biostratigraphic position of this horizon is not yet finalised; based on current data, this bentonite horizon is constrained to either the late MFZ 7 or the MZF 8 foraminifera biozones (G. Sevastopulo, pers. comm., 2011; Fig. 3.1). Conodonts may provide additional constraints on this horizon but this research is not sufficiently far along to be of use in this thesis. The sample of this bentonite horizon is blue-grey, poorly consolidated and exhibits a putty-like consistency. XRD analysis of sample material reveals the presence of illite-mica (probably occurring as mixed-layer clay), which is typical of K-bentonite horizons (e.g. Weaver, 1953; Trewin, 1968; section 1.5.1), together with feldspar and pyrite (Appendix 2 Table 2). Quartz is notably absent from this sample (Appendix 2 Table 2), which could signify a lack of detrital contamination within this bentonite horizon.

The zircons separated from this sample are euhedral to subhedral, comprising both whole crystals and fragments. The zircons are 50 – 350 μm in length and have high aspect ratios (*c.* 3 – 8; Fig. 3.3). The grains are relatively clear with few fractures or inclusions, although some grains contain melt inclusions. Petrographic observations under transmitted light show no obvious signs of xenocrystic inheritance.

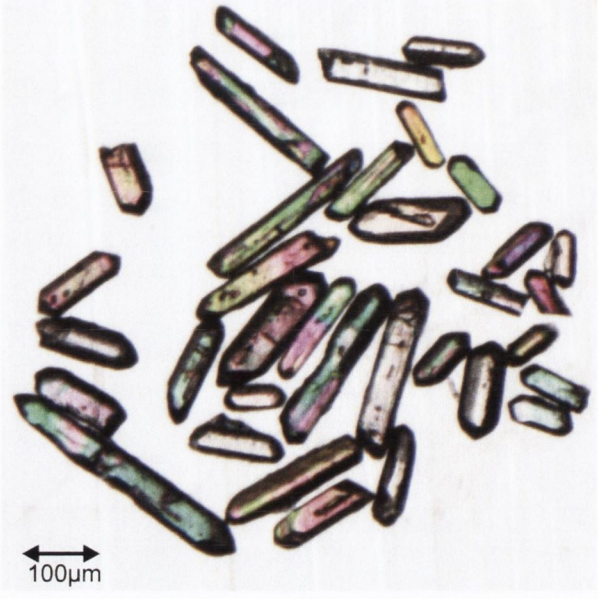

Figure 3.3. Zircons separated from bentonite 300 imaged under a binocular microscope equipped with an analyzer. The bright colours are interference colours.

Several elongate, euhedral grains were selected for U-Pb CA-ID-TIMS dating, the results of which are presented in Fig. 3.4 and in Appendix 1 Table 1.

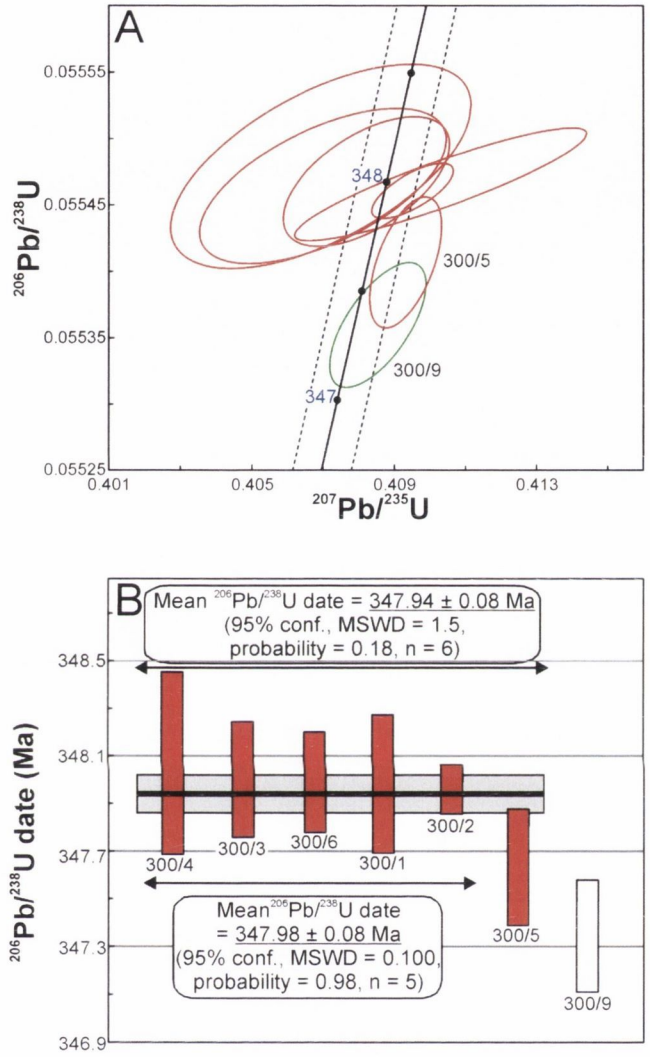

Figure 3.4. U-Pb zircon CA-ID-TIMS data from bentonite 300 illustrated as a Wetherill concordia diagram (A) and a weighted mean $^{206}Pb/^{238}U$ date plot (B). In plot A, the red and green error ellipses represent data points included in and excluded from the weighted mean date calculation shown at the top of plot B respectively. The solid black line in plot A is the concordia drawn using the decay constants of Jaffey *et al.* (1971). The dashed black lines drawn parallel to the concordia represent the uncertainty in the position of the concordia arising from uncertainties in the U decay constants. Blue numbers are concordant ages (in units of Ma). Error ellipses are drawn at the 2σ confidence level. In plot B, the grey band represents the uncertainty of the weighted mean (95 % confidence level). Box heights (representing date uncertainties) are drawn at the 2σ confidence level.

One analysis (300/10; Appendix 1 Table 1) is not illustrated in Fig. 3.4 because it is significantly older than all the other analyses ($^{206}Pb/^{238}U$ date of 520.59 ± 0.51 Ma, 2σ; Appendix 1 Table 1) and is very discordant. This grain likely contained a xenocrystic core that was not detected during hand-picking. Five analyses yielded overlapping and concordant dates (within analytical and decay constant uncertainties) which cluster at *c.* 348 Ma (Fig. 3.4). Two analyses (300/5, 9; Fig. 3.4) yielded younger dates: analysis 300/9 is significantly younger ($^{206}Pb/^{238}U$ date of 347.34 ± 0.23 Ma, 2σ; Appendix 1 Table 1) than the *c.* 348 Ma data cluster and does not overlap at the 2σ confidence level, whereas analysis 300/5 is slightly younger ($^{206}Pb/^{238}U$ date of 347.63 ± 0.25 Ma, 2σ; Appendix 1 Table 1) and partially overlaps (within analytical uncertainties) with the

c. 348 Ma cluster of analyses. The cluster of analyses at *c.* 348 Ma is interpreted to represent the eruption age of this sample. Analysis 300/9 is interpreted to reflect residual lead loss not completely removed by the chemical abrasion method. Analysis 300/5 may also contain an element of residual lead loss; however, its inclusion in the weighted mean $^{206}Pb/^{238}U$ date calculation does not significantly alter the calculated date, as illustrated in Fig. 3.4b. The weighted mean $^{206}Pb/^{238}U$ date of the six analyses, including 300/5 (red analyses in Fig. 3.4b), is 347.94 ± 0.08 Ma (95 % conf., MSWD = 1.5, p = 0.18) and this date is taken as approximating the eruption age of this bentonite.

3.3. Visean Stage

3.3.1. The Namur-Dinant Basin: an introduction

The Namur-Dinant Basin (also known as the Franco-Belgian Basin; Fig. 3.2 and Fig. 3.5) of southern Belgium lies within the northwestern part of the Rhenohercynian fold belt (Poty *et al.*, 2001). The basin initiated during Devonian times as two separate basins (the Namur Basin to the north and the Dinant Basin to the south) that were connected by early Carboniferous times (McCann *et al.*, 2008). The main structural feature of the basin is the Midi Fault, a major E-W trending Variscan thrust fault (Fig. 3.5) which separates the Brabant Para-autochthon to the north from the southern Ardenne Allochthon (Fig. 3.5; Poty *et al.*, 2001).

Mississippian carbonate strata crop out on both sides of the Midi Fault and these strata are inferred to have been originally deposited within the same sedimentary basin (Poty *et al.*, 2001). There are six sedimentation 'areas' recognised within the basin (Fig. 3.5; see Hance *et al.*, 2001, 2002, or Poty *et al.*, 2001, for details). These areas were coeval sites of deposition and were characterised by different sedimentation patterns during Tournaisian and early Visean times, when differential subsidence and Waulsortian mud mounds generated topographic irregularities (Hance *et al.*, 2006). From late Moliniacian times onwards, however, sedimentation within the basin became more uniform and lithostratigraphic units can readily be traced between the different sedimentation areas (Fig. 3.6).

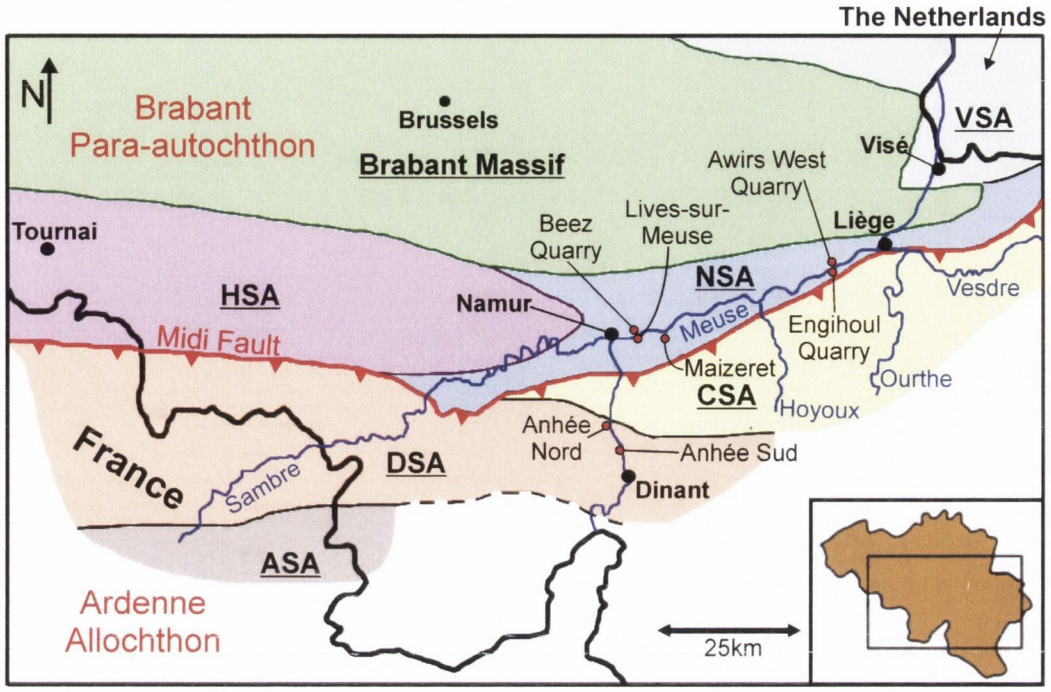

Figure 3.5. Sedimentation areas within the Namur-Dinant Basin (redrawn from Poty *et al.* 2001; not palinspastic). Black circles denote major towns and cities. Red circles denote localities mentioned in this chapter. ASA = southern Avesnois sedimentation area, CSA = Condroz sedimentation area, DSA = Dinant sedimentation area, HSA = Hainaut sedimentation area, NSA = Namur sedimentation area, VSA = Visé-Maastricht sedimentation area. The inset shows the area of Belgium covered by the main diagram.

The Namur-Dinant basin is inferred to have evolved from a south-facing homoclinal ramp during early Tournaisian times to a rimmed shelf during early Visean times and then into an aggrading carbonate platform during mid-to-late Visean times (Hance *et al.*, 2002). Similar changes in platform evolution have been reported from other Lower Carboniferous carbonate shelves within Great Britain (Walkden, 1987) and Ireland (Gallagher & Somerville, 2003), although the timing of such changes differs between these geographical areas. The transition from ramp to shallow-water carbonate platform sedimentation appears somewhat earlier in Belgium (Livian / Holkerian times; Hance *et al.*, 2002) than in Great Britain (early Asbian times; Walkden, 1987; Waters & Davies, 2006) and Ireland (late Asbian times; Gallagher & Somerville, 2003). Wright & Vanstone (2001) suggested that the transition from ramp to platform sedimentation within Great Britain was triggered by global climate change (i.e. the onset of major Carboniferous glaciation). However, additional factors (regional tectonics?) are required to account for the diachroneity of this transition within western Europe.

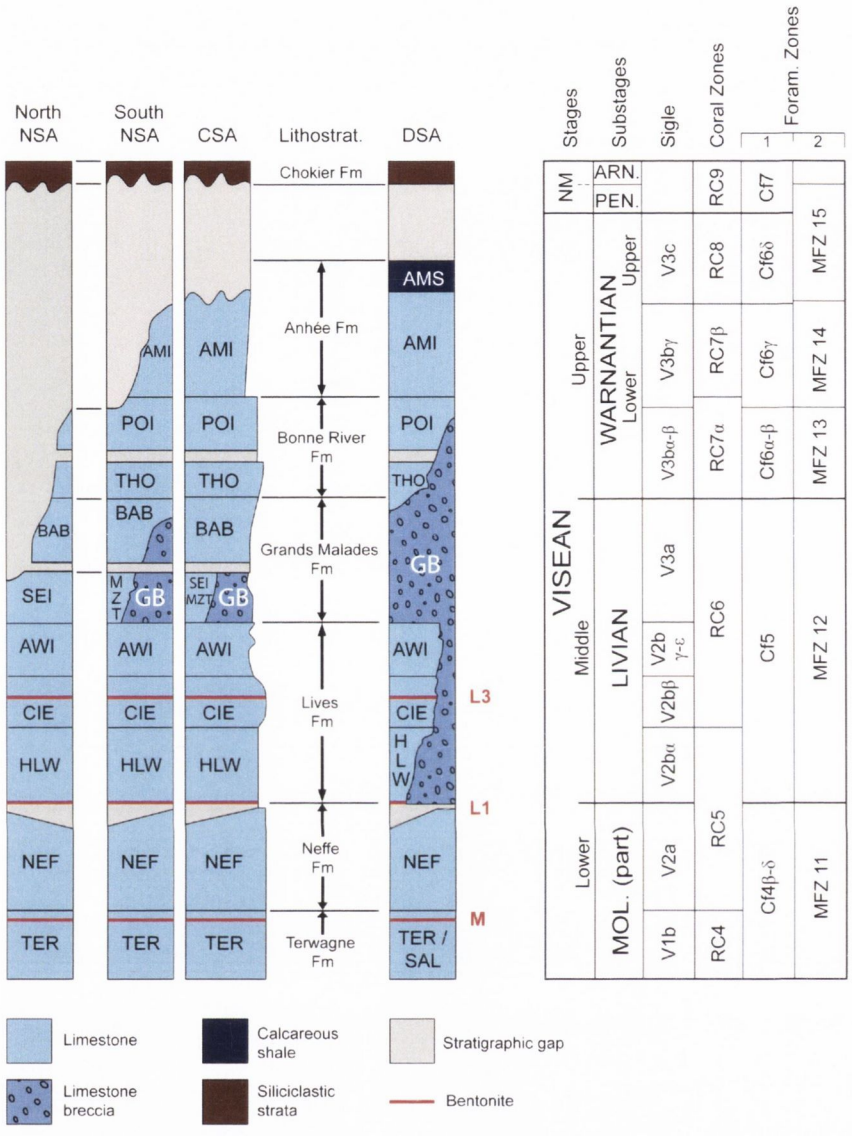

Figure 3.6. Lithostratigraphic framework of the Namur-Dinant Basin (after Poty *et al.*, 2001). The figure is schematic; no vertical scaling is implied. Lithostratigraphic unit abbreviations: AMI and AMS = Lower and Upper members of the Anhée Formation respectively; AWI = Awirs Member; BAB = Bay Bonnet Member; CIE = Corphalie Member; GB = Grande Brèche Viséenne; HLW = Haut-le-Wastia Member; MZT = Maizeret Member; NEF = Neffe Formation; POI = Poilvache Member; SAL = Salet Formation; SEI = Seilles Member; TER = Terwagne Formation; THO = Thon Samson Member. Fm = Formation. Chronostratigraphic unit abbreviations: ARN = Arnsbergian; MOL = Moliniacian; NM = Namurian; PEN = Pendleian. Foraminifera biozones and subzones: 1) Conil *et al.* (1990); 2) Poty *et al.* (2006). Coral biozones and subzones are from Poty *et al.* (2006). Sigles are historical lithostratigraphic units from Conil *et al.* (1967). The figure is redrawn from figures presented in Poty & Hance (2006a, b).

3.3.2. Mid-to-upper Visean stratigraphic framework of the Namur-Dinant Basin

The diagenetically altered volcanic ash layers sampled from the Namur-Dinant Basin in this study (section 3.3.3.2) occur within the mid-to-upper Visean (Livian and Warnantian substages). The chrono-, bio- and lithostratigraphic frameworks for this stratigraphic interval are described in the following sections.

3.3.2.1. Chronostratigraphy

The current chronostratigraphic framework for the Namur-Dinant Basin was proposed by Conil *et al.* (1977), who defined five stages within the Tournaisian and Visean series (the Hastarian, Ivorian, Moliniacian, Livian and Warnantian; Fig. 3.1). The basal stage boundaries were selected to correspond with major sedimentary cycles and significant biostratigraphic events (Paproth *et al.*, 1983a).

Three stages were defined within the Visean Series: the Moliniacian, Livian and Warnantian (Conil *et al.*, 1977), which are often informally referred to as the lower, middle (or mid) and upper Visean respectively. The Visean has recently been ratified as a global stage by the Subcommission on Carboniferous Stratigraphy of the International Commission on Stratigraphy (see Heckel & Clayton, 2006). Thus, the Molinacian, Livian and Warnantian, which were originally defined as stages, are now relegated to the status of regional substages (Heckel & Clayton, 2006). Accounts of the histories of these three substages and their current definitions are well summarised in Devuyst *et al.* (2006) and Poty & Hance (2006a, b) respectively; as such, only brief descriptions are presented here. The base of the Moliniacian Substage is currently defined by the earliest appearance of the benthic foraminifera *Eoparastaffella simplex* in the Salet road section (Dinant sedimentation area) and correlates with the base of the Visean (Devuyst *et al.*, 2006). The base of the Livian Substage is currently defined as at the base of the Banc d'Or de Bachant bed (= bentonite L1; Fig. 3.1) within the sections at Lives-sur-Meuse and is equated with the base of the Cf5 foraminifera zone of Conil *et al.* (1990) and the base of the MFZ12 foraminifera zone of Poty *et al.* (2006; Fig. 3.6). The base of the Warnantian Substage is defined as at the base of the Thon Samson Member of the Bonne River Formation (Poty & Hance, 2006b) and corresponds to the base of the Cf6

zone of Conil *et al.* (1990) and to the base of the MFZ13 zone of Poty *et al.* (2006; Fig. 3.6). The top of the Warnantian corresponds to the base of the Namurian Regional Stage (Poty & Hance, 2006b). There are problems with the current boundary stratoypes for the Livian and Warnantian substages, which are discussed in Poty & Hance (2006a, b) and briefly explained in sections 3.4.3.1 and 3.4.3.2.

The Warnantian is incompletely preserved within the Namur-Dinant Basin. The most complete records are preserved in the Dinant (DSA) and the Condroz (CSA) sedimentation areas (Fig. 3.5), where only the latest Warnantian strata are missing (Fig. 3.6; Poty & Hance, 2006b). However, to the north and east within the basin, the amount of stratigraphic omission increases and extends stratigraphically downwards; in the northern Namur sedimentation area (NSA), Namurian siliciclastic strata rest upon uppermost Livian to lowermost Warnantian strata (Fig. 3.6).

The Warnantian is informally divided into the lower and upper Warnantian. The base of the lower Warnantian is equated with the base of the Warnantian Substage, whereas the base of the upper Warnantian corresponds with the base of the Cf6δ subzone of Conil *et al.* (1990; Fig. 3.6) and the base of the RC8 coral biozone (Poty & Hance, 2006b). In order to simplify the descriptions of strata within the lower Warnantian in later sections and avoid terms such as 'lower lower Warnantian' strata, the lower and upper Warnantian are hereafter treated as formal stratigraphic divisions (and are capitalised accordingly). In support of this practice, these are long-established terms with precise and stable definitions.

The Moliniacian is correlated with the late Chadian and Arundian in Britain and Ireland (Devuyst *et al.*, 2006). The Livian is correlated with the British Holkerian Substage (Poty & Hance, 2006a). The Lower and Upper Warnantian are correlated with the British Asbian and Brigantian substages respectively (Poty & Hance, 2006b).

3.3.2.2. Biostratigraphy

The primary biostratigraphic controls on the Visean stratigraphy of the Namur-Dinant Basin are derived from benthic foraminifera (Conil *et al.*, 1990; Poty *et al.*, 2006). Conil *et al.* (1990) established a biostratigraphic scheme of foraminifera zones and subzones

for the Namur-Dinant Basin that has since been extended to other regions within Western Europe (e.g. Ireland; Somerville, 2008). Poty *et al.* (2006) have recently produced a revised foraminifera zonation for the Namur-Dinant Basin; however, most of their new zones, especially those within the mid-to-upper Visean, correspond closely to the zones and subzones already established by Conil *et al.*, (1990; see Somerville, 2008). Corals provide secondary biostratigraphic constraints (Poty *et al.*, 2006) but conodonts, which are important biostratigraphic markers earlier in the Carboniferous (Tournaisian), are of limited use in mid-to-late Visean times because they comprise only long-ranging taxa and are relatively scarce (Paproth *et al.*, 1983a; Poty *et al.*, 2006). The biostratigraphic framework for the Livian and Warnantian substages of the Namur-Dinant Basin is shown in Fig. 3.6.

3.3.2.3. Lithostratigraphy

The current lithostratigraphic framework for the Visean of the Namur-Dinant Basin is that of Poty *et al.* (2001). As already noted in section 3.3.1, the stratigraphy of the Livian and Warnantian substages is relatively uniform and the lithostratigraphic units can be traced laterally within the basin. The lithostratigraphy provides a means of correlation at a finer scale than can be attained using the existing biostratigraphic constraints. Additionally, several bentonite layers have also been directly correlated between multiple localities within the basin using zircon typology (Delcambre, 1989, 1996; section 3.3.3.1), providing a firm basis for correlation between the studied outcrop sections.

The following is intended as a brief overview of the Livian and Warnantian lithostratigraphy; for further details regarding the lithostratigraphic framework refer to Poty *et al.* (2001) and Poty & Hance (2006a, b). All unit thicknesses cited in this section are from Poty *et al.* (2001). The Livian and Warnantian substages are *c.* 124 –144 m and *c.* 121 m thick (respectively) and are characterised by shallow-water, cyclically-bedded carbonate facies. The sedimentary cycles comprise alternations of bioclastic and micritic limestones that are interpreted to represent shallowing-upwards cycles (Poty & Hance, 2006a, b; section 3.4.1.1). The Livian Substage includes the Lives and Grands Malades formations (Fig. 3.6). The Lives Formation is formally divided into three units: the Haut-le-Wastia, Corphalie and Awirs members (Poty *et al.*, 2001; Figs. 3.1 and 3.6).

The Haut-le-Wastia Member (*c.* 30 m thick) comprises metre-scale sedimentary cycles dominated by micrite. The Corphalie Member comprises a single, anomalously thick (*c.* 16 m) sedimentary cycle that contains roughly equal proportions of bioclastic limestones and micrite beds. The Awirs Member (*c.* 35 m thick) comprises metre-scale sedimentary cycles dominated by bioclastic limestones. The Grands Malades Formation includes the Maizeret and Seilles members, which are thought to be laterally equivalent (Poty & Hance, 2006a; Fig. 3.6), and the overlying Bay Bonnet Member (Fig. 3.6). Across a large area of the basin, the Grands Malades Formation is brecciated and is often referred to as the Grande Brèche Viséenne (Poty *et al.*, 2001; Fig. 3.6). Its brecciated origin is thought to be related to the dissolution of evaporite horizons and possibly also an early phase of Variscan shortening (Poty *et al.*, 2001; references therein). Where the Grands Malades Formation is not brecciated (e.g. in the north NSA; Fig 3.6), the Seilles Member (*c.* 35 – 55 m thick) comprises metre-scale sedimentary cycles dominated by bioclastic limestones (Poty & Hance, 2006a). The overlying Bay Bonnet Member comprises *c.* 8 m of thickly-bedded stromatolitic micrites (Poty & Hance, 2006a). The Warnantian stratigraphy is subdivided into the Bonne River Formation and the Anhée Formation (Poty *et al.*, 2001; Fig 3.6). The Bonne River Formation is formally subdivided into the Thon Samson (*c.* 8 m thick) and the Poilvache members (*c.* 80 m thick). Both are cyclically bedded; cycles in the Thon Samson Member are dominated by bioclastic limestones, whereas those of the Poilvache Member are dominated by micritic limestones. The Anhée Formation (*c.* 25m thick) is formally divided into Lower and Upper members (Poty *et al.*, 2001). The Lower Member comprises metre-scale parasequences dominated by bioclastic limestones, whereas the Upper Member comprises up to 8 m of argillaceous limestones and shales (both siliceous and calcareous; Poty *et al.*, 2001).

3.3.3. Diagenetically altered volcanic ash layers

Several clay-rich layers occur interbedded with the Visean limestones of the Namur-Dinant Basin and have been interpreted as diagenetically altered volcanic ash layers (e.g. Thorez & Pirlet, 1978; Anceau, 1992, 1996; Delcambre, 1996; section 3.3.3.1). In outcrop, these clay horizons typically exhibit sharp, recessed contacts with the surrounding limestones and thicknesses of 3 – 30 cm. Some horizons rest on undulose, palaeokarstic surfaces (Fig. 3.7). The bentonite layers are strongly coloured, ranging

from dark grey to orange-red (Fig. 3.8). Most of the bentonite horizons are poorly consolidated. At some localities, the horizons exhibit a putty-like texture where the clays have swelled in the presence of water (e.g. the L5 horizon at Awirs West Quarry). More rarely, some layers are well consolidated and exhibit blocky fracture patterns (e.g. bentonite W8 at Anhée Nord). The majority of bentonite horizons contain little internal structure (such as layering). The exception to this is the L4 horizon at Awirs West Quarry, which exhibits two clearly distinguishable layers (Fig. 3.8d).

Figure 3.7. Bentonite M at Lives-sur-Meuse. It is located within the Terwagne Formation (see Fig. 3.6), a limestone unit of late Molinician age that is characterised by peritidal facies (Devuyst *et al.*, 2006).

The colour and texture of a bentonite layer are not characteristic and can vary laterally between outcrop exposures of the same bentonite. Instead, the colour and texture of a bentonite seem to be related to the duration of time that the horizon has been exposed to the modern environment, as suggested previously by Delcambre (1996). This was demonstrated in this study by sampling the same bentonite horizons in recent and mature quarry sections (the active Engihoul Quarry and the disused Awirs West Quarry respectively). In Engihoul Quarry, the L3 and L4 horizons (Fig. 3.1) were dark grey, well consolidated and were similar in appearance to laminated mudstones (Fig. 3.8a, c).

In contrast, at the Awirs West Quarry (less than 2 km north of Engihoul Quarry; Fig. 3.5), a disused quarry that is now a popular rock climbing location, the laterally equivalent horizons were orange-brown (L4 is stratified with an orange and a black layer; Fig 3.8d) and exhibit a putty-like consistency. Delcambre (1996) noted that some of the Lower Warnantian bentonites exposed in the (then active) Transcar Quarry at Maizeret (location is labelled as Maizeret in Fig. 3.5) exhibited transformations in colour and texture over relatively short timescales (less than 5 years since the bentonite layers were first exposed) and suggested that the oxidation of pyrite was an important process during these transformations.

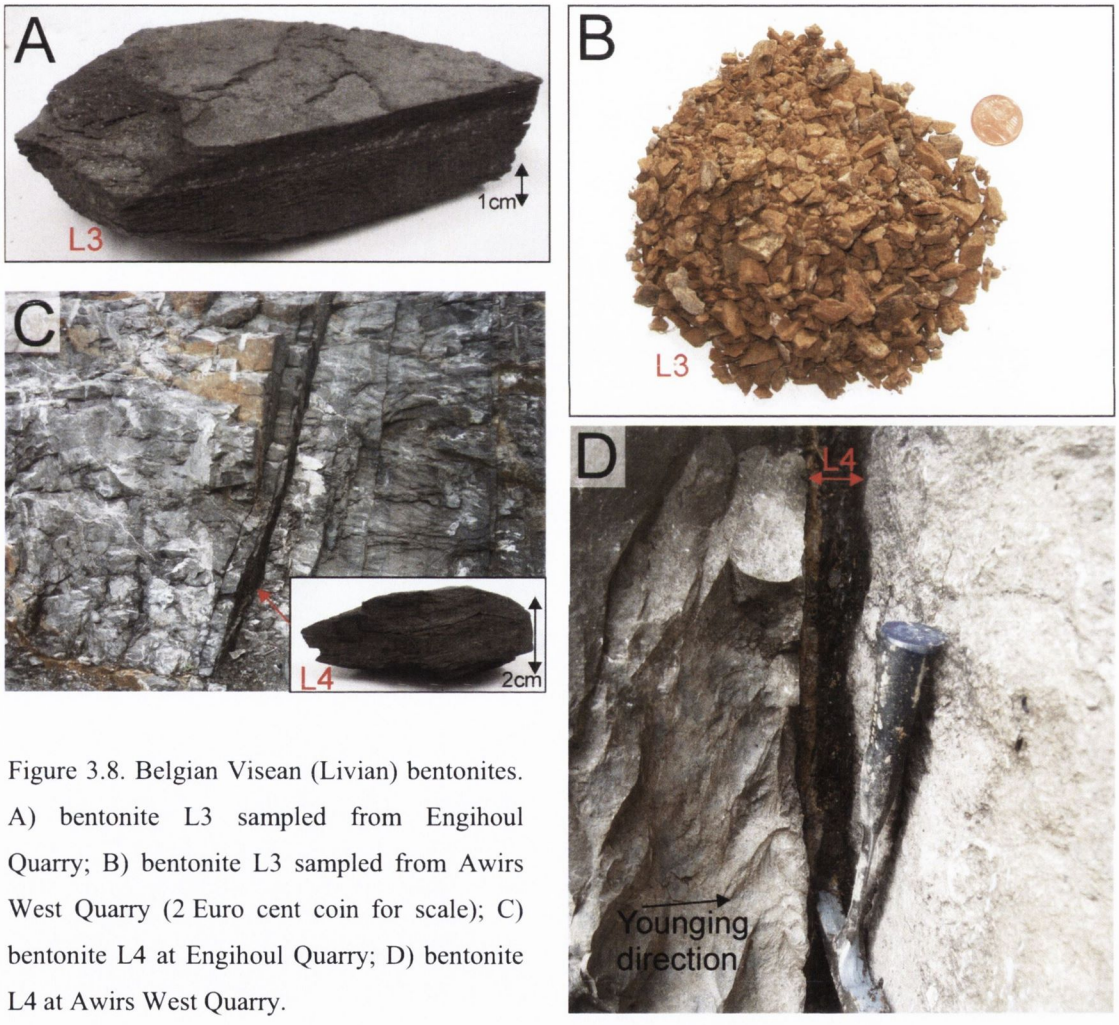

Figure 3.8. Belgian Visean (Livian) bentonites. A) bentonite L3 sampled from Engihoul Quarry; B) bentonite L3 sampled from Awirs West Quarry (2 Euro cent coin for scale); C) bentonite L4 at Engihoul Quarry; D) bentonite L4 at Awirs West Quarry.

3.3.3.1. Previous research

The composition of these clay-rich horizons is well studied (e.g. Thorez & Pirlet, 1978; Delcambre, 1989, 1996; Anceau, 1992, 1996). The clay mineralogy of these horizons

includes ordered illite / smectite mixed-layer clays, illite, sudoite, kaolinite and chlorite / smectite mixed-layers (Anceau, 1996; references therein). Most horizons comprise poly-mineralic clay mineral assemblages that vary laterally within a single layer and also between successive horizons (Thorez & Pirlet, 1978; Anceau, 1996). It has been suggested that the clay mineralogy could have formed through the combination of subaqueous weathering of volcanic ashes in a marine environment and subsequent diagenetic alteration (Thorez & Pirlet, 1978).

These horizons also contain a minor, coarser grained fraction comprising euhedral zircon and apatite, splintery quartz and partially altered biotite that are interpreted to represent volcanic phenocrysts (Thorez & Pirlet, 1978; Anceau, 1996; Delcambre, 1996). Some layers also contain possible pseudomorphs of earlier feldspar and biotite grains that have been subsequently replaced by kaolinite and chlorite (Thorez & Pirlet, 1978). Pyrite is abundant in some horizons and is thought to be of diagenetic origin (Anceau, 1996).

Delcambre (1989, 1996) investigated the typology (external morphology) of zircon grains within these clay horizons. Using the zircon typology scheme of Pupin (1980), Delcambre (1996) was able to correlate a number of these horizons between different outcrop localities, thus demonstrating that these bentonite layers are laterally continuous within the basin. Based on the clay mineral assemblages, the nature of the subordinate coarse fraction (phenocrysts) and lateral continuity arguments, these horizons have been interpreted to represent diagenetically altered volcanic ash layers (e.g. Thorez & Pirlet, 1978; Delcambre, 1996) and have been classified as K-bentonites (Thorez & Pirlet, 1978; Anceau, 1996; defined in section 1.5.1). Whole-rock geochemical analyses of samples taken from several of the Belgian Visean bentonites (documented in chapter 7) suggest that they were originally extracted from an evolved, possibly mildly alkaline (trachyandesitic) magmatic source (section 7.5.1).

3.3.3.2. Horizons dated by U-Pb zircon CA-ID-TIMS and sampling localities

While the mineralogy of these bentonite horizons is well established (section 3.3.3.1), there have been no previous attempts made to date any of these horizons using geochronology. This is unfortunate as isotopic dates from these biostratigraphically well

constrained horizons could potentially be used to improve the calibration of the Mississippian timescale. The work presented in the following sections is an attempt to address this.

The abundance of bentonite horizons within the stratigraphy (see Fig. 3.1) meant that only a subset of the altered volcanic horizons could be dated by the U-Pb CA-ID-TIMS method within the time constraints of this project. Included in this subset were bentonite horizons that occur close to important stratigraphic boundaries (e.g. bentonites L2, W1; Fig. 3.1) to provide temporal calibration of stratigraphic substages. Some bentonite horizons that are located between these stratigraphically important horizons were also sampled (e.g. bentonites L3, W8; Fig. 3.1) to enable average periodicities of cyclic sedimentation to be calculated over short stratigraphic intervals, thus enabling secular variations in cycle periodicities to be resolved.

During this PhD project, high-precision U-Pb zircon CA-ID-TIMS dating was undertaken on six Belgian Visean bentonite layers (L2, L3, W1, W8, W12, W13; Fig. 3.1). U-Pb zircon CA-ID-TIMS data from one additional bentonite (L1 horizon; Fig. 3.1) that were obtained prior to this PhD project (by M. Ovtcharova, University of Geneva and D. Chew, Trinity College Dublin) are also presented and discussed in subsequent sections because they are of relevance to the discussion (section 3.4) and have not been presented elsewhere.

U-Pb zircon CA-ID-TIMS dating was undertaken on samples of Livian bentonites L1, L2 and L3 (Fig. 3.1) that were collected from the two cliff sections exposed at Lives-sur-Meuse (Fig. 3.9). Bentonites L1 and L2 were sampled from section 1 at Lives-sur-Meuse (50.4692°N, 4.9291°E; all latitude / longitude coordinates are given relative to the WGS 84 datum), whereas bentonite L3 was sampled from section 2 at Lives-sur-Meuse (50.4686°N, 4.9285°E). Sedimentological logs of these cliff sections are presented in section 6.3.2 (Figs. 6.4 – 6.6). The base of the L1 bentonite at Lives-sur-Meuse currently defines the base of the Livian Substage in Belgium (Poty & Hance, 2006a; section 3.3.2.1). Bentonite L2 occurs within the lower part of the Haut-le-Wastia Member of the Lives Formation (Figs. 3.1 and 6.4) and bentonite L3 occurs within the upper part of the Corphalie Member of the Lives Formation (Figs. 3.1 and 6.5).

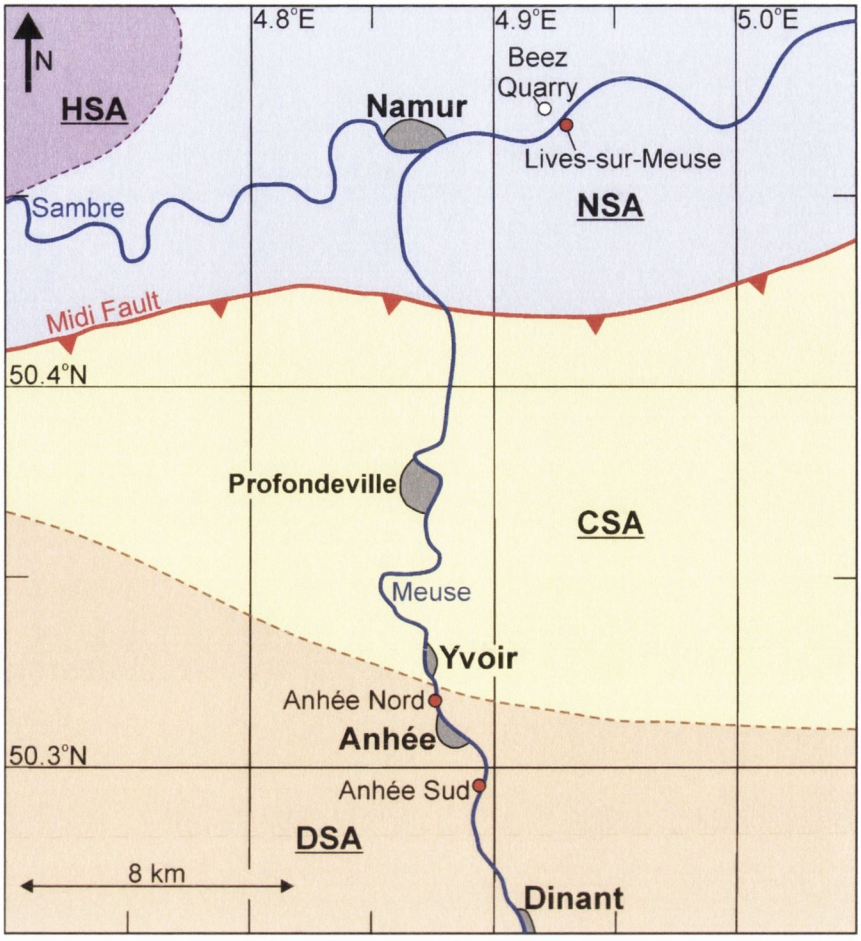

Figure 3.9. Map showing the sampling localities of the Livian and Warnantian bentonites dated using the U-Pb zircon CA-ID-TIMS method (indicated by red circles). Grey areas denote population centres. CSA = Condroz sedimentation area, DSA = Dinant sedimentation area, HSA = Hainaut sedimentation area, NSA = Namur sedimentation area. Sedimentation areas and the trace of the Midi Fault are schematic (redrawn from Poty *et al.*, 2001). The sedimentation areas are described further in section 3.3.1.

Bentonite horizons W1 and W8 (Fig. 3.1) were sampled from an ancient quarry section to the north of the village of Anhée, near Dinant (50.3170°N, 4.8760°E), which has been referred to as the Anhée Nord locality (Delcambre, 1996; Fig. 3.9) and Yvoir (Pirlet, 1968); the former name is used hereafter. Bentonite W1 is of latest Livian age, whereas the W8 bentonite is of early Early Warnantian age (Fig. 3.1). As W1 is of Livian age, it would be more accurate to describe it as an 'L' level. However, the existing bentonite nomenclature (from Delcambre, 1996) is well established and to rename this bentonite horizon would cause disruption to the existing nomenclature and may lead to confusion. Thus, the original designation of 'W1' is retained in this thesis. A sedimentological log

of the Anhee Nord section can be found in section 3.3.4.4 (Fig. 3.16) and also in section 6.4.3 (Fig. 6.9).

Two further bentonite horizons, one corresponding to the W12 horizon of Delcambre (1996) and a second previously unreported layer (herein named W13) were collected from a disused quarry section (Watrisse Quarry) to the south of the village of Anhée, at a locality known as Anhée Sud (Pirlet, 1968; Delcambre, 1996; Fig. 3.9; 50.2940°N, 4.8936°E). Both bentonite layers are of late Early Warnantian age and occur within the Lower Member of the Anhée Formation (Figs. 3.1 and 6.10). Data from these bentonites are presented in stratigraphic order (Fig. 3.1) in subsequent sections.

3.3.4. U-Pb zircon CA-ID-TIMS age constraints: Livian bentonite layers

3.3.4.1. Bentonite L1 (also known as the Banc d'Or de Bachant)

This bentonite horizon was dated prior to this PhD project as a proof-of-concept pilot study that such horizons could yield high-precision isotopic dates using the U-Pb zircon CA-ID-TIMS method. U-Pb zircon CA-ID-TIMS dating of grains from L1 at Lives-sur-Meuse was undertaken by M. Ovtcharova (University of Geneva) and D. Chew (Trinity College Dublin). The results from CA-ID-TIMS dating of this layer are presented here because they are not published elsewhere and are of relevance to the other bentonite horizons dated during this PhD project.

At Lives-sur-Meuse, bentonite L1 comprises a single, orange, poorly consolidated, *c.* 25 cm thick, recessive layer that is located at the boundary between the Neffe and Lives Formations (Fig. 3.1). It has an undulose, erosive lower boundary, which is consistent with prolonged emergence and thus suggests that there is a stratigraphic gap beneath the L1 bentonite in the Livian boundary stratotype.

XRD analysis of material from the L1 horizon at Lives-sur-Meuse suggests the presence of illite-mica (Appendix 2 Table 2), which would account for the high potassium concentrations of this sample (8.20 % K_2O; determined by ICP-OES; Appendix 2 Table 1). The zircon separate from this horizon comprises predominantly euhedral to

subhedral grains of 50 – 280 μm length and aspect ratios of 1.5 – 4. Some grains contain oscillatory zonation that is visible under a petrographic microscope. Fractures and inclusions are common within grains; melt inclusions orientated parallel to the c-axis and euhedral apatite inclusions can be identified. Some grains contain obvious inherited cores.

Several single grains were analysed using the U-Pb CA-ID-TIMS method, the results of which are illustrated in Fig. 3.10 and are presented as a data table in Appendix 1 Table 1.

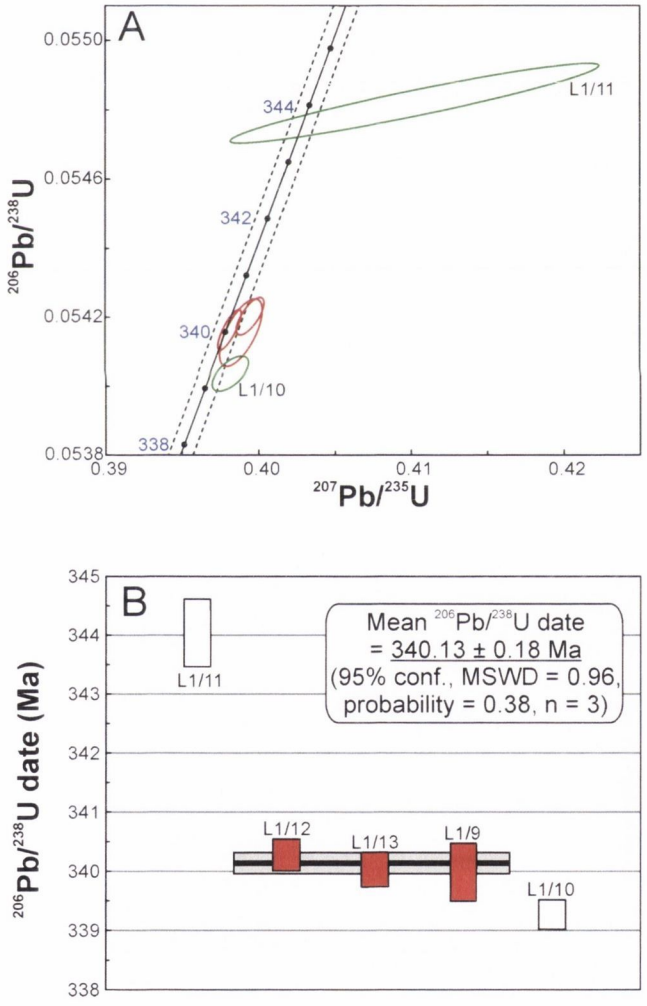

Figure 3.10. U-Pb zircon CA-ID-TIMS data from bentonite L1 illustrated as a Wetherill concordia diagram (A) and a weighted mean $^{206}Pb/^{238}U$ date plot (B). In plot A, the red and green error ellipses represent data points included in and excluded from the weighted mean calculation shown in plot B respectively. The solid black line in plot A is the concordia drawn using the decay constants of Jaffey *et al.* (1971). The dashed black lines drawn parallel to the concordia represent the uncertainty in the position of the concordia arising from uncertainties in the U decay constants. Blue numbers are concordant ages (in units of Ma). Error ellipses are drawn at the 2σ confidence level. In plot B, the grey band represents the uncertainty of the weighted mean (95 % confidence level). Box heights (representing date uncertainties) are drawn at the 2σ confidence level.

One data point is significantly older than the rest (L1/11; Fig. 3.10; Appendix 1 Table 1) and is interpreted to represent an inherited grain. Three analyses (red analyses in Fig. 3.10) overlap within analytical uncertainties and are interpreted to represent the eruption

age of this horizon. One analysis (L1/10; Fig. 3.10; Appendix 1 Table 1) is considerably younger than the three overlapping analyses (it only overlaps marginally at the 2σ confidence level). This analysis is inconsistent with the U-Pb data obtained from the overlying L2 horizon (section 3.3.4.2) and is interpreted to contain residual lead loss not completely removed by the chemical abrasion method. The weighted mean $^{206}Pb/^{238}U$ date of the three overlapping analyses is 340.13 ± 0.18 Ma (95 % conf., MSWD = 0.96, probability = 0.38; Fig. 3.10b) and this date is taken to approximate the eruption age of this bentonite layer.

3.3.4.2. Bentonite L2

Delcambre (1996) noted that this bentonite horizon was encountered more infrequently within the Namur-Dinant Basin compared to the L1 and L3 horizons. The L2 horizon was not originally reported by Delcambre (1996) from Lives-sur-Meuse. However, there is a conspicuous orange, clay-rich and recessive horizon at this locality (Fig. 3.11) that occurs at a comparable stratigraphic level to the L2 horizon reported by Delcambre (1996) from the nearby Beez Quarry (Fig. 3.12; the location of Beez Quarry is shown in Fig. 3.9; = 50.4735°N, 4.9211°E).

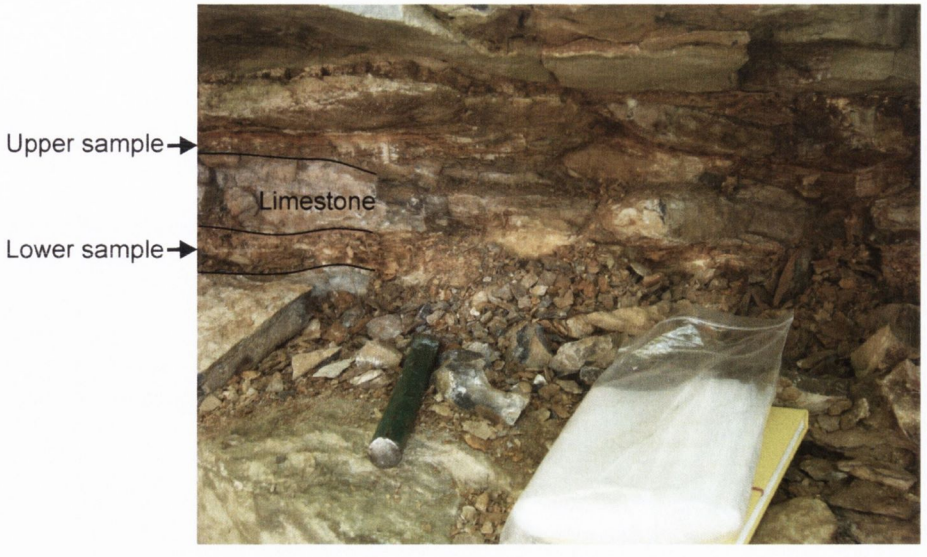

Figure 3.11. Bentonite L2 (?) at Lives-sur-Meuse.

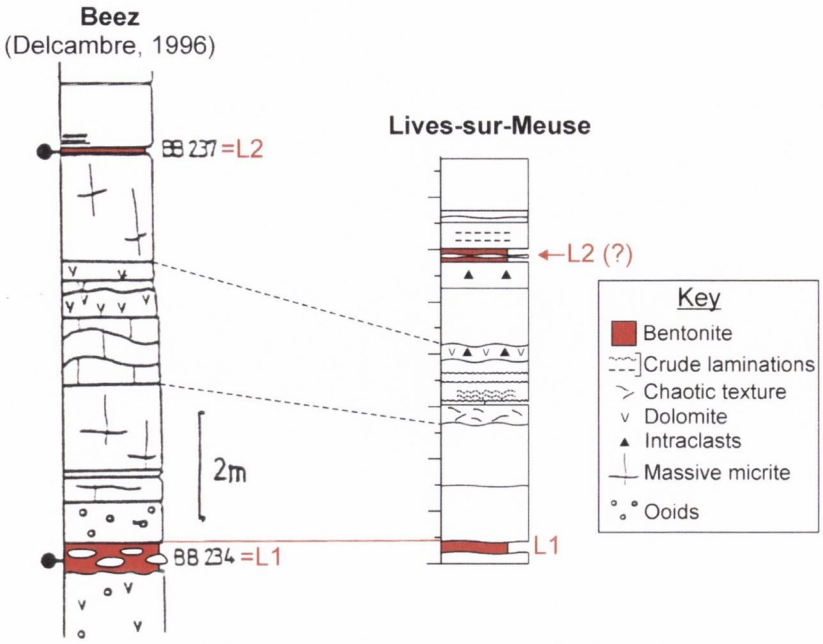

Figure 3.12. Logs of the sections exposed at Beez Quarry (from Delcambre, 1996) and Lives-sur-Meuse. The logs are of the same scale. The strata between the bentonite layers are almost exclusively micritic limestones.

At Lives-sur-Meuse, this horizon occurs in the lower part of the Haut-le-Wastia Member, *c.* 5.4 m above the L1 horizon. The horizon is *c.* 25 cm thick, orange-brown and contains thin lenses of limestone (Fig. 3.11). Two samples were collected from this horizon (lower and upper samples in Fig. 3.11). Abundant euhedral zircon grains were separated from the lower sample, whereas the upper sample yielded very few zircon grains.

XRD analysis of sample material from this bentonite horizon suggests the presence of illite-mica and goethite (Appendix 2 Table 2), which could account for the relatively high concentrations of K_2O and Fe_2O_3 (6.66 % and 6.69 % respectively; determined by ICP-OES; Appendix 2 Table 1) observed in this sample.

The zircon separate from the lower sample comprises relatively coarse (100 – 400 μm in length), predominantly euhedral grains with aspect ratios of *c.* 2 – 4.5. A few grains contain radial fractures and possible xenocrystic cores. Fracturing, oscillatory zonation and euhedral apatite inclusions are abundant in grains of this sample (Fig. 3.13). The latter two features were suggested by Delcambre (1996) to be characteristic of the L2

horizon. On the basis of the available data it seems likely that this horizon at Lives-sur-Meuse is the L2 bentonite of Delcambre (1996).

Figure 3.13. A photomicrograph of zircon grains separated from the L2 (?) horizon at Lives-sur-Meuse. The bright colours are interference colours.

U-Pb zircon CA-ID-TIMS dating was undertaken on grains from the lower sample of bentonite L2, the results of which are presented in Fig. 3.14 and in Appendix 1 Table 1. All analyses are equivalent and concordant within analytical and decay constant uncertainties (Fig. 3.14). The weighted mean $^{206}Pb/^{238}U$ date of all analyses is 339.89 ± 0.06 Ma (95 % conf., MSWD = 0.79, probability = 0.56, n = 6; Fig. 3.14b) and this date is taken to approximate the eruption age of this bentonite horizon.

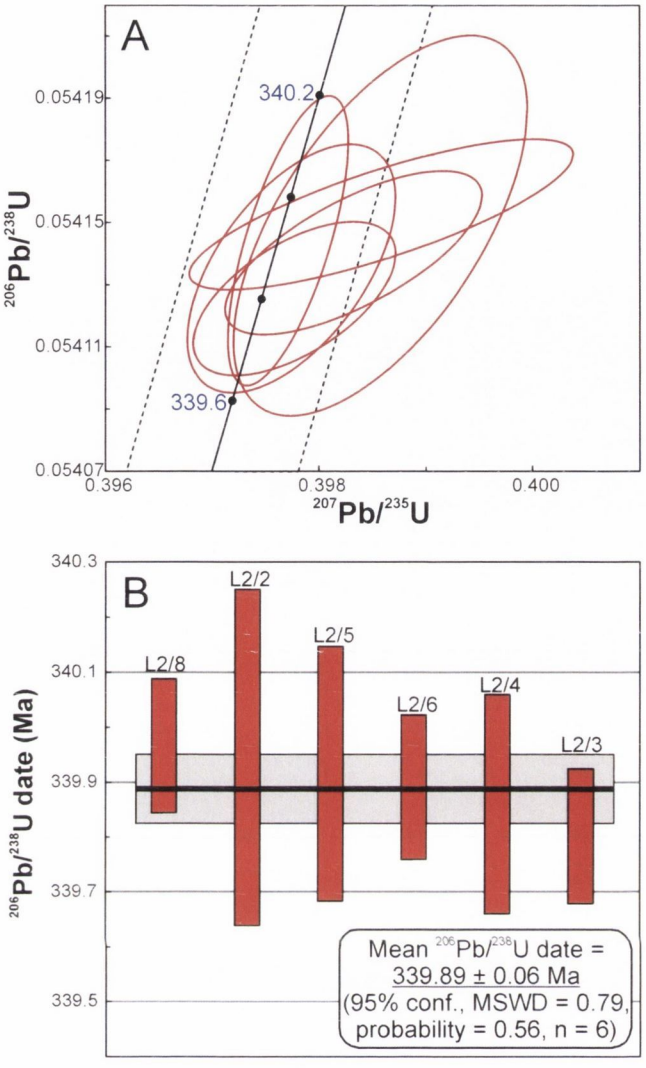

Figure 3.14. U-Pb zircon CA-ID-TIMS data from bentonite L2 illustrated as a Wetherill concordia diagram (A) and a weighted mean $^{206}Pb/^{238}U$ date plot (B). The solid black line in plot A is the concordia drawn using the decay constants of Jaffey *et al.* (1971). The dashed black lines drawn parallel to the concordia represent the uncertainty in the position of the concordia arising from uncertainties in the U decay constants. Blue numbers are concordant ages (in units of Ma). Error ellipses are drawn at the 2σ confidence level. In plot B, the grey band represents the uncertainty of the weighted mean (95 % confidence level). Box heights (representing date uncertainties) are drawn at the 2σ confidence level.

3.3.4.3. Bentonite L3

L3 is observed at numerous localities across the Namur-Dinant Basin (Delcambre, 1996) and always occurs within the upper, micritic portion of the Corphalie Member of the Lives Formation (Fig. 3.1; Fig. 3.6). At Lives-sur-Meuse, bentonite L3 occurs 13.9 m above the base of the Corphalie Member and is 10 cm thick, orange and poorly consolidated (Fig. 3.15).

XRD analysis of material from the L3 horizon at Lives-sur-Meuse suggests the presence of illite-mica (probably occurring as a mixed-layer clay), calcite, chlorite, kaolinite and quartz (Appendix 2 Table 2). The occurrence of calcite is consistent with the high CaO concentrations in this sample (6.26 %; determined by ICP-OES; Appendix 2 Table 1) relative to the L1 and L2 horizons (0.42 % and 1.20 % CaO respectively; Appendix 2

Table 1). This horizon is less enriched in potassium than the L1 and L2 horizons at Lives-sur-Meuse (2.60 % K_2O; Appendix 2 Table 1). This is probably due to the greater abundance of kaolinite and calcite (and therefore lower abundance of illite-mica) in this sample.

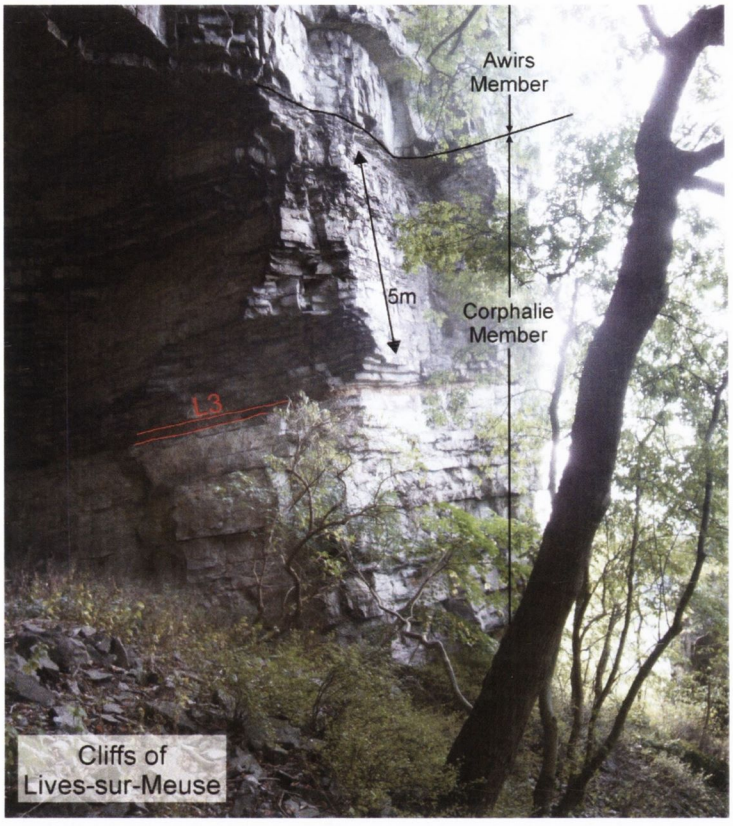

Figure 3.15. The L3 bentonite horizon at Lives-sur-Meuse.

The sample of L3 from Lives-sur-Meuse yielded euhedral to subhedral zircon grains (in roughly equal proportions) of 100 – 200 μm length that exhibit small aspect ratios (*c.* 1.5 – 3). Oscillatory zonation is visible in several grains under a petrographic microscope. Some grains contain fractures and / or inclusions (melt and euhedral apatite inclusions are recognisable). A few grains contain possible inherited cores surrounded by radial fractures.

Euhedral grains were hand picked for analysis by the U-Pb CA-ID-TIMS method, the results of which are presented in Fig. 3.16. Sample data can be found in Appendix 1 Table 1. The data show some dispersion, i.e. not all the analyses overlap within analytical uncertainties at the 2σ confidence level. There are five analyses that overlap within analytical uncertainties (red ellipses in Fig. 3.16), four slightly older analyses

(L3/2, 4, 6, 13; Fig. 3.16; Appendix 1 Table 1) and one analysis which is comparatively young (L3/10; Fig. 3.16). The cluster of five analyses that are equivalent and concordant within analytical and decay constant uncertainties are interpreted as representing the youngest magmatic population in this sample. The four slightly older grains are interpreted to represent antecrystic grains (*sensu* Miller *et al.*, 2007; section 2.3.2.3). These grains are excluded from the weighted mean date calculation because they do not represent the youngest concordant age population within the sample. Analysis L3/10 is significantly younger than all other analyses and is tentatively attributed to residual lead loss; therefore, it is also excluded from the weighted mean calculation. The weighted mean $^{206}Pb/^{238}U$ date of the five concordant and equivalent analyses is 338.28 ± 0.09 Ma (95 % conf., MSWD = 2.1, probability = 0.075; Fig. 3.16b) and this date is taken to approximate the eruption age of this bentonite horizon.

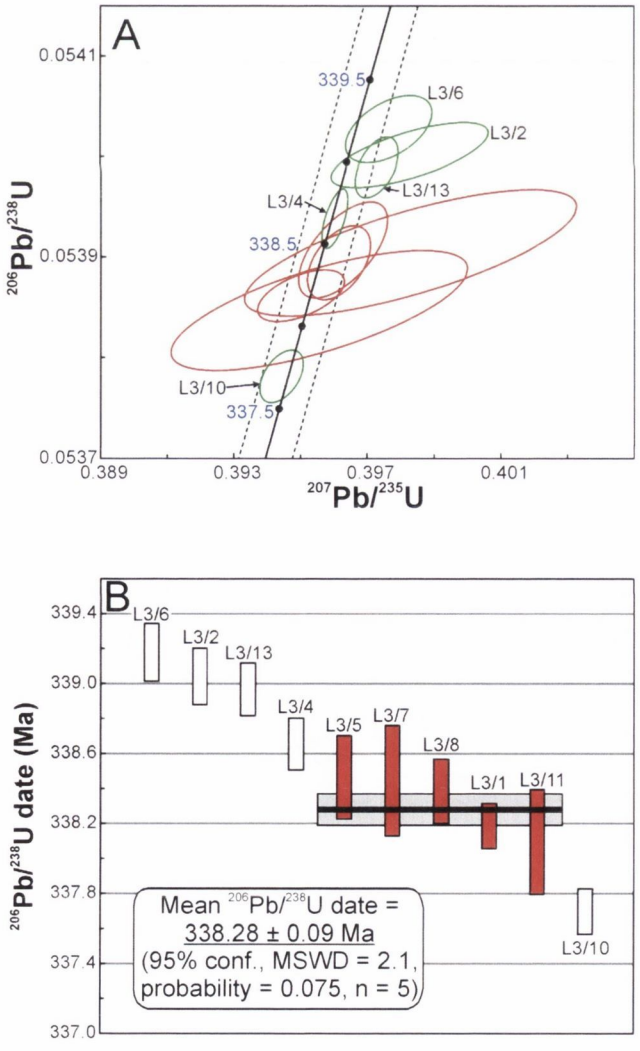

Figure 3.16. U-Pb zircon CA-ID-TIMS data from bentonite L3 illustrated as a Wetherill concordia diagram (A) and a weighted mean $^{206}Pb/^{238}U$ date plot (B). In plot A, the red and green error ellipses represent data points included in and excluded from the weighted mean calculation shown in plot B respectively. The solid black line in plot A is the concordia drawn using the decay constants of Jaffey *et al.* (1971). The dashed black lines drawn parallel to the concordia represent the uncertainty in the position of the concordia arising from uncertainties in the U decay constants. Blue numbers are concordant ages (in units of Ma). Error ellipses are drawn at the 2σ confidence level. In plot B, the grey band represents the uncertainty of the weighted mean (95 % confidence level). Box heights (representing date uncertainties) are drawn at the 2σ confidence level.

3.3.4.4. Bentonite W1

The W1 bentonite horizon was recognised by Delcambre (1996) from two localities within the Namur-Dinant Basin (Transcar Quarry, Maizeret and Anhée Nord; Fig. 3.5) using zircon typology. Within the Transcar Quarry at Maizeret, the W1 horizon occurs within the Bay Bonnet Member of the Lives Formation, *c.* 4 m below the base of the Thon-Samson Member (Bonne River Formation) and the base of the Warnantian Substage (Poty & Hance, 2006b). Unfortunately, the Maizeret section is no longer accessible and the W1 horizon was instead sampled from the Anhée Nord locality, where it rests upon the Grande Brèche Viséenne (Fig. 3.17).

XRD analysis of material from the W1 horizon at Anhée Nord suggests the presence of illite-mica (probably occurring as a mixed-layer clay), calcite, chlorite, quartz and possibly kaolinite (Appendix 2 Table 2). Whole-rock geochemical analysis of the W1 horizon (determined by ICP-OES/MS) shows that it contains greater MgO concentrations than the 'L' horizons discussed in previous sections (5.34 % MgO *c.f.* 1 – 2 % for L1 – L3 at Lives-sur-Meuse; Appendix 2 Table 1). The presence of a magnesium-rich chlorite phase (e.g. sudoite or clinochlore), which have been reported previously from bentonite horizons within the Anhée Nord section (Anceau, 1992), could account for the high magnesium concentrations. This sample also contains a substantial amount of calcium (9.23 % CaO; Appendix 2 Table 1), which can be attributed to the presence of calcite in this sample.

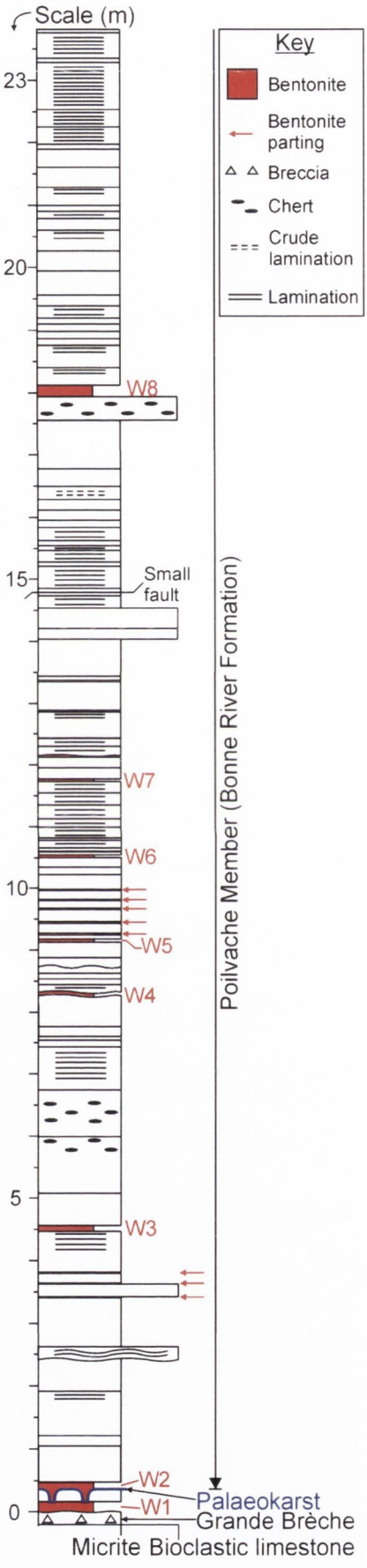

Figure 3.17. Log of the outcrop section exposed at Anhée Nord.

The zircon separate from this horizon comprises mostly euhedral to subhedral zircon grains (80 – 280 μm in length) with aspect ratios of *c.* 2 – 4, although rare euhedral, elongate grains (aspect ratios up to 6) are also present. Most grains are heavily fractured and / or contain visible oscillatory zonation. Some grains contain a few radial fractures which may indicate the presence of small cores; however, no obvious inherited cores were identifiable.

Euhedral grains were hand picked for U-Pb CA-ID-TIMS analysis, the results of which are illustrated in Fig. 3.18. U-Pb zircon CA-ID-TIMS data from bentonite W1 are also presented in Appendix 1 Table 1.

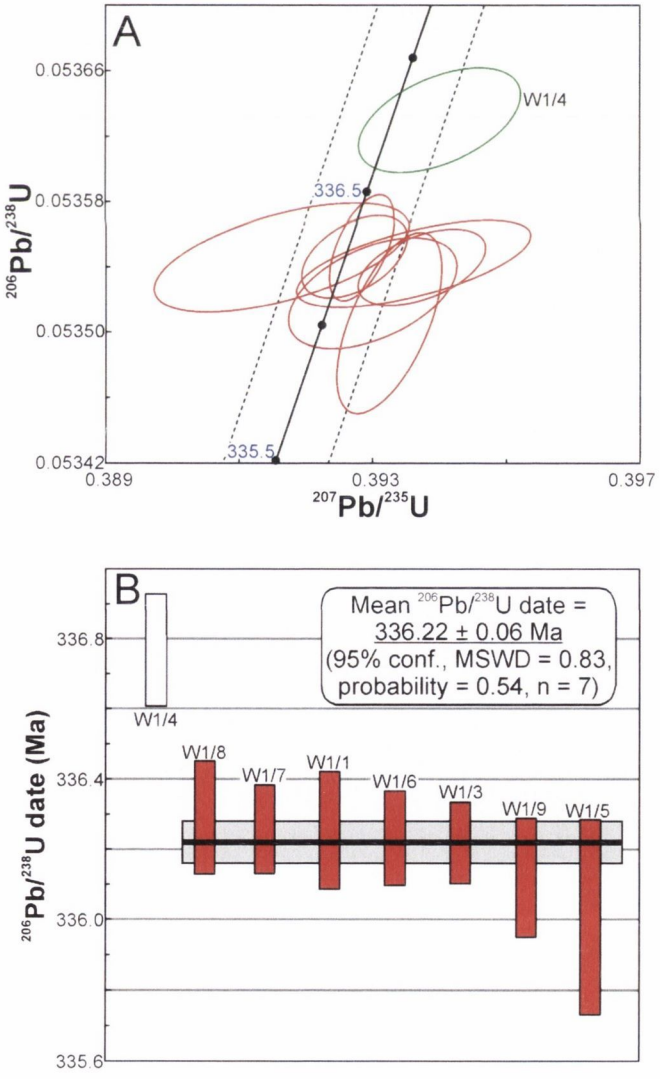

Figure 3.18. U-Pb zircon CA-ID-TIMS data from bentonite W1 illustrated as a Wetherill concordia diagram (A) and a weighted mean $^{206}Pb/^{238}U$ date plot (B). In plot A, the red and green error ellipses represent data points included in and excluded from the weighted mean date calculation shown in plot B respectively. The solid black line in plot A is the concordia drawn using the decay constants of Jaffey *et al.* (1971). The dashed black lines drawn parallel to the concordia represent the uncertainty in the position of the concordia arising from uncertainties in the U decay constants. Blue numbers are concordant ages (in units of Ma). Error ellipses are drawn at the 2σ confidence level. In plot B, the grey band represents the uncertainty of the weighted mean (95 % confidence level). Box heights (representing date uncertainties) are drawn at the 2σ confidence level.

One analysis is distinctly older (W1/4; Fig. 3.18) than all other analyses and is interpreted to represent inheritance, possibly of antecrystic origin (*sensu* Miller *et al.*, 2007) and is accordingly excluded from the weighted mean calculation. The weighted mean $^{206}Pb/^{238}U$ date of all other analyses is 336.22 ± 0.06 Ma (95 % conf., MSWD = 0.83, probability = 0.54; Fig. 3.18b) and this is taken as the best estimate for the eruption age of this bentonite horizon.

3.3.5. U-Pb zircon CA-ID-TIMS age constrains: Warnantian bentonite layers

3.3.5.1. Bentonite W8

Bentonite W8 occurs within the lower part of the Poilvache Member of the Bonne River Formation and is of early Early Warnantian age. W8 was sampled from the Anhée Nord locality, where it occurs 18 m above bentonite W1 (Fig. 3.17). It is the uppermost bentonite horizon exposed within this section. In outcrop, W8 is *c.* 18 cm thick, red-brown, homogeneous and well-consolidated. XRD analysis of material from W8 at Anhée Nord suggests that it contains quartz and chlorite (Appendix 2 Table 2). Illite-mica is either absent or present in minor amounts that are undetectable using powder XRD analysis. The presence of quartz probably accounts for the high silica content in this sample (54.36 – 57.60 % SiO_2; determined by ICP-OES; Appendix 2 Table 1). The presence of an Mg-rich chlorite phase in this sample could account for the relatively high magnesium concentration (8.63 % MgO; determined by ICP-OES; Appendix 2 Table 1).

The sample of W8 yielded a small zircon population of notably finer grain size (50 – 150 μm in length) compared to most of the other Belgian bentonite layers discussed in previous sections. The grains from this sample are predominantly euhedral and are characterised by relatively high aspect ratios (*c.* 3 – 9). Most grains are relatively clear and contain few fractures or inclusions. Some grains contain melt inclusions parallel to the c-axis. A small amount of rounded, cloudy and fractured grains are also present in the zircon separate.

The euhedral, elongate grains were selected preferentially for U-Pb zircon CA-ID-TIMS analysis, the results of which are presented in Fig 3.19 and in Appendix 1 Table 1. Compared to the samples discussed previously, the data are more complex to interpret. There is one relatively old and imprecise analysis (W8/5 in Fig. 3.19), a cluster of analyses at *c.* 336.3 Ma (green analyses excluding W8/5 in Fig. 3.19) and three younger analyses yielding $^{206}Pb/^{238}U$ dates of *c.* 335.6 Ma (red analyses; Fig 3.18). The oldest analysis is interpreted to represent an inherited grain. The cluster of analyses at *c.* 336.3 Ma are equivalent and concordant within analytical uncertainties and yield a weighted mean $^{206}Pb/^{238}U$ date of 336.35 ± 0.13 Ma (95 % conf., MSWD = 0.62, probability = 0.65, n = 5; Fig. 3.19b). This date is inconsistent with the $^{206}Pb/^{238}U$ date from the underlying W1 horizon (336.22 ± 0.06 Ma; section 3.3.4.4) and as such these grains are tentatively interpreted to be antecrystic (*sensu* Miller *et al.*, 2007). The three youngest grains in this sample are equivalent and concordant within analytical and decay constant uncertainties and yield a weighted mean $^{206}Pb/^{238}U$ date of 335.59 ± 0.19 Ma (95 % conf., MSWD = 0.16, probability = 0.86; Fig 3.19b). This latter date is taken to be the best approximation for the eruption age of this bentonite horizon. The precision of this age determination is notably worse than most of the other samples reported in this chapter. This is a consequence of the small grain size and low uranium concentrations of the zircon grains analysed from this sample. Several zircon grains were too small to be weighed accurately using the balance in the isotope laboratory at the University of Geneva. However, the larger zircon grains that did register on the balance contained 42 – 169 ppm of uranium (Appendix 1 Table 1). The small grain size and low uranium concentrations (and therefore also low radiogenic lead concentrations) negatively impact on the counting statistics of the analyses and exacerbate uncertainties in the common lead correction.

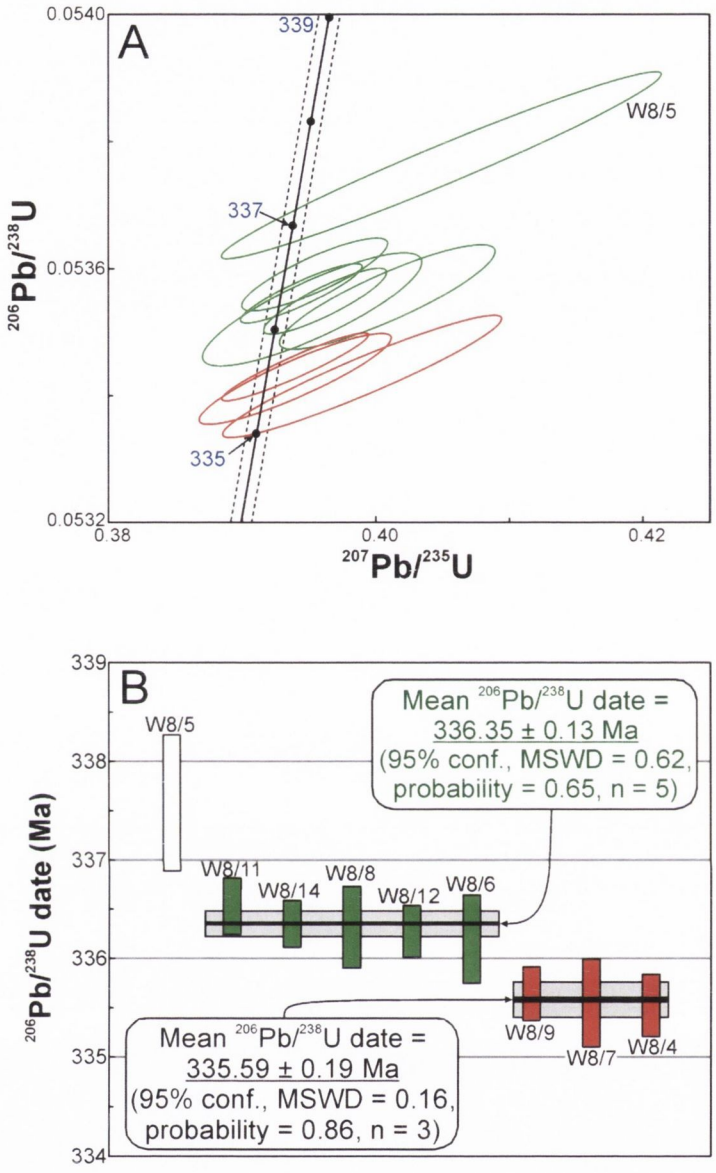

Figure 3.19. U-Pb zircon CA-ID-TIMS data from bentonite W8 illustrated as a Wetherill concordia diagram (A) and a weighted mean $^{206}Pb/^{238}U$ date plot (B). In plot A, the red and green error ellipses represent data points included in and excluded from the weighted mean calculation shown in plot B respectively. The solid black line in plot A is the concordia drawn using the decay constants of Jaffey *et al.* (1971). The dashed black lines drawn parallel to the concordia represent the uncertainty in the position of the concordia arising from uncertainties in the U decay constants. Blue numbers are concordant ages (in units of Ma). Error ellipses are drawn at the 2σ confidence level. In plot B, the grey band represents the uncertainty of the weighted mean (95 % confidence level). Box heights (representing date uncertainties) are drawn at the 2σ confidence level.

3.3.5.2. Bentonites W12 and W13: introduction

These two bentonite layers are very close within the stratigraphy (separated by 0.5 m of limestone at Anhée Sud; Fig. 3.20), to the extent that they should yield similar, if not identical ages within analytical uncertainties. W12 was the youngest Visean bentonite reported by Delcambre (1996), whereas W13 is a recently discovered bentonite at the Anhée Sud locality and is named following the nomenclature established by Delcambre (1996). Both W12 and W13 occur within the Lower Member of the Anhée Formation and are of late Early Warnantian age (Fig. 3.1).

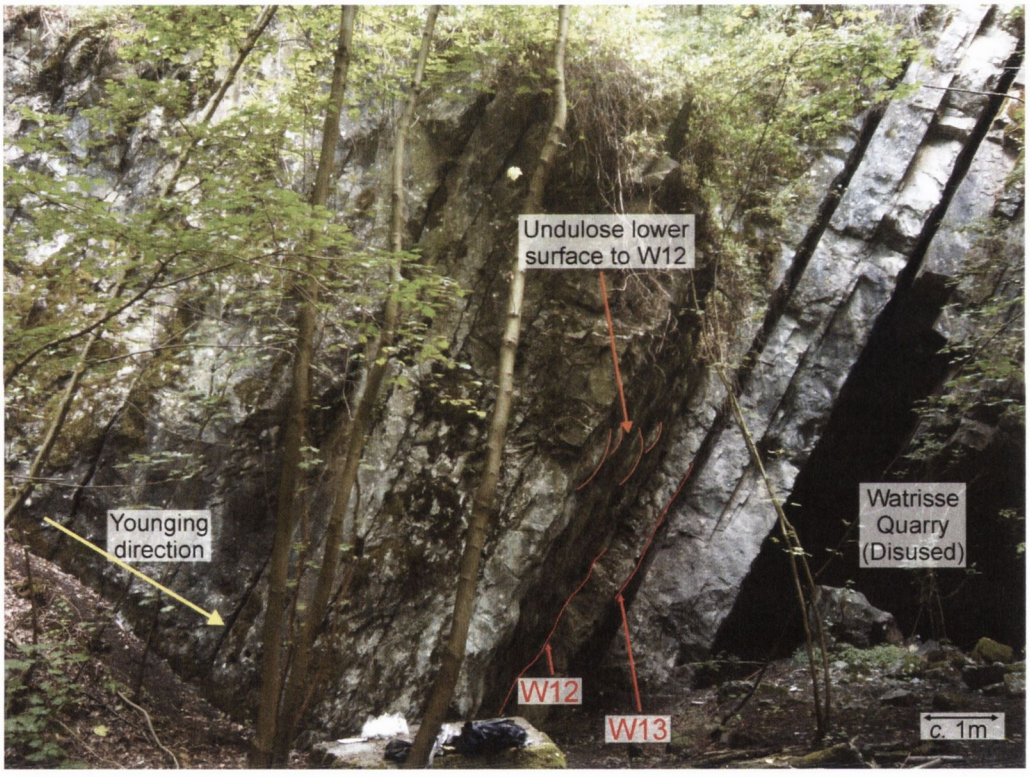

Figure 3.20. The Anhée Sud (Watrisse Quarry) locality. Bentonite W12 overlies an undulose, possibly palaeokarstic surface. Bentonite W13 occurs at the base of a recessive mudstone bed. The strata are overturned.

Bentonite W12 was dated by the U-Pb zircon CA-ID-TIMS method but yielded complex, inconclusive results (section 3.3.5.2.1). W13 was subsequently dated as a 'replacement' for W12 and to provide an age constraint on the base of the Upper Warnantian (Fig. 3.1).

3.3.5.2.1. Bentonite W12

In outcrop, W12 is *c.* 5 cm thick, black and poorly consolidated. It rests on a strongly undulose, possibly palaeokarstic surface (Fig. 3.20). XRD analysis of sample material from this horizon suggests the presence of illite-mica (probably occurring as a mixed-layer clay), chlorite and kaolinite (Appendix 2 Table 2).

The sample from bentonite W12 yielded an abundant zircon population comprising a diverse range of morphologies, i.e. from anhedral to euhedral and from sub-spherical to acicular. The anhedral grains are typically *c.* 40 – 100 μm in length and exhibit low aspect ratios (less than 3). The subhedral and euhedral grains are 40 – 150 μm in length and exhibit a wider range of aspect ratios (*c.* 1.5 – 8) than the anhedral sub-population. Oscillatory zonation is visible in a number of grains of all morphologies. Several grains contain inclusions; euhedral apatite and melt inclusions can be identified. Tiny, round inclusions are present in a number of grains. In contrast, fracturing is relatively sparse in grains from this sample. Some of the elongate subhedral and euhedral grains contain melt inclusions orientated parallel to the c-axis, whereas some of the more equant grains contain inherited cores and / or radial fractures.

The euhedral, elongate grains were targeted preferentially for U-Pb CA-ID-TIMS analysis. The results from CA-ID-TIMS dating are shown in Fig. 3.21 and are also presented in Appendix 1 Table 1. All analyses are concordant within analytical and decay constant uncertainties. Most of the analyses cluster between *c.* 332 – 333 Ma (red analyses in Fig. 3.21), with the exception of two analyses (W12/4, 8; Fig. 3.21) that yielded significantly younger dates ($^{206}Pb/^{238}U$ dates of *c.* 331.4 Ma). It is not clear from these data alone whether the two relatively young analyses record late-stage growth of magmatic zircon or contain residual lead loss that was not completely removed by the chemical abrasion technique. To shed light on this problem, U-Pb zircon CA-ID-TIMS dating of grains from the adjacent W13 bentonite was undertaken. In contrast to bentonite W12, no grains of *c.* 331.4 Ma age were obtained from bentonite W13 (section 3.3.5.2.2). Instead, the data from the W13 horizon mostly cluster at *c.* 332.5 Ma (see Fig. 3.22 in section 3.3.5.2.2). This suggests that the two anomalously young analyses in the W12 sample (analyses W12/4, 8) are affected by residual lead loss and that the true age of this bentonite lies within the *c.* 332 – 333 Ma data cluster. However, it is difficult to further refine the age of the W12 bentonite layer. The analyses clustered

between *c.* 332 – 333 Ma are too dispersed to represent a single age population, i.e. the oldest and youngest analyses within this cluster do not overlap at the 2σ confidence level (Fig. 3.21). Also, when the weighted mean $^{206}Pb/^{238}U$ date of these analyses is computed the MSWD is considerably higher (MSWD = 10.8) than is acceptable at the 95 % confidence level for 12 degrees of freedom (MSWD of 1.74; Wendt & Carl, 1991; section 2.3.5.2.5). A number of analyses from this sample contain elevated analytical blanks, but inaccuracies in the common lead correction are not the primary source of the data scatter as there is no significant correlation between the calculated age and the magnitude of the analytical blank. Additionally, when those analyses with high analytical blanks (> 2 pg) are excluded from the weighted mean $^{206}Pb/^{238}U$ date calculation, the MSWD of the age calculation increases significantly (MSWD = 17). The high-blank analyses, which are inherently less precise (due to the greater common lead correction), mask some of the scatter within the dataset. There is a strong argument for the two *c.* 331.4 Ma grains being affected by residual lead loss and it is possible that some of the 332 – 333 Ma analyses are also affected by residual lead loss, but to a lesser extent. Additionally, the possibility that antecrystic zircons are present cannot be excluded; the rounding of grains observed in this sample could possibly be due to partial resorption during prolonged magmatic residence. In summary, the available data support an age for the W12 bentonite horizon of *c.* 332 – 333 Ma but no further refinement is possible at this present time.

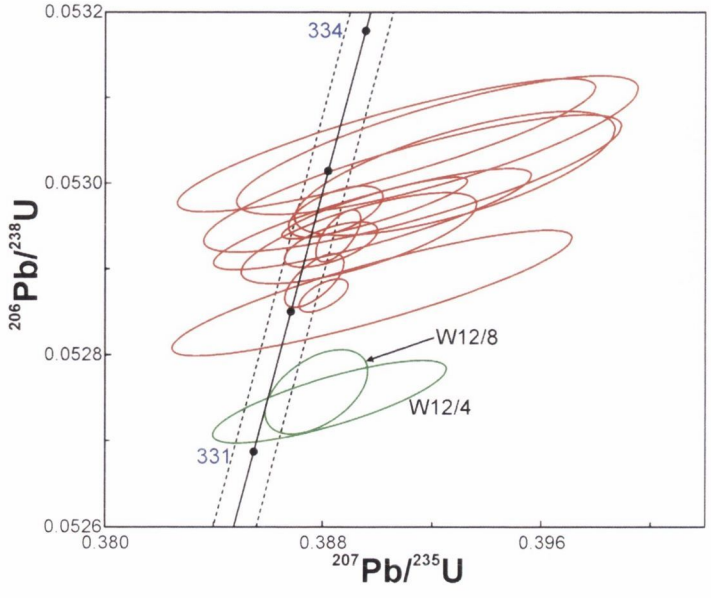

Figure 3.21. U-Pb concordia diagram of CA-ID-TIMS data from bentonite W12. The solid black line is the concordia drawn using the decay constants of Jaffey *et al.* (1971). The dashed black lines drawn parallel to the concordia represent the uncertainty in the position of the concordia arising from uncertainties in the U decay constants. Blue numbers are concordant ages (in units of Ma). Error ellipses are drawn at the 2σ confidence level.

3.3.5.2.2. Bentonite W13

This horizon occurs *c.* 0.5 m above the W12 horizon and at the base of a 20 cm thick, recessive mudstone horizon (Fig. 3.20). In outcrop, the W13 horizon is a 1 cm thick, internally homogeneous, pale-grey clay-rich layer with orange margins. The whole-rock mineralogy (as determined by XRD analysis) and the whole-rock geochemistry of this horizon (as determined by ICP-OES/MS) appear very similar to that of W12 (section 3.3.5.2.1; Appendix 2 Tables 1 and 2). XRD analysis of sample material suggests the presence of illite-mica (probably occurring as a mixed-layer clay), chlorite and kaolinite (Appendix 2 Table 2).

The sample of bentonite W13 yielded abundant zircon with a population of similar diversity to that recovered from the W12 horizon (section 3.3.5.2.1). The zircon separate is characterised by grains 50 – 220 μm long with anhedral to euhedral morphologies and aspect ratios of *c.* 1.5 – 4.5 (most are less than 4). Subhedral grains are the most common morphology observed. Apatite inclusions are visible in some sample grains. Some grains are oscillatory zoned and a few grains contain possible inherited cores. Fractures are relatively rare in grains from bentonite W13.

Euhedral grains with elongate aspect ratios and containing few inclusions were selected preferentially for CA-ID-TIMS analysis, the results of which are presented in Fig. 3.22 and in Appendix 1 Table 1. The U-Pb zircon CA-ID-TIMS data from this sample are less complicated than the data obtained from bentonite W12; most analyses cluster at *c.* 332.5 Ma (Fig. 3.22). One analysis (W13/3; Fig. 3.22; Appendix 1 Table 1) is significantly older and is interpreted to represent an inherited grain that is possibly of antecrystic origin (section 2.3.2.3). The remaining analyses overlap within analytical uncertainties and yield a weighted mean $^{206}Pb/^{238}U$ date of 332.50 ± 0.07 Ma (95 % conf., MSWD = 2.4, probability = 0.051; Fig. 3.22b), which is taken to approximate the eruption age of this bentonite layer.

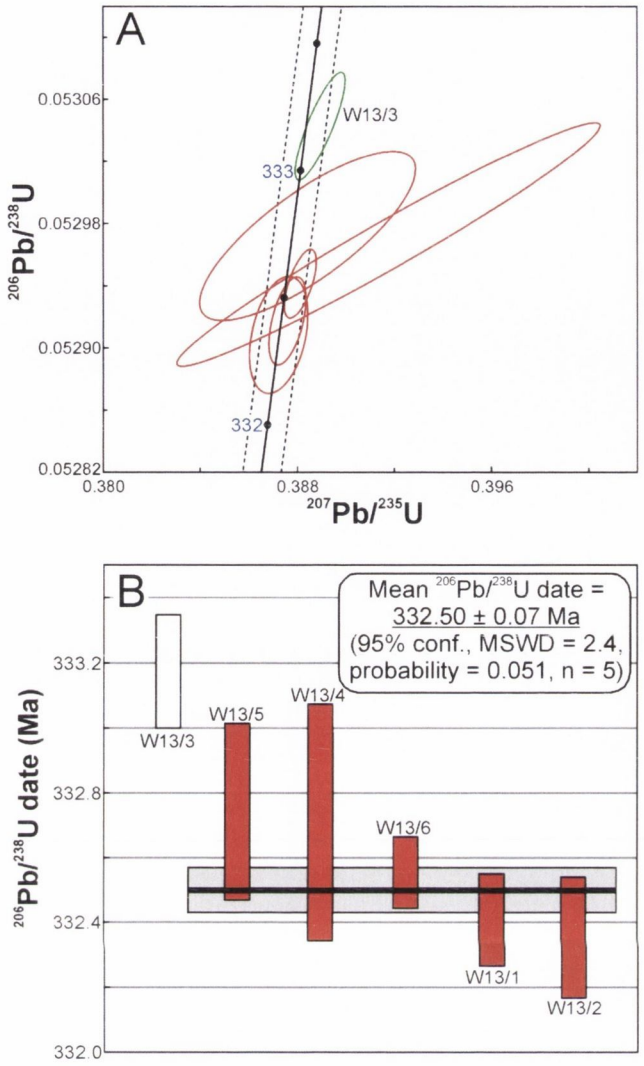

Figure 3.22. U-Pb zircon CA-ID-TIMS data from bentonite W13 illustrated as a Wetherill concordia diagram (A) and a weighted mean $^{206}Pb/^{238}U$ date plot (B). In plot A, the red and green error ellipses represent data points included in and excluded from the weighted mean calculation shown in plot B respectively. The solid black line in plot A is the concordia drawn using the decay constants of Jaffey *et al.* (1971). The dashed black lines drawn parallel to the concordia represent the uncertainty in the position of the concordia arising from uncertainties in the U decay constants. Blue numbers are concordant ages (in units of Ma). Error ellipses are drawn at the 2σ confidence level. In plot B, the grey band represents the uncertainty of the weighted mean (95 % confidence level). Box heights (representing date uncertainties) are drawn at the 2σ confidence level.

3.4. Discussion

The U-Pb zircon CA-ID-TIMS isotopic dates described in the previous sections are summarised in Table 3.1 and are the focus of the following discussion. The age of the W12 horizon (section 3.3.5.2.1) is of insufficient precision to merit its inclusion in the subsequent data interpretation.

The new isotopic dates from the Belgian Visean bentonite layers are employed to estimate the average periodicities of mid-to-upper Visean sedimentary cycles within the Namur-Dinant Basin (section 3.4.1). During late Visean times, widespread cyclic sedimentation appears within the stratigraphic record of western Europe (section 3.4.1). There have been several suggestions within the literature that the sedimentary cycles are glacio-eustatic in origin and that their appearance within the stratigraphic record may

signify the onset of major Carboniferous glaciation (e.g. Wright & Vanstone, 2001). The calculated periodicities are compared with Milankovitch frequencies, which have been shown to modulate Pleistocene glacial ice volumes (e.g. Hays *et al.*, 1976). This is undertaken to determine if the periodicity of the Belgian Visean (Livian and Lower Warnantian) cycles is comparable to that of the Pleistocene glacial cycles, which may lend support to the former being of glacio-eustatic origin. In addition to the periodicity calculations, comparisons are drawn between existing (published) Mississippian isotopic age data and the new U-Pb zircon CA-ID-TIMS dates (Table 3.1), in section 3.4.2. The implications that the new CA-ID-TIMS data have for calibration of the Carboniferous timescale are discussed in section 3.4.3.

Bentonite horizon	Stratigraphic position	Weighted mean $^{206}Pb/^{238}U$ date	Uncertainties (95% conf.)			MSWD	Probability of fit	No. of analyses
			± X	± Y	± Z			
300	upper Tournaisian	347.94	0.08	0.19	0.42	1.5	0.18	6
L1	lowermost Livian	340.13	0.18	0.25	0.44	0.96	0.38	3
L2	lower Livian	339.89	0.06	0.18	0.41	0.79	0.56	6
L3	lower Livian	338.28	0.09	0.19	0.41	2.1	0.075	5
W1	uppermost Livian	336.22	0.06	0.18	0.40	0.83	0.54	7
W8	lower Lower Warnantian	335.59	0.19	0.25	0.44	0.16	0.86	3
W13	upper Lower Warnantian	332.50	0.07	0.18	0.40	2.4	0.051	5

Table 3.1. A summary of the U-Pb zircon CA-ID-TIMS data used in the discussion. ± X / Y / Z uncertainty levels are explained in section 2.3.5.2.5.

3.4.1. Mid-to-upper Visean cyclic sedimentation and the onset of major Gondwanan glaciation

Cyclic sedimentation is a common feature of upper Visean shallow-water carbonate platform sequences from the palaeo-equatorial realm. Cyclic sedimentation has been reported from North America (e.g. Smith & Read, 2000), Great Britain (Somerville 1979a, b, c; Walkden, 1987; Wright & Vanstone, 2001), Ireland (Gallagher, 1996; Gallagher & Somerville, 1997; Gallagher *et al.*, 2006), Belgium (Pirlet, 1968; Poty & Hance, 2006a, b), France (e.g. Hoyez, 1971) and Poland (Walkden, 1987; references therein). Within western Europe (Belgium, Britain, Ireland), the cycles display

regressive (shallowing upwards) facies and are typically 1 – 20 m thick (e.g. Walkden, 1987).

It is notoriously difficult to identify the processes that generated such carbonate cycles. This is because markedly different causal mechanisms (e.g. eustasy, tectonism, climate, autocyclic processes) can generate sedimentary cycles of similar morphology (Satterley, 1996). There is currently no definitive method for determining the mechanisms that generated individual carbonate cycles (Lehrmann & Goldhammer, 1999). The origins of such cycles are often inferred from multiple, independent lines of evidence, including arguments based on lateral continuity and cycle periodicities (e.g. Walkden, 1987).

There have been numerous suggestions that British and Irish Asbian and Brigantian shallowing-upwards carbonate sedimentary cycles are the result of glacio-eustatic sea-level oscillations (Walkden, 1987; Leeder, 1988; Vanstone, 1993; Gallagher, 1996; Wright & Vanstone, 2001; Barnett *et al.*, 2002; Gallagher *et al.*, 2006). This interpretation is based on the following arguments:

1. The inferred lateral continuity of the sedimentary cycles. Several studies of British Asbian cycles have argued that individual cycles can be traced across carbonate platforms and shelves within the British province (e.g. Gray, 1981; Horbury, 1987; Walkden, 1987; Vanstone, 1993). Similarly, the Brigantian mixed carbonate – siliciclastic 'Yoredale' cycles of northern England and southern Scotland, which were deposited in more proximal marine environments than the pure carbonate sequences of central England and Wales (Ramsbottom, 1973), have been correlated over considerable geographic areas (*c.* 10,000 km^2; Tucker *et al.*, 2003). Such correlations are primarily based upon lithostratigraphic evidence because biostratigraphic constraints are too coarse to provide precise correlation of individual cycles. There are inherent assumptions in such correlations; for example, that geographically distinct cycles are coeval and share a common causal mechanism. However, there appear to be broadly comparable numbers of cycles preserved on different carbonate shelves and platforms within Britain and Ireland (e.g. Vanstone, 1993).

2. The appearance of cyclic sedimentation within the stratigraphic record only slightly predates and occurs almost continuously until the widespread appearance of direct glacial records on Gondwana (Leeder, 1988), which are thought to appear close to the base of the Namurian Stage (section 1.1).

3. The cycles are everywhere characterised by regressive facies and typically comprise subtidal limestones overlain by peritidal deposits and features consistent with emergence (e.g. Walkden, 1987). Transgressive facies are generally poorly represented or absent (Walkden, 1987; Vanstone, 1993). This has been suggested to indicate that sea-level rose rapidly and fell slowly (e.g. Leeder, 1988). Comparisons have been drawn between these inferred sea-level changes and the slow build-up of glacial ice and rapid melting inferred from the proxy records of Pleistocene ice volumes ('saw-tooth' pattern; Hays *et al.*, 1976; Imbrie & Imbrie, 1980; Clark *et al.*, 1999). However, this is not the only possible explanation for the asymmetry of these sedimentary cycles. The lack of transgressive facies could represent a preservation bias, with early transgressive deposits having been reworked by subsequent transgression (e.g. Walkden, 1987), or alternatively may arise due to a time lag between the initial flooding of the carbonate platform and the resumption of carbonate production (Lehrmann & Goldhammer, 1999). It is also important to note that some British and Irish cycles, particularly those within the late Asbian, demonstrate incomplete shoaling upwards sequences, with emergent surfaces developed over subtidal bioclastic limestones (Walkden, 1987; Vanstone, 1993). This has been interpreted as evidence for rapid eustatic drawdown rather than the passive build-up of the carbonate platform to sea-level (Walkden, 1987).

4. There are few known geological processes (apart from glacio-eustasy) that can generate sea-level oscillations of comparable magnitude to those inferred from British Asbian and Brigantian sedimentary cycles, over the short timescales (< 1 Myrs) that the sedimentary cycles are inferred to represent (Fig. 3.23). Sea-level oscillations of 10 – 50 m have been inferred for the British Asbian and lower Brigantian cycles (Wright & Vanstone, 2001), and up to 95 m for the upper Brigantian cycles (Wright & Vanstone, 2001). Simple periodicity calculations based on counting the number of sedimentary cycles and

comparisons to contemporary published timescales (such as Menning *et al.*, 2000 and Davydov *et al.*, 2004) demonstrates that these cycles are of high frequency (< 1 Myrs duration per cycle; see argument 5 below).

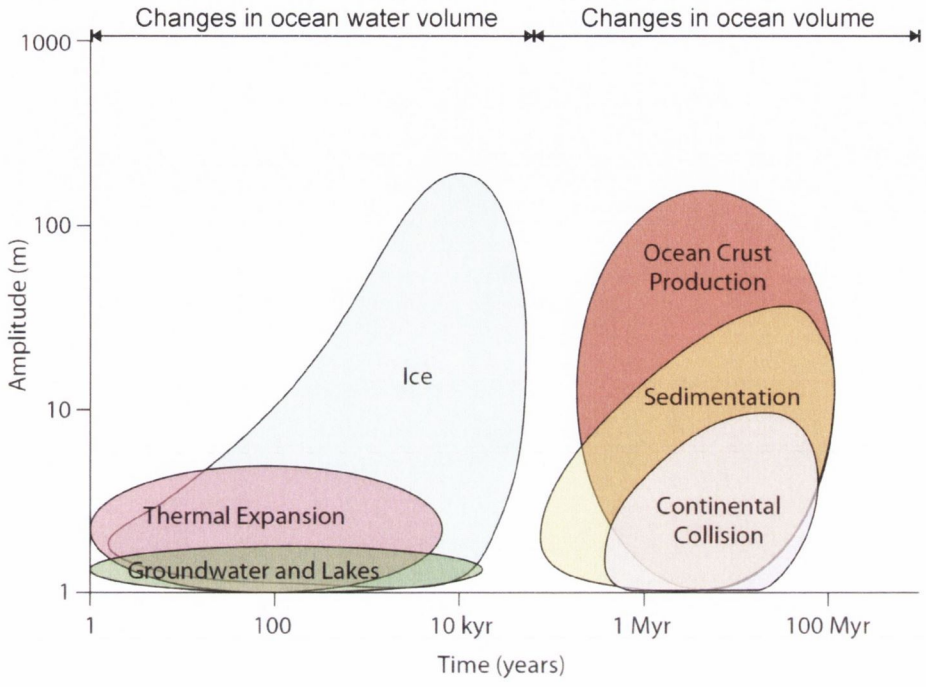

Figure 3.23. Mechanisms for driving sea-level change. Sedimentation = large scale changes in ocean sedimentation (e.g. progradation of new delta systems) that affects the volume of the ocean. The diagram is reproduced from Miller *et al.* (2011).

5. There have been suggestions that British Asbian cycles have periodicities comparable to those of Milankovitch cycles (e.g. Vanstone, 1993; Wright & Vanstone, 2001), which have been shown to modulate recent Pleistocene glacial ice volumes (e.g. Hays *et al.*, 1976; Imbrie *et al.*, 1993). These calculations are relatively crude. This is because there are no direct isotopic age constraints from the studied sections and hence contemporary published Carboniferous timescales were employed to estimate the time duration encompassing a package of sedimentary cycles. Unfortunately, the Mississippian timescale is relatively poorly constrained (section 1.4) and it is questionable whether these periodicity estimates are of sufficient precision to resolve Milankovitch frequencies (*c.* 100 kyrs, *c.* 404 kyrs; section 1.3) from other, non-Milankovitch frequencies. These existing periodicity estimates suggest that the cycle frequencies may be compatible with Milankovitch cycles, but they are of insufficient precision to demonstrate this conclusively.

Thus, the evidence for upper Visean British and Irish sedimentary cycles being of glacio-eustatic origin is strong. Furthermore, it has also been suggested that the appearance of these glacio-eustatic sedimentary cycles within the stratigraphic record may signify the onset of major Gondwanan glaciation (e.g. Wright & Vanstone, 2001). However, at least within the western European realm the appearance of cyclic sedimentation is regionally diachronous based on current biostratigraphic correlations, appearing first in Belgium during Livian (Holkerian) times (Fig. 3.1). The Belgian Livian sedimentary cycles appear to be an isolated occurrence as elsewhere in western Europe (e.g. Britain and Ireland) similar aged (Holkerian) strata contain little evidence of high-frequency shallowing-upwards sedimentary cycles (Walkden 1987; Wright & Vanstone, 2001). There are only sparse, local reports of cyclic sedimentation within the Holkerian strata of the UK (e.g. Jefferson, 1980). The absence of Holkerian and lower Asbian shallowing-upwards cyclicity from the Irish stratigraphic record could be due to the greater water depths of the prevailing carbonate ramp environment (section 3.3.1) and thus a diminished sensitivity of the depositional environment to eustatic oscillations. However, the Holkerian strata preserved in parts of Britain represent very shallow water depositional settings, which should be sensitive to relatively minor sea-level oscillations (Wright & Vanstone, 2001). Widespread sedimentary cyclicity does not appear within the British stratigraphic record until the base of the Asbian Substage (e.g. Wright & Vanstone, 2001; Fig 3.1) and during the upper Asbian within the Irish stratigraphic record (base of the Cf6γ foraminifera biozone; Gallagher *et al.*, 2006; Fig. 3.1). This diachroneity may extend to regions outside of western Europe but the biostratigraphic correlations to other palaeogeographic provinces (e.g. North America) are not as precise as those between the different basins within western Europe. It is therefore more difficult to determine the extent of these potential diachroneities on a global scale.

The origin of the Belgian Livian cycles is not as well understood as the British and Irish Asbian and Brigantian cycles. There have been suggestions that the Belgian Livian cycles are glacio-eustatic (Aretz *et al.*, 2011) based on the lateral continuity of cycles within the basin, which has been demonstrated by Gerards & Michot (1963), Pirlet (1963, 1968) and Aretz *et al.* (2011). There have also been suggestions that the Livian cycles possess periodicities that are consistent with Milankovitch frequencies (Aretz *et*

al., 2011). However, these latter periodicity estimates were based upon poor temporal constraints and thus their accuracy is uncertain.

The significance of these early Belgian (Livian) sedimentary cycles is important because it has repercussions for our understanding of the onset of major Carboniferous glaciation. If these Belgian cycles represent an early record of glacio-eustasy, it would support a much earlier onset of glaciation than is currently inferred from the British stratigraphic record (Wright & Vanstone, 2001). To shed further light on whether these cycles are glacio-eustatically driven the new U-Pb zircon CA-ID-TIMS dates from Belgian bentonites are used to estimate average periodicities of the sedimentary cycles that occur between the bentonite horizons. These estimates are compared to Milankovitch cycle periodicities (section 1.3).

3.4.1.1. Belgian mid-to-upper Visean carbonate cycles

Widespread evidence for sedimentary cyclicity appears within the stratigraphic record of the Namur-Dinant Basin during early Livian times (e.g. Hance *et al.*, 2006). There are isolated instances of older pulses of cyclic sedimentation within the basin, such as from the 'black marble' of Denée within the Molignée Formation (lower Moliniacian; Mottequin, 2008). These are, however, of limited lateral extent and it is not until Livian times that sedimentary cyclicity is observed from multiple sedimentation areas within the basin (Fig. 3.5). The strata are almost continuously cyclically bedded throughout the Livian and Warnantian substages, with only the 8 m of stromatolitic limestones that comprise the Bay Bonnet Member not displaying clear evidence of cyclicity. However, the Bay Bonnet Member represents a relatively small proportion of the total thickness of the Livian and Warnantian stratigraphy within the basin (*c.* 3 %; taking the total thickness of Livian and Warnantian strata to be *c.* 245 – 265 m; section 3.3.2.3).

The Livian and Warnantian sedimentary cycles have been described by several previous studies (Gerards & Michot, 1963; Pirlet, 1963, 1968; Chevalier & Aretz, 2005; Poty & Hance, 2006a, b) and thus only an overview is given here. The cyclicity is expressed as alternations of bioclastic limestone beds containing a diverse faunal assemblage (brachiopods, crinoids, corals, foraminifera, etc.; Fig. 3.24a, b) overlain by micrites and stromatolitic boundstones (e.g. Gerards & Michot, 1963; Pirlet 1963; Chevalier &

Aretz, 2005; Poty & Hance, 2006a, b). The base of a cycle is traditionally defined as at the base of the first bioclastic limestone bed overlying a micritic bed (Pirlet, 1963) and the boundary is typically sharp, undulose and erosive (Gerards & Michot, 1963). The lower bioclastic portion typically shows evidence of fining upwards and the contact between the bioclastic and micritic beds is either transitional within a bed or occurs across a bedding plane. The cycles range in thickness from *c.* 0.7 m to *c.* 20 m, although most are less than 10 m thick. There is no discernable systematic trend in cycle thickness upwards through the Livian and Warnantian substages, unlike time-equivalent cycles in Britain which thicken upwards (Walkden, 1987; Wright & Vanstone, 2001). Some cycles, particularly within their upper micritic portions, contain features consistent with emergence (e.g. Fig. 3.25).

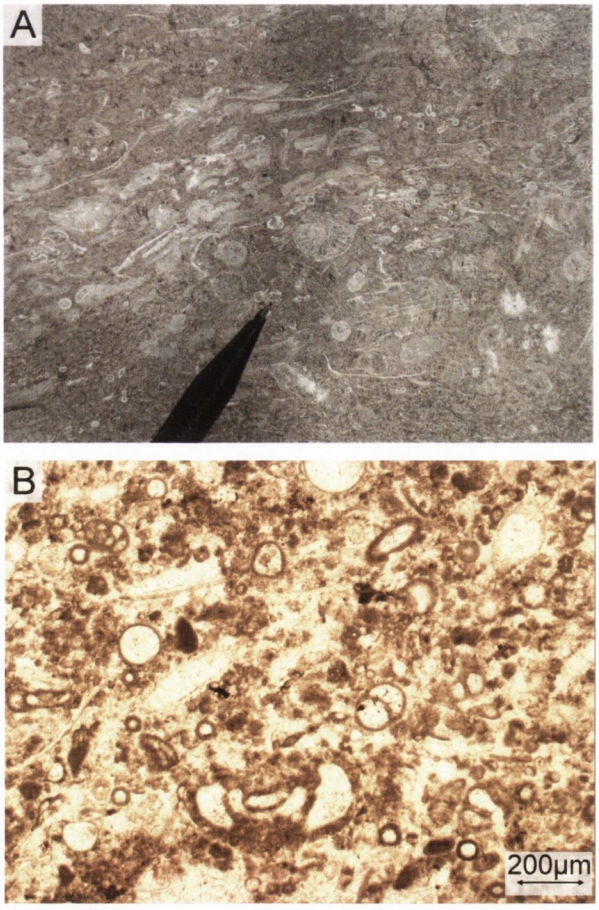

Figure 3.24. A) Field photograph of a bioclastic limestone bed within the lower Corphalie Member at Lives-sur-Meuse. B) Thin section of a bioclastic limestone from the Haut-le-Wastia Member at Lives-sur-Meuse (plane-polarised light).

Figure 3.25. A palaeosol horizon resting on a strongly undulose, palaeokarstic surface. The horizon occurs within the upper Corphalie Member at Lives-sur-Meuse.

Most of the mid-to-upper Visean bentonites described in the previous sections occur within the upper micritic portions of the carbonate cycles, which may be a preservation bias rather than a true reflection of when volcanism occurred. Some cycles culminate in undulose, palaeokarstic surfaces overlain by a bentonite horizon (e.g. W12 in Fig. 3.20); however, most do not and are instead characterised by the repetition of bioclastic and micritic facies.

The sedimentary cycles have been interpreted to represent shallowing upwards trends in water depth (e.g. Pirlet, 1963; Poty & Hance, 2006a, b) and have been described as parasequences (i.e. a relatively conformable series of genetically related beds bounded by marine flooding surfaces; Poty & Hance, 2006a, b; Aretz *et al.*, 2011). The lower bioclastic limestones are inferred to have been deposited in a subtidal environment with good ocean connectivity, whereas the overlying micrites and stromatolitic boundstones are thought to have been deposited in a restricted (lagoonal) intertidal to supratidal environment (Pirlet, 1963; Chevalier & Aretz, 2005; Aretz *et al.*, 2011).

3.4.1.2. Average periodicity estimates for Belgian Livian and Warnantian sedimentary cycles

The available U-Pb zircon age constraints from the bentonite horizons (Table 3.1) are too dispersed within the stratigraphy to calculate the periodicities of individual sedimentary cycles. However, it is possible to calculate the average periodicities for three different packages of sedimentary cycles within the Livian Substage, i.e. the sedimentary cycles that occur between bentonites L1 – L2, L2 – L3 and L3 – W1 (Fig. 3.26). Average periodicities are also computed for the Lower Warnantian sedimentary cycles between bentonites W1 – W8 and W8 – W13 (Fig. 3.26). By calculating the average periodicities of sedimentary cycles within these different stratigraphic intervals, it is possible to examine how consistent cyclic sedimentation was during Livian and Early Warnantian times. All of the periodicity calculations were computed using the methodology outlined in section 2.9.

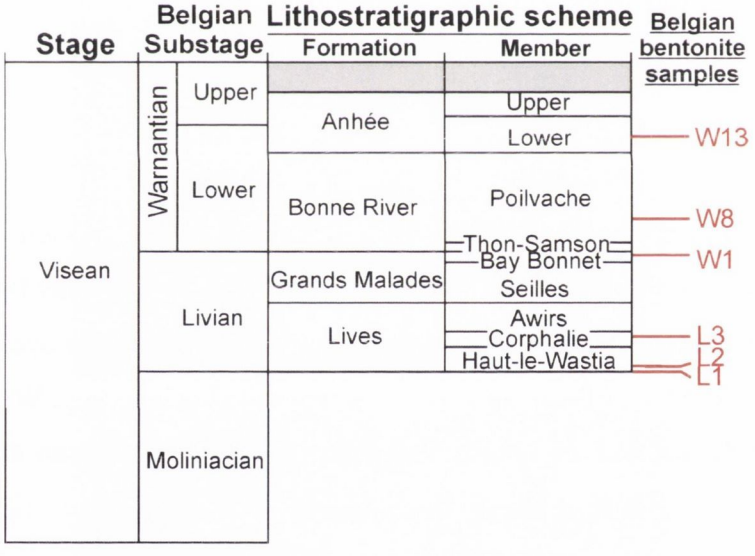

Figure 3.26. Stratigraphic positions of the bentonites used in the periodicity calculations. The lithostratigraphic divisions follow Poty *et al.* (2001). The grey area represents the stratigraphic omission within the Namur-Dinant Basin (see section 3.3.2.1 for details).

3.4.1.2.1. Livian sedimentary cycles

For the Livian average periodicity calculations, the composite stratigraphic section of Aretz *et al.* (2011) is used to estimate the number of intervening sedimentary cycles. This composite standard has not yet been published and thus the periodicity calculations for Livian sedimentary cycles should be regarded as preliminary estimates. Between

bentonites L1 and L2 there are 1 – 2 sedimentary cycles; between bentonites L2 and L3 there are approximately 10 sedimentary cycles; and between bentonites L3 and W1 there are approximately 23 cycles (M. Aretz, pers. comm., 2011).

The most uncertain part of the cycle record corresponds to the interval between L3 and W1. This is because over a large area of the basin (CSA, DSA and southern NSA; Fig. 3.5) the stratigraphy has been brecciated (Grand Brèche Viséenne; Fig. 3.6) and thus any record of sedimentary cyclicity has since been lost. Additionally, there is a stratigraphic gap between the Visean limestones and Namurian siliciclastic rocks that increases in magnitude from the northeast to the southwest (Fig. 3.6). Thus, the record of upper Livian sedimentary cycles can only be reconstructed from a limited geographical area within the basin (northern NSA), between the brecciated strata to the southwest and the truncated stratigraphic record to the northeast.

Based on the numbers of sedimentary cycles listed above and the U-Pb zircon dates from the bentonites shown in Table 3.1, the average periodicities of Livian sedimentary cycles between bentonites L1, L2, L3 and W1 were calculated and are shown in Table 3.2. Taking into consideration the uncertainty in the number of sedimentary cycles between bentonites L1 and L2 (1 – 2 sedimentary cycles), the average periodicity of the intervening sedimentary cycles lies between 120 ± 95 kyrs / cycle (Table 3.2) and 240 ± 190 kyrs / cycle (Table 3.2), which can be abbreviated to 25 – 430 kyrs / cycle.

Bentonites	Number of sedimentary cycles	Time duration (Myrs)	Uncertainty in time duration (± Myrs)	Average periodicity (kyrs / cycle)	Uncertainty in average periodicity (± kyrs / cycle)
L1 - L2	1	0.24	0.19	240	190
	2	0.24	0.19	120	95
L2 - L3	10	1.61	0.11	161	11
L3 - W1	23	2.06	0.11	90	5

Table 3.2. The average periodicities of Livian sedimentary cycles between bentonites L1, L2, L3 and W1. The calculations follow the method detailed in section 2.9. The time duration is calculated using the U-Pb zircon dates from the bentonite horizons shown in Table 3.1. Uncertainties are at the 95 % confidence level.

3.4.1.2.2. Lower Warnantian cycles

The periodicity calculations for the Lower Warnantian cycles predominantly employ the stratigraphic record from the DSA, where the stratigraphic record is most complete (section 3.3.2.1; Fig. 3.6) and where the bentonites W1, W8 and W13 were sampled for isotopic dating using the U-Pb zircon CA-ID-TIMS method (section 3.3.3.2). The record of Warnantian sedimentary cycles used in the periodicity calculations is shown in Fig. 3.27. The periodicity estimates for the cycles between bentonites W1 – W8 and W8 – W13 are discussed in subsequent sections.

3.4.1.2.2.1. Lower Warnantian cyclicity between bentonites W1 and W8

There are two contrasting interpretations for the basal portion of the Anhée Nord section, both of which depict the W1 horizon at approximately the same stratigraphic level (i.e. uppermost Livian) but which lead to a marked difference in the number of intervening sedimentary cycles between the W1 and W8 horizons. The classic interpretation is that the base of the Warnantian is located at the base of the first bioclastic limestone bed (base of cycle 5 in Fig. 3.27; Conil *et al.*, 1967; Pirlet 1968). However, subsequent work by Delcambre (1996), who correlated bentonite horizons (using zircon typology) cropping out at the Anhée Nord locality with bentonite horizons exposed within Transcar Quarry, Maizeret (NSA; Fig. 3.27), suggested that the Livian – Warnantian boundary is located between the W1 and W2 bentonite horizons at Anhée Nord, which is somewhat lower than the traditional interpretation (*c.* 2.4 m lower; Fig. 3.27). More importantly, however, Delcambre (1996) suggested that there is a stratigraphic hiatus at the Anhée Nord locality between bentonites W1 and W2 and that the lowermost Warnantian strata (corresponding to the Thon-Samson Member and lowermost Poilvache Member; Fig. 3.27) are not represented at Anhée Nord. Based on the correlations of Delcambre (1996) and the cycle interpretations of Pirlet (1963) from the Maizeret section (NSA), there are 3 – 4 sedimentary cycles missing from the Anhée Nord section (Fig. 3.27). The uncertainty in the number of missing cycles arises because at other localities within the vicinity of Transcar Quarry (i.e. within the Samson Valley), Pirlet (1963) noted an additional cycle at the base of the Warnantian Substage (which he termed sequence 0) that was not represented at Maizeret (Pirlet, 1963). The significance of this cycle is unclear. It appears to be discontinuous on a local scale and therefore may be of limited significance. Nevertheless, it is factored into the periodicity calculations.

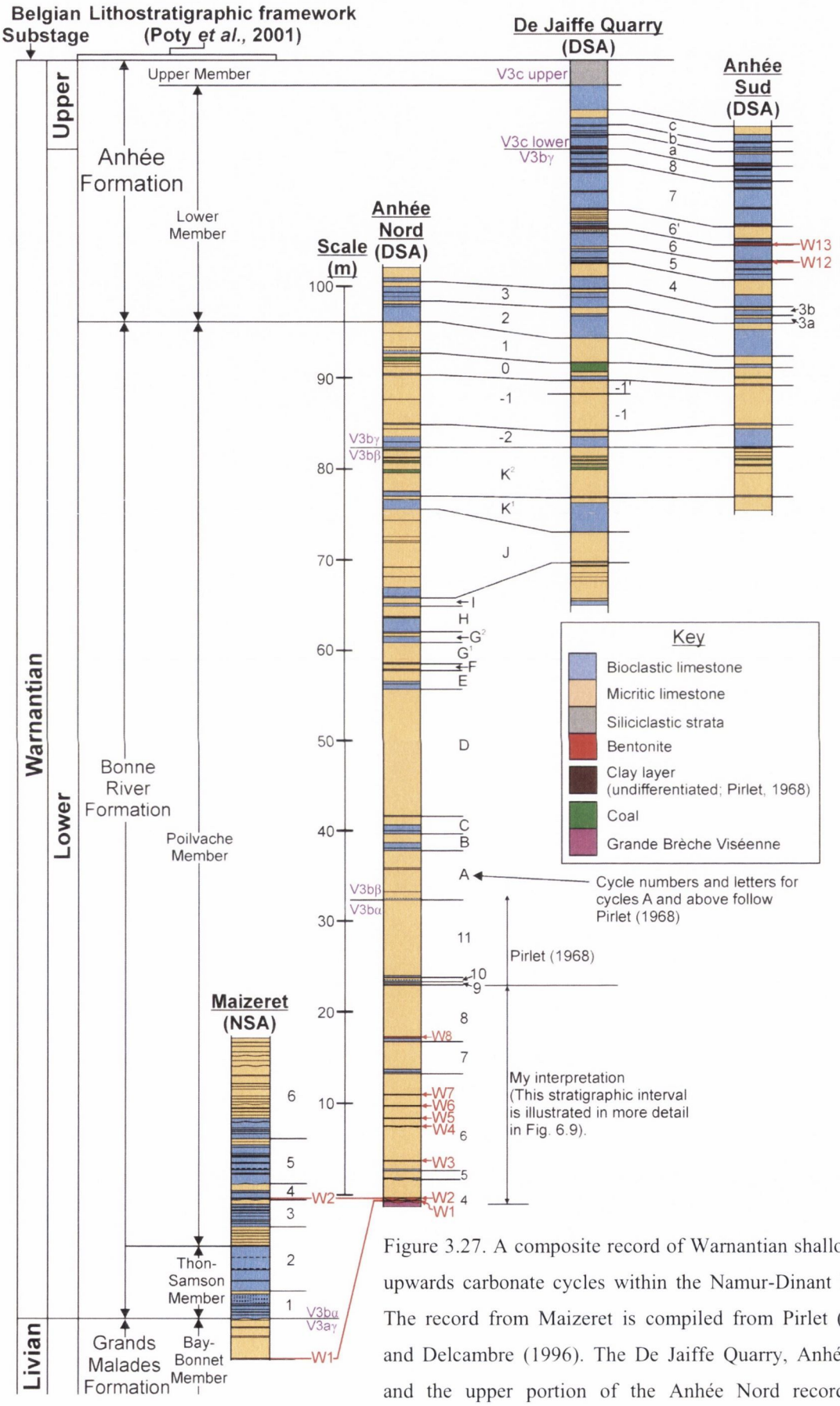

Figure 3.27. A composite record of Warnantian shallowing-upwards carbonate cycles within the Namur-Dinant Basin. The record from Maizeret is compiled from Pirlet (1963) and Delcambre (1996). The De Jaiffe Quarry, Anhée Sud and the upper portion of the Anhée Nord records are redrawn from Pirlet (1968). Correlations between Maizeret and Anhée Nord are from Delcambre (1996).

An interpretation of the cyclicity at the Anhée Nord section was presented by Pirlet (1968). However, several of the cycles of Pirlet (1968) within the lowermost 23 m of the section exposed do not conform to the standard cycle pattern defined for this stratigraphic interval in the Namur-Dinant Basin (i.e. alternations of bioclastic and micritic beds; section 3.4.1.1) and are instead characterised by repetitions of micritic strata. The significance of these repetitions is unclear and the entirely micritic cycles of Pirlet (1968) are not treated as separate cycles in this thesis. It is important to note that it is only within this stratigraphic interval that Pirlet (1968) subdivided the micritic facies into separate cycles. At other stratigraphic levels within the Warnantian Substage, the cycles of Pirlet (1968) comprise both bioclastic and micritic beds, several of which contain repetitions of micritic facies that are not subdivided into individual cycles. Thus, the interpretations of Pirlet (1968) for this stratigraphic interval appear inconsistent. Based on the traditional standard definition of a sedimentary cycle (defined in section 3.4.1.1), there are three complete sedimentary cycles between bentonites W2 and W8 at the Anhée Nord locality (cycles 5 – 7 in Figs. 3.27 and 6.9) and two partial cycles corresponding to the part of cycle 4 above the W2 horizon and the part of cycle 8 beneath the W8 horizon (Fig. 3.27).

3.4.1.2.2.2. Periodicity of sedimentary cycles between bentonites W1 and W8

There are either 7.5 or 8.5 sedimentary cycles between bentonites W1 and W8 (Fig. 3.27) when the uncertain significance of the basal Warnantian cycle 0 of Pirlet (1963) is considered. The half cycle corresponds to the fraction of sedimentary cycle 8 (Fig. 3.27) beneath bentonite W8. It is unclear how much time resides in the 4 m of the Bay Bonnet Member between bentonite W1 and the base of the Thon Samson Member (Fig. 3.27) and thus how to treat this interval within the periodicity calculations. No correction was applied for the amount of time residing within the Bay Bonnet Member. If this approach is grossly inaccurate then the calculated periodicities will be overestimated. Based on the presence of 7.5 to 8.5 intervening cycles, the average periodicity of these sedimentary cycles is between 74 ± 24 kyrs / cycle and 84 ± 27 kyrs / cycle (Table 3.3), which can be simplified to 50 – 111 kyrs / cycle.

Number of sedimentary cycles	Time duration (Myrs)	Uncertainty in time duration (± Myrs)	Average periodicity (kyrs / cycle)	Uncertainty in average periodicity (± kyrs / cycle)
7.5	0.63	0.20	84	27
8.5	0.63	0.20	74	24

Table 3.3. The average periodicity of sedimentary cycles between bentonites W1 and W8. The calculations follow the method detailed in section 2.9. The ages of bentonites W1 and W8 are from Table 3.1. Uncertainties are at the 95 % confidence level.

3.4.1.2.2.3. Lower Warnantian cyclicity between bentonites W8 and W13

The record of sedimentary cycles between bentonites W8 and W13 (Fig. 3.27) draws heavily on the work of Pirlet (1968). Unfortunately, the upper portion of the stratigraphic section at Anhée Nord that was originally described by Pirlet (1968) (corresponding to cycle 9 and above in Fig. 3.27) could not be re-examined. The stratigraphic interval immediately above cycle 8 (Fig. 3.27) is now inaccessible, whereas the upper third of the section studied by Pirlet (1968) is still exposed but is located on private property and the current owner would not allow access. Thus, there is little choice at this present time than to rely on the cycle interpretations of Pirlet (1968), which are at least consistent with the traditional standard cycle definition (section 3.4.1.1) in this stratigraphic interval.

The stratigraphic interval between W8 and W13 is incomplete at Anhée Nord (Fig. 3.27). Instead, this uppermost interval was constructed from the Anhée Sud locality, where W13 was sampled for U-Pb zircon CA-ID-TIMS dating. The correlation between the Anhée Nord and Anhée Sud sections is from Pirlet (1968) and is primarily based on lithostratigraphic controls. The entirety of the Anhée Sud section described by Pirlet (1968) is still exposed, allowing his interpretations to be re-examined. The cycle interpretations of Pirlet (1968) from this locality comply with the standard cycle definition (section 3.4.1.1) and appear representative of the cycles exposed.

3.4.1.2.2.4. Periodicity of sedimentary cycles between bentonites W8 and W13

There are 25.5 to 27.5 sedimentary cycles between bentonites W8 and W13 (Fig. 3.27). The uncertainty in the number of cycles arises because two of the cycles of Pirlet (1968) are locally subdivided into multiple cycles; cycle -1 at De Jaiffe Quarry is subdivided into cycles -1 and -1' (Fig. 3.27) and cycle 3 at Anhée Sud is subdivided into cycles 3 and 3' (Fig. 3.27). In both instances, the extra cycles occur at only a single locality. Whether these additional cycles reflect basin-wide events that are not represented elsewhere or more localised phenomena is unclear and this uncertainty must thus be factored into the periodicity calculations.

Using the U-Pb zircon dates from bentonites W8 and W13 (Table 3.1), the average periodicity of the intervening sedimentary cycles is between 112 ± 7 kyrs / cycle and 121 ± 8 kyrs / cycle (Table 3.4), which can be simplified to 105 – 129 kyrs / cycle.

Number of sedimentary cycles	Time duration (Myrs)	Uncertainty in time duration (± Myrs)	Average periodicity (kyrs / cycle)	Uncertainty in average periodicity (± kyrs / cycle)
25.5	3.09	0.20	121	8
27.5	3.09	0.20	112	7

Table 3.4. The average periodicity of sedimentary cycles between bentonites W8 and W13. The calculations follow the method detailed in section 2.9. The ages of bentonites W8 and W13 are from Table 3.1. Uncertainties are at the 95 % confidence level.

3.4.1.2.3. Synthesis of periodicity calculations

A summary of the average periodicity estimates obtained from the Livian and Lower Warnantian sedimentary cycles is presented in Fig. 3.28. The imprecision on the periodicity estimate for the sedimentary cycles between the L1 and L2 bentonite horizons, which is a function of the short time duration and small number of intervening cycles, negates a definitive interpretation. The preliminary average periodicity estimates for the Livian cycles between bentonites L2, L3 and W1 suggest that the periodicity of the Livian cycles is not constant. There is also a poor overlap between the average periodicity estimates from the Livian cycles and the Milankovitch frequencies; the

average periodicity of cycles between L3 and W1 overlaps marginally (at the upper 95 % confidence limit) with the *c.* 100 kyrs 'short' eccentricity frequency (Fig. 3.28), whereas the average periodicity of cycles between bentonites L2 and L3 is substantially longer than the 'short' eccentricity band (Fig. 3.28). The available preliminary periodicity estimates for the Livian sedimentary cycles therefore do not lend support to these cycles being controlled by Milankovitch cycles. However, it is not possible at this time to definitively exclude a Milankovitch control for the Livian sedimentary cycles. The accuracy of the Livian periodicity estimates is limited by a lack of detailed information about the Livian sedimentary cycle record (section 3.4.1.2.1). If in the future the record of Livian sedimentary cycles is better characterised, it may be possible to generate more robust periodicity estimates and better evaluate whether the Livian sedimentary cycles possess a Milankovitch beat. Additional U-Pb zircon CA-ID-TIMS dates from bentonites L4 or L5 (Fig. 3.1) would also provide further insight into the periodicity of Livian sedimentary cycles.

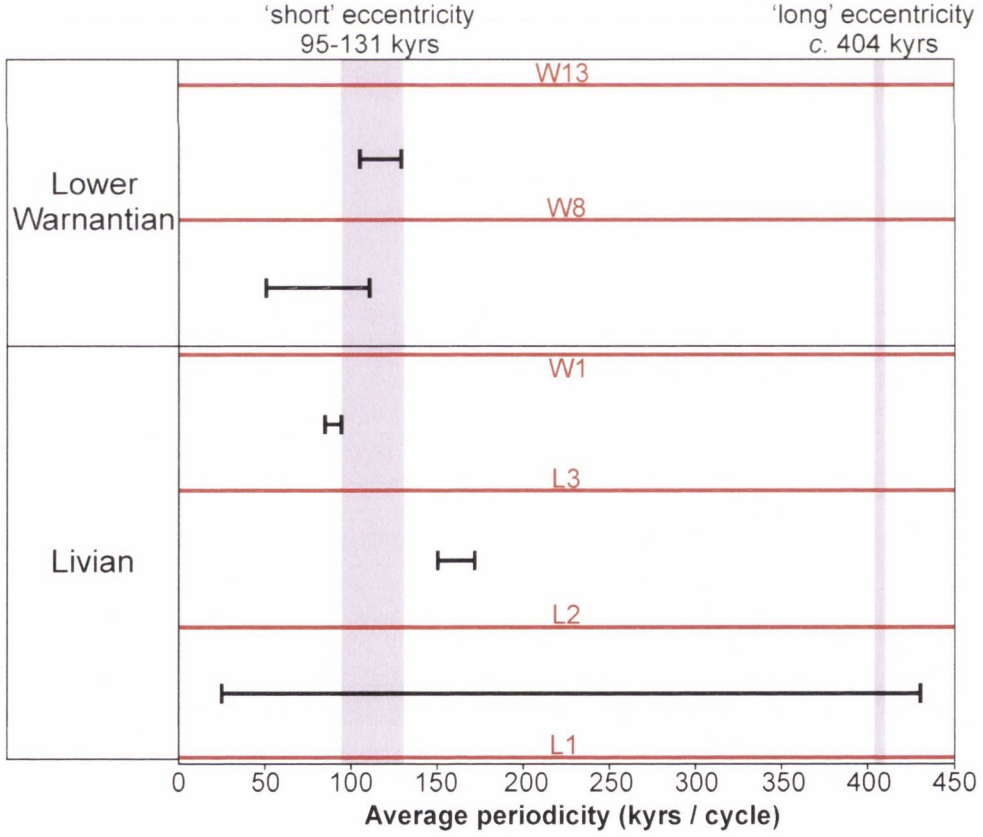

Figure 3.28. A summary of the average periodicity estimates for Livian and Lower Warnantian sedimentary cycles calculated against the new U-Pb zircon CA-ID-TIMS age constraints. The uncertainties on the periodicity estimates are illustrated as black horizontal lines and are drawn at the 95 % confidence level. Milankovitch eccentricity frequencies are illustrated as purple bands. The spacing of bentonite horizons on the y-axis is not to scale.

In contrast to the Livian cycles, the average periodicities of Lower Warnantian cycles show good overlap with the Milankovitch 100 kyrs 'short' eccentricity frequency, which is the dominant Milankovitch frequency identified in Pleistocene glacial records (e.g. Hays *et al.*, 1976; Imbrie *et al.*, 1993; Lisiecki, 2010). Therefore, the available periodicity calculations could be argued to support the hypothesis that these cycles record glacio-eustatic oscillations.

The available periodicity calculations may support the hypothesis that the onset of major Carboniferous glaciation occurred close to the base of the Warnantian Substage. This is in agreement with the suggestions of Wright & Vanstone (2001) that major Carboniferous glaciation commenced at the base of the Asbian Substage (equivalent to the Lower Warnantian). Furthermore, the new U-Pb zircon CA-ID-TIMS dates from the Belgian bentonites (Table 3.1) constrain this inferred onset of glaciation to between 336.22 ± 0.40 Ma and 335.59 ± 0.44 Ma (dates from bentonites W1 and W8 in Table 3.1; uncertainties are at the 95 % confidence level and include systematic uncertainties arising from the calibration of the isotopic tracer solution and the ^{238}U decay constant).

3.4.2. Comparisons between the new U-Pb zircon CA-ID-TIMS data and existing age constraints

In this section, comparisons are made between the new U-Pb zircon CA-ID-TIMS dates from the Belgian Visean bentonite horizons presented in previous sections (summarised in Table 3.1) and existing isotopic age data from comparable stratigraphic levels that have been included in previous Carboniferous timescale calibrations (e.g. Davydov *et al.*, 2004). Five existing age constraints are discussed, which comprise two U-Pb zircon ID-TIMS dates (Trapp, 2001; Fig. 3.29) and three U-Pb zircon SHRIMP dates (Roberts *et al.*, 1995a; Kryza *et al.*, 2010; Claoué-Long *et al.*, unpublished; Fig. 3.29). Only one of the Davydov *et al.* (2010) U-Pb zircon CA-ID-TIMS dates is from a comparable stratigraphic level to the Belgian horizons dated in this study (sample C1ve2; Fig. 3.29). This date discussed within the context of the timing of the base of the Livian Substage in section 3.4.3.1.

There are also two Mississippian $^{207}Pb/^{206}Pb$ zircon (evaporation method) dates from comparable stratigraphic levels but these are not discussed in detail. One date is from a

bentonite of early to late Tournaisian age (*Siphonodella crenulata* to *Scaliognathus anchoralis* conodont zones) that was sampled from the Thuringian Slate Mountains, Germany (Obernitz sample = 352 ± 8 Ma; discussed in Weyer & Menning, 2006). The second $^{207}Pb/^{206}Pb$ date is from a bentonite horizon of late Asbian or early Brigantian age that was sampled from northwest Frankenberg, Saxony, Germany (Frankenberg sample = 330 ± 4 Ma; discussed in Weyer & Menning, 2006). These dates are of uncertain accuracy (because there is no internal consistency check on a zircon age when only the Pb isotopes are analysed), are imprecise and are from bentonite horizons that are not well constrained biostratigraphically. These limitations negate meaningful comparisons with the new U-Pb zircon CA-ID-TIMS dates.

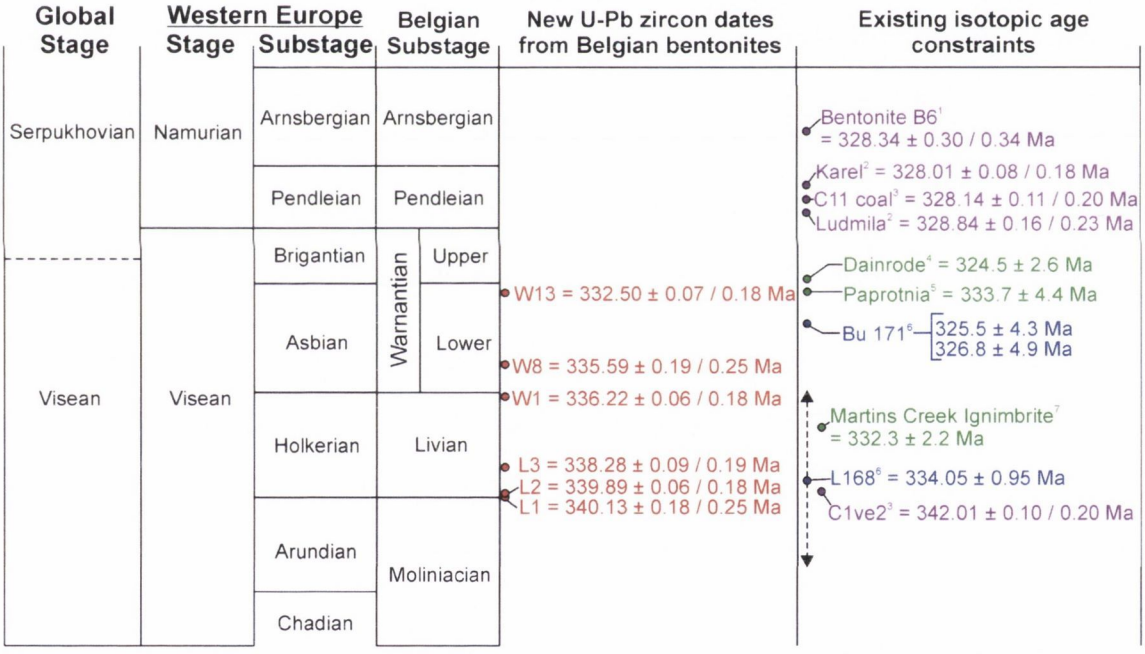

Figure 3.29. A comparison between the new U-Pb zircon CA-ID-TIMS dates from Belgian bentonite horizons (dates shown in red) and published isotopic dates from comparable stratigraphic levels. Existing isotopic dates are colour-coded accordingly to the methodology used: blue = U-Pb zircon ID-TIMS dates; purple = U-Pb zircon CA-ID-TIMS dates; green = U-Pb zircon SHRIMP dates. Reference sources for the existing isotopic data: 1) Waters & Condon (2012); 2) Gastaldo *et al.* (2009); 3) Davydov *et al.* (2010); 4) Claoué-Long *et al.* (unpublished); 5) Kryza *et al.* (2010); 6) Trapp (2001); 7) Roberts *et al.* (1995a). All date uncertainties are shown at the 2σ or 95 % confidence level. Uncertainties on the U-Pb zircon CA-ID-TIMS dates (red and purple dates) are shown as ± internal error / internal error plus tracer uncertainties (± 0.05 %, 2σ). The stratigraphic uncertainty of sample L168 is redrawn from Trapp (2001).

3.4.2.1. Trapp (2001) U-Pb zircon ID-TIMS dates (samples L168 and Bu 171)

Trapp (2001) reported two U-Pb zircon ID-TIMS dates from mid-to-upper Visean bentonite horizons interbedded with siliciclastic strata within the Harz Mountains, Germany (samples L168 and Bu 171). Most of the analyses undertaken by Trapp (2001) were of 1 – 2 grain aliquots that were air abraded (*sensu* Krogh, 1982) prior to dissolution. These dates have never been published in a peer-reviewed journal but have become entrained into published Carboniferous timescale calibrations (e.g. Davydov *et al.*, 2004; Weyer & Menning, 2006) because of the dearth of published high-precision Carboniferous isotopic age constraints (section 1.4).

3.4.2.1.1. Sample L168 (Lerbach)

This sample was collected from a bentonite layer constrained to within the conodont *Gnathodus texanus* biozone. As noted by Menning *et al.* (2001) and Weyer & Menning (2006), this conodont zone is of extremely long duration (Chadian to Holkerian) and thus the stratigraphic position of this bentonite horizon is imprecise. Weyer & Menning (2006) considered this horizon to be located within the upper part of the *Gnathodus texanus* conodont zone. The U-Pb zircon ID-TIMS data from this sample are redrawn from Trapp (2001) in Fig. 3.30. Two data points are not drawn in Fig. 3.30 because they yield very young and discordant dates (analyses 4 and 12 of Trapp, 2001; $^{206}Pb/^{238}U$ dates of 112.2 ± 0.5 Ma and 307.8 ± 1.2 Ma respectively) that are consistent with lead loss. The data show some dispersion beyond analytical uncertainties. Trapp (2001) interpreted the oldest, concordant analyses to be representative of the crystallisation age of this sample (red analyses in Fig. 3.30) and suggested the concordia age (*sensu* Ludwig, 1998) of these analyses (334.0 ± 0.6 Ma) to be the best estimate for the crystallisation age of this horizon. The MSWD of this age determination exceeds the acceptable range of values at the 95 % confidence level (section 2.3.5.2.5), suggesting that there is complexity present within this sample. Taking the same data points as used by Trapp (2001) for the concordia age calculation but instead calculating the weighted mean $^{206}Pb/^{238}U$ date yields a date of 334.05 ± 0.95 Ma (95 % conf., MSWD = 2.3, p = 0.042; Fig. 3.30). The uncertainty on this latter calculation is expanded to account for the additional data scatter (see section 2.3.5.2.5 for details).

The Lerbach bentonite should correlate to a horizon close to or lower than the W1 horizon (Fig. 3.29); however, the date from this horizon is over 1 Myrs younger than the W1 horizon (336.22 ± 0.18 Ma, 95 % conf., includes tracer calibration uncertainties). There is evidence of lead loss in some of the grains analysed from this sample and it is possible that some of the analyses included in the concordia age and weighted mean $^{206}Pb/^{238}U$ date calculations are also affected by subtle lead loss, which is biasing the concordia age and weighted mean date calculations towards younger ages. Re-analysing grains from this sample using the chemical abrasion method (Mattinson, 2005), which is a more efficient method of mitigating lead loss, would test the accuracy of this age determination. Although, this is not recommended because of the large biostratigraphic uncertainty attached to this bentonite horizon.

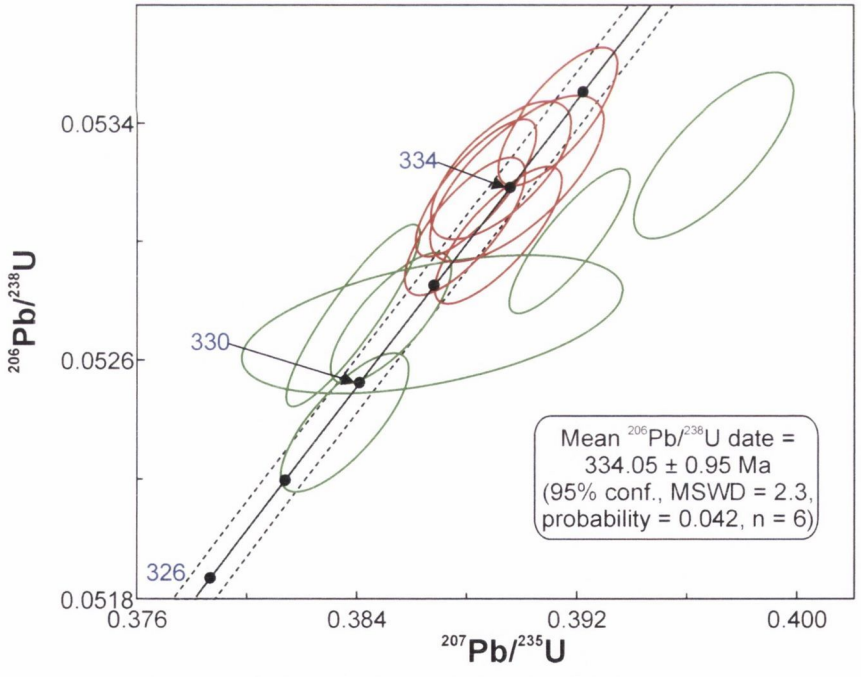

Figure 3.30. U-Pb zircon ID-TIMS data from sample L168 of Trapp (2001). Data are redrawn from Trapp (2001). Red and green ellipses denote data points included in and excluded from the average age calculations (weighted mean $^{206}Pb/^{238}U$ date, concordia age) respectively. Error ellipses are drawn at the 2σ confidence level.

3.4.2.1.2. Sample Bu 171 (Büchenberg)

Sample Bu 171 was collected from a bentonite horizon within the *Entogonites nasutus* ammonoid zone (Trapp, 2001). U-Pb zircon ID-TIMS dating yielded a heterogeneous distribution of dates (Fig. 3.31). There is a concordant population at *c.* 342 Ma (indicated by the red ellipses in Fig. 3.31b); however, Trapp (2001) considered this to represent an older, inherited population. Instead, Trapp (2001) fitted two discordia lines to subsets of the data (Fig. 3.31b). One discordia was interpreted to represent recent lead loss (blue label in Fig. 3.31b) and the other was inferred to represent xenocrystic inheritance (purple label in Fig. 3.31b). The two discordia intercepts overlap within uncertainty at *c.* 326 Ma (325.5 ± 4.3 Ma and 326.8 ± 4.9 Ma) and this age was interpreted by Trapp (2001) to represent the crystallisation age of this sample.

These two discordia intercept ages (325.5 ± 4.3 Ma and 326.8 ± 4.9 Ma) are inconsistent with the new U-Pb zircon CA-ID-TIMS dates from the Belgian samples. Based on the correlations between the ammonoid and foraminifera zones of Herbig (2006), who considered the *Entogonites nasutus* ammonoid zone to be older than the Cf6γ foraminifera subzone, bentonite Bu 171 should correlate to a horizon below the W13 bentonite (Fig. 3.29). However, the two discordia intercepts suggested by Trapp (2001) yield dates very much younger than that of bentonite W13 (332.50 ± 0.18 Ma, 95 % conf., includes tracer calibration uncertainties). The Bu 171 bentonite horizon is certainly older than the base of the Namurian, yet the discordia intercept ages obtained by Trapp (2001) for this sample are substantially younger than several recently published high-precision U-Pb zircon CA-ID-TIMS dates from early Serpukhovian / Namurian bentonites (bentonite B6, C11 coal, Karel and Ludmila samples; Gastaldo *et al.*, 2009; Davydov *et al.*, 2010; Waters & Condon, 2012; illustrated in Fig. 3.29) and recent estimates for the age of the base of the western European regional Namurian Stage (329.2 – 329.7 Ma; Gastaldo *et al.*, 2009; Davydov *et al.*, 2010).

The double discordia interpretation of Trapp (2001) is a novel approach to interpreting a complex dataset; however, it is of questionable accuracy. The fact that the two discordia intercepts overlap within uncertainty may be a coincidence without any geological significance, which arises through filtering of the dataset.

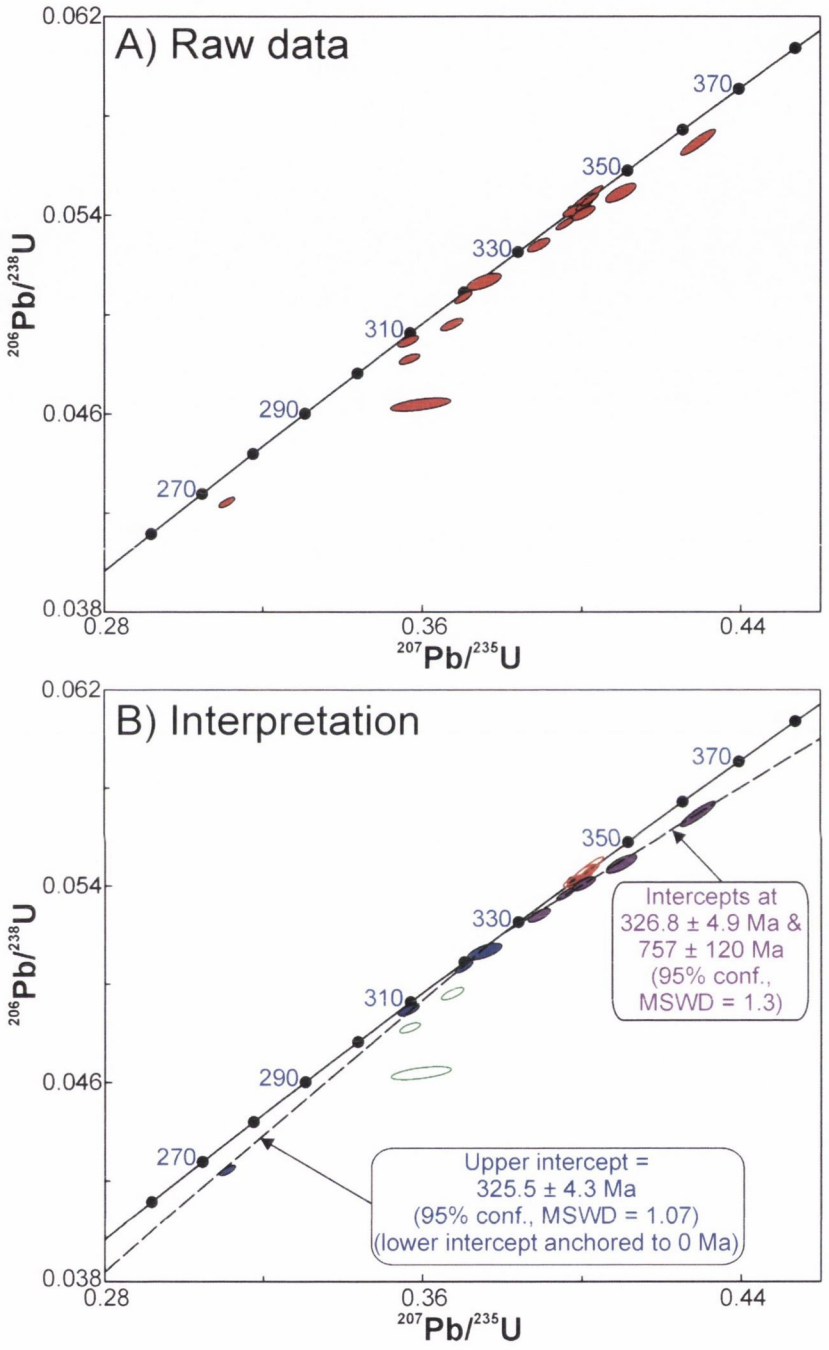

Figure 3.31. U-Pb zircon ID-TIMS data from sample Bu 171 (redrawn from Trapp, 2001). In plot B, the blue filled error ellipses are analyses included in the lower discordia calculation and the purple filled ellipses are analyses included in the upper discordia calculation. The two discordias are redrawn from Trapp (2001). Green error ellipses are data points not used in the interpretation. In both plots, the error ellipses are drawn at the 2σ confidence level.

3.4.2.2. U-Pb zircon SHRIMP dates

3.4.2.2.1. Martins Creek Ignimbrite (Roberts et al., 1995a)

The Martins Creek ignimbrite of eastern Australia is constrained to lie above the *Linoprotonia tenuirugosa* brachiopod subzone and either below or within the lower part of the *Rhipidomella fortimuscula* brachiopod zone (Roberts *et al.*, 1995a). It is suggested to correlate to a horizon within the Holkerian Substage of western Europe (Roberts *et al.*, 1995a). U-Pb SHRIMP dating of zircon grains from the Martins Creek ignimbrite (calibrated against the SL-13 zircon standard) was undertaken by Roberts *et al.* (1995a). The data obtained revealed the presence of inheritance and subtle lead loss within the sample. Nine analyses out of 32 were interpreted to contain small amounts of lead loss and were excluded from the weighted mean $^{206}Pb/^{238}U$ date calculation. The remaining 23 analyses yielded a weighted mean $^{206}Pb/^{238}U$ date of 332.3 ± 2.2 Ma (2σ, MSWD = 1.41). Based on the biostratigraphic correlation scheme suggested by Roberts *et al.* (1995a), this horizon should correlate to a horizon between L1 and W1 (Fig. 3.29). However, this U-Pb SHRIMP date is substantially younger than the $^{206}Pb/^{238}U$ date from the W1 horizon (336.22 ± 0.18 Ma, 95 % conf., includes tracer calibration uncertainties).

Within the Martins Creek ignimbrite sample there is clear evidence of lead loss. It is possible that several analyses included in the weighted mean date calculation are also affected by lead loss, but that this is unresolvable within the analytical uncertainties of these early-to-mid 1990s SHRIMP analyses, and is biasing the weighted mean calculation towards a younger date.

3.4.2.2.2. Paprotnia Beds bentonite (Kryza et al., 2010)

Kryza *et al.* (2010) recently reported a U-Pb zircon SHRIMP date from a bentonite layer within the Paprotnia Beds, Poland, NE Bohemian Massif. The bentonite is constrained to the upper Asbian *Goniatites crenistria* (Go IIIα) ammonoid zone (Kryza *et al.*, 2010). 12 out of 15 analyses were reported by Kryza *et al.* (2010) to yield a concordia age of 334 ± 3 Ma. Taking the same data points but instead calculating the weighted mean $^{206}Pb/^{238}U$ date yields a date of 333.7 ± 4.4 Ma (95 % conf, MSWD = 2.3, p = 0.007). These data are more scattered than can be accounted for by analytical

uncertainties alone and thus the uncertainty on this $^{206}Pb/^{238}U$ weighted mean date is expanded to take into consideration this excess scatter (as described in section 2.3.5.2.5). Based on the correlations between ammonoid and foraminifera biozones suggested by Herbig (2006), this bentonite should correlate to a horizon close to that of the W13 bentonite (Fig. 3.29) and indeed the U-Pb zircon CA-ID-TIMS date from W13 (332.50 ± 0.18 Ma, 95 % conf., includes tracer calibration uncertainties) and the U-Pb SHRIMP date from this bentonite (333.7 ± 4.4 Ma) are indistinguishable within analytical uncertainties.

3.4.2.2.3. Dainrode bentonite (Claoué-Long et al., unpublished; discussed in Weyer & Menning, 2006)

This bentonite horizon was sampled from a quarry *c.* 1 km east of Dainrode, Hessen, within the Rhenish Mountains, Germany (Weyer & Menning, 2006). The bentonite layer occurs within the *Goniatites spirifer* ammonoid zone (Weyer & Menning, 2006), which is correlated to the P1b (*Arnsbergites Falcatus*) ammonoid zone of the British Isles (Korn, 1994). The P1b ammonoid zone is the lowest zone of the Brigantian Substage (Riley, 1993; Fig. 4.1) and thus the Dainrode bentonite is of early Brigantian age.

U-Pb SHRIMP dating of several zircon grains from this horizon was undertaken by J. Claoué-Long during the early 1990s and yielded a weighted mean $^{206}Pb/^{238}U$ date of 324.5 ± 2.6 Ma (calibrated against the standard zircon SL-13; Weyer & Menning, 2006). J. Claoué-Long has subsequently stated that this age determination may be inaccurate, citing problems of high uranium concentrations and lead loss from grains in this sample (discussed in Weyer & Menning, 2006). However, Weyer & Menning (2006) contended that in the light of the Trapp (2001) date from the Büchenberg sample (Bu 171; section 3.4.2.1.2) this SHRIMP date has geological significance. The U-Pb date from this sample, like the Bu 171 date of Trapp (2001) discussed previously (section 3.4.2.1.2), is stratigraphically inconsistent with the current age for the base of the Namurian Stage (see section 3.4.2.1.2). It is also very much younger than the new U-Pb zircon CA-ID-TIMS date from bentonite W13 and the Kryza *et al.* (2010) SHRIMP date from an upper Asbian bentonite (section 3.4.2.2.2), which both occupy similar stratigraphic positions to the Dainrode bentonite (Fig. 3.29).

3.4.3. Implications for timescale calibration

The new U-Pb zircon CA-ID-TIMS dates (Table 3.1) provide additional age constraints for the temporal calibration of the Belgian substages (the base of the Livian, Warnantian and Upper Warnantian boundaries). In this section, the boundary ages determined using the new U-Pb zircon CA-ID-TIMS dates are compared to estimates from recent published Carboniferous timescales (Davydov *et al.*, 2004, 2010; Menning *et al.*, 2006).

The bentonite 300 horizon (Fig. 3.32) is located too far below the Tournaisian – Visean boundary (*c.* 100 m) to provide a direct estimate of the age of this stratigraphic boundary. Without resorting to assumptions based upon constant sedimentation rates to correct for the amount of time within the intervening *c.* 100 m of stratigraphy, it is only possible to state that this age determination is consistent with the boundary age of 346.3 Ma suggested by Davydov *et al.* (2010; Fig. 3.32). This age constraint, however, is an additional constraint that can be integrated in future iterations of the Carboniferous timescale.

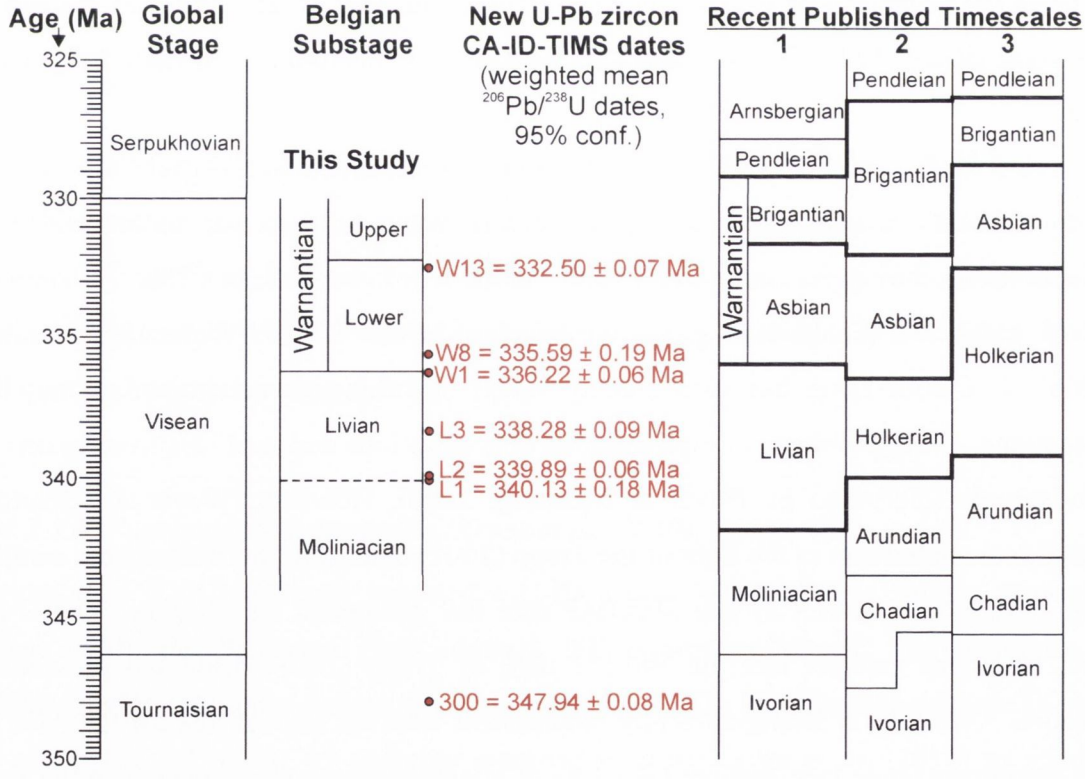

Figure 3.32. Revised absolute age estimates for some western European regional stratigraphic boundaries, derived using the new U-Pb zircon CA-ID-TIMS dates and astronomical tuning. These are compared to recent published Carboniferous timescales. Published timescales: 1) Davydov *et al.* (2010); 2) Menning *et al.* (2006); 3) Davydov *et al.* (2004). The ages of the global stage boundaries are from Davydov *et al.* (2010).

3.4.3.1. Base of the Livian Substage

The base of the Livian Substage (correlated with the base of the British Holkerian Substage; Poty & Hance, 2006a) is currently defined as at the base of the Banc d'Or de Bachant (= L1 bentonite; Poty & Hance, 2006a) and is equated with the base of the Cf5 foraminifera zone of Conil *et al.* (1990) and the base of the MFZ 12 (*Pojarkovella nibelis*) foraminifera zone of Poty *et al.* (2006). This is an unsatisfactory boundary definition because the Banc d'Or de Bachant horizon is of limited geographical extent (i.e. restricted to the Namur-Dinant Basin) and, more importantly, it is unclear whether this horizon coincides with the first occurrence of the Livian guide taxa *Pojarkovella nibelis* (Poty & Hance, 2006a). This is because in the Namur-Dinant Basin the Moliniacian – Livian boundary interval is characterised by very shallow water depths and an impoverished faunal assemblage (Poty & Hance, 2006a). It has been suggested that in more open marine environments the Livian guide taxa may enter at a lower level than the L1 bentonite horizon (Poty & Hance, 2006a).

Davydov *et al.* (2010) recently determined a date of 341.9 Ma for the base of the MFZ 12 (equated with the base of the Livian Substage; Fig. 3.32) in the Donets Basin, Ukraine. This estimate is tightly constrained by an isotopic date from a bentonite horizon within the lower Styl'skaya Formation (sample C1ve2; 342.01 ± 0.10 Ma; 2σ; Davydov *et al.*, 2010) that correlates to a horizon within the lower Livian (Davydov *et al.*, 2010; Fig. 3.29). This estimate for the base of the Livian is considerably older than the new CA-ID-TIMS date from the L1 horizon (340.13 ± 0.18 Ma; 95 % conf; Fig. 3.32).

The discrepancy between these two dates can be reconciled by either the guide taxa entering earlier in regions outside of the Namur-Dinant Basin or that there is a substantial hiatus (1 – 2 Myrs) within the Namur-Dinant Basin, across the Molinacian – Livian boundary interval. Unfortunately these two possibilities cannot be distinguished on the basis of the available data. There is, however, field evidence to support the latter; the lower boundary of the L1 bentonite is often erosive and conglomeratic (Delcambre, 1989, 1996), which is consistent with prolonged sub-aerial exposure. Additionally, Delcambre (1989, 1996) noted that towards the south and east of the basin, multiple (up to three) closely-spaced bentonite layers (separated by thin limestone horizons) are present that yield the zircon typology assemblage characteristic of the L1 bentonite.

Delcambre (1989) noted that these horizons appear to coalesce towards the north and west, where L1 is represented by only a single layer (e.g. at Lives-sur-Meuse). Further age constraints from the L1 horizon(s) at localities in the south and east of the basin would help to resolve how much time is contained within this stratigraphic interval.

3.4.3.2. Base of the Warnantian Substage

The base of the Warnantian Substage (correlated with the base of the British Asbian Substage; Poty & Hance, 2006b) is defined as at the base of the Bonne River Formation (Poty & Hance, 2006b) and corresponds with the bases of the Cf6 (Conil *et al.*, 1990) and MFZ 13 foraminifera biozones (Poty *et al.*, 2006). The boundary stratotype for the base of the Warnantian was chosen within the Samson Valley (NSA; Poty & Hance 2006b) at the boundary between the Bay Bonnet Member (Grands Malades Formation) and the Thon Samson Member (Bonne River Formation; Poty & Hance, 2006). The current stratotype locality is unsatisfactory because the appearance of the Warnantian guide fossils coincides with a major change in the depositional environment, from a restricted to an open marine environment (Poty & Hance, 2006b). The search for a more suitable boundary stratotype is ongoing (Poty & Hance, 2006b).

The new CA-ID-TIMS date from bentonite W1 provides insights into the age of the base of the Warnantian as it is currently defined. W1 occurs within the middle of the Bay Bonnet Member (Delcambre, 1996), 4 m below the base of the Warnantian Substage and thus the age of the W1 horizon (336.22 ± 0.06 Ma; 95 % conf.) can approximate the age of this stratigraphic boundary. This is substantially older than the base of the Asbian suggested in the Geologic Time Scale 2004 (Davydov *et al.*, 2004; 332.5 Ma; Fig. 3.32) but is comparable to values shown in the more recent timescales of Davydov *et al.* (2010; 336.0 Ma) and Menning *et al.* (2006; 336.5 Ma; Fig. 3.32).

3.4.3.3. Base of the Upper Warnantian and the duration of the Early Warnantian

The Upper Warnantian corresponds to the Cf6δ foraminifera zone of Conil *et al.* (1990; section 3.3.2.1) and is correlated with the British Brigantian Substage (Poty & Hance, 2006b; section 3.3.2.1). Bentonite W13 occurs three sedimentary cycles (8.5 m) beneath the base of the Upper Warnantian. Assuming these sedimentary cycles adhere to the

c. 100 kyrs Milankovitch eccentricity cycle, and tuning the intervening three sedimentary cycles to this astronomical beat, constrains the base of the Upper Warnantian to *c.* 332.2 Ma. This is substantially older than the base of the Brigantian suggested by Davydov *et al.* (2004; 328.8 Ma; Fig. 3.32) but is similar to the boundary ages shown in Davydov *et al.* (2010; 331.6 Ma; Fig. 3.32) and Menning *et al.* (2006; 332 Ma; Fig. 3.32).

The new CA-ID-TIMS dates from bentonites W1 and W13 suggest that the Early Warnantian is of approximately 4 Myrs duration. This is similar to the duration of the Asbian Substage suggested in all of the recent published Carboniferous timescale compilations illustrated in Fig. 3.32 (Davydov *et al.*, 2004, 2010; Menning *et al.*, 2006).

3.5. Conclusions

Several western European diagenetically altered volcanic ash layers were dated by the U-Pb zircon CA-ID-TIMS method and yielded high-precision isotopic dates. New U-Pb zircon dates from mid-to-upper Visean bentonite horizons within the Namur-Dinant Basin (Belgium) were employed to estimate the periodicity of Belgian Livian and Warnantian sedimentary cycles. These estimates suggested that the periodicity of Livian sedimentary cycles was not constant and the cycles show poor overlap with the periodicities of Milankovitch cycles. In contrast, periodicity estimates from the Lower Warnantian sedimentary cycles overlap with the Milankovitch *c.* 100 kyrs eccentricity band. This is the dominant Milankovitch band observed in the Pleistocene glacial record (e.g. Hays *et al.*, 1976) and it is possible that these cycles were the result of glacio-eustatic oscillations. The available periodicity estimates therefore support an appearance of glacio-eustatic cyclic sedimentation and the onset of major Gondwanan glaciation close to the base of the Belgian Warnantian Substage (which is correlated with the base of the Asbian Substage; Poty & Hance, 2006b). This interpretation is in agreement with the views of Wright & Vanstone (2001), who proposed that major Carboniferous glaciation commenced at the base of the Asbian. The new Belgian U-Pb zircon CA-ID-TIMS dates provide a high-precision temporal framework for the western European stratigraphic record and constrain the inferred onset of glaciation to between 336.22 ± 0.40 Ma and 335.59 ± 0.44 Ma (dates from bentonites W1 and W8 in Table 3.1; uncertainties are at the 95 % confidence level and include both tracer calibration

and decay constant uncertainties). In the future, as more isotopic age data become available from the 'direct' Gondwanan glacial records, it may be possible to use high-precision geochronology as a means of correlating between the ice-distal proxy records and direct glacial records on Gondwana independently of biostratigraphic correlations that are complicated by faunal endemism. Ultimately, this will elucidate a better understanding of the onset of major Carboniferous glaciation.

The new U-Pb zircon CA-ID-TIMS age constraints from Belgian Visean bentonites suggest that the existing U-Pb zircon ID-TIMS dates of Trapp (2001) and some U-Pb SHRIMP dates from the 1990s (Roberts *et al.*, 1995a; Claoué-Long *et al.*, unpublished; section 3.4.2.2) are anomalously young. The new dates presented in this chapter, in conjunction with the Mississippian dates presented by Davydov *et al.* (2010), go some way towards addressing the deficit of high-precision absolute age constraints from the Mississippian Subsystem.

Chapter 4

Irish Visean (Mississippian) clay partings

4.1. Introduction

Several Irish Asbian and Brigantian clay-rich horizons that occur interbedded with carbonate and siliciclastic sedimentary strata (respectively) were investigated to determine if they contained volcanic zircon populations of Carboniferous age, which could be used to provide absolute age constraints on the adjacent stratigraphy. Some of the investigated samples yielded zircon populations which were characterised using a combination of binocular optical microscopy, scanning electron microscopy with cathodoluminescence imaging (SEM-CL) and U-Pb zircon LA-MC-ICP-MS dating. The samples are presented in stratigraphic order (Fig. 4.1) in this chapter.

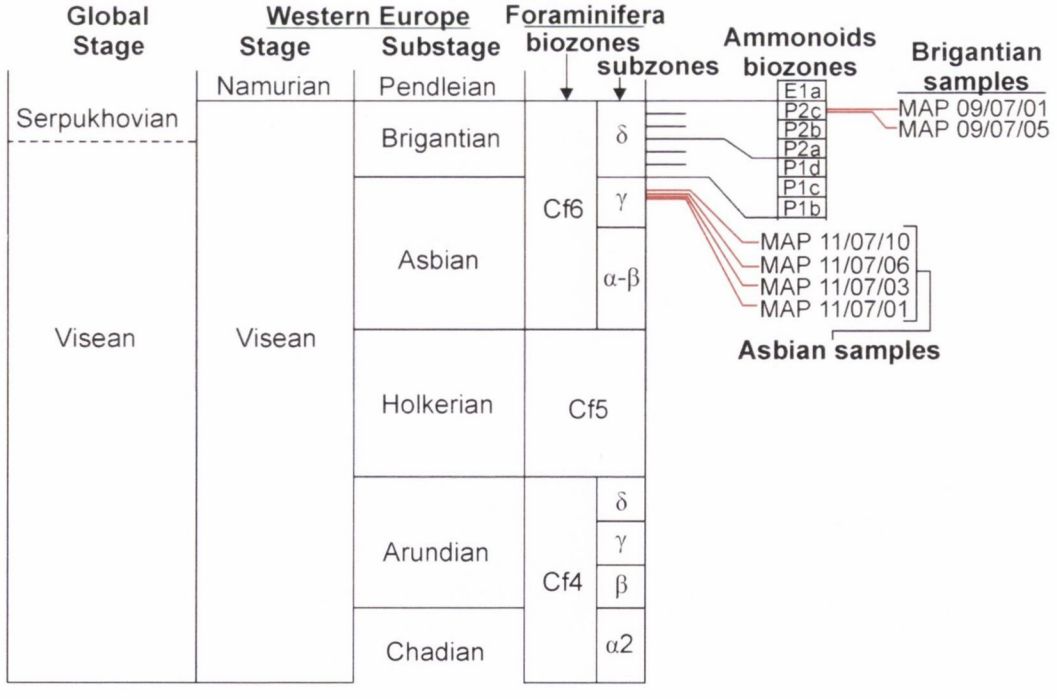

Figure 4.1. A stratigraphic column of the samples discussed in this chapter. The stratigraphic positions of the Asbian samples are from Cózar & Somerville (2005) and the positions of the Brigantian samples are from Legg *et al.* (1998). Foraminifera biozones and subzones are from Conil *et al.* (1990). Ammonoid biozones are from Riley (1993). The position of the Visean – Serpukhovian boundary is from Sevastopulo & Barham (2011).

4.2. Irish Asbian clay-rich horizons

Numerous clay-rich palaeosols and shale partings are interbedded with upper Asbian cyclically bedded limestones in the Carlow area (Cózar & Somerville, 2005). Several clay-rich and shale layers were sampled in November 2007 from quarry faces within Ballyadams Quarry, County Laois (Fig. 4.2; Irish Grid Reference: S6216 9157) and processed for zircon. The rationale for this investigation was to search for volcanic horizons that could help to constrain the timing of the appearance of upper Visean cyclic sedimentation in Ireland.

Samples from four horizons were selected for zircon separation (Fig. 4.2a). These horizons are poorly consolidated and rest on undulose, palaeokarstic surfaces (e.g. MAP 11/07/06 in Fig. 4.2a). They are interpreted to represent palaeosols. Three of the horizons are dark brown (MAP 11/07/01, 03, 06), whereas horizon MAP 11/07/10 is orange and similar in appearance to the clay wayboards described by Walkden (1972). XRD analysis of material from these clay-rich horizons suggests the presence of illite-mica and quartz (Appendix 2 Table 2). Calcite is present in sample MAP 11/07/03 and is abundant in sample MAP 11/07/06 (Appendix 2 Table 2). The whole-rock geochemical data from these samples (determined by ICP-OES/MS; section 2.7) are discussed in section 7.3.2.

Two horizons yielded sparse (< 20 grains) but predominantly euhedral zircon populations (MAP 11/07/01, MAP 11/07/03). No zircons were recovered from the other two horizons (MAP 11/07/06, MAP 11/07/10). Zircon grains from the two productive horizons were imaged using SEM-CL at the British Geological Survey, Keyworth, UK (section 2.3.4.2.1).

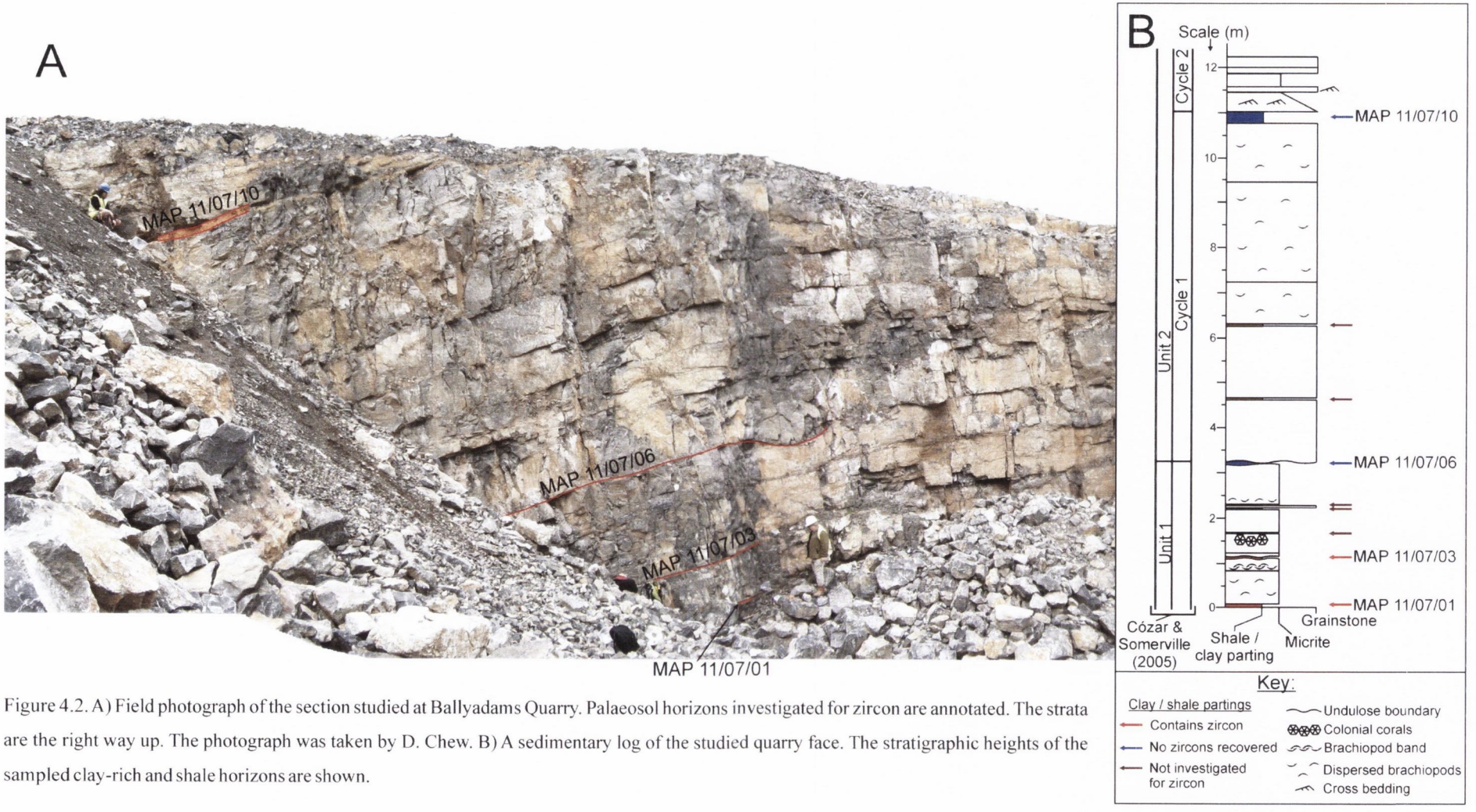

Figure 4.2. A) Field photograph of the section studied at Ballyadams Quarry. Palaeosol horizons investigated for zircon are annotated. The strata are the right way up. The photograph was taken by D. Chew. B) A sedimentary log of the studied quarry face. The stratigraphic heights of the sampled clay-rich and shale horizons are shown.

4.2.1. SEM imaging of grains from Irish Asbian clay partings

Several grains from sample MAP 11/07/01 display oscillatory zonation under SEM-CL (Fig. 4.3). Grain Z5 in Fig. 4.3 is an obvious exception to this trend and is a rounded grain with a patchy internal texture. There is little evidence of xenocrystic cores within the imaged grain populations, with the exception of grain Z3 which has a thin, bright overgrowth (Fig. 4.3). In contrast, the grains from sample MAP 11/07/03 were very dark under SEM-CL (suggesting high uranium contents), making it difficult to obtain useful textural information. U-Pb LA-MC-ICP-MS dating was subsequently undertaken on grains from both samples, following the methodology described in section 2.3.4.2.2.

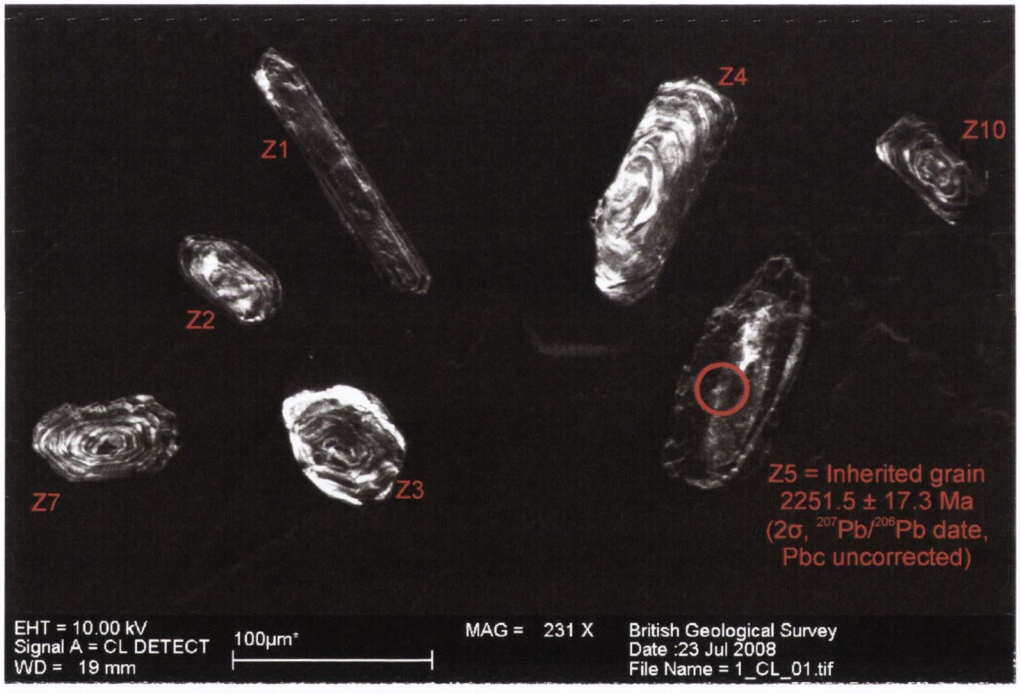

Figure 4.3. SEM-CL images of grains from sample MAP 11/07/01. Pbc = common lead.

4.2.2. U-Pb zircon LA-MC-ICP-MS dating

The results from U-Pb zircon LA-MC-ICP-MS dating of grains from samples MAP 11/07/01 and MAP 11/07/03 are illustrated in Fig. 4.4 and are also presented in Appendix 1 Table 2. Both samples yielded a suite of discordant analyses (filled purple ellipses in Fig. 4.4). Several analyses from sample MAP 11/07/01 and all of the analyses from sample MAP 11/07/03 contained measureable amounts of common lead. Before an interpretation can be attempted for these data, it is necessary to employ a

common lead correction (see section 2.3.4.2.2 for details of this correction). The common lead correction vastly improves the concordance of the data (open ellipses in Fig. 4.4), but adversely affects the precision of the U-Pb dates. The data uncorrected for common lead are not discussed further; the interpretation instead focuses on the common-lead corrected data.

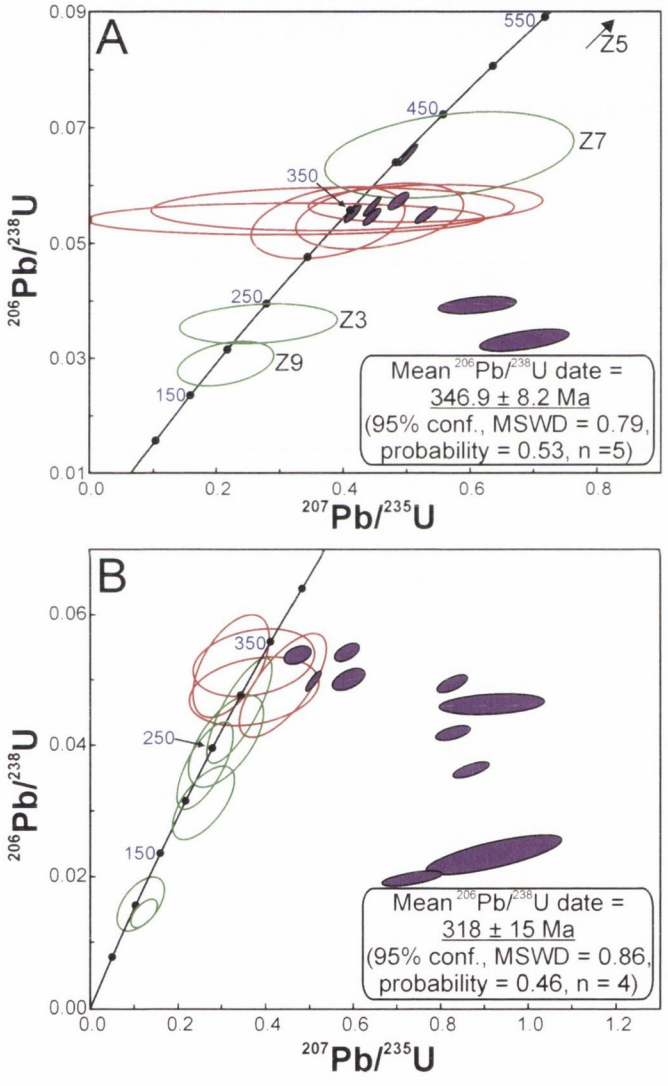

Figure 4.4. U-Pb concordia diagrams of LA-MC-ICP-MS data from samples MAP11/07/01 (plot A) and MAP 11/07/03 (plot B). Data uncorrected for common lead are drawn as filled purple ellipses. Open ellipses represent data corrected for common lead. Red and green ellipse outlines denote common-lead corrected analyses included in and excluded from the weighted mean $^{206}Pb/^{238}U$ date calculations respectively. The LA-MC-ICP-MS data drawn in this figure are presented in Appendix 1 Table 2.

Five grains from sample MAP 11/07/01 yielded concordant dates that are indistinguishable within analytical uncertainties (red ellipses in Fig. 4.4a). These five data points yield a Carboniferous weighted mean $^{206}Pb/^{238}U$ date of 346.9 ± 8.2 Ma (Fig. 4.4a). Two analyses (MAP110701/Z3 and MAP110701/Z9; Appendix 1 Table 2) yielded dates younger than the base of the Permian System (298.7 Ma; Davydov *et al.*,

2010) and are interpreted to have been affected by lead loss. Two further grains (MAP110701/Z5, MAP110701/Z7; Appendix 1 Table 2) yielded near-concordant dates (even before correction for common lead) that are older than the main cluster of analyses; grain Z5 yielded a $^{206}Pb/^{238}U$ date of 2309.8 ± 84.9 Ma (2σ, not corrected for common lead; Appendix 1 Table 2), whereas grain Z7 yielded a $^{206}Pb/^{238}U$ date of 407.4 ± 9.0 Ma (2σ, not corrected for common lead; Appendix 1 Table 2). Both of these grains are significantly older the base of the Carboniferous System (359.2 Ma; Davydov *et al.*, 2010) and are thus inconsistent with the stratigraphic position of this clay-rich horizon. These two grains are interpreted to represent inheritance and are possibly of detrital origin.

Data from sample MAP 11/07/03 are shown in Fig. 4.4b. A number of analyses yielded dates that are younger than the base of the Permian System (298.7 Ma; Davydov *et al.*, 2010) and are interpreted to contain lead loss. All of the grains analysed from this sample are uranium rich (> 900 ppm; Appendix 1 Table 2), which may account for the dark appearance of the grains when viewed under SEM-CL (see section 2.3.4.2.1). The oldest four grains analysed are of Carboniferous age and yield a weighted mean $^{206}Pb/^{238}U$ date of 318 ± 15 Ma (95 % confidence level; Fig 4.4b). This is significantly younger than the weighted mean $^{206}Pb/^{238}U$ date calculated from grains in sample MAP 11/07/01 (Fig 4.4a), although individual data points from these two samples overlap significantly at the 2σ confidence level. The weighted mean $^{206}Pb/^{238}U$ date from this sample is relatively young compared to the stratigraphic position of this sample; based on biostratigraphic constraints from benthic foraminifera, this clay-rich layer (Cf6γ foraminifera subzone; Fig. 4.1) should correlate to a horizon close to that of bentonite W13 in Belgium (also Cf6γ foraminifera subzone; Fig. 3.1). However, only towards the upper 95 % confidence limit does the weighted mean $^{206}Pb/^{238}U$ date approach a value that is consistent with the W13 U-Pb zircon CA-ID-TIMS date (332.50 ± 0.18 Ma; 95 % confidence level; includes tracer calibration uncertainties; Table 3.1). It is probable that one or more of the analyses included in the weighted mean calculation for this sample exhibits a small amount of lead loss, which is biasing the weighted mean date towards a younger value.

4.2.3. Potential for U-Pb zircon CA-ID-TIMS dating

U-Pb zircon LA-MC-ICP-MS data from samples MAP 11/07/01 and MAP 11/07/03 (section 4.2.2) confirm that both samples contain a zircon population (or populations) of Carboniferous age, although the source of these zircons is uncertain. The whole-rock geochemical data from these horizons (presented in chapter 7) suggests that they were originally sourced from a mafic, possibly alkaline magma (section 7.5.2). Such magmas could have been locally derived from volcanic centres within Great Britain and Ireland (section 7.5.2). Whether these magmas crystallised zircon is uncertain and it may be that the sparse zircon grains in these samples originated from elsewhere. One possibility is that the zircon grains were transported in from more distal, felsic volcanic centres but this is not represented in the whole-rock geochemistry because the amount of exotic ash in these horizons is small. Alternatively, the sparse zircon grains in samples MAP 11/07/01 and MAP 11/07/03 may originate from the local reworking of older Carboniferous lithologies. The presence of rounded and inherited grains in sample MAP 11/07/01 (section 4.2.2) may lend support to this hypothesis. Unfortunately, the available U-Pb zircon LA-MC-ICP-MS data (section 4.2.2) are of insufficient precision to differentiate between these possibilities; however, further insights into the origins of the Carboniferous sample grains may be gained from high-precision U-Pb CA-ID-TIMS analyses. Such an undertaking would require large samples (> 2 kg) as these layers are not very zircon rich.

If these horizons do contain a primary volcanic Carboniferous population, they could potentially provide useful age constraints on the adjacent stratigraphy and the appearance of upper Visean cyclic sedimentation in Ireland.

4.3. Brigantian clay-rich horizons

Several thin clay bands interpreted to be K-bentonites have been reported from within the upper Brigantian Carraun Shale Formation (adjacent to the Camderry Limestone Member; Fig. 4.5a) to the north and east of Lough Allen, Ireland (Brandon & Hodson, 1984; Legg *et al.*, 1998). These clay-rich layers occur close to the Visean – Namurian boundary (Fig. 4.5a), which is precisely located within the region (the index ammonoid *Cravenoceras leion* has been reported from nearby exposures; Legg *et al.*, 1998). Isotopic dates from these horizons would better constrain the age of this stratigraphic boundary.

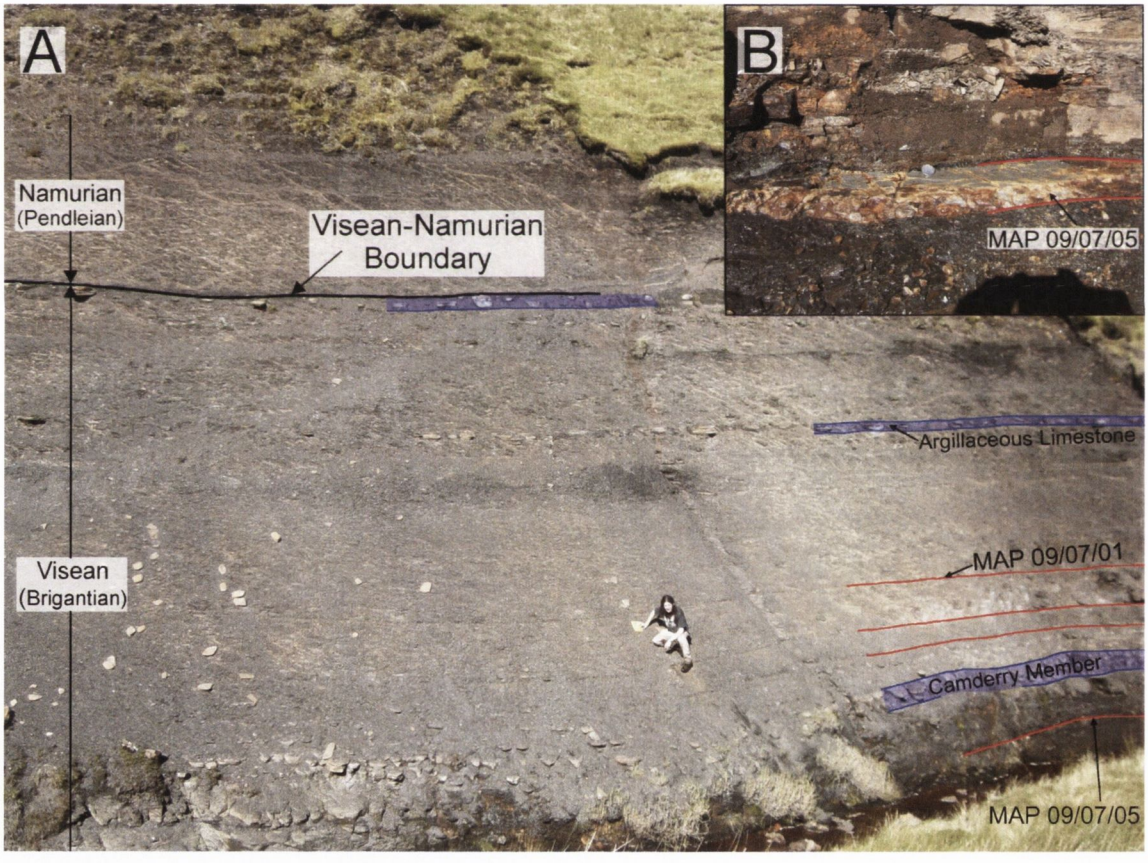

Figure 4.5. A) The section exposed at Altscraghy, Cuilcagh Mountain. Red lines denote the thin (< 5 cm) clay-rich horizons. Blue bands are limestone / dolomite horizons. The Visean stratigraphy is part of the Caurraun Shale Formation and the overlying Namurian stratigraphy is part of the Gubaveeny Shale Member (Dergvone Shale Formation; Legg *et al.*, 1998). B) A close-up of horizon MAP 09/07/05. The silver coin is a 10 pence piece (for scale). Both photographs were taken by D. Chew.

The clay bands were sampled at a locality called Altscraghy (Legg *et al.*, 1998), on Cuilcagh Mountain, Ireland (Irish Grid Reference: H1290 2893). Samples from two horizons were collected (MAP 09/07/01 and MAP 09/07/05; Fig. 4.5a) and processed for zircon separation. In outcrop, these clay bands are laterally continuous, pyritic, 2 – 3 cm thick, grey putty-like bands with sharp, orange-stained boundaries (Fig. 4.5b). XRD analysis of sample material from these two horizons suggests that they possess similar bulk mineralogies that include illite-mica (probably occurring as a mixed-layer clay), quartz and feldspar (possibly albite; Appendix 2 Table 2). Sample MAP 09/07/05 may also contain a small amount of kaolinite. Whole-rock geochemical data from these horizons are discussed in section 7.3.3. Both samples yielded rounded zircon populations (Fig. 4.6); no euhedral zircons were recovered from either sample. Nevertheless, SEM-CL imaging and U-Pb LA-MC-ICP-MS dating of grains from sample MAP 09/07/01 was undertaken.

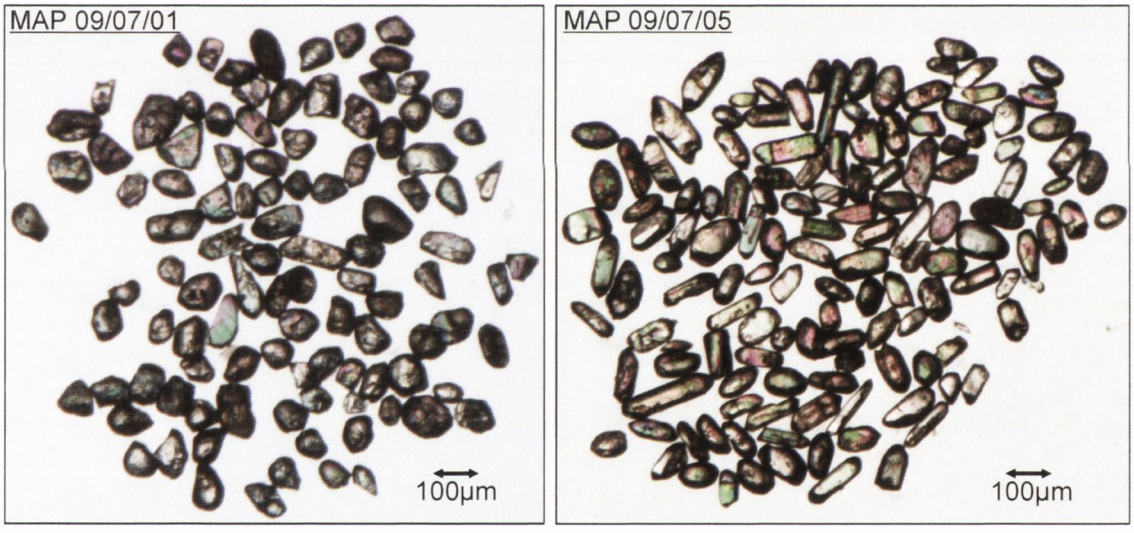

Figure 4.6. Optical photomicrographs (crossed polars) of zircons separated from samples MAP 09/07/01 and MAP 09/07/05. Bright colours are interference colours.

4.3.1. SEM-CL imaging of grains from sample MAP 09/07/01

Grains from sample MAP 09/07/01 show a range of internal textures under SEM-CL (Fig. 4.7). Oscillatory zonation, intra-grain cores with patchy or homogeneous overgrowths and evidence of localised recrystallisation (e.g. labelled areas of grains in Fig. 4.7) are recognisable. Additionally, some grains have patchy, chaotic internal

textures. The truncation of internal textures against external grain surfaces is common in grains from this sample.

Figure 4.7. SEM-CL image of grains from sample MAP 09/07/01.

4.3.2. U-Pb zircon LA-MC-ICP-MS results

The least rounded grains from sample MAP 09/07/01 were hand picked for U-Pb zircon LA-MC-ICP-MS dating, the results of which are illustrated in Fig. 4.8 and are also presented in Appendix 1 Table 2. Grains yielded a range of dates that are mostly concordant to near-concordant. No zircons of Carboniferous age were identified; the youngest concordant / near-concordant grain (< 15 % discordance; $^{207}Pb/^{206}Pb$ – $^{206}Pb/^{238}U$) identified has a $^{206}Pb/^{238}U$ date of 433.8 ± 10.5 Ma (2σ; analysis MAP090701/Z35 in Appendix 1 Table 2). The U-Pb dates obtained are inconsistent with the stratigraphic position of the sample horizon (uppermost Brigantian) and thus the zircon grains are interpreted to represent inheritance.

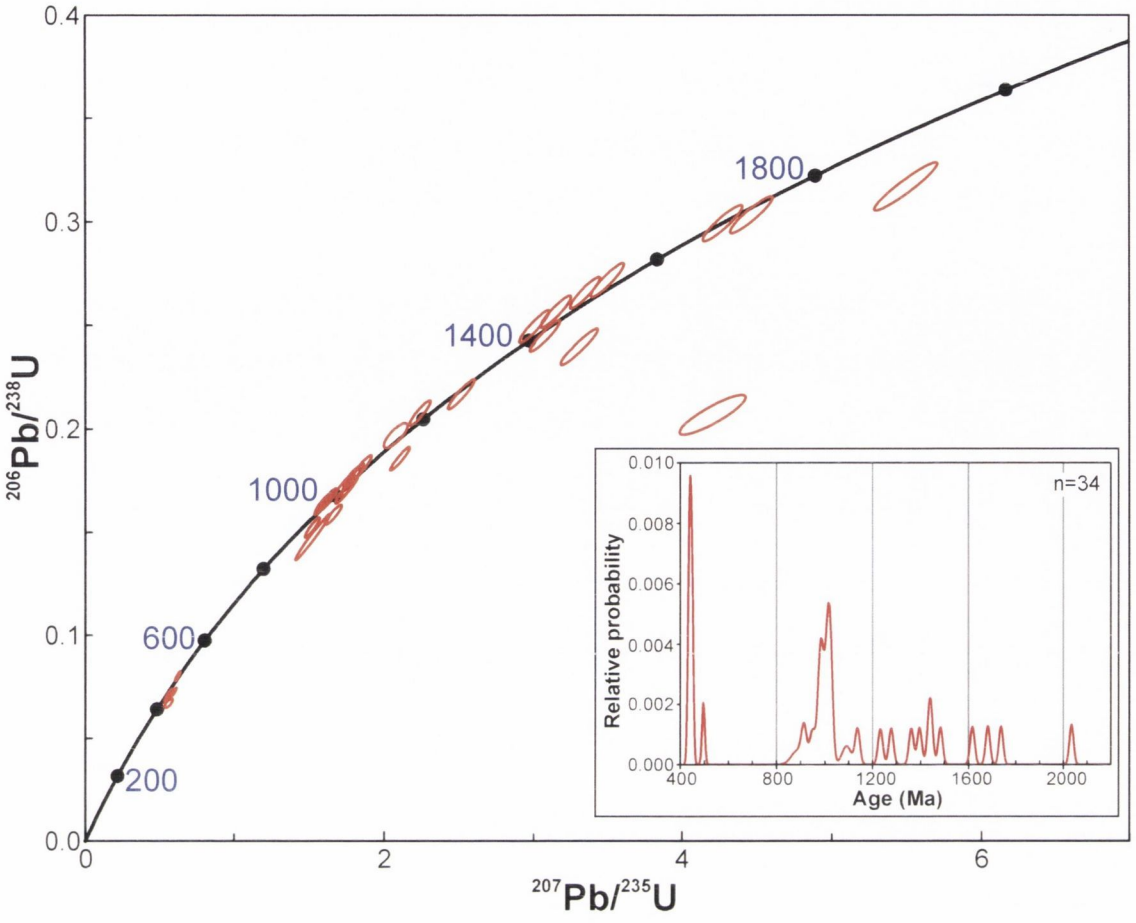

Figure 4.8. A concordia diagram of U-Pb zircon LA-MC-ICP-MS data from sample MAP 09/07/01. Error ellipses are drawn at the 2σ confidence level. The inset shows a probability density plot for analyses with < 15 % discordance (two data points are excluded). In the probability density plot, $^{206}Pb/^{238}U$ dates are used for grains younger than 1000 Ma, whereas $^{207}Pb/^{206}Pb$ dates are used for grains older than 1000 Ma, as $^{207}Pb/^{206}Pb$ dates are generally more precise for grains older than 1000 Ma. Sample LA-MC-ICP-MS data illustrated in this figure can be found in Appendix 1 Table 2.

The source of these grains is less certain; they could represent detrital contamination. In support of this hypothesis, it could be argued that the rounding of grains may be indicative of transportation. Thin section analysis of both sampled horizons reveals that they both contain rounded quartz grains. Additionally, in the nearby Lackagh Hills – Dough Mountain region, clay-rich horizons of similar appearance and stratigraphic position (probable lateral equivalents of the layers sampled herein) are observed that have been suggested to exhibit features consistent with both K-bentonite horizons and pyrite-cemented distal turbidites (Brandon & Hodson, 1984). Alternatively, these zircon grains could represent very late-stage assimilated material that was incompletely

resorbed into a zircon-undersaturated parent magma. In this scenario, the rounding of grains could be due to magmatic resorption. In Britain and Ireland, the majority of Mississippian (Tournaisian and Visean) magmatism was of mafic composition (Stephenson *et al.*, 2003) and thus there are known local magmatic centres that could be the source of such zircon-undersaturated ash. Unfortunately, the whole-rock geochemical data from these bentonites yield inconsistent information about the magmatic source from which these horizons were originally derived (summarised in section 7.5.3). It is likely that their whole-rock geochemistry has been modified by the assimilation of country rock into the parent magma and / or by post-eruption detrital additions. Thus, the whole-rock geochemistry of these bentonites may no longer preserve an accurate record of their magmatic source (section 7.5.3).

Some provenance information can be extracted from these U-Pb data, the extent of which is limited by the small number of robust analyses (i.e. analyses with < 15 % discordance; n = 34), which total fewer than are generally considered to be necessary for a statistically-robust provenance analyses; Vermeesch (2004) suggested that 117 analyses were necessary in order to attain 95 % confidence that an age population of ≥ 5 % was not overlooked. Because fewer than 117 analyses were obtained from sample MAP 09/07/01 it is possible that some minor age populations are unrepresented within the sample dataset; based on equations presented in Vermeesch (2004) there is 95 % confidence for this dataset that no age population of ≥ 14 % has been missed. Using the available U-Pb sample data, sample age peaks (Fig. 4.8 inset) at *c.* 400 Ma (Caledonian) and 900 – 1100 Ma (Grenvillian), and the absence of 500 – 700 Ma aged grains (Cadomian / Avalonian), are characteristic of a Laurentian provenance (e.g. Hallsworth *et al.*, 2000; McConnell *et al.*, 2010). Such grains potentially could have been sourced locally; for example, a source comprising upper crustal lithologies within the Grampian Terrane of northern Ireland or Scotland, such as the Dalradian Supergroup and the late Caledonian granite suites, would be consistent with the analysed zircon populations.

4.3.3. Potential for U-Pb zircon CA-ID-TIMS dating

Regardless of the origins of the zircon population in sample MAP 09/07/01, the absence of a zircon population of Carboniferous age and the abundance of inherited grains make this sample a poor choice for high-precision CA-ID-TIMS analysis. The similar

rounded morphology of the grains in sample MAP 09/07/05 suggests that it may contain similar complexities and therefore may also prove unsuitable for CA-ID-TIMS dating. Further work is necessary to determine if the inheritance observed in sample MAP 09/07/01 is endemic to this cluster of upper Brigantian clay-rich horizons.

4.4. Conclusions

SEM-CL imaging and U-Pb LA-MC-ICP-MS analysis are powerful techniques for rapid characterisation of zircon populations. The information gained from these techniques can help to distinguish between samples that are unsuitable for CA-ID-TIMS dating (e.g. sample MAP 09/07/01; sections 4.3.1 and 4.3.2) and samples that are potentially viable dating targets (e.g. sample B9; section 5.2.3.3), thus aiding sample selection for the time intensive and expensive CA-ID-TIMS dating method.

Two of the investigated Irish Asbian samples contained zircon populations of Carboniferous age (samples MAP 11/07/01 and MAP 11/07/03; section 4.2.2), although the origin of these grains is unclear. Whole-rock geochemical data from these horizons suggests a mafic, possible alkaline magmatic source (section 7.5.2) that may not have crystallised significant zircon. Whether these Carboniferous sample grains represent primary volcanic grains derived from distal (i.e. outside of the UK and Ireland) volcanic centres or reworked detrital grains is unclear and cannot be determined from the available U-Pb zircon LA-MC-ICP-MS data. Further insight into the origins of these grains may be obtained by employing the high-precision U-Pb zircon CA-ID-TIMS method.

In contrast, the two investigated Brigantian bentonite horizons (samples MAP 09/07/01 and MAP 09/07/05) yielded rounded zircon populations. U-Pb LA-MC-ICP-MS dating of grains from one of these horizons demonstrated that the zircon population was inherited (section 4.3.2). No grains of Carboniferous age were identified during LA-MC-ICP-MS analysis suggesting that either Carboniferous magmatic grains are modally poorly represented or are not present at all. The reasons for this are unclear; one possibility is that the original ash was of mafic composition and thus magmatic zircon did not crystallise.

Chapter 5

U-Pb zircon dates from western European Namurian and Westphalian (Serpukhovian – Moscovian) diagenetically altered volcanic ash layers

5.1. Introduction

The aim of this chapter is to present new U-Pb zircon LA-MC-ICP-MS and CA-ID-TIMS data obtained from Namurian and Westphalian western European diagenetically altered volcanic ash layers (bentonites and tonsteins; see section 1.5.1 for definitions). The Namurian bentonite samples were collected from outcrop exposures within the Pennine Basin, northern England (section 1.5; Fig. 1.5). The Westphalian tonsteins were originally sampled from collieries and boreholes within the Campine and Ruhr Basins (Belgium and Germany respectively; section 1.5; Fig. 1.5) by Dr. Bernard Delcambre (Université Catholique de Louvain). All of the Westphalian samples investigated were derived from Dr. Bernard Delcambre's personal collection.

The new U-Pb zircon CA-ID-TIMS dates from Namurian horizons are employed to estimate the periodicity of high-frequency sedimentary cycles that occur between the dated bentonites and tonsteins (section 5.4.1), which have been suggested to be an expression of glacio-eustasy (e.g. Maynard & Leeder, 1992; Martinsen *et al.*, 1995; Davies *et al.*, 1999). These calculations were undertaken to determine if the sedimentary cycles exhibit periodicities compatible with Milankovitch cycles (section 1.3) and may therefore reinforce the glacio-eustatic hypothesis (section 1.2). The new U-Pb CA-ID-TIMS dates also provide additional age constraints for the temporal calibration of the western European Carboniferous stratigraphic record, which is discussed in section 5.4.2. Lastly, the new U-Pb zircon CA-ID-TIMS dates have implications for the correlation between the western European regional stratigraphic scheme and the global stratigraphic scheme (section 5.4.3).

The data are presented in stratigraphic order (Fig. 5.1) and the chapter sections are subdivided according to the western European regional stage divisions (Fig. 5.1).

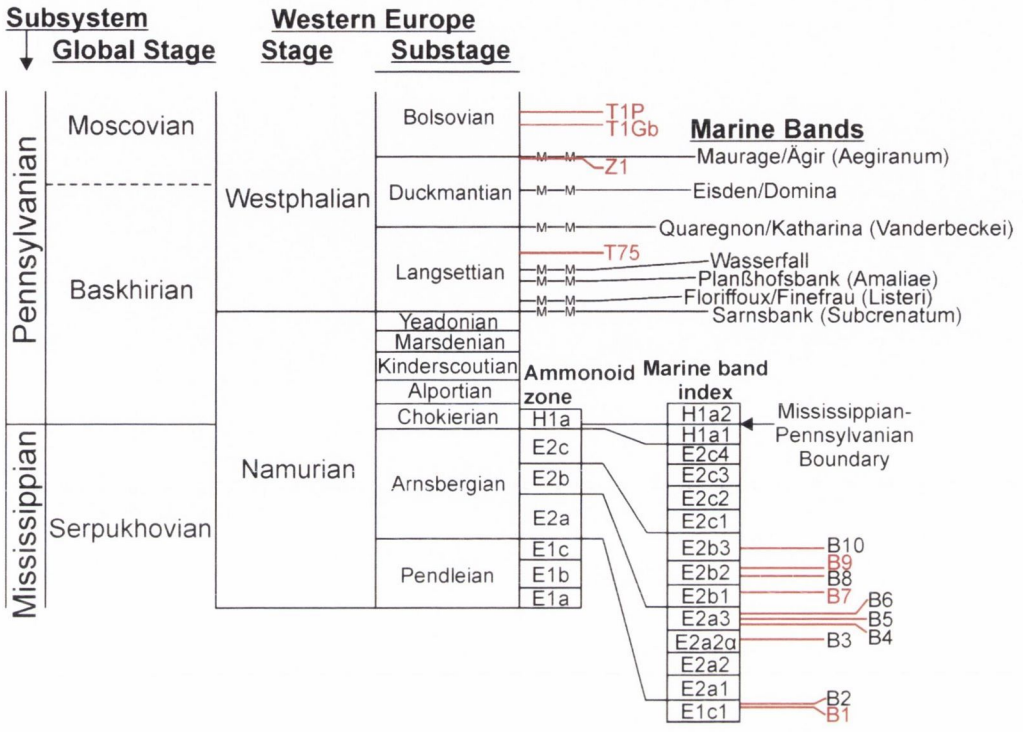

Figure 5.1. Stratigraphic column showing the positions of the Namurian and Westphalian bentonites and tonsteins discussed in this chapter. The positions of the Namurian bentonites (B horizons) are from Trewin (1968) and Trewin & Holdsworth (1972). Red labels denote horizons dated using the U-Pb zircon LA-MC-ICP-MS and / or U-Pb zircon CA-ID-TIMS methods. The stratigraphic positions of the Westphalian tonsteins are from Delcambre (1996). Namurian marine band indices correspond to those of Waters *et al.* (2007). Only the most significant Westphalian marine bands are drawn; local names for these marine bands are shown followed in brackets by the standard names suggested by Ramsbottom *et al.* (1978). The position of the Mississippian – Pennsylvanian (Mid-Carboniferous) boundary within the western European regional stratigraphic framework is from Riley *et al.* (1993).

5.2. Namurian Stage

Ten Arnsbergian bentonites were reported by Trewin (1968) and Trewin & Holdsworth (1972) from outcrop exposures in the Edale Gulf and North Staffordshire Sub-basin areas of the Pennine Basin, northern England (Fig. 5.2). Trewin (1968) termed the lowest seven bentonite horizons B1 to B7 (Fig. 5.1). Three further bentonite horizons were subsequently discovered by Trewin & Holdsworth (1972). These were not assigned 'B' numbers but have been referred to in subsequent publications (e.g. Spears *et al.*, 1999) as B8, B9 and B10, and this practice is continued in this thesis.

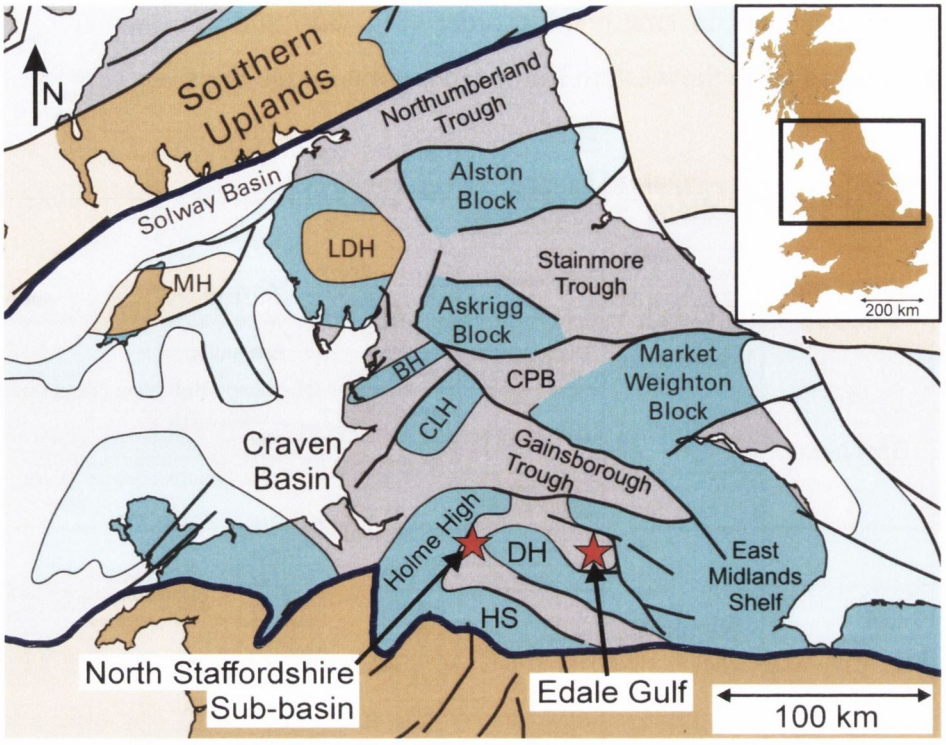

Figure 5.2. The Pennine Basin. The northern and southern extremities of the basin are indicated by the heavy blue lines. The main sub-basins within the Pennine basin are shown in grey and intervening structural highs in blue. Emergent land masses (during Carboniferous times) are shown in brown. BH = Bowland High, CLH = Central Lancashire High, CPB = Central Pennine Basin, DH = Derbyshire High, HS = Hathern Shelf, MH = Manx High, LDH = Lake District High. The inset shows the area of Great Britain covered by the main diagram. The figure is redrawn and simplified from Waters *et al.* (2007).

The bentonite horizons occur interbedded with paralic siliciclastic sedimentary strata that demonstrate simple cyclicity in the form of alternations of rocks which are barren of marine fossils and thin bands of shale, mudstone or limestone that contain abundant marine invertebrates (Holdsworth & Collinson, 1988; further described in section 5.4.1). The latter are often referred to as 'marine bands' and contain thick-shelled ammonoids which provide the primary biostratigraphic controls on the Namurian strata of the Pennine Basin. During Namurian times, ammonoid radiation rates were very high and thus the majority of marine bands contain a different characteristic ammonoid (Ramsbottom *et al.*, 1978; Holdsworth & Collinson, 1988; Riley *et al.*, 1993; Waters & Condon, 2012; see Fig. 5.20).

Trewin (1968) suggested a number of possible correlations between these bentonite horizons and conspicuous horizons (green to brown mudstones and pyritic partings)

observed in three drillcores taken in Derbyshire (Tansley, Uppertown, Highoredish; Trewin, 1968). Additionally, probable correlatives (based on marine band correlations) of these bentonite horizons have also been reported from drillcores within the Central Pennine Basin (Fig. 5.2; Riley *et al.*, 1993; Spears *et al.*, 1999). Thus, these bentonite horizons are potentially geographically widespread within the basin.

5.2.1. Namurian bentonite samples

Samples of bentonites B1, B2, B7, B8 and B9 (Fig. 5.1) were collected from outcrops previously described by Trewin (1968) and Trewin & Holdsworth (1972). The names and grid references of the sampling localities are shown in Table 5.1. In outcrop, bentonite B1 is *c.* 1.5 cm thick, laterally continuous and orange / brown. The lower half of B1 is laminated and its lower boundary is transitional with the underlying shale. Bentonite B2 is *c.* 0.5 cm thick, internally homogeneous and orange / brown (Fig. 5.3a). Bentonite B7 in outcrop is 1.5 cm thick and grey to pale blue (Fig. 5.3b). B8 and B9 at Oakenclough Brook are orange / brown, internally homogeneous and 2.5 cm and 3 cm thick respectively. B8 is extremely pyritic at this locality.

The mineralogy of these horizons has been investigated previously by Trewin (1968) and Trewin & Holdworth (1972), who determined that the bentonite horizons comprise polymineralic clays (mica / montmorillonite mixed-layer clays and kaolinite) and pyrite. Powder XRD analysis of sample material from the bentonite samples (presented in Appendix 2 Table 2) are consistent with the interpretations of Trewin (1968) and Trewin & Holdsworth (1972). The samples collected from bentonites B8 and B9 additionally contain a mineral closely corresponding to rhodochrosite ($MnCO_3$), which is probably of diagenetic origin. XRD analysis of material from B2 reveals relatively small clay peaks and large quartz peaks compared to the other bentonite samples. The B2 horizon is very thin (*c.* 0.5 cm) and was therefore difficult to sample. It is possible that this sample was contaminated by some of the enclosing shales. Whole-rock geochemical analysis of material from bentonites B1, B7, B8 and B9 (the sample from B2 was of insufficient size to use for whole-rock geochemical analysis) was conducted and is discussed in section 7.3.4. The whole-rock geochemical analyses suggest these bentonite horizons were originally sourced from intermediate, sub-alkaline (andesitic) magmas (discussed in section 7.5.4).

Bentonite	Grid Reference	Sub-basin	Sampling locality
B1	SK 1037 8512	Edale Gulf	Locality 74 [1]
B2	SK 1124 8473	Edale Gulf	Locality 105 [1]
B7	SK 1235 8595	Edale Gulf	Locality 145 [1]
B8	SK 0501 6369	North Staffordshire Sub-basin	Oakenclough Brook [2]
B9	SK 0501 6369	North Staffordshire Sub-basin	Oakenclough Brook [2]

Table 5.1. Grid references and sampling localities for Namurian bentonite samples. Sampling localities: 1) locality described by Hudson & Cotton (1945) and sampled by Trewin (1968); 2) sampled by Trewin & Holdsworth (1972).

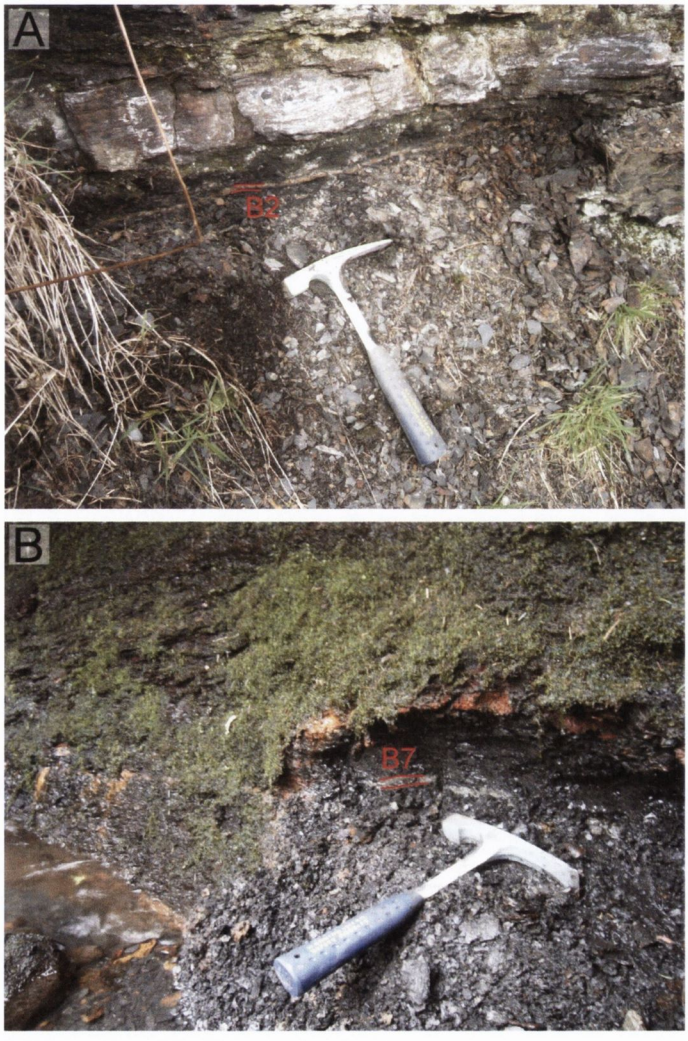

Figure 5.3. Field photographs of Namurian bentonites from the Pennine Basin, northern England. A) Bentonite B2; B) Bentonite B7.

5.2.2. Zircon populations from Namurian bentonites

All samples yielded zircon grains; however, the sample from bentonite B2 yielded a very sparse, fine-grained zircon population that was not investigated further.

5.2.2.1. Bentonite B1

The zircon separate from the B1 bentonite yielded a bimodal population composed of rounded and euhedral grains, both possessing low aspect ratios (*c.* 1.5 – 3). Approximately 60 of the grains separated from bentonite B1 were imaged using scanning electron microscopy with cathodoluminescence imaging (SEM-CL), which revealed that the rounded population comprises CL-bright grains whereas the euhedral grain population is very dark under CL (Fig. 5.4), possibly suggesting high uranium concentrations (section 2.3.4.2.1).

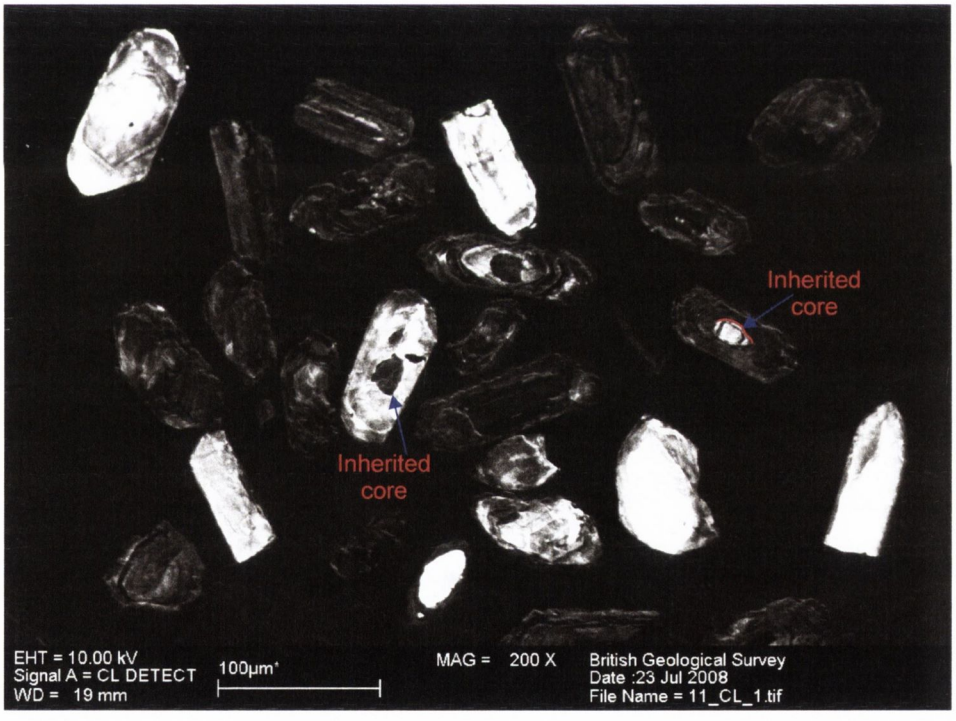

Figure 5.4. SEM-CL image of grains separated from bentonite B1.

Some grains (both light and dark grains under SEM-CL) contain evidence of inherited cores (e.g. the labelled grains in Fig. 5.4). Additionally, several of the dark grains under SEM-CL display oscillatory zonation (made visible through substantial contrast enhancements; Fig. 5.5).

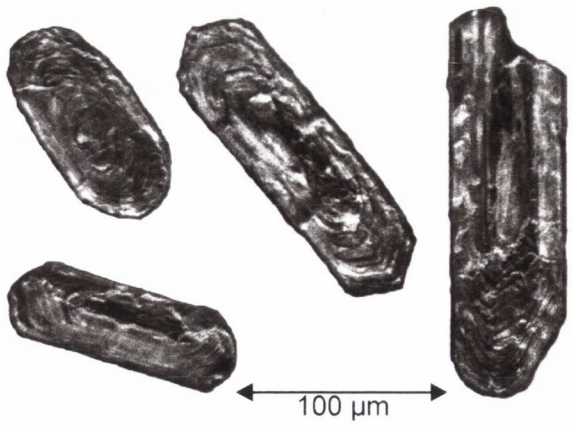

Figure 5.5. Oscillatory zonation in grains from bentonite B1.

5.2.2.2. Bentonite B7

The sample of bentonite B7 yielded an abundant population of relatively small (grain lengths of 40 – 150 µm; most are < 100 µm), euhedral zircon grains possessing low aspect ratios (*c.* 1.5 – 3). Most zircon grains separated from this bentonite are reasonably clear with few fractures or inclusions. There is no visible evidence of inherited cores within the sample grains.

5.2.2.3. Bentonites B8 and B9

Bentonites B8 and B9 yielded notably fewer grains than bentonite B7 despite similar sample sizes. Zircons from these bentonites are fine grained (generally < 120 µm in length) and are characterised by low aspect ratios (typically 1.5 – 3). Inclusions and fractures are rare in grains from these samples. Some grains from B9 were imaged using SEM-CL and display oscillatory zonation.

5.2.3. U-Pb zircon LA-MC-ICP-MS dating of Namurian bentonites

Reconnaissance U-Pb LA-MC-ICP-MS analysis was undertaken on zircons separated from bentonites B1, B7 and B9, to screen for inheritance and evaluate the suitability of these sample grains for U-Pb CA-ID-TIMS dating. The results from U-Pb zircon LA-MC-ICP-MS dating are presented in the subsequent sections, as concordia diagrams. The sample U-Pb zircon LA-MC-ICP-MS data from bentonites B1, B7 and B9 are also presented as data tables in Appendix 1 Table 2.

5.2.3.1. Bentonite B1

The results from LA-MC-ICP-MS dating of grains from bentonite B1 are shown in Fig. 5.6. The data show some complexity, evidenced by the presence of different age populations within this sample. The bright grains in the SEM-CL images (section 5.2.2.1) have low uranium concentrations (< 200 ppm) and yield concordant / near-concordant dates that are substantially older than the base of the Carboniferous System (359.2 Ma; Davydov *et al.*, 2010). These grains are interpreted to represent inheritance. The rounding of these grains could be due to transportation and may point towards detrital contamination within this sample.

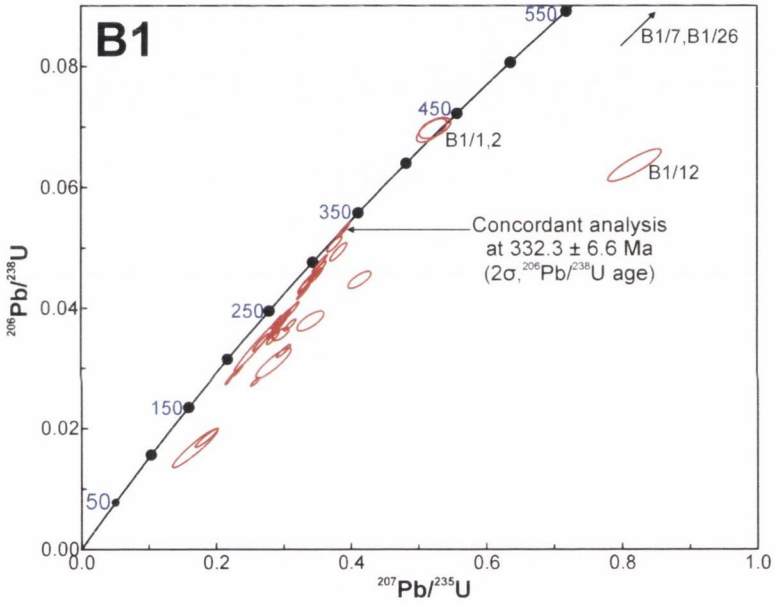

Figure 5.6. Concordia diagram of U-Pb zircon LA-MC-ICP-MS data from bentonite B1. Analyses B1/7 and B1/26 are not drawn; both analyses are concordant (within uncertainties) and yield $^{207}Pb/^{206}Pb$ dates of 1562.5 ± 18.8 Ma (2σ) and 1676.1 ± 18.5 (2σ) respectively. Sample U-Pb data drawn in this figure are presented in Appendix 1 Table 2.

The euhedral, dark grains (under SEM-CL) have higher uranium concentrations (*c.* 700 – 3800 ppm) and several grains contain measureable amounts of common lead. Most grains yielded $^{206}Pb/^{238}U$ dates younger than the base of the Permian System (298.7 Ma; Davydov *et al.*, 2010), which are inconsistent with the stratigraphic position of the B1 horizon (upper Pendleian; Fig. 5.1). These grains are thus interpreted to have suffered lead loss. Several data form a weak linear array in Fig. 5.6, although it is not possible to fit a statistically robust chord without substantial filtering of the dataset. Some of this dispersion can be attributed to variable incorporation of common lead

within the sample grains, which shifts analyses to the right of the concordia (section 2.3.2.4). A correction for common lead using the method of Horstwood *et al.* (2003) is possible for these data but substantially worsens the precision of the data, such that the data corrected for common lead do not provide much additional information. There is a single concordant analysis at 332.3 ± 6.6 Ma (2σ, $^{206}Pb/^{238}U$ date; analysis B1/34; Appendix 1 Table 2), which may approximate the eruption age of this horizon. In summary, these data support the presence of a Carboniferous magmatic population within this bentonite horizon that is characterised by high uranium concentrations, variable amounts of lead loss and common lead contamination.

5.2.3.2. Bentonite B7

The results from U-Pb zircon LA-MC-ICP-MS dating of grains from bentonite B7 are shown in Fig. 5.7. The data define a relatively simple age population, with the exception of a single data point (B7/7; Fig. 5.7) which is significantly discordant, most likely due to common lead contamination.

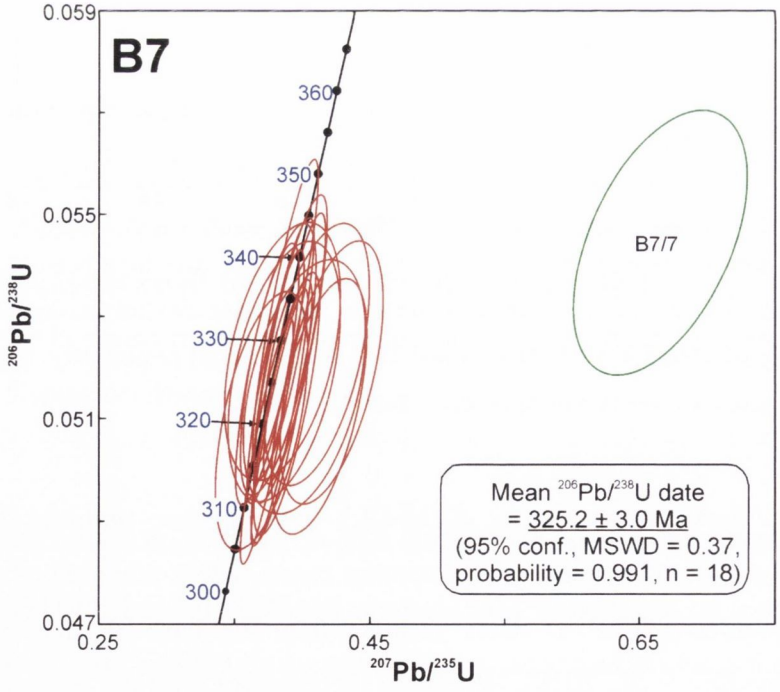

Figure 5.7. U-Pb zircon LA-MC-ICP-MS data from bentonite B7 presented as a concordia diagram. Error ellipses are drawn at the 2σ confidence level. Red and green error ellipses denote data points included in and excluded from the weighted mean $^{206}Pb/^{238}U$ date shown in the figure respectively. Sample U-Pb data drawn in this figure are presented in Appendix 1 Table 2.

Within the main data cluster, there is a slight displacement of some data points horizontally to the right of concordia (analyses B7/8, 12, 13, 14; Appendix 1 Table 2), which is probably the result of minor common lead contamination. The weighted mean $^{206}Pb/^{238}U$ date of all analyses except B7/7 is 325.2 ± 3.0 Ma (95 % conf., MSWD = 0.37, probability = 0.991, n = 18; Fig. 5.7). The inclusion of data points interpreted to contain slight common lead contamination has a negligible impact on the weighted mean $^{206}Pb/^{238}U$ date calculation (excluding analyses B7/8, 12, 13, 14 yields a weighted mean $^{206}Pb/^{238}U$ date of 325.2 ± 3.4 Ma, 95 % conf., MSWD = 0.44).

5.2.3.3. Bentonite B9

The U-Pb zircon LA-MC-ICP-MS data from bentonite B9 define a relatively simple population with no clear evidence of inheritance or lead loss (Fig. 5.8). The weighted mean $^{206}Pb/^{238}U$ date of all data is 326.9 ± 2.1 Ma (95 % conf. MSWD = 2.1, excludes decay constant errors). The MSWD value of the weighted average exceeds the acceptable range of MSWD values at the 95 % confidence level (for n = 24 degrees of freedom the upper limit for the MSWD is 1.52; Wendt & Carl, 1991), indicating that the data are more scattered than can be accounted for by analytical errors alone. Accordingly, the weighted mean date uncertainty is expanded by the square root of the MSWD multiplied by student's t-factor (see section 2.3.5.2.5).

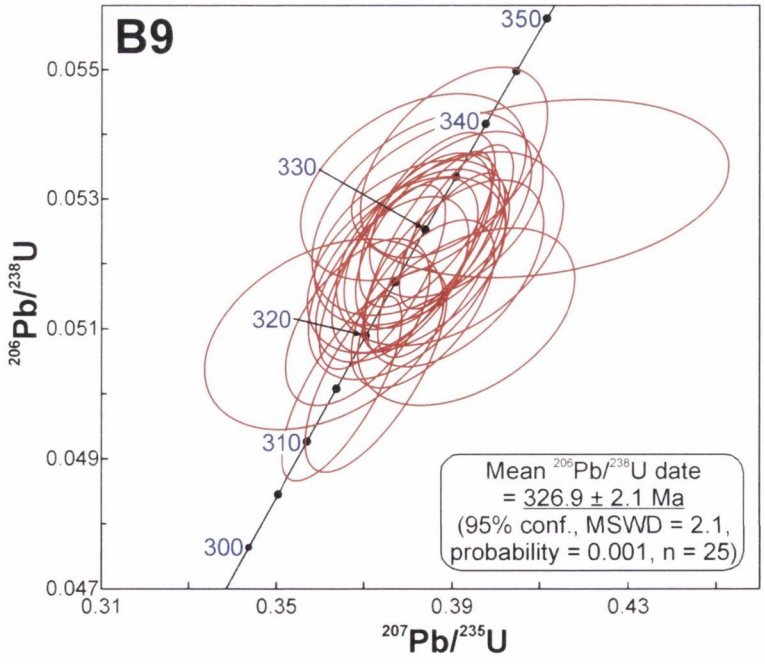

Figure. 5.8. U-Pb zircon LA-MC-ICP-MS data from bentonite B9 presented as a concordia diagram. Error ellipses are drawn at the 2σ confidence level. Sample U-Pb data drawn in this figure are presented in Appendix 1 Table 2.

The weighted mean $^{206}Pb/^{238}U$ date of this sample is slightly older than was obtained from B7 (section 5.2.3.2), despite bentonite B7 occupying a slightly lower stratigraphic level. However, the two weighted mean dates are indistinguishable within uncertainty (at the 95 % confidence level), and individual analyses from these two samples show considerable overlap at the 2σ confidence level. These two bentonites are separated by only a small amount of stratigraphy and as such it is not surprising that they yield isotopic dates that are indistinguishable within the analytical precision attainable using the LA-MC-ICP-MS method.

5.2.3.4. Synthesis of LA-MC-ICP-MS data

U-Pb zircon LA-MC-ICP-MS dating supports the presence of a Carboniferous magmatic population in all three of the samples analysed. Bentonites B7 and B9 yielded simple age populations, whereas the sample of B1 showed greater complexity. Based on these data, bentonites B7 and B9 are the obvious targets for CA-ID-TIMS dating. However, these bentonite horizons are very close together in the stratigraphy, and combined with the small zircon grain size that is an endemic feature of these Namurian bentonite horizons, it is probable that U-Pb zircon CA-ID-TIMS dating of grains from B7 and B9 would yield dates that are indistinguishable within analytical uncertainties. To maximise the stratigraphic spacing for the periodicity calculations, high-precision U-Pb zircon CA-ID-TIMS dating was undertaken on samples B1 and B9. Isotopic dating of the B1 horizon also has the added advantage that it is sufficiently close to the Pendleian – Arnsbergian boundary to constrain the age of this stratigraphic boundary (Fig. 5.1).

5.2.4. U-Pb zircon CA-ID-TIMS dating of Namurian bentonites

5.2.4.1. Bentonite B1

The euhedral zircon population in sample B1 was preferentially targeted for CA-ID-TIMS analysis. Unfortunately, U-Pb CA-ID-TIMS dating of this sample proved problematic and the results are inconclusive. Although 13 single grain CA-ID-TIMS analyses were undertaken from bentonite B1, only five yielded sample data; the small size of grains from this bentonite sample caused considerable handling difficulties and

consequently several grains intended for analysis were not successfully delivered to the Teflon bombs. U-Pb zircon CA-ID-TIMS data from the five sample grains are documented in Appendix 1 Table 1. Only two analyses yielded Carboniferous dates (B1/2, B1/12; Fig. 5.9; Appendix 1 Table 1), and these are younger than the U-Pb zircon CA-ID-TIMS data from bentonite B9 (data drawn in Fig. 5.9 and described in section 5.2.4.2), which occupies a higher stratigraphic level than bentonite B1 (Fig. 5.1). Analysis B1/2 (Fig. 5.9) is also stratigraphically inconsistent with CA-ID-TIMS data from the Langsettian tonstein T75 (section 5.3.1.1). The two Carboniferous dates from grains within bentonite B1 almost certainly contain residual lead loss which was not completely removed by the chemical abrasion method. Variable amounts of lead loss were inferred to be present in the LA-MC-ICP-MS data from bentonite B1 (section 5.2.3.1), which corroborates this interpretation.

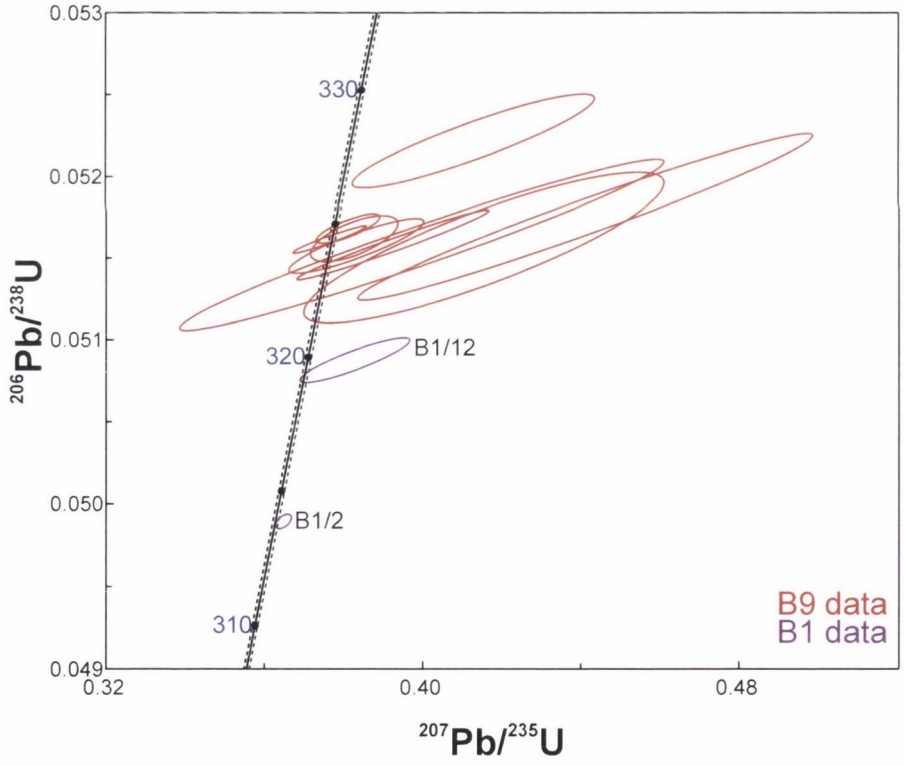

Figure 5.9. U-Pb zircon CA-ID-TIMS data from bentonites B1 (purple ellipses) and B9 (red ellipses), presented as a concordia diagram. Error ellipses are drawn at the 2σ confidence level.

Three analyses (B1/10, 11, 13; Appendix 1 Table 1) yielded dates older than the base of the Carboniferous System (359.2 Ma; Davydov *et al.*, 2010) and are accordingly interpreted as inherited grains. Two are concordant (within analytical and decay

constant uncertainties) and yield $^{206}Pb/^{238}U$ dates of 421.14 ± 7.93 Ma and 951.45 ± 0.67 Ma (B1/10, B1/13 respectively; Appendix 1 Table 1). These may reflect detrital inheritance akin to the rounded, inherited grains identified during LA-MC-ICP-MS analysis (section 5.2.3.1). The third grain (B1/11) is very discordant, and probably contained multiple internal age domains. Grains with obvious internal cores were observed in the SEM-CL images (Fig. 5.4), and may support this interpretation.

The inferred presence of residual lead loss suggests an insufficient amount of chemical abrasion. However, very little sample material remained available for dating by ID-TIMS following chemical abrasion. It may not be possible to attain a balance between chemically abrading these sample grains enough to remove lead loss and preserving enough sample material for dating by ID-TIMS analysis, because of the fine grain size and high uranium concentrations of the Carboniferous grains in bentonite B1. Further work on this sample was abandoned in the light of the poor initial results.

5.2.4.2. Bentonite B9

The results of U-Pb zircon CA-ID-TIMS dating of grains from bentonite B9 are shown in Fig. 5.10. The U-Pb zircon CA-ID-TIMS data from bentonite B9 is also presented in Appendix 1 Table 1. Nine single grain fractions were dated by the U-Pb zircon CA-ID-TIMS method. One analysis is discordant and is significantly older than the other analyses (B9/3; Fig. 5.10; Appendix 1 Table 1). This analysis is interpreted to reflect inheritance, possibly arising from an intra-grain core. The remaining eight analyses yield comparable $^{206}Pb/^{238}U$ ratios. There is some dispersion in $^{207}Pb/^{235}U$ ratios, particularly between analyses with high analytical blanks (> 3 pg; B9/2, 5, 9, 16; Appendix 1 Table 1). The $^{207}Pb/^{235}U$ ratio is more sensitive to the composition of the analytical blank and the shifting of high-blank analyses to the right of concordia probably represents inaccuracies in the common lead correction.

The high-blank analyses are excluded from the weighted mean $^{206}Pb/^{238}U$ date calculation, although these data have very little effect on the calculation (as shown in Fig. 5.10b). This is because they are significantly less precise (due to the greater common lead correction) than the four analyses with lower analytical blanks (B9/ 10, 11, 14, 15; Fig. 5.10; Appendix 1 Table 1), and so are assigned a lower weighting in the

weighted mean date calculation. The four analyses with lower analytical blanks (< 1.5 pg) yield a weighted mean $^{206}Pb/^{238}U$ date of 324.54 ± 0.26 Ma (95 % conf., MSWD = 0.94, probability = 0.42; Fig. 5.10b) and this is taken to approximate the eruption age of bentonite B9.

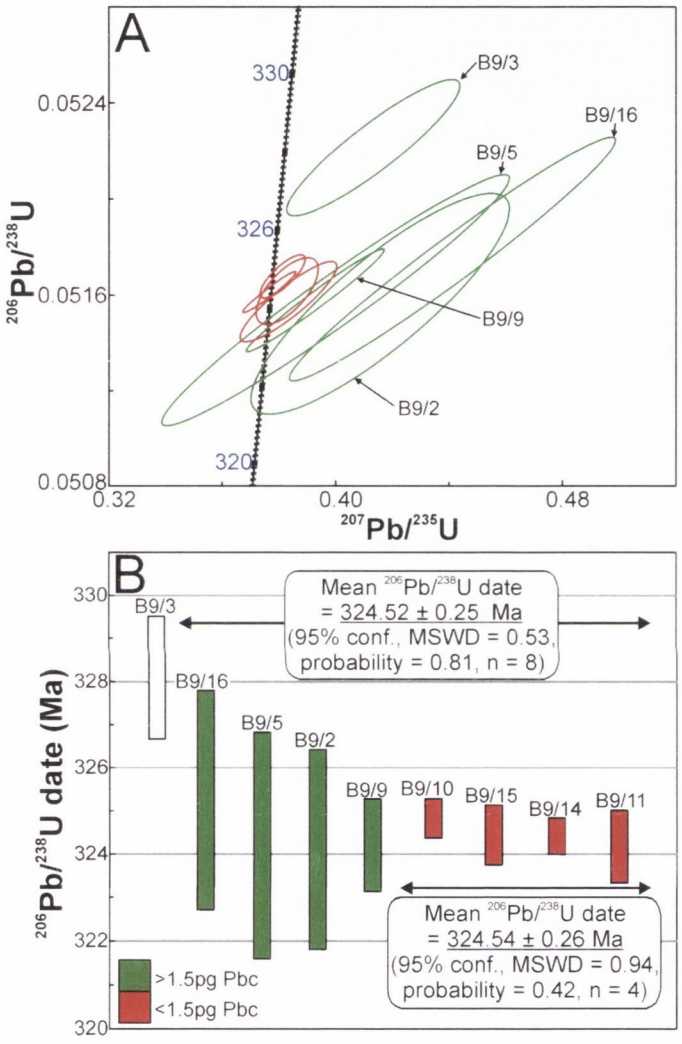

Figure 5.10. U-Pb zircon CA-ID-TIMS data from bentonite B9 illustrated as a concordia diagram (A) and a weighted mean $^{206}Pb/^{238}U$ date plot (B). In plot A, red and green error ellipses represent data points included in and excluded from the lower of the two weighted mean calculations shown in plot B respectively. The solid black line in plot A is the concordia (drawn using the decay constants of Jaffey *et al.*, 1971). The dashed black lines drawn parallel to the concordia represent the uncertainty in the position of the concordia arising from uncertainties in the U decay constants. Blue numbers are concordant ages (Ma). Error ellipses are drawn at the 2σ confidence level. In plot B, box heights (representing date uncertainties) are drawn at the 2σ confidence level. Pbc = common lead.

This weighted mean date only marginally overlaps at the 95 % confidence level with the weighted mean $^{206}Pb/^{238}U$ date from bentonite B9 determined using the U-Pb zircon LA-MC-ICP-MS method (section 5.2.3.3; to make such a comparison, uncertainties in the composition of the Earthtime isotopic tracer must be added to the B9 CA-ID-TIMS weighted mean, increasing its uncertainty to ± 0.31 Ma; Table 5.2). However, the individual CA-ID-TIMS and LA-MC-ICP-MS data are mostly indistinguishable within analytical uncertainties (Fig. 5.11).

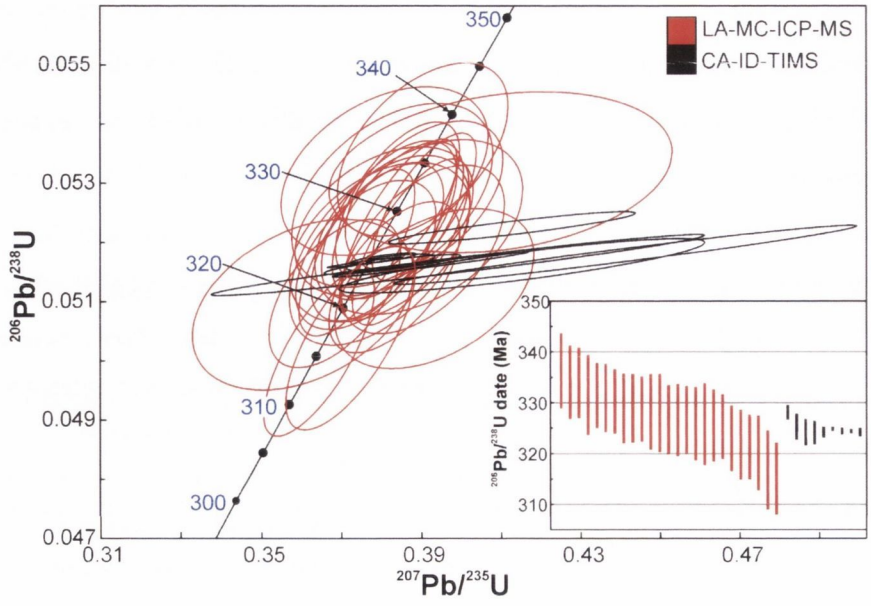

Figure. 5.11. U-Pb zircon LA-MC-ICP-MS and CA-ID-TIMS data from bentonite B9 drawn as a concordia diagram and as a weighted mean $^{206}Pb/^{238}U$ date plot (inset). The solid black line is the concordia drawn using the decay constants of Jaffey *et al.* (1971). Blue numbers are concordant ages (in units of Ma). Error ellipses (main diagram) and box heights (inset) are drawn at the 2σ confidence level.

5.2.4.2.1. Comparison to the B6 U-Pb CA-ID-TIMS date of Waters & Condon (2012)

Waters & Condon (2012) have recently determined a weighted mean $^{206}Pb/^{238}U$ date of 328.34 ± 0.30 / 0.55 Ma (2σ; ± X / ± Z uncertainty levels; section 2.3.5.2.5) using the U-Pb zircon CA-ID-TIMS method and the Earthtime 'ET535' tracer, for a bentonite that is probably laterally equivalent to the B6 bentonite of Trewin (1968; labelled B6 in Fig. 5.1). It is noteworthy that when the isotopic dates from bentonites B6 (Waters & Condon, 2012) and B9 (section 5.2.4.2) are compared (Fig. 5.12) they imply that a substantial time duration exists between these bentonites (*c.* 3.8 Myrs). This is in contrast to the close stratigraphic proximity of bentonites B6 and B9, which are separated by only six marine bands (Fig. 5.20). It is unclear why such a large time duration exists between these two bentonite horizons, when it would appear that they should be separated by only a short time interval. Differences in the composition of the Earthtime tracer solutions used during data reduction in this study compared to Waters & Condon (2012) account for only a very minor amount of the age difference between the B6 and B9 weighted mean $^{206}Pb/^{238}U$ dates; Waters & Condon (2012) employed a value of 100.18 for the $^{235}U/^{205}Pb$ ratio of the Earthtime 'ET535' tracer, *c.f.* a value of

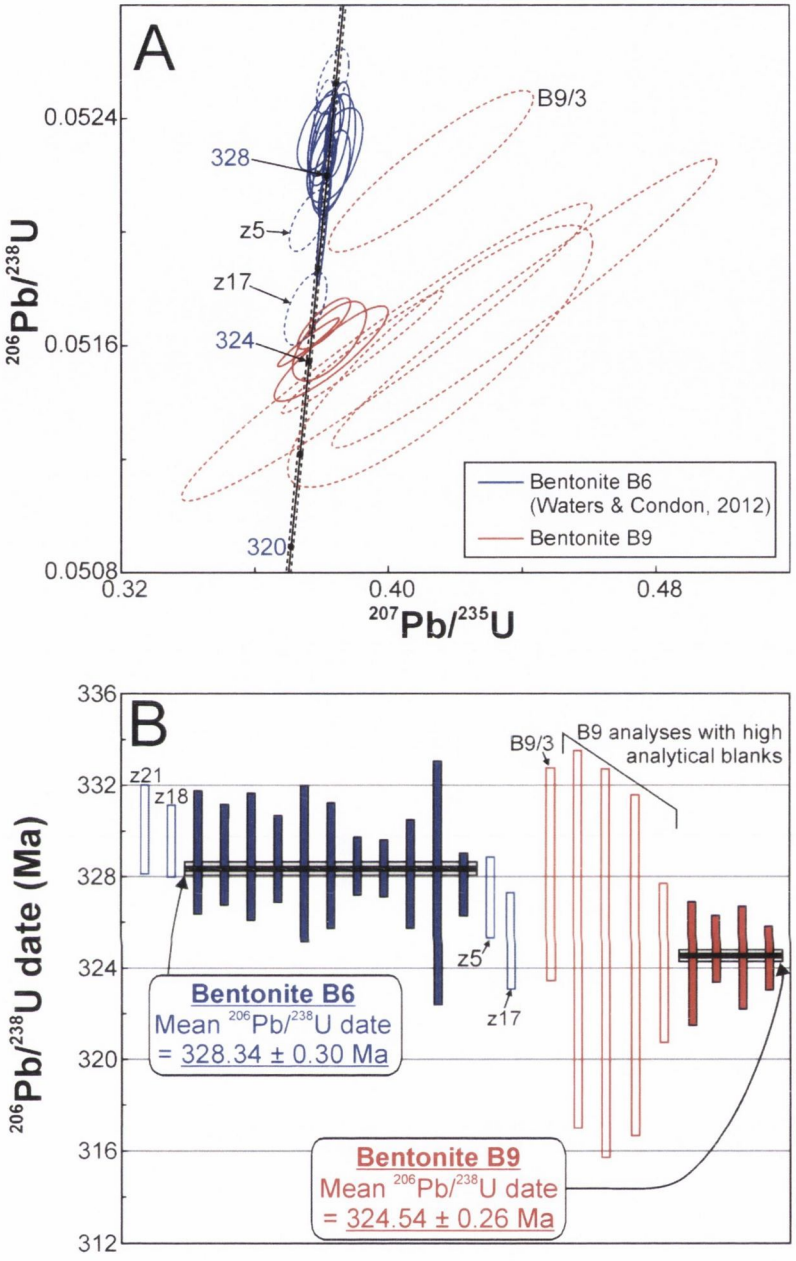

Figure 5.12. U-Pb zircon CA-ID-TIMS data from bentonites B6 (redrawn from Waters & Condon, 2012) and B9 illustrated as a concordia diagram (A) and a weighted mean $^{206}Pb/^{238}U$ date plot (B). Two data points from the bentonite B6 dataset of Waters & Condon (2012) are not illustrated in this figure; these analyses yielded $^{206}Pb/^{238}U$ dates substantially younger (analysis zA2) and older (analysis zA1) than the majority of the sample data and were interpreted by Waters & Condon (2012) to reflect residual lead loss and inheritance respectively. In plot A, the solid black line is the concordia drawn using the decay constants of Jaffey *et al.* (1971). The dashed black lines drawn parallel to the concordia represent the uncertainty in the position of the concordia arising from uncertainties in the U decay constants. Blue numbers are concordant ages (Ma). Error ellipses (plot A) and box heights (plot B) are drawn at the 2σ confidence level. Error ellipses with solid and dashed outlines denote data points included in and excluded from the weighted mean calculations (plot B) respectively. In plot B, weighted mean $^{206}Pb/^{238}U$ date uncertainties are cited at the 95 % confidence level (± X uncertainty level; see section 2.3.5.2.5 for an explanation).

100.20 used for the Earthtime tracers in this study (Table 2.1). Recalculating the bentonite B9 CA-ID-TIMS data using a $^{235}U/^{205}Pb$ tracer ratio of 100.18 increases the weighted mean $^{206}Pb/^{238}U$ date of bentonite B9 (shown in Fig. 5.12b) by *c.* 0.06 Myrs.

From an analytical perspective, neither of the two datasets are ideal; some of the data from B9 trend towards the right of concordia (Fig. 5.12a), which has been interpreted to represent inaccuracies in the common lead correction (section 5.2.4.2). It may be of significance to note that there is one analysis from bentonite B9 that yields a similar $^{206}Pb/^{238}U$ date to the main age population in the B6 data of Waters & Condon (2012), but that this analysis is discordant within analytical uncertainties (B9/3; Fig. 5.12a). In contrast, the B6 dataset of Waters & Condon (2012) contains evidence of both inheritance and lead loss, with a more-or-less equivalent population at *c.* 328.3 Ma (Fig. 5.12; the MSWD of the weighted mean date is slightly greater than the acceptable range of values at the 95 % confidence level; section 2.3.5.2.5). Within the bentonite B6 dataset, there is one analysis of comparable age to the majority of the data from B9 (analysis z17 of Waters & Condon, 2012; Fig. 5.12), which was discarded by Waters & Condon (2012) as probably affected by residual lead loss. However, this interpretation appears to be largely based on the fact that it is distinctly younger than most other analyses. This analysis is not discordant within analytical or decay constant uncertainties, nor are there precise isotopic dates from younger Namurian horizons (e.g. Fig. 1.4) that would provide a minimum age constraint on this horizon and conclusively demonstrate that this grain has suffered lead loss.

Alternatively, if the U-Pb zircon CA-ID-TIMS dates from bentonites B6 (Waters & Condon, 2012) and B9 (section 5.2.4.2) are robust, the large time duration between these closely spaced bentonite horizons could indicate the presence of stratigraphic omission. Waters & Condon (2012) have suggested previously the possibility of stratigraphic omission within the Arnsbergian record of the Pennine Basin.

The available isotopic age data are insufficient to differentiate between these possibilities. Further insights may be gained through the U-Pb zircon CA-ID-TIMS dating of additional Namurian bentonites. Bentonite B7, which is intermediate between the dated B6 and B9 bentonite horizons (Fig. 5.1) and yielded encouraging U-Pb zircon LA-MC-ICP-MS data (section 5.2.3.2), is a potential target for CA-ID-TIMS dating.

5.3. Westphalian Stage

Numerous tonstein horizons have been reported from the Westphalian paralic coal fields of western Europe (Belgium, France, Germany, United Kingdom). Tonsteins are predominantly kaolinitic rocks and are typically fine-grained (Spears, 2006), with a markedly different mineralogy and geochemistry compared to the enclosing coal measures (e.g. Spears & Kanaris-Sotiriou, 1979). They are important stratigraphic markers within the coal measures of western Europe because of their widespread distribution (> 400 km), distinctive appearance and inferred rapid deposition (Lyons *et al.*, 1994).

Today, it is widely accepted that tonstein horizons arose from the alteration of volcanic ash (Spears, 2006). This has been supported by their considerable lateral extent, their markedly different geochemistry compared to the enclosing siliciclastic strata and the recovery of volcanic phenocrysts from these horizons (e.g. euhedral zircon and apatite, sanidine, biotite, β-form and splintery quartz, as well as volcanic glass shards; Bohor & Triplehorn, 1993). The work of Bouroz (1967), who compared tonstein horizons from the paralic coalfields of northern France with less extensively altered tonsteins in the limnic coalfields of southern France (Lyons *et al.*, 1994; Spears, 2006), has also contributed to the consolidation of this hypothesis.

Unfortunately, present-day opportunities for the collection of western European tonstein samples are sparse, due to the decline of coal mining in western Europe. All of the samples investigated were obtained from Dr. Bernard Delcambre's (Université Catholique de Louvain) personal collection. U-Pb zircon CA-ID-TIMS dating was undertaken on three tonstein layers from the Belgian Campine Basin (T75, T1Gb, T1P) and tonstein Z1 from the Ruhr Basin, Germany, the stratigraphic positions of which are shown in Fig. 5.1. The whole-rock geochemistry and possible volcanic sources of these horizons are discussed in chapter 7. The primary biostratigraphic controls on this stratigraphic interval are from ammonoids within marine bands, similar to the underlying Namurian stratigraphy. In contrast to the Namurian marine bands, however, only a few Westphalian marine bands contain ammonoids. These include: the ammonoid-bearing Subcrenatum, Vanderbeckei and Aegiranum marine bands, which define the bases of the Langsettian, Duckmantian and Bolsovian substages respectively

(Fig. 5.1); the Langsettian Listeri and Amaliae marine bands (Fig. 5.1); and the Bolsovian Cambriense marine band, although the latter is not well known outside of Great Britain (Dusar *et al.*, 2000). Ammonoids have not been widely reported from the other Westphalian marine bands and as such these bands are generally not correlated beyond their immediate sedimentary basins.

5.3.1. U-Pb zircon CA-ID-TIMS dating of Westphalian tonsteins

5.3.1.1. Tonstein T75

T75 is a late Langsettian-aged tonstein from the Campine Basin, Belgium. The sample investigated was originally obtained from the Zwartberg colliery (51.0136°N, 5.5038°E; now disused). Tonstein T75 is correlated with tonstein Wilhelm of the Ruhr Basin (Paproth *et al.*, 1983b; Delcambre, 1996) and occurs between the Wasserfall and Quaregnon marine bands (Fig. 5.1). XRD analysis of sample material from tonstein T75 reveals an abundance of quartz and kaolinite, with probable trace amounts of mica and chlorite (Appendix 2 Table 2).

Zircons separated from the sample of tonstein T75 are predominantly euhedral with lengths of 50 – 260 μm (most are > 100 μm) and aspect ratios of *c.* 2 – 8 (most grains > 3). Some grains contain inclusions, of which melt inclusions parallel to the c-axis are the most common and occur preferentially in the grains with high aspect ratios. A few grains display evidence of xenocrystic inheritance (small, round, high-relief cores and radial fractures). The distribution of fractures is bimodal; some grains are heavily fractured whereas other grains contain none.

Eleven single grain U-Pb zircon CA-ID-TIMS analyses were undertaken from the sample of tonstein T75 (presented in Appendix 1 Table 1). Ten analyses are shown in Fig. 5.13; one data point is not drawn (T75/5) because it is substantially older ($^{206}Pb/^{238}U$ date of 321.53 ± 0.83 Ma, 2σ; Appendix 1 Table 1). This sample shows some age complexity: there are four relatively old analyses (T75/5, 7, 8, 11); a cluster of data points that are equivalent and concordant within analytical and decay constant uncertainties (red ellipses in Fig. 5.13a); and two relatively young analyses with high analytical blanks (> 3 pg common lead; analyses T75/4 and T75/9 in Fig. 5.13).

The two youngest analyses (T75/4, 9) only marginally overlap (at the 2σ confidence level) with each other and with the concordia band (Fig. 5.13a). These grains probably represent residual lead loss not completely mitigated by the chemical abrasion method and therefore they are not included in the weighted mean $^{206}Pb/^{238}U$ date calculation. Of the four relatively old analyses (Fig. 5.13a; analyses T75/5, 7, 8, 11), T75/5 is substantially older than the rest and is considered to represent an inherited grain. Analyses T75/7, T75/8 and T75/11 are marginally older (< 1 Myrs) than the main concordant data cluster and may represent antecrystic grains (*sensu* Miller *et al.*, 2007; section 2.3.2.3). The five analyses that are equivalent and concordant (within analytical and decay constant uncertainties; red ellipses in Fig. 5.13a) are interpreted to provide the best estimate for the eruption age of this tonstein horizon. The weighted mean $^{206}Pb/^{238}U$ date of these analyses is 317.63 ± 0.12 Ma (95 % conf., MSWD = 0.70, p = 0.59; Fig. 5.13b).

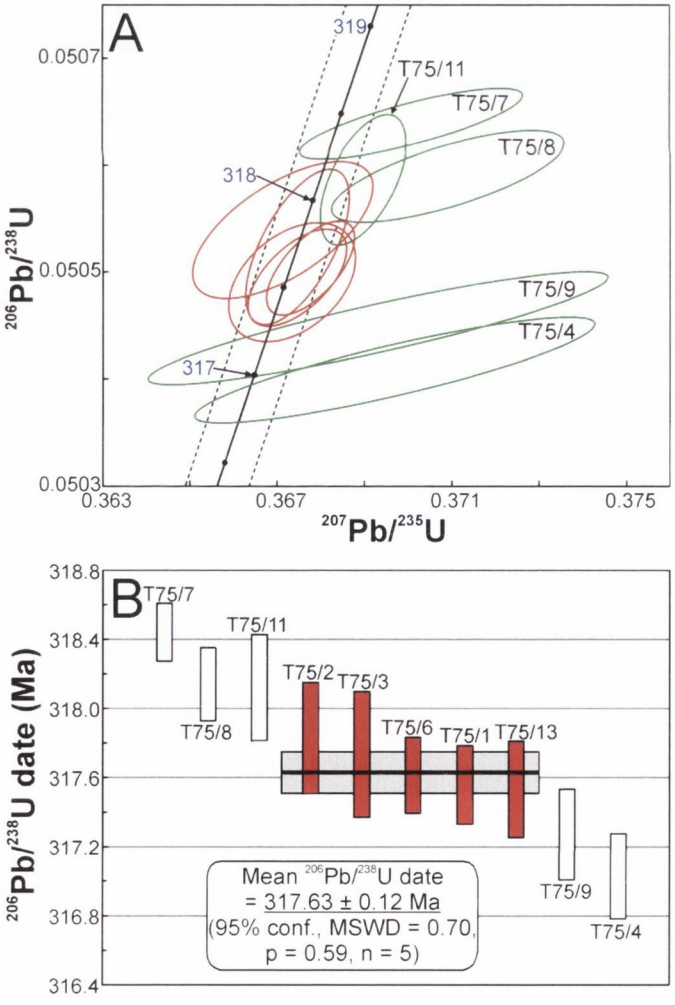

Figure 5.13. U-Pb zircon CA-ID-TIMS data from T75 illustrated as a Wetherill concordia diagram (A) and a weighted mean $^{206}Pb/^{238}U$ date plot (B). In plot A, red and green error ellipses represent data points included in and excluded from the weighted mean calculation respectively. The solid black line in plot A is the concordia drawn using the decay constants of Jaffey *et al.* (1971). The dashed black lines drawn parallel to the concordia represent the uncertainty in the position of the concordia arising from uncertainties in the U decay constants. Blue numbers are concordant ages (Ma). Error ellipses are drawn at the 2σ confidence level. In plot B, the grey band represents the uncertainty of the weighted mean (95 % confidence level). Box heights (representing date uncertainties) are drawn at the 2σ confidence level.

5.3.1.2. Tonstein Z1

The sample of tonstein Z1 investigated was originally collected from the Furst Leopold colliery, Dorsten (51.6713°N, 6.9777°E), located in the Ruhr Basin, Germany. Tonstein Z1 occurs 10 – 12 m below the Ägir marine band (Fiebig, 1969), which defines the base of the Bolsovian (Westphalian C) Substage, and is thus of latest Duckmantian (Westphalian B) age (Fig. 5.1). XRD analysis of sample material from this tonstein horizon revealed an abundance of kaolinite, the presence of feldspar and trace amounts of illite-mica (Appendix 2 Table 2). The feldspar is sanidine, which was successfully separated from this horizon and identified using energy dispersive X-ray spectroscopy (SEM-EDS).

The zircon separate from this sample has similar attributes to that reported by Claoué-Long *et al.* (1995); the population is bimodal, comprising both well rounded and euhedral zircons. Rounded grains account for *c.* 80 % of the total zircon separate. The euhedral grains are typically 100 – 250 μm in length with aspect ratios of 2 – 6. The euhedral grains are also heavily fractured and some contain melt inclusions.

The euhedral grains were selected preferentially for CA-ID-TIMS analysis. Seven single grain U-Pb zircon CA-ID-TIMS analyses were undertaken from this sample, the data from which are presented in Appendix 1 Table 1. Six analyses (Z1/4 – 9; Appendix 1 Table 1) are shown in Fig. 5.14. The seventh analysis (Z1/1; Appendix 1 Table 1) has an unacceptably high analytical blank (11.45 pg; Appendix 1 Table 1) and is not illustrated, nor is it included in further interpretations.

The remaining six analyses yield a simple age population (Fig. 5.14a) and a weighted mean $^{206}Pb/^{238}U$ date of 313.78 ± 0.08 Ma (95 % conf., MSWD = 2.2, p = 0.056; Fig. 5.14b). This is within error of (but substantially more precise than) previous age determinations from tonstein Z1 (Fig. 5.15) that were obtained using the $^{40}Ar/^{39}Ar$ sandine (Lippolt *et al.*, 1984; Hess & Lippolt, 1986) and U-Pb zircon SHRIMP methods (Claoué-Long *et al.*, 1995).

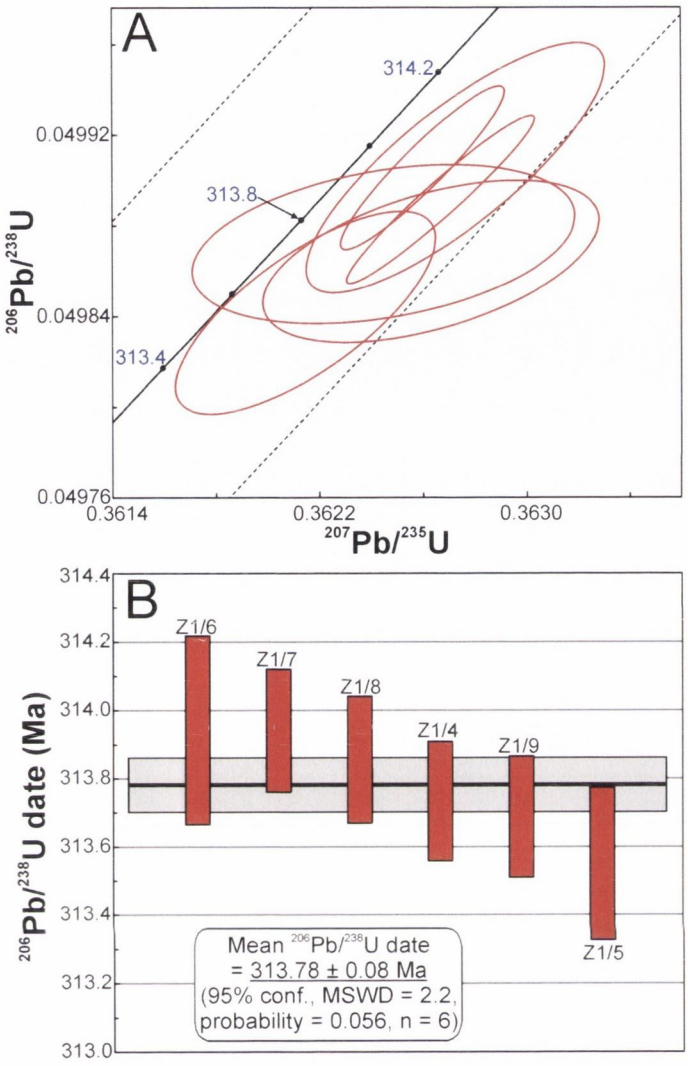

Figure 5.14. U-Pb zircon CA-ID-TIMS data from tonstein Z1 illustrated as a concordia diagram (A) and a weighted mean $^{206}Pb/^{238}U$ date plot (B). In plot A, the solid black line is the concordia drawn using the decay constants of Jaffey *et al.* (1971). The dashed black lines drawn parallel to the concordia represent the uncertainty in the position of the concordia arising from uncertainties in the U decay constants. Blue numbers are concordant ages (Ma). Error ellipses are drawn at the 2σ confidence level. In plot B, the grey band represents the uncertainty of the weighted mean (95 % confidence level). Box heights (representing date uncertainties) are drawn at the 2σ confidence level.

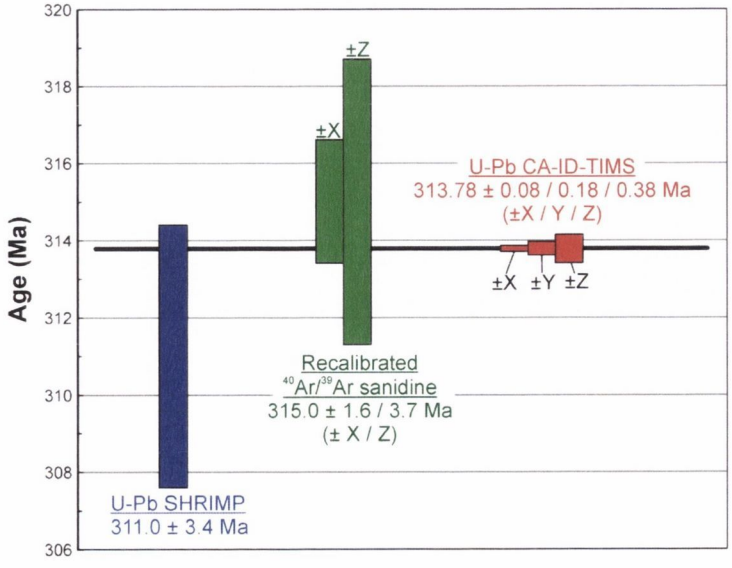

Figure 5.15. A comparison of isotopic age data from tonstein Z1. All data are drawn at the 95 % / 2σ confidence level. U-Pb SHRIMP data includes decay constant uncertainties. For the $^{40}Ar/^{39}Ar$ data, X = internal error only, Z = internal error plus standard and decay constant uncertainties. The U-Pb zircon SHRIMP date is from Claoué-Long *et al.* (1995) and the $^{40}Ar/^{39}Ar$ sanidine date is recalibrated from Lippolt *et al.* (1984) following the methodology described in section 2.8.

5.3.1.2.1. Comparison to the Sub-High Main Tonstein U-Pb zircon CA-ID-TIMS date of Waters & Condon (2012)

Waters & Condon (2012) determined a weighted mean $^{206}Pb/^{238}U$ date of 314.37 ± 0.25 / 0.53 Ma (2σ; ± X / ± Z uncertainty levels; section 2.3.5.2.5) for the Sub-High Main tonstein using the U-Pb zircon CA-ID-TIMS method and the Earthtime 'ET535' tracer solution. This tonstein is reported to occur 14 m above the Aegiranum marine band (Waters & Condon, 2012; Fig. 5.1) and is in close stratigraphic proximity to the Z1 tonstein that was dated in this study (section 5.3.1.2; tonstein Z1 occurs 10 – 12 m below the Aegiranum marine band), to the extent that these horizons should yield similar, if not equivalent dates within analytical uncertainties. It is therefore pertinent to compare the U-Pb zircon CA-ID-TIMS isotopic dates from these two tonstein horizons for internal consistency.

U-Pb data from both the Sub-High Main tonstein and tonstein Z1 are presented in Fig. 5.16. The data from tonstein Z1 yield slightly younger dates than several of the analyses from Sub-High Main tonstein (Fig. 5.16). This is with the exception of analysis z4 from the Sub-High Main tonstein (Fig. 5.16).

The calculated weighted mean $^{206}Pb/^{238}U$ dates from the Sub-High Main tonstein and tonstein Z1 (Fig. 5.16b) do not overlap within analytical uncertainties (at the ± X uncertainty level). The weighted mean $^{206}Pb/^{238}U$ date from the Sub-High Main tonstein is slightly older than that of tonstein Z1, despite the latter tonstein horizon occupying a slightly lower stratigraphic position. The reasons for this discrepancy are uncertain. A small proportion (*c.* 0.06 Myrs) of the age discrepancy can be attributed to differences in the composition of the Earthtime tracer solutions used during the data reduction in this study and by Waters & Condon (2012; see section 5.2.4.2.1). Recalculating the tonstein Z1 data using a $^{235}U/^{205}Pb$ tracer ratio of 100.18 (the value used by Waters & Condon, 2012; section 5.2.4.2.1) increases the weighted mean $^{206}Pb/^{238}U$ date of tonstein Z1 (shown in Fig. 5.16b; section 5.3.1.2) by *c.* 0.06 Myrs, but this correction is of insufficient magnitude to account for the difference in age between these two tonstein samples.

The data from tonstein Z1 are significantly more precise than the Sub-High Main tonstein dataset. Thus, there is a greater chance of resolving subtle complexities, such as

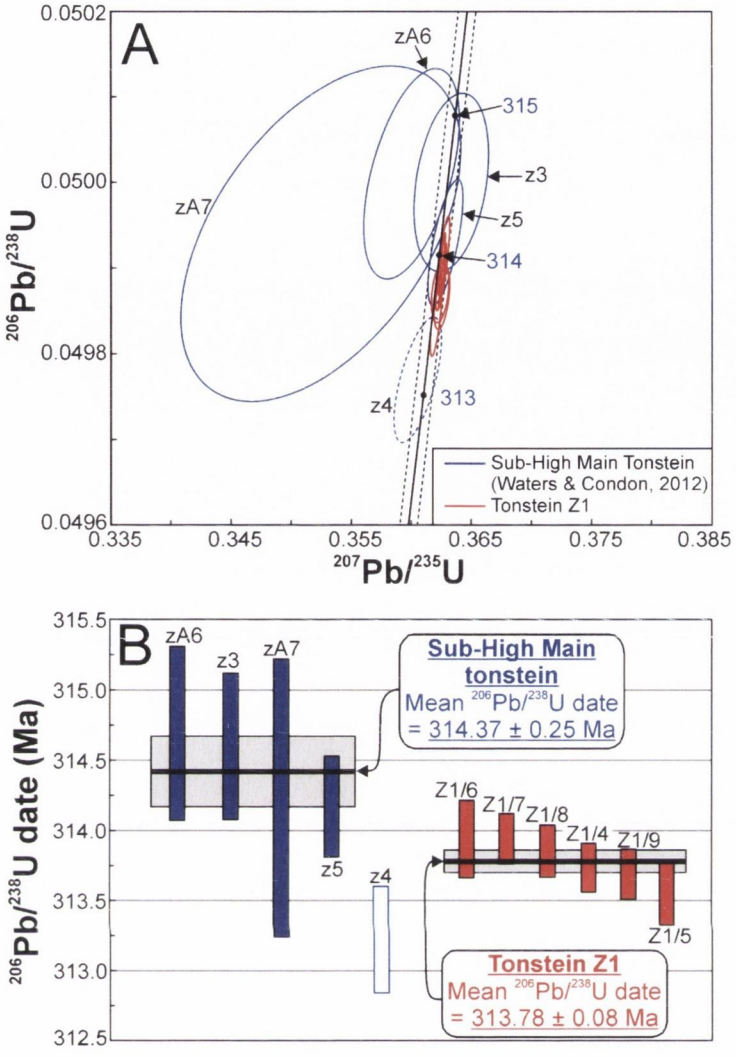

Figure 5.16. U-Pb zircon CA-ID-TIMS data from the Sub-High Main tonstein (redrawn from Waters & Condon, 2012) and tonstein Z1 illustrated as a concordia diagram (A) and a weighted mean $^{206}Pb/^{238}U$ date plot (B). Four data points from the Sub-High Main tonstein sample of Waters & Condon (2012) are not illustrated in this figure; these analyses yielded $^{206}Pb/^{238}U$ dates substantially younger (n = 1; analysis zA9) or older (n = 3; analyses z2, z6, zA8) than the majority of the sample data and were interpreted by Waters & Condon (2012) to reflect residual lead loss and inheritance respectively. In plot A, the solid black line is the concordia drawn using the decay constants of Jaffey *et al.* (1971). The dashed black lines drawn parallel to the concordia represent the uncertainty in the position of the concordia arising from uncertainties in the U decay constants. Blue numbers are concordant ages (in units of Ma). Error ellipses are drawn at the 2σ confidence level. Error ellipses with solid and dashed outlines denote data points included in and excluded from the weighted mean calculations (plot B) respectively. In plot B, box heights (representing date uncertainties) are drawn at the 2σ confidence level and the grey bands represents the uncertainty of the weighted mean calculations (95 % confidence level). Weighted mean $^{206}Pb/^{238}U$ date uncertainties shown in plot B are at the 95 % confidence level (± X uncertainty level; see section 2.3.5.2.5 for an explanation).

minor lead loss or antecrystic inheritance, within the tonstein Z1 dataset. Bearing this in mind, one possible explanation for the age discrepancy between these two tonstein samples is that analyses zA6 and z3 in the Sub-High Main tonstein dataset (Fig. 5.16) represent antecrystic zircons (*sensu* Miller *et al.*, 2007; section 2.3.2.3) and thus their inclusion in the weighed mean $^{206}Pb/^{238}U$ date calculation (Fig. 5.16b) is biasing the calculated date towards an older value. Excluding these analyses from the weighted mean $^{206}Pb/^{238}U$ date calculation yields a date of 314.18 ± 0.33 Ma (95% conf.; n = 2; analyses zA7 and z5), which is equivalent (within uncertainty) to the tonstein Z1 $^{206}Pb/^{238}U$ weighted mean date (Fig. 5.16b).

Alternatively, it could be that analysis z4 from the Sub-High Main tonstein (Fig. 5.16), which was discarded by Waters & Condon (2012) as containing residual lead loss, may represent late-stage magmatic crystallisation and thus may better approximate the age of this horizon. The inference that analysis z4 represents residual lead loss appears to be based largely on this analysis being distinctly younger than the main cluster of sample data (analyses z3, z5, zA6, zA7; Fig. 5.16). Analysis z4 is neither discordant (within analytical and decay constant uncertainties; Fig. 5.16a), nor are there precise isotopic dates from younger Bolsovian volcanic horizons that would provide a minimum age constraint on this horizon and conclusively demonstrate that this analysis contains residual lead loss.

5.3.1.3. Tonsteins T1Gb and T1P: introduction

Tonsteins T1Gb and T1P are both of early Bolsovian age (Fig. 5.1) and are from the Campine Basin, Belgium. These two horizons are relatively close together within the stratigraphy, separated by *c.* 100 m of siliciclastic strata (Delcambre, 1996) and thus should yield similar ages. Tonstein T1P was the youngest tonstein sample investigated during this project. U-Pb CA-ID-TIMS dating of zircon grains from tonstein T1P was undertaken to provide an upper age bracket on Bolsovian sedimentary cycles. Unfortunately, the results from T1P were complex and subsequently zircon grains from tonstein T1Gb were instead dated using the U-Pb CA-ID-TIMS method. Due to time constraints, only preliminary results from T1Gb were obtained, and further work is necessary before a statistically robust date from this tonstein horizon can be reported. However, initial results are presented in this thesis.

5.3.1.3.1. Tonstein T1P

The sample of tonstein T1P was obtained from drillcore KS6 (Campine Basin, Belgium; 51.0917°N, 5.2250°E; 789.41 – 789.42 m depth; B. Delcambre, pers. comm., 2008). In this drillcore, tonstein T1P is 1 cm thick and pale grey. XRD analysis of material from tonstein T1P reveals an abundance of kaolinite in this sample. The sample yielded an abundant and diverse zircon population; external grain morphologies range from anhedral through to euhedral, of which subhedral grains are the most abundant. The euhedral and subhedral grains both have lengths of 40 – 200 μm (most are < 120 μm) and aspect ratios of *c.* 2 – 5. Some grains contain inclusions, the most common of which are melt inclusions orientated parallel to the c-axis. Fractures are relatively rare in the sample grains.

Euhedral grains were selected preferentially for CA-ID-TIMS analysis, the results of which are shown in Fig. 5.17 and are also presented in Appendix 1 Table 1. The data show significant dispersion, yielding $^{206}Pb/^{238}U$ dates between *c.* 307 Ma and *c.* 312 Ma. It is not clear from these data whether the data scatter represents residual lead loss, inheritance or a combination of these factors. Further work on this sample was not undertaken because of the poor initial results.

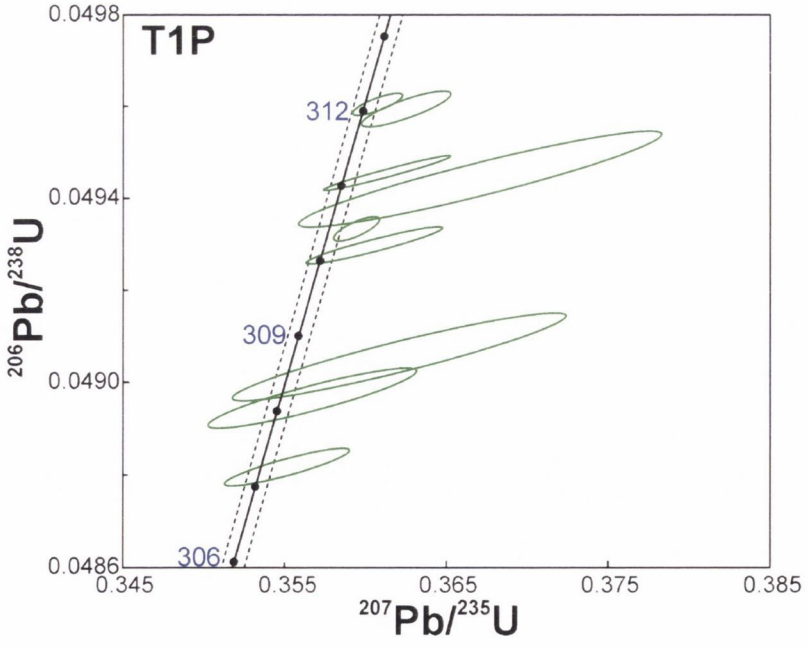

Figure. 5.17. U-Pb zircon CA-ID-TIMS data from tonstein T1P illustrated as a concordia diagram. The solid black line is the concordia. The uncertainty in the position of the concordia arising from the U decay constant uncertainties is denoted by the black dashed lines parallel to the concordia. Blue numbers are concordant ages (in units of Ma). Error ellipses are drawn at the 2σ confidence level.

5.3.1.3.2. Tonstein T1Gb

The sample of tonstein T1Gb was obtained from drillcore KS20 (Campine Basin, Belgium; 51.1018°N, 5.1853°E; 791.00 – 791.08 m depth; B. Delcambre, pers. comm., 2008), where the tonstein horizon is 8 cm thick and dark grey. XRD analysis of material from tonstein T1Gb reveals that it comprises abundant kaolinite and possibly also trace amounts of quartz (Appendix 2 Table 2). The zircon separate contains a diversity of zircon morphologies with anhedral, subhedral and euhedral grains all represented. Most grains show some rounding / corrosion of pyramidal terminations. Euhedral grains are less frequent in this sample than in the sample of tonstein T1P. Euhedral and subhedral grains both have lengths of 50 – 230 μm (most are < 150 μm) and possess aspect ratios of *c.* 2 – 8. The zircon grains are generally heavily fractured and oscillatory zonation is visible in some of the grains.

Six CA-ID-TIMS analyses were undertaken on the euhedral grains. Unfortunately, in only three analyses were the zircons successfully delivered successfully to the Teflon bombs. These three analyses yielded precise dates, which are illustrated in Fig. 5.18 and are also presented in Appendix 1 Table 1. One analysis (T1Gb/1; Fig. 5.18; Appendix 1 Table 1) is substantially older than the other two. This analysis is older than the U-Pb dates from bentonite B9 (section 5.2.4.2) and tonstein T75 (section 5.3.1.1), and is thus interpreted to represent an inherited grain. The other two analyses are equivalent and concordant within analytical and decay constant uncertainties (Fig. 5.18), and yield a weighted mean $^{206}Pb/^{238}U$ date of 312.57 ± 0.24 Ma (95 % conf., Fig. 5.18). Further analyses are required to confirm that these two grains represent the youngest magmatic population present within this sample. However, if these grains are representative of the youngest magmatic population, then this may suggest (based on the stratigraphic proximity of this horizon to the T1P tonstein) that the age of tonstein T1P lies towards the older end of the 307 – 312 Ma range of dates observed from tonstein T1P (section 5.3.1.3.1). If this is true, then some of the complexity in the T1P sample may be the result of residual lead loss. Further analysis of grains from tonstein T1P, employing more aggressive chemical abrasion, would test this hypothesis.

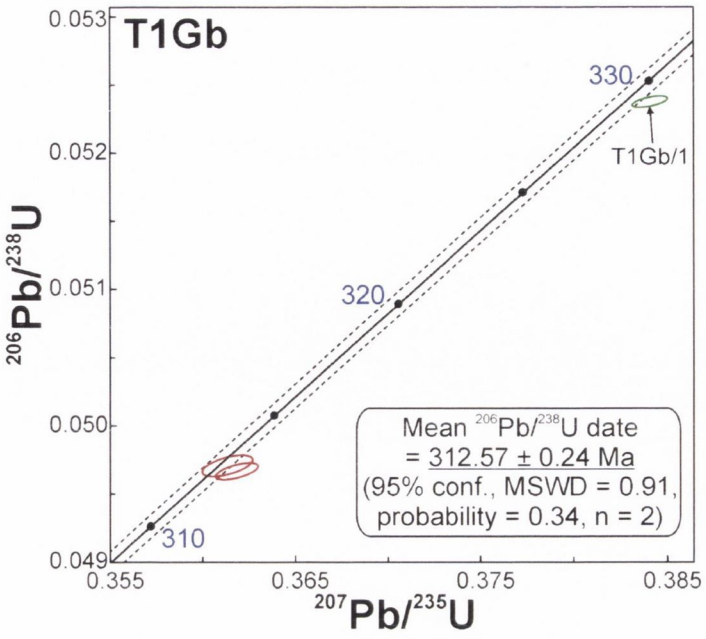

Figure 5.18. U-Pb zircon CA-ID-TIMS data from tonstein T1Gb illustrated as a concordia diagram. The solid black line is the concordia drawn using the decay constants of Jaffey *et al.* (1971). The dashed black lines drawn parallel to the concordia represent the uncertainty in the position of the concordia arising from uncertainties in the U decay constants. Blue numbers are concordant ages (Ma). Error ellipses are drawn at the 2σ confidence level. Red and green error ellipses denote analyses included in and excluded from the weighted mean $^{206}Pb/^{238}U$ date calculation respectively.

5.4. Discussion

U-Pb zircon CA-ID-TIMS dating of samples B9, T75 and Z1 yielded precise age constraints (summarised in Table 5.2) that are the focus of this discussion. U-Pb zircon CA-ID-TIMS data from samples B1, T1P and T1Gb are not discussed further.

Horizon	Stratigraphic position	Weighted mean $^{206}Pb/^{238}U$ date	Uncertainties (95% conf.)			MSWD	Probability of fit	No. of analyses
			± X	± Y	± Z			
B9	Arnsbergian (E2b2)	324.54	0.26	0.31	0.46	0.94	0.42	4
T75	upper Langsettian	317.63	0.12	0.20	0.39	0.70	0.59	5
Z1	uppermost Duckmantian	313.78	0.08	0.18	0.38	2.2	0.056	6

Table 5.2. Summary of U-Pb zircon CA-ID-TIMS data discussed in this section. ± X / Y / Z uncertainty levels are explained in section 2.3.5.2.5.

The isotopic dates from horizons B9, T75 and Z1 are used to estimate the periodicity of sedimentary cycles that occur between these altered ash layers, to determine if there is any compatibility between the periodicity of these sedimentary cycles and Milankovitch cycles. These calculations are discussed in section 5.4.1. The implications that the new CA-ID-TIMS dates have for the calibration of the Carboniferous timescale are discussed in section 5.4.2. The new U-Pb zircon CA-ID-TIMS dates from tonsteins T75 and Z1 also facilitate correlation of the base of the global Moscovian Stage boundary with the western European regional stratigraphic framework (discussed in section 5.4.3).

5.4.1. Upper Carboniferous cyclic sedimentation

The Namurian and Westphalian regional stages of western Europe are characterised by siliciclastic facies that demonstrate simple cyclicity in the form of the alternation of marine bands (thin horizons of limestone, mudstone or shale that contain a diverse fauna) and strata that are barren of marine organisms (Holdsworth & Collinson, 1988). A detailed investigation of the sedimentary cycles by Ramsbottom *et al.* (1962) has demonstrated that they contain cycles of faunal phases (Fig. 5.19; Ramsbottom *et al.*, 1962), which were interpreted by Ramsbottom *et al.* (1962) to reflect variations in salinity, a view that has largely been upheld by subsequent studies (e.g. Holdsworth & Collinson, 1988). Several of the marine bands can be traced across western Europe, from Ireland through to Germany (Ramsbottom *et al.*, 1978), on the basis of the thick-shelled ammonoids contained within the bands. The marine bands have been suggested to represent eustatic highstands (e.g. Holdsworth & Collinson, 1988), during which time marine waters impinged on otherwise brackish or non-marine basins (Holdsworth & Collinson, 1988). Furthermore, some authors have suggested glacio-eustasy as the mechanism driving the eustatic oscillations (Maynard & Leeder, 1992; Martinsen *et al.*, 1995; Davies *et al.*, 1999), based on the known occurrence of coeval ice centres on Gondwana at this time (section 1.1).

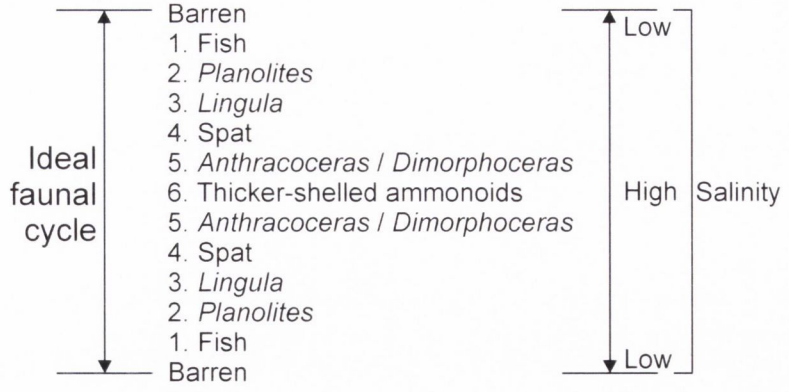

Figure 5.19. The idealised faunal cycle (after Ramsbottom *et al.*, 1962). Spat = immature mollusc shells. *Anthracoceras* and *Dimorphoceras* are thinner-shelled ammonoids

5.4.1.1. Periodicity of upper Carboniferous marine bands

Several previous periodicity estimates have been published for western and central European Namurian and Westphalian sedimentary cycles (Table 5.3).

Reference source	Stratigraphic interval	Average cycle periodicity (kyrs / cycle)
Pennine Basin, northern England		
Holdsworth & Collinson (1988)	Namurian Stage	*c.* 185
Leeder (1988)	Namurian Stage	*c.* 180
Leeder (1988)	Langsetttian to lower Bolsovian	*c.* 200 *
Maynard & Leeder (1992)	Kinderscoutian to Duckmantian	160 ± 64
Riley *et al.* (1993)	Arnsbergian to Duckmantian	*c.* 65
Upper Silesian Basin, Czech Republic		
Gastaldo *et al.* (2009)	lower Pendleian	54 – 107

Table 5.3. Recent published periodicity estimates for Namurian and Westphalian cycles. * Leeder (1988) noted that this estimate may be distorted by the heterogeneous vertical distribution of the marine bands (see Fig. 5.21); the periodicity of these cycles could be as short as 100 kyrs / cycle (Leeder, 1988).

The majority of previous estimates (Table 5.3) have assumed that the marine bands adhere to a constant forcing mechanism (i.e. that the cycles share a common periodicity) and have employed the following equation to estimate the average periodicity of sedimentary cycles:

$$\text{Average cycle periodicity (kyrs / cycle)} = \frac{\text{Time duration (kyrs)}}{\text{Number of cycles}}$$

With the exception of the Gastaldo *et al.* (2009) estimate, the other estimates shown in Table 5.3 were based upon imprecise temporal controls ($^{40}Ar/^{39}Ar$ sanidine dates, U-Pb SHRIMP dates and contemporary published timescales). The estimate by Gastaldo *et al.* (2009) is, in contrast, based upon precise U-Pb zircon CA-ID-TIMS dates from altered ash layers that occur interbedded with the sedimentary cycles of the Upper Silesian Basin and is thus considered to be a robust periodicity estimate.

There is some disagreement between the different periodicity estimates. The estimates from the late 1980s imply a longer average periodicity than more recent estimates (such as that of Riley *et al.*, 1993; Table 5.3). The estimate of Maynard & Leeder (1992) overlaps within uncertainty with the 'short' (*c.* 100 kyrs) eccentricity Milankovitch band. However, the uncertainty of this estimate is large, negating a definitive evaluation. The periodicity estimate of Gastaldo *et al.* (2009) also overlaps (at the 95 % confidence level) with the *c.* 100 kyrs eccentricity Milankovitch cycle, which led Gastaldo *et al.* (2009) to propose a possible 'short' eccentricity control over the Pendleian cycles of the Upper Silesian Basin.

More recently, Waters & Condon (2012) suggested that the Namurian and Westphalian marine bands of the Pennine Basin may preserve multiple orders of cyclicity, which would potentially invalidate the periodicity estimates for Pennine Basin sedimentary cycles which assume that the cycles adhere to a uniform periodicity. Within the Pennine Basin, there are numerous marine bands that contain distinct ammonoid faunas (e.g. see Fig. 5.20 in section 5.4.1.1.1); however, there are also several instances where successive marine bands contain the same ammonoid faunas (e.g. the E2a1a – c, E2b2a – c, R2a1a – c marine bands; Fig. 5.20). In mudstone-dominated sequences, successive marine bands bearing the same ammonoid faunas typically occur as distinct beds separated by tens of centimetres to metres of fossil-barren shales and mudstones (e.g. E2b2a – c marine bands in Fig. 5.20; Waters & Condon, 2012). Conversely, in more sand-rich stratigraphic sections (e.g. sections containing deltaic strata), the stratigraphic separation between such marine bands is typically much greater (tens of

metres; e.g. R1c1-3 marine bands in Fig. 5.20; Waters & Condon, 2012). Working under the assumption that ammonoid morphological evolution rates were relatively constant during Namurian times, Waters & Condon (2012) proposed that the marine bands containing the same ammonoid fauna represent higher frequency eustatic oscillations than the marine bands containing distinct ammonoid faunas. Using the U-Pb zircon CA-ID-TIMS dates from bentonite B6 (section 5.2.4.2.1; Waters & Condon, 2012) and the Sub-High Main tonstein (section 5.3.1.2.1; Waters & Condon, 2012), together with recent age estimates for the base of the Namurian Regional Stage and the Mississippian-Pennsylvanian boundary (from Davydov *et al.* 2010), Waters & Condon (2012) suggested that several of the marine bands that contain distinct ammonoid faunas represented 'long' (*c.* 404 kyrs) eccentricity forcing, whereas the marine bands possessing the same ammonoid faunas represented *c.* 100 kyrs eccentricity or possibly shorter Milankovitch frequencies (obliquity or precession; section 1.3).

It is not clear at this present time whether the assumption that ammonoid morphological evolution rates were constant during Namurian and Westphalian times is a valid one. Elsewhere, it has been suggested that the heterogeneous distribution of distinct ammonoid faunas within the marine bands could indicate that the ammonoid biozones represent unequal time durations (e.g. Menning *et al.*, 2000), although, this argument assumes that the marine bands of the Pennine Basin possess a uniform periodicity. Unfortunately, there are insufficient absolute age constraints from the Namurian and Westphalian stratigraphy of the Pennine Basin, which would otherwise provide a basis for testing the constancy of ammonoid morphological evolution rates and the uniformity of cycle periodicities. Thus, at this time it is not certain which approach yields periodicity estimates that are more representative of the actual periodicities of these sedimentary cycles.

In subsequent chapters, average periodicity estimates are computed assuming equal durations for the sedimentary cycles. Using the new precise U-Pb zircon CA-ID-TIMS dates (Table 5.2), it is possible to calculate the average periodicity of sedimentary cycles between bentonite B9 and tonstein T75 and also between tonsteins T75 and Z1 (Fig. 5.1). These calculations are discussed in subsequent sections.

5.4.1.1.1. Arnsbergian to lower Langsettian cycles (bentonite B9 to tonstein T75)

Combining the Namurian stratigraphic record from the Pennine Basin, northern England, with the Langsettian record from the Ruhr Basin, Germany, 59 marine bands are recognised between bentonite B9 and tonstein T75 (= tonstein Wilhelm of the Ruhr Basin; Paproth *et al.*, 1983b; Delcambre, 1996), as shown in Figs. 5.20 and 5.21. Within the Langsettian of the Ruhr Basin (Fig. 5.21) there are also 16 faunal bands that contain ostracodes of the genus *Jonesina*, the trace fossil *Planolites ophthalmoides,* arenaceous foraminifera and / or inarticulate brachiopods (*Lingula*; Fiebig, 1969; Bachmann *et al.*, 1970), which are thought to be indicative of brackish (near-marine) conditions (Rabitz, 1966; Calver, 1968; Bless *et al.*, 1987; Paproth *et al.*, 1994; Dusar *et al.*, 2000). It is difficult to trace these bands beyond the immediate vicinity of the Ruhr Basin; consequently, their lateral continuity is not known and thus the likelihood that they reflect eustatic oscillations is difficult to assess. This uncertainty is taken into consideration in the periodicity calculations; the number of faunal bands attributable to eustasy is between 59 (marine bands only; Table 5.4) and 75 (marine and brackish bands; Table 5.4).

Using the new CA-ID-TIMS dates for horizons B9 and T75, the average periodicty of Namurian (Arnsbergian) to lower Langsettian sedimentary cycles is between 88 and 122 kyrs / cycle (95 % confidence; Table 5.4). This is comparable (within uncertainty) to the dominant *c.* 100 kyrs cycle frequency observed in Pleistocene glacial records (e.g. Hays *et al.*, 1976), which is though to result from the Milankovitch 100 kyrs eccentricity orbital-forcing (Hays *et al.*, 1976; Imbrie *et al.*, 1993; Lisiecki, 2010). The similarity between the periodicity of Pleistocene glacial cycles and western European Arnsbergian to lower Langsettian sedimentary cycles strengthens the argument that these Carboniferous sedimentary cycles are the product of glacio-eustatic oscillations.

	Number of cycles between bentonite B9 and tonstein T75	Time duration (Myrs)	Uncertainty in time duration (± Myrs)	Average periodicity (kyrs)	Uncertainty in average periodicity (± kyrs / cycle)
Marine bands	59	6.91	0.29	117	5
Marine and brackish bands	75	6.91	0.29	92	4

Table 5.4. Average periodicities of the sedimentary cycles between bentonite B9 and tonstein T75; calculated using the methodology presented in section 2.9. Uncertainties are at the 95 % conf. level.

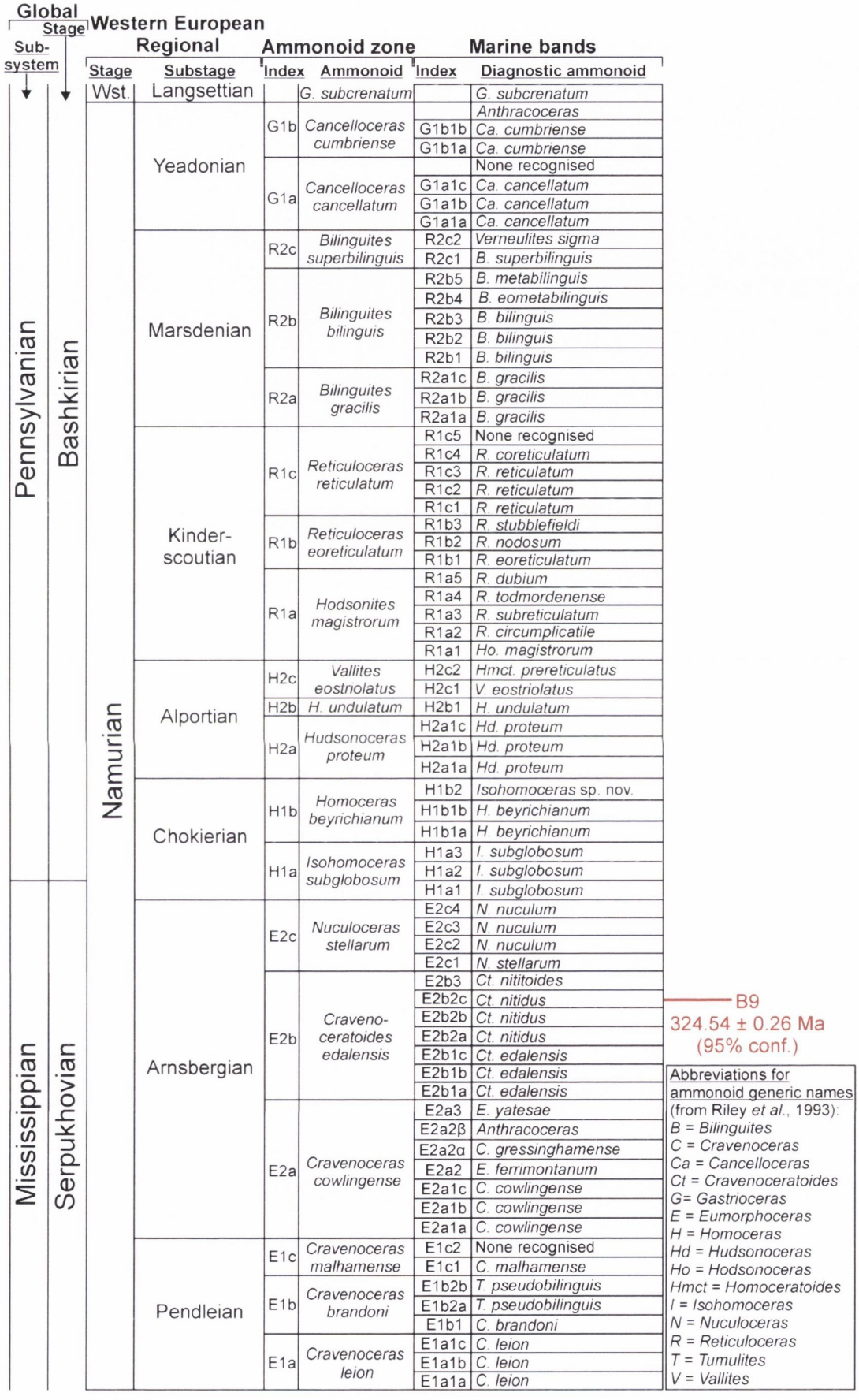

Figure 5.20. Namurian marine bands observed within the Pennine Basin, northern England (redrawn from Waters & Condon, 2012). Wst = Westphalian.

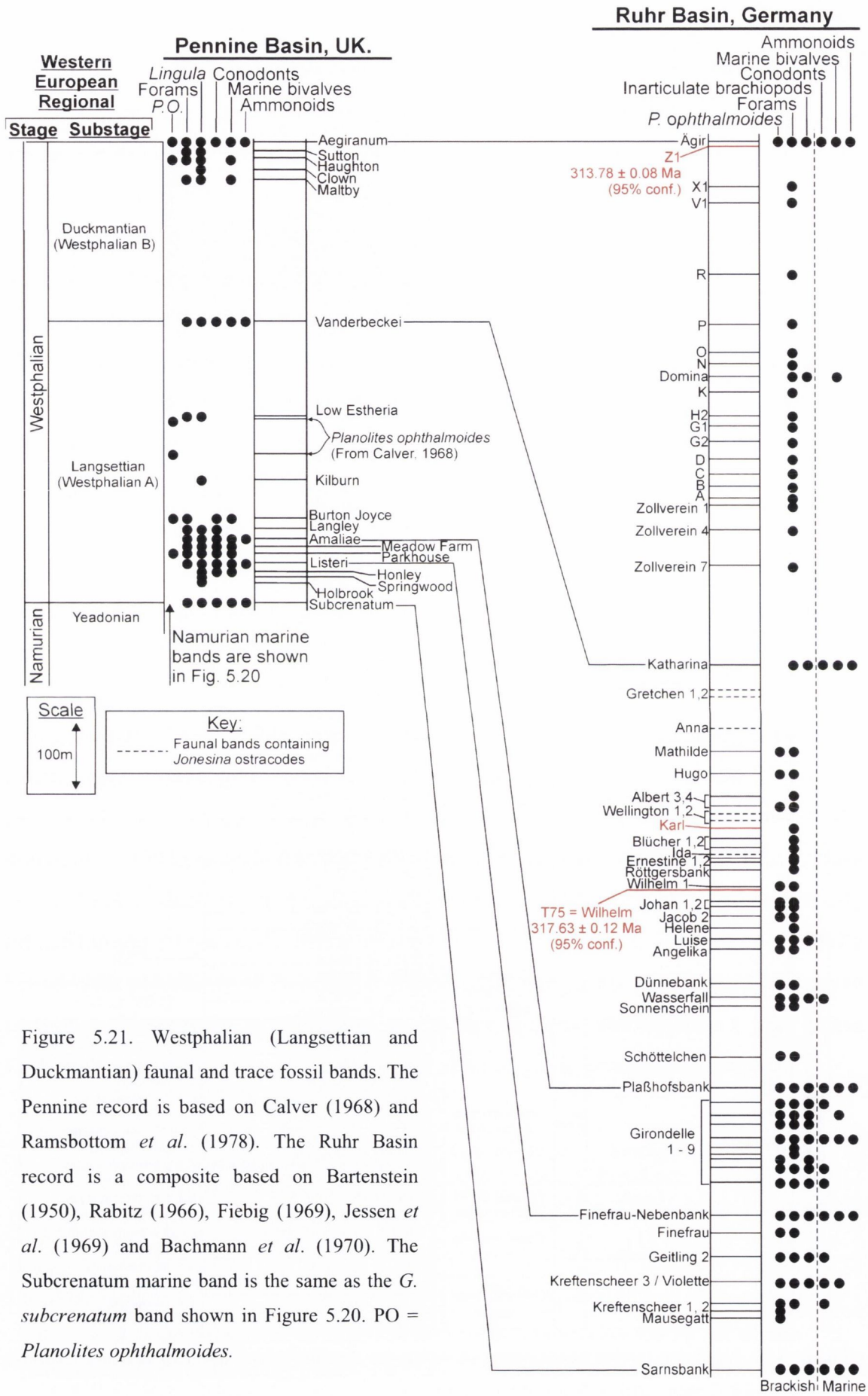

Figure 5.21. Westphalian (Langsettian and Duckmantian) faunal and trace fossil bands. The Pennine record is based on Calver (1968) and Ramsbottom *et al.* (1978). The Ruhr Basin record is a composite based on Bartenstein (1950), Rabitz (1966), Fiebig (1969), Jessen *et al.* (1969) and Bachmann *et al.* (1970). The Subcrenatum marine band is the same as the *G. subcrenatum* band shown in Figure 5.20. PO = *Planolites ophthalmoides.*

5.4.1.1.2. Upper Langsettian to Duckmantian sedimentary cycles

The Westphalian Stage of western Europe contains notably fewer marine bands than the Namurian Stage. Ramsbottom *et al.* (1978) recognised 19 laterally extensive Westphalian marine bands within the Pennine Basin and a further two bands from only the East Midlands (Notts. – Derby) coalfield (the Kilburn and Low Estheria bands in Fig. 5.21). Additionally, Calver (1968) noted the occurrence of two *Planolites ophthalmoides* bands within the upper Langsettian succession of the East Midlands coalfield (Fig. 5.21). Most of the faunal and trace fossil bands occur in the lower Langsettian and the upper Duckmantian to lower Bolsovian (Calver, 1968, 1969). The reduction in the number of marine bands during the mid-to-upper Langsettian is coincident with an increased prevalence of non-marine mussel bands (Calver, 1968, 1969) and sedimentological changes that suggest a landward shift in the depositional environment from a lower to an upper delta plain (Guion & Fielding, 1988; Guion *et al.*, 1995).

A similar reduction in the number of marine bands is observed in the Campine and Ruhr Basins (Belgium and Germany respectively). Lower Langsettian strata contain numerous marine bands but few have been found in younger rocks (Fiebig, 1969; Paproth, *et al.*, 1994; Fig. 5.21). There are, however, numerous upper Langsettian and Duckmantian brackish faunal and trace fossil bands. In the Ruhr Basin, between tonsteins Wilhelm (= tonstein T75) and Z1, there are only two fully marine bands (Katharina and Domina horizons in Fig. 5.21), whereas 34 bands containing ostracodes of the genus *Jonesina*, the trace fossil *Planolites ophthalmoides,* arenaceous foraminifera and / or *Lingula* have been recognised (Fig. 5.21). Thus, within this stratigraphic interval there are between two and 36 faunal bands that could be eustatic. Using the same methodology as employed to the Arnsbergian to lower Langsettian cycles (section 5.4.1.1.1; i.e. calculating the periodicity of marine bands only and marine plus brackish bands) yields average cycle periodicity values for upper Langsettian to Duckmantian sedimentary cycles within the Ruhr Basin of between 107 ± 4 kyrs / cycle (marine and brackish bands; Table 5.5) and 1925 ± 70 kyrs / cycle (marine bands only; Table 5.5), or expressed as a single range, 103 – 1995 kyrs / cycle.

	Number of cycles between tonsteins T75 and Z1	Time duration (Myrs)	Uncertainty in time duration (± Myrs)	Average periodicity (kyrs)	Uncertainty in average periodicity (± kyrs / cycle)
Ruhr Basin, Germany					
Marine bands	2	3.85	0.14	1925	70
Marine and brackish bands	36	3.85	0.14	107	4
Pennine Basin, northern England					
Minimum number of faunal bands	5	3.85	0.14	770	28
Maximum number of faunal bands	11	3.85	0.14	350	13

Table 5.5. Average periodicities of the upper Langsettian to Duckmantian sedimentary cycles between tonsteins T75 and Z1; calculated using the methodology presented in section 2.9. Uncertainties are at the 95 % confidence level.

In contrast, if the stratigraphic record of the Pennine Basin (northern England) is used, there are between five and eleven faunal and trace fossil bands between tonsteins T75 and Z1 (Fig. 5.21). The uncertainty in the number of intervening faunal and trace fossil bands arises because of uncertainties in the correlation of tonstein T75 to the Pennine Basin stratigraphic record. Lateral correlatives of tonsteins T75 and Z1 have thus far not been identified from the Pennine Basin. Instead, the correlation of tonsteins T75 and Z1 to the Pennine Basin stratigraphy relies upon biostratigraphic controls from the ammonoid-bearing marine bands, which are firmly correlated between Pennine and Ruhr Basins (solid lines of correlation in Fig. 5.21). Tonstein Z1 occurs adjacent to the Ägir marine band, which is firmly correlated with the Aegiranum marine band in the Pennine Basin (Fig. 5.21) and therefore can be reliably correlated to the Pennine Basin stratigraphy. In contrast, Tonstein T75 (= tonstein Wilhelm of the Ruhr Basin; Paproth *et al.*, 1983b; Delcambre, 1996) occurs roughly equidistance between the Plaßhofsbank and Quaregnon (= Katharina band in the Ruhr Basin) ammonoid-bearing marine bands (Figs. 5.1 and 5.21), which are correlated to the Amalie and Vanderbeckei marine bands respectively in the Pennine Basin (Fig. 5.21). Within the limits of the ammonoid biostratigraphic controls, tonstein T75 could correlate to a horizon beneath the Langley marine band (Fig. 5.21), above the Low Estheria faunal band (Fig. 5.21) or to an intermediate level between these limits (Fig. 5.21). Thus, between tonsteins T75 and Z1 within the Pennine Basin record there are between a minimum of five (if tonstein T75

correlates to above the Low Estheria band) and a maximum of 11 faunal and trace fossil bands (if tonstein T75 correlates to below the Langley band). This constrains the average periodicity of Pennine sedimentary cycles to between 350 ± 13 kyrs / cycle (11 faunal bands; Table 5.5) and 770 ± 28 kyrs / cycle (5 faunal bands; Table 5.5), or expressed as a single range, 337 – 798 kyrs / cycle.

The above periodicity calculations highlight differences in the amount of time residing between the Pennine and Ruhr Basin faunal bands. There are a sufficient number of brackish and marine faunal bands preserved within the Ruhr Basin to yield an average periodicity that is similar to the underlying Namurian cycles (section 5.4.1.1.1) and to the *c.* 100 kyrs Milankovitch eccentricity cycle. The periodicity calculations are consistent with the hypothesis that the brackish faunal bands in the Ruhr Basin could represent the distal expression of glacio-eustasy. However, this is not definitive proof and further research is necessary to confirm this hypothesis. There are more tonstein horizons known from the Ruhr Basin that are interbedded with these cryptic brackish bands (e.g. Fiebig, 1969; Burger *et al.*, 2005). Additional U-Pb zircon CA-ID-TIMS dates from such horizons would evaluate whether the above calculated average periodicity is representative on a finer scale of analysis.

The average periodicity of sedimentary cycles within the Pennine Basin is significantly longer than the *c.* 100 kyrs 'short' eccentricity cycle. However, it is uncertain whether the average cycle periodicity is representative of the periodicity of individual sedimentary cycles; the heterogeneous vertical distribution of the faunal bands (as noted by Leeder, 1988; Fig. 5.21) may render the average periodicity calculations inaccurate. It is possible that the Pennine Basin sedimentary cycles possess much shorter periodicities (similar to Ruhr Basin sedimentary cycles?) than the calculated average cycle periodicity, which may be is biased towards longer values by the occurrence of so called 'missing beats' within the upper Langsettian to lower Duckmantian of the Pennine Basin. However, alternative explanations for the longer average cycle periodicity within the upper Langsettian to Duckmantian of the Pennine Basin, such as a possible change in the dominant Milankovitch cycle expressed within this stratigraphic interval (e.g. from *c.* 100 kyrs to *c.* 404 kyrs eccentricity forcing) or the superimposition of multiple Milankovitch frequencies (as suggested by Waters & Condon, 2012; section 5.4.1.1), cannot be excluded on the basis of the available age data. Further high-

precision isotopic dates from tonstein horizons intermediate between tonsteins T75 and Z1 are required to test these different hypotheses.

5.4.2. Carboniferous timescale calibration and astronomical tuning

As shown in previous sections, the periodicity of Arnsbergian to lower Langsettian cycles is compatible with the Milankovitch *c.* 100 kyrs eccentricity frequency. This Milankovitch frequency, in conjunction with the CA-ID-TIMS date from bentonite B9, is used to astronomically tune the Namurian stratigraphy of the Pennine Basin in northern England, enabling revised dates for the base of the Westphalian Regional Stage and the global Mid-Carboniferous boundary to be determined. Extending the astronomical tuning approach to the base of the Namurian Stage is problematic and is discussed in section 5.4.2.1. These astronomically tuned estimates are then compared to published timescale calibrations (Davydov *et al.*, 2004, 2010; timescale B of Menning *et al.*, 2000; Peterson, 2011).

Astronomical tuning is not extended into the Westphalian Stage because it is controversial whether the numerous brackish bands are eustatically driven and hence if they preserve a genuine Milankovitch signal. However, tonstein Z1 occurs adjacent to the base of the Bolsovian Substage and its new U-Pb zircon CA-ID-TIMS date approximates the age of this boundary, allowing a comment on the duration of the Langsettian and Duckmantian substages combined.

5.4.2.1. Base of the Namurian Stage

The basal boundary of the Namurian Regional Stage is defined as at the base of strata containing the earliest occurrence of the ammonoid *Cravenoceras leion* (van Leckwijck, 1960). In the Pennine Basin, this corresponds to the base of the E1a1 (*C. leion*) marine band, which occurs 20.5 sedimentary cycles below bentonite B9 (Fig. 5.20); the half cycle corresponds to the part of a cycle between bentonite B9 and the underlying E2b2c marine band. If it is assumed that these cycles reflect the *c.* 100 kyrs eccentricity cycle, then the age of the base of the Namurian is calculated as approximately 326.6 Ma (Fig. 5.22). This value is close to that reported in the Geologic Time Scale 2004 (326.4 ± 1.6 Ma; Davydov *et al.* 2004; Fig. 5.22) and timescale B of Menning *et al.* (2000,

326.5 Ma; Fig. 5.22), but is substantially younger than that shown by Gastaldo *et al.* (2009; 329.7 Ma) and Davydov *et al.* (2010; 329.2 Ma; Fig 5.22). The true date of the base of the Namurian is almost certainly older than 326.6 Ma because Davydov *et al.* (2010) reported the date of a tonstein within the C11 coal of the Donets Basin, which is correlated with a horizon in the Pendleian Substage of western Europe, as 328.14 ± 0.11 Ma (2σ, $^{206}Pb/^{238}U$ date; Davydov *et al.*, 2010). Gastaldo *et al.* (2009) similarly reported an age of 328.84 ± 0.16 Ma (2σ) for a tonstein correlated with the Pendleian in the Ostrava Formation of the Upper Silesian Basin, Czech Republic. Using the estimate of 329.2 Ma in Davydov *et al.* (2010) for the age of the base of the Namurian, the average periodicity of the Pendleian and Arnsbergian cycles below bentonite B9 is calculated to be approximately 227 kyrs / cycle (Table 5.6).

Number of sedimentary cycles between the base of Namurian Stage and bentonite B9 (from Fig. 5.20)	Time duration (Myrs)	Average periodicity (kyrs / cycle)
20.5	4.66 *	227

Table 5.6. Average periodicity of the sedimentary cycles between the base of the Namurian and bentonite B9; calculated using the methodology presented in section 2.9. * The time duration is calculated as 329.2 Ma (base of Namurian Stage; Davydov *et al.*, 2010) - 324.54 Ma (U-Pb zircon CA-ID-TIMS date from bentonite B9; section 5.2.4.2). No uncertainty is calculated for this average periodicity estimate because the uncertainty of the Davydov *et al.* (2010) estimate for the base of the Namurian Stage is not known.

The available data are not sufficient to discriminate between different possibilities such as a combination of *c.* 100 kyrs and *c.* 404 kyrs eccentricity control over the sedimentary cycles in this stratigraphic interval or that there was a switch in the dominant Milankovitch frequency from *c.* 404 kyrs to *c.* 100 kyrs eccentricity several sedimentary cycles above the base of the Namurian. The former possibility, that the sedimentary cycles represent a combination of multiple Milankovitch frequencies, has been suggested previously by Waters & Condon (2012), who proposed that successive marine bands bearing the same ammonoid faunas (Fig. 5.20) represent shorter time durations than marine bands possessing distinct ammonoid faunas (section 5.4.1.1).

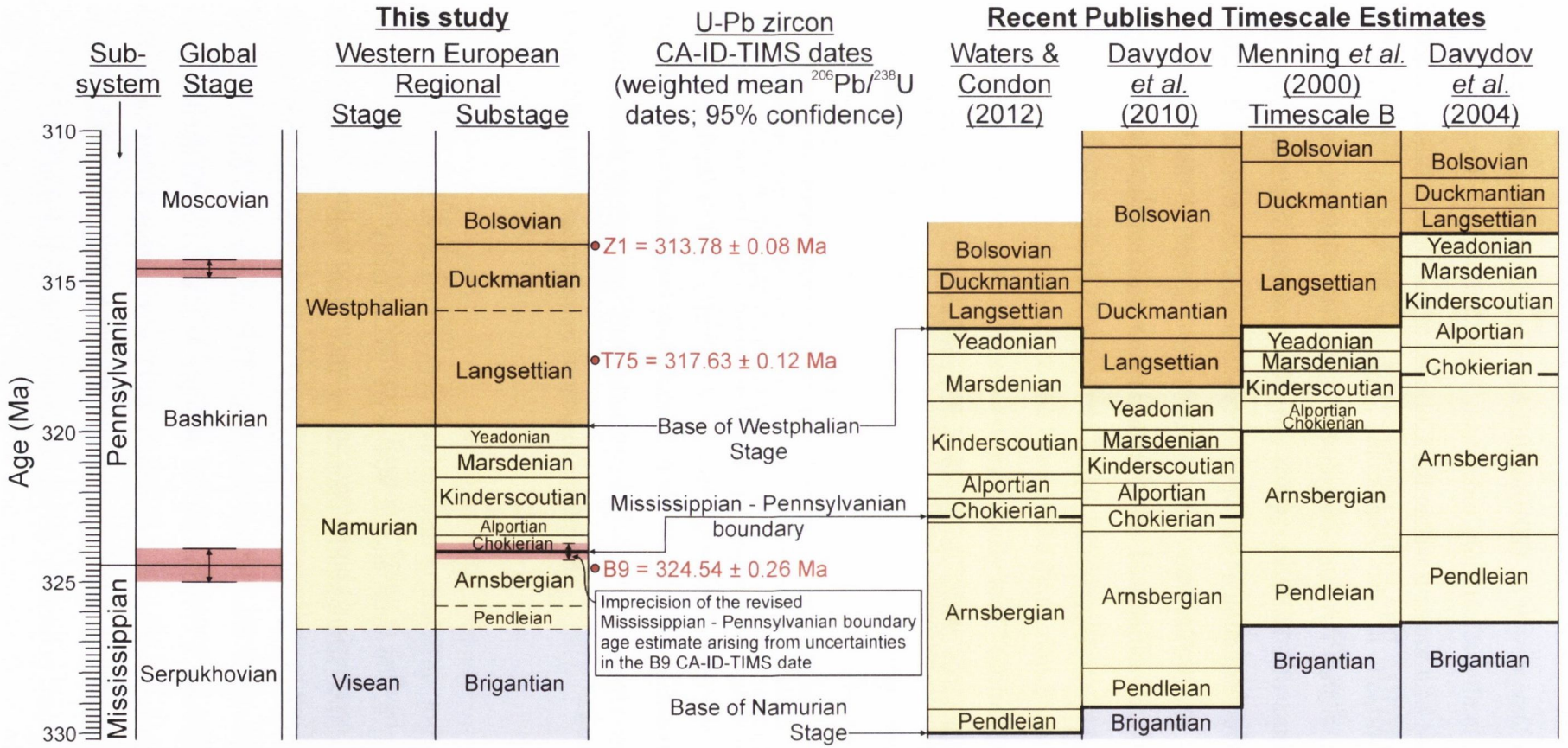

Figure 5.22. Revised absolute age estimates for some western European regional stratigraphic boundaries derived using astronomical tuning and the new U-Pb CA-ID-TIMS dates. These are compared to recent published timescale estimates (Menning *et al.*, 2000; Davydov *et al.*, 2004, 2010; Waters & Condon, 2012) and contemporary age estimates for the global Carboniferous stage boundaries (Peterson, 2011). Zircon date uncertainties exclude systematic uncertainties arising from the tracer calibration and the ^{238}U decay constant. Namurian Stage boundaries and the substage boundaries therein are astronomically tuned to the 100 kyrs eccentricity cycle; these are at best as precise as the U-Pb zircon CA-ID-TIMS from bentonite B9, against which the astronomical timescale is anchored (this is illustrated for Mississippian-Pennsylvanian boundary). The base of the Bolsovian Substage is constrained by the CA-ID-TIMS date from tonstein Z1. Red bands are uncertainty bounds on the stratigraphic boundary age determinations (2σ / 95 % conf. level).

5.4.2.2. Mississippian – Pennsylvanian (Mid-Carboniferous) Boundary

The Mississippian – Pennsylvanian boundary is correlated with the base of the H1a2 marine band in the European parastratotype at Stonehead Beck, northern England (Riley *et al.*, 1993, p. 281). In recent Carboniferous timescale compilations, this boundary has been successively revised towards older ages by *c.* 6.3 Ma (from 318.1 ± 1.3 Ma to 324.42 ± 0.54 Ma; Davydov *et al.*, 2004, and Peterson, 2011, respectively). This substantial age shift reflects the paucity of precise isotopic age constraints from near to this stratigraphic boundary.

Further confusion surrounding the age of this boundary arises from inconsistencies within the published isotopic dataset. For example, the isotopic age constraints from closest to the Mid-Carboniferous boundary, i.e. two U-Pb SHRIMP determinations from bentonites within the Pennine Basin, northern England (Riley *et al.*, 1993) and a $^{40}Ar/^{39}Ar$ sanidine date from tonstein 479 of the Upper Silesian Basin, Czech Republic (Lippolt *et al.*, 1984; Hess & Lippolt, 1986), diverge significantly. The two Pennine bentonites, which are probable lateral equivalents of bentonites B6 and B8 (Fig. 5.1), were sampled from the Harewood Borehole (British Grid reference: SE 3220 4410; Riley *et al.*, 1993) and dated by the U-Pb SHRIMP method, yielding weighted mean $^{206}Pb/^{238}U$ dates of 314.4 ± 4.6 Ma and 314.5 ± 4.6 Ma respectively (Riley *et al.*, 1993). Hess & Lippolt (1986) originally determined a plateau age of 319.5 ± 2.4 / 7.8 Ma (2σ internal error / internal error plus standard uncertainties) for tonstein 479. This tonstein is reported to occur within the Max coal seam (Lippolt *et al.*, 1984), which is located above the Enna marine horizon (contains *Cravenoceratoides edalensis;* E2b1; Dzik, 1997) and below the Roemer marine horizon (contains *Cravenoceratoides nitidus* and *Cravenoceratoides nitidoides*; E2b2 – E2b3; Hartung & Patteisky, 1960; Dzik, 1997), and is thus constrained to the E2b1 group of marine bands (Fig. 5.20). Before the tonstein 479 $^{40}Ar/^{39}Ar$ date is compared to the U-Pb SHRIMP date, it first requires recalibration against modern values for the age of the monitor standard and the ^{40}K decay constant. Following recalibration of this sanidine date using the methodology described in section 2.8, the age of tonstein 479 is revised to 323.7 ± 1.0 / 3.6 Ma (2σ; internal error / internal error plus standard and decay constant uncertainties). The recalibrated $^{40}Ar/^{39}Ar$ date and U-Pb SHRIMP dates are statistically distinct at the 95 % confidence level (Fig. 5.23).

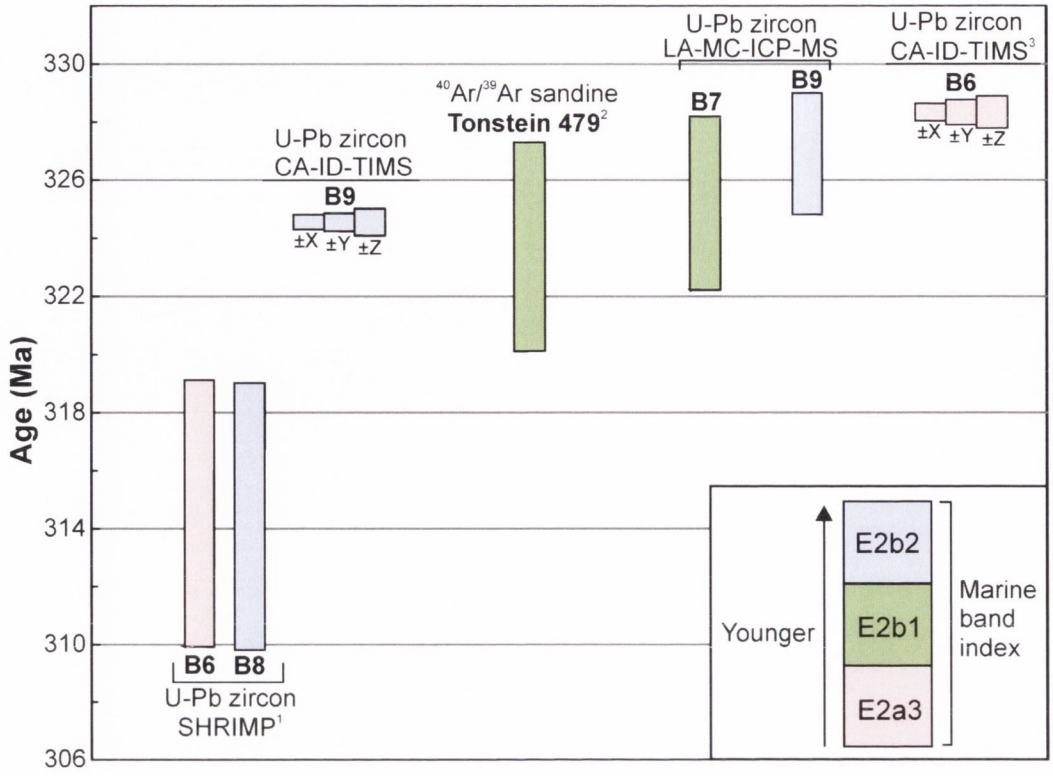

Figure 5.23. Comparison of isotopic age constraints from several Arnsbergian bentonites and tonsteins. Data are colour-coded based on their biostratigraphic position (constrained by thick-shelled ammonoids within the marine bands). The height of the coloured bars represents date uncertainties (2σ or 95 % confidence level). Uncertainties on the U-Pb SHRIMP data, LA-MC-ICP-MS data and $^{40}Ar/^{39}Ar$ sanidine data include systematic uncertainties arising from the age of standard materials and decay constants. The uncertainty levels shown on the CA-ID-TIMS dates correspond to the ± X/ Y/ Z uncertainty notation of Schoene *et al.* (2006; see section 2.3.5.2.5. for an explanation). Published data included in this figure: 1) Riley *et al.* (1993); 2) Lippolt *et al.* (1984) – data are recalibrated (as described in section 2.8); 3) Waters & Condon (2012).

Waters & Condon (2012) have subsequently resampled the Harewood Borehole drillcore (originally sampled by Riley *et al.*, 1993; see above) and re-dated bentonite B6 using the U-Pb zircon CA-ID-TIMS method. Waters & Condon (2012) determined a $^{206}Pb/^{238}U$ date of 328.34 ± 0.30 / 0.55 Ma (2σ; internal error / internal error plus tracer calibration and ^{238}U decay constant uncertainties; section 5.2.4.2.1) for the B6 bentonite. This age determination is in excess of 10 Myrs older than the U-Pb SHRIMP date of bentonite B6 determined by Riley *et al.* (1993).

Although the Namurian bentonite horizons dated in this study (bentonites B7, B9) are different to those dated by Hess & Lippolt (1986), Riley *et al.* (1993) and Waters & Condon (2012), they occupy similar stratigraphic positions based on the ammonoid biostratigraphic constraints (Fig. 5.1). As such, the new CA-ID-TIMS date from bentonite B9 (section 5.2.4.2), together with LA-MC-ICP-MS data from bentonites B7 and B9 (sections 5.2.3.2 and 5.2.3.3), provide additional information that can clarify the discrepancies that exist between the published age data. Six marine bands are recognised in the Pennine Basin between the stratigraphically lowest bentonite (B6; E2a3; Fig. 5.20) and highest bentonite of interest (B9; E2b2c; Fig. 5.20). This would imply, based on the estimated average periodicity of these cycles (88 – 122 kyrs / cycle; section 5.4.1.1.1.), that there should be no more than *c.* 0.73 Myrs difference in age between these altered ash horizons. However, as illustrated in Fig. 5.23, this is not the case; the U-Pb SHRIMP dates are substantially younger than all other data.

Using the U-Pb zircon CA-ID-TIMS date from bentonite B9 as an anchor point and astronomically tuning the cycle record between bentonite B9 and the Mid-Carboniferous boundary (6.5 sedimentary cycles; the half cycle corresponds to the top part of cycle E2b2c between bentonite B9 and the overlying E2b3 marine band; Fig. 5.20), the age of this boundary is constrained to *c.* 323.9 Ma. This is considerably older than the estimates of Davydov *et al.* (2004) and Menning *et al.* (2000; timescale B), slightly older than the estimate of Davydov *et al.* (2010; Fig. 5.22) but indistinguishable within uncertainty with the most recent estimate of 324.42 ± 0.54 Ma by Peterson (2011; Fig. 5.22).

5.4.2.3. Base of the Westphalian Regional Stage

The base of the Westphalian Regional Stage is defined as at the base of the marine band containing the earliest occurrence of *Gastrioceras subcrenatum* (Waters & Davies, 2006). In recent timescale calibrations, this boundary has been progressively revised towards older ages, shifting by *c.* 4 Myrs over the last decade (*c.f.* Davydov *et al.*, 2004 and Davydov *et al.*, 2010 in Fig. 5.22). This reflects a lack of precise isotopic dates from close to this boundary, thus requiring considerable interpolation in published Carboniferous timescale calibrations to constrain the age of this stratigraphic boundary.

Revised age estimates for the base of the Westphalian Stage can be computed using the new U-Pb zircon CA-ID-TIMS dates from bentonite B9 and tonstein T75, in conjunction with astronomical tuning. It is possible to determine a boundary age by astronomical tuning of the upper Namurian stratigraphic record of the Pennine basin (between bentonite B9 and the base of the Westphalian; Fig. 5.20), or alternatively by astronomical tuning of the lower Langsettian cycle record of the Ruhr Basin (between the base of the Westphalian and tonstein T75; Fig. 5.21). Neither approach is ideal. The former involves astronomical tuning over a greater number of sedimentary cycles, whereas the latter approach requires astronomical tuning to be employed to a stratigraphic interval that contains several sedimentary cycles of uncertain significance (cycles bounded by brackish faunal and trace fossil bands; see section 5.4.1.1.1).

Using the CA-ID-TIMS date from bentonite B9 and tuning the intervening 47.5 sedimentary cycles (the half cycle corresponds to the top part of cycle E2b2c between bentonite B9 and the overlying E2b3 marine band; Fig. 5.20) between bentonite B9 and the base of the Westphalian Stage (Fig. 5.20) to the *c.* 100 kyrs eccentricity cycle yields an age of *c.* 319.8 Ma for the base of the Westphalian. In contrast, tuning of the sedimentary cycles between base of the Langsettian and tonstein T75 (Fig. 5.21) to the *c.* 100 kyr eccentricity cycle yields an age of between *c.* 318.8 Ma (calculated for marine bands only; Fig. 5.21) and *c.* 320.4 Ma (includes marine and brackish bands; Fig. 5.21) for the base of the Westphalian Stage. The former age estimate derived using the bentonite B9 CA-ID-TIMS date and the Namurian stratigraphic record is the preferred estimate because the record of Namurian sedimentary cycles from the Pennine Basin is less ambiguous than the lower Langsettian record of the Ruhr Basin. It should be noted that this estimate is potentially more inaccurate than that suggested for the Mississippian – Pennsylvanian boundary (section 5.4.2.2) because of the greater number of intervening cycles involved. This is the oldest estimate for the base of the Westphalian Stage to date (Fig. 5.22).

5.4.2.4. Base of the Bolsovian Substage

Tonstein Z1 occurs 10 – 12 m below the Aegiranum marine band (Fiebig, 1969), which defines the base of the Bolsovian Substage. Tonstein Z1 is sufficiently close to this boundary that the new CA-ID-TIMS date (313.78 ± 0.08 Ma; Table 5.2) can be used to

constrain the age of this stratigraphic boundary. This boundary estimate is older than was estimated by Davydov *et al.* (2004) and Menning *et al.* (2000) but younger than that suggested by Davydov *et al.* (2010) and Waters & Condon (2012; Fig. 5.22).

5.4.2.5. Duration of Chokierian to Duckmantian substages

Using the astronomically-tuned boundary ages for the base of the Chokierian Regional Substage and the Westphalian Stage (Fig. 5.22), the duration of the intervening stratigraphic interval is estimated to be *c.* 4.2 Ma, which is similar to the durations presented in the timescales of Davydov *et al.* (2004, 2010; 5.1 Myrs and 4.8 Myrs respectively; Fig. 5.22) and Menning *et al.* (2000; 3.5 Myrs; Fig. 5.22) but somewhat shorter than was estimated by Waters & Condon (2012; 6.4 Myrs; Fig. 5.22). Similarly, taking the astronomically-tuned age for the base of the Westphalian Stage (*c.* 319.8 Ma; section 5.4.2.3) and the new U–Pb CA-ID-TIMS date from tonstein Z1, the duration of Langsettian and Duckmantian substages combined is revised to *c.* 6.0 Ma. This compares favourably with the *c.* 5.5 Ma duration shown in timescale B of Menning *et al.* (2000; Fig. 5.22) but is substantially longer than was suggested by Davydov *et al.* (2004, 2010; Fig. 5.22) and Waters & Condon (2012; Fig. 5.22).

It is noteworthy that the three new U–Pb zircon CA-ID-TIMS dates yield similar time duration relationships for the intervening stratigraphic intervals as presented in timescale B of Menning *et al.* (2000). Between bentonite B9 and tonstein T75 there is a duration of *c.* 6.9 Ma, compared to the *c.* 7.4 Ma duration shown in timescale B of Menning *et al.* (2000). Likewise, between tonsteins T75 and Z1 there is a *c.* 3.9 Ma duration compared to 3.2 Ma shown in Menning *et al.* (2000). Both the timescale B of Menning *et al.* (2000) and the duration estimates herein are based upon isotopic age datasets obtained from a single (albeit different) decay system and standard ($^{40}Ar/^{39}Ar$ data and U–Pb CA-ID-TIMS data respectively); thus, isotopic age data from different decay systems and standards yield similar time duration relationships for the studied stratigraphic interval. Whilst the time durations calculated in this study are similar to the values presented in timescale B of Menning *et al.* (2000) there is a 3 – 4 Ma systematic offset between the stratigraphic boundary ages determined in this study (Fig. 5.22) and those presented in timescale B of Menning *et al.* (2000; Fig. 5.22). This discrepancy is likely to arise because the $^{40}Ar/^{39}Ar$ dates that underpin the Menning *et al.* (2000)

timescale were calibrated against values for the age of the monitor standard and ^{40}K decay constant that are now considered obsolete. Recalibrating these legacy $^{40}Ar/^{39}Ar$ data against modern values for the monitor standard and ^{40}K decay constant increases the sample ages by *c.* 4 Ma (e.g. see section 2.8), which is similar in magnitude to the observed systematic offset.

5.4.3. Correlation of the base of the Moscovian Stage with the regional stages of western Europe

The Moscovian Stage is the second oldest of the four global stages of the Pennsylvanian Subsystem (Heckel & Clayton, 2006). Heckel & Clayton (2006) showed the base of this stage as equivalent to a level in the upper part of the Duckmantian Regional Substage of western Europe (Fig. 5.24). However, Wagner & Álvarez-Vázquez (2010; references therein) contended that the base of the Moscovian should be correlated with a level slightly below the base of the Langsettian in western Europe (Fig. 5.24). Correlation of the base of the Moscovian cannot yet be precise because a GSSP for the base of the stage has yet to be selected. However, it seems probable that the base will be chosen to coincide with the evolutionary first occurrence of conodonts *Declinognathodus donetzianus*, *Idiognathoides postsulcatus* or *Diplognathodus ellesmerensis*. Within the Donets Basin these taxa first occur in limestones K_1, K_2 and K_3 respectively (Davydov *et al.*, 2010), all of which are contained within a single orbitally-tuned 400 kyrs cycle (Davydov *et al.*, 2010).

Taking the base of the K_1 limestone as a preliminary base for the Moscovian, Davydov *et al.* (2010) and Peterson (2011) estimated the boundary at 314.6 Ma and 314.61 ± 0.33 Ma respectively. This is very close to the 313.78 Ma CA-ID-TIMS date from the Z1 tonstein and constrains the base of the Moscovian to be *c.* 800 kyrs older than tonstein Z1. Assuming that the brackish faunal bands within the Ruhr Basin (Fig. 5.21) are controlled by the *c.* 100 kyrs eccentricity cycle (section 5.4.1.1.2), the base of the Moscovian Stage is constrained to within the middle of the Duckmantian Regional Substage of western Europe (between the H2 and K brackish faunal bands; Fig. 5.21). This is very close to the level shown in Heckel & Clayton (2006; Fig. 5.24), and confirms that the base of the Moscovian should be correlated to within the upper part of the Duckmantian Substage. The base is certainly located at a higher stratigraphic level

than the upper Langsettian tonstein T75 (317.63 ± 0.12 Ma). High-precision U-Pb zircon CA-ID-TIMS data thus have the potential to aid correlation between different palaeogeographic regions with non-equivalent faunas.

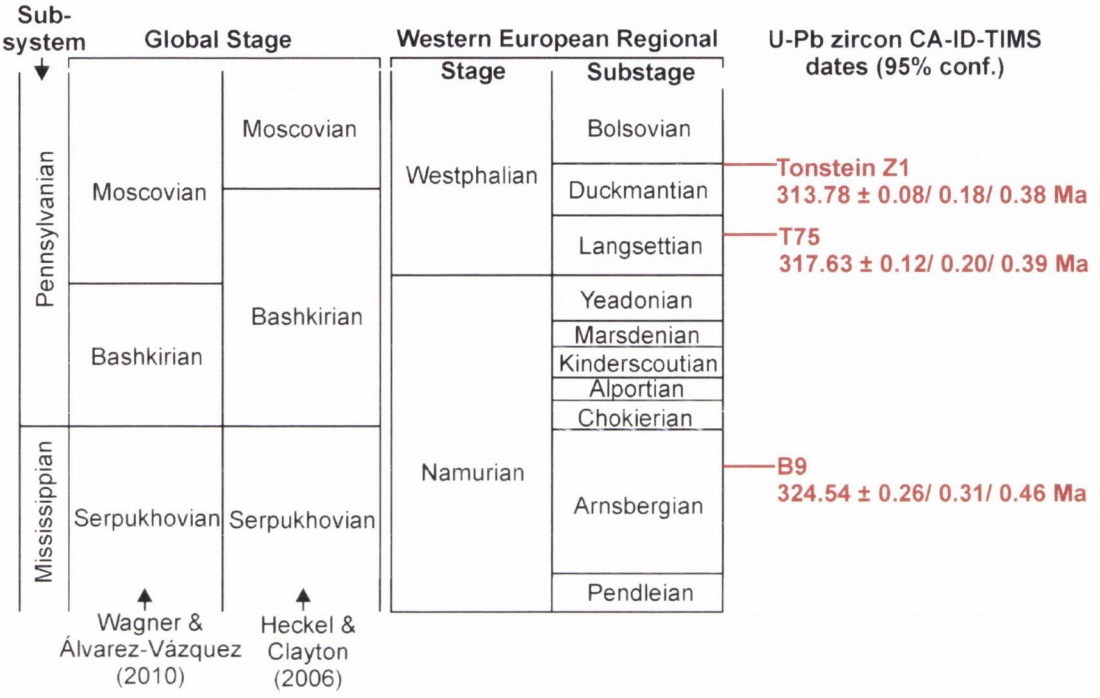

Figure 5.24. Stratigraphic column showing two interpretations for the position of the base of the Moscovian Stage within the western European stratigraphic framework.

5.5. Conclusions

Numerous diagenetically altered volcanic ash layers (bentonites and tonsteins) occur interbedded with western European, Mississippian and Pennsylvanian paralic sediments. Zircon phenocrysts from within these horizons are amenable to U-Pb CA-ID-TIMS dating and yield high-precision isotopic dates. The new U-Pb zircon CA-ID-TIMS dates are substantially more precise than existing published data derived using the U-Pb zircon SHRIMP and $^{40}Ar/^{39}Ar$ sanidine methodologies. They also help to address the dearth of high-precision Carboniferous isotopic dates.

The new U-Pb zircon CA-ID-TIMS data were used to estimate the periodicity of cyclic sedimentation. The average periodicity of Namurian (Arnsbergian) to lower Langsettian cycles is between 88 and 122 kyrs / cycle. This is comparable to the dominant *c.* 100 kyrs Pleistocene glacial cycle that is widely attributed to the *c.* 100 kyrs 'short'

eccentricity Milankovitch cycle and may therefore support the hypothesis that these Carboniferous sedimentary cycles are the product of glacio-eustasy.

The new U-Pb zircon CA-ID-TIMS dates were also employed to estimate the average periodicity of upper Langsettian to Duckmantian sedimentary cyclicity within the Pennine and Ruhr Basins (northern England and Germany respectively). Upper Langsettian to Duckmantian sedimentary cycles within the Ruhr Basin yielded an average cycle periodicity of 103 – 1995 kyrs / cycle (section 5.4.1.1.2), which may be compatible with 100 kyrs eccentricity forcing. In contrast, time-equivalent sedimentary cycles within the Pennine Basin yield a notably longer average periodicity (337 – 798 kyrs / cycle; section 5.4.1.1.2). However, the heterogeneous distribution of the Pennine Basin sedimentary cycles may render the calculated average cycle periodicity unrepresentative of individual cycle periodicities. It is possible that the Pennine Basin cycles represent much shorter periodicities than are implied by the average periodicity calculations, which may be biased towards longer values by the occurrence of 'missing beats' within the stratigraphy of the Pennine Basin.

There is evidence within the available periodicity calculations to support the continued occurrence of a *c.* 100 kyrs eccentricity signal throughout the Namurian to Duckmantian interval. Additionally, this stratigraphic interval is characterised by a pronounced and continuous cyclic motif. Taken together, the data may lend support to the idea of a continuous Carboniferous glaciation during Namurian to Duckmantian times. This has been suggested previously (e.g. Veevers & Powell, 1987), although several recent regional studies of direct (near-field) glacial deposits (e.g. Fielding *et al.*, 2008; Gulbranson *et al.*, 2010) have questioned this view and have instead favoured a punctuated glaciation. It has yet to be established how representative the regional near-field studies are of Gondwanan glaciation as a whole; it is possible that whilst one area of Gondwana was glaciated another area was being de-glaciated. At this present time, it is not possible to correlate between the different regional near-field studies at a high enough temporal resolution in order to reconstruct an overall picture of Carboniferous glaciation on Gondwana. In the future, as more high-precision age constraints become available from the near-field records, it may become possible to achieve this; however, until then the palaeo-equatorial far-field records may provide a better overall record of Carboniferous glaciation.

Astronomical tuning of Namurian cycles to the *c.* 100 kyrs Milankovitch eccentricity cycles constrains the global Mississippian – Pennsylvanian boundary to *c.* 323.9 Ma and the base of the Westphalian Stage to *c.* 319.8 Ma. The new U-Pb CA-ID-TIMS dates also provide a basis for the correlation of the base of the global Moscovian Stage to the regional stratigraphic scheme of Western Europe. New data confirms that the base of the global Moscovian Stage should be correlated to a horizon within the Duckmantian Regional Substage.

Chapter 6

Magnetic susceptibility and stable isotope ($\delta^{13}C$ and $\delta^{18}O$) data from Belgian Livian and Lower Warnantian carbonate cycles

6.1. Introduction

This chapter presents stable isotope data ($\delta^{13}C$ and $\delta^{18}O$ analyses of whole-rock samples) and low-field magnetic susceptibility (MS) measurements from Livian and Lower Warnantian shallowing-upwards carbonate cycles in the Namur-Dinant Basin, southern Belgium. The stable isotope analyses were undertaken to ascertain if the sedimentary cycles exhibit systematic and reproducible isotopic excursions, which may support a glacio-eustatic origin for these cycles. The use of whole-rock analyses is not ideal but is borne out of necessity; other potential targets for stable isotope analyses such as brachiopods and conodonts, which are generally considered to be less prone to diagenetic alteration (e.g. Marshall, 1992), occur too infrequently within the stratigraphy to provide an isotopic record on the scale of individual cycles.

MS variations in marine limestones are thought to reflect primarily changes in the flux of detrital grains into the marine environment (section 2.4.2), which is thought to be related to temporal variations in parameters such as eustasy, climate and tectonism (da Silva *et al.*, 2009b; section 2.4.2). The MS analyses were undertaken to determine if there is any correlation between the MS records and the sedimentary cycles, which may suggest an allocyclic (i.e. external) influence on the Belgian sedimentary cycles.

6.2. Samples and stratigraphy

Five outcrop sections within the Namur-Dinant Basin, Belgium, were sampled for magnetic susceptibility and stable isotope analyses (Fig. 6.1). Bentonite horizons from these localities were sampled and dated using the U-Pb zircon CA-ID-TIMS method (section 3.3.3.2) and thus the MS and stable isotope ($\delta^{13}C$ and $\delta^{18}O$) records have high-precision absolute age control. Three sections of Livian age were sampled, including the two sections exposed at the cliffs of Lives-sur-Meuse (Fig. 6.2; section 1 = 50.4692°N, 4.9291°E; section 2 = 50.4686°N, 4.9285°E) and the (now disused) quarry face at Awirs West Quarry (Fig. 6.2; 50.5905°N, 5.4089°E). These sections together cover the Lives Formation and the lower part of the Seilles Member of the Grands Malades Formation (Fig. 6.1). Two Warnantian localities were sampled; the Anhée Nord (Fig. 6.2; 50.3170°N, 4.8760°E) and Anhée Sud sections (Fig. 6.2; 50.2940°N; 4.8936°E). At Anhée Nord, strata from the lower part of the Poilvache Member were sampled, whereas at the Anhée Sud locality strata corresponding to the uppermost Poilvache Member and the lower part of the Lower Member of the Anhée Formation (Fig. 6.1) were sampled.

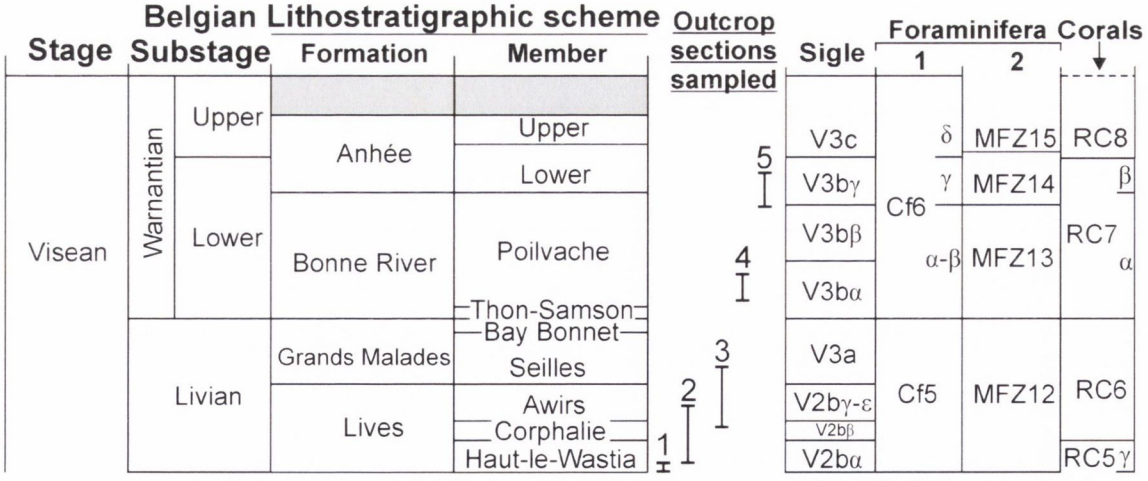

Figure 6.1. Sampling localities for stable isotope and magnetic susceptibility analyses. 1, 2 = cliff sections at Lives-sur-Meuse; 3 = Awirs West Quarry; 4 = Anhée Nord; 5 = Anhée Sud. Foraminifera biozones and subzones are from: 1) Conil *et al.* (1990); 2) Poty *et al.* (2006). Coral biozones and subzones are from Poty *et al.* (2006). The lithostratigraphic framework is from Poty *et al.* (2001). The sigles are historical lithostratigraphic divisions (from Conil *et al.*, 1967).

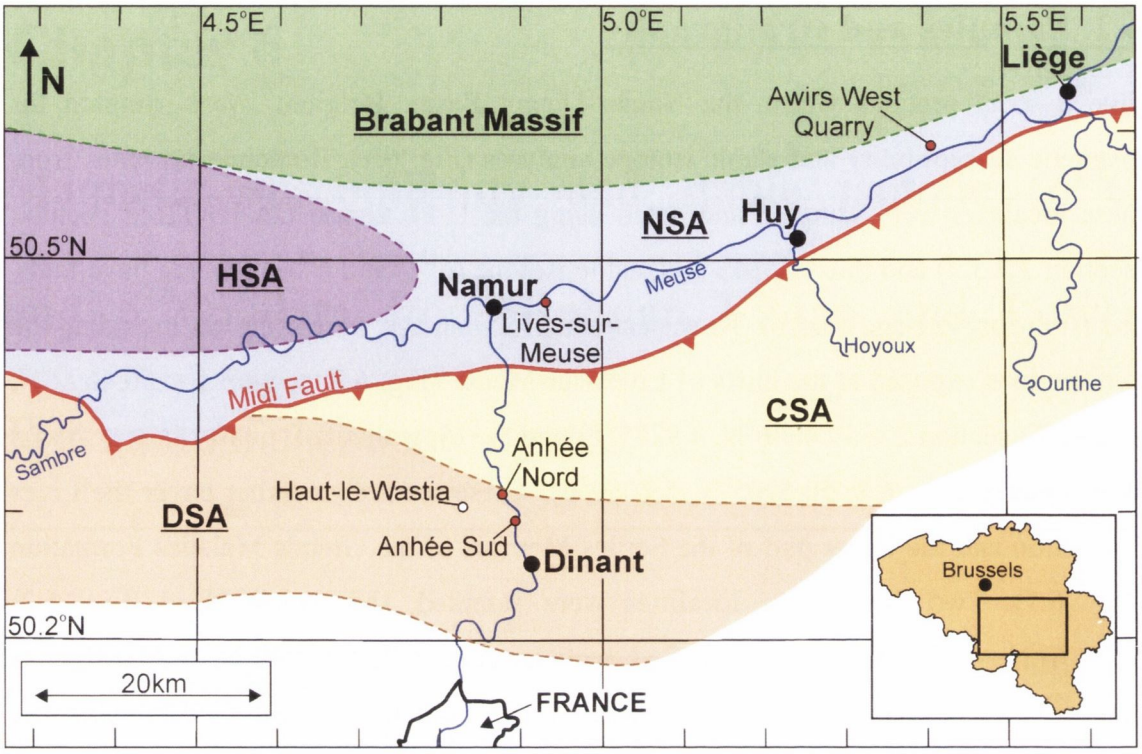

Figure 6.2. Map showing the localities sampled for magnetic susceptibility analysis and stable isotope analysis (indicated by red circles). The black circles denote major towns and cities. CSA = Condroz sedimentation area, DSA = Dinant sedimentation area, HSA = Hainaut sedimentation area, NSA = Namur sedimentation area. Sedimentation areas are schematic (redrawn from Poty *et al.*, 2001) and are described further in section 3.3.1. The inset shows the area of Belgium covered by the main diagram.

6.3. Results

6.3.1. Overview

1596 samples were analysed for low-field magnetic susceptibility analysis following the method described in section 2.4.3. The number of analyses from each of the five sampled sections is presented in Table 6.1. Samples from section 1 at Lives-sur-Meuse yielded the highest average MS values (Table 6.1), whereas samples from Awirs West Quarry, particularly those from the Seilles Member, yielded the lowest average MS values (less than 0.1 x 10^{-8} m^3 / kg; Table 6.1).

	MS ($\times 10^{-8}$ m^3 / kg)			$\delta^{13}C$ (‰ V-PDB)		$\delta^{18}O$ (‰ V-PDB)		Stable isotope analyses (n)
	Mean	SD	n	Mean	SD	Mean	SD	
Lives-sur-Meuse								
Section 1								
Haut-le-Wastia Member	0.80	0.91	68					
Section 2								
Haut-le-Wastia Member	0.45	0.44	215	2.03	0.28	-6.79	1.81	49
Corphalie Member	0.70	0.68	186	2.37	0.29	-7.30	0.54	32
Awirs Member	0.60	0.44	117	2.46	0.32	-7.21	0.32	26
Awirs West Quarry								
Corphalie Member	0.73	0.30	44	2.46	0.08	-7.77	0.63	2
Awirs Member	0.18	0.26	319	2.13	0.73	-8.97	0.98	54
Seilles Member	0.06	0.10	192					
Anhée Nord								
Poilvache Member	0.46	0.51	241	-0.43	0.87	-10.06	0.98	56
Anhée Sud								
Poilvache Member	0.58	0.77	100					
Lower Member (Anhée Fm.)	0.46	0.49	114					

Table 6.1. Summary statistics for the magnetic susceptibility and carbonate stable isotope ($\delta^{13}C$ and $\delta^{18}O$) data. SD = standard deviation. n = number of analyses. Fm = formation. The raw sample MS and stable isotope data are presented in Appendix 3 Tables 1 – 8. The stratigraphic positions of the lithostratigraphic members cited in this table are drawn in Fig. 6.1.

Because of the greater time and cost of the stable isotope analyses, a subset of the total number of samples analysed for MS was selected to evaluate if there were systematic and reproducible isotopic excursions within the sedimentary cycles. 219 samples were selected for stable isotope analyses, from section 2 at Lives-sur-Meuse, Awirs West Quarry and Anhée Nord. A breakdown of the distribution of these analyses is given in Table 6.1. These localities were chosen to ensure both Livian and Warnantian samples were represented in the results. Additionally, samples from the same stratigraphic interval (the upper Corphalie Member and lower Awirs Member) were selected from both Lives-sur-Meuse and Awirs West Quarry (Fig. 6.1) to determine if there was any lateral variability in the stable isotopic signatures on a local scale (Lives-sur-Meuse and Awirs West Quarry are *c.* 37 km apart). All stable isotope analyses were prepared according to the methodology described in section 2.5.5. All $\delta^{13}C$ and $\delta^{18}O$ values cited are with respect to V-PDB. The results of the stable isotope analyses are complex and show little clear evidence of correlation with the sedimentary cycles. In the light of these initial results further stable isotope analyses were not undertaken. However, the initial results are presented in this thesis for future reference.

6.3.1.1. $\delta^{13}C$ data

Samples analysed from Lives-sur-Meuse yielded the narrowest range and the most positive $\delta^{13}C$ values of the three localities investigated (Fig. 6.3; Table 6.1). Most analyses from Lives-sur-Meuse overlap with the stable isotope data fields ($\delta^{13}C$ and $\delta^{18}O$) from western European brachiopods of a similar age (early Livian data of Bruckschen & Veizer, 1997; Fig. 6.3).

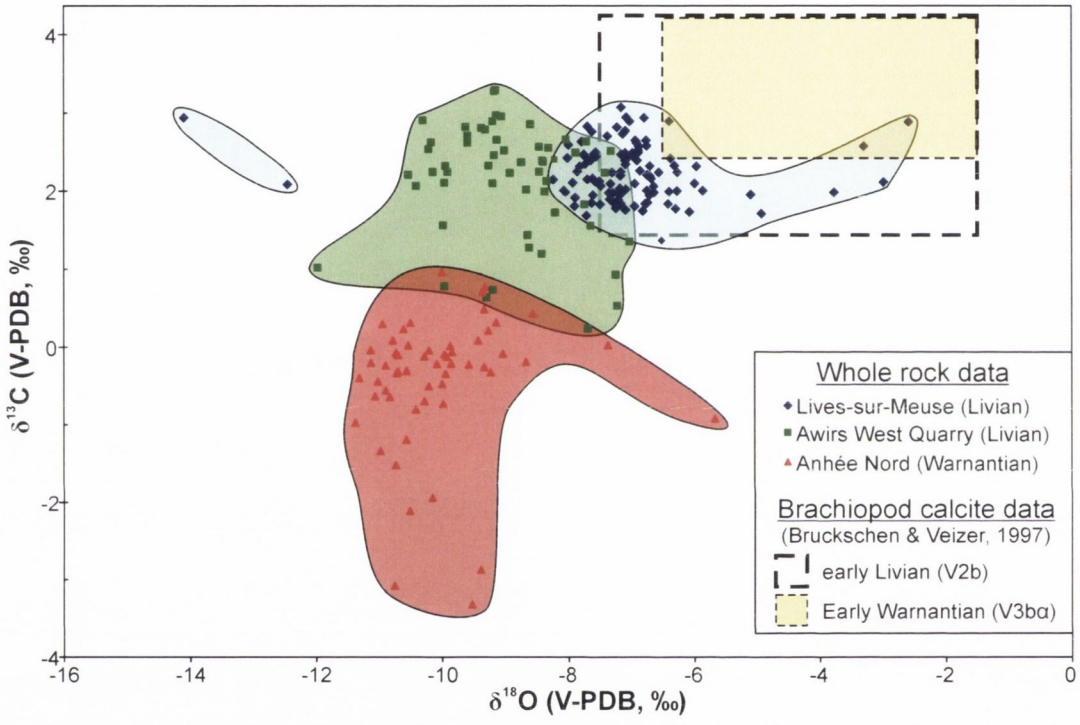

Figure 6.3. A cross plot of $\delta^{13}C$ and $\delta^{18}O$ values from Belgian Livian and Warnantian samples. The brachiopod calcite box dimensions are ± 2 standard deviations of the mean $\delta^{13}C$ and $\delta^{18}O$ values from early Livian and Early Warnantian aged brachiopods (from Bruckschen & Veizer, 1997).

The majority of samples from Awirs West Quarry yielded $\delta^{13}C$ values comparable to samples from Lives-sur-Meuse. However, a few analyses from Awirs West Quarry yielded markedly lower $\delta^{13}C$ values (Fig. 6.3). The samples from Anhée Nord yielded notably lower and more dispersed $\delta^{13}C$ values than samples from both Lives-sur-Meuse and Awirs West Quarry (Table 6.1; Fig. 6.3). The $\delta^{13}C$ values of samples from Anhée Nord are also distinctly lower than data from western European brachiopods of a similar age (Early Warnantian data in Fig. 6.3; Bruckschen & Veizer, 1997).

6.3.1.2. $\delta^{18}O$ data

All of the samples analysed yielded negative $\delta^{18}O$ values with respect to V-PDB (Fig. 6.3). Samples from Lives-sur-Meuse yielded the least negative $\delta^{18}O$ values of the three localities investigated but show more dispersion than $\delta^{13}C$ values from the same samples (Fig. 6.3; Table 6.1). Two analyses from Lives-sur-Meuse are obvious outliers with very negative $\delta^{18}O$ values. These occur within the Haut-le-Wastia Member and are discussed in section 6.3.2.1.2. A large proportion of the $\delta^{18}O$ values from the Lives-sur-Meuse samples overlap with values from western European brachiopods of a similar age (Fig. 6.3). A few analyses from Awirs West Quarry yield comparable $\delta^{18}O$ values to those of the Lives-sur-Meuse samples, although most yield more negative values (Fig. 6.3). The $\delta^{18}O$ values from the Anhée Nord samples mostly fall within a narrow range of highly negative values (-8.6 to -11.4 ‰) and are substantially more negative than data from brachiopods of a similar age (Fig. 6.3).

There are no statistically significant correlations (at the 95 % confidence level) between $\delta^{13}C$ and $\delta^{18}O$ values from the three localities. Nor is there significant correlation between $\delta^{13}C$ and $\delta^{18}O$ data within the different lithostratigraphic units exposed in the two sections at Lives-sur-Meuse (the Haut-le-Wastia, Corphalie and Awirs members).

In the following sections, detailed results of the magnetic susceptibility and stable isotope analyses from the sampled sections are given. The sampled sections are discussed in stratigraphic order (see Fig. 6.1).

6.3.2. Lives-sur-Meuse (Livian Substage)

6.3.2.1. Haut-le-Wastia Member

6.3.2.1.1. Magnetic susceptibility data

The magnetic susceptibility and stable isotope data from the Haut-le-Wastia Member at Lives-sur-Meuse are illustrated in Fig. 6.4 and are presented as data tables in Appendix 3 Tables 1, 2 and 6. Within cliff section 1 at Lives-sur-Meuse (Fig. 6.4), MS values decrease between the top of bentonite L1 and *c.* 1.25 m elevation (Fig. 6.4). Above *c.* 1.25 m MS values remain relatively stable and are weakly positive ($0 - 1 \times 10^{-8}$ m^3 / kg), with the exceptions of an interval at 2.6 – 4.2 m, which yielded an erratic MS signature, and two analyses from the L2 bentonite horizon (5.8 m and 5.9 m; Fig 6.4). The erratic signal between 2.6 – 4.2 m closely corresponds with an interval of increased lithological diversity (undulose bedding planes, shaley limestone partings, chaotic textures and dolomitisation). The paramagnetic clay minerals and goethite contained within bentonite L2 (section 3.3.4.2) account for the high MS values from this layer.

The MS and stable isotope ($\delta^{13}C$ and $\delta^{18}O$) records from cliff section 2 at Lives-sur-Meuse are presented against two different interpretations of the sedimentary cycles exposed at this locality (Fig. 6.4; Vanneste, 1999, and my subsequent reinterpretation). Traditionally, the Corphalie Member (a single *c.* 16 – 20 m thick sedimentary cycle) is termed cycle 0 and cycles within the underlying Haut-le-Wastia Member are assigned negative numbers (Fig. 6.4), whereas the overlying cycles of the Awirs Member are assigned positive numbers. This numbering system is retained in this thesis. There is a close correspondence between the two cyclicity models for several of the sedimentary cycles (e.g. cycles -1, -2). The main disagreement between the two interpretations concerns the thin -3, -5 and -7 to -12 cycles of Vanneste (1999), which could not be located and are thus not included in my reinterpretation. There are three main intervals of high MS in the Haut-le-Wastia Member of cliff section 2 at Lives-sur-Meuse (*c.* 4.0 – 5.5 m; *c.* 6.8 – 8.3 m; *c.* 12.5 – 16 m; Fig. 6.4). The latter interval (12.5 – 16 m) contains three higher frequency MS oscillations. The intervening stratigraphic intervals yielded weakly positive MS values ($0 - 0.5 \times 10^{-8}$ m^3 / kg). There is little evidence of correlation between the MS and the sedimentary cycles (compared to both cyclicity models; Fig. 6.4).

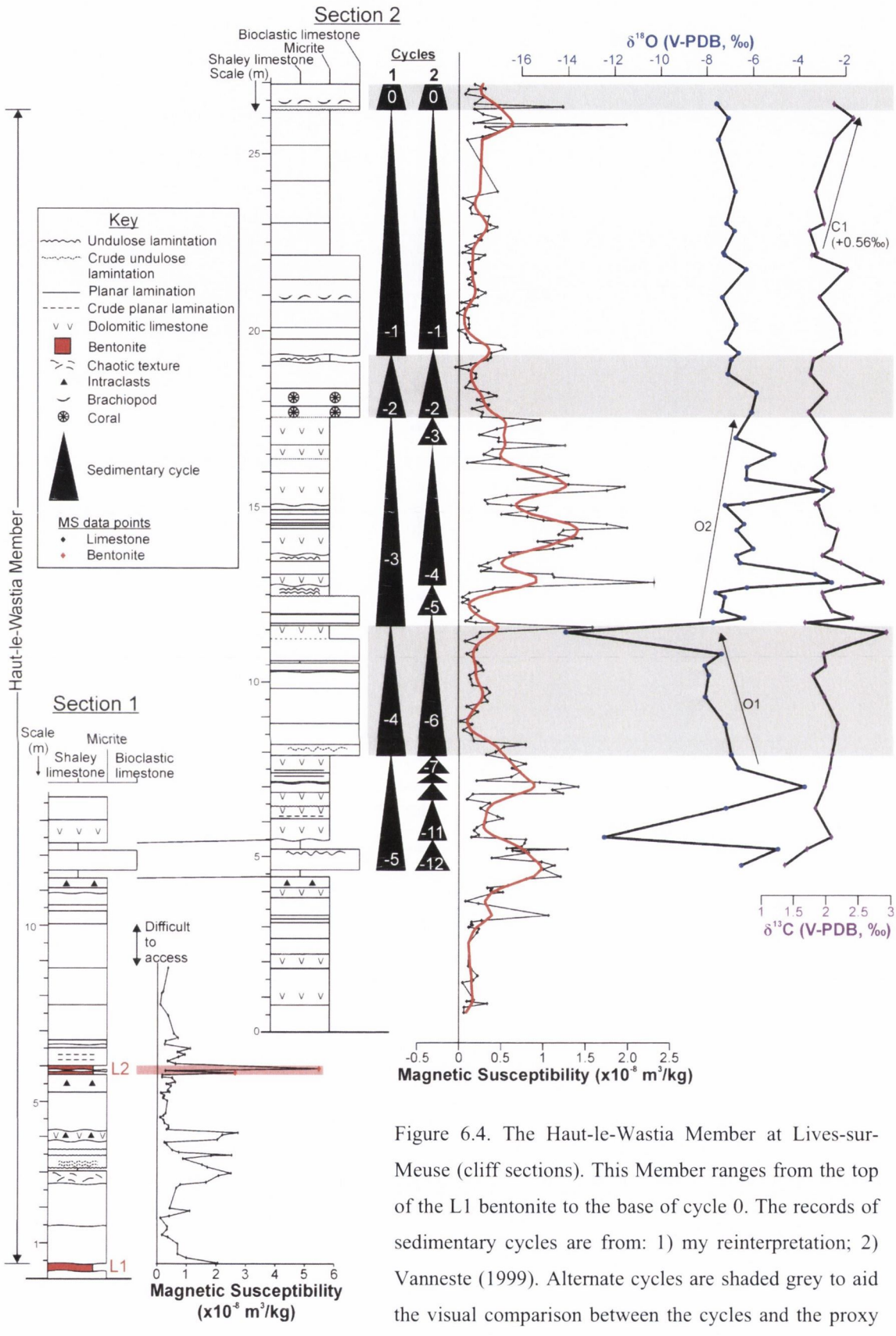

Figure 6.4. The Haut-le-Wastia Member at Lives-sur-Meuse (cliff sections). This Member ranges from the top of the L1 bentonite to the base of cycle 0. The records of sedimentary cycles are from: 1) my reinterpretation; 2) Vanneste (1999). Alternate cycles are shaded grey to aid the visual comparison between the cycles and the proxy records. The thick red line running through the MS data is a smoothing spline. Sample MS and stable isotope ($\delta^{13}C$ and $\delta^{18}O$) data illustrated in this figure are presented as data tables in Appendix 3 Tables 1, 2 and 6.

Hereafter, all cycle numbers cited within the text refer to my reinterpretation of the sedimentary cyclicity. The first positive MS excursion (*c.* 4.0 – 5.5 m) appears to commence below cycle -5 and continues into the base of this cycle (Fig. 6.4). Likewise, the second positive MS excursion commences in the upper part of cycle -5 but continues into the lower part of cycle -4. The third positive MS excursion (*c.* 12.5 – 16 m) occurs within the micritic beds of cycle -3. There is a slight increase in MS values at the base of cycle -1, but otherwise cycles -2 and -1 are characterised by only weakly positive MS values. It is also noteworthy that some of the MS peaks observed from section 2 correspond to dolomitised beds (e.g. cycle -3; Fig. 6.4), although this trend is not consistent throughout the section as there are some other dolomitised beds that are not associated with MS peaks (e.g. the dolomitised beds at 1 m, 2 m and between 5.5 – 6.7 m; Fig. 6.4). The correlation between some of the dolomitised beds and high MS values may indicate that the MS record from this section has undergone some diagenetic alteration.

6.3.2.1.2. Stable isotope ($\delta^{13}C$ and $\delta^{18}O$) data

There is little evidence to support a correlation between the stable isotope analyses and the sedimentary cycles of the Haut-le-Wastia Member. The $\delta^{18}O$ values show more dispersion than the $\delta^{13}C$ values (Fig. 6.4). Two analyses at 5.56 m and 11.42 m yielded markedly negative $\delta^{18}O$ values and are the most conspicuous feature of the stable isotope data from the Haut-le-Wastia Member (Fig. 6.4). These obvious outliers occur in dolomitised horizons and probably reflect diagenetic alteration.

Three analyses at 12.83 m, 13.08 m and 15.46 m (Fig. 6.4) show markedly greater $\delta^{18}O$ values than adjacent analyses. The analyses at 12.83 m and 13.08 m are also associated with greater $\delta^{13}C$ values. These positive $\delta^{13}C$ and $\delta^{18}O$ excursions could be due to the presence of significant dolomite in these analyses. If these three data points are excluded, then the $\delta^{13}C$ and $\delta^{18}O$ values from cycles -3 to -1 show little covariation and range between 1.7 to 2.4 ‰ $\delta^{13}C$ and -7.7 to -5.1 ‰ $\delta^{18}O$.

Within the $\delta^{18}O$ data there is a weak trend towards more negative $\delta^{18}O$ values upwards through cycle -4 (O1 arrow; Fig. 6.4) and another weak trend towards more positive $\delta^{18}O$ values upwards through cycle -3 (O2 arrow; Fig. 6.4). The former trend could

represent increasing emergence and meteoric diagenesis (Fig. 2.9) upwards through cycle -4, whereas the latter may reflect an increasing evaporation or salinity trend (Fig. 2.9). The top of the Haut-le-Wastia Member also shows a weak trend towards more positive $\delta^{13}C$ values up-section (C1 arrow; Fig. 6.4). The reasons for this increase are not certain; it could indicate an increasingly restricted carbon pool (decreased ocean connectivity; Fig. 2.9) or an increase in organic productivity (Fig. 2.9).

6.3.2.2. Corphalie Member

6.3.2.2.1. Magnetic susceptibility data

The magnetic susceptibility data obtained from the Corphalie Member at Lives-sur-Meuse (cliff section 2) are illustrated in Fig. 6.5 and are presented as a data table in Appendix 3 Table 2. There is no significant change in MS values across the boundary between the Haut-le-Wastia Member and the Corphalie Member (base of cycle 0 in Fig. 6.5). MS values remain low ($< 1 \times 10^{-8}$ m^3 / kg) within the bioclastic beds of the lower Corphalie Member (Fig. 6.5). There is a subtle trend of decreasing MS values from the base of the Corphalie Member to *c.* 30.6 m (Fig. 6.5). Above this level, MS values marginally increase until *c.* 37 m and then rapidly increase to a level slightly above bentonite L3 (*c.* 39.3 m). The rapid MS increase between 37 m and 39.3 m correlates with the appearance of several orange clay-rich partings between the limestone beds (red band in Fig. 6.5) and occurs at a significantly higher stratigraphic level than the major lithological change within this member, from bioclastic to micritic limestones (*c.* 34.8 m; Fig. 6.5). Above *c.* 39.3 m, MS values define a decreasing trend to *c.* 43.5 m, at which point the MS values return to background values (i.e. values that characterise the majority of the lower levels of the member). It is likely given the close correspondence between the appearance of the orange clay partings and this positive MS excursion, which peaks near the L3 bentonite, that the MS excursion represents a pulse of volcanic activity. There is a final increase in MS values towards the top of the Corphalie Member; however, this is not associated with any orange clay partings. The anomalously strongly positive MS analysis at 32.4 m is from a shaley, siliciclastic parting between two limestone beds.

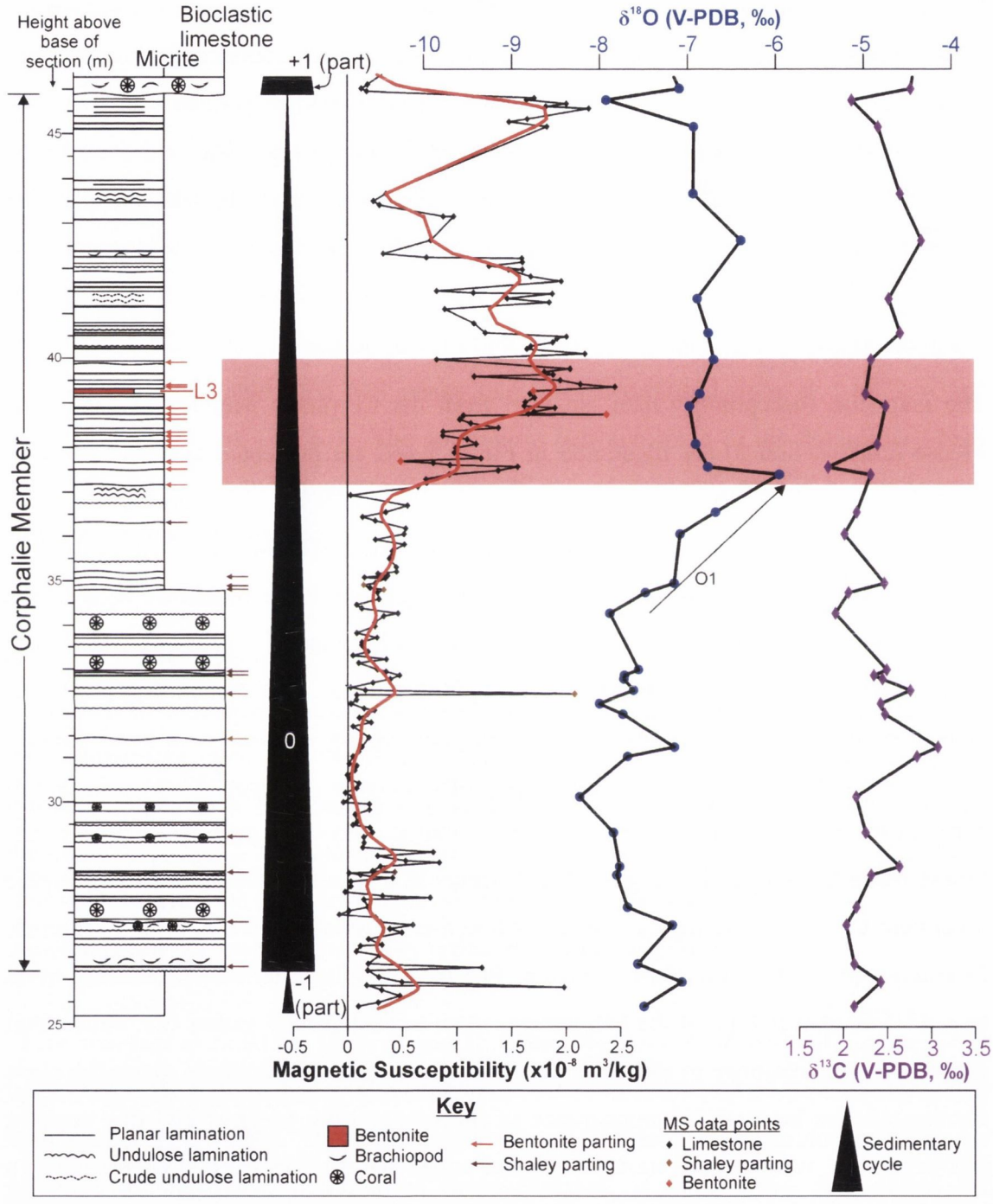

Figure 6.5. The Corphalie Member (= sedimentary cycle 0) at Lives-sur-Meuse (section 2). The red band denotes an interval containing numerous orange, clay-rich partings between the limestone beds. The thick red line running through the MS data is a smoothing spline. Sample MS and stable isotope ($\delta^{13}C$ and $\delta^{18}O$) data drawn in this figure are presented in Appendix 3 Tables 2 and 6 respectively.

6.3.2.2.2. Stable isotope ($\delta^{13}C$ and $\delta^{18}O$) data

The stable isotope data obtained from the Corphalie Member at Lives-sur-Meuse (cliff section 2) are presented in Fig. 6.5. These data are also presented in Appendix 3 Table 6. The main features of the $\delta^{18}O$ record from the Corphalie Member are that the lower bioclastic beds yielded on average more negative $\delta^{18}O$ values (-7.7 ‰) than the upper micritic beds (-6.9 ‰) and that there is a trend of increasing $\delta^{18}O$ values across the transition between the bioclastic and micritic limestones (between 34.3 m and 37.4 m; Fig. 6.5). The higher average $\delta^{18}O$ values within the micritic beds relative to the bioclastic beds could reflect an environmental change such as increased evaporation or salinity (Fig. 2.9). Alternatively, the difference in $\delta^{18}O$ values could be a diagenetic effect, possibly related to the differences in porosity and permeability (and therefore fluid flow) between the two lithologies.

In contrast to the $\delta^{18}O$ values, there is no obvious difference in the $\delta^{13}C$ values between the bioclastic and the micritic limestones of the Cophalie Member. The small fluctuations in $\delta^{13}C$ values within the bioclastic beds (Fig. 6.5) may represent the sampling of different carbonate components (allochems and cement).

6.3.2.3. Awirs Member

6.3.2.3.1. Magnetic susceptibility data

The magnetic susceptibility data obtained from the Awirs Member at Lives-sur-Meuse (section 2) are drawn in Fig. 6.6 and are also presented as a data table in Appendix 3 Table 2. There is a substantial decrease in MS values across the boundary between the Corphalie Member and the Awirs Member (Fig. 6.6).

Within the Awirs Member at Lives-sur-Meuse, there is good correlation between the MS excursions and the sedimentary cycles, with the MS values increasing upwards through the sedimentary cycles. This correlation is in contrast to the lack of obvious correlation within the underlying strata (sections 6.3.2.1.1). Generally, the bioclastic limestone beds exhibit low MS values ($< 0.5 \times 10^{-8}$ m^3 / kg; Fig. 6.6), whereas the micrite beds exhibit higher MS values (up to 1.7×10^{-8} m^3 / kg; Fig. 6.6). In cycle +2 there are two thin bioclastic beds (52.23 – 52.50 m; Fig. 6.6), the upper of which

exhibits low-angle cross stratification (52.40 – 52.50 m elevation in Fig. 6.6). These beds could be argued to define the base of another sedimentary cycle; however, no equivalent of these beds is observed at Awirs West Quarry (section 6.3.2.1) and thus they are probably only of local significance.

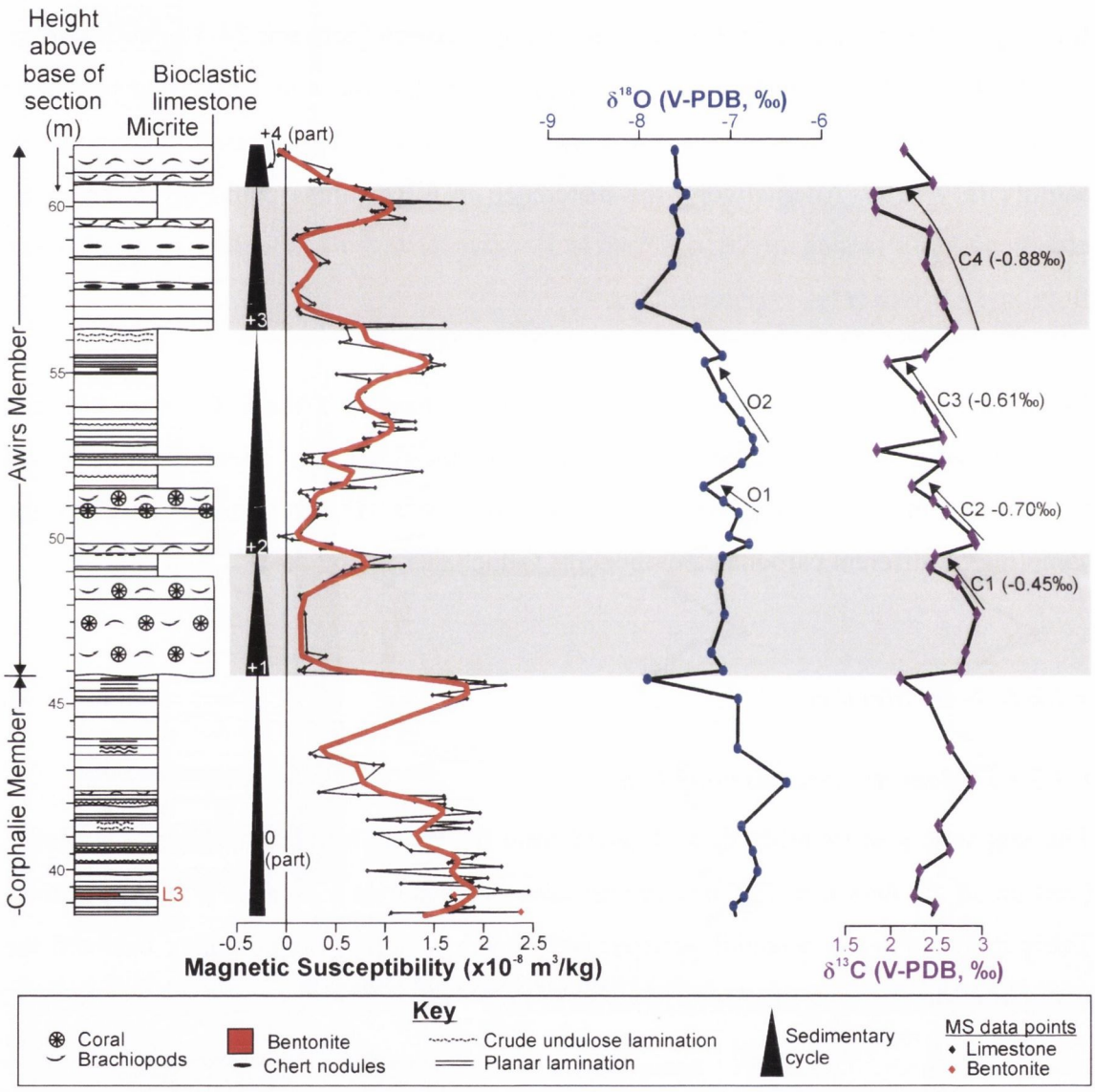

Figure 6.6. The upper Corphalie Member and lower Awirs Member exposed at Lives-sur-Meuse (section 2). The Awirs Member is not complete at Lives-sur-Meuse; only the lower part is represented. The thick red line running through the MS data is a smoothing spline. Sedimentary cycles are numbered with respect to the Corphalie member (cycle 0; see section 6.3.2.1.1 for an explanation). Sample MS and stable isotope ($\delta^{13}C$ and $\delta^{18}O$) data illustrated in this figure are presented as data tables in Appendix 3 Tables 2 and 6 respectively.

6.3.2.3.2. Stable isotope ($\delta^{13}C$ and $\delta^{18}O$) data

The stable isotope ($\delta^{13}C$ and $\delta^{18}O$) data obtained from the Awirs Member at Lives-sur-Meuse (cliff section 2) are illustrated in Fig. 6.6 and are also presented in Appendix 3 Table 6. The samples from cycle +1 yielded relatively stable $\delta^{18}O$ values (*c.* -7.1 ‰). There are small fluctuations (*c.* 0.5 ‰ magnitude) in $\delta^{18}O$ values within the +2 cycle (indicated by the O1 and O2 arrows in Fig. 6.6). The top of the section yields relatively uniform $\delta^{18}O$ values of *c.* -7.6 ‰. There is some evidence to support a systematic reduction in $\delta^{18}O$ values from the upper Corphalie Member (average = -6.8 ‰) through cycles +1 and +2 (average = -7.0 ‰) and into cycle +3 (average = -7.6 ‰). The significance of this trend is unclear; it may indicate a trend of increasing meteoric diagenesis, although changes in environmental parameters (e.g. higher temperatures, reduced evaporation or lower salinity; Fig. 2.9) cannot be excluded.

$\delta^{13}C$ data from the Awirs Member are inversely correlated with the MS data and this correlation is significant at the 99 % confidence level ($r = -0.508$, $n = 26$, $p = 0.008$, two tailed). Cycles +1 and +3 exhibit trends of decreasing $\delta^{13}C$ values upwards through the cycles, whereas cycle +2 contains two such trends (arrows labelled C1 to C4 in Fig. 6.6). The two $\delta^{13}C$ shifts within cycle 2 correlate with similar shifts in $\delta^{18}O$ values (arrows labelled O1 and O2 in Fig. 6.6). These trends are discussed in section 6.4.3.

6.3.3. Awirs West Quarry (Livian Substage)

6.3.3.1. Awirs Member

6.3.3.1.1. Magnetic susceptibility data

The magnetic susceptibility data from the Awirs member at Awirs West Quarry are illustrated in Fig. 6.7. These data are also presented as a data table in Appendix 3 Table 3. Within cycles +1 to +3 there is evidence of a correlation between MS and the sedimentary cycles, with MS values increasing upwards within these cycles (Fig. 6.7). This is a comparable trend to that observed from the Awirs Member at Lives-sur-Meuse (section 6.3.2.3.1; cycles +1 to +3 in Fig. 6.6). Above cycle +3, the MS signal becomes progressively weaker; cycles +4 and +5 show weakly increasing trends up-section.

Above cycle +5, the correlation between MS and lithology is no longer observed, and above 32 m the MS signal becomes uniform (Fig. 6.7). Possible reasons for this trend are discussed in section 6.4.1. Anomalous, strongly positive MS analyses at *c.* 19.3 m, 27 m, 31.5 m and 44.8 m are from interbedded bentonites and shaley partings and thus their relatively high MS values, compared to the adjacent limestones, reflect mineralogical differences.

6.3.3.1.2. Stable isotope ($\delta^{13}C$ and $\delta^{18}O$) data

The stable carbon and oxygen isotope dataset from Awirs West Quarry (Fig. 6.7; Appendix 3 Table 7) is noisy and contains few clear trends, particularly for the interval above cycle +2 (Fig. 6.7). Cycles +1 and +2 show trends of increasing $\delta^{18}O$ values upwards through the cycles (arrows O1 and O3 in Fig. 6.7) and significant decreases in $\delta^{18}O$ values across the cycle boundaries (arrows O2 and O4 in Fig. 6.7). This trend contrasts strongly with the $\delta^{18}O$ record from the same stratigraphic interval at Lives-sur-Meuse (cycles +1 to +3 in Fig. 6.6). The increasing $\delta^{18}O$ values within a cycle may record a local trend of increasing evaporation or salinity (Fig. 2.9). Alternatively, this may be a diagenetic trend, whereby the bioclastic beds are more diagenetically altered than the overlying micritic beds, possibly driven by differences in porosity and permeability, as has already been suggested for the Corphalie Member at Lives-sur-Meuse (section 6.3.2.2.2).

Cycles +1 and +2 show a trend of decreasing $\delta^{13}C$ values up-section (Fig. 6.7), similar to the $\delta^{13}C$ data from Lives-sur-Meuse, but without the high frequency excursions towards lower values seen at Lives-sur-Meuse (i.e. arrows C1 to C3 in Fig. 6.6).

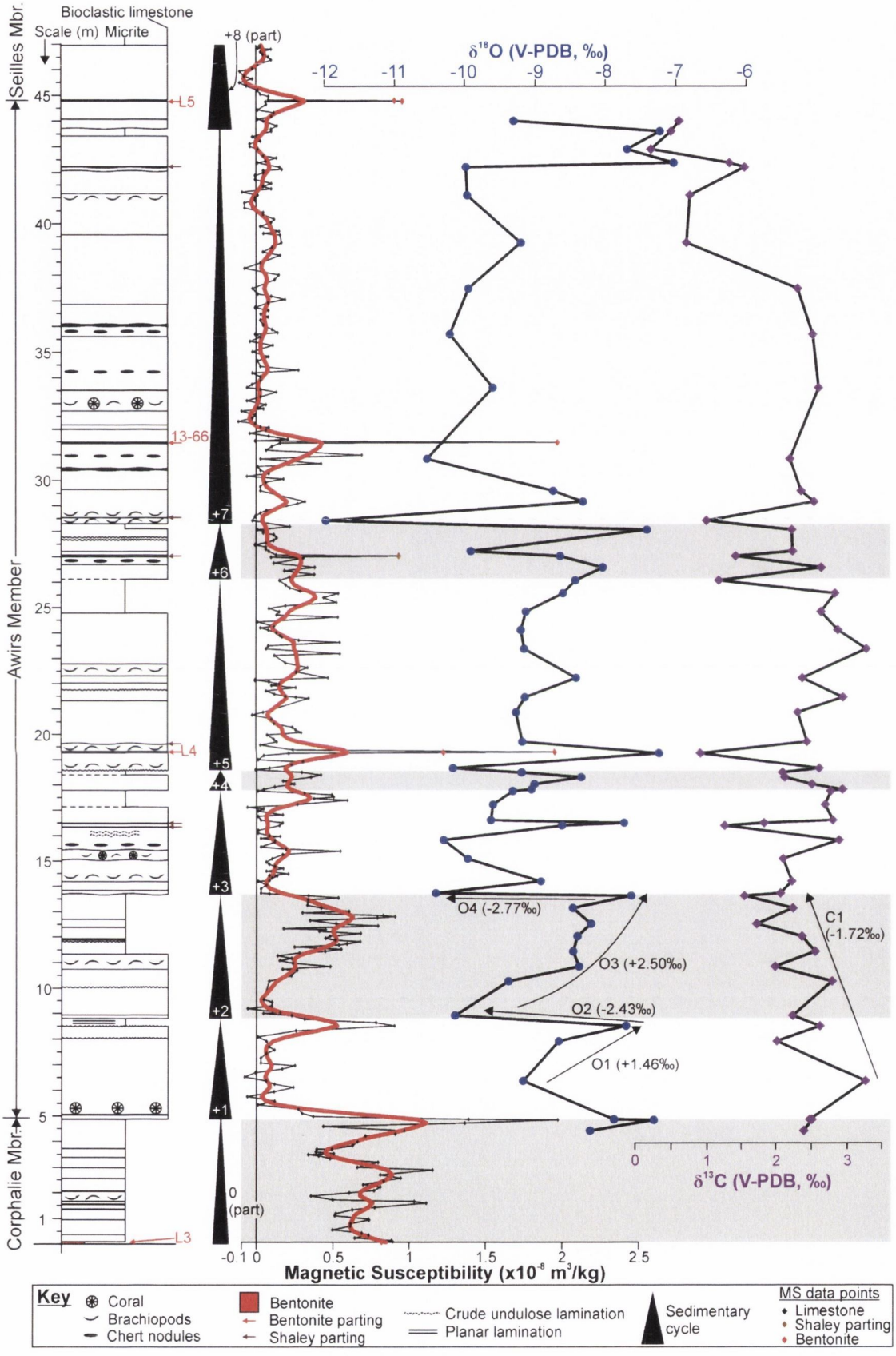

Figure 6.7. The uppermost Corphalie Member and the Awirs Member at Awirs West Quarry. The red line running through the MS data is a smoothing spline. Mbr = Member. Sedimentary cycles are numbered with respect to the Corphalie member (cycle 0; see section 6.3.2.1.1 for an explanation). Sample MS and stable isotope data drawn in this figure are presented in Appendix 3 Tables 3 and 7.

6.3.3.2. Seilles Member

6.3.3.2.1. Magnetic susceptibility data

The lowest 25 m of the Seilles Member exposed at Awirs West Quarry yielded a relatively uniform diamagnetic to weakly positive MS signal (Fig. 6.8; Appendix 3 Table 3), which is a continuation of the weak MS values observed in the upper parts of the underlying Awirs Member (section 6.3.3.1). Above 55 m, the MS signal becomes very monotonous and there is no correlation between MS variation and lithology. The two analyses yielding comparatively high MS values at *c.* 44.9 m are from the L5 bentonite.

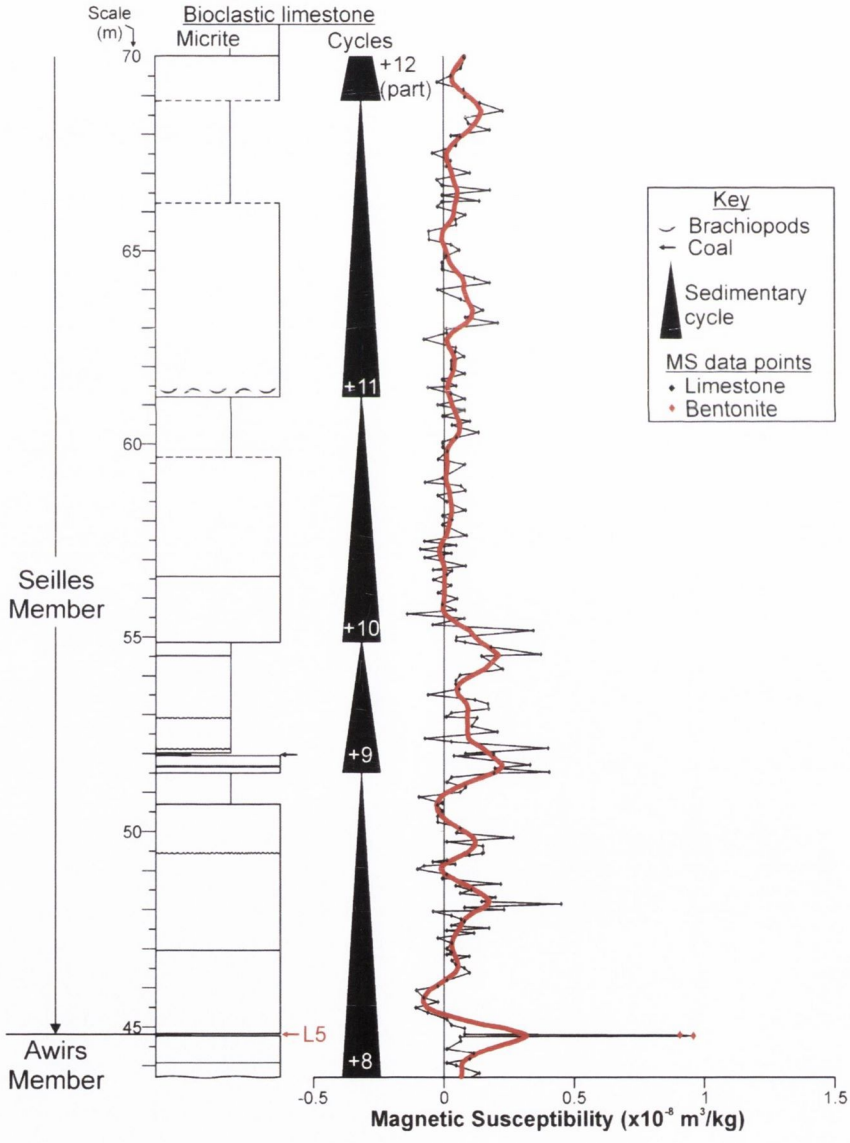

Figure 6.8. The uppermost Awirs Member and lower part of the Seilles Member at Awirs West Quarry. The thick red line running through the MS data is a smoothing spline. Sedimentary cycles are numbered with respect to the Corphalie Member (cycle 0; see section 6.3.2.1.1 for an explanation). Sample MS data drawn in this figure are presented in Appendix 3 Table 3.

6.3.4. Anhée Nord (Lower Warnantian; Poilvache Member)

6.3.4.1. Magnetic susceptibility data

The results from the MS, $\delta^{13}C$ and $\delta^{18}O$ analyses at the Anhée Nord locality are illustrated in Fig. 6.9. These data are also presented as data tables in Appendix 3 Tables 4 and 8. The MS of samples from this locality ranges between $0 - 3 \times 10^{-8}$ m^3 / kg. Several peaks in the MS record can be correlated with the occurrence of interbedded bentonites or bentonite partings (Fig. 6.9; red bands indicate bentonites or clusters of bentonites). Thus, it seems likely that the MS analyses from this locality, to a large extent, record intermittent volcanic activity. There is little evidence to support a correlation between the sedimentary cycles and MS data from this locality.

6.3.4.2. Stable isotope ($\delta^{13}C$ and $\delta^{18}O$) data

There is no correlation between $\delta^{18}O$ values and the sedimentary cycles at this locality. Most analyses yield $\delta^{18}O$ values of -8.6 to -11.4 ‰, excluding two analyses with notably less negative $\delta^{18}O$ values (analyses at 0.7 m = -5.67 ‰ and 10.8 m = -7.4 ‰; Fig. 6.9). Samples from the basal 2.5 m of strata yield the widest range of $\delta^{13}C$ ‰ values (-1.53 ‰ to +0.3 ‰). Above the basal 2.5 m, there is a prominent negative $\delta^{13}C$ isotopic excursion (arrow labelled C1 in Fig. 6.9) followed by an interval where $\delta^{13}C$ trends towards *c.* 0 ‰ (arrow labelled C2 in Fig. 6.9). The cause of this negative $\delta^{13}C$ excursion is not certain and could arise from a number of possible sources such as elevated organic carbon content, an interval of decreased organic productivity or enhanced meteoric diagenesis (Fig. 2.9). Above 8 m, the $\delta^{13}C$ values are relatively uniform, with values between -1 ‰ and 0 ‰ (V-PDB), except for a single analysis at 22.5 m (-3.1 ‰ $\delta^{13}C$).

The $\delta^{13}C$ and $\delta^{18}O$ values are substantially more negative at this site compared to the data from Lives-sur-Meuse and Awirs West Quarry and also compared to coeval brachiopod calcite data (Bruckschen & Veizer, 1997; Fig 6.3). It is probable that these samples have experienced greater diagenetic alteration than samples from Lives-sur-Meuse and Awirs West Quarry. Such alteration could arise from near surface alteration (meteoric diagenesis) and / or higher temperature burial diagenesis. The sedimentary cycles at this site comprise predominantly micritic limestones characteristic of intertidal

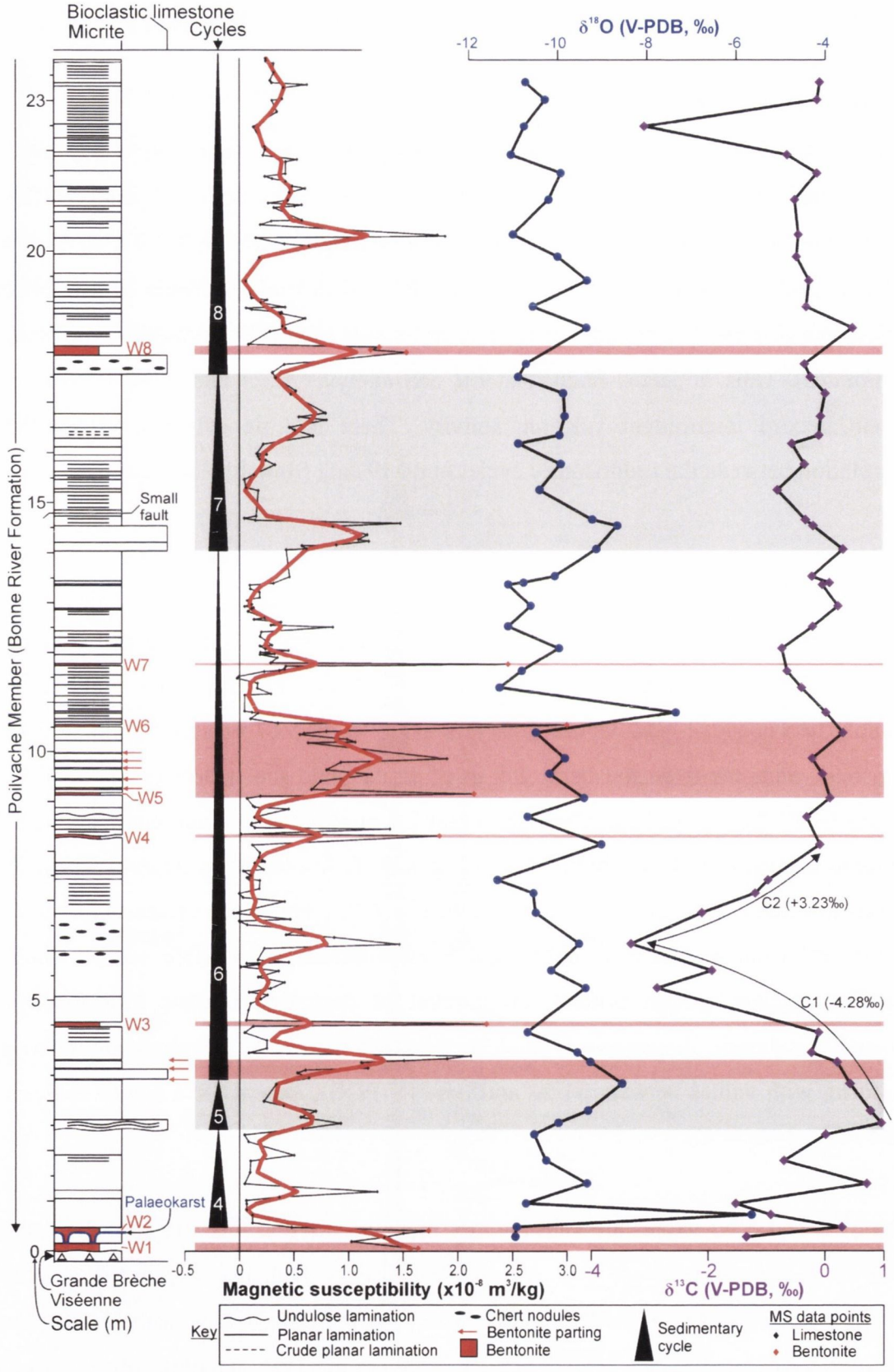

Figure 6.9. MS and stable isotopic analyses from the Anhée Nord section. Red shaded areas denote stratigraphic intervals with a high density of bentonites or bentonite partings. Alternate sedimentary cycles are shaded grey to aid visual comparisons between the cycles and the proxy records. The thick red line running through the MS data is a smoothing spline. Sample MS and stable isotope data drawn in this figure are presented in Appendix 3 Tables 4 and 8. Cycle numbers follow Fig. 3.27.

to supratidal depositional environments (section 3.4.1.1), and thus these sedimentary cycles may have experienced longer periods of emergence compared to the Livian cycles, which comprise greater proportions of subtidal bioclastic limestones. Additionally, the DSA (Anhée Nord; Fig. 6.2) has undergone greater thermal maturation than the NSA (Lives-sur-Meuse and Awirs West Quarry; Fig. 6.2) based on conodont alteration indices (CAI). The DSA yields CAI values of 4.0 – 4.5 (190 – 250 °C; Helsen, 1992), compared with CAI values of 3 – 4 (125 – 190 °C) from the NSA (Helsen, 1992).

6.3.5. Anhée Sud (Lower Warnantian; Poilvache Member to Lower Member of the Anhée Formation)

6.3.5.1. Magnetic susceptibility data

The results from MS analysis of samples from the Anhée Sud locality are illustrated in Fig. 6.10 and are presented as a data table in Appendix 3 Table 5. Most analyses yielded weakly positive magnetic susceptibilities (less than 1 x 10^{-8} m^3 / kg). The exceptions are a prominent MS excursion at the top of cycle -1 / -2 (Fig. 6.10), a siliciclastic parting at 19.68 m (2.63 x 10^{-8} m^3 / kg; Appendix 3 Table 5) and the W12 bentonite (2.48 x 10^{-8} m^3 / kg; Appendix 3 Table 5). There is a notable decrease in MS values across the boundary between cycles -1 and 0, but there is little change in MS values across important lithostratigraphic boundaries (i.e. the V3bβ – V3bγ boundary and the boundary between the Bonne River and Anheé formations; Fig. 6.10).

Within the Anhée Sud section, there is evidence of an up-section increase in water depths. This is inferred from an up-section decrease in the proportion of intertital / supratidal micrite beds relative to subtidal bioclastic limestones within the sedimentary cycles (see cycles 2 to c in Fig. 3.27), together with an increase in the siliciclastic content of the sedimentary cycles; cycles 3', 4 and 5 contain thin siliciclastic, shaley partings within their lower, bioclastic beds (Fig. 6.10), whereas the overlying cycles (cycles 6' – 8 in Fig. 3.27; cycle 6' in Fig. 6.10) contain thicker mudstone beds.

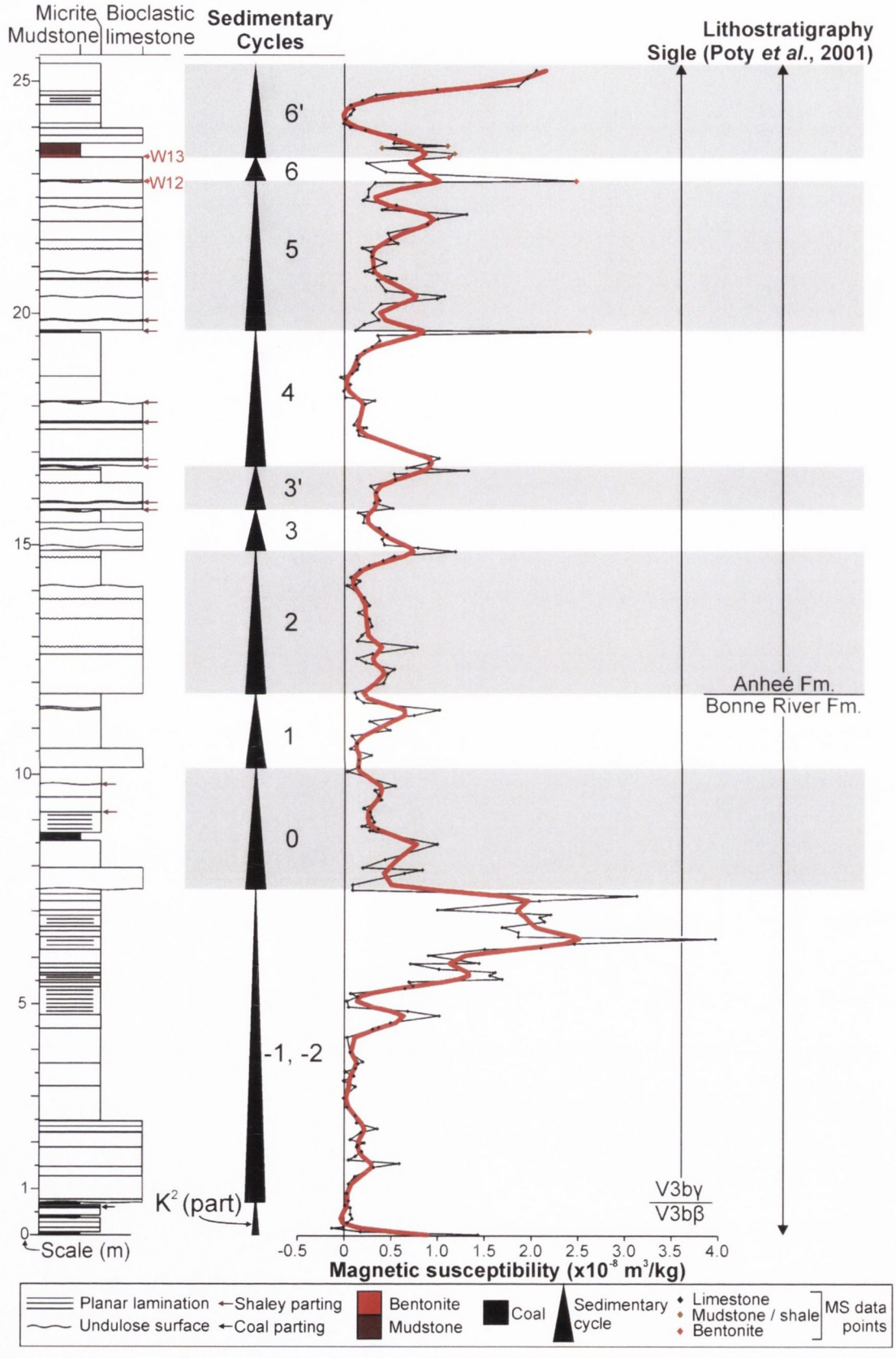

Figure 6.10. Magnetic susceptibility data from the Anheé Sud. Cycle names and the position of the V3bβ – V3bγ boundary follow Pirlet (1968). The base of Pirlet's (1968) cycle -1 could not be precisely located, thus the cycle shown encompasses cycles -2 and -1 of Pirlet (1968). The red line running through the MS data is a smoothing spline. The sigles are historical lithostratigraphic units (from Conil *et al.*, 1967). Sample MS data drawn in this figure can be found in Appendix 3 Table 5.

MS trends within the Anhée Sud sedimentary cycles are inconsistent; some cycles show increasing MS trends up-section (e.g. cycles -1 and 1; Fig. 6.10), other cycles show trends of decreasing MS values (cycles 0 and 3; Fig. 6.10), while some cycles show no obvious trend (e.g. cycle 5; Fig. 6.10). There is no clear correlation between MS and lithology (micrite, bioclastic limestone) within the sampled stratigraphic interval, nor is there any clear indication of a long-term change in MS as a response to changing water depths.

6.4. Discussion

6.4.1. Correlation between MS and the sedimentary cycles

A correlation between the MS data and the sedimentary cycles first appears within the Corphalie Member and continues into the lower Awirs Member. MS values increase up-section, i.e. MS values are low within the lower bioclastic (subtidal) beds and greater in the upper micritic (intertidal to supratidal) beds. This correlation is observed within the MS data from both Lives-sur-Meuse and Awirs West Quarry (Fig. 6.11). Thus, MS values appear to decrease from proximal (intertidal / supratidal) to more distal (subtidal) depositional environments on the carbonate platform. Similar trends between MS values and depositional environment have been observed from other shallow-water carbonate platforms. For example, da Silva & Boulvain (2006) noted that MS values increased systematically from distal, offshore carbonates to proximal, supratidal deposits on a middle Frasnian carbonate platform in Belgium. The observed proximal-distal trends in MS values are compatible with the ideas of Crick *et al.* (1997); i.e. cyclic variations in MS primarily reflects variations in detrital additions into the marine realm as a result of eustatic, climatic or tectonic processes. The close correspondence between the shallowing-upwards sedimentary cycles and MS variations could be interpreted as evidence for a eustatic control on these cycles.

In contrast, the underlying cycles within the Haut-le-Wastia Member at Lives-sur-Meuse do not show clear correlation with MS values. It could be that these cycles formed independently of the processes controlling the flux of detrital grains into the marine environment. Alternatively, it is possible that the MS record from this stratigraphic interval has experienced some diagenetic modification and thus any

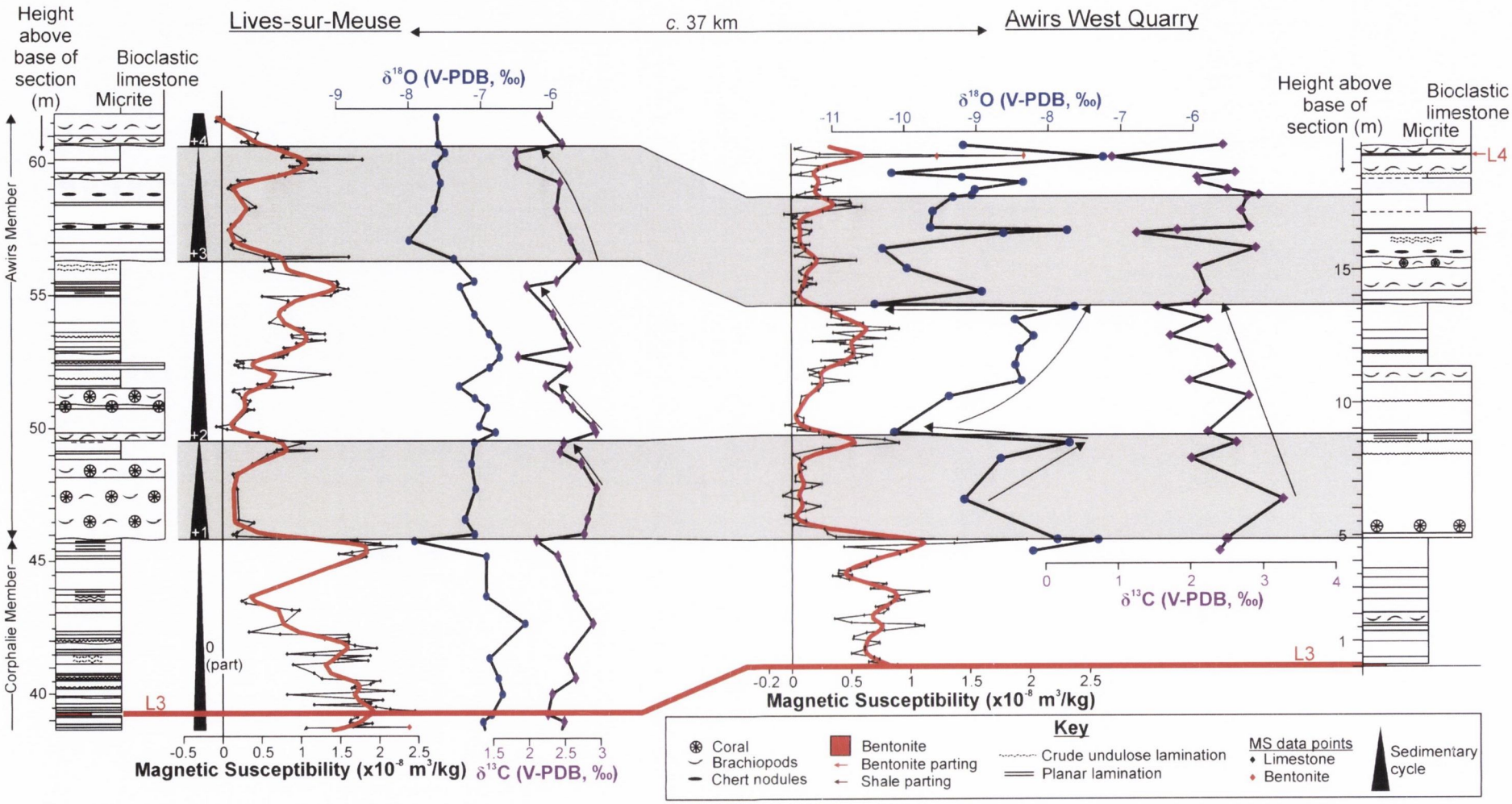

Figure 6.11. Proxy records from the upper Corphalie Member and lower Awirs Member at Lives-sur-Meuse and Awirs West Quarry. The black triangles represent individual sedimentary cycles (numbered relative to the Corphalie Member / cycle 0, as explained in section 6.3.2.1.1).

correlation between the sedimentary cycles and the MS record has been subsequently overprinted. The correlation between some of the dolomitised beds and high MS values (section 6.3.2.1.1), and the occurrence of strongly negative $\delta^{18}O$ values in some of the limestone samples (section 6.3.2.1.2), may lend support to the latter hypothesis. Further work is necessary to establish how representative the MS record from the Haut-le-Wastia Member at Lives-sur-Meuse is of the basin as a whole.

The relationship between the sedimentary cycles and the MS records breaks down within the middle of the Awirs Member at Awirs West Quarry (section 6.3.3.1). Above this stratigraphic level, the MS signal intensity weakens over several sedimentary cycles and then remains weakly positive within the lower part of the overlying Seilles Member (sections 6.3.3.1 and 6.3.3.2). This trend of a decrease in the MS signal correlates with stratigraphic evidence for a longer term increase in water depths within the Lives Formation; the sequence stratigraphic interpretations of Hance *et al.* (2001, 2002) suggest that there is a third order (*sensu* Vail *et al.*, 1977) maximum flooding surface located within the upper Awirs Member (cycle +7 of Fig. 6.7; equivalent to the V2bδ sigle unit of Conil *et al.*, 1967). Thus, it seems likely that the MS fluctuations on the scale of individual sedimentary cycles are modulated or dampened by lower frequency eustatic oscillations. The interplay of different frequencies of eustatic oscillation has been inferred within MS data from other carbonate platform deposits; for example, da Silva & Boulvain (2006) observed that the average MS values of fourth-order sequences (packages of sedimentary cycles) varied depending on their position within third-order sequences (packages of fourth-order sequences). The significance of this, however, is unclear. It has been suggested that during greenhouse (ice-free) conditions, high-frequency, climatically driven cycles (fourth and fifth order; *sensu* Vail *et al.*, 1977) have reduced amplitude and therefore that third-order changes in sea-level should dominate the stratigraphic record (Lehrman & Goldhammer, 1999). Thus, if the dominant signal in the MS record is from third-order processes then this could tentatively be interpreted to argue against these cycles being glacio-eustatic (and hence against the presence of significant glacial ice on Gondwana). It must be stressed, however, that further research is necessary to establish whether the MS trends observed at Awirs West Quarry are representative of MS variations on a basin-wide scale.

The Warnantian sections do not show convincing evidence of a correlation between the MS record and the sedimentary cycles. Several of the MS excursions recorded within the Anhée Nord section correspond closely with bentonite horizons or intervals containing numerous bentonite partings. It therefore appears that the MS record from this section is dominated by a volcanic signature. There are a few MS peaks from the Anhée Nord section that do not readily correlate with the occurrence of bentonites (e.g. MS peaks at 6.1 m and 20.2 m; Fig. 6.9); these may represent minor volcanic events with no obvious expression of volcanism, possibly caused by the volcanic ash being diluted within the limestones. It is not clear why the sedimentary cycles at Anhée Sud do not show a relationship with MS. Within this section, there is an up-section increase in lithological diversity (increase in abundance of siliciclastic mudstones and shales; section 6.3.5.1) and evidence to support an up-section increase in water depth (section 6.3.5.1). It is possible that these factors generated MS variations which are superimposed upon the MS variations at the scale of individual sedimentary cycles and thus complicate the MS record at this locality. Analysing additional coeval sections for MS may shed further light on the wider geographical significance of the MS records obtained from the Anhée Sud section.

6.4.2. Magnetic susceptibility analysis as a correlation tool

The analysis of samples for both MS and stable isotopes from the same stratigraphic interval (the upper Corphalie Member and the lower Awirs Member) at Lives-sur-Meuse and Awirs West Quarry reveals an excellent correlation between the MS records (cycles 0 to +3; Fig. 6.11). On the basis of this data, it appears that MS has some potential to be a useful correlation tool, which is in agreement with several other studies (e.g. da Silva & Boulvain, 2006; Bábek *et al.*, 2010; Whalen & Day, 2010). Thus, MS may provide a means of local correlation between different sections within the Namur-Dinant Basin, at a finer scale of resolution than is possible using lithostratigraphic and biostratigraphic controls. It is important to note, however, that this conclusion is based upon data from a relatively short stratigraphic interval within which there is strong evidence of a relationship between lithology and MS (sections 6.3.2.3.1 and 6.3.3.1.1). It remains to be established whether it is as straightforward to correlate using MS between sections which demonstrate complex relationships between MS and lithology (e.g. Haut-le-Wastia member; section 6.3.2.1). Characterising a greater number of

overlapping (laterally equivalent) sections, including sections that demonstrate complex relationships between MS and lithology, would better evaluate the potential of MS as a correlation tool in carbonate successions.

6.4.3. Significance of the stable isotope ($\delta^{13}C$ and $\delta^{18}O$) analyses

Within the majority of the investigated stratigraphic interval, there is limited evidence to support the occurrence of systematic and reproducible isotopic shifts (both $\delta^{13}C$ and $\delta^{18}O$) within the sedimentary cycles. Notable exceptions to this statement within the $\delta^{18}O$ dataset include cycle 0 within the Corphalie Member (sampled at Lives-sur-Meuse; section 6.3.2.2), which shows some evidence of a correlation between lithology and $\delta^{18}O$; the lower bioclastic beds are characterised by more negative $\delta^{18}O$ values compared to the overlying micrite beds (section 6.3.2.2.2). This may arise from diagenetic alteration or it could reflect environmental changes such as increased evaporation or salinity (see section 6.3.2.2.2). Additionally, cycles +1 and +2 within the Awirs Member at Awirs West Quarry (section 6.3.3.1.2) show evidence of an upwards increasing trend in $\delta^{18}O$ values. The latter trend appears to be of limited lateral extent though, as the same cycles (+1 and +2) sampled from Lives-sur-Meuse show markedly different trends in $\delta^{18}O$ values (Fig. 6.11). This is in contrast to the MS data, which can be readily correlated between these two localities (Fig. 6.11; section 6.4.2). The up-section increase in $\delta^{18}O$ values within the sedimentary cycles at Awirs West Quarry may arise from diagenetic alteration, possibly linked to changes in porosity and fluid flow (as noted in sections 6.3.2.2.2 and 6.3.3.1.2), although changes in environmental parameters (e.g. increasing salinity up-section) cannot be excluded. Localised diagenetic alteration or local variations in environmental parameters (such as salinity) may account for the poor correlation between the $\delta^{18}O$ datasets from Lives-sur-Meuse and Awirs West Quarry (Fig. 6.11).

Notable exceptions to the above, opening statement within the $\delta^{13}C$ dataset include the Awirs Member at Lives-sur-Meuse (section 6.3.2.3), which demonstrates a strong correlation between $\delta^{13}C$ values and both the sedimentary cycles ($\delta^{13}C$ values decrease upwards within cycles) and MS (inversely correlated; section 6.3.1.3.2). Similar vertical trends in $\delta^{13}C$ values have been observed from other ancient shallowing-upwards carbonate cycles, where they have been attributed to meteoric diagenesis (e.g. Allan &

Matthews, 1982; Algeo *et al.*, 1992). It is possible that the vertical trends in $\delta^{13}C$ values within the cycles of the Awirs Member at Lives-sur-Meuse also reflect meteoric diagenesis. The significance of the inverse correlation between MS and $\delta^{13}C$ is unclear. It may be a coincidence (without a genetic linkage), as both MS intensity and the extent of sub-aerial exposure (and thus potential for meteoric diagenesis) increase from distal to more proximal environments on carbonate platforms.

The lack of correlation between whole-rock stable isotope analyses ($\delta^{13}C$ and $\delta^{18}O$) and the sedimentary cycles of the Haut-le-Wastia Member (Lives Formation), at both Haut-le-Wastia (Fig. 6.2) and Awirs West Quarry, has been noted previously by Smeesters *et al.* (2003; in preparation). The data presented in previous sections show that this lack of correlation is also observed at Lives-sur-Meuse and that it is not limited to the Haut-le-Wastia Member, but is widespread within the Lives Formation. One possible interpretation for the lack of correlation is that the sedimentary cycles were formed by processes independent of those controlling the isotopic composition of the limestones (e.g. autocyclic processes). However, it is more likely, given that many of the stable isotope analyses yielded more negative $\delta^{13}C$ and / or $\delta^{18}O$ values than have been obtained from similar-aged brachiopods (Bruckschen & Veizer, 1997; Fig. 6.3), that the primary environmental signal of these samples has been subsequently modified by diagenetic alteration. Thus, the whole-rock analyses undertaken in this study may no longer provide an accurate record of the primary environmental conditions under which these sedimentary cycles were formed.

6.5. Conclusions

The MS data from Belgian Livian and Warnantian sedimentary cycles is complex. Some sedimentary cycles within the Corphalie and Awirs members (Lives Formation) show a close correspondence with the MS record, with low MS signal intensities within the lower, bioclastic limestones and higher MS values within the upper intertidal to supratidal micrites. Such MS variations are consistent with the hypothesis that the MS record primarily reflects the input of detrital grains into the marine environment (section 2.4.2). However, not all of the sedimentary cycles show the same strong correlation with the MS record. Further research is necessary to establish: 1) the geographic and stratigraphic extent of the correlation between MS and the sedimentary

cycles; 2) why some cycles show strong correlation with MS whilst others do not; 3) to what extent the MS record is affected by diagenesis.

The strong correlation between MS records from Lives-sur-Meuse and Awirs West Quarry suggests that the MS technique has some potential as a correlation tool in marine sequences, which is in agreement with several other studies (e.g. da Silva & Boulvain, 2006; Bábek *et al.*, 2010; Whalen & Day, 2010). In contrast to the MS data, the stable isotope data from the same stratigraphic interval at Lives-sur-Meuse and Awirs West Quarry show markedly different trends between the two localities and are probably only of local significance or have been altered by subsequent diagenesis.

Without a detailed investigation into the diagenetic histories of the limestone samples (which would require considerable time and expense), it is difficult to confidently interpret the whole-rock stable isotopic records. This is because many of the features within these records could be diagenetic, primary (environmental) or a combination of these two possibilities.

Chapter 7

Whole-rock geochemistry of western European diagenetically altered volcanic ash layers

7.1. Introduction

The purpose of this chapter is to present whole-rock geochemical data from several western European diagenetically altered volcanic ash layer samples. These analyses were undertaken to gain insight into the magmatic composition of the ash layers prior to diagenesis. Several authors have employed whole-rock geochemical analyses to elucidate the original compositions of altered volcanic lithologies (e.g. Huff *et al.*, 1996; Spears *et al.*, 1999). A number of elements, including those that are routinely used to classify fresh volcanic lithologies (such as Na, K, Si), are known to be mobile during alteration and thus cannot be used to infer the original source composition of altered volcanic lithologies. Instead, the classification of altered volcanic rocks often relies on several elements which are thought to be immobile during alteration and are also inferred to be indicators of magmatic composition (e.g. Zr, Nb, Y, Ti; see section 7.4 for details).

The samples analysed are described in section 7.2. This is followed by the presentation of the whole-rock geochemical data in section 7.3. Within the data several major elemental trends can be linked to the bulk mineralogy of samples (determined by XRD analysis), which are discussed in section 7.3. The remainder of the chapter (sections 7.4 and 7.5) focuses on elucidating the magmatic parentage of the altered ash layer samples using trace element discrimination diagrams (section 7.4.1) and rare-earth element data (section 7.4.2).

7.2. Samples

52 samples of diagenetically altered volcanic ash layers were analysed for whole-rock geochemistry (major, trace and rare-earth elements), using the methodology described in section 2.7. This sample set includes several Belgian Visean bentonites (horizons M to W13 in Fig. 7.1). A number of Belgian Moliniacian and Livian bentonite horizons were sampled from several localities within the Namur-Dinant Basin (Table 7.1; Fig. 7.2) to determine if there is significant lateral variation in the whole-rock geochemistry of these horizons. The 13-66 horizon (Fig 7.1) is a Livian bentonite horizon that was sampled from Awirs West Quarry (50.5905°N, 5.4089°E). It occurs between bentonites L4 and L5 (Fig. 7.1) and is not currently assigned an 'L' number. The most appropriate designation for this horizon would be L5, but this would require the current 'L5' bentonite to be renumbered as L6, which may cause unnecessary confusion. As such, this horizon is referred to only by a sample number (MAP 13-66) in this thesis.

Bentonite	Sampling localities	Latitude / longitude (WGS 84 datum)
M	Lives-sur-Meuse	50.4720°N, 4.9328°E
	Malonne	50.4337°N, 4.7949°E
L1, L2	Lives-sur-Meuse (cliff section 1†)	50.4692°N, 4.9291°E
	Royseux	50.4690°N, 5.2679°E
	Sosoye*	50.3017°N, 4.7762°E
L3	Anhée Nord+	50.3180°N, 4.8758°E
	Awirs West Quarry	50.5905°N, 5.4089°E
	Engihoul Quarry	50.5764°N, 5.4241°E
	Lives-sur-Meuse (cliff section 2†)	50.4686°N, 4.9285°E
L4, L5	Awirs West Quarry	50.5905°N, 5.4089°E
	Engihoul Quarry	50.5764°N, 5.4241°E

Table 7.1. Sampling localities of Belgian Moliniacian and Livian bentonites. * Two horizons at Sosoye (separated by *c.* 1m of limestone) yield zircon shapes characteristic of the L1 horizon (Delcambre 1996) and are accordingly termed L1a (lower) and L1b (upper) following Delcambre (1996). †Cliff sections 1 and 2 at Lives-sur-Meuse are further described in section 6.3.2. +Bentonite L3 is exposed at Anhée Nord *c.* 110m to the north of the section containing bentonites W1 – W8 (= 50.3170°N, 4.8760°E). Sampling localities are drawn in Fig. 7.2.

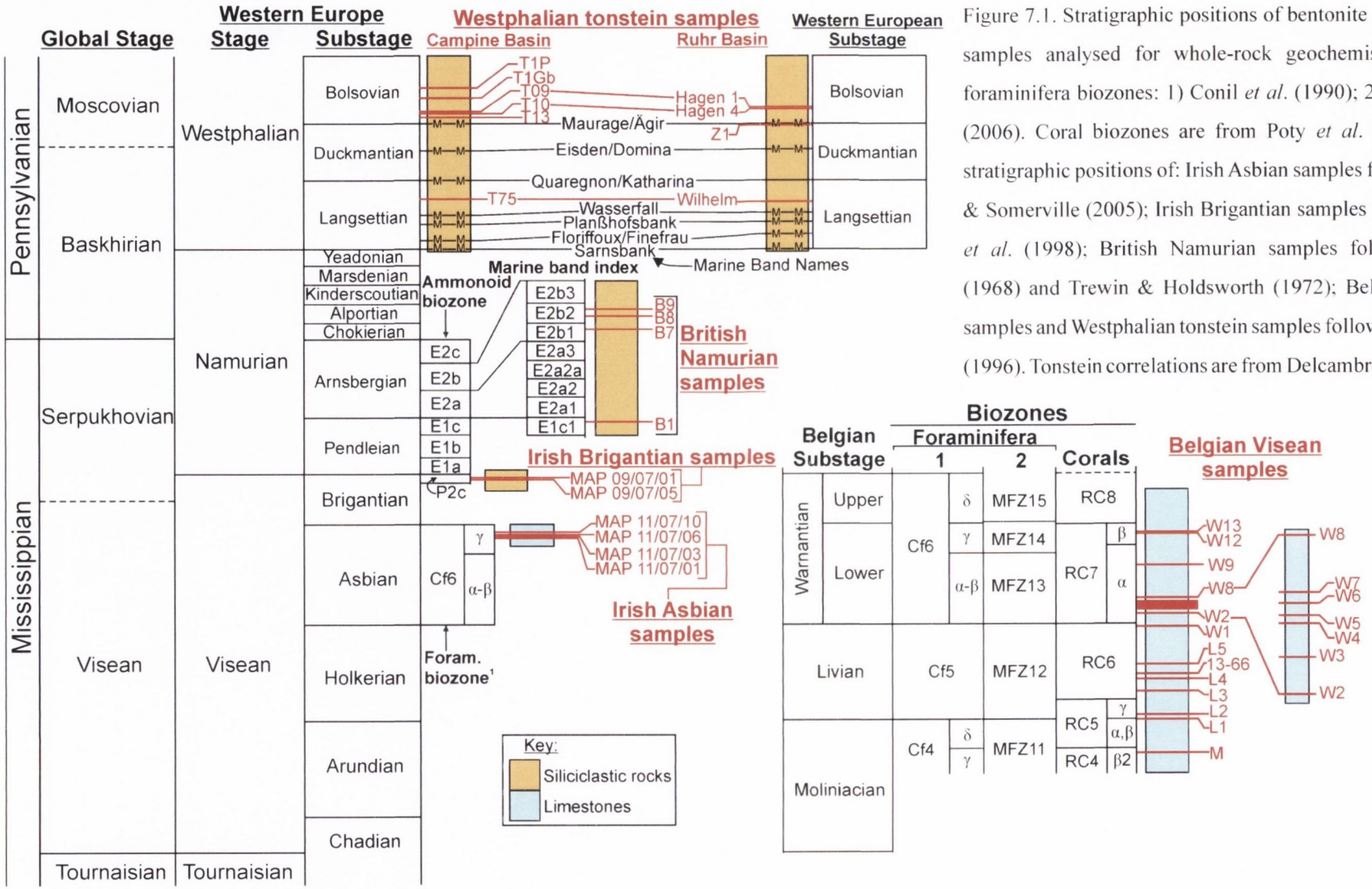

Figure 7.1. Stratigraphic positions of bentonite and tonstein samples analysed for whole-rock geochemistry. Visean foraminifera biozones: 1) Conil *et al.* (1990); 2) Poty *et al.* (2006). Coral biozones are from Poty *et al.* (2006). The stratigraphic positions of: Irish Asbian samples follow Cózar & Somerville (2005); Irish Brigantian samples follow Legg *et al.* (1998); British Namurian samples follow Trewin (1968) and Trewin & Holdsworth (1972); Belgian Visean samples and Westphalian tonstein samples follow Delcambre (1996). Tonstein correlations are from Delcambre (1996).

The Belgian Visean horizons W1 through to W8 (Fig. 7.1) were sampled from Anhée Nord (50.3170°N, 4.8760°E; Fig. 7.2), whereas horizons W12 and W13 were collected from the Anhée Sud section (50.2940°N, 4.8936°E; Fig. 7.2). W9 was sampled from Dullière Quarry at Monceau-sur-Sambre by Dr. Bernard Delcambre (pers. comm., 2008; corresponds to the locality labelled Monceau in Fig. 7.2; 50.3949°N, 4.3749°E). Additionally, three Belgian Visean horizons (L4 and L5 from Awirs West Quarry and W8 from Anhée Nord) were sampled at both their base and top to investigate if there is vertical geochemical stratification within these layers. Bentonite L4 at Awirs West Quarry comprises two distinct layers (a lower orange layer and an upper black layer; Fig. 3.8d), bentonite L5 at Awirs West Quarry appears internally homogeneous and is *c.* 5 cm thick, whereas bentonite W8 at Anhée Nord is *c.* 18 cm thick, well consolidated and is also internally homogeneous.

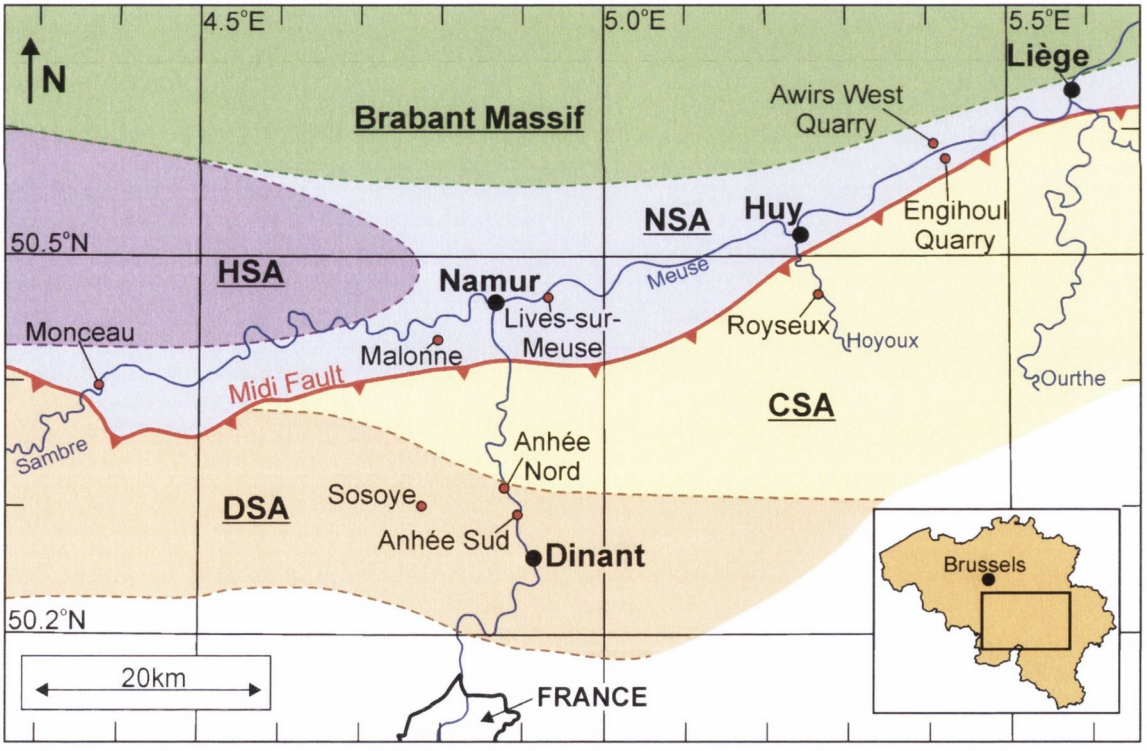

Figure 7.2. Map of the Namur-Dinant Basin showing the sampling localities of Belgian Visean bentonites discussed in this chapter. Black circles denote major towns and cities. Red circles denote localities mentioned in this chapter. CSA = Condroz sedimentation area, DSA = Dinant sedimentation area, HSA = Hainaut sedimentation area, NSA = Namur sedimentation area. Sedimentation areas are schematic (redrawn from Poty *et al.*, 2001). The inset shows the area of Belgium covered by the main diagram.

In addition to the Belgian Visean samples, the four Irish Asbian palaeosol horizons investigated for zircon (samples MAP 11/07/01, 03, 06, 10; see section 4.2 for further details) and the two Irish Brigantian bentonites sampled from Cuilcagh Mountain (samples MAP 09/07/01, 05; see section 4.3 for details) were analysed for their whole-rock geochemistry. Four British Namurian bentonite samples from the Pennine Basin, northern England (bentonites B1, B7, B8, B9; see section 5.2.1 for details) and ten Westphalian tonstein samples from the Campine and Ruhr basins (Belgium and Germany respectively) were also analysed for their whole-rock geochemistry (Table 7.2). The tonstein samples included the Langsettian tonsteins T75 (Campine Basin) and Wilhelm (Ruhr Basin) that are considered to be laterally equivalent (Paproth *et al.*, 1983b; Delcambre 1996; Fig. 7.1), the Duckmantian tonstein Z1 (Ruhr) and several Bolsovian tonsteins from the Campine (tonsteins T13, T10, T09, T1Gb, T1P) and Ruhr basins (tonsteins Hagen 1, Hagen 4; Fig. 7.1). Additionally, the whole-rock geochemistry of three Belgian Visean limestone samples and two British Namurian shale samples was also determined (as explained in section 2.7); the details of which are presented in Table 2.4. The stratigraphic positions of all diagenetically altered volcanic ash layer samples discussed in this chapter are shown in Fig. 7.1. The whole-rock geochemical composition of the upper Tournaisian bentonite 300 (section 3.2.1) was not determined because of insufficient sample material.

Tonstein	**Stratigraphic age**	**Sedimentary basin**	**Sampling locality**	**Latitude / longitude (WGS 84 datum)**
T75	Langsettian	Campine Basin	Zwartberg colliery	51.0136°N, 5.5038°E
Wilhelm	Langsettian	Ruhr Basin	Unser Fritz colliery	51.5408°N, 7.1343°E
Z1	Duckmantian	Ruhr Basin	Furst Leopold colliery	51.6713°N, 6.9777°E
T13	Bolsovian	Campine Basin	Eisden colliery	51.0016°N, 5.7044°E
T10	Bolsovian	Campine Basin	Eisden colliery	51.0016°N, 5.7044°E
T09	Bolsovian	Campine Basin	Eisden colliery	51.0016°N, 5.7044°E
T1Gb	Bolsovian	Campine Basin	Drillcore KS20 (791.00 – 791.08 m)	51.1018°N, 5.1853°E
T1P	Bolsovian	Campine Basin	Drillcore KS21 (464.02 – 464.03m)	51.0902°N, 5.3025°E
Hagen 1	Bolsovian	Ruhr Basin	Furst Leopold colliery	51.6713°N, 6.9777°E
Hagen 4	Bolsovian	Ruhr Basin	Altendorf colliery	51.6394°N, 7.0187°E

Table 7.2. Sampling localities of the Westphalian tonsteins analysed. All of the Westphalian tonstein samples investigated were provided by Dr. Bernard Delcambre (Université Catholique de Louvain).

7.3. Whole-rock geochemistry

The whole-rock geochemical data from western European diagenetically altered volcanic ash layers are presented in stratigraphic order, under the section headings of Belgian Visean, Irish Asbian, Irish Brigantian, Namurian and Westphalian samples. In subsequent sections, the whole-rock geochemical data are normalised to the composition of the continental crust (Rudnick & Gao, 2003) and are illustrated as multi-element diagrams (Figs. 7.3 – 7.9). These diagrams were drawn using the sample data that are presented in Appendix 2 Table 1.

7.3.1. Belgian Visean samples

The Belgian Visean bentonite samples (Fig. 7.3a – e) show much stronger enrichment in all elements, except for CaO, MnO and Sr, compared to the samples of the enclosing limestones (samples MAP 02-28, 03-02, 07-41; Fig. 7.3a). Bentonites M to L5 (Fig. 7.3a – c; Moliniacian to Livian age) are generally enriched in Al_2O_3, K_2O, Hf, Nb, Rb, Sn, Ta, Th, U and Zr and are depleted in Ba (except bentonite M from Lives-sur-Meuse and bentonites L4 and L5 from Engihoul Quarry; Fig. 7.3a, c), MgO, MnO, NaO, Eu and Sr (except bentonite M at Malonne; Fig. 7.3a) with respect to the bulk continental crust. Bentonites L3, L4, MAP13-66 and L5 are also strongly depleted in Cr_2O_3 (Fig. 7.3b, c). There is a clear difference in enrichment / depletion trends for the rare-earth elements (La to Lu; see section 7.4.2 for further details) between bentonite L3, which shows a decreasing trend of enrichment from La to Lu (excluding Eu; Fig. 7.3b), and bentonites L4 and L5 (excluding L5 from Engihoul Quarry), which are characterised by increasing trends from Nd to Lu (Fig 7.3c). Several samples are enriched in CaO (M from Malonne and L1b from Sosoye, Fig. 7.3a; bentonite L3 from Anhée Nord and Engihoul Quarry, Fig. 7.3b; bentonite L5 from Engihoul Quarry, Fig. 7.3c), which can be linked to the presence of calcite in these samples (as determined by XRD analysis; Appendix 2 Table 2). The enrichment in K_2O and Al_2O_3 can be attributed to the presence of clay minerals (illite-mica, probable mixed-layer clays and kaolinite) as identified using XRD analysis (Appendix 2 Table 2). The concentration of Al_2O_3 in most samples exceeds what can reasonably be expected to occur in a fresh volcanic lithology (most samples contain 20 – 30 % Al_2O_3; Appendix 2 Table 1) and has likely been residually enriched through the loss of mobile elements.

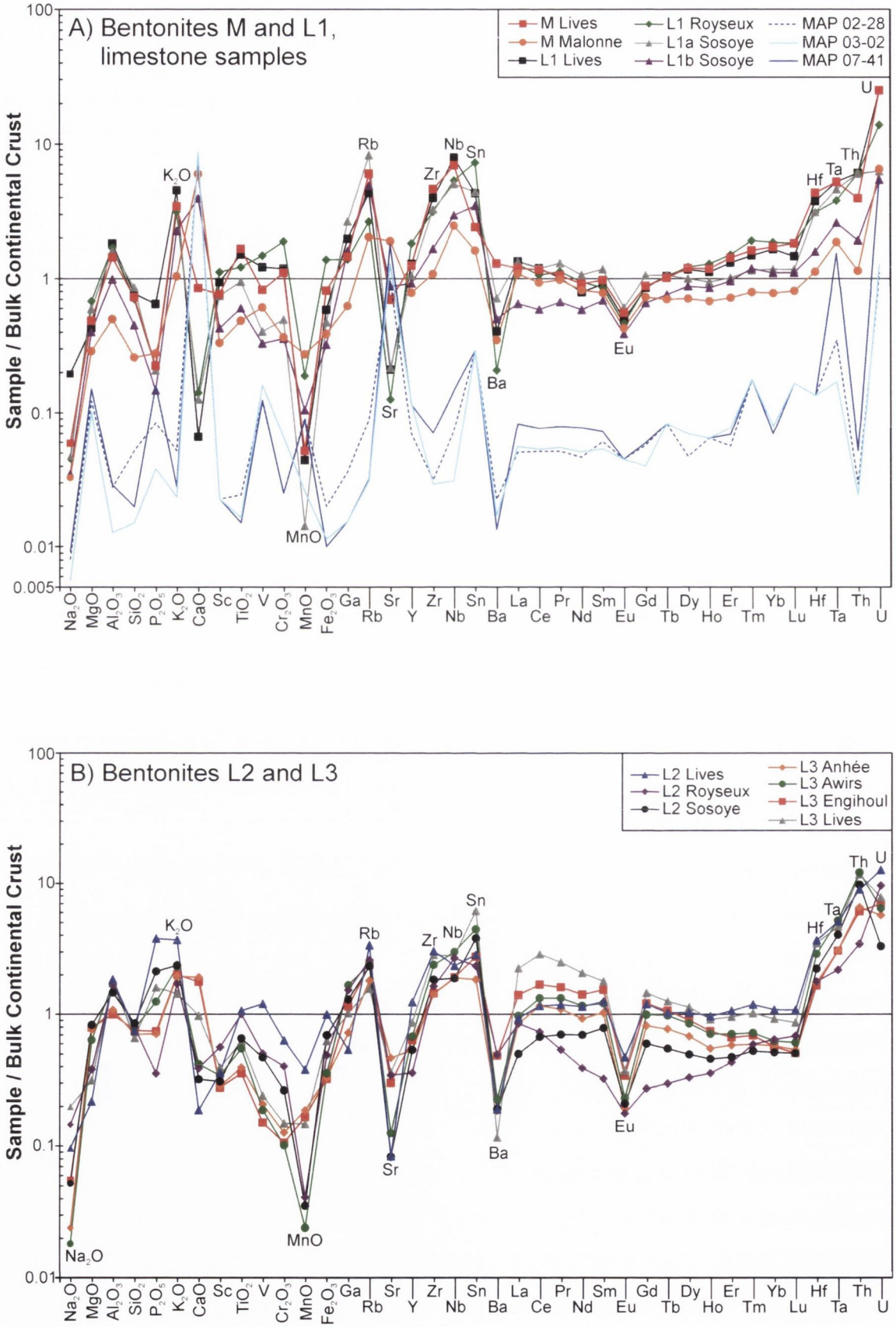

Figure 7.3 (*continued overleaf*)

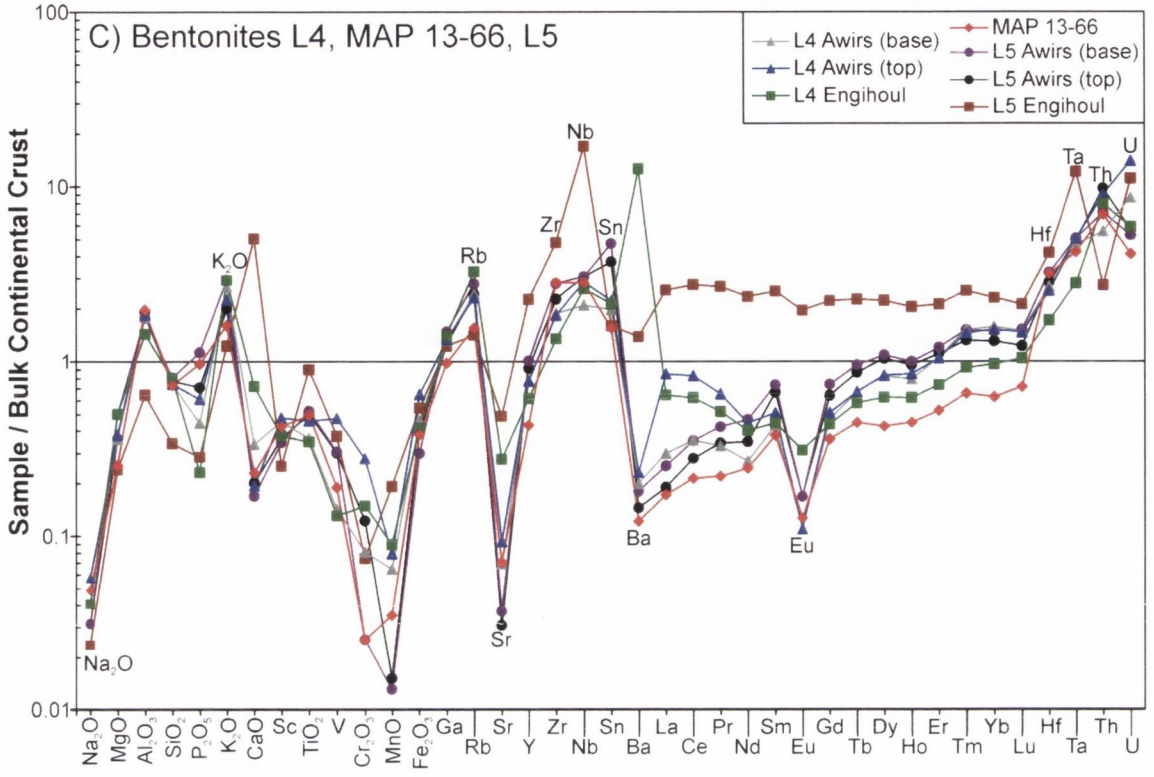

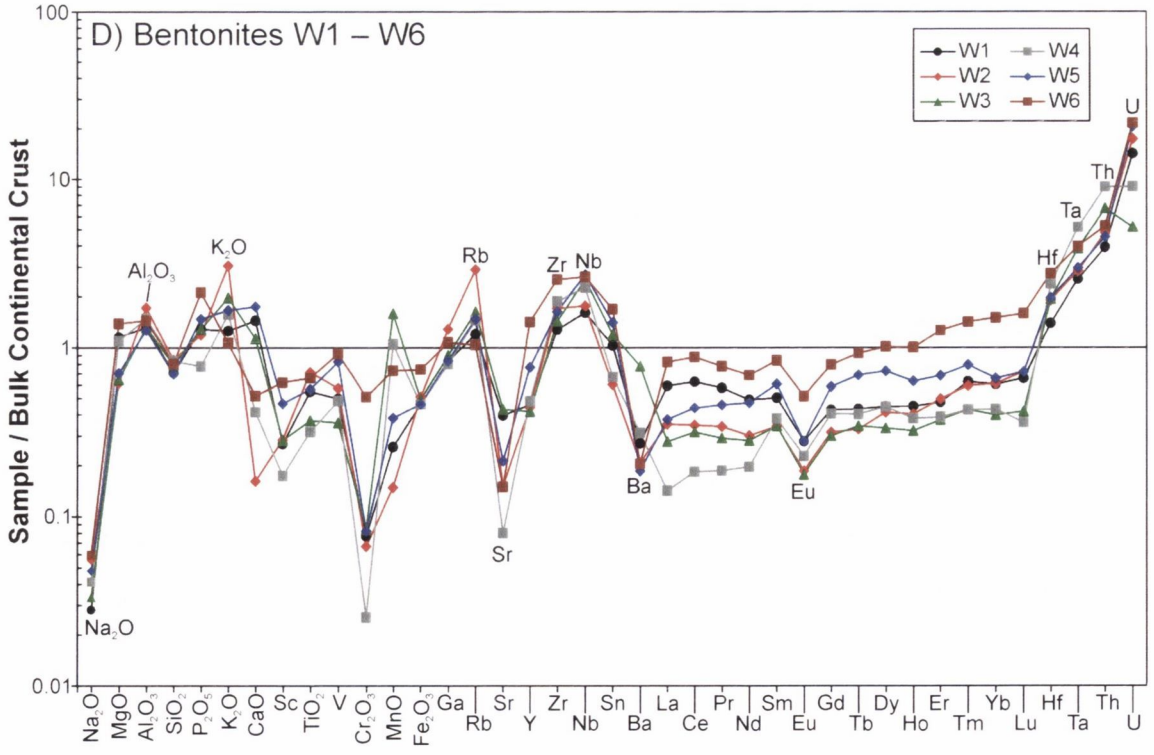

Figure 7.3 (*continued overleaf*)

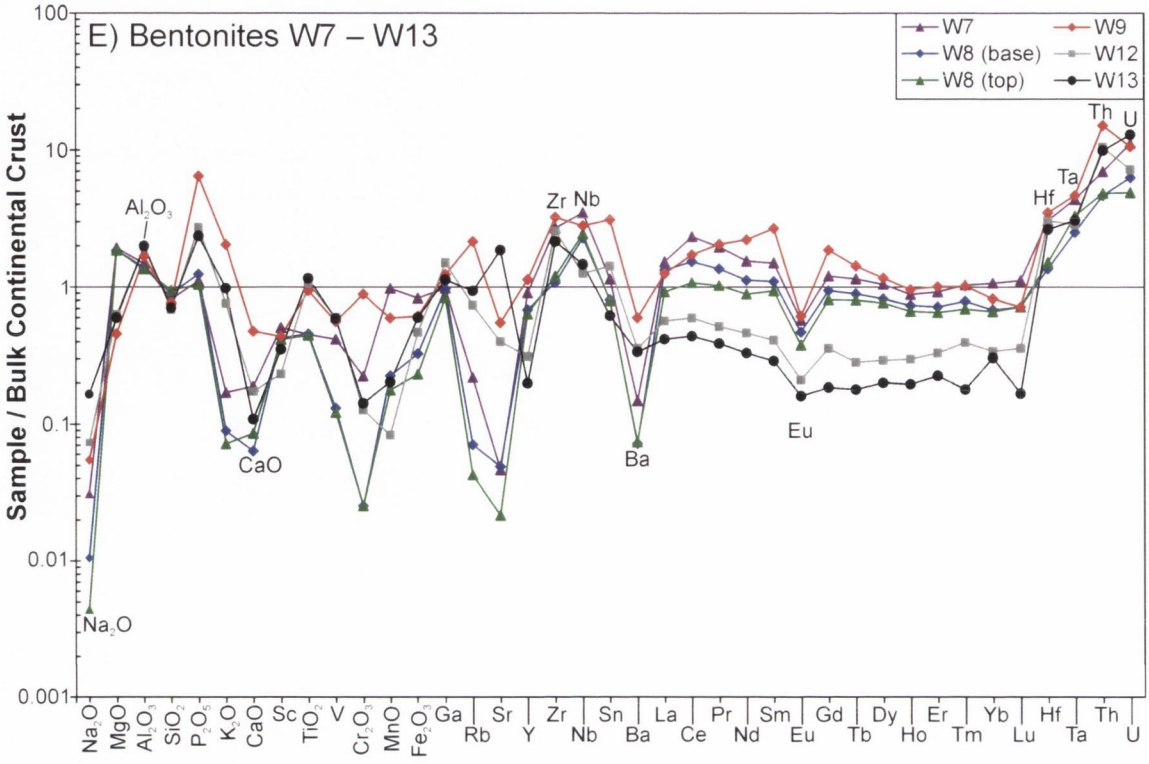

Figure 7.3 (a – e). Major and trace element data from the Belgian Visean bentonite and limestone samples normalised to bulk continental crust values (Rudnick & Gao, 2003). The stratigraphic positions of the sampled bentonites are shown in Fig. 7.1. Elements are arranged in order of increasing atomic number.

The Belgian 'W' bentonites (Fig. 7.3d, e; latest Livian to Warnantian age) show similar elemental trends, with respect to the bulk continental crust, compared to the Belgian 'M' and 'L' horizons (Fig. 7.3a – c; Moliniacian and Livian age). A notable deviation from this pattern is that several 'W' level samples are enriched in MgO (W1, W4, W6, W7, W8; Fig. 7.3d, e). These samples contain chlorite (as determined by XRD analysis; Appendix 2 Table 2), and Mg-rich chlorites (e.g. sudoite) have been reported from some of the 'W' bentonites at Anhée Nord (Anceau, 1992). Thus, the chlorites are a likely source of the extra MgO in these samples. Additionally, samples W7 and W8 are depleted in K_2O and Rb (with respect to the bulk continental crust; Fig. 7.3e). Illite-mica was not detected in the XRD analyses from these two horizons (Appendix 2 Table 2). This is in contrast to most of the other Belgian Visean samples analysed and may account for the lower K_2O and Rb concentrations observed in these two samples.

7.3.1.1. Vertical chemical structure of bentonite samples

Samples were collected from the base and top of three Belgian bentonite horizons (L4 and L5 from Awirs West Quarry and W8 from Anhée Nord) to determine if there is any vertical geochemical stratification within these horizons. The results from the three bentonites are shown in Fig. 7.4 as cross plots of the elemental data obtained from the base and top of the sampled horizons. Data from the base and top of these altered ash horizons are very similar and suggest that there are no major variations in elemental composition within these three horizons (Fig. 7.4). The results from the L4 horizon were particularly surprising because it contains two distinctive layers (Fig. 3.8d). The upper sample from L4 at Awirs West Quarry exhibits a slight enrichment in Ce, La, Nd, Pr, U and Th (Fig. 7.4a), which, together with a slightly increased P_2O_5 concentration (0.08 % *c.f.* 0.06 % in the lower sample; Appendix 2 Table 1), may indicate the presence of apatite that is of insufficient concentration to be detected by XRD analysis. The colour differences within the L4 horizon can be attributed to the presence of goethite in the lower sample (identified by XRD analysis; Appendix 2 Table 2) that is not recorded from the upper sample. It is also possible that the upper layer within the L4 horizon may contain more organic matter, which would account for the slightly higher loss-on-ignition from this sample (14.20 % *c.f.* 12.86 % in the lower sample; Appendix 2 Table 1) and its dark colouration (Fig. 3.8d).

The samples collected from the base and top of bentonite L5 at Awirs West Quarry have very similar major and trace elemental concentrations (Fig. 7.4b). This is with the exception of chromium which is more concentrated in the top of the L5 horizon (Fig. 7.4b). It is unclear why chromium is concentrated in the top of this horizon; it may arise from the diagenetic redistribution of chromium. There is a slight enrichment in Na and Sr within the base of the W8 bentonite horizon (relative to its top; Fig. 7.4c). Again, the cause of this enrichment is not certain but could reflect temporal changes in magma composition, the sorting of the volcanic ash material during deposition (coarser Na- and Sr-rich phenocrysts deposited first) or the diagenetic redistribution of Na and Sr (both are mobile elements; e.g. Christidis, 1998) within the bentonite horizon.

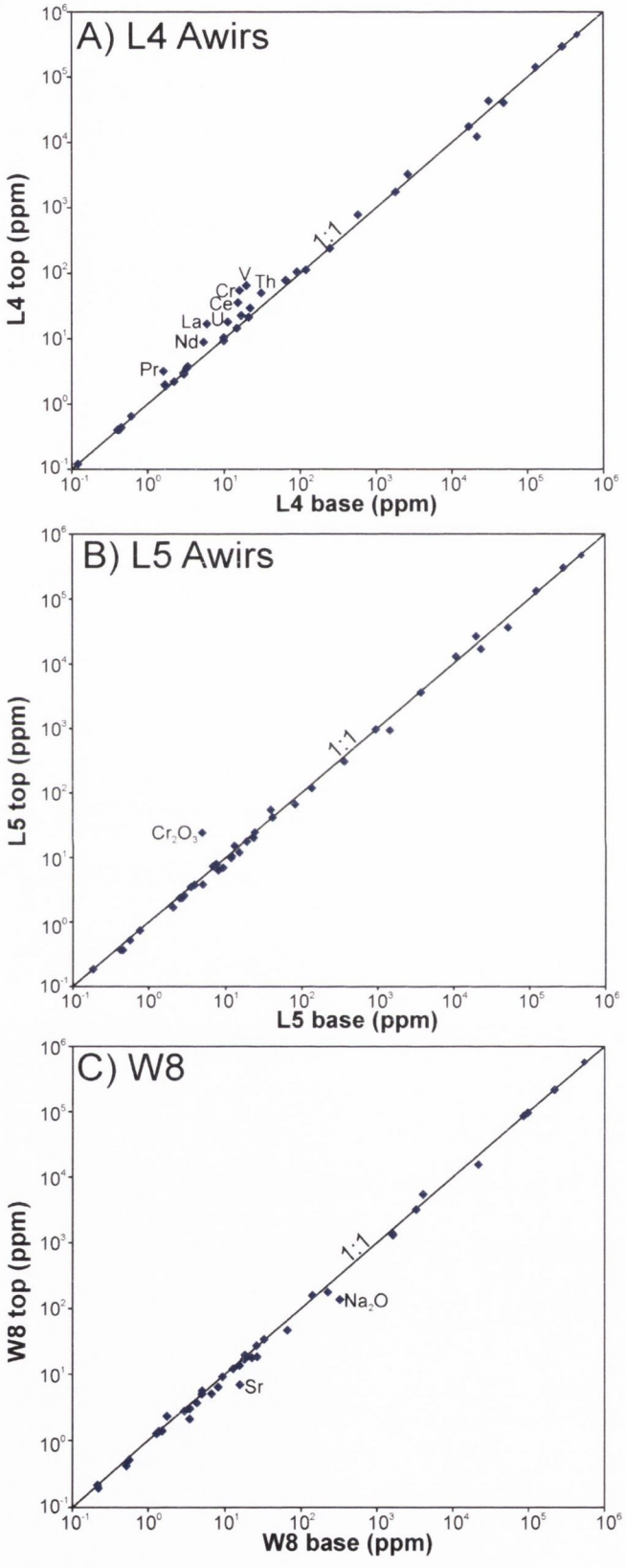

Figure 7.4. Cross plots of whole-rock geochemical data from samples taken at the base and top of the same bentonite horizons. All elemental data are presented in units of ppm.

7.3.1.2. Lateral variations in composition

Several Belgian Visean horizons were sampled from multiple localities within the Namur-Dinant Basin (Table 7.1) and analysed for their whole-rock geochemical composition to investigate if there are significant lateral variations in geochemistry within the bentonites. The four samples from bentonite L3 yield the most similar results. There is particularly good agreement within the trace element data, which is apparent in Fig 7.3b and also in the trace element discrimination diagrams presented in later sections (section 7.4.1; Figs. 7.10 and 7.11). In contrast to the L3 bentonite, bentonites L4 and L5 show much greater lateral variation. The samples of these horizons collected from Awirs West Quarry and Engihoul Quarry (Fig. 7.2) have different bulk mineralogies; the samples of L4 and L5 from Awirs West Quarry contain probable mixed-layer clays and kaolinite (Fig. 7.5), whereas the equivalent horizons at Engihoul Quarry contain significant calcite, quartz and pyrite, plus small amounts of clay minerals (probable mixed-layer clays; Fig. 7.5; Appendix 2 Table 2).

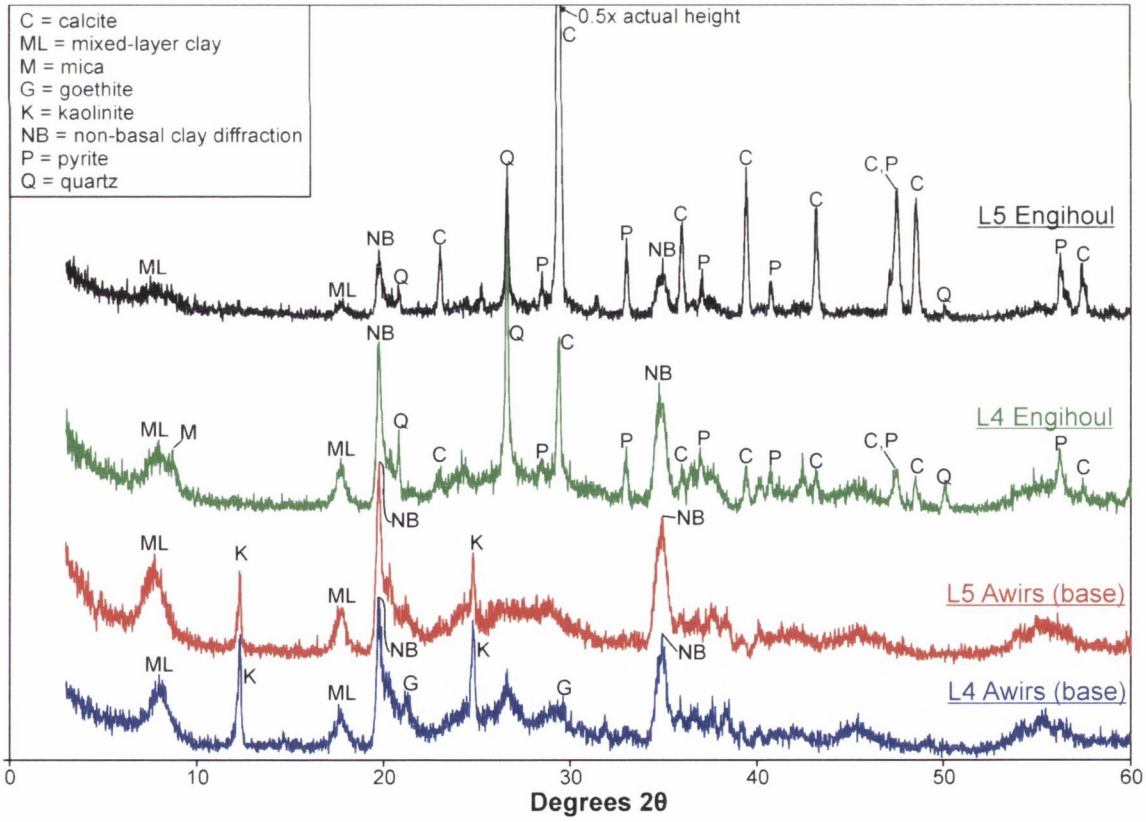

Figure 7.5. X-ray diffraction (XRD) traces of samples taken from bentonites L4 and L5 at Awirs West Quarry and Engihoul Quarry. The mixed-layer clay could be illite-smectite but this cannot be proven from these analyses.

L4 and L5 from Engihoul Quarry also contain more CaO, Ba and Sr but less MgO and Fe_2O_3 than the equivalent horizons at Awirs West Quarry (Fig. 7.3c). This is consistent with the presence of calcite (detected in the XRD traces; Fig. 7.5) in the samples from Engihoul Quarry, which is probably diluting the signal from the Fe- and Mg-bearing clay minerals. The absence of quartz and calcite in samples from Awirs West Quarry, and the presence of these minerals in samples from Engihoul Quarry, could be an indication that there is local detrital contamination within the latter samples or, more likely, that these samples have experienced local fluid-related diagenetic alteration. The occurrence of pyrite in samples from Engihoul Quarry but not in samples from Awirs West Quarry likely reflects the shorter time that the Engihoul horizons have been exposed to the modern environment compared to the same horizons at Awirs West Quarry, as noted in section 3.3.3.

7.3.2. Irish Asbian samples

The four Irish Asbian samples show comparable trends with respect to the bulk continental crust (Fig. 7.6). Samples MAP 11/07/01, 03, 10 show enrichment in Al_2O_3, K_2O, TiO_2, Cr_2O_3, Ga, Nb, Rb, Sn, Ta, Th, U (Fig. 7.6). Samples MAP 11/07/01 and MAP 11/07/03 are also enriched in Zr (with respect to the bulk continental crust). Sample 11/07/03 shows a slight enrichment in CaO, whereas sample MAP 11/07/06 shows a strong enrichment in CaO and a slight enrichment in Sr with respect to both the bulk continental crust and the other Irish Asbian samples (Fig. 7.6). The presence of illite-mica in these samples (as determined by XRD analysis; Appendix 2 Table 2) probably accounts for the relative enrichment in K_2O and Al_2O_3. The presence of zircon in samples MAP 11/07/01 and MAP 11/07/03 (section 4.2) accounts for the relative enrichment in zirconium observed in both of these samples. Samples MAP 11/07/03 and MAP 11/07/06 both contain calcite (as determined by XRD analysis; Appendix 2 Table 2). The characteristic XRD peaks for calcite are particularly strong in the data from sample 11/07/06, suggesting that this sample contains abundant calcite. It is likely that the abundance of calcite in this sample is diluting other phases and their chemical signatures, which would explain the lower concentrations of most other elements in this sample compared to the other Irish Asbian samples (Fig. 7.6).

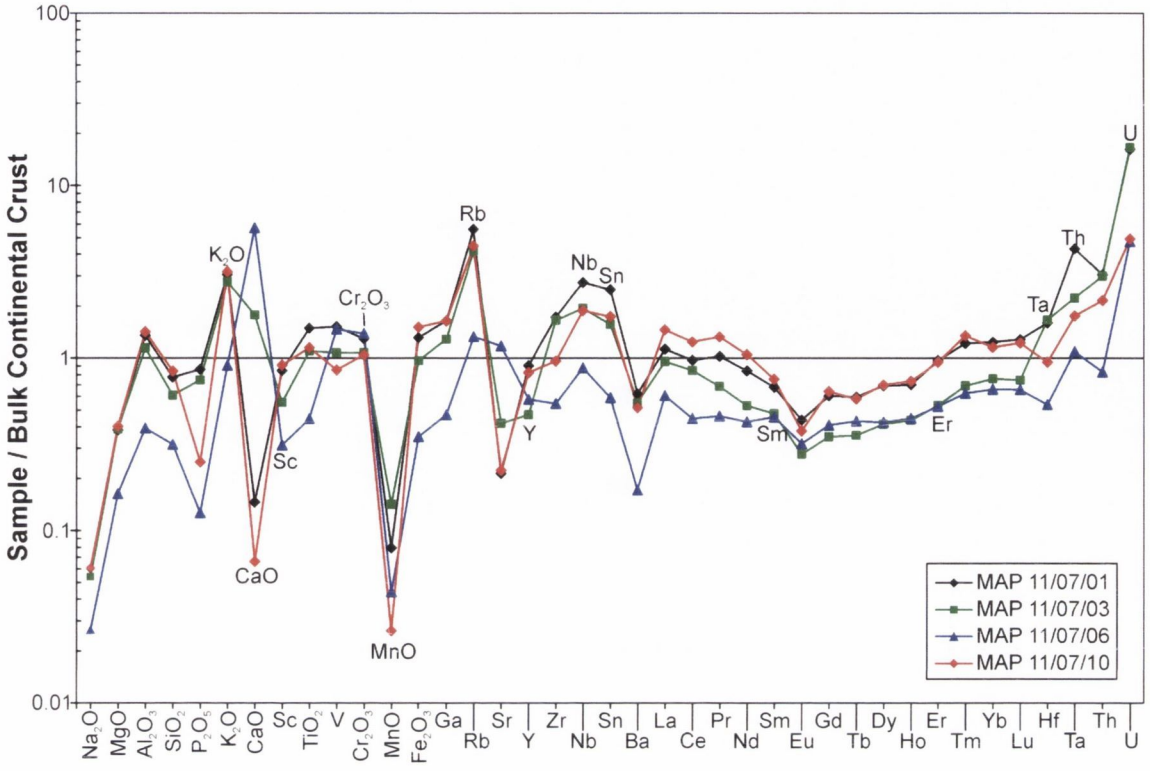

Figure 7.6. Major and trace element data from the Irish Asbian samples normalised to bulk continental crust values (Rudnick & Gao, 2003). Elements are arranged in order of increasing atomic number.

7.3.3. Irish Brigantian samples

The two Irish Brigantian samples are enriched in Al_2O_3, Fe_2O_3 and most trace elements except for Ba, Ga, La, Rb, Sc, Sr and V (Fig. 7.7). There is a strong enrichment in trace elements compared to the other Visean samples discussed in previous sections. Interestingly, these two Brigantian samples show a smaller depletion in Na_2O compared to all other samples analysed. XRD analysis of material from these horizons suggests the presence of pyrite and feldspar (albite?), which are likely sources of the iron and sodium in these samples respectively. The relative enrichment in Al_2O_3 with respect to the bulk continental crust can be attributed to the presence of clay minerals (probable mixed-layer clays) and feldspar in these samples (as identified by XRD analysis; Appendix 2 Table 2).

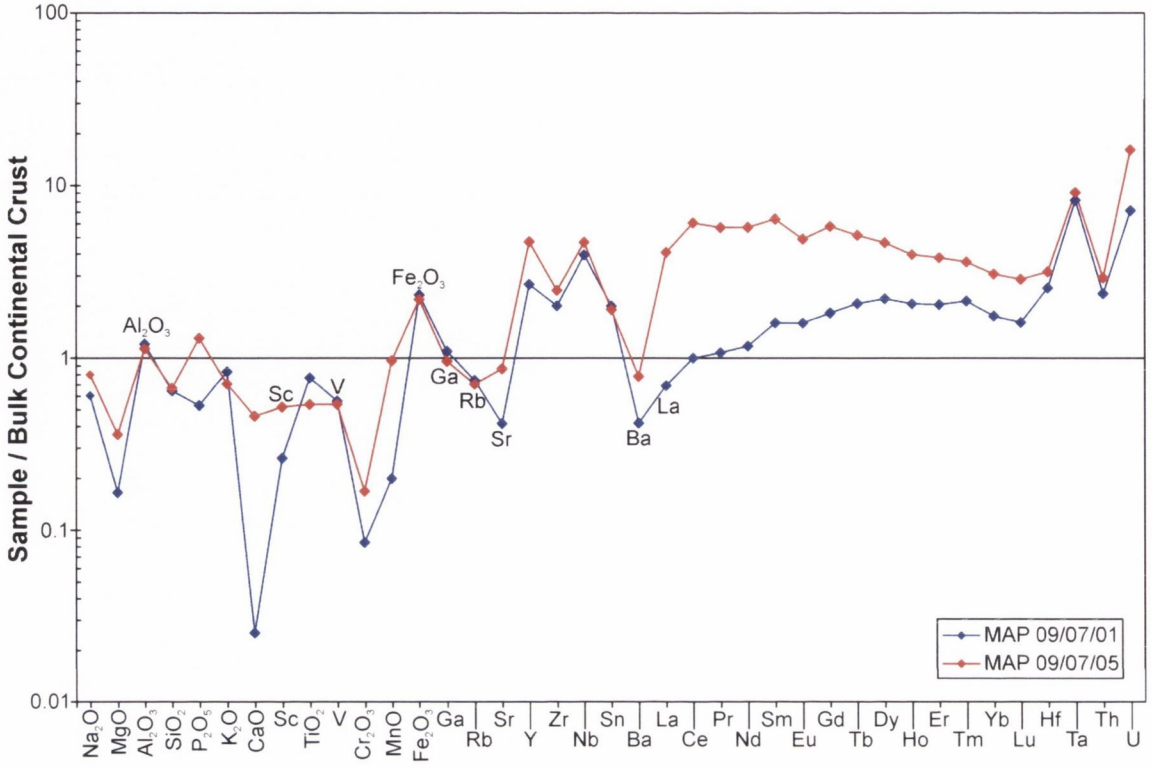

Figure 7.7. Major and trace element data from the Irish Brigantian bentonite samples normalised to bulk continental crust values (Rudnick & Gao, 2003). Elements are arranged in order of increasing atomic number.

7.3.4. Namurian bentonite samples

The Namurian bentonite samples analysed are enriched in Fe_2O_3 (except B7), MnO, Sn, Y and elements heavier than La (with the exception of Eu in sample B1; Fig. 7.8) with respect to the bulk continental crust. All samples are depleted in CaO, Cr_2O_3, MgO, Na_2O, Sc, Sr and V. The enrichment in iron can be attributed to the presence of pyrite in these samples (identified by XRD analysis; Appendix 2 Table 2). Samples B8 and B9 contain substantial amounts of iron (32.59 % and 27.70 % Fe_2O_3 respectively; Appendix 2 Table 1), which is unlikely to be representative of the parent ash. It is more likely that some of the iron has been taken up during diagenesis under reducing conditions. This explanation could also account for the enrichment in MnO within these samples. XRD analysis of material from bentonites B8 and B9 suggests that at least some of the Mn occurs as a phase closely corresponding to rhodochrosite ($MnCO_3$).

The two Namurian shales that were sampled from the strata adjacent to bentonites B1 and B7 (samples MAP 03/02/08 and MAP 12/07/09 respectively; Fig. 7.8; Table 2.4)

are enriched in Cr_2O_3, P_2O_5, Rb and Sr and are depleted in Hf, Ta and Th compared to the bentonite samples (Fig. 7.8). The greater concentrations of Rb and Sr in the shale samples can be attributed to the presence of chlorite (determined by XRD analysis, using the same method as presented in section 2.6; Appendix 2 Table 2), which is not represented in the bentonite samples (Appendix 2 Table 2). The enrichment of MnO in shale sample MAP 12/07/09 likely arises from the presence of a phase closely corresponding to rhodochrosite (identified by XRD analysis).

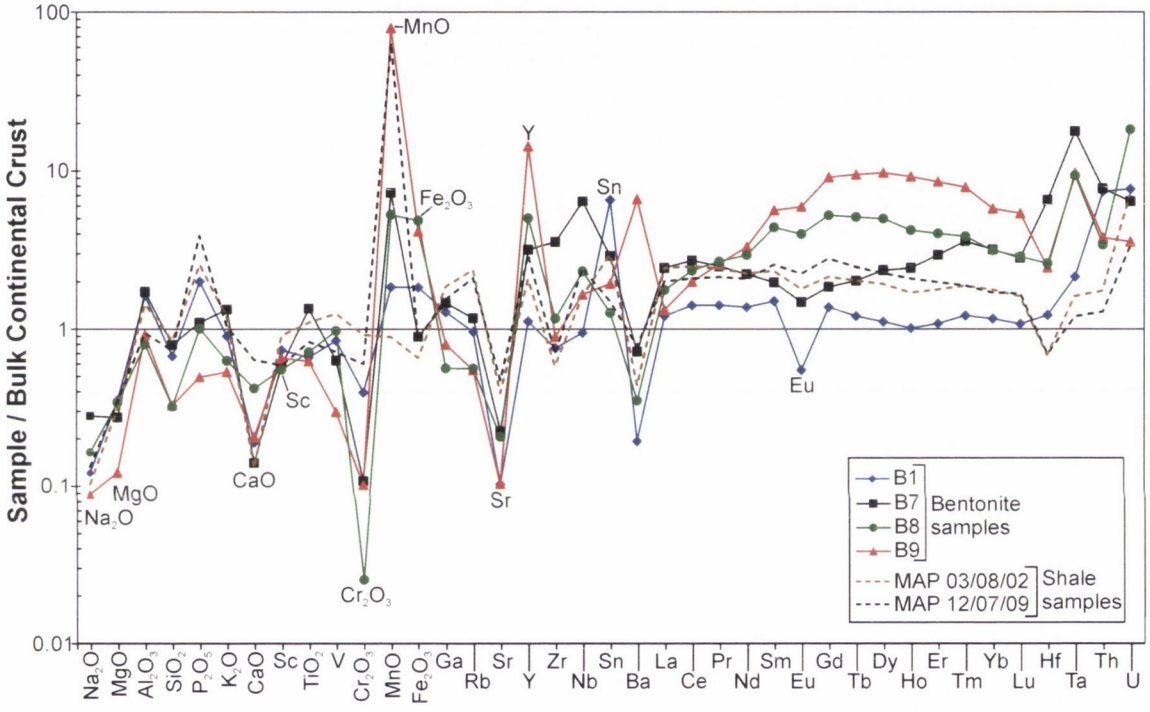

Figure 7.8. Major and trace element data from the Namurian bentonite and shale samples normalised to bulk continental crust values (Rudnick & Gao, 2003).

7.3.5. Westphalian tonstein samples

All Westphalian tonstein samples show similar elemental trends (Fig. 7.9). The samples are generally enriched in Al_2O_3, Ce, Ga (except tonstein Z1), Gd (except T1Gb), La, Nb (except Wilhelm), Nd, Pr (except T1Gb), Sm (except T1Gb), Sn, Ta, Th and U and are depleted in CaO, MgO, MnO, Na_2O, Ba, Sc, Sr (except T10), TiO_2 (except T1P) and V. Samples T75, Hagen 1 and Hagen 4, and to a lesser extent samples T13 and Z1, are notably less depleted to slightly enriched in K_2O (with respect to the continental crust; Fig. 7.9a, b). XRD analysis of material from these horizons reveals the presence of a mica peak (*c.* $8-9^{o}$ 2θ) that is absent from the other tonstein samples (Appendix 2

Table 2). Additionally, K-bearing minerals were recovered from Z1 (sanidine) and Hagen 1 (sanidine), which were identified optically following mineral separation and confirmed using SEM-EDS. The nature of the mica phase is not well constrained; however, a K-bearing mica phase could account for the elevated K_2O concentrations in these samples. The enrichment in Al_2O_3 in the tonstein samples can be attributed to the presence of kaolinite (as identified using XRD analysis; Appendix 2 Table 2).

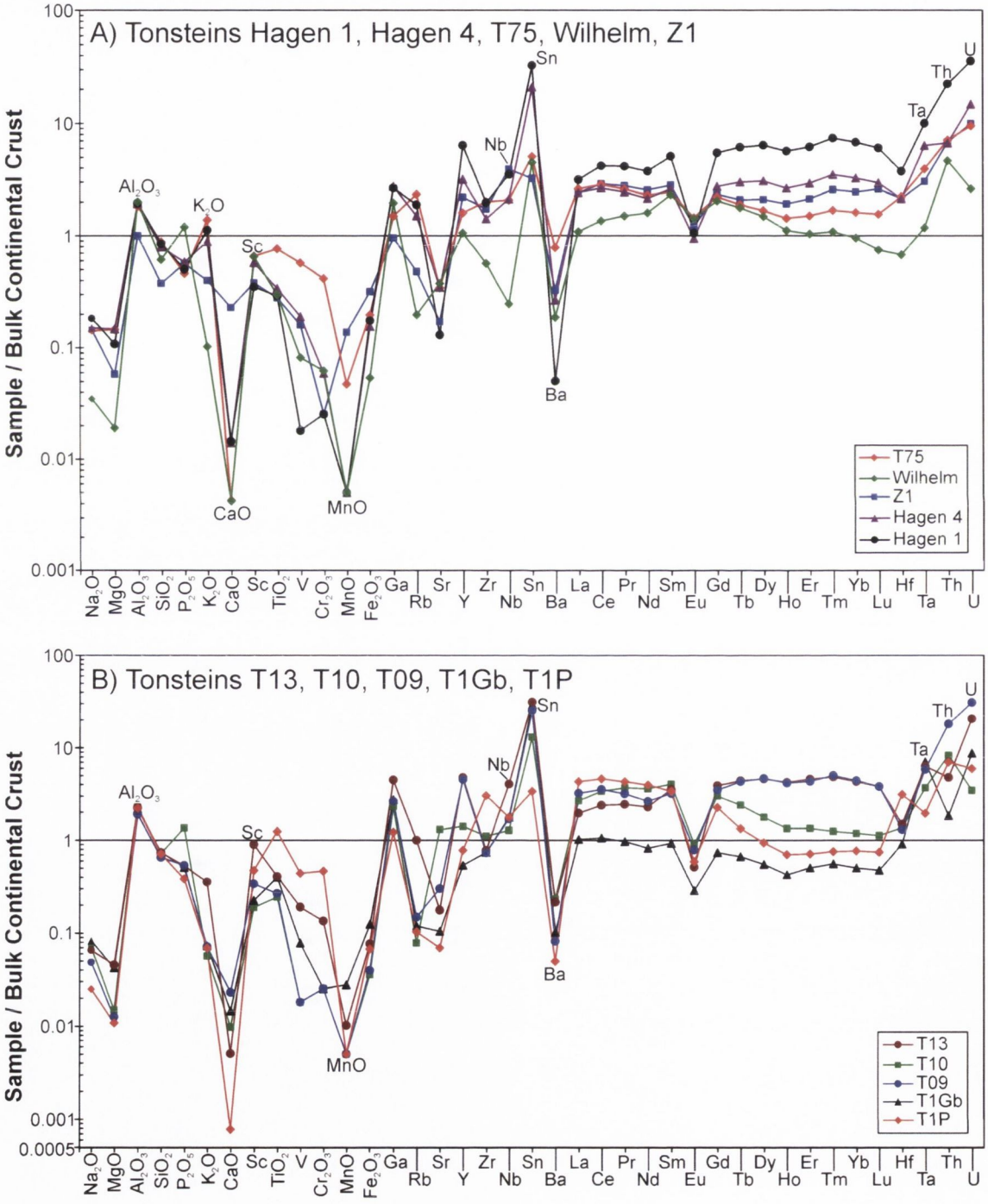

Figure 7.9 (a – b). Major and trace element data from the Westphalian tonstein samples normalised to bulk continental crust values (Rudnick & Gao, 2003).

7.4. Magma parentage of the altered ash layer samples

The whole-rock geochemistry of altered volcanic lithologies has been employed by several authors to deduce information about the composition of the original ash layers and hence the magma from which they were derived (e.g. Spears & Lyons, 1995; Huff *et al.*, 1996; Spears *et al.*, 1999; Pellenard *et al.*, 2003). The major elements (Si, Al, Na, K, Mg, Ca and Fe) that are routinely used to classify fresh or slightly altered volcanic lithologies (e.g using a total alkali versus silica diagram) are of limited use for classifying extensively altered volcanic lithologies (such as bentonites and tonsteins), because several of these elements are known to be mobile during weathering and diagenesis (Winchester & Floyd, 1977; Zielinski, 1985; Christidis, 1998; Spears *et al.*, 1999). For example, Christidis (1998) observed within the alteration profiles of two Greek ignimbrites that during the alteration of volcanic glass to bentonitic clays the alkalis were leached, Fe and Mg were taken up, Ti and Al were immobile, whereas the behaviours of Ca and Si were inconsistent between the two profiles and were possibly dependent upon the original composition of the ash.

The classification of altered volcanic lithologies instead relies on several trace elements including Ti, the high-field-strength elements (high ionic charge, small ionic radius) Zr, Nb, Hf, Ta and rare-earth elements that are generally considered to be immobile during most upper crustal processes and are also indicators of petrogenetic processes (Winchester & Floyd, 1977; Huff *et al.*, 1996). These elements are thought to reside primarily within unaltered volcanic phenocrysts (Huff *et al.*, 1996). It should be noted, however, that the concentrations of these elements can be modified by sedimentary processes including detrital additions and sediment reworking (e.g. Clayton *et al.*, 1996). Thus, the trace elements may offer insight into the chemistry and tectonic setting of the parent magma but should always be interpreted with caution.

Trace element discrimination diagrams are presented in section 7.4.1, followed by rare-earth element profiles (section 7.4.2) and the calculations of europium (Eu) anomalies (section 7.4.2.3).

7.4.1. Trace element geochemistry: discrimination diagrams

Several tectonic and magmatic discrimination diagrams have been employed to gain insight into the source magma from which the altered volcanic ash layers were originally extracted (e.g. Winchester & Floyd, 1977). Such discrimination diagrams are empirically derived, using igneous lithologies of known origin (Huff *et al.*, 1996). Sample data are presented on the Zr / TiO_2 – Nb / Y plot of Winchester & Floyd (1977) and the Ti / Th x 10 – Ce x 10 / Y – Zr / Nb ternary diagram of Batchelor & Jeppsson (1999).

7.4.1.1. Zr / TiO_2 – Nb / Y diagram (Winchester & Floyd, 1977)

Winchester & Floyd (1977) proposed a number of discrimination diagrams using various combinations of Ce, Ga, Nb, Sc, Ti, Y and Zr to make inferences about the magmatic parentage of altered volcanic lithologies. The Zr / TiO_2 – Nb / Y plot is probably the most commonly cited classification diagram proposed by Winchester & Floyd (1977). The Zr / TiO_2 and Nb / Y ratios are both indices of alkalinity, whereas the Zr / TiO_2 ratio is also a measure of magmatic differentiation (Winchester & Floyd, 1977). Sample data are plotted on the Zr / TiO_2 – Nb / Y diagram in Fig. 7.10.

There is reasonable separation between the Belgian Visean, Irish Asbian, British Namurian and the Westphalian samples when plotted on the Zr / TiO_2 – Nb / Y diagram (Fig. 7.10). The Belgian Visean bentonite samples cluster mostly within the trachyandesite field. The sample data from bentonites M, L1 and L2 plot lower within the trachyandesite field than data from bentonites L3, L4 and L5, which may indicate a slightly less evolved source composition for the former horizons. The Irish Asbian samples and British Namurian samples yield (mostly) lower Zr / TiO_2 ratios than the Belgian Visean and the Westphalian samples, suggesting a less evolved magma source for these samples. The Irish Asbian samples exhibit greater Nb / Y ratios than the Namurian samples, suggesting a more alkaline source for the former (alkali-basalt to trachyandesite). The Namurian samples yield similar Zr / TiO_2 ratios but more variable Nb / Y ratios (Fig. 7.10). The Zr / TiO_2 versus Nb / Y plot for the Namurian samples suggests a sub-alkaline, andesitic composition for the parent magma. The two Irish Brigantian bentonites investigated overlap with the Westphalian tonstein samples and plot within the rhyodacite / dacite field. The Westphalian tonstein samples plot mostly

within the rhyodacite / dacite field, suggesting a sub-alkaline, evolved (felsic) source composition.

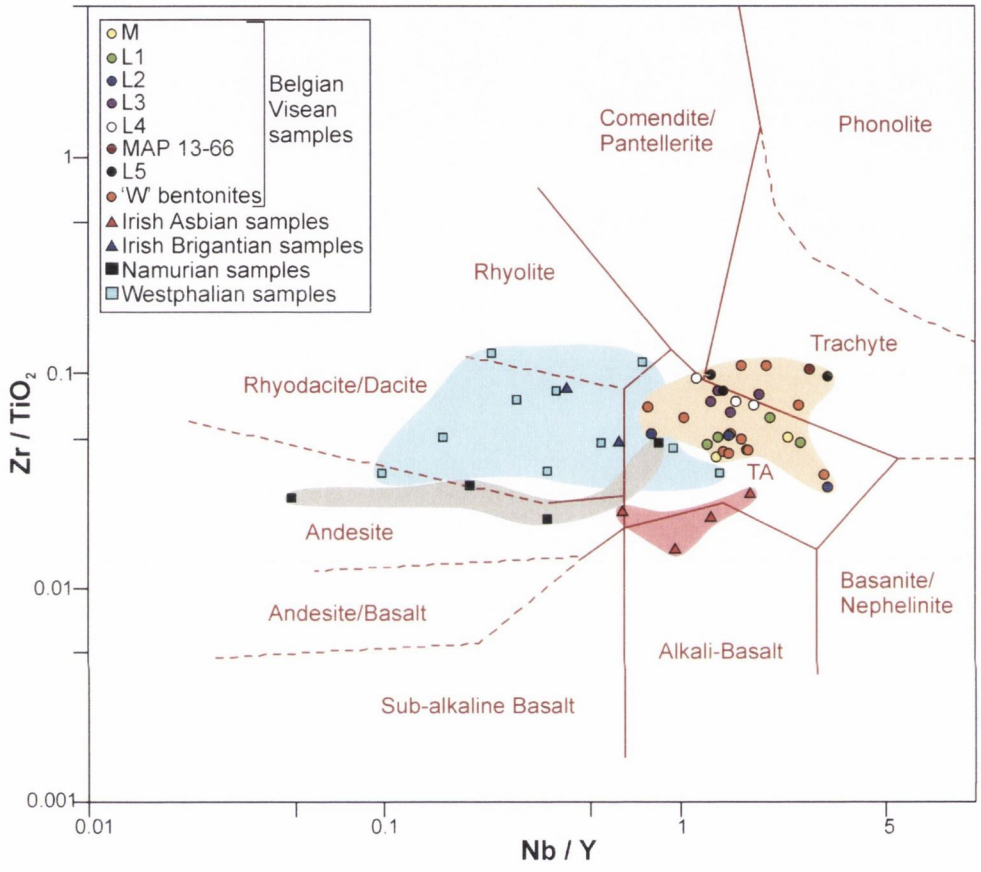

Figure 7.10. $Zr / TiO_2 - Nb / Y$ discrimination diagram (after Winchester & Floyd, 1977). TA = trachyandesite. The diagram was drawn using the GCDkit v. 2.3 (Janoušek *et al.*, 2006). The coloured fields illustrate the compositional ranges of the following samples: blue = Westphalian samples; grey = Namurian samples; orange = Belgian Visean samples; red = Irish Asbian samples.

Since the Winchester & Floyd (1977) publication there have been suggestions that yttrium can be mobilised during the alteration of volcanic rocks to bentonites (Christidis, 1998; Hill *et al.*, 2000); thus, the measured Nb / Y ratios should be regarded as maximum estimates for the alkalinity of the original ash layers.

7.4.1.2. Batchelor & Jeppsson (1999) ternary diagram

The Ti / Th x 10 – Ce x 10 / Y – Zr / Nb ternary diagram of Batchelor & Jeppsson (1999) is another magmatic discrimination diagram (Fig. 7.11). The different compositional fields are not precisely delineated within this plot. The sample data are plotted as a Batchelor & Jeppsson (1999) ternary diagram in Fig. 7.11.

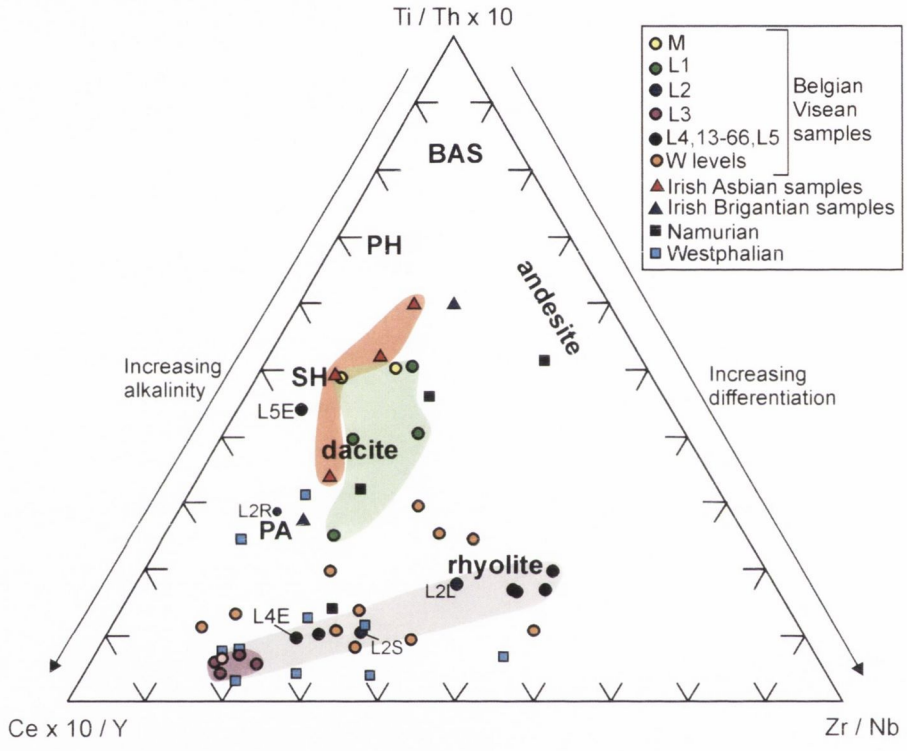

Figure 7.11. Ternary diagram of Ti / Th x 10 versus Ce x 10 / Y versus Zr / Nb from Batchelor & Jeppsson (1999). BAS = basalt; PA = pantellerite; PH = phonolite; SH = shoshonite. L2L = L2 Lives-sur-Meuse; L2R = L2 Royseux; L2S = L2 Sosoye; L4E and L5E = L4 and L5 sampled from Engihoul Quarry. The coloured fields contain the following samples: red = Irish Asbian samples; green = bentonites M and L1; grey = bentonites L3 to L5 (excluding L5 from Engihoul Quarry); purple = samples of bentonite L3.

The Belgian Visean M and L1 bentonites occupy a different area of the ternary diagram (green field in Fig. 7.11) than bentonites L3, L4, 13-66 and L5 which, apart from L5 from Engihoul, plot towards the base of the diagram (grey field in Fig. 7.11). This could be interpreted to indicate that the M and L1 bentonites were sourced from a less evolved magma than the L3 – L5 horizons. The samples from the L2 bentonite are scattered

within the ternary diagram; L2 from Royseux plots higher (L2R in Fig. 7.11) than the samples of L2 collected from Sosoye (L2S in Fig 7.11) and Lives-sur-Meuse (L2L in Fig. 7.11), which overlap with the L3 – L5 field (grey field in Fig. 7.11). The Belgian 'W' horizon samples and the Westphalian tonstein samples occupy positions towards the base of the diagram (Fig. 7.11), suggesting an evolved magma source. The Irish Asbian samples plot towards the top left of the ternary diagram, suggesting a less evolved, possibly alkaline magma source. The Irish Brigantian samples are dispersed; sample MAP 09/07/01 plots towards the top of the diagram, between andesite and phonolite, whereas sample MAP 09/07/05 plots closer to pantellerite (Fig. 7.11). The Namurian bentonite samples also show some dispersion within this plot; B1 plots within the L3 –L5 field, whereas the other three samples (B7 – B9) plot close to the andesite and dacite fields, suggesting an intermediate, sub-alkaline source.

The information obtained from both the Zr / TiO_2 – Nb / Y discrimination diagram (section 7.4.1.1) and the Ti / Th x 10 – Ce x 10 / Y – Zr / Nb ternary diagram are discussed further in section 7.5.

7.4.2. Rare-earth element geochemistry

In geochemistry, the rare-earth elements (REEs) are taken to comprise the 15 lanthanide elements (mass numbers 57 – 71), although promethium (mass number 61) does not occur in nature (it has no long-lived or stable isotope) and thus was not measured. In altered volcanic ash layers, the REEs are thought to reside mostly within non-carbonate minerals, including heavy minerals (e.g. zircon and apatite) and clay minerals (Wray, 1995; Pellenard *et al.*, 2003). REE profiles are routinely normalised to a standard reference material in order to reduce the Oddo-Harkins effect (i.e. elements with an even atomic number are more abundant in nature than elements with an odd atomic number). REE sample data from diagenetically altered volcanic ash layers have been presented normalised to CI-chondrite values (e.g. Huff *et al.*, 1996; Spears *et al.*, 1999; Pellenard *et al.* 2003) and / or various shale standards such as the USGS Cody Shale (e.g Wray, 1995; Wray & Wood, 1998; Jeans *et al.*, 2000; Pellenard *et al.*, 2003) and the Post-Archean Australian shales composite (PAAS; e.g. Clayton *et al.*, 1996). REE data are presented normalised to CI-chondrite values and Cody Shale values in subsequent sections.

7.4.2.1. CI-Chondrite normalised REE profiles

Sample REE data are presented normalised to the CI-chondrite values of McDonough & Sun (1995) in Fig. 7.12. All of the samples investigated show enrichment in REEs compared to CI-chondrite values (Fig. 7.12) and most samples show greater enrichment in LREEs compared to HREEs, which is typical of the continental crust (Rudnick & Gao, 2003). The Belgian Visean bentonite samples (Fig. 7.12a – d) show decreasing enrichment in LREEs (negative slope; La_N / Sm_N = 1.4 – 14.3; where La_N and Sm_N denote measured sample elemental concentrations normalised to the CI-chondrite values of McDonough & Sun, 1995) and moderate to large negative Eu anomalies (explained in section 7.4.2.3). Some Belgian Visean samples demonstrate a continuous decrease in enrichment from La to Lu (except for the negative Eu anomaly), whereas other samples show slight increasing trends in HREEs (Fig. 7.12a – d); however, there is no clear stratigraphic pattern to this variation. The four Irish Asbian palaeosol samples yield very similar REE plots (Fig. 7.12e), with a steep trend of decreasing LREE enrichment (La_N / Sm_N = 6.7 – 12.4), small negative Eu anomalies and an increasing trend of HREE enrichment (Fig. 7.12e; Gd_N / Sm_N = 0.73 – 0.98). The two Irish Brigantian bentonite samples exhibit negative slopes and small negative Eu anomalies (Fig. 7.12f). Sample MAP 09/07/05 has a markedly greater total REE concentration compared to sample MAP 09/07/01 (576 ppm versus 120 ppm ΣREE) and a steeper slope (La_N / Yb_N = 9.5 *c.f.* La_N / Yb_N = 2.8). The British Namurian samples yield heterogeneous REE trends (Fig. 7.12f); the B1 bentonite sample yields a markedly larger negative Eu anomaly than the other three bentonite samples. Additionally, bentonite B9 shows a trend of increasing LREE enrichment (La_N / Sm_N = 0.7), in contrast to all of the other samples analysed. The Westphalian tonsteins (Fig. 7.12g) show the greatest enrichment in REEs with respect to CI-chondrite values (La_N = 86.4 – 364.2; excluding tonsteins Wilhelm and T1Gb, La_N values are > 150). The Westphalian tonstein samples show negative trends in LREEs (La_N / Sm_N = 2.3 – 8.7), with pronounced negative Eu anomalies (Fig. 7.12g). HREE trends vary between tonstein samples; some samples show steeper slopes in HREEs (samples Wilhelm, T75, T10, T1Gb, T1P; Gd_N / Yb_N = 2.2 – 4.6) than others (Z1, Hagen 4, Hagen 1, T13, T09; Gd_N / Yb_N = 1.2 – 1.5).

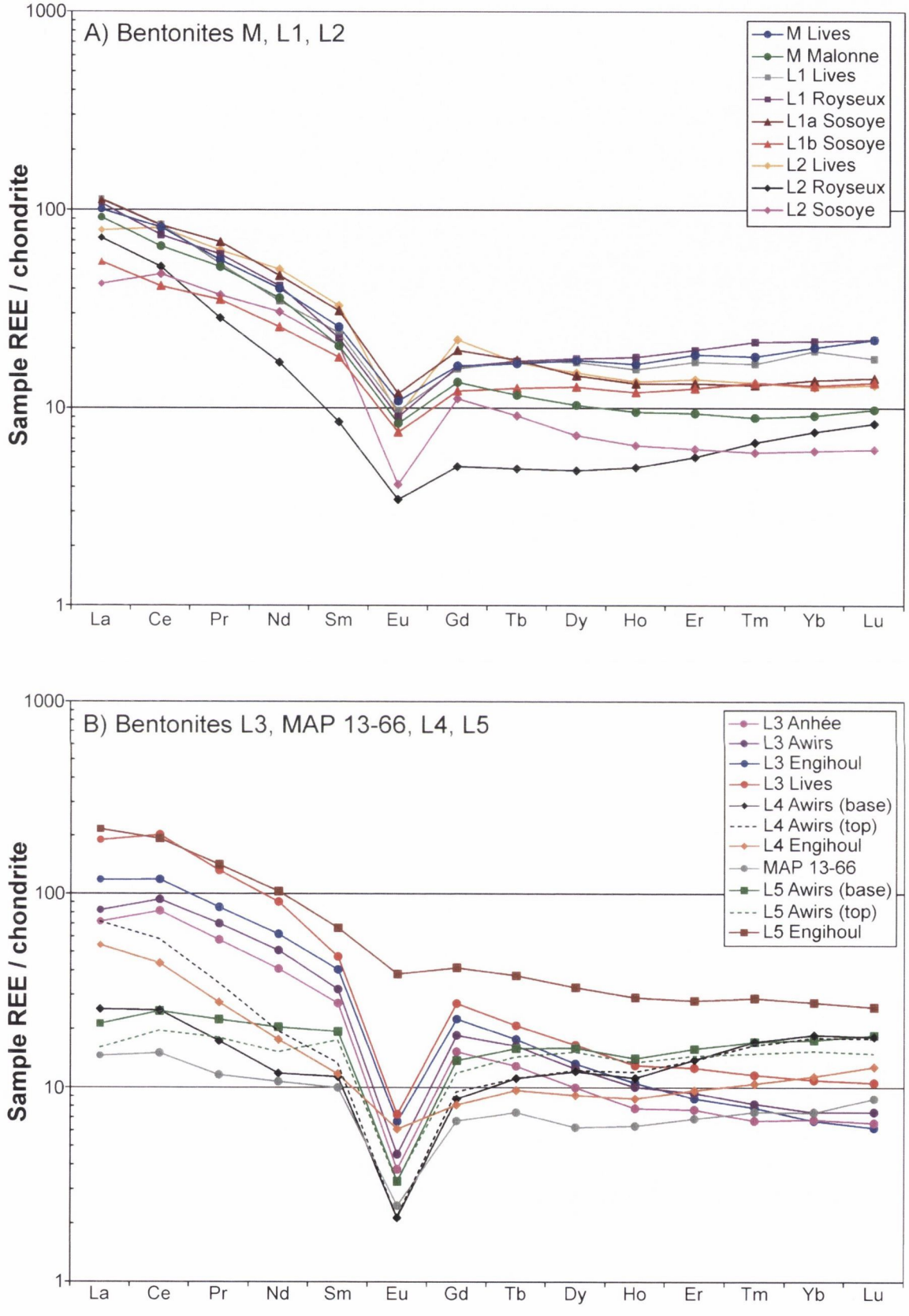

Figure 7.12 (*continued overleaf*)

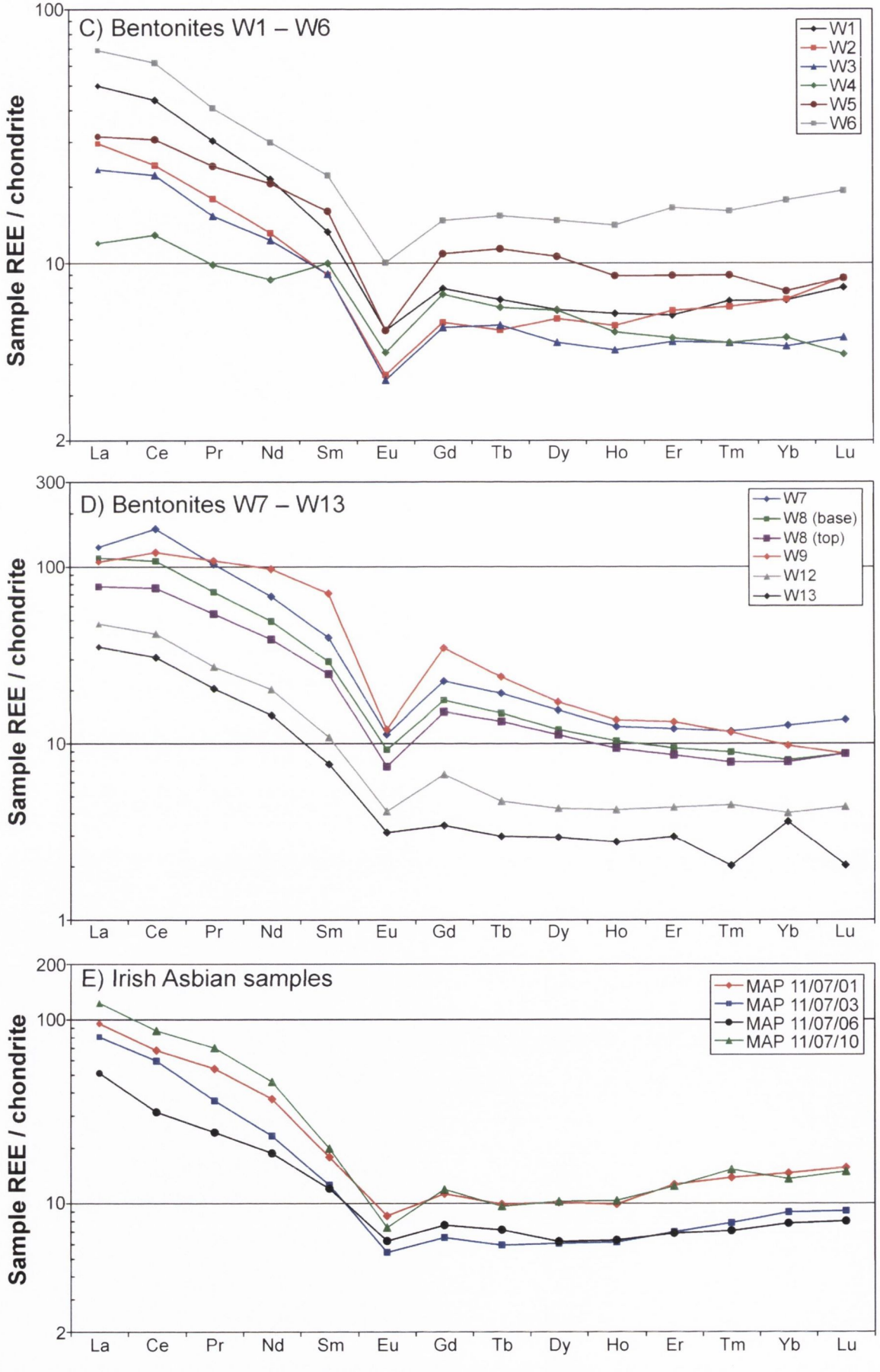

Figure 7.12 (*continued overleaf*)

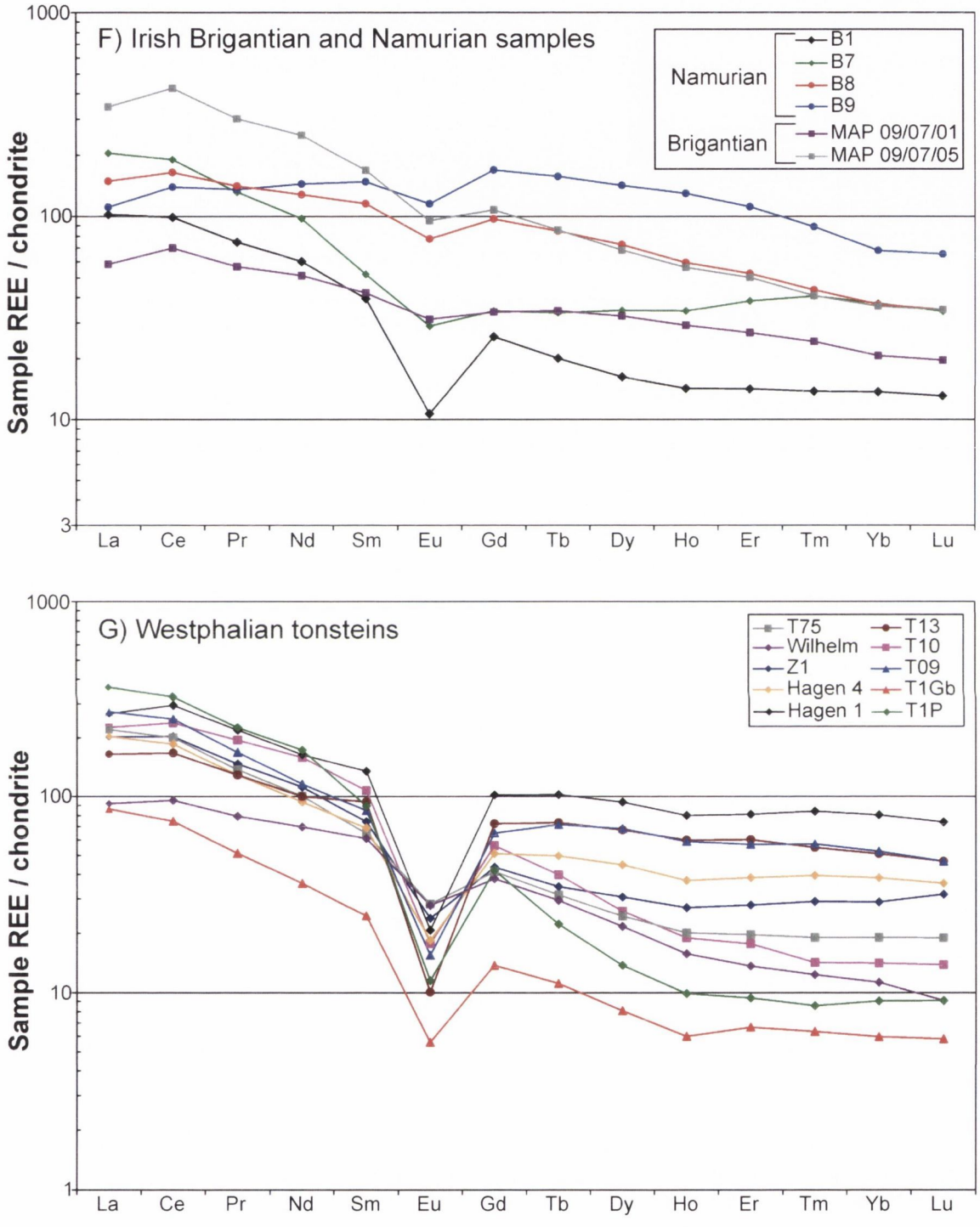

Figure 7.12 (a – g). Sample REE data normalised to CI-chondrite values (McDonough & Sun, 1995). A – D = Belgian Visean bentonites; E = Irish Asbian samples; F = Irish Brigantian and British Namurian bentonites; G = Westphalian tonsteins.

7.4.2.2. Shale-normalised REE profiles

Normalising REE sample data from diagenetically altered volcanic ash layers against composite or standard shale values has been utilised by a number of studies (e.g. Wray, 1995; Pellenard *et al.*, 2003) and has two main advantages over chondritic normalisation. Firstly, the composition of most samples is closer to shale than chondritic values and hence it is easier to resolve subtle trends between the sample data when they are normalised against shale values. Secondly, normalisation against shales can resolve, in some instances, detrital contamination as samples containing significant detritus often yield sub-horizontal shale-normalised REE profiles (e.g. Wray, 1995).

Sample REE data normalised to Cody Shale values are shown in Fig. 7.13. A notable feature of Fig. 7.13 is that the Visean limestone-hosted samples are predominantly depleted in REEs relative to the Cody Shale (Fig. 7.13a – e; L5 from Engihoul Quarry shown in Fig. 7.13c is an exception to this statement), whereas the siliciclastic-hosted samples (Brigantian, Namurian and Westphalian samples; Fig. 7.13f, g) are mostly enriched with respect to the Cody Shale. This trend does not readily correlate with the variations in magmatic source composition inferred from trace element discrimination diagrams (section 7.4.1). Trends between the immobile trace element concentrations of bentonite horizons and the lithological facies of the enclosing stratigraphy have been reported in other studies; for example, Kiipli *et al.* (2006, 2008) observed that in some eastern European Silurian-aged bentonites, immobile trace element concentrations increased systematically between a shallow water carbonate platform environment and a deeper water siliciclastic shelf environment. In these studies (Kiipli *et al.*, 2006, 2008), the bentonites were correlated laterally using chemical variations in sanidine phenocrysts. Kiipli *et al.* (2006, 2008) attributed the trend between immobile trace element concentrations and variations in the enclosing lithology to differences in the intensity of alteration (of the original volcanic ash material) in different depositional environments, with volcanic ash deposited in the deeper water shelf environments experiencing more intense alteration and leaching of major elements, resulting in a greater residual enrichment in immobile elements (Kiipli *et al.*, 2006, 2008). A similar interpretation could reconcile the observed relationship between the REE enrichment / depletion patterns and the host lithology of the samples studied herein; i.e. more intense alteration of the siliciclastic-hosted samples deposited in paralic environments (Brigantian and Namurian samples) and acidic coal swamps (Westphalian

tonsteins) resulted in a greater loss of major elements and a greater residual enrichment of immobile rare-earth elements compared to the limestone-hosted bentonites, which were deposited in a shallow marine, carbonate platform environment.

Between the Belgian Visean samples, the M and L1 horizons show similar REE trends when normalised against the Cody Shale; the samples are generally depleted with respect to the Cody Shale and exhibit relatively flat to slightly decreasing LREE trends, small negative Eu anomalies and constant to slightly increasing HREE trends (Fig. 7.13a). Samples from bentonite L3 demonstrate a slight increasing trend from La to Sm, a large Eu anomaly and constant to slightly decreasing HREE patterns (Fig. 7.13b). Samples from the L2 horizon show less consistent results. The samples of L2 from Lives-sur-Meuse and Sosoye have similar trends to those obtained from samples of the L3 horizon (Fig 7.13b); however, the sample of L2 from Royseux yields a smaller Eu anomaly and an REE pattern that is similar to the samples of bentonites M and L1 (Fig. 7.13a).

With the exception of the top sample from L4 at Awirs West Quarry, the remaining analyses from bentonites L4, 13-66 and L5 from Awirs West Quarry (Fig. 7.13c) have comparable REE patterns that are different to those from samples of the L3 horizon (as mentioned in section 7.3.1). REE traces from horizons L4, 13-66 and L5 at Awirs West Quarry are depleted with respect to the Cody Shale and show a trend of decreasing depletion from the La to Lu as well as large negative Eu anomalies (Fig. 7.13c). The upper (top) sample of the L4 horizon at Awirs West Quarry, in contrast, shows a negative slope from La to Sm (Fig 7.13c). L4 sampled from Engihoul Quarry shows a similar trend to the upper sample of L4 from Awirs West Quarry (Fig 7.13c) but without the prominent Eu anomaly, whereas L5 sampled from Engihoul Quarry has a markedly different, sub-horizontal trend (Fig. 7.13c).

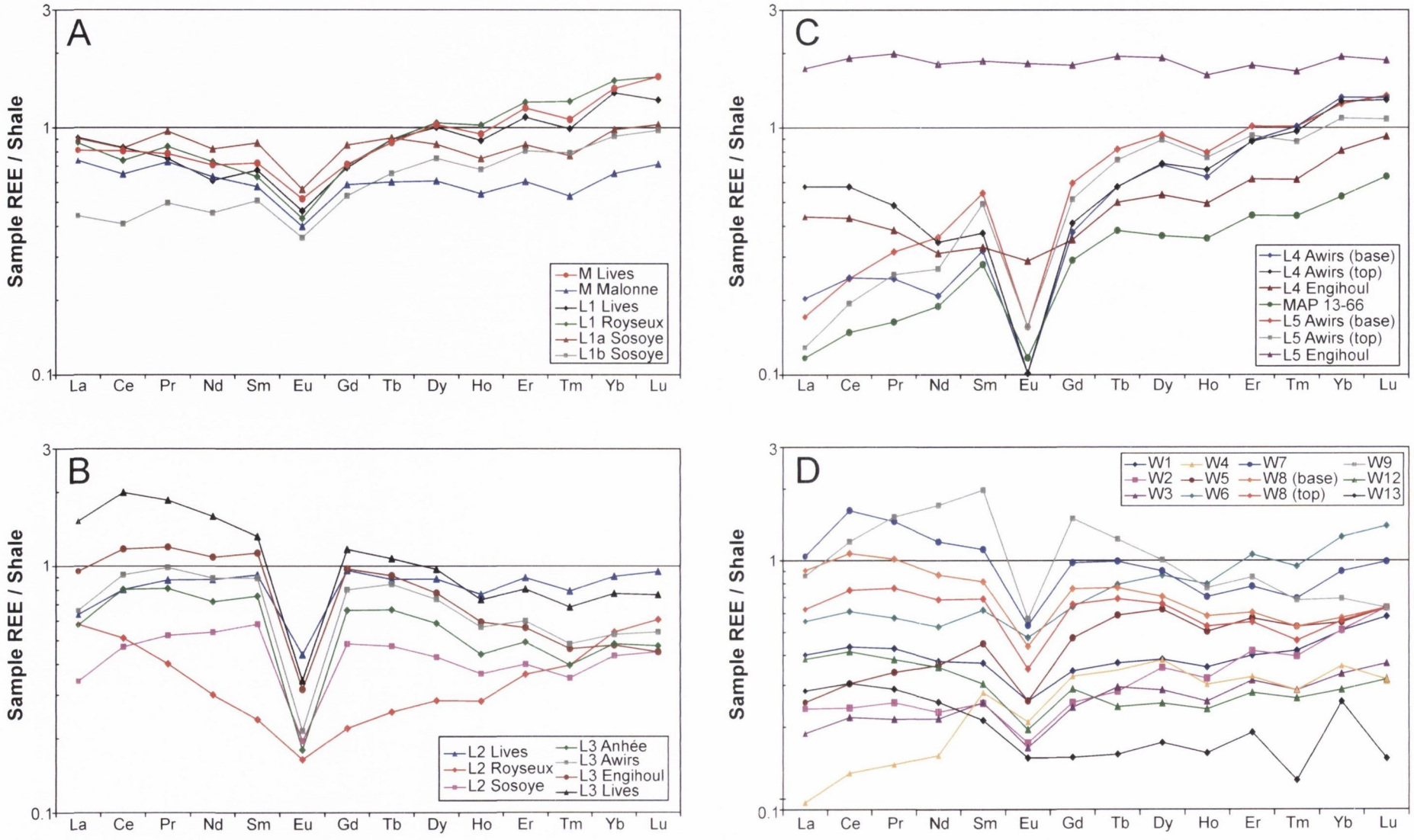

Figure 7.13 (*continued overleaf*)

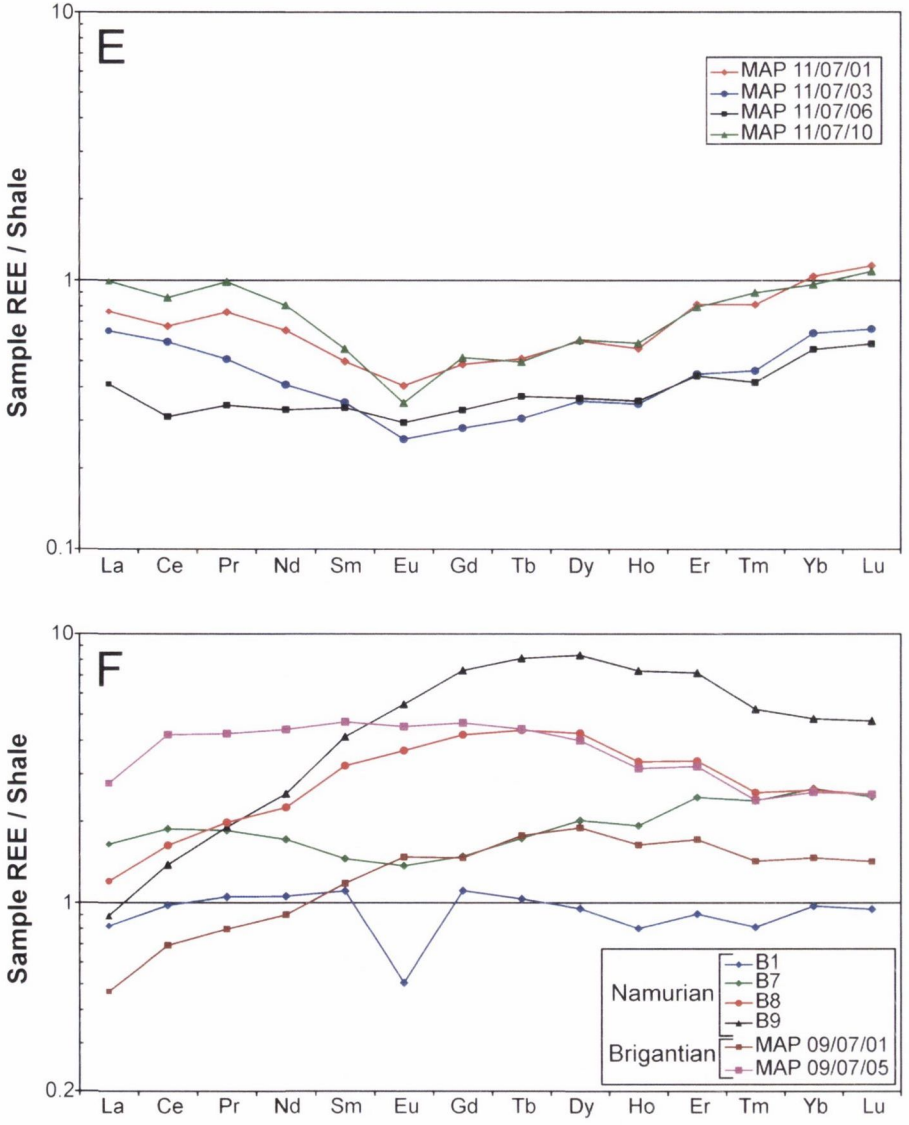

Figure 7.13. Sample REE data normalised to Cody Shale values (Govindaraju, 1994). A–D = Belgian Visean bentonites; E = Irish Asbian samples; F = Irish Brigantian and British Namurian bentonites; G = Westphalian tonsteins.

The Belgian 'W' levels have similar REE profiles; most are depleted with respect to the Cody Shale and show sub-horizontal trends with moderate negative Eu anomalies (Fig. 7.13d). The Irish Asbian palaeosol samples yield comparable REE patterns with respect to the Cody Shale; i.e. samples are depleted in REEs with respect to the Cody Shale and show decreasing LREE trends and increasing HREE trends (Fig. 7.13e). The Irish Brigantian and British Namurian samples yield markedly different REE trends (Fig. 7.13f). These samples are generally enriched in REEs with respect to the Cody Shale. The sample of bentonite B1 shows similar REE enrichment to the Cody Shale and yields a sub-horizontal trend with a pronounced negative Eu anomaly (Fig. 7.13f). The Westphalian tonstein samples yield similar REE patterns, with most samples enriched in REEs with respect to the Cody Shale and displaying large negative Eu anomalies (Fig. 7.13g).

7.4.2.3. Europium anomalies

The europium (Eu) anomaly is a measure of the amount of Eu that is present in a sample compared to how much is predicted to be present within a sample based on interpolation between the adjacent elements to Eu: samarium (Sm) and gadolinium (Gd). The Eu anomaly is calculated as follows:

$$\text{Europium anomaly} = \text{Eu/Eu}^* = \frac{\text{Eu}_N}{\sqrt{\text{Sm}_N \times \text{Gd}_N}}$$

where Eu_N, Sm_N and Gd_N denote measured elemental concentrations that are normalised to CI-chondrite values (McDonough & Sun, 1995) and Eu* represents the amount of Eu predicted to be present based on the measured concentrations of Sm and Gd.

Eu / Eu* ratios of > 1 are termed positive anomalies, Eu / Eu* ratios of < 1 are termed negative anomalies and a ratio of 1 indicates no anomaly (Huff *et al.*, 1996). Negative Eu anomalies in altered volcanic ash layers are often interpreted as evidence for an evolved, sub-alkaline magma parentage (Wray, 1995; Huff *et al.*, 1996; Jeans *et al.*, 2000; Pellenard *et al.*, 2003) and are thought to arise through the partitioning of europium into feldspar, with feldspar fractionation resulting in a depletion of europium within the residual melt (Wray, 1995; Pellenard *et al.*, 2003). The calculated Eu

anomalies for all sample data are presented in Fig 7.14 and are also shown in Appendix 2 Table 1.

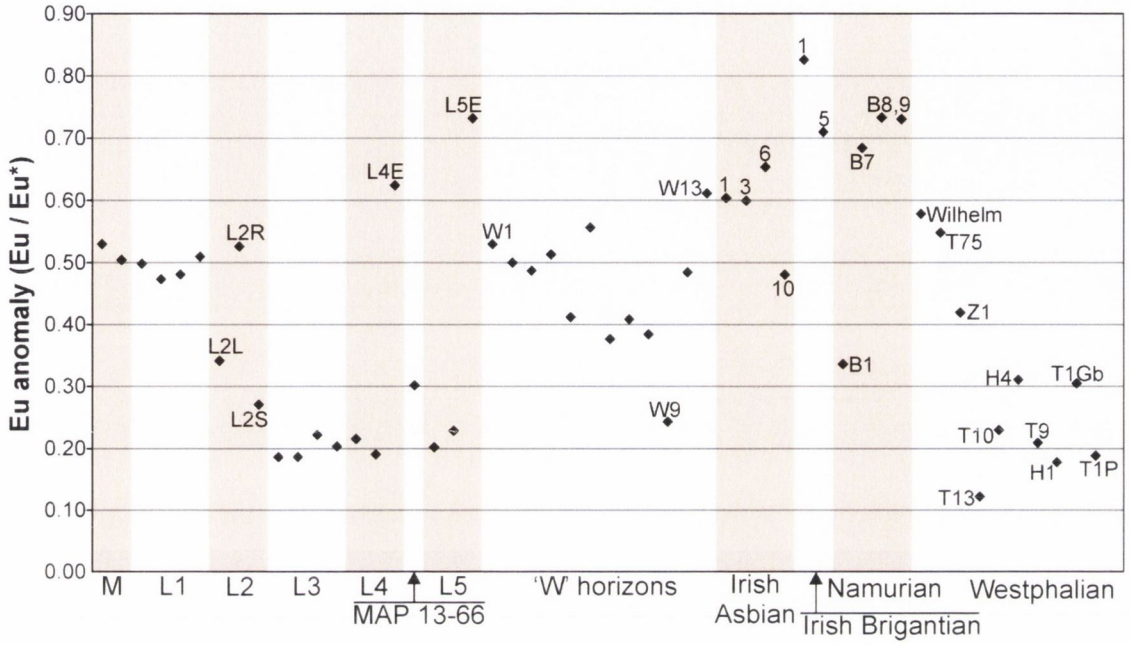

Figure 7.14. Europium anomalies calculated for the analysed bentonites and tonsteins. L4E and L5E = L4 and L5 sampled from Engihoul Quarry. L2L = L2 from Lives-sur-Meuse; L2R = L2 sampled from Royseux; L2S = L2 from Sosoye. H1 = Hagen 1; H4 = Hagen 4. Data point numbers for Irish Asbian and Brigantian samples correspond to sample numbers (prefix MAP 11/07/ and MAP 09/07/ to the numbers shown for Irish Asbian and Brigantian samples respectively to obtain the full sample numbers). The pink bars are shown to aid visualisation.

Belgian Livian samples of bentonites M and L1, and L2 from Royseux, demonstrate moderate negative Eu anomalies (0.47 – 0.53; Fig. 7.14). The remaining Belgian 'L' samples (L2 from Sosoye and Lives-sur-Meuse, L3, L4, 13-66, L5; Fig. 7.14), excluding L4 and L5 sampled from Engihoul Quarry, have large negative Eu anomalies (0.19 – 0.34). The latter two samples yield relatively small negative Eu anomalies (0.62 and 0.73 respectively). Most of the Belgian 'W' bentonite samples show moderate negative Eu anomalies (0.38 – 0.61), with the exception of the W9 bentonite, which shows a particularly large negative anomaly (0.24). Irish Asbian levels yield similar small to moderate negative anomalies (0.48 – 0.65), whereas the Irish Brigantian bentonite samples (MAP 09/07/01, MAP 09/07/05) have small negative anomalies (0.83

and 0.71 respectively). Of the British Namurian samples, B1 shows a large negative anomaly (0.34), while the other three Namurian samples (B7 – B9) all show smaller negative anomalies (0.68 – 0.73). The Westphalian tonsteins Wilhelm and T75, which are thought to be lateral equivalents (Delcambre, 1996), demonstrate comparable, moderate negative Eu anomalies (0.58 and 0.55 respectively), whereas the Bolsovian tonsteins (all tonstein samples except Wilhelm, T75 and Z1) are characterised by large negative Eu anomalies (0.12 – 0.31).

7.5. Discussion: magmatic parentage of the original ash layers

7.5.1. Belgian Visean samples

The trace element discrimination diagrams (section 7.4.1) suggest an evolved, possibly mildly alkaline (trachyandesite) parent magma composition for the Belgian Visean bentonite samples. This is reinforced by the presence of negative Eu anomalies (section 7.4.2.3) in these samples. There is evidence to suggest a possible change in source composition from late Moliniacian – early Livian times (bentonites M and L1) to mid-to-late Livian times (bentonites L3, 13-66, L4 and L5). The samples from the M and L1 horizons yielded lower Zr / TiO_2 values (Fig. 7.10), plot towards less evolved compositions on the Batchelor & Jeppsson (1999) ternary diagram (Fig. 7.11) and exhibit smaller negative Eu anomalies (Fig. 7.14) compared to the samples from bentonites L3, L4, 13-66 and L5. Taken together these data suggest that the source of the upper Moliniacian – lower Livian bentonite horizons may have been slightly less evolved than the source of the mid-to-upper Livian bentonites.

The presence of quartz and calcite in samples of the L4 and L5 bentonites from Engihoul Quarry and the absence of these minerals from the same horizons at Awirs West Quarry (section 7.3.1.2) suggests that the samples from Engihoul Quarry have been affected by diagenetic fluids or are contaminated by detritus. There is better agreement between the samples of L4 from Awirs West and Engihoul when plotted on trace element discrimination diagrams (Figs. 7.10 and 7.11) and as shale-normalised rare-earth element data (Fig. 7.13c) than between samples of the L5 bentonite from the same localities. This may indicate that L5 is more altered (or contaminated) than L4 at Engihoul Quarry.

In terms of possible source locations for the Belgian Visean samples, there are known intrusive rocks of Visean age within the Variscan orogenic belt. These intrusive rocks are high-K diorites and granites (e.g. Schaltegger, 1997) that occur in a belt parallel to the axis of the Variscan orogen (Schaltegger, 1997; Kotková *et al.*, 2010) and have been suggested to trace a major Variscan palaeosuture (Kotková *et al.*, 2010). These rocks are thought to have formed through adiabatic melting of lithospheric mantle and lower crust, probably in association with a supra-subduction setting (Kotková *et al.*, 2010; references therein). Several of these intrusions have been isotopically dated previously, mostly using the U-Pb zircon ID-TIMS method, although some were dated using other methodologies including the U-Pb zircon SHRIMP, U-Pb rutile ID-TIMS, $^{207}Pb/^{206}Pb$ zircon evaporation and $^{40}Ar/^{39}Ar$ (biotite, hornblende) methods (see Table 6 of Kotková *et al.*, 2010, for a detailed summary of the available age data). The published U-Pb zircon ID-TIMS isotopic dates from these intrusions predominantly cluster between 340 Ma and 330 Ma (Kotková *et al.*, 2010). The Belgian Visean bentonite horizons dated using the U-Pb zircon CA-ID-TIMS method (sections 3.3.4 and 3.3.5) are compatible with this range of dates (L1 = 340.13 ± 0.18 Ma; W13 = 332.50 ± 0.07 Ma; Table 3.1). Thus, it may be that the investigated Belgian Visean bentonites represent an extrusive expression of these widespread, high-K Variscan intrusive rocks.

7.5.2. Irish Asbian samples

The trace element discrimination plots (Figs. 7.10 and 7.11) suggest a less evolved (basaltic to andesitic), possibly alkaline magmatic source for the Irish Asbian samples. This is corroborated by the small negative Eu anomalies and the rarity of zircon in these samples (section 4.2). There are several known local volcanic centres of similar age within Great Britain and Ireland that contain predominantly basaltic volcanic rocks; for example, within the Limerick syncline (Somerville *et al.*, 1992), the Midland Valley of Scotland (Timmerman, 2004) and Derbyshire, northern England (MacDonald *et al.*, 1984). These are all possible source locations for the ash material within these Irish Asbian palaeosol horizons. It is unclear where the few zircons of Carboniferous age in samples MAP 11/07/01 and MAP 11/07/03 (see section 4.2.2) originated from; it is possible that these grains may have been transported in from volcanic centres further afield or that they may represent detrital reworking of older Carboniferous lithologies (section 4.2.3).

7.5.3. Irish Brigantian samples

The trace element discrimination diagrams yielded inconsistent information for the Irish Brigantian samples; the Zr / TiO_2 – Nb / Y (Winchester & Floyd, 1977) plot suggests an evolved source composition for these samples (rhyodacite / dacite; Fig. 7.10); however, the sample data show more dispersion when plotted on the Batchelor & Jeppsson (1999) ternary diagram (Fig. 7.11), with sample MAP 09/07/01 plotting between andesite and phonolite and sample MAP 09/07/05 plotting closer to pantellerite (Fig. 7.11). Additionally, the small negative Eu anomalies obtained from these samples (section 7.4.2.3) and the lack of an obvious Carboniferous magmatic zircon population (section 4.3.2) may argue against an evolved magma source. As discussed in section 4.3.2, these samples contain evidence of inherited zircon grains that may arise from detrital contamination or xenocrystic inheritance. It is possible that detrital and / or xenocrystic additions have modified the whole-rock geochemistry of these bentonite horizons to the extent that their whole-rock geochemistry no longer reflects the original composition of the parent magma (section 4.3.2).

7.5.4. British Namurian samples

The trace element discrimination diagrams (Figs. 7.10 and 7.11) suggest an intermediate, sub-alkaline source composition (andesitic) for these samples. Bentonites B7, B8 and B9 yielded minor negative Eu anomalies, which could be interpreted to reflect a less evolved magma source. The presence of magmatic zircon (sections 5.2.2 and 5.2.3) and the lack of significant quartz as shown from the sample XRD analyses (Appendix 2 Table 2) further support an intermediate composition for these bentonites. The sub-horizontal shale-normalised REE profile obtained from bentonite B1 (section 7.4.2.2; Fig. 7.13f), together with the presence of quartz (as identified by XRD analysis; Appendix 2 Table 2) and rounded, inherited zircon grains in this sample (sections 5.2.2.1 and 5.2.3.1) strongly suggests that bentonite B1 is contaminated by sedimentary detritus.

Spears *et al.* (1999) investigated a number of Namurian bentonites within the central Pennine Basin that are considered to be lateral equivalents of the Namurian samples investigated in this thesis. Using a similar approach to that undertaken in this project

(whole-rock geochemistry; trace element discrimination diagrams and rare-earth element profiles), Spears *et al.* (1999) inferred a slightly more evolved (rhyodacite / dacite), sub-alkaline original composition for the central Pennine bentonites. Spears *et al.* (1999) further suggested a magma source location outside of Great Britain and Ireland, probably within the Variscan orogenic belt or, less likely, from the more distal eastern (destructive) margin of the East European Craton (Spears *et al.*, 1999). A magma source external to Great Britain and Ireland seems likely as magmatism within Great Britain and Ireland during Namurian times was predominantly of mafic composition (Stephenson *et al.*, 2003).

7.5.5. Westphalian tonstein samples

The trace element discrimination diagrams (Figs. 7.10 and 7.11) suggest an evolved, sub-alkaline magma source (dacite / rhyodacite), which is corroborated by the large negative Eu anomalies calculated for these samples (section 7.4.2.3). Similar interpretations have been suggested for Westphalian tonsteins preserved on mainland Europe (e.g. some French and German tonsteins; Spears & Kanaris-Sotiriou, 1979) and some British tonsteins (Spears & Kanaris-Sotiriou, 1979; Spears & Lyons, 1995). There have been suggestions that these tonsteins originated within the Variscan orogenic belt (Spears & Kanaris-Sotiriou, 1979).

7.6. Conclusions

The whole-rock geochemistry of bentonite and tonstein samples can provide insight into the original magmatic parentage of these altered volcanic ash horizons. The major elemental geochemistry is of limited use in this respect because several elements are known to be mobile during diagenetic alteration. Using several trace elements and rare-earth elements, which are thought to be relatively immobile during alteration and are also indicators of source composition (e.g. differentiation, alkalinity), differences in source compositions between the Belgian Visean, Irish Asbian, British Namurian and the Westphalian tonstein samples have been inferred. The Belgian Visean bentonite horizons were probably sourced from an evolved, possibly mildly alkaline magma that was probably derived from within the Variscan orogenic belt. The trace element data from the Irish Asbian palaeosol horizons suggests a more mafic source composition for

these horizons, which could have originated locally from known magmatic centres in Great Britain and Ireland. The original composition and source location of the Irish Brigantian samples is uncertain. There is evidence to support possible detrital contamination within these horizons and it is unclear whether their whole-rock geochemistry still preserves a record of the original ash composition. The geochemical data from the British Namurian samples suggests an intermediate, sub-alkaline source. The source of these horizons was probably external to Britain and Ireland as there is a lack of volcanic centres of suitable composition within this region. The Variscan orogenic belt is the likely location of the volcanoes that sourced these horizons but further work is necessary to confirm this. The geochemical data from the Westphalian tonstein samples indicate an evolved, sub-alkaline (dacite / rhyodacite) original ash composition that was most likely sourced from within the Variscan orogenic belt.

Chapter 8

Conclusions

High-precision U-Pb zircon CA-ID-TIMS dating was undertaken on several diagenetically altered volcanic ash layers that occur interbedded with western European sedimentary strata. Eight horizons yielded precise U-Pb zircon age constraints (< 0.1 % uncertainty on weighted mean $^{206}Pb/^{238}U$ dates, 2σ), which are summarised in Fig. 8.1. U-Pb zircon CA-ID-TIMS dating was undertaken on four additional layers (horizons W12, B1, T1P and T1Gb; Fig. 8.1); however, these samples failed to yield statistically robust isotopic dates and, with the exception of tonstein T1Gb, these samples yielded complex results. Some of the complexity may arise from residual lead loss that was not removed using the chemical abrasion method, although the presence of further complexities (particularly in the data from W12 and T1P), such as antecrystic grains (*sensu* Miller *et al.*, 2007), cannot be excluded on the basis of the available data. Only preliminary data were obtained from T1Gb, which are encouraging but are of insufficient quantity to provide a robust age estimate for this tonstein horizon.

The new U-Pb zircon CA-ID-TIMS dates are from biostratigraphically well constrained horizons and provide additional high-precision age constraints for improved calibration of the Carboniferous timescale. These dates are substantially more precise than the majority of existing published data from western European diagenetically altered ash layers, which were mostly obtained using the U-Pb zircon SHRIMP (e.g. Riley *et al.*, 1993) and $^{40}Ar/^{39}Ar$ sanidine methods (e.g. Hess & Lippolt, 1986). Additionally, the new U-Pb zircon dates presented in this thesis complement the recently published U-Pb zircon datasets of Gastaldo *et al.* (2009) and Davydov *et al.* (2010), providing absolute age constraints on stratigraphic intervals that are not well constrained by these datasets (i.e. the mid-to-upper Visean and the upper Serpukhovian to Baskhirian; see Fig. 1.4).

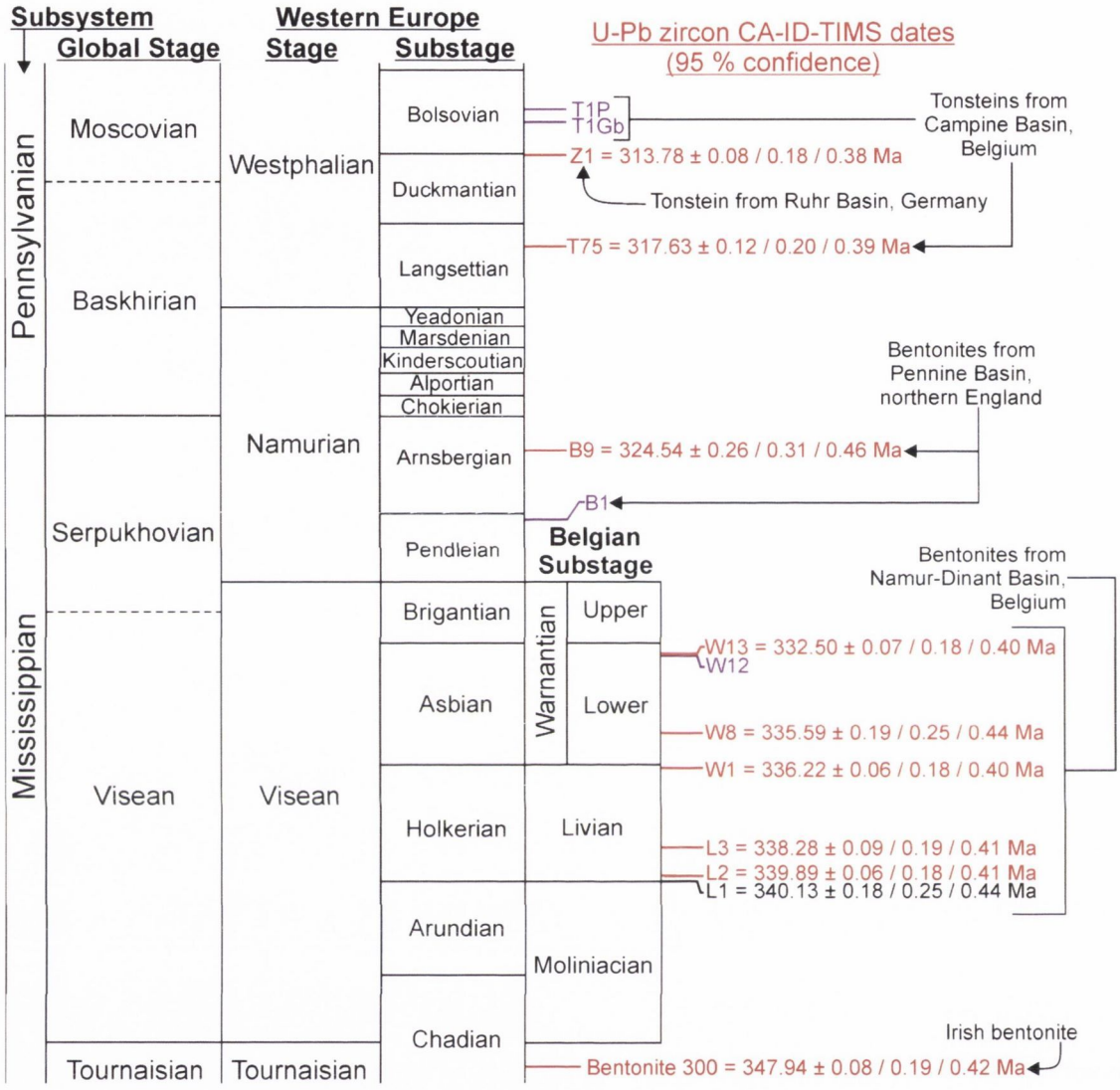

Fig. 8.1. Stratigraphic column summarising the high-precision U-Pb zircon CA-ID-TIMS dates reported in this thesis (dates shown in red). Bentonites and tonsteins shown in purple were dated using the U-Pb zircon CA-ID-TIMS method but yielded inconclusive results (W12, B1, T1P) or only preliminary data were obtained (T1Gb). The L1 horizon was dated prior to this PhD project by D. Chew and M. Ovtcharova (section 3.3.4.1). The U-Pb dates are quoted as weighted mean $^{206}Pb/^{238}U$ dates and the uncertainties are given in the ± X / Y / Z notation of Schoene *et al.* (2006), where the X uncertainty level represents the internal error only, the Y uncertainty level is the internal error plus isotopic tracer calibration uncertainties and the Z uncertainty level includes the internal error, tracer calibration uncertainties and ^{238}U decay constant uncertainties.

The new U-Pb zircon dates from western European diagenetically altered volcanic ash layers were employed to estimate the average periodicity of mid-to-upper Visean (Livian and Lower Warnantian) sedimentary cycles from the Namur-Dinant Basin, Belgium, and Namurian to Westphalian siliciclastic sedimentary cycles within the Pennine and Ruhr basins (England and Germany respectively). A summary of these periodicity estimates is shown in Fig. 8.2.

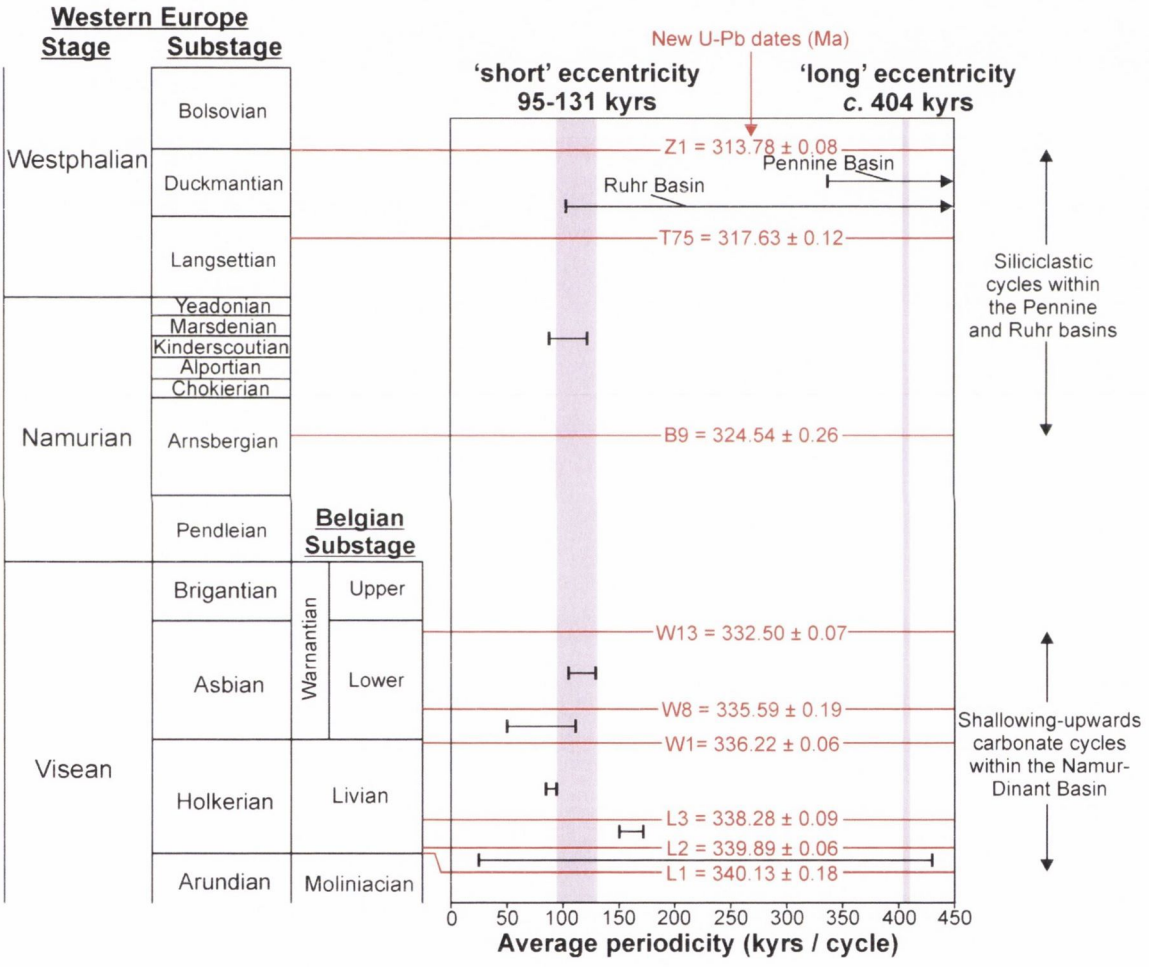

Figure 8.2. Average periodicities of sedimentary cycles that occur between the dated bentonite and tonstein horizons. It is not possible to compute a periodicity for cycles between W13 and B9 due to a major change in sedimentation style across western Europe during late Visean to early Namurian times. The periodicity estimate for cycles between bentonite B9 and tonstein T75 uses the Namurian cycle record from the Pennine Basin and the lower Langsettian cycle record from the Ruhr Basin. The new U-Pb dates quoted are $^{206}Pb/^{238}U$ weighted mean dates. U-Pb zircon date uncertainties are shown at the 95 % confidence level and exclude systematic uncertainties arising from the calibration of the isotopic tracer solution and the ^{238}U decay constant.

The calculated average periodicities suggest that the Livian sedimentary cycles of the Namur-Dinant Basin, Belgium, do not adhere to a uniform periodicity (Fig. 8.2). These cycles also show limited overlap with Milankovitch cycle periodicities (Fig. 8.2). In contrast, periodicity estimates from the Lower Warnantian cycles within the Namur-Dinant Basin (between horizons W1 and W13 in Fig. 8.2) and the Arnsbergian to Langsettian siliciclastic cycles within the Ruhr and Pennine Basins (between horizons B9 and T75 in Fig. 8.2) overlap within uncertainty with the *c.* 100 kyrs Milankovitch eccentricity cycle, which is the dominant Milankovitch frequency observed in the Pleistocene glacial record (e.g. Hays *et al.*, 1976). Thus, the periodicity calculations may support the hypothesis that the Lower Warnantian and the Arnsbergian to Langsettian cycles are of glacio-eustatic origin. It is not possible to generate precise periodicity estimates for the upper Langsettian to Duckmantian sedimentary cycles (between tonsteins T75 and Z1) because there is considerable uncertainty in the number of eustatic sedimentary cycles that occur between these tonsteins.

The appearance of glacio-eustatic sedimentary cyclicity has been suggested to signify the onset of major Gondwanan glaciation (e.g. Wright & Vanstone, 2001). However, in western Europe the appearance of sedimentary cyclicity is diachronous. Sedimentary cyclicity appears earlier in Belgium (Livian / Holkerian times) than in Britain and Ireland (Asbian times). The average cycle periodicities calculated for the Livian sedimentary cycles do not lend support for these cycles being of glacio-eustatic origin. These cycles appear to be an isolated occurrence within western Europe despite the occurrence of similar shallow-water depositional settings in parts of Britain, which should be sensitive to even small eustatic oscillations (Wright & Vanstone, 2001). It could be that the Belgian Livian sedimentary cycles are only of local significance (i.e. not glacio-eustatic). In contrast to the Livian cycles, Belgian Lower Warnantian cycles have comparable lateral equivalents in Britain and Ireland (e.g. Wright & Vanstone, 2001; Gallagher *et al.*, 2006) and yield periodicities that are compatible with Milankovitch *c.* 100 kyrs eccentricity forcing, which may support a glacio-eustatic origin for these cycles. The available data therefore support the suggestions of Wright & Vanstone (2001) that major Carboniferous glaciation commenced at close to the base of the Asbian Substage (correlated with the base of the Belgian Warnantian Substage). Furthermore, the new U-Pb zircon CA-ID-TIMS dates from the Belgian Visean bentonite horizons constrain the onset of glaciation to between 336.22 ± 0.40 Ma and

335.59 ± 0.44 Ma (i.e. between bentonites W1 and W8; uncertainties are at the 95 % confidence level and include systematic uncertainties in the calibration of the isotopic tracer solution and the ^{238}U decay constant).

Stable isotope ($\delta^{13}C$ and $\delta^{18}O$) and magnetic susceptibility (MS) analyses were undertaken on whole-rock carbonate samples from Livian and Lower Warnantian shallowing-upwards carbonate sedimentary cycles within the Namur-Dinant Basin, Belgium. The relationship between the sedimentary cycles and the MS record is complex. Some sedimentary cycles, such as those within the Corphalie Member and the lower part of the Awirs Member (Lives Formation; lower Livian), show a close correspondence with the MS record (within the studied sections: Lives-sur-Meuse, Awirs West Quarry), with weak MS signal intensities within the lower (subtidal) bioclastic limestones and greater MS intensities within the upper (intertidal / supratidal) micrites. These MS variations are consistent with the general theory of Crick *et al.* (1997), that MS signal of marine carbonates primarily reflects changes in the flux of detrital grains into the marine environment. It is possible that these cycles were controlled by eustasy, although characterisation of additional stratigraphic sections for MS to establish basin-wide MS trends would better evaluate the eustatic hypothesis. It must be noted, however, that these sedimentary cycles represent an isolated occurrence within the Livian stratigraphy; sedimentary cycles within the underlying Haut-le-Wastia Member and the overlying upper Awirs Member (at Lives-sur-Meuse and Awirs West Quarry respectively) do not demonstrate the same strong relationship with MS. It is unclear why the correlation between the sedimentary cycles and MS record is not continuous throughout the Livian stratigraphic record; possibilities such as diagenetic alteration of the MS record and / or contributions to the MS record from lower (third) order processes (section 6.4.1) cannot be excluded. Further insights into the origins of the Livian sedimentary cycles may be gained by analysing more laterally equivalent sections.

It is noteworthy that MS analyses from geographically distinct, laterally equivalent sections within the Namur-Dinant Basin (Lives-sur-Meuse, Awirs West Quarry) yielded comparable MS trends, suggesting that MS may prove useful as a local correlation tool within some carbonate successions. This is certainly an area for future research, as it may prove possible to correlate using MS at a greater resolution than can be attained

using biostratigraphic and lithostratigraphic controls. In contrast to the MS data, the stable isotopic compositions of the whole-rock carbonate samples analysed appear to be of only local significance or have been modified by diagenesis. These data are likely of limited use as a proxy for global climatic processes or as a correlation tool.

Whole-rock geochemical analyses were undertaken for several western European diagenetically altered volcanic ash layers to gain insight into their magmatic parentage. Several major elements that are used to classify unaltered igneous lithologies are known to be mobile during alteration processes and thus cannot be used to infer the magmatic parentage of the altered volcanic horizons. Instead, several trace elements that are thought to be both immobile during alteration and indicators of magmatic parentage are routinely used to provide insight into the composition of the parent magmas of bentonite and tonstein horizons (e.g. Huff *et al.*, 1996). Using such an approach, the data obtained suggest that there were differences in the original ash composition between the Belgian Visean bentonites (trachyandesite), the Irish Asbian clay-rich horizons (alkali-basalt to andesite), the British Namurian bentonites (andesite) and the Westphalian tonstein horizons (dacite / rhyodacite). Such whole-rock geochemical data can help to rationalise why some bentonite horizons yield abundant euhedral zircon, whereas other horizons yield only sparse or no zircon grains. Whole-rock geochemical data potentially could be employed as a rapid screening tool to identify bentonites derived from igneous lithologies that are likely to contain sufficient quantities of zircon (e.g. lithologies of intermediate to felsic composition) and are thus potential targets for U-Pb dating.

Bibliography

Algeo, T. J., Wilkinson, B. H. & Lohmann, K. C. 1992. Meteoric-burial diagenesis of Middle Pennsylvanian limestones in the Orogrande Basin, New Mexico: water/rock interactions and basin geothermics. *Journal of Sedimentary Petrology,* **62,** 652-670.

Allan, J. R. & Matthews, R. K. 1982. Isotope signatures associated with early meteoric diagenesis. *Sedimentology,* **29,** 797-817.

Anceau, A. 1992. Sudoite in some Visean (Lower Carboniferous) K-bentonites of Belgium. *Clay Minerals,* **27,** 283-292.

Anceau, A. 1996. Sudoite, Al-rich Li-Mg-bearing chlorite, clinochlore and kaolinite as alteration products of biotite in Visean K-bentonites from Belgium. *European Journal of Mineralogy,* **8,** 493-505.

Anderson, T. F. & Arthur, M. A. 1983. Stable isotopes of oxygen and carbon and their application to sedimentologic and paleoenvironmental problems. *In:* Arthur, M. A., Anderson, T. F., Kaplan, I. R., Veizer, J. & Land, L. S. (Eds.) *Stable Isotopes in Sedimentary Geology*. Society for Sedimentary Geology (SEPM), Short Course, **10,** 1-151.

Aretz, M., Chevalier, E., Poty, E. & Chevalier, J. 2011. Cyclicity in the Middle Visean strata of Belgium. *Programme & Abstracts, The XVII Internation Congress on the Carboniferous and Permian, Perth 3-8 July 2011: Geological Survey of Western Australia,* 41.

Bábek, O., Kalvoda, J., Aretz, M., Cossey, P. J., Devuyst, F.-X., Herbig, H.-G. & Sevastopulo, G. 2010. The correlation potential of magnetic susceptibility and outcrop gamma-ray logs at Tournaisian-Viséan boundary sections in western Europe. *Geologica Belgica,* **13,** 291-308.

Bachmann, M., Herbst, G. & Kimpe, W. F. M. 1970. Derzeitiger Stand Der Flözparallelisierung zwischen den Steinkohlenrevieren Der Niederlande, von Aachen-Erkelenz vom Niederrheingebiet. *Compte Rendu: 6me Congrès International de Stratigraphie et de Géologie du Carbonifère, Sheffield 1967,* **2,** 445-452.

Bachmann, O., Oberli, F., Dungan, M. A., Meier, M., Mundil, R. & Fischer, H. 2007. $^{40}Ar/^{39}Ar$ and U–Pb dating of the Fish Canyon magmatic system, San Juan volcanic field, Colorado: Evidence for an extended crystallization history. *Chemical Geology,* **236,** 134-166.

Barnett, A. J., Burgess, P. M. & Wright, V. P. 2002. Icehouse world sea-level behaviour and resulting stratal patterns in late Visean (Mississippian) carbonate platforms: integration of numerical forward modelling and outcrop studies. *Basin Research,* **14,** 417-438.

Bartenstein, H. 1950. Micropalaeontological Research in European Upper Carboniferous Stratigraphy. *Geological Magazine,* **87,** 253-260.

Batchelor, R. A. & Jeppsson, L. 1999. Wenlock metabentonites from Gotland, Sweden: geochemistry, sources and potential as chemostratigraphic markers. *Geological Magazine,* **136,** 661-669.

Berger, A., Loutre, M. F. & Laskar, J. 1992. Stability of the astronomical frequencies over the Earth's history for paleoclimate studies. *Science,* **255,** 560-566.

Bishop, J. W., Montañez, I. P., Gulbranson, E. L. & Brenckle, P. L. 2009. The onset of Mid-Carboniferous glacio-eustasy: Sedimentologic and diagenetic constraints, Arrow Canyon, Nevada. *Palaeogeography, Palaeoclimatology, Palaeoecology,* **276,** 217-243.

Black, L. P., Kamo, S. L., Williams, I. S., Mundil, R., Davis, D. W., Korsch, R. J. & Foudoulis, C. 2003. The application of SHRIMP to Phanerozoic geochronology; a critical appraisal of four zircon standards. *Chemical Geology,* **200,** 171-188.

Black, L. P., Kamo, S. L., Allen, C. M., Davis, D. W., Aleinikoff, J. N., Valley, J. W., Mundil, R., Campbell, I. H., Korsch, R. J., Williams, I. S. & Foudoulis, C. 2004. Improved $^{206}Pb/^{238}U$ microprobe geochronology by the monitoring of a trace-element-related matrix effect; SHRIMP, ID–TIMS, ELA–ICP–MS and oxygen isotope documentation for a series of zircon standards. *Chemical Geology,* **205,** 115-140.

Bless, M. J. M., Streel, M. & Becker, G. 1987. Distribution and paleoenvironment of Devonian to Permian ostracode assemblages in Belgium with reference to some late Famennian to Permian marine nearshore to brackish-water assemblages dated by miospores. *Annales de la Société Géologique de Belgique,* **110,** 347-362.

Bohor, B. F. & Triplehorn, D. M. 1993. *Tonsteins: Altered volcanic-ash layers in coal-bearing sequences.* Geological Society of America, Special Paper, **285,** 44pp.

Bouroz, A. 1967. Correlations des tonsteins d'origine volcanique entre les bassins houillers de Sarre-Lorraine et du Nord-Pas-de-Calais. *Comptes Rendus, Series D: Sciences Naturelles,* **264,** 2729-2732.

Bowring, J. F., McLean, N. M. & Bowring, S. A. 2011. Engineering Cyber Infrastructure for U-Pb Geochronology: Tripoli and U-Pb Redux. *Geochemistry Geophysics Geosystems- G^3,* **12,** 19pp.

Bowring, S. A., Schoene, B., Crowley, J. L., Ramezani, J. & Condon, D. J. 2006. High-precision U-Pb zircon geochronology and the stratigraphic record: Progress and promise. *In:* Olszewski, T. D. (Ed.) *Geochronology: Emerging Opportunities.* Paleontological Society, Papers, **12,** 25-46.

Brandon, A. & Hodson, F. 1984. *The stratigraphy and palaeontology of the late Visean and early Namurian rocks of north-east Connaught.* Geological Survey of Ireland, Special Paper, **6,** 54pp.

Bruckschen, P., Bruhn, F., Veizer, J. & Buhl, D. 1995. $^{87}Sr/^{86}Sr$ isotopic evolution of Lower Carboniferous seawater: Dinantian of western Europe. *Sedimentary Geology,* **100,** 63-81.

Bruckschen, P. & Veizer, J. 1997. Oxygen and carbon isotopic composition of Dinantian brachiopods: Paleoenvironmental implications for the Lower Carboniferous of Western Europe. *Palaeogeography, Palaeoclimatology, Palaeoecology,* **132,** 243-264.

Bruckschen, P., Oesmann, S. & Veizer, J. 1999. Isotope stratigraphy of the European Carboniferous: proxy signals for ocean chemistry, climate and tectonics. *Chemical Geology,* **161,** 127-163.

Buggisch, W., Joachimski, M. M., Sevastopulo, G. & Morrow, J. R. 2008. Mississippian $\delta^{13}C_{carb}$ and conodont apatite $\delta^{18}O$ records – Their relation to the Late Palaeozoic Glaciation. *Palaeogeography, Palaeoclimatology, Palaeoecology,* **268,** 273-292.

Buhrke, V. E., Creasy, L. E., Croke, J. F., Feret, F., Jenkins, R., Kanare, H. M. & Kocman, V. 1998. Specimen Preparation in X-Ray Fluorescence. *In:* Buhrke, V. E., Jenkins, R. & Smith, D. K. (Eds.) *A Practical Guide for the Preparation of Specimens for X-Ray Fluorescence and X-Ray Diffraction Analysis.* Wiley-VCH, United States, 59-122.

Burger, K., Bieg, G. & Pfisterer, W. 2005. Klassische und primitive Kaolin-Kohlentonsteine im Ruhroberkarbon. *Courier Forschungsinstitut Senckenberg,* **254,** 169-180.

Calver, M. A. 1968. Distribution of Westphalian marine faunas in northern England and adjoining areas. *Proceedings of the Yorkshire Geological Society,* **37,** 1-72.

Calver, M. A. 1969. Westphalian of Britain. *Compte Rendu: 6me Congrès International de Stratigraphie et de Géologie du Carbonifère, Sheffield 1967,* **1,** 233-254.

Capo, R. C. & DePaolo, D. J. 1990. Seawater strontium isotopic variations from 2.5 million years ago to the present. *Science,* **249,** 51-55.

Chao, G. Y. 1969. 2θ (Cu) table for common minerals. *Carleton University, Department of Geology, Geological Paper,* **69-2,** 42pp.

Cherniak, D. J. & Watson, E. B. 2001. Pb diffusion in zircon. *Chemical Geology,* **172,** 5-24.

Chevalier, E. & Aretz, M. 2005. A microbe-bryozoan reef from the middle Visean of the Namur Syncline (Engihoul Quarry). *Geologica Belgica,* **8,** 109-119.

Chew, D. M., Fallon, N., Kennelly, C., Crowley, Q. & Pointon, M. A. 2010. Basic volcanism contemporaneous with the Sturtian glacial episode in NE Scotland. *Transactions of the Royal Society of Edinburgh,* **100,** 399-415.

Christidis, G. E. 1998. Comparative study of the mobility of major and trace elements during alteration of an andesite and a rhyolite to bentonite, in the islands of Milos and Kimolos, Aegean, Greece. *Clays and Clay Minerals,* **46,** 379-399.

Claoué-Long, J. C., Compston, W., Roberts, J. & Fanning, C. M. 1995. Two Carboniferous ages: a comparison of SHRIMP zircon dating with conventional zircon ages and $^{40}Ar/^{39}Ar$ analysis. *In:* Berggren, W. A., Kent, D. V., Aubry, M.-P. & Hardenbol, J. (Eds.) *Geochronology Timescales and Global Stratigraphic Correlations.* Society for Sedimentary Geology (SEPM), Special Publication, **54**, 3-21.

Clark, P. U., Alley, R. B. & Pollard, D. 1999. Northern Hemisphere ice-sheet influences on global climate change. *Science,* **286,** 1104-1111.

Clayton, T., Francis, J. E., Hillier, S. J., Hodson, F., Saunders, R. A. & Stone, J. 1996. The implications of reworking on the mineralogy and chemistry of Lower Carboniferous K-bentonites. *Clay Minerals,* **31,** 377-390.

Condon, D. J., McLean, N., Schoene, B., Bowring, S., Parrish, R. & Noble, S. 2008. Synthetic U-Pb 'standard' solutions for ID-TIMS geochronology. *Geochimica et Cosmochimica Acta,* **72,** A175.

Condon, D. J., McLean, N. M., Noble, S. R. & Bowring, S. A. 2010. Isotopic composition ($^{238}U/^{235}U$) of some commonly used uranium reference materials. *Geochimica et Cosmochimica Acta,* **74,** 7127-7143.

Conil, R., Pirlet, H. & Lys, M. 1967. Echelle Biostratigraphique du Dinantien de la Belgique. *Service Géologique de Belgique, Professional Paper,* **13,** 56pp.

Conil, R., Groessens, E. & Pirlet, H. 1977. Nouvelle charte stratigraphique du Dinantien type de la Belgique. *Annales de la Société Géologique du Nord,* **96,** 363–371.

Conil, R., Groessens, E., Laloux, M., Poty, E. & Tourneur, F. 1990. Carboniferous guide foraminifera, corals and conodonts in the Franco-Belgian and Campine basins: their potential for widespread correlation. *Courier Forschungsinstitut Senckenberg,* **130,** 15-30.

Corfu, F., Hanchar, J. M., Hoskin, P. W. O. & Kinny, P. D. 2003. Atlas of zircon textures. *In*: Hanchar, J. M. & Hoskin, P. W. O. (Eds.) *Zircon.* Reviews in Mineralogy and Geochemistry, **53,** 469-500.

Cózar, P. & Somerville, I. D. 2005. Stratigraphy of upper Viséan carbonate platform rocks in the Carlow area, southeast Ireland. *Geological Journal,* **40,** 35-64.

Crick, R. E., Ellwood, B. B., El Hassani, A., Feist, R. & Hladil, J. 1997. Magnetosusceptibility event and cyclostratigraphy (MSEC) of the Eifelian-Givetian GSSP and associated boundary sequences in North Africa and Europe. *Episodes,* **20,** 167-175.

Crick, R. E., Ellwood, B. B., Hladil, J., El Hassani, A., Hrouda, F. & Chlupác, I. 2001. Magnetostratigraphy susceptibility of the Přídolian-Lochkovian (Silurian-Devonian) GSSP (Klonk, Czech Republic) and a coeval sequence in Anti-Atlas Morocco. *Palaeogeography, Palaeoclimatology, Palaeoecology,* **167,** 73-100.

Crowley, J. L., Schoene, B. & Bowring, S. A. 2007. U-Pb dating of zircon in the Bishop Tuff at the millennial scale. *Geology,* **35,** 1123-1126.

Crucifix, M., Loutre, M. F. & Berger, A. 2006. The climate response to the astronomical forcing. *Space Science Reviews,* **125,** 213-226.

da Silva, A.-C. & Boulvain, F. 2006. Upper Devonian carbonate platform correlations and sea level variations recorded in magnetic susceptibility. *Palaeogeography, Palaeoclimatology, Palaeoecology,* **240,** 373-388.

da Silva, A.-C., Potma, K., Weissenberger, J. A. W., Whalen, M. T., Humblet, M., Mabille, C. & Boulvain, F. 2009a. Magnetic susceptibility evolution and sedimentary environments on carbonate platform sediments and atolls, comparison of the Frasnian from Belgium and Alberta, Canada. *Sedimentary Geology,* **214,** 3-18.

da Silva, A.-C., Mabille, C. & Boulvain, F. 2009b. Influence of sedimentary setting on the use of magnetic susceptibility: examples from the Devonian of Belgium. *Sedimentology,* **56,** 1292-1306.

Das, A. & Davis, D. W. 2010. Response of Precambrian zircon to the chemical abrasion (CA-TIMS) method and implications for improvement of age determinations. *Geochimica et Cosmochimica Acta,* **74,** 5333-5348.

Davies, S., Hampson, G., Flint, S. & Elliott, T. 1999. Continental-scale sequence stratigraphy of the Namurian, Upper Carboniferous and its applications to reservoir prediction. *In:* Fleet, A. J. & Boldy, S. A. R. (Eds.) *Petroleum Geology of Northwest Europe: Proceedings of the 5th Conference.* Geological Society, London, **2**, 757-770.

Davydov, V., Wardlaw, B. R. & Gradstein, F. M. 2004. The Carboniferous Period. *In:* Gradstein, F. M., Ogg, J. G. & Smith, A. G. (Eds.) *A Geologic Time Scale 2004.* Cambridge University Press, Cambridge, United Kingdom, 222-248.

Davydov, V. I., Crowley, J. L., Schmitz, M. D. & Poletaev, V. I. 2010. High-precision U-Pb zircon age calibration of the global Carboniferous time scale and Milankovitch band cyclicity in the Donets Basin, eastern Ukraine. *Geochemistry, Geophysics, Geosystems- G^3,* **11,** 22pp.

De Laeter, J. R., Böhlke, J. K., De Bièvre, P., Hidaka, H., Peiser, H. S., Rosman, K. J. R. & Taylor, P. D. P. 2003. Atomic weights of the elements: Review 2000 (IUPAC technical report). *Pure and Applied Chemistry,* **75,** 683-800.

Delcambre, B. 1989. Marqueurs téphrostratigraphiques au passage des calcaires de Neffe vers ceux de Lives. *Bulletin de la Société Belge de Géologie,* **98,** 163-170.

Delcambre, B. 1996. *Application de la Typologie du Zircon à la Téphrostratigraphie du Carbonifère de Belgique et des Régions voisines: Implications pétrologiques et diagénétiques*. PhD thesis, Université Catholique de Louvain.

Devuyst, F.-X., Hance, L. & Poty, E. 2005. *The Dinantian of Southern Belgium revisited: sedimentary history and biostratigraphy. A guidebook of key sections. I.U.G.S. Subcommission on Carboniferous Stratigraphy field trip, May 2005.* 79pp.

Devuyst, F.-X., Hance, L. & Poty, E. 2006. Moliniacian. *Geologica Belgica,* **9,** 123-131.

Dia, A. N., Cohen, A. S., O'Nions, R. K. & Shackleton, N. J. 1992. Seawater Sr isotope variation over the past 300 kyr and influence of global climate cycles. *Nature,* **356,** 786-788.

Dickens, G. R., O'Neil, J. R., Rea, D. K. & Owen, R. M. 1995. Dissociation of oceanic methane hydrate as a cause of the carbon isotope excursion at the end of the Paleocene. *Paleoceanography,* **10,** 965-972.

Dunlop, D. J. & Özdemir, Ö. 1997. *Rock Magnetism: Fundamentals and Frontiers.* Cambridge University Press, Cambridge, United Kingdom, 576pp.

Dusar, M., Paproth, E., Streel, M. & Bless, M. J. M. 2000. Palaeogeographic and palaeoenvironmental characteristics of major marine incursions in northwestern Europe during the Westphalian C (Bolsovian). *Geologica Belgica,* **3,** 331-347.

Dzik, J. 1997. Emergence and succession of Carboniferous conodont and ammonoid communities in the Polish part of the Variscan sea. *Acta Palaeontologica Polonica,* **42,** 57-170.

Ellwood, B. B. 2007. Magnetic susceptibility (MS), low-field. *In:* Fairbridge, R. W. & Rampino, M. (Eds.) *Encyclopedia of geomagnetism and paleomagnetism.* Springer, Netherlands, 566-572.

Ellwood, B. B., Crick, R. E., El Hassani, A., Benoist, S. L. & Young, R. H. 2000. Magnetosusceptibility event and cyclostratigraphy method applied to marine rocks: Detrital input versus carbonate productivity. *Geology,* **28,** 1135-1138.

Ellwood, B. B., Crick, R. E., García-Alcalde Fernandez, J. L., Soto, F. M., Truyóls-Massoni, M., El Hassani, A. & Kovas, E. J. 2001. Global correlation using magnetic susceptibility data from Lower Devonian rocks. *Geology,* **29,** 583-586.

Ellwood, B. B., Brett, C. E. & MacDonald, W. D. 2007a. Magnetostratigraphy susceptibility of the Upper Ordovician Kope Formation, northern Kentucky. *Palaeogeography, Palaeoclimatology, Palaeoecology,* **243,** 42-54.

Ellwood, B. B., Tomkin, J. H., Richards, B. C., Benoist, S. L. & Lambert, L. L. 2007b. MSEC data sets record glacially driven cyclicity: Examples from the Arrow Canyon Mississippian–Pennsylvanian GSSP and associated sections. *Palaeogeography, Palaeoclimatology, Palaeoecology,* **255,** 377-390.

Ellwood, B. B., Tomkin, J. H., Febo, L. A. & Stuart, C. N. 2008a. Time series analysis of magnetic susceptibility variations in deep marine sedimentary rocks: A test using the upper Danian–lower Selandian proposed GSSP, Spain. *Palaeogeography, Palaeoclimatology, Palaeoecology,* **261,** 270-279.

Ellwood, B. B., Tomkin, J. H., Ratcliffe, K. T., Wright, M. & Kafafy, A. M. 2008b. High-resolution magnetic susceptibility and geochemistry for the Cenomanian/Turonian boundary GSSP with correlation to time equivalent core. *Palaeogeography, Palaeoclimatology, Palaeoecology,* **261,** 105-126.

Emrich, K., Ehhalt, D. H. & Vogel, J. C. 1970. Carbon isotope fractionation during the precipitation of calcium carbonate. *Earth and Planetary Science Letters,* **8,** 363-371.

Fiebig, H. E. R. 1969. Das Namur C und Westfal im Niederrheinisch-Westfälischen Steinkohlengebiet. *Compte Rendu: 6^{me} Congrès International de Stratigraphie et de Géologie du Carbonifère, Sheffield 1967,* **1,** 79-89.

Fielding, C. R., Frank, T. D., Birgenheier, L. P., Rygel, M. C., Jones, A. T. & Roberts, J. 2008. Stratigraphic imprint of the late Palaeozoic ice age in eastern Australia: a record of alternating glacial and nonglacial climate regime. *Journal of the Geological Society, London,* **165,** 129-140.

Frakes, L. A., Francis, J. E. & Syktus, J. I. 1992. *Climate modes of the Phanerozoic: the history of the Earth's climate over the past 600 million years.* Cambridge University Press, Cambridge, United Kingdom, 274pp.

Frank, T. D., Birgenheier, L. P., Montañez, I. P., Fielding, C. R. & Rygel, M. C. 2008. Late Paleozoic climate dynamics revealed by comparison of ice-proximal stratigraphic and ice-distal isotopic records. *In*: Fielding, C. R., Frank, T. D., & Isbell, J. L. (Eds.) *Resolving the late Palaeozoic Ice Age in Space and Time.* Geological Society of America, Special Paper, **441,** 331-342.

Gallagher, S. J. 1996. The stratigraphy and cyclicity of the late Dinantian platform carbonates in parts of southern and western Ireland. *In:* Strogen, P., Somerville, I. D. & Jones, L. L. (Eds.) *Recent Advances in Lower Carboniferous Geology.* Geological Society, London, Special Publications, **107,** 239-251.

Gallagher, S. J. & Somerville, I. D. 1997. Late Dinantian (Lower Carboniferous) platform carbonate stratigraphy of the Buttevant area North Co. Cork, Ireland. *Geological Journal,* **32,** 313-335.

Gallagher, S. J., MacDermot, C. V., Somerville, I. D., Pracht, M. & Sleeman, A. G. 2006. Biostratigraphy, microfacies and depositional environments of Upper Viséan limestones from the Burren region, County Clare, Ireland. *Geological Journal,* **41,** 61-91.

Gastaldo, R. A., Purkyňová, E., Šimůnek, Z. & Schmitz, M. D. 2009. Ecological persistence in the Late Mississippian (Serpukhovian, Namurian A) megafloral record of the Upper Silesian Basin, Czech Republic. *Palaios,* **24,** 336-350.

Gerards, J. & Michot, P. 1963. Le Viseen Moyen, partie supérieure: V2b. *In:* Michot, P., Gerards, J., Monty, C. & Pirlet, H. (Eds.) *Excursion G – 1^{e} partie: Sédimentologie des formations viséennes du Synclinorium de Namur, dans la vallée de la Meuse. 6^{e} Congrès International de Sédimentologie Belgique & Pays-Bas.* 10-12.

Gerstenberger, H. & Haase, G. 1997. A highly effective emitter substance for mass spectrometric Pb isotope ratio determinations. *Chemical Geology,* **136,** 309-312.

Gray, D. I. 1981. *Lower Carboniferous shelf carbonate palaeoenvironments in North Wales*. PhD thesis, University of Newcastle-upon-Tyne.

Guion, P. D. & Fielding, C. R. 1988. Westphalian A and B sedimentation in the Pennine Basin, UK. *In:* Besly, B. M. & Kelling, G. (Eds.) *Sedimentation in a Synorogenic Basin Complex: the Upper Carboniferous of Northwest Europe.* Blackie, Glasgow, 153-177.

Guion, P. D., Fulton, I. M. & Jones, N. S. 1995. Sedimentary facies of the coal-bearing Westphalian A and B north of the Wales-Brabant High. *In:* Whateley, M. K. G. & Spears, D. A. (Eds.) *European Coal Geology.* Geological Society, London, Special Publications, **82**, 45-78.

Gulbranson, E. L., Montañez, I. P., Schmitz, M. D., Limarino, C. O., Isbell, J. L., Marenssi, S. A. & Crowley, J. L. 2010. High-precision U-Pb calibration of Carboniferous glaciation and climate history, Paganzo Group, NW Argentina. *Bulletin of the Geological Society of America,* **122,** 1480-1498.

Hallsworth, C. R., Morton, A. C., Claoué-Long, J. & Fanning, C. M. 2000. Carboniferous sand provenance in the Pennine Basin, UK: constraints from heavy mineral and detrital zircon age data. *Sedimentary Geology,* **137,** 147-185.

Hance, L., Poty, E. & Devuyst, F.-X. 2001. Stratigraphie séquentielle du Dinantien type (Belgique) et corrélation avec le Nord de la France (Boulonnais, Avesnois). *Bulletin de la Societe Geologique de France,* **172,** 411-426.

Hance, L., Devuyst, F.-X. & Poty, E. 2002. Sequence stratigraphy of the Belgian Lower Carboniferous – tentative correlation with the British Isles. *In:* Hills, L.V., Henderson, C.M. & Bamber, E.W (Eds.) *Carboniferous and Permian of the World.* Canadian Society of Petroleum Geologists, Memoir, **19,** 41-51.

Hance, L., Poty, E. & Devuyst, F.-X. 2006. Viséan. *Geologica Belgica,* **9,** 55-62.

Hanchar, J. M. & Miller, C. F. 1993. Zircon zonation patterns as revealed by cathodoluminescence and backscattered electron images: Implications for interpretation of complex crustal histories. *Chemical Geology,* **110,** 1-13.

Harrison, R. J. & Feinberg, J. M. 2009. Mineral magnetism: providing new insights into geoscience processes. *Elements,* **5,** 209-215.

Hartung, W. & Patteisky, K. 1960. Die Flora der Goniatiten-Zonen im Visé und Namur des ostsudetischen Karbons. *Compte Rendu: 4^{me} Congrès International de Stratigraphie et de Géologie du Carbonifère, Heerlen 1958,* **1,** 247-262.

Hays, J. D., Imbrie, J. & Shackleton, N. J. 1976. Variations in the Earth's Orbit: Pacemaker of the Ice Ages. *Science,* **194,** 1121-1132.

Heckel, P. H. & Clayton, G. 2006. The Carboniferous System. Use of the new official names for the subsystems, series, and stages. *Geologica Acta,* **4,** 403-407.

Helsen, S. 1992. Conodont colour alteration maps for Paleozoic strata in Belgium, northern France and westernmost Germany – preliminary results. *Annales de la Société Géologique de Belgique,* **115,** 135-143.

Henderson, G. M., Martel, D. J., O'Nions, R. K. & Shackleton, N. J. 1994. Evolution of seawater $^{87}Sr/^{86}Sr$ over the last 400 ka: the absence of glacial/interglacial cycles. *Earth and Planetary Science Letters,* **128,** 643-651.

Herbig, H.-G. 2006. Kalkschalige Kleinforaminiferen. *In:* Deutsche Stratigraphische Kommission (Eds.) *Stratigraphie von Deutschland VI. Unterkarbon (Mississippium).* Schriftenreihe der Deutschen Gesellschaft für Geowissenschaften, **41**, 250-270.

Hess, J. C. & Lippolt, H. J. 1986. $^{40}Ar/^{39}Ar$ ages of tonstein and tuff sanidines: new calibration points for the improvement of the Upper Carboniferous time scale. *Chemical Geology: Isotope Geoscience Section,* **59,** 143-154.

Higgins, J. A. & Schrag, D. P. 2006. Beyond methane: Towards a theory for the Paleocene–Eocene thermal maximum. *Earth and Planetary Science Letters,* **245,** 523-537.

Hill, I. G., Worden, R. H. & Meighan, I. G. 2000. Yttrium: The immobility-mobility transition during basaltic weathering. *Geology,* **28,** 923-926.

Hinnov, L. A. & Ogg, J. G. 2007. Cyclostratigraphy and the astronomical time scale. *Stratigraphy,* **4,** 239-251.

Holdsworth, B. K. & Collinson, J. D. 1988. Millstone Grit cyclicity revisited. *In:* Besly, B. M. & Kelling, G. (Eds.) *Sedimentation in a Synorogenic Basin Complex: the Upper Carboniferous of Northwest Europe.* Blackie, Glasgow, 132-152.

Horbury, A. D. 1987. *Sedimentology of the Urswick Limestone in South Cumbria and North Lancashire.* PhD thesis, University of Manchester.

Horstwood, M. S. A. 2008. Data reduction strategies, uncertainty assessment and resolution of LA–(MC–)ICP–MS isotope data. *In:* Sylvester, P. (Ed.) *Laser ablation ICP-MS in the Earth Sciences: current practices and outstanding issues.* Mineralogical Association of Canada, Short Course, **40,** 283-303.

Horstwood, M. S. A., Foster, G. L., Parrish, R. R., Noble, S. R. & Nowell, G. M. 2003. Common-Pb corrected *in situ* U–Pb accessory mineral geochronology by LA-MC-ICP-MS. *Journal of Analytical Atomic Spectrometry,* **18,** 837-846.

Hoskin, P. W. O. & Schaltegger, U. 2003. The composition of zircon and igneous and metamorphic petrogenesis. *In:* Hanchar, J. M. & Hoskin, P. W. O. (Eds.) *Zircon.* Reviews in Mineralogy and Geochemistry, **53,** 27-62.

Hoyez, B. 1971. Le Viséen du Boulonnais: analyse et corrélation séquentielles. *Annales de la Société Géologique du Nord,* **91,** 113-128.

Hudson, R. G. S. & Cotton, G. 1945. The Carboniferous rocks of the Edale Anticline, Derbyshire. *Quarterly Journal of the Geological Society of London,* **101,** 1-36.

Huff, W. D. 1983. Misuse of the term "bentonite" for ash beds of Devonian age in the Appalachian Basin: discussion and reply. *Geological Society of America Bulletin,* **94,** 681-683.

Huff, W. D., Morgan, D. J. & Rundle, C. C. 1996. Silurian K-bentonites of the Welsh Borderlands: Geochemistry, mineralogy and K-Ar ages of illitization. *British Geological Survey Technical Report WG/96/45,* 25pp.

Hunt, C. P., Moskowitz, B. M. & Banerjee, S. K. 1995. Magnetic properties of rocks and minerals. *In:* Ahrens, T. J. (Ed.) *Rock Physics & Phase Relations: A Handbook of Physical Constants*. AGU Reference Shelf, **3,** 189-204.

Imbrie, J. & Imbrie, J. Z. 1980. Modeling the climatic response to orbital variations. *Science,* **207,** 943-953.

Imbrie, J., Berger, A., Boyle, E. A., Clemens, S. C., Duffy, A., Howard, W. R., Kukla, G., Kutzbach, J., Martinson, D. G., McIntyre, A., Mix, A. C., Molfino, B., Morley, J. J., Peterson, L. C., Pisias, N. G., Prell, W. L., Raymo, M. E., Shackleton, N. J. & Toggweiler, J. R. 1993. On the structure and origin of major glaciation cycles 2. The 100,000-year cycle. *Paleoceanography,* **8,** 699-735.

Isbell, J. L., Miller, M. F., Wolfe, K. L. & Lenaker, P. A. 2003. Timing of late Paleozoic glaciation in Gondwana: Was glaciation responsible for the development of Northern Hemisphere cyclothems? *In:* Chan, M. A. & Archer, A. A. (Eds.) *Extreme Depositional Environments: Mega End Members in Geologic Time*. Geological Society of America, Special Paper, **370,** 5-24.

Jaffey, A. H., Flynn, K. F., Glendenin, L. E., Bentley, W. C. & Essling, A. M. 1971. Precision measurement of half-lives and specific activities of ^{235}U and ^{238}U. *Physical Review C,* **4,** 1889-1906.

Janoušek, V., Farrow, C. M. & Erban, V. 2006. Interpretation of whole-rock geochemical data in igneous geochemistry: introducing Geochemical Data Toolkit (GCDkit). *Journal of Petrology,* **47,** 1255-1259.

Jeans, C. V., Wray, D. S., Merriman, R. J. & Fisher, M. J. 2000. Volcanogenic clays in Jurassic and Cretaceous strata of England and the North Sea Basin. *Clay Minerals,* **35,** 25-55.

Jefferson, D. P. 1980. Cyclic sedimentation in the Holkerian (Middle Visean) North of Settle, Yorkshire. *Proceedings of the Yorkshire Geological Society,* **42,** 483-503.

Jessen, W., Josten, K.-H., Knauff, W., Paproth, E., Stadler, G. & Wolf, M. 1969. Die Bochumer Schichten im Ruhrbezirk (Oberes Westfal A). *Compte Rendu: 6^{me} Congrès International de Stratigraphie et de Géologie du Carbonifère, Sheffield 1967,* **1,** 91-97.

Kalsbeek, F. 1992. The statistical distribution of the mean squared weighted deviation – Comment: Isochrons, errorchrons, and the use of MSWD-values. *Chemical Geology: Isotope Geoscience Section,* **94,** 241-242.

Kiipli, E., Kiipli, T. & Kallaste, T. 2006. Identification of the O-bentonite in the deep shelf sections with implication on stratigraphy and lithofacies, East Baltic Silurian. *GFF,* **128,** 255-260.

Kiipli, T., Soesoo, A., Kallaste, T. & Kiipli, E. 2008. Geochemistry of Telichian (Silurian) K-bentonites in Estonia and Latvia. *Journal of Volcanology and Geothermal Research,* **171,** 45-58.

Korn, D. 1994. Revision of the Rhenish late Visean goniatite stratigraphy. *Annales de la Société Géologique de Belgique,* **117,** 129-136.

Košler, J. & Sylvester, P. J. 2003. Present trends and the future of zircon in geochronology: laser ablation ICPMS. *In:* Hanchar, J. M. & Hoskin, P. W. O. (Eds.) *Zircon.* Reviews in Mineralogy and Geochemistry, **53,** 243-275.

Kotková, J., Schaltegger, U. & Leichmann, J. 2010. Two types of ultrapotassic plutonic rocks in the Bohemian Massif – Coeval intrusions at different crustal levels. *Lithos,* **115,** 163-176.

Krogh, T. E. 1973. A low-contamination method for hydrothermal decomposition of zircon and extraction of U and Pb for isotopic age determinations. *Geochimica et Cosmochimica Acta,* **37,** 485-494.

Krogh, T. E. 1982. Improved accuracy of U-Pb zircon ages by the creation of more concordant systems using an air abrasion technique. *Geochimica et Cosmochimica Acta,* **46,** 637-649.

Kryza, R., Muszer, J., Haydukiewicz, J., August, C., Jurasik, M. & Rodionov, N. 2010. A SIMS zircon age for a biostratigraphically dated Upper Viséan (Asbian) bentonite in the Central-European Variscides (Bardo Unit, Polish Sudetes). *International Journal of Earth Sciences (Geologische Rundschau),* **100,** 1227-1235.

Kuiper, K. F., Deino, A., Hilgen, F. J., Krijgsman, W., Renne, P. R. & Wijbrans, J. R. 2008. Synchronizing rock clocks of Earth history. *Science,* **320,** 500-504.

Laskar, J. 1999. The limits of Earth orbital calculations for geological time-scale use. *Philosophical Transactions of the Royal Society: Mathematical, Physical and Engineering Sciences,* **357,** 1735-1759.

Le Maitre, R. W., Streckeisen, A., Zanettin, B., Le Bas, M. J., Bonin, B., Bateman, P., Bellieni, G., Dudek, A., Efremova, S., Keller, J., Lameyre, J., Sabine, P. A., Schmid, R., Sorensen, H. & Woolley, A. R. 2002. *Igneous rocks: a classification and glossary of terms: recommendations of the International*

Union of Geological Sciences Subcommission on the Systematics of Igneous Rocks. Cambridge University Press, Cambridge, United Kingdom, 252pp.

Leeder, M. R. 1988. Recent developments in Carboniferous geology: a critical review with implications for the British Isles and N.W. Europe. *Proceedings of the Geologists' Association,* **99,** 73-100.

Legg, I. C., Johnston, T. P., Mitchell, W. I., Smith, R. A., Arthur, M. J., Reay, D. M., Riley, N. J. & Strank, A. R. E. 1998. *Geology of the country around Derrygonnelly and Marble Arch: memoir for 1:50,000 geological sheets 44, 56 and 43 (Northern Ireland).* Memoirs of the Geological Survey of Northern Ireland, 82pp.

Lehrmann, D. J. & Goldhammer, R. K. 1999. Secular variation in parasequence and facies stacking patterns of platform carbonates: a guide to application of stacking-patterns analysis in strata of diverse ages and settings. *In:* Harris, P. M., Saller, A. H. & Simo, J. A. (Eds.) *Advances in Carbonate Sequence Stratigraphy: Applications to Outcrops, Reservoirs and Models.* Society for Sedimentary Geology (SEPM), Special Publication, **63,** 187-225.

Lippolt, H. J., Hess, J. C. & Burger, K. 1984. Isotopische Alter von pyroklastischen Sanidinen aus Kaolin-Kohlentonsteinen als Korrelationsmarken für das mitteleuropäische Oberkarbon. *Fortschritte in der Geologie von Rheinland und Westfalen,* **32,** 119-150.

Lisiecki, L. E. 2010. Links between eccentricity forcing and the 100,000-year glacial cycle. *Nature Geoscience,* **3,** 349-352.

Ludwig, K. R. 1998. On the treatment of concordant uranium-lead ages. *Geochimica et Cosmochimica Acta,* **62,** 665-676.

Ludwig, K. R. 2003a. User's manual for Isoplot 3.00: A geochronological toolkit for Microsoft Excel. *Berkeley Geochronology Center Special Publication*, **4,** 70pp.

Ludwig, K. R. 2003b. Mathematical-statistical treatment of data and errors for ^{230}Th/U geochronology. *In:* Bourdon, B., Henderson, G. M., Lundstrom, C. C & Turner, S. P. (Eds.) *Uranium-series Geochemistry.* Reviews in Mineralogy and Geochemistry, **52,** 631-656.

Lyons, P. C., Spears, D. A., Outerbridge, W. F., Congdon, R. D. & Evans, H. T.. 1994. Euramerican tonsteins: overview, magmatic origin, and depositional-tectonic implications. *Palaeogeography, Palaeoclimatology, Palaeoecology,* **106,** 113-134.

Macdonald, R., Gass, K. N., Thorpe, R. S. & Gass, I. G. 1984. Geochemistry and petrogenesis of the Derbyshire Carboniferous basalts. *Journal of the Geological Society, London,* **141,** 147-159.

Marshall, D. J. 1988. *Cathodoluminescence of Geological Materials.* Unwin Hyman, London, United Kingdom, 146pp.

Marshall, J. D. 1992. Climatic and oceanographic isotopic signals from the carbonate rock record and their preservation. *Geological Magazine,* **129,** 143-160.

Martinsen, O. J., Collinson, J. D. & Holdsworth, B. K. 1995. Millstone Grit cyclicity revisited, II: sequence stratigraphy and sedimentary responses to changes of relative sea-level. *In:* Plint, A. G. (Ed.) *Sedimentary Facies Analysis.* International Association of Sedimentologists, Special Publications, **22,** 305-327.

Mattinson, J. M. 2005. Zircon U–Pb chemical abrasion ("CA-TIMS") method: Combined annealing and multi-step partial dissolution analysis for improved precision and accuracy of zircon ages. *Chemical Geology,* **220,** 47-66.

Mattinson, J. M. 2010. Analysis of the relative decay constants of ^{235}U and ^{238}U by multi-step CA-TIMS measurements of closed system natural zircon samples. *Chemical Geology,* **275,** 186-198.

Mattinson, J. M., Graubard, C. M., Parkinson, D. L. & McClelland, W. C. 1996. U-Pb reverse discordance in zircons; the role of fine-scale oscillatory zoning and sub-micron transport of Pb. *In:* Basu, A. & Hart, S. R. (Eds.) *Earth Processes: Reading the Isotopic Code.* Geophysical Monograph, **95,** 355-370.

Maynard, J. R. & Leeder, M. R. 1992. On the periodicity and magnitude of Late Carboniferous glacio-eustatic sea-level changes. *Journal of the Geological Society, London,* **149,** 303-311.

McCann, T., Skompski, S., Poty, E., Dusar, M., Vozárová, A., Schneider, J., Wetzel, A., Krainer, K., Kornpihl, K., Schäefer, A., Krings, M., Oplustil, S. & Tait, J. 2008. Carboniferous. *In:* McCann, T. (Ed.) *The Geology of Central Europe: Volume 1, Precambrian and Palaeozoic.* Geological Society, London, United Kingdom, 411-529.

McConnell, B., Crowley, Q. G. & Riggs, N. 2010. Laurentian origin of the Ordovician Grangegeeth volcanic arc terrane, Ireland. *Journal of the Geological Society, London,* **167,** 469-474.

McDonough, W. F. & Sun, S.-s. 1995. The composition of the Earth. *Chemical Geology,* **120,** 223-253.

Menning, M., Weyer, D., Drozdzewski, G., van Amerom, H. W. J. & Wendt, I. 2000. A Carboniferous Time Scale 2000: discussion and use of geological parameters as time indicators from Central and Western Europe. *Geologisches Jahrbuch, Reihe A,* **156,** 3-44.

Menning, M., Weyer, D., Drozdzewski, G. & Wendt, I. 2001. More radiometric ages for the Carboniferous time scale. *Newsletter on Carboniferous Stratigraphy,* **19,** 16-18.

Menning, M., Alekseev, A. S., Chuvashov, B. I., Davydov, V. I., Devuyst, F.-X., Forke, H. C., Grunt, T. A., Hance, L., Heckel, P. H., Izokh, N. G., Jin, Y.-G., Jones, P. J., Kotlyar, G. V., Kozur, H. W., Nemyrovska, T. I., Schneider, J. W., Wang, X. -D., Weddige, K., Weyer, D. & Work, D. M. 2006. Global time scale and regional stratigraphic reference scales of Central and West Europe, East Europe, Tethys, South China, and North America as used in the Devonian–Carboniferous–Permian Correlation Chart 2003 (DCP 2003). *Palaeogeography, Palaeoclimatology, Palaeoecology,* **240,** 318-372.

Mii, H.-S., Grossman, E. L. & Yancey, T. E. 1999. Carboniferous isotope stratigraphies of North America: Implications for Carboniferous paleoceanography and Mississippian glaciation. *Bulletin of the Geological Society of America,* **111,** 960-973.

Mii, H.-S., Grossman, E. L., Yancey, T. E., Chuvashov, B. & Egorov, A. 2001. Isotopic records of brachiopod shells from the Russian Platform – evidence for the onset of Mid-Carboniferous glaciation. *Chemical Geology,* **175,** 133-147.

Miller, J. S., Matzel, J. E. P., Miller, C. F., Burgess, S. D. & Miller, R. B. 2007. Zircon growth and recycling during the assembly of large, composite arc plutons. *Journal of Volcanology and Geothermal Research,* **167,** 282-299.

Miller, K. G., Mountain, G. S., Wright, J. D. & Browning, J. V. 2011. A 180-million-year record of sea level and ice volume variations from continental margin and deep-sea isotopic records. *Oceanography,* **24,** 40-53.

Min, K., Mundil, R., Renne, P. R. & Ludwig, K. R. 2000. A test for systematic errors in $^{40}Ar/^{39}Ar$ geochronology through comparison with U/Pb analysis of a 1.1-Ga rhyolite. *Geochimica et Cosmochimica Acta,* **64,** 73-98.

Mottequin, B. 2008. The 'black marble' of Denée, a fossil conservation deposit from the Lower Carboniferous (Viséan) of southern Belgium. *Geological Journal,* **43,** 197-208.

Nasdala, L., Zhang, M., Kempe, U., Panczer, G., Gaft, M., Andrut, M. & Plötze, M. 2003. Spectroscopic methods applied to zircon. *In:* Hanchar, J. M. & Hoskin, P. W. O. (Eds.) *Zircon.* Reviews in Mineralogy and Geochemistry, **53,** 427-467.

Paproth, E., Conil, R., Bless, M. J. M., Boonen, P., Bouckaert, J., Carpentier, N., Coen, M., Delcambre, B., Deprijck, Ch., Deuzon, S., Dreesen, R., Groessens, E., Hance, L., Hennebert, M., Hibo, D., Hahn, G. & R., Hislaire, O., Kasig, W., Laloux, M., Lauwers, A., Lees, A., Lys, M., Op de Beek, K., Overlau, P., Pirlet, H., Poty, E., Ramsbottom, W. H. C., Streel, M., Swennen, R., Thorez, J., Vanguestaine, M., van Steenwinkel, M. & Vieslet, J. L. 1983a. Bio- and lithostratigraphic subdivisions of the Dinantian in Belgium, a review. *Annales de la Société Géologique de Belgique,* **106,** 185-239.

Paproth, E., Dusar, M., Bless, M. J. M., Bouckaert, J., Delmer, A., Fairon-Demaret, M., Houlleberghs, E., Laloux, M., Pierart, P., Somers, Y., Streel, M., Thorez, J. & Tricot, J. 1983b. Bio- and lithostratigraphic subdivisions of the Silesian in Belgium, a review. *Annales de la Société Géologique de Belgique,* **106,** 241-283.

Paproth, E., Dusar, M., Verkaeren, P. & Bless, M. J. M. 1994. Stratigraphy and cyclic nature of lower Westphalian deposits in the boreholes KB174 and KB206 in the Belgian Campine. *Annales de la Société Géologique de Belgique,* **117,** 169-189.

Pellenard, P., Deconinck, J., Huff, W. D., Thierry, J., Marchand, D., Fortwengler, D. & Trouiller, A. 2003. Characterization and correlation of Upper Jurassic (Oxfordian) bentonite deposits in the Paris Basin and the Subalpine Basin, France. *Sedimentology,* **50,** 1035-1060.

Peterson, J. A. 2011. Better mathematical constraints on ages of Carboniferous stage boundaries using radiometric tuff dates and cyclostratigraphy. *Geochemistry, Geophysics, Geosystems - G^3,* **12,** 7pp.

Pirlet, H. 1963. Sédimentologie des formations du Viséen supérieur, V3b dans la Vallée du Samson (Bassin de Namur, Belgique). *Annales de la Société Géologique de Belgique,* **86,** Mémoire no. 1, 46pp.

Pirlet, H. 1968. La sédimentation rythmique et la stratigraphie du Viséen supérieur V3b, V3c inférieur dans les synclinoriums de Namur et de Dinant. *Académie royale da Belgique, classe des Sciences, Mémoires collection, 4, deuxième série,* **17,** 7-98.

Poller, U., Huth, J., Hoppe, P. & Williams, I. S. 2001. REE, U, Th and Hf distribution in zircon from Western Carpathian Variscan granitoids: A combined cathodoluminescence and ion microprobe study. *American Journal of Science,* **301,** 858-867.

Poty, E., Hance, L., Lees, A. & Hennebert, M. 2001. Dinantian lithostratigraphic units (Belgium). *Geologica Belgica,* **4,** 69-93.

Poty, E., Devuyst, F.-X. & Hance, L. 2006. Upper Devonian and Mississippian foraminiferal and rugose coral zonations of Belgium and northern France: a tool for Eurasian correlations. *Geological Magazine,* **143,** 829-857.

Poty, E. & Hance, L. 2006a. Livian. *Geologica Belgica,* **9,** 133-138.

Poty, E. & Hance, L. 2006b. Warnantian. *Geologica Belgica,* **9,** 139-144.

Pupin, J. P. 1980. Zircon and granite petrology. *Contributions to Mineralogy and Petrology,* **73,** 207-220.

Rabitz, A. 1966. Die marinen Horizonte des flözführenden Ruhrkarbons. Rückschau und Ausblick. *Fortschritte in der Geologie von Rheinland und Westfalen,* **13,** 243-296.

Ramezani, J., Schmitz, M. D., Davydov, V. I., Bowring, S. A., Snyder, W. S. & Northrup, C. J. 2007. High-precision U–Pb zircon age constraints on the Carboniferous–Permian boundary in the southern Urals stratotype. *Earth and Planetary Science Letters,* **256,** 244-257.

Ramsbottom, W. H. C., Rhys, G. H. & Smith, E. G. 1962. Boreholes in the Carboniferous rocks of the Ashover District, Derbyshire. *Bulletin of the Geological Survey of Great Britain,* **19,** 75-168.

Ramsbottom, W. H. C. 1973. Transgressions and regressions in the Dinantian: a new synthesis of British Dinantian stratigraphy. *Proceedings of the Yorkshire Geological Society,* **39,** 567-607.

Ramsbottom, W. H. C., Calver, M. A., Eagar, R. M. C., Hodson, F., Holliday, D. W., Stubblefield, C. J. & Wilson, R. B. 1978. *A Correlation of Silesian Rocks in the British Isles.* Geological Society, London, Special Report, **10,** 82pp.

Rasbury, E. T., Hanson, G. N., Meyers, W. J., Holt, W. E., Goldstein, R. H. & Saller, A. H. 1998. U-Pb dates of paleosols: Constraints on late Paleozoic cycle durations and boundary ages. *Geology,* **26,** 403-406.

Renne, P. R., Swisher, C. C., Deino, A. L., Karner, D. B., Owens, T. L. & DePaolo, D. J. 1998. Intercalibration of standards, absolute ages and uncertainties in $^{40}Ar/^{39}Ar$ dating. *Chemical Geology,* **145,** 117-152.

Revesz, K.M., Landwehr, J. M. & Keybl, J. 2001. Measurement of $\delta^{13}C$ and $\delta^{18}O$ isotopic ratios of $CaCO_3$ using a Thermoquest Finnigan GasBench II Delta Plus XL continuous flow isotope ratio mass spectrometer with application to Devils Hole Core DH-11 calcite. *U.S. Geological Survey Open-File Reports,* **01-257,** 22pp.

Richards, B. 2009. Report of the task group to establish a GSSP close to the existing Viséan–Serpukhovian boundary. *Newsletter on Carboniferous Stratigraphy,* **27,** 10-12.

Riley, N. J. 1993. Dinantian (Lower Carboniferous) biostratigraphy and chronostratigraphy in the British Isles. *Journal of the Geological Society, London,* **150,** 427-446.

Riley, N. J., Claoué-Long, J., Higgins, A. C., Owens, B., Spears, A., Taylor, L. & Varker, W. J. 1993. Geochronometry and geochemistry of the European Mid-Carboniferous boundary global stratotype proposal, Stonehead Beck, North Yorkshire, UK. *Annales de la Société Géologique de Belgique,* **116,** 275–289.

Roberts, J., Claoué-Long, J. C. & Jones, P. 1995a. Australian Early Carboniferous time. *In:* Berggren, W. A., Kent, D. V., Aubry, M.-P. & Hardenbol, J. (Eds.) *Geochronology Timescales and Global Stratigraphic Correlations.* Society for Sedimentary Geology (SEPM), Special Publication, **54,** 23-40.

Roberts, J., Claoué-Long, J., Jones, P. J. & Foster, C. B. 1995b. SHRIMP zircon age control of Gondwanan sequences in Late Carboniferous and Early Permian Australia. *In:* Dunay, R.E. & Hailwood, E.A. (Eds.) *Non-biostratigraphical methods of dating and correlation.* Geological Society, London, Special Publications, **89,** 145-174.

Roen, J. B. & Hosterman, J. W. 1982. Misuse of the term "bentonite" for ash beds of Devonian age in the Appalachian Basin. *Geological Society of America Bulletin,* **93,** 921-925.

Rosenbaum, S. & Brownfield, I. K. 1999. Magnetic susceptibilities of minerals. *U.S. Geological Survey Open-File Reports,* **99-529,** 37pp.

Rudnick, R. L. & Gao, S. 2003. Composition of the continental crust. *In:* Rudnick, R. L. (Ed.) *Treatise on Geochemistry*, **3,** 1-64.

Satterley, A. K. 1996. The interpretation of cyclic successions of the Middle and Upper Triassic of the Northern and Southern Alps. *Earth-Science Reviews,* **40,** 181-207.

Schaltegger, U. 1997. Magma pulses in Central Variscan Belt: episodic melt generation and emplacement during lithospheric thinning. *Terra Nova,* **9,** 242-245.

Schärer, U. 1984. The effect of initial ^{230}Th disequilibrium on young U-Pb ages: the Makalu case, Himalaya. *Earth and Planetary Science Letters,* **67,** 191-204.

Schmitz, M. D. & Schoene, B. 2007. Derivation of isotope ratios, errors, and error correlations for U-Pb geochronology using ^{205}Pb-^{235}U-(^{233}U)-spiked isotope dilution thermal ionization mass spectrometric data. *Geochemistry, Geophysics, Geosystems - G^3,* **8,** 20pp.

Schoene, B., Crowley, J. L., Condon, D. J., Schmitz, M. D. & Bowring, S. A. 2006. Reassessing the uranium decay constants for geochronology using ID-TIMS U–Pb data. *Geochimica et Cosmochimica Acta,* **70,** 426-445.

Schoene, B., Guex, J., Bartolini, A., Schaltegger, U. & Blackburn, T. J. 2010. Correlating the end-Triassic mass extinction and flood basalt volcanism at the 100 ka level. *Geology,* **38,** 387-390.

Schwarzacher, W. 1993. *Cyclostratigraphy and the Milankovitch Theory.* Developments in Sedimentology, **52,** 225pp.

Sevastopulo, G. & Barham, M. 2011. Correlation of the base of the Serpukhovian Stage in Northwest Europe and North America. *Programme & Abstracts, The XVII International Congress on the Carboniferous and Permian, Perth 3-8 July 2011: Geological Survey of Western Australia,* 109.

Sharp, Z. 2007. *Principles of Stable Isotope Geochemistry.* Pearson Education, Upper Saddle River, New Jersey, United States, 360pp.

Simon, J. I., Renne, P. R. & Mundil, R. 2008. Implications of pre-eruptive magmatic histories of zircons for U-Pb geochronology of silicic extrusions. *Earth and Planetary Science Letters,* **266,** 182-194.

Sircombe, K. N. & Stern, R. A. 2002. An investigation of artificial biasing in detrital zircon U-Pb geochronology due to magnetic separation in sample preparation. *Geochimica et Cosmochimica Acta,* **66,** 2379-2397.

Sláma, J., Košler, J., Condon, D. J., Crowley, J. L., Gerdes, A., Hanchar, J. M., Horstwood, M. S. A., Morris, G. A., Nasdala, L., Norberg, N., Schaltegger, U., Schoene, B., Tubrett, M. N. & Whitehouse, M. J. 2008. Plesovice zircon – A new natural reference material for U-Pb and Hf isotopic microanalysis. *Chemical Geology,* **249,** 1-35.

Smeesters, A., Muchez, P. & Keppens, E. 2003. Diagenesis at exposure surfaces in a transgressive systems tract in a third-order sequence (Lower Carboniferous, Belgium). *Journal of Geochemical Exploration,* **78-79,** 565-569.

Smeesters, A., Muchez, P., Swennen, R. & Keppens, E. In Preparation. Diagenesis at exposure surfaces in a transgressive systems tract in a third order sequence (Lower Carboniferous, Belgium).

Smith, L. B. & Read, J. F. 2000. Rapid onset of late Paleozoic glaciation on Gondwana: Evidence from Upper Mississippian strata of the Midcontinent, United States. *Geology,* **28,** 279-282.

Somerville, I. D. 1979a. A sedimentary cyclicity in early Asbian (lower D1) limestones in the Llangollen district of North Wales. *Proceedings of the Yorkshire Geological Society,* **42,** 397-404.

Somerville, I. D. 1979b. Minor sedimentary cyclicity in late Asbian (upper D1) limestones in the Llangollen district of North Wales. *Proceedings of the Yorkshire Geological Society,* **42,** 317-342.

Somerville, I. D. 1979c. A cyclicity in the early Brigantian (D2) limestones east of the Clwydian Range, North Wales and its use in correlation. *Geological Journal,* **14,** 69-87.

Somerville, I. D. 2008. Biostratigraphic zonation and correlation of Mississippian rocks in Western Europe; some case studies in the late Viséan/Serpukhovian. *Geological Journal,* **43,** 209-240.

Somerville, I. D., Strogen, P. & Jones, G. L. 1992. Biostratigraphy of Dinantian limestones and associated volcanic rocks in the Limerick Syncline, Ireland. *Geological Journal,* **27,** 201-220.

Spears, D. A. 2006. Clay mineralogy of onshore UK Carboniferous mudrocks. *Clay Minerals,* **41,** 395-416.

Spears, D. A. & Kanaris-Sotiriou, R. 1979. A geochemical and mineralogical investigation of some British and other European tonsteins. *Sedimentology,* **26,** 407-425.

Spears, D. A. & Lyons, P. C. 1995. An update on British tonsteins. *In:* Whateley, M. K. G. & Spears, D. A. (Eds.) *European Coal Geology.* Geological Society, London, Special Publications, **82,** 137-146.

Spears, D. A., Kanaris-Sotiriou, R., Riley, N. & Krause, P. 1999. Namurian bentonites in the Pennine Basin, UK – origin and magmatic affinities. *Sedimentology,* **46,** 385-401.

Stacey, J. S. & Kramers, J. D. 1975. Approximation of terrestrial lead isotope evolution by a two-stage model. *Earth and Planetary Science Letters,* **26,** 207-221.

Steiger, R. H. & Jäger, E. 1977. Subcommission on geochronology: Convention on the use of decay constants in geo- and cosmochronology. *Earth and Planetary Science Letters,* **36,** 359-362.

Stephenson, D., Goodenough, K. M., Loughlin, S. C., Millward, D. & Waters, C. N. 2003. Carboniferous and Permian igneous rocks of Great Britain north of the Variscan Front: an introduction. *In:* Stephenson, D., Loughlin, S. C., Millward, D., Waters, C. N. & Williamson, I. T. (Eds.) *Carboniferous and Permian Igneous Rocks of Great Britain North of the Variscan Front.* Geological Conservation Review Series, **27,** 3-34.

Tarling, D. H. & Hrouda, F. 1993. *The Magnetic Anisotropy of Rocks.* Chapman & Hall, London, United Kingdom, 217pp.

Thorez, J. & Pirlet, H. 1978. Petrology of K-bentonite beds in the Carboniferous Series of the Visean and Tournaisian Stages of Belgium. *In:* Mortland, M. M. & Farmer, V. C. (Eds.) *International Clay Conference 1978.* Developments in Sedimentology, **27,** 323-332.

Timmerman, M. J. 2004. Timing, geodynamic setting and character of Permo-Carboniferous magmatism in the foreland of the Variscan Orogen, NW Europe. *In:* Wilson, M., Neumann, E. R., Davies, G. R., Timmerman, M. J., Heeremans, M. & Larsen, B. T. (Eds.) *Permo-Carboniferous Magmatism and Rifting in Europe.* Geological Society, London, Special Publications, **223,** 41-74.

Trapp, E. 2001. *U-Pb-Geochronologie an unterkarbonischen Pyroklastika des Harzes; der Schluessel zu einer verbesserten Zeitskala des Unterkarbons.* PhD Thesis, University of Braunschweig - Institute of Technology, Germany.

Trapp, E., Kaufmann, B., Mezger, K., Korn, D. & Weyer, D. 2004. Numerical calibration of the Devonian-Carboniferous boundary: two new U-Pb isotope dilution–thermal ionization mass spectrometry single-zircon ages from Hasselbachtal (Sauerland, Germany). *Geology,* **32,** 857-860.

Trewin, N. H. 1968. Potassium bentonites in the Namurian of Staffordshire and Derbyshire. *Proceedings of the Yorkshire Geological Society,* **37,** 73-91.

Trewin, N. H. & Holdsworth, B. K. 1972. Further K-bentonites from the Namurian of Staffordshire. *Proceedings of the Yorkshire Geological Society,* **39,** 87-88.

Triplehorn, D. M., Bohor, B. F. & Betterton, W. J. 2002. Chemical disaggregation of kaolinitic claystones (tonsteins and flint clays). *Clays and Clay Minerals,* **50,** 766-770.

Tucker, M. E., Gallagher, J., Lemon, L. & Leng, M. 2003. The Yoredale cycles of Northumbria: high-frequency clastic-carbonate Sequences of the Mid-Carboniferous icehouse world. *Open University Geological Society Journal,* **24,** 5-10.

Vail, P. R., Todd, R. G. & Sangree, J. B. 1977. Seismic stratigraphy and global changes of sea level: Part 5, Chronostratigraphic significance of seismic reflections. *In:* Payton, C.E. (Ed.) *Seismic Stratigraphy – Applications to hydrocarbon exploration.* American Association of Petroleum Geologists Memoir, **26,** 99-116.

van Leckwijck, W. P. 1960. Report of the Subcommission on Carboniferous Stratigraphy. *Compte Rendu: 4^{me} Congrès International de Stratigraphie et de Géologie du Carbonifère, Heerlen 1958,* **1,** XXIV-XXVI.

Vanneste, C. 1999. *Le calcaire de Lives (Viséen moyen) entre Namur et Dinant (Belgique). Stratigraphie séquentielle et biostratigraphie.* MS thesis, Université Catholique de Louvain.

Vanstone, S. D. 1993. *Soil development and the use of palaeosols in the assessment of palaeoclimate: a case study from the late Dinantian of Britain and Newfoundland.* PhD Thesis, University of Reading.

Veevers, J. J. & Powell, M. 1987. Late Paleozoic glacial episodes in Gondwanaland reflected in transgressive-regressive depositional sequences in Euramerica. *Bulletin of the Geological Society of America,* **98,** 475-487.

Vermeesch, P. 2004. How many grains are needed for a provenance study? *Earth and Planetary Science Letters,* **224,** 441-451.

Wagner, R. H. & Álvarez-Vázquez, C. 2010. The Carboniferous floras of the Iberian Peninsula: A synthesis with geological connotations. *Review of Palaeobotany and Palynology,* **162,** 239-324.

Walkden, G. M. 1972. The mineralogy and origin of interbedded clay wayboards in the Lower Carboniferous of the Derbyshire Dome. *Geological Journal,* **8,** 143-160.

Walkden, G. M. 1987. Sedimentary and diagenetic styles in late Dinantian carbonates of Britain. *In:* Miller, J., Adams, A. E. & Wright, V. P. (Eds.) *European Dinantian Environments.* John Wiley & Sons, Chichester, United Kingdom, 131-155.

Waters, C. N. & Davies, S. J. 2006. Carboniferous: extensional basins, advancing deltas and coal swamps. *In:* Brenchley, P. J. & Rawson, P. F. (Eds.) *The Geology of England and Wales.* 2nd Edition. Geological Society, London, United Kingdom, 173-224.

Waters, C. N., Browne, M., Dean, M. & Powell, J. H. 2007. Lithostratigraphical framework for Carboniferous successions of Great Britain (Onshore). *British Geological Survey Research Report,* **RR/07/01,** 60pp.

Waters, C. N., Somerville, I. D., Jones, N. S., Cleal, C. J., Collinson, J. D., Waters, R. A., Besly, B. M., Dean, M. T., Stephenson, M. H., Davies, J. R., Freshney, E. C., Jackson, D. I., Mitchell, W. I., Powell, J. H., Barclay, W. J., Browne, M. A. E., Leveridge, B. E., Long, S. E. & McLean, D. 2011. *A Revised Correlation of Carboniferous Rocks in the British Isles*. Geological Society, London, Special Report, **26,** 186pp

Waters, C. N. & Condon, D. J. 2012. Nature and timing of Late Mississippian to Mid-Pennsylvanian glacio-eustatic sea-level changes of the Pennine Basin, UK. *Journal of the Geological Society, London*, **169,** 37-51.

Watson, E. B. 1979. Zircon saturation in felsic liquids: Experimental results and applications to trace element geochemistry. *Contributions to Mineralogy and Petrology,* **70,** 407-419.

Weaver, C. E. 1953. Mineralogy and petrology of some Ordovician K-bentonites and related limestones. *Geological Society of America Bulletin,* **64,** 921-944.

Wefer, G. & Berger, W. H. 1991. Isotope paleontology: growth and composition of extant calcareous species. *Marine Geology,* **100,** 207-248.

Wendt, I. & Carl, C. 1991. The statistical distribution of the mean squared weighted deviation. *Chemical Geology: Isotope Geoscience Section,* **86,** 275-285.

Wetherill, G. W. 1956. An interpretation of the Rhodesia and Witwatersrand age patterns. *Geochimica et Cosmochimica Acta,* **9,** 290-292.

Weyer, D. & Menning, M. 2006. Geologische Zeitskala, stratigraphische Nomenklatur und Magnetostratigraphie. *In:* Deutsche Stratigraphische Kommission (Eds.) *Stratigraphie von Deutschland VI. Unterkarbon (Mississippium).* Schriftenreihe der Deutschen Gesellschaft für Geowissenschaften, **41,** 27-50.

Whalen, M. T. & Day, J. E. 2010. Cross-basin variations in magnetic susceptibility influenced by changing sea level, paleogeography, and paleoclimate: Upper Devonian, Western Canada Sedimentary Basin. *Journal of Sedimentary Research,* **80,** 1109-1127.

Wiedenbeck, M. 1995. An example of reverse discordance during ion microprobe zircon dating: An artifact of enhanced ion yields from a radiogenic labile Pb. *Chemical Geology,* **125,** 197-218.

Wiedenbeck, M., Allé, P., Corfu, F., Griffin, W. L., Meier, M., Oberli, F., von Quadt, A., Roddick, J. C. & Spiegel, W. 1995. Three natural zircon standards for U-Th-Pb, Lu-Hf, trace element and REE analyses. *Geostandards Newsletter,* **19,** 1-23.

Winchester, J. A. & Floyd, P. A. 1977. Geochemical discrimination of different magma series and their differentiation products using immobile elements. *Chemical Geology,* **20,** 325-343.

Wray, D. S. 1995. Origin of clay-rich beds in Turonian chalks from Lower Saxony, Germany – a rare-earth element study. *Chemical Geology,* **119,** 161-173.

Wray, D. S. & Wood, C. J. 1998. Distinction between detrital and volcanogenic clay-rich beds in Turonian–Coniacian chalks of eastern England. *Proceedings of the Yorkshire Geological Society,* **52,** 95-105.

Wright, V. P. & Vanstone, S. D. 2001. Onset of late Palaeozoic glacio-eustasy and the evolving climates of low latitude areas: a synthesis of current understanding. *Journal of the Geological Society, London,* **158,** 579-582.

Ziegler, P. A. 1990. *Geological Atlas of Western and Central Europe* (2nd Edition). Shell Internationale Petroleum Maatschappij B.V., Netherlands, 239pp.

Zielinski, R. A. 1985. Element mobility during alteration of silicic ash to kaolinite – a study of tonstein. *Sedimentology,* **32,** 567-579.

Appendices

Appendix 1: U-Pb isotopic data

Table 1 U-Pb zircon CA-ID-TIMS data

Table 2 U-Pb zircon LA-MC-ICP-MS data

Appendix 2: Whole-rock geochemistry and mineralogy data from bentonite and tonstein samples

Table 1 Whole-rock geochemical data

Table 2 Summary of X-ray diffraction data

Appendix 3: Magnetic susceptibility (MS) and stable isotope ($\delta^{13}C$ and $\delta^{18}O$) data from Belgian Livian and Warnantian strata

Table 1 MS data from section 1 at Lives-sur-Meuse

Table 2 MS data from section 2 at Lives-sur-Meuse

Table 3 MS data from Awirs West Quarry

Table 4 MS data from Anhée Nord

Table 5 MS data from Anhée Sud

Table 6 Stable isotope data from section 2 at Lives-sur-Meuse

Table 7 Stable isotope data from Awirs West Quarry

Table 8 Stable isotope data from Anhée Nord

Appendix 1

U-Pb isotopic data

Appendix 1 Table 1: U-Pb zircon CA-ID-TIMS data

(a) /1, /2 etc. are labels for the different single zircon grain analyses; all analyses were annealed and chemically abraded following a method modified after Mattinson (2005). Analyses shown in bold are data points used in the weighted mean $^{206}Pb/^{238}U$ date calculation.

(b) Nominal fraction weights measured after chemical abrasion. Weights that are underlined represent grains that were too small to be accurately weighed using the available balance. These weights may therefore be inaccurate.

(c) Nominal U and total Pb concentrations subject to the uncertainty in zircon weights. Concentration values for grains too small to be weighed accurately are likely to be inaccurate.

(d) Model Th/U ratio calculated from the radiogenic $^{208}Pb/^{206}Pb$ ratio and $^{206}Pb/^{238}U$ date.

(e) Pb* and Pbc represent radiogenic and common Pb respectively.

(f) Measured ratio corrected for tracer and fractionation only. Pb and U mass fractionation were controlled online using the $^{202}Pb/^{205}Pb$ and $^{233}U/^{235}U$ ratios of the Earthtime isotopic tracer respectively.

(g) Corrected for fractionation, tracer, and common Pb. All common lead was attributed to the analytical blank and corrected using: $^{206}Pb/^{204}Pb = 18.30 \pm 0.26$, $^{207}Pb/^{204}Pb = 15.47 \pm 0.32$, $^{208}Pb/^{204}Pb = 37.60 \pm 0.74$ (all uncertainties 2σ absolute). $^{206}Pb/^{238}U$ and $^{207}Pb/^{206}Pb$ ratios corrected for initial disequilibrium in $^{230}Th/^{238}U$ using Th/U [magma] of 4.

(h) Error correlation between $^{207}Pb/^{235}U$ and $^{206}Pb/^{238}U$ ratios.

(i) Calculations are based on the decay constants of Jaffey *et al.* (1971). $^{206}Pb/^{238}U$ and $^{207}Pb/^{206}Pb$ dates are corrected for initial disequilibrium in $^{230}Th/^{238}U$ using Th/U [magma] = 4.

(j) Date uncertainties are 2σ absolute (Ma), propagated using the algorithms of Schmitz & Schoene (2007) and Crowley *et al.* (2007).

(k) Discordance = 100 - (100 x ($^{206}Pb/^{238}U$ date / $^{207}Pb/^{206}Pb$ date)).

		Compositional Parameters						Radiogenic Isotope Ratios								Isotopic Dates (Ma)						
Sample ID	Wt. (mg)	U (ppm)	Pb (ppm)	Th / U	Pb* / Pb_c	Pb_c (pg)	$^{206}Pb/^{204}Pb$	$^{208}Pb/^{206}Pb$	$^{207}Pb/^{206}Pb$	± (2σ, %)	$^{207}Pb/^{235}U$	± (2σ, %)	$^{206}Pb/^{238}U$	± (2σ, %)	ρ	$^{207}Pb/^{206}Pb$	± (2σ, abs)	$^{207}Pb/^{235}U$	± (2σ, abs)	$^{206}Pb/^{238}U$	± (2σ, abs)	Discordance (%)
(a)	(b)	(c)	(c)	(d)	(e)	(e)	(f)	(g)	(g)		(g)		(g)		(h)	(i)	(j)	(i)	(j)	(i)	(j)	(k)
Bentonite 300																						
300/1	**0.0018**	**123**	**7.4**	**0.331**	**10.8**	**1.13**	**697**	**0.104**	**0.05322**	**0.65**	**0.4070**	**0.70**	**0.05546**	**0.09**	**0.597**	**338.0**	**14.7**	**346.69**	**2.05**	**347.98**	**0.29**	**-2.9**
300/2	**0.0026**	**223**	**12.7**	**0.304**	**28.1**	**1.13**	**1794**	**0.096**	**0.05355**	**0.21**	**0.4095**	**0.23**	**0.05546**	**0.03**	**0.719**	**352.2**	**4.7**	**348.51**	**0.67**	**347.96**	**0.10**	**1.2**
300/3	**0.0027**	**97**	**5.8**	**0.429**	**15.4**	**0.96**	**960**	**0.135**	**0.05337**	**0.43**	**0.4082**	**0.47**	**0.05547**	**0.07**	**0.576**	**344.7**	**9.8**	**347.57**	**1.38**	**348.00**	**0.24**	**-1.0**
300/4	**0.0004**	**311**	**18.6**	**0.300**	**10.7**	**0.64**	**694**	**0.095**	**0.05320**	**0.79**	**0.4069**	**0.85**	**0.05548**	**0.11**	**0.600**	**337.1**	**17.8**	**346.65**	**2.50**	**348.07**	**0.38**	**-3.2**
300/5	**0.0022**	**232**	**13.1**	**0.328**	**36.0**	**0.78**	**2280**	**0.104**	**0.05358**	**0.17**	**0.4093**	**0.20**	**0.05541**	**0.07**	**0.555**	**353.3**	**3.9**	**348.37**	**0.60**	**347.63**	**0.25**	**1.6**
300/6	**0.0020**	**137**	**8.3**	**0.259**	**8.1**	**1.82**	**539**	**0.082**	**0.05365**	**0.77**	**0.4103**	**0.82**	**0.05547**	**0.06**	**0.900**	**356.4**	**17.3**	**349.09**	**2.43**	**347.99**	**0.21**	**2.4**
300/9	0.0009	638	36.6	0.321	22.2	1.42	1417	0.101	0.05352	0.23	0.4085	0.27	0.05536	0.07	0.655	350.9	5.2	347.81	0.80	347.34	0.23	1.0
300/10	0.0005	378	35.4	0.433	16.5	1.01	1003	0.135	0.08386	0.21	0.9725	0.27	0.08411	0.10	0.693	1289.3	4.2	689.76	1.36	520.59	0.51	59.6

Appendix 1 Table 1 continued

		Compositional Parameters						Radiogenic Isotope Ratios								Isotopic Dates (Ma)						
Sample ID	Wt. (mg)	U (ppm)	Pb (ppm)	Th / U	Pb* / Pb_c	Pb_c (pg)	$^{206}Pb/^{204}Pb$	$^{208}Pb/^{206}Pb$	$^{207}Pb/^{206}Pb$	± (2σ, %)	$^{207}Pb/^{235}U$	± (2σ, %)	$^{206}Pb/^{238}U$	± (2σ, %)	ρ	$^{207}Pb/^{206}Pb$	± (2σ, abs)	$^{207}Pb/^{235}U$	± (2σ, abs)	$^{206}Pb/^{238}U$	± (2σ, abs)	Discordance (%)
(a)	(b)	(c)	(c)	(d)	(e)	(e)	(f)	(g)	(g)		(g)		(g)		(h)	(i)	(j)	(i)	(j)	(i)	(j)	(k)
L1 (Lives-sur-Meuse)																						
L1/9	**0.0026**	**807**	**45.1**	**0.368**	**38.2**	**3.00**	**2390**	**0.116**	**0.05340**	**0.22**	**0.3988**	**0.29**	**0.05416**	**0.15**	**0.663**	**346.0**	**5.0**	**340.75**	**0.83**	**339.98**	**0.49**	**1.7**
L1/10	0.0019	748	41.9	0.366	31.8	2.42	1999	0.115	0.05342	0.21	0.3980	0.25	0.05404	0.08	0.632	346.8	4.8	340.22	0.72	339.26	0.25	2.2
L1/11	0.0020	302	23.5	0.536	2.9	12.11	189	0.169	0.05427	2.26	0.4102	2.42	0.05482	0.17	0.945	382.1	50.7	348.99	7.14	344.04	0.57	10.0
L1/12	**0.0006**	**1560**	**86.7**	**0.369**	**53.5**	**0.95**	**3342**	**0.116**	**0.05344**	**0.14**	**0.3993**	**0.18**	**0.05420**	**0.08**	**0.722**	**347.3**	**3.1**	**341.17**	**0.53**	**340.27**	**0.27**	**2.0**
L1/13	**0.0069**	**801**	**44.3**	**0.384**	**89.4**	**3.38**	**5550**	**0.121**	**0.05329**	**0.10**	**0.3980**	**0.16**	**0.05416**	**0.09**	**0.813**	**341.3**	**2.2**	**340.19**	**0.45**	**340.03**	**0.30**	**0.4**
L2 (Lives-sur-Meuse)																						
L2/2	**0.0058**	**152**	**8.6**	**0.355**	**23.7**	**2.02**	**1497**	**0.112**	**0.05338**	**0.24**	**0.3986**	**0.28**	**0.05415**	**0.09**	**0.614**	**345.2**	**5.4**	**340.61**	**0.82**	**339.94**	**0.31**	**1.5**
L2/3	**0.0074**	**167**	**9.5**	**0.404**	**33.4**	**2.04**	**2075**	**0.128**	**0.05330**	**0.18**	**0.3978**	**0.20**	**0.05413**	**0.04**	**0.586**	**341.5**	**4.0**	**340.02**	**0.57**	**339.80**	**0.12**	**0.5**
L2/4	**0.0088**	**100**	**5.9**	**0.579**	**35.0**	**1.45**	**2075**	**0.183**	**0.05329**	**0.17**	**0.3977**	**0.20**	**0.05414**	**0.06**	**0.571**	**341.0**	**4.0**	**340.00**	**0.58**	**339.86**	**0.20**	**0.3**
L2/5	**0.0119**	**201**	**11.0**	**0.337**	**77.0**	**1.68**	**4848**	**0.106**	**0.05327**	**0.09**	**0.3977**	**0.12**	**0.05414**	**0.07**	**0.687**	**340.4**	**1.9**	**339.98**	**0.34**	**339.91**	**0.23**	**0.1**
L2/6	**0.0103**	**77**	**4.3**	**0.358**	**25.3**	**1.69**	**1594**	**0.113**	**0.05336**	**0.22**	**0.3983**	**0.25**	**0.05414**	**0.04**	**0.697**	**344.1**	**5.0**	**340.43**	**0.72**	**339.89**	**0.13**	**1.2**
L2/8	**0.0017**	**600**	**35.7**	**0.492**	**18.3**	**3.14**	**1117**	**0.155**	**0.05338**	**0.34**	**0.3986**	**0.37**	**0.05415**	**0.04**	**0.793**	**345.1**	**7.7**	**340.62**	**1.07**	**339.97**	**0.12**	**1.5**
L3 (Lives-sur-Meuse)																						
L3/1	**0.0022**	**281**	**16.5**	**0.528**	**26.3**	**1.32**	**1589**	**0.167**	**0.05318**	**0.25**	**0.3949**	**0.27**	**0.05386**	**0.04**	**0.549**	**336.5**	**5.7**	**337.98**	**0.78**	**338.18**	**0.13**	**-0.5**
L3/2	0.0033	220	13.2	0.476	14.4	2.82	890	0.150	0.05348	0.46	0.3982	0.49	0.05400	0.05	0.688	349.4	10.3	340.36	1.41	339.04	0.16	3.0
L3/4	0.0049	317	17.6	0.420	111.3	0.77	6843	0.133	0.05324	0.06	0.3960	0.08	0.05394	0.04	0.629	339.1	1.4	338.71	0.23	338.65	0.15	0.1
L3/5	**0.0032**	**185**	**10.5**	**0.431**	**30.2**	**1.08**	**1866**	**0.136**	**0.05331**	**0.24**	**0.3962**	**0.28**	**0.05391**	**0.07**	**0.620**	**341.8**	**5.4**	**338.89**	**0.80**	**338.46**	**0.24**	**1.0**
L3/6	0.0028	113	6.6	0.465	28.0	0.63	1712	0.147	0.05337	0.25	0.3976	0.27	0.05402	0.05	0.494	344.7	5.6	339.89	0.77	339.18	0.17	1.6
L3/7	**0.0020**	**234**	**15.0**	**0.487**	**6.9**	**3.81**	**433**	**0.154**	**0.05358**	**0.96**	**0.3982**	**1.03**	**0.05390**	**0.10**	**0.731**	**353.5**	**21.7**	**340.37**	**2.97**	**338.45**	**0.31**	**4.3**
L3/8	**0.0018**	**471**	**26.7**	**0.449**	**41.0**	**1.14**	**2515**	**0.142**	**0.05330**	**0.18**	**0.3961**	**0.20**	**0.05389**	**0.06**	**0.476**	**341.7**	**4.0**	**338.81**	**0.57**	**338.38**	**0.18**	**1.0**
L3/10	0.0024	470	26.0	0.389	55.3	1.11	3439	0.123	0.05318	0.12	0.3944	0.14	0.05378	0.04	0.476	336.5	2.8	337.54	0.39	337.70	0.13	-0.4
L3/11	**0.0006**	**314**	**19.4**	**0.425**	**7.9**	**1.31**	**501**	**0.134**	**0.05327**	**0.86**	**0.3955**	**0.92**	**0.05385**	**0.09**	**0.698**	**340.3**	**19.5**	**338.38**	**2.66**	**338.09**	**0.30**	**0.7**
L3/13	0.0017	578	32.2	0.407	60.5	0.89	3738	0.129	0.05336	0.12	0.3972	0.13	0.05399	0.05	0.494	344.2	2.7	339.63	0.39	338.97	0.15	1.5

Appendix 1 Table 1 continued

		Compositional Parameters						Radiogenic Isotope Ratios								Isotopic Dates (Ma)						
Sample ID	Wt. (mg)	U (ppm)	Pb (ppm)	Th / U	Pb* / Pb_c	Pb_c (pg)	$^{206}Pb/^{204}Pb$	$^{208}Pb/^{206}Pb$	$^{207}Pb/^{206}Pb$	± (2σ, %)	$^{207}Pb/^{235}U$	± (2σ, %)	$^{206}Pb/^{238}U$	± (2σ, %)	ρ	$^{207}Pb/^{206}Pb$	± (2σ, abs)	$^{207}Pb/^{235}U$	± (2σ, abs)	$^{206}Pb/^{238}U$	± (2σ, abs)	Discordance (%)
(a)	(b)	(c)	(c)	(d)	(e)	(e)	(f)	(g)	(g)		(g)		(g)		(h)	(i)	(j)	(i)	(j)	(i)	(j)	(k)
W1 (Anhée Nord)																						
W1/1	**0.0010**	**229**	**13.3**	**0.461**	**20.3**	**0.62**	**1247**	**0.146**	**0.05304**	**0.37**	**0.3916**	**0.40**	**0.05355**	**0.05**	**0.584**	**330.7**	**8.5**	**335.55**	**1.15**	**336.25**	**0.17**	**-1.7**
W1/3	**0.0044**	**142**	**8.2**	**0.507**	**37.5**	**0.93**	**2265**	**0.160**	**0.05334**	**0.18**	**0.3937**	**0.20**	**0.05354**	**0.04**	**0.500**	**343.1**	**4.2**	**337.09**	**0.57**	**336.22**	**0.12**	**2.0**
W1/4	0.0041	494	32.2	1.009	33.2	3.87	1774	0.318	0.05328	0.23	0.3940	0.25	0.05363	0.05	0.488	340.8	5.3	337.28	0.72	336.77	0.16	1.2
W1/5	**0.0033**	**290**	**16.5**	**0.508**	**51.6**	**1.04**	**3109**	**0.160**	**0.05330**	**0.13**	**0.3932**	**0.16**	**0.05351**	**0.08**	**0.601**	**341.7**	**3.0**	**336.73**	**0.47**	**336.01**	**0.28**	**1.7**
W1/6	**0.0044**	**95**	**5.5**	**0.494**	**19.5**	**1.18**	**1193**	**0.156**	**0.05332**	**0.34**	**0.3936**	**0.37**	**0.05354**	**0.04**	**0.639**	**342.3**	**7.7**	**337.00**	**1.05**	**336.23**	**0.13**	**1.8**
W1/7	**0.0016**	**447**	**25.5**	**0.507**	**46.5**	**0.86**	**2807**	**0.160**	**0.05319**	**0.15**	**0.3927**	**0.17**	**0.05355**	**0.04**	**0.473**	**337.0**	**3.4**	**336.35**	**0.47**	**336.26**	**0.13**	**0.2**
W1/8	**0.0025**	**688**	**38.2**	**0.443**	**85.9**	**1.10**	**5252**	**0.140**	**0.05320**	**0.08**	**0.3928**	**0.10**	**0.05355**	**0.05**	**0.574**	**337.4**	**1.9**	**336.43**	**0.29**	**336.29**	**0.16**	**0.3**
W1/9	**0.0013**	**523**	**31.7**	**0.702**	**29.3**	**1.36**	**1686**	**0.222**	**0.05325**	**0.24**	**0.3930**	**0.26**	**0.05352**	**0.05**	**0.486**	**339.5**	**5.5**	**336.55**	**0.75**	**336.12**	**0.17**	**1.0**
W8 (Anhée Nord)																						
W8/4	**0.0022**	**73**	**5.4**	**0.990**	**5.3**	**1.89**	**301**	**0.313**	**0.05346**	**1.40**	**0.3938**	**1.50**	**0.05343**	**0.11**	**0.900**	**348.4**	**31.8**	**337.15**	**4.31**	**335.52**	**0.36**	**3.7**
W8/5	0.0009	169	15.2	1.000	2.3	4.10	143	0.316	0.05461	3.13	0.4048	3.35	0.05376	0.22	0.974	396.4	70.2	345.14	9.79	337.58	0.73	14.8
W8/6	0.0010	96	7.2	0.948	5.0	1.20	287	0.299	0.05352	1.59	0.3951	1.70	0.05354	0.14	0.838	351.1	35.9	338.08	4.90	336.19	0.45	4.2
W8/7	**0.0018**	**107**	**8.5**	**0.959**	**3.6**	**3.35**	**210**	**0.303**	**0.05414**	**2.02**	**0.3988**	**2.15**	**0.05343**	**0.15**	**0.945**	**376.9**	**45.3**	**340.81**	**6.24**	**335.55**	**0.48**	**11.0**
W8/8	0.0019	42	3.3	1.132	5.2	1.01	286	0.357	0.05427	1.55	0.4007	1.66	0.05356	0.13	0.872	382.2	34.8	342.18	4.82	336.31	0.41	12.0
W8/9	**0.0010**	**132**	**9.3**	**0.940**	**7.0**	**1.17**	**392**	**0.297**	**0.05344**	**1.06**	**0.3938**	**1.14**	**0.05345**	**0.08**	**0.941**	**347.5**	**24.0**	**337.14**	**3.27**	**335.64**	**0.27**	**3.4**
W8/11	0.0010	123	8.6	0.861	7.1	1.06	405	0.272	0.05349	1.06	0.3953	1.14	0.05359	0.09	0.852	349.8	24.1	338.21	3.27	336.53	0.29	3.8
W8/12	0.0010	155	10.7	0.891	8.6	1.11	486	0.281	0.05364	0.88	0.3961	0.95	0.05355	0.08	0.875	356.1	20.0	338.79	2.75	336.27	0.26	5.6
W8/14	0.0020	70	4.8	0.940	8.5	1.02	475	0.297	0.05339	0.88	0.3943	0.95	0.05356	0.07	0.899	345.3	20.0	337.49	2.72	336.35	0.23	2.6

Appendix 1 Table 1 continued

		Compositional Parameters						Radiogenic Isotope Ratios								Isotopic Dates (Ma)						
Sample ID	Wt. (mg)	U (ppm)	Pb (ppm)	Th / U	Pb* / Pb_c	Pb_c (pg)	$^{206}Pb/^{204}Pb$	$^{208}Pb/^{206}Pb$	$^{207}Pb/^{206}Pb$	± (2σ, %)	$^{207}Pb/^{235}U$	± (2σ, %)	$^{206}Pb/^{238}U$	± (2σ, %)	ρ	$^{207}Pb/^{206}Pb$	± (2σ, abs)	$^{207}Pb/^{235}U$	± (2σ, abs)	$^{206}Pb/^{238}U$	± (2σ, abs)	Discordance (%)
(a)	(b)	(c)	(c)	(d)	(e)	(e)	(f)	(g)	(g)		(g)		(g)		(h)	(i)	(j)	(i)	(j)	(i)	(j)	(k)
W12 (Anhée Sud)																						
W12/2	0.0010	265	18.8	0.700	4.6	3.36	280	0.221	0.05336	1.51	0.3902	1.61	0.05304	0.12	0.869	344.0	34.1	334.55	4.59	333.18	0.39	3.2
W12/3	0.0020	439	27.6	0.839	21.5	2.45	1205	0.265	0.05319	0.34	0.3882	0.36	0.05293	0.04	0.631	337.1	7.6	333.05	1.03	332.47	0.13	1.4
W12/4	0.0010	257	16.5	0.654	8.3	1.77	496	0.206	0.05337	0.84	0.3882	0.90	0.05275	0.07	0.798	344.7	19.1	333.02	2.56	331.36	0.24	3.9
W12/5	0.0010	386	26.0	0.668	6.0	3.71	364	0.211	0.05337	1.15	0.3897	1.22	0.05296	0.09	0.867	344.7	25.9	334.17	3.48	332.66	0.30	3.5
W12/6	0.0024	143	9.3	0.696	8.4	2.37	499	0.220	0.05333	0.85	0.3892	0.91	0.05294	0.08	0.743	342.8	19.2	333.81	2.59	332.52	0.27	3.0
W12/7	0.0009	550	36.7	1.105	22.7	1.40	1192	0.349	0.05318	0.34	0.3884	0.37	0.05297	0.05	0.586	336.4	7.7	333.18	1.04	332.71	0.15	1.1
W12/8	0.0014	412	24.6	0.626	19.8	1.65	1169	0.198	0.05329	0.37	0.3877	0.40	0.05276	0.08	0.490	341.3	8.3	332.66	1.13	331.43	0.25	2.9
W12/9	0.0009	367	25.9	0.731	4.8	4.00	291	0.231	0.05346	1.44	0.3897	1.54	0.05287	0.11	0.880	348.3	32.6	334.16	4.39	332.13	0.37	4.6
W12/11	0.0015	84	5.7	0.723	6.5	1.14	384	0.228	0.05373	1.15	0.3927	1.23	0.05301	0.11	0.714	359.9	25.9	336.37	3.51	332.98	0.36	7.5
W12/12	0.0010	166	11.8	0.763	4.7	2.06	284	0.241	0.05353	1.50	0.3912	1.61	0.05300	0.12	0.837	351.4	34.0	335.24	4.58	332.91	0.40	5.3
W12/13	0.0021	383	22.5	0.623	28.8	1.59	1696	0.197	0.05315	0.20	0.3876	0.23	0.05289	0.05	0.664	335.3	4.6	332.61	0.66	332.22	0.16	0.9
W12/14	0.0040	72	4.7	0.787	10.6	1.62	611	0.248	0.05337	0.67	0.3898	0.71	0.05297	0.06	0.884	344.6	15.1	334.22	2.03	332.73	0.18	3.4
W12/15	0.0009	217	15.5	0.825	5.1	2.27	303	0.260	0.05361	1.44	0.3921	1.54	0.05304	0.12	0.816	354.8	32.5	335.91	4.40	333.18	0.40	6.1
W12/16	0.0024	171	10.1	0.684	45.1	0.53	2600	0.216	0.05322	0.15	0.3885	0.17	0.05294	0.05	0.660	338.3	3.3	333.26	0.49	332.54	0.15	1.7
W12/17	0.0025	164	9.7	0.705	40.2	0.59	2307	0.223	0.05322	0.17	0.3879	0.19	0.05287	0.03	0.617	338.1	3.9	332.86	0.54	332.11	0.10	1.8
W13 (Anhée Sud)																						
W13/1	**0.0156**	**138**	**8.2**	**0.711**	**46.1**	**2.72**	**2639**	**0.224**	**0.05312**	**0.14**	**0.3875**	**0.16**	**0.05292**	**0.04**	**0.516**	**333.7**	**3.3**	**332.57**	**0.46**	**332.41**	**0.14**	**0.4**
W13/2	**0.0130**	**77**	**4.6**	**0.702**	**40.1**	**1.45**	**2306**	**0.222**	**0.05308**	**0.24**	**0.3872**	**0.26**	**0.05291**	**0.06**	**0.346**	**332.1**	**5.5**	**332.32**	**0.73**	**332.35**	**0.19**	**-0.1**
W13/3	0.0116	35	2.0	0.627	30.4	0.76	1781	0.198	0.05318	0.18	0.3889	0.22	0.05304	0.05	0.847	336.4	4.0	333.58	0.62	333.17	0.17	1.0
W13/4	**0.0110**	**27**	**2.0**	**0.678**	**4.0**	**4.33**	**246**	**0.214**	**0.05364**	**1.71**	**0.3917**	**1.83**	**0.05297**	**0.12**	**0.975**	**356.0**	**38.6**	**335.64**	**5.23**	**332.71**	**0.39**	**6.5**
W13/5	**0.0099**	**19**	**1.3**	**0.896**	**9.1**	**1.28**	**511**	**0.283**	**0.05318**	**0.88**	**0.3884**	**0.94**	**0.05297**	**0.08**	**0.790**	**336.3**	**19.9**	**333.19**	**2.68**	**332.74**	**0.27**	**1.1**
W13/6	**0.0112**	**62**	**3.6**	**0.664**	**48.3**	**0.82**	**2797**	**0.210**	**0.05317**	**0.12**	**0.3881**	**0.14**	**0.05294**	**0.03**	**0.640**	**335.8**	**2.8**	**332.97**	**0.41**	**332.56**	**0.11**	**1.0**

Appendix 1 Table 1 continued

		Compositional Parameters						Radiogenic Isotope Ratios								Isotopic Dates (Ma)						
Sample ID	Wt. (mg)	U (ppm)	Pb (ppm)	Th / U	Pb* / Pb_c	Pb_c (pg)	$^{206}Pb/^{204}Pb$	$^{208}Pb/^{206}Pb$	$^{207}Pb/^{206}Pb$	± (2σ, %)	$^{207}Pb/^{235}U$	± (2σ, %)	$^{206}Pb/^{238}U$	± (2σ, %)	ρ	$^{207}Pb/^{206}Pb$	± (2σ, abs)	$^{207}Pb/^{235}U$	± (2σ, abs)	$^{206}Pb/^{238}U$	± (2σ, abs)	Discordance (%)
(a)	(b)	(c)	(c)	(d)	(e)	(e)	(f)	(g)	(g)		(g)		(g)		(h)	(i)	(j)	(i)	(j)	(i)	(j)	(k)
Bentonite B1																						
B1/2	0.0004	1344	78.0	0.722	18.4	1.60	1064	0.228	0.05291	0.41	0.3640	0.44	0.04989	0.07	0.514	325.2	9.3	315.22	1.19	313.87	0.22	3.5
B1/10	0.0010	5	1.8	0.235	0.2	1.48	33	0.074	0.05659	31.05	0.5267	32.64	0.06751	1.95	0.827	475.5	686.5	429.65	114.33	421.14	7.93	11.4
B1/11	0.0010	88	15.9	0.438	5.8	2.34	343	0.135	0.16216	0.36	3.0818	0.45	0.13783	0.11	0.852	2478.3	6.1	1428.17	3.46	832.41	0.88	66.4
B1/12	0.0010	57	3.9	0.187	2.4	1.16	173	0.059	0.05449	2.78	0.3823	2.98	0.05088	0.22	0.891	391.5	62.5	328.70	8.36	319.89	0.68	18.3
B1/13	0.0010	251	40.7	0.283	39.6	1.00	2509	0.086	0.07101	0.12	1.5572	0.15	0.15904	0.08	0.634	957.8	2.4	953.37	0.93	951.45	0.67	0.7
Bentonite B9																						
B9/2	0.0010	53	7.1	1.466	1.0	3.53	67	0.463	0.05839	8.41	0.4151	9.03	0.05156	0.73	0.858	544.5	183.8	352.56	26.89	324.11	2.30	40.5
B9/3	0.0010	23	2.8	1.862	1.7	1.03	93	0.588	0.05731	5.70	0.4126	6.10	0.05221	0.44	0.908	503.5	125.4	350.73	18.08	328.09	1.42	34.8
B9/5	0.0010	32	5.1	1.108	0.6	3.16	51	0.350	0.05614	11.82	0.3992	12.62	0.05158	0.83	0.970	457.9	262.1	341.10	36.56	324.20	2.62	29.2
B9/9	0.0010	109	11.1	1.044	1.5	4.41	98	0.330	0.05512	4.75	0.3920	5.09	0.05158	0.34	0.980	417.0	106.2	335.81	14.55	324.20	1.07	22.3
B9/10	**0.0010**	**87**	**6.6**	**1.187**	**5.1**	**1.09**	**276**	**0.375**	**0.05338**	**1.62**	**0.3804**	**1.73**	**0.05168**	**0.14**	**0.802**	**345.1**	**36.6**	**327.32**	**4.84**	**324.82**	**0.45**	**5.9**
B9/11	**0.0010**	**31**	**2.7**	**0.988**	**2.3**	**0.80**	**142**	**0.312**	**0.05381**	**3.43**	**0.3826**	**3.66**	**0.05157**	**0.27**	**0.885**	**362.9**	**77.4**	**328.95**	**10.30**	**324.17**	**0.84**	**10.7**
B9/14	**0.0010**	**64**	**4.8**	**0.985**	**4.3**	**0.91**	**247**	**0.311**	**0.05281**	**1.89**	**0.3758**	**2.02**	**0.05161**	**0.14**	**0.967**	**320.5**	**42.9**	**323.93**	**5.60**	**324.41**	**0.43**	**-1.2**
B9/15	**0.0010**	**90**	**6.8**	**0.945**	**3.9**	**1.39**	**228**	**0.298**	**0.05369**	**2.23**	**0.3821**	**2.37**	**0.05162**	**0.22**	**0.663**	**357.9**	**50.3**	**328.56**	**6.65**	**324.44**	**0.70**	**9.3**
B9/16	0.0010	56	8.7	1.088	0.7	5.22	53	0.344	0.06177	9.95	0.4407	10.73	0.05175	0.80	0.975	666.1	213.1	370.77	33.33	325.25	2.54	51.2

Appendix 1 Table 1 continued

Sample ID	Wt.	Compositional Parameters						Radiogenic Isotope Ratios								Isotopic Dates (Ma)						Discordance
		U	Pb	Th	Pb*	Pb_c	^{206}Pb	^{208}Pb	^{207}Pb	±	^{207}Pb	±	^{206}Pb	±	ρ	^{207}Pb	±	^{207}Pb	±	^{206}Pb	±	
				U	Pb_c		^{204}Pb	^{206}Pb	^{206}Pb	(2σ, %)	^{235}U	(2σ, %)	^{238}U	(2σ, %)		^{206}Pb	(2σ, abs)	^{235}U	(2σ, abs)	^{238}U	(2σ, abs)	(%)
(a)	(b)	(c)	(c)	(d)	(e)	(e)	(f)	(g)	(g)		(g)		(g)		(h)	(i)	(j)	(i)	(j)	(i)	(j)	(k)
Tonstein T75																						
T75/1	**0.0009**	**750**	**42.7**	**0.671**	**27.4**	**1.36**	**1591**	**0.212**	**0.05277**	**0.22**	**0.3674**	**0.25**	**0.05049**	**0.07**	**0.596**	**319.0**	**4.9**	**317.73**	**0.69**	**317.56**	**0.23**	**0.5**
T75/2	**0.0014**	**261**	**14.3**	**0.447**	**17.2**	**1.10**	**1065**	**0.141**	**0.05268**	**0.40**	**0.3671**	**0.46**	**0.05054**	**0.10**	**0.634**	**314.9**	**9.2**	**317.48**	**1.26**	**317.83**	**0.32**	**-0.9**
T75/3	**0.0026**	**296**	**16.4**	**0.549**	**27.9**	**1.47**	**1673**	**0.173**	**0.05274**	**0.21**	**0.3674**	**0.26**	**0.05052**	**0.12**	**0.631**	**317.7**	**4.8**	**317.73**	**0.72**	**317.73**	**0.36**	**0.0**
T75/4	0.0006	706	41.6	0.408	6.7	3.24	431	0.129	0.05319	0.95	0.3697	1.02	0.05041	0.08	0.871	336.7	21.5	319.40	2.79	317.03	0.25	5.8
T75/5	0.0010	446	38.5	0.598	1.7	14.15	119	0.189	0.05449	3.76	0.3843	4.02	0.05114	0.27	0.984	391.5	84.4	330.17	11.34	321.53	0.83	17.9
T75/6	**0.0011**	**477**	**26.5**	**0.599**	**34.8**	**0.81**	**2053**	**0.189**	**0.05281**	**0.19**	**0.3677**	**0.23**	**0.05050**	**0.07**	**0.645**	**320.5**	**4.3**	**317.96**	**0.62**	**317.61**	**0.22**	**0.9**
T75/7	0.0006	302	17.5	0.577	13.1	0.75	788	0.182	0.05300	0.52	0.3700	0.57	0.05064	0.05	0.803	328.7	11.9	319.68	1.55	318.44	0.17	3.1
T75/8	0.0018	233	13.3	0.500	12.3	1.80	755	0.158	0.05317	0.54	0.3709	0.59	0.05059	0.07	0.725	336.1	12.3	320.31	1.62	318.14	0.21	5.3
T75/9	0.0008	517	32.0	0.544	6.0	3.64	377	0.172	0.05309	1.09	0.3693	1.17	0.05045	0.09	0.901	332.5	24.8	319.10	3.21	317.27	0.26	4.6
T75/11	0.0022	182	9.8	0.504	37.5	0.56	2269	0.159	0.05289	0.18	0.3689	0.22	0.05059	0.10	0.577	324.3	4.1	318.86	0.60	318.12	0.31	1.9
T75/13	**0.0015**	**181**	**9.6**	**0.420**	**31.1**	**0.45**	**1927**	**0.133**	**0.05276**	**0.30**	**0.3673**	**0.33**	**0.05049**	**0.09**	**0.402**	**318.5**	**6.8**	**317.64**	**0.89**	**317.53**	**0.28**	**0.3**
Tonstein Z1																						
Z1/1	0.0057	218	14.2	0.774	6.1	11.45	357	0.244	0.05313	1.15	0.3653	1.23	0.04987	0.11	0.767	334.4	26.0	316.17	3.34	313.70	0.33	6.2
Z1/4	**0.0055**	**152**	**8.4**	**0.689**	**67.3**	**0.68**	**3866**	**0.218**	**0.05271**	**0.16**	**0.3624**	**0.17**	**0.04987**	**0.06**	**0.351**	**316.3**	**3.6**	**314.04**	**0.45**	**313.73**	**0.17**	**0.8**
Z1/5	**0.0042**	**444**	**24.4**	**0.675**	**84.8**	**1.19**	**4884**	**0.213**	**0.05270**	**0.08**	**0.3621**	**0.11**	**0.04984**	**0.07**	**0.733**	**315.8**	**1.8**	**313.81**	**0.31**	**313.55**	**0.22**	**0.7**
Z1/6	**0.0053**	**177**	**9.8**	**0.685**	**59.5**	**0.86**	**3428**	**0.216**	**0.05271**	**0.08**	**0.3627**	**0.13**	**0.04991**	**0.09**	**0.818**	**316.5**	**1.8**	**314.25**	**0.35**	**313.94**	**0.28**	**0.8**
Z1/7	**0.0048**	**378**	**20.8**	**0.689**	**121.1**	**0.82**	**6946**	**0.218**	**0.05270**	**0.03**	**0.3626**	**0.07**	**0.04991**	**0.06**	**0.935**	**315.7**	**0.6**	**314.15**	**0.19**	**313.94**	**0.18**	**0.6**
Z1/8	**0.0057**	**157**	**8.7**	**0.693**	**80.5**	**0.61**	**4615**	**0.219**	**0.05272**	**0.03**	**0.3627**	**0.08**	**0.04989**	**0.06**	**0.964**	**316.8**	**0.7**	**314.20**	**0.22**	**313.86**	**0.19**	**0.9**
Z1/9	**0.0056**	**149**	**8.1**	**0.636**	**61.1**	**0.73**	**3559**	**0.201**	**0.05274**	**0.13**	**0.3626**	**0.15**	**0.04986**	**0.06**	**0.509**	**317.8**	**2.9**	**314.18**	**0.40**	**313.69**	**0.18**	**1.3**

Appendix 1 Table 1 continued

		Compositional Parameters						Radiogenic Isotope Ratios								Isotopic Dates (Ma)						
Sample ID	Wt. (mg)	U (ppm)	Pb (ppm)	Th / U	Pb* / Pb_c	Pb_c (pg)	$^{206}Pb/^{204}Pb$	$^{208}Pb/^{206}Pb$	$^{207}Pb/^{206}Pb$	± (2σ, %)	$^{207}Pb/^{235}U$	± (2σ, %)	$^{206}Pb/^{238}U$	± (2σ, %)	ρ	$^{207}Pb/^{206}Pb$	± (2σ, abs)	$^{207}Pb/^{235}U$	± (2σ, abs)	$^{206}Pb/^{238}U$	± (2σ, abs)	Discordance (%)
(a)	(b)	(c)	(c)	(d)	(e)	(e)	(f)	(g)	(g)		(g)		(g)		(h)	(i)	(j)	(i)	(j)	(i)	(j)	(k)
Tonstein T1Gb																						
T1Gb/1	0.0010	1805	102.6	0.544	33.7	2.95	2021	0.172	0.05319	0.17	0.3841	0.20	0.05237	0.07	0.590	336.9	3.9	330.04	0.57	329.07	0.22	2.3
T1Gb/2	**0.0006**	**897**	**47.6**	**0.441**	**24.8**	**1.11**	**1528**	**0.139**	**0.05270**	**0.26**	**0.3612**	**0.31**	**0.04971**	**0.13**	**0.570**	**316.0**	**5.9**	**313.11**	**0.83**	**312.72**	**0.39**	**1.0**
T1Gb/6	**0.0010**	**522**	**26.8**	**0.348**	**30.5**	**0.85**	**1922**	**0.110**	**0.05282**	**0.21**	**0.3617**	**0.26**	**0.04967**	**0.10**	**0.612**	**321.0**	**4.9**	**313.49**	**0.70**	**312.48**	**0.31**	**2.7**
Tonstein T1P																						
T1P/2	0.0007	579	29.2	0.261	20.8	0.94	1348	0.082	0.05282	0.29	0.3593	0.32	0.04933	0.04	0.774	321.1	6.6	311.69	0.86	310.43	0.13	3.3
T1P/3	0.0010	265	14.3	0.373	12.6	1.05	798	0.118	0.05299	0.57	0.3624	0.62	0.04959	0.06	0.840	328.5	13.0	313.98	1.69	312.03	0.20	5.0
T1P/4	0.0010	258	15.1	0.519	7.5	1.78	465	0.164	0.05302	0.89	0.3604	0.96	0.04930	0.07	0.940	329.7	20.3	312.51	2.58	310.21	0.20	5.9
T1P/5	0.0010	220	12.3	0.423	8.1	1.36	513	0.134	0.05274	0.83	0.3550	0.89	0.04882	0.07	0.890	317.6	18.9	308.46	2.37	307.26	0.20	3.2
T1P/6	0.0010	543	28.3	0.349	19.3	1.40	1226	0.110	0.05272	0.32	0.3606	0.35	0.04960	0.04	0.800	316.7	7.3	312.64	0.95	312.09	0.12	1.5
T1P/8	0.0010	128	8.9	0.457	2.8	2.37	186	0.144	0.05383	2.35	0.3670	2.51	0.04944	0.17	0.935	363.9	53.0	317.39	6.84	311.09	0.52	14.5
T1P/11	0.0010	155	10.6	0.508	3.0	2.66	197	0.161	0.05351	2.20	0.3620	2.34	0.04906	0.16	0.934	350.7	49.6	313.68	6.32	308.72	0.48	12.0
T1P/13	0.0008	120	6.9	0.190	4.5	0.99	315	0.060	0.05281	1.39	0.3565	1.48	0.04897	0.11	0.901	320.6	31.5	309.63	3.96	308.18	0.32	3.9
T1P/14	0.0010	259	14.3	0.299	7.6	1.66	499	0.094	0.05297	0.83	0.3612	0.89	0.04945	0.06	0.972	327.4	18.9	313.09	2.41	311.17	0.19	5.0

Appendix 1 Table 2: U-Pb zircon LA-MC-ICP-MS data

1) Error correlation between $^{207}Pb/^{235}U$ and $^{206}Pb/^{238}U$ ratios

2) Discordance (%) = 100 - (100 x ($^{206}Pb/^{238}U$ date / $^{207}Pb/^{206}Pb$ date))

	Radiogenic isotopic ratios							Isotopic dates (Ma)							
Sample ID	$^{207}Pb/^{206}Pb$	±(2σ,%)	$^{207}Pb/^{235}U$	±(2σ,%)	$^{206}Pb/^{238}U$	±(2σ,%)	ρ[1]	$^{207}Pb/^{206}Pb$	±(2σ abs)	$^{207}Pb/^{235}U$	±(2σ abs)	$^{206}Pb/^{238}U$	±(2σ abs)	Discordance[2] (%)	U conc[n] (ppm)
MAP 11/07/01 (Not corrected for common lead)															
MAP110701/Z1	0.07001	1.4	0.5298	2.6	0.05488	2.2	0.838	928.6	29.3	431.7	9.2	344.4	7.4	62.9	1086
MAP110701/Z2	0.05709	1.1	0.4437	2.6	0.05637	2.4	0.908	494.9	23.9	372.9	8.1	353.5	8.1	28.6	655
MAP110701/Z3	0.11270	7.6	0.6104	8.3	0.03928	3.2	0.386	1843.4	138.3	483.8	31.9	248.4	7.8	86.5	1230
MAP110701/Z4	0.05437	1.3	0.4130	2.6	0.05509	2.2	0.861	386.3	29.8	351.0	7.8	345.7	7.6	10.5	523
MAP110701/Z5	0.14198	1.0	8.7893	4.4	0.44899	4.2	0.973	2251.5	17.3	2316.4	39.8	2390.8	84.9	-6.2	239
MAP110701/Z7	0.05577	1.0	0.5017	2.5	0.06524	2.3	0.916	443.3	22.2	412.8	8.5	407.4	9.0	8.1	899
MAP110701/Z8	0.06158	1.8	0.4865	2.8	0.05730	2.1	0.762	659.5	38.8	402.5	9.3	359.2	7.4	45.5	559
MAP110701/Z9	0.14998	7.1	0.6855	8.5	0.03315	4.7	0.553	2345.7	120.9	530.1	35.1	210.2	9.7	91.0	1866
MAP110701/Z10	0.05899	1.4	0.4438	2.6	0.05457	2.2	0.841	566.7	30.3	372.9	8.0	342.5	7.2	39.6	992
MAP 11/07/01 (Corrected for common lead)															
MAP110701/Z1	0.05066	24.9	0.3744	26.7	0.05359	9.4	0.355	225.5	576.0	322.9	73.7	336.6	31.0	-49.2	1086
MAP110701/Z2	0.04944	61.4	0.3815	61.7	0.05597	5.4	0.088	168.7	1434.5	328.1	172.9	351.0	18.6	-108.1	655
MAP110701/Z3	0.05313	37.8	0.2642	38.6	0.03607	7.8	0.203	334.3	856.8	238.1	81.9	228.4	17.6	31.7	1230
MAP110701/Z4	0.04121	83.6	0.3081	83.7	0.05422	4.1	0.049	-274.6	2125.9	272.7	200.2	340.4	13.6	224.0	523
MAP110701/Z5	0.14352	4.0	8.7145	19.9	0.44037	19.5	0.979	2270.2	69.7	2308.6	181.5	2352.3	384.6	-3.6	239
MAP110701/Z7	0.06294	27.1	0.5666	28.6	0.06529	9.3	0.326	706.1	575.5	455.8	105.1	407.7	36.8	42.3	899
MAP110701/Z8	0.06739	28.4	0.5290	28.8	0.05693	4.7	0.163	850.0	590.1	431.1	101.1	356.9	16.3	58.0	559
MAP110701/Z9	0.05289	27.3	0.2122	29.4	0.02910	10.9	0.370	324.1	619.7	195.4	52.2	184.9	19.8	43.0	1866
MAP110701/Z10	0.06041	22.4	0.4558	23.9	0.05472	8.5	0.355	618.4	482.8	381.3	76.1	343.4	28.4	44.5	992
MAP 11/07/03 (Not corrected for common lead; data continued overleaf)															
MAP110703/Z1	0.07807	3.4	0.5831	4.0	0.05417	2.1	0.538	1148.6	66.5	466.5	14.9	340.1	7.1	70.4	1357
MAP110703/Z2	0.14323	3.2	0.8270	3.9	0.04187	2.2	0.564	2266.6	55.5	611.9	17.9	264.4	5.7	88.3	1972
MAP110703/Z3	0.26924	5.9	0.7326	7.7	0.01974	4.9	0.633	3301.6	93.2	558.1	33.0	126.0	6.1	96.2	3122
MAP110703/Z5	0.17375	2.9	0.8678	4.0	0.03622	2.7	0.688	2594.1	48.1	634.4	18.7	229.4	6.1	91.2	2218

Appendix 1 Table 2 continued

	Radiogenic isotopic ratios							Isotopic dates (Ma)							
Sample ID	$^{207}Pb/^{206}Pb$	±(2σ,%)	$^{207}Pb/^{235}U$	±(2σ,%)	$^{206}Pb/^{238}U$	±(2σ,%)	ρ^1	$^{207}Pb/^{206}Pb$	±(2σ abs)	$^{207}Pb/^{235}U$	±(2σ abs)	$^{206}Pb/^{238}U$	±(2σ abs)	Discordance[2] (%)	U conc[n] (ppm)
MAP 11/07/03 (Not corrected for common lead)															
MAP110703/Z6	0.12107	2.7	0.8243	3.5	0.04938	2.2	0.645	1972.1	47.3	610.4	15.9	310.7	6.8	84.2	1675
MAP110703/Z10	0.06344	5.1	0.4701	5.5	0.05374	2.1	0.383	723.1	107.8	391.2	17.9	337.4	6.9	53.3	931
MAP110703/Z11	0.28639	9.1	0.9212	13.9	0.02333	10.5	0.755	3398.1	141.4	663.0	67.5	148.7	15.4	95.6	4263
MAP110703/Z12	0.14354	10.5	0.9156	10.8	0.04626	2.8	0.259	2270.3	180.2	660.0	52.5	291.5	8.0	87.2	1671
MAP110703/Z14	0.07383	1.5	0.5067	2.9	0.04977	2.5	0.860	1036.7	30.1	416.2	10.0	313.1	7.7	69.8	1096
MAP110703/Z16	0.08507	4.5	0.5867	5.2	0.05002	2.7	0.519	1317.1	86.8	468.8	19.7	314.7	8.4	76.1	1499
MAP 11/07/03 (Corrected for common lead)															
MAP110703/Z1	0.04422	18.8	0.3178	22.5	0.05212	12.3	0.547	-98.3	462.2	280.2	55.0	327.5	39.3	433.3	1357
MAP110703/Z2	0.05073	14.7	0.2582	20.7	0.03691	14.7	0.708	228.8	338.4	233.2	43.2	233.6	33.7	-2.1	1972
MAP110703/Z3	0.05900	17.0	0.1176	21.0	0.01446	12.3	0.587	566.9	369.5	112.9	22.4	92.5	11.3	83.7	3122
MAP110703/Z5	0.05905	17.6	0.2543	22.9	0.03123	14.6	0.637	569.0	384.1	230.1	47.1	198.3	28.5	65.2	2218
MAP110703/Z6	0.05402	10.9	0.3375	18.1	0.04530	14.5	0.800	372.1	244.6	295.2	46.4	285.6	40.5	23.2	1675
MAP110703/Z10	0.05105	29.6	0.3705	30.7	0.05264	8.1	0.262	243.2	682.3	320.0	84.2	330.7	26.0	-36.0	931
MAP110703/Z11	0.05061	33.6	0.1108	39.7	0.01589	21.1	0.531	223.0	776.9	106.7	40.2	101.6	21.2	54.4	4263
MAP110703/Z12	0.05460	18.0	0.3059	22.9	0.04064	14.1	0.617	395.8	403.7	271.0	54.4	256.8	35.5	35.1	1671
MAP110703/Z14	0.05571	31.6	0.3704	32.8	0.04823	8.8	0.269	440.7	702.5	320.0	90.0	303.6	26.1	31.1	1096
MAP110703/Z16	0.06441	13.0	0.4368	18.5	0.04918	13.2	0.711	755.1	274.9	368.0	57.2	309.5	39.8	59.0	1499
MAP 09/07/01 (Not corrected for common lead; data continued overleaf)															
MAP090701/Z1	0.14694	2.0	4.1909	4.3	0.20686	3.8	0.878	2310.6	35.1	1672.2	35.1	1212.1	41.5	47.5	277
MAP090701/Z2	0.06998	1.0	1.5910	2.6	0.16490	2.4	0.924	927.7	20.5	966.7	16.3	984.0	22.0	-6.1	109
MAP090701/Z3	0.07588	1.9	2.0583	3.1	0.19674	2.5	0.793	1091.8	38.2	1135.0	21.4	1157.8	26.3	-6.0	32
MAP090701/Z4	0.06937	1.0	1.5637	2.6	0.16348	2.4	0.923	909.9	20.6	955.9	16.1	976.1	21.7	-7.3	195
MAP090701/Z5	0.09089	1.0	3.3276	2.5	0.26553	2.3	0.920	1444.3	19.0	1487.5	19.9	1518.1	31.7	-5.1	110
MAP090701/Z6	0.10636	1.0	4.4477	2.6	0.30328	2.4	0.923	1738.0	18.3	1721.3	21.6	1707.6	36.0	1.7	263
MAP090701/Z7	0.05714	1.0	0.5729	2.6	0.07272	2.4	0.922	496.8	22.0	459.9	9.5	452.5	10.4	8.9	959
MAP090701/Z8	0.07505	1.1	1.6406	2.7	0.15855	2.5	0.907	1069.9	22.9	986.0	17.1	948.7	21.6	11.3	120

Appendix 1 Table 2 continued

Sample ID	Radiogenic isotopic ratios							Isotopic dates (Ma)						Discordance[2] (%)	U conc[n] (ppm)
	$^{207}Pb/^{206}Pb$	±(2σ,%)	$^{207}Pb/^{235}U$	±(2σ,%)	$^{206}Pb/^{238}U$	±(2σ,%)	ρ[1]	$^{207}Pb/^{206}Pb$	±(2σ abs)	$^{207}Pb/^{235}U$	±(2σ abs)	$^{206}Pb/^{238}U$	±(2σ abs)		
MAP 09/07/01 (Not corrected for common lead)															
MAP090701/Z9	0.07294	1.0	1.7630	2.7	0.17530	2.5	0.929	1012.3	20.3	1031.9	17.5	1041.2	24.1	-2.9	478
MAP090701/Z10	0.09051	1.0	3.0563	2.7	0.24490	2.5	0.930	1436.3	19.1	1421.8	20.9	1412.1	32.2	1.7	360
MAP090701/Z11	0.07762	1.0	2.2227	2.6	0.20768	2.4	0.922	1137.2	19.9	1188.2	18.1	1216.4	26.4	-7.0	266
MAP090701/Z12	0.07317	1.0	1.8351	2.6	0.18190	2.4	0.925	1018.6	20.3	1058.1	17.4	1077.4	24.2	-5.8	229
MAP090701/Z13	0.05812	2.8	0.5387	3.9	0.06723	2.8	0.713	534.1	60.6	437.6	14.0	419.5	11.4	21.5	191
MAP090701/Z14	0.07278	1.0	1.7837	2.7	0.17775	2.5	0.929	1007.8	20.3	1039.5	17.6	1054.7	24.4	-4.7	277
MAP090701/Z15	0.05597	1.3	0.5492	2.7	0.07116	2.4	0.886	451.2	28.0	444.5	9.8	443.2	10.3	1.8	258
MAP090701/Z18	0.07042	1.0	1.6113	2.7	0.16596	2.5	0.930	940.5	20.5	974.6	17.0	989.8	23.1	-5.2	142
MAP090701/Z20	0.07274	1.3	1.7824	2.8	0.17771	2.4	0.881	1006.8	26.6	1039.0	18.0	1054.5	23.8	-4.7	58
MAP090701/Z21	0.08340	1.0	2.4925	2.9	0.21676	2.7	0.938	1278.6	19.5	1269.9	20.9	1264.7	31.1	1.1	134
MAP090701/Z22	0.07185	1.0	1.7059	2.7	0.17220	2.5	0.929	981.6	20.4	1010.7	17.3	1024.2	23.8	-4.3	232
MAP090701/Z23	0.08861	1.0	3.1343	2.6	0.25655	2.4	0.924	1395.7	19.2	1441.2	20.2	1472.2	31.9	-5.5	101
MAP090701/Z24	0.07347	1.0	1.7460	2.6	0.17236	2.4	0.923	1026.9	20.2	1025.7	16.7	1025.1	22.7	0.2	257
MAP090701/Z25	0.07128	1.0	1.4981	2.7	0.15244	2.5	0.928	965.4	20.4	929.6	16.3	914.6	21.2	5.3	411
MAP090701/Z26	0.05474	1.0	0.5446	2.7	0.07216	2.5	0.927	401.7	22.4	441.5	9.6	449.2	10.7	-11.8	371
MAP090701/Z27	0.08703	1.0	2.9906	2.8	0.24923	2.6	0.932	1361.1	19.3	1405.2	21.0	1434.5	33.0	-5.4	224
MAP090701/Z29	0.05587	1.0	0.6165	2.6	0.08004	2.4	0.921	447.1	22.2	487.7	9.9	496.3	11.3	-11.0	248
MAP090701/Z32	0.05559	1.0	0.5402	2.6	0.07048	2.4	0.923	436.0	22.3	438.5	9.2	439.0	10.2	-0.7	585
MAP090701/Z33	0.05442	1.2	0.5287	2.7	0.07046	2.4	0.888	388.5	27.6	430.9	9.4	438.9	10.0	-13.0	220
MAP090701/Z34	0.10313	1.0	4.2550	2.6	0.29924	2.4	0.923	1681.2	18.5	1684.7	21.4	1687.5	35.7	-0.4	242
MAP090701/Z35	0.05496	1.0	0.5274	2.7	0.06960	2.5	0.929	410.4	22.4	430.1	9.5	433.8	10.5	-5.7	332
MAP090701/Z36	0.07332	1.0	1.7129	2.8	0.16943	2.6	0.934	1022.9	20.2	1013.4	17.9	1009.0	24.4	1.4	178
MAP090701/Z38	0.05553	2.9	0.5486	3.8	0.07165	2.5	0.651	433.7	65.0	444.1	13.8	446.1	10.8	-2.9	77
MAP090701/Z39	0.09280	1.0	3.4784	2.7	0.27183	2.5	0.926	1483.9	18.9	1522.3	20.9	1550.1	33.9	-4.5	117
MAP090701/Z40	0.12546	1.0	5.4820	3.2	0.31690	3.0	0.948	2035.3	17.7	1897.8	27.1	1774.6	46.4	12.8	69
MAP090701/Z45	0.07401	1.0	1.5074	6.2	0.14772	6.1	0.987	1041.7	20.2	933.4	37.9	888.2	50.8	14.7	221
MAP090701/Z46	0.08149	1.0	2.0855	2.7	0.18562	2.5	0.927	1233.2	19.6	1144.0	18.3	1097.6	25.0	11.0	394
MAP090701/Z47	0.09961	1.0	3.2925	3.1	0.23973	3.0	0.948	1616.8	18.6	1479.3	24.4	1385.3	37.0	14.3	308

Appendix 1 Table 2 continued

	Radiogenic isotopic ratios							Isotopic dates (Ma)							
Sample ID	$^{207}Pb/^{206}Pb$	±(2σ,%)	$^{207}Pb/^{235}U$	±(2σ,%)	$^{206}Pb/^{238}U$	±(2σ,%)	ρ[1]	$^{207}Pb/^{206}Pb$	±(2σ abs)	$^{207}Pb/^{235}U$	±(2σ abs)	$^{206}Pb/^{238}U$	±(2σ abs)	Discordance[2] (%)	U conc[n] (ppm)
Bentonite B9 (Not corrected for common lead)															
B9/1	0.05284	3.9	0.3902	4.5	0.05356	2.2	0.504	321.7	87.6	334.5	12.7	336.3	7.4	-4.5	126
B9/2	0.05290	2.9	0.3818	3.6	0.05235	2.1	0.587	324.4	66.4	328.4	10.1	328.9	6.8	-1.4	172
B9/3	0.05322	2.8	0.3841	3.5	0.05235	2.1	0.597	338.0	63.5	330.0	9.8	328.9	6.7	2.7	180
B9/4	0.05405	2.1	0.3873	3.0	0.05197	2.2	0.731	373.0	46.8	332.4	8.6	326.6	7.1	12.4	256
B9/5	0.05274	4.3	0.3805	4.8	0.05232	2.0	0.417	317.8	98.6	327.4	13.4	328.8	6.4	-3.5	112
B9/6	0.05590	8.3	0.4098	8.6	0.05316	2.1	0.246	448.5	184.6	348.7	25.3	333.9	6.9	25.5	51
B9/7	0.05371	3.6	0.3907	4.1	0.05276	2.0	0.479	358.8	82.0	334.9	11.8	331.4	6.4	7.6	137
B9/8	0.05261	4.8	0.3828	5.4	0.05277	2.4	0.452	311.9	109.0	329.1	15.1	331.5	7.8	-6.3	100
B9/9	0.05287	2.9	0.3789	3.6	0.05197	2.1	0.588	323.4	65.7	326.2	10.0	326.6	6.7	-1.0	189
B9/10	0.05337	2.0	0.3841	3.1	0.05220	2.4	0.764	344.7	45.7	330.1	8.8	328.0	7.6	4.9	274
B9/11	0.05308	4.1	0.3793	4.9	0.05184	2.5	0.522	332.0	94.1	326.6	13.6	325.8	8.1	1.9	125
B9/12	0.05193	5.1	0.3808	5.5	0.05318	2.2	0.401	282.4	115.8	327.6	15.5	334.0	7.2	-18.3	100
B9/13	0.05225	3.0	0.3681	3.7	0.05110	2.0	0.557	296.2	69.4	318.3	10.0	321.3	6.4	-8.4	183
B9/14	0.05292	4.4	0.3793	4.9	0.05198	2.1	0.439	325.4	99.3	326.5	13.6	326.7	6.8	-0.4	119
B9/15	0.05233	2.2	0.3737	3.2	0.05180	2.2	0.707	300.0	50.8	322.4	8.7	325.5	7.1	-8.5	253
B9/16	0.05287	2.5	0.3840	3.3	0.05268	2.1	0.634	323.4	57.8	330.0	9.3	330.9	6.7	-2.3	211
B9/17	0.05133	5.8	0.3604	6.2	0.05091	2.3	0.377	255.8	132.4	312.5	16.7	320.1	7.3	-25.1	90
B9/18	0.05278	2.0	0.3645	3.1	0.05008	2.3	0.751	319.5	46.2	315.5	8.4	315.0	7.1	1.4	292
B9/19	0.05404	4.9	0.3892	5.4	0.05223	2.3	0.427	372.7	110.9	333.8	15.5	328.2	7.4	11.9	100
B9/20	0.05568	4.7	0.3929	5.2	0.05118	2.2	0.423	439.6	103.9	336.5	14.8	321.8	6.8	26.8	109
B9/21	0.05457	3.6	0.3901	4.3	0.05185	2.3	0.530	394.7	81.3	334.5	12.2	325.9	7.2	17.4	151
B9/22	0.05361	2.5	0.3722	3.5	0.05035	2.5	0.711	354.8	56.3	321.3	9.8	316.7	7.8	10.7	225
B9/23	0.05268	3.2	0.3760	3.8	0.05176	2.0	0.526	315.2	73.5	324.1	10.5	325.3	6.3	-3.2	168
B9/24	0.05407	2.8	0.3831	3.5	0.05138	2.1	0.588	373.9	63.4	329.3	9.8	323.0	6.5	13.6	190
B9/25	0.05391	1.9	0.3907	2.7	0.05257	2.0	0.727	367.4	41.8	334.9	7.7	330.3	6.3	10.1	310

Appendix 2

Whole-rock geochemistry and mineralogy data from bentonite and tonstein samples

Appendix 2 Table 1: Whole-rock geochemical data

1) Samples underlined were comminuted using a Tema mill. Data for samples shown in italics are averages of the sample replicate data presented towards the bottom of the table.
2) Geographical coordinates of the sampled localities: Belgian and German localities = latitude / longitude (WGS 84 datum); British and Irish localities = National grid references.
3) Analytes that were below the limit of detection are underlined; the values shown for these analytes are half of the limit of detection.
4) Loss-on-ignition determined at 1000°C
5) Europium anomaly calculated using CI-chondrite normalised values (from McDonough & Sun, 1995)

	Sampling locality			Major elements (%)[3]											
Sample ID[1]	Country	Locality Name	Geographical coordinates[2]	SiO_2	Al_2O_3	CaO	Cr_2O_3	Fe_2O_3	K_2O	MgO	MnO	Na_2O	P_2O_5	TiO_2	LOI[4]
M Lives-sur-Meuse	Belgium	Lives-sur-Meuse	50.4720°N, 4.9328°E	44.02	22.88	5.44	0.022	5.47	6.23	2.26	0.005	0.18	0.03	1.20	11.86
M Malonne	Belgium	Malonne	50.4337°N, 4.7949°E	15.72	7.93	38.33	0.007	2.61	1.88	1.34	0.027	0.10	0.04	0.35	32.84
L1 Lives-sur-Meuse	Belgium	Lives-sur-Meuse	50.4692°N, 4.9291°E	46.86	28.92	0.42	0.023	3.93	8.20	1.99	0.004	0.60	0.08	1.09	8.03
L1 Royseux	Belgium	Royseux	50.4690°N, 5.2679°E	42.81	26.93	0.90	0.037	9.27	5.70	3.15	0.019	0.14	0.03	0.88	11.20
L1a Sosoye	Belgium	Sosoye	50.3017°N, 4.7762°E	52.00	25.46	0.81	0.010	3.19	6.46	2.76	0.001	0.15	0.03	0.68	8.58
L1b Sosoye	Belgium	Sosoye	50.3017°N, 4.7762°E	27.30	15.70	25.29	0.007	2.16	4.08	1.87	0.010	0.11	0.02	0.43	24.17
L2 Lives-sur-Meuse	Belgium	Lives-sur-Meuse	50.4692°N, 4.9291°E	45.28	29.38	1.20	0.013	6.69	6.66	1.01	0.038	0.30	0.49	0.77	9.02
L2 Royseux	Belgium	Royseux	50.4690°N, 5.2679°E	48.66	26.81	2.49	0.01	3.28	3.10	1.77	0.00	0.45	0.05	0.73	12.65
L2 Sosoye	Belgium	Sosoye	50.3017°N, 4.7762°E	51.71	23.16	2.05	0.005	4.67	4.29	3.87	0.004	0.16	0.28	0.47	10.17
L3 Anhée Nord	Belgium	Anhée Nord	50.3180°N, 4.8758°E	42.74	17.11	12.29	0.002	2.21	3.54	3.57	0.019	0.07	0.09	0.28	15.07
L3 Awirs	Belgium	Awirs West Quarry	50.5905°N, 5.4089°E	47.71	27.07	2.68	0.00	2.40	4.18	2.98	0.00	0.06	0.16	0.40	12.63
L3 Engihoul	Belgium	Engihoul Quarry	50.5764°N, 5.4241°E	45.90	15.89	11.35	0.00	2.16	3.63	3.69	0.02	0.17	0.10	0.26	16.19
L3 Lives-sur-Meuse	Belgium	Lives-sur-Meuse	50.4686°N, 4.9285°E	40.14	27.50	6.26	0.003	4.21	2.60	1.46	0.015	0.61	0.21	0.45	15.26
L4 Awirs (base)	Belgium	Awirs West Quarry	50.5905°N, 5.4089°E	45.15	28.66	2.16	0.002	3.08	4.85	1.68	0.006	0.18	0.06	0.26	12.86
L4 Awirs (top)	Belgium	Awirs West Quarry	50.5905°N, 5.4089°E	44.97	29.36	1.24	0.005	4.35	4.07	1.77	0.008	0.18	0.08	0.33	14.20
L4 Engihoul	Belgium	Engihoul Quarry	50.5764°N, 5.4241°E	48.58	22.81	4.63	0.003	2.79	5.30	2.33	0.009	0.13	0.03	0.25	12.31
MAP 13-66	Belgium	Awirs West Quarry	50.5905°N, 5.4089°E	44.45	31.42	1.48	0.0005	2.57	2.92	1.19	0.004	0.15	0.13	0.36	13.86
L5 Awirs (base)	Belgium	Awirs West Quarry	50.5905°N, 5.4089°E	48.93	28.34	1.09	0.0005	2.01	5.31	2.33	0.001	0.10	0.15	0.38	12.44
L5 Awirs (top)	Belgium	Awirs West Quarry	50.5905°N, 5.4089°E	46.95	30.55	1.29	0.002	2.65	3.63	1.68	0.002	0.10	0.09	0.36	13.33
L5 Engihoul	Belgium	Engihoul Quarry	50.5764°N, 5.4241°E	20.59	10.25	32.32	0.001	3.64	2.23	1.12	0.019	0.07	0.04	0.65	25.70
W1	Belgium	Anhée Nord	50.3170°N, 4.8760°E	42.87	20.89	9.23	0.002	3.09	2.27	5.34	0.026	0.09	0.17	0.39	15.81
W2	Belgium	Anhée Nord	50.3170°N, 4.8760°E	51.08	27.34	1.03	0.001	3.42	5.51	2.86	0.015	0.17	0.15	0.51	9.37
W3	Belgium	Anhée Nord	50.3170°N, 4.8760°E	47.96	20.85	7.23	0.002	3.31	3.56	3.00	0.159	0.10	0.17	0.27	14.48
W4	Belgium	Anhée Nord	50.3170°N, 4.8760°E	50.38	23.52	2.66	0.0005	3.09	2.85	5.08	0.105	0.13	0.10	0.23	11.20
W5	Belgium	Anhée Nord	50.3170°N, 4.8760°E	42.33	20.17	11.16	0.002	3.10	3.01	3.28	0.038	0.15	0.19	0.41	16.67
W6	Belgium	Anhée Nord	50.3170°N, 4.8760°E	48.56	22.92	3.31	0.010	4.97	1.92	6.44	0.073	0.18	0.27	0.48	12.41

Appendix 2 Table 1 continued

		Trace elements (ppm)[3]																				
Sample ID[1]	**Sampling locality**	Ba	Ce	Dy	Er	Eu	Ga	Gd	Hf	Ho	La	Lu	Nb	Nd	Pr	Rb	Sc	Sm	Sn	Sr	Ta	Tb
M Lives-sur-Meuse	Lives-sur-Meuse	589.7	49.9	4.3	3.0	0.6	23.3	3.3	16	0.9	23.9	0.5	55.4	18.3	5.2	295.0	17	3.8	4	222.7	3.6	0.6
M Malonne	Malonne	159.4	40.1	2.5	1.5	0.5	10.0	2.7	4	0.5	21.7	0.2	19.7	16.4	4.8	99.4	7	3.0	3	605.3	1.3	0.4
L1 Lives-sur-Meuse	Lives-sur-Meuse	184.8	51.5	4.2	2.7	0.5	31.4	3.2	14	0.9	26.9	0.4	63.1	15.8	5.0	212.4	21	3.6	7	67.1	3.7	0.6
L1 Royseux	Royseux	94.5	45.6	4.4	3.2	0.5	22.2	3.2	11	1.0	25.6	0.5	43.0	18.9	5.5	129.4	25	3.3	12	40.3	2.7	0.6
L1a Sosoye	Sosoye	325.0	51.2	3.6	2.1	0.7	42.4	3.9	11	0.7	26.6	0.3	40.4	21.3	6.4	402.9	16	4.6	7	69.2	3.2	0.6
L1b Sosoye	Sosoye	228.1	25.3	3.2	2.0	0.4	25.6	2.4	6	0.7	13.0	0.3	23.6	11.7	3.3	239.9	9	2.7	6	279.8	1.8	0.5
L2 Lives-sur-Meuse	Lives-sur-Meuse	86.6	49.7	3.7	2.2	0.5	8.6	4.4	13	0.7	18.7	0.3	18.8	22.9	5.8	164.6	8	4.9	5	26.9	3.6	0.6
L2 Royseux	Royseux	225.4	31.6	1.2	0.9	0.2	24.5	1.0	7	0.3	17.1	0.2	21.5	7.8	2.6	127.3	12	1.3	4	110.0	1.5	0.2
L2 Sosoye	Sosoye	87.3	29.1	1.8	1.0	0.2	20.7	2.2	8	0.4	10.0	0.2	15.1	14.0	3.4	114.6	7	3.1	6	26.5	2.8	0.3
L3 Anhée Nord	Anhée Nord	84.6	49.8	2.5	1.2	0.2	11.6	3.0	6	0.4	17.0	0.2	15.2	18.6	5.4	88.6	6	4.0	3	149.0	2.1	0.5
L3 Awirs	Awirs West Quarry	103.4	57.1	3.1	1.5	0.3	26.8	3.7	11	0.5	19.5	0.2	24.0	23.2	6.5	118.6	7	4.7	8	40.1	3.6	0.6
L3 Engihoul	Engihoul Quarry	220.4	72.6	3.3	1.4	0.4	18.3	4.5	6	0.6	28.0	0.2	15.3	28.2	7.9	116.2	6	6.0	5	96.4	2.1	0.6
L3 Lives-sur-Meuse	Lives-sur-Meuse	53.0	123.5	4.1	2.0	0.4	16.3	5.4	13	0.7	44.9	0.3	22.3	41.4	12.2	76.7	9	7.0	10	115.3	3.3	0.8
L4 Awirs (base)	Awirs West Quarry	90.9	15.3	3.0	2.2	0.1	21.1	1.7	10	0.6	6.0	0.4	16.8	5.4	1.6	119.6	10	1.7	3	22.1	3.3	0.4
L4 Awirs (top)	Awirs West Quarry	105.3	35.7	3.0	2.2	0.1	21.4	1.9	9	0.7	17.0	0.4	22.8	8.9	3.2	113.3	10	2.0	4	29.7	3.5	0.4
L4 Engihoul	Engihoul Quarry	5764.4	26.7	2.2	1.5	0.3	22.5	1.6	6	0.5	12.8	0.3	20.8	8.1	2.5	160.4	8	1.7	4	88.3	2.0	0.3
MAP 13-66	Awirs West Quarry	55.2	9.2	1.5	1.1	0.1	15.7	1.3	12	0.3	3.4	0.2	22.6	4.9	1.1	76.1	9	1.5	3	22.7	3.0	0.3
L5 Awirs (base)	Awirs West Quarry	82.4	15.2	3.9	2.5	0.2	23.7	2.7	12	0.8	5.0	0.5	24.5	9.3	2.1	136.6	8	2.9	8	11.8	3.5	0.6
L5 Awirs (top)	Awirs West Quarry	66.2	12.0	3.7	2.3	0.2	20.0	2.4	10	0.7	3.8	0.4	24.4	6.9	1.7	118.6	8	2.6	6	9.8	3.5	0.5
L5 Engihoul	Engihoul Quarry	631.8	118.2	8.0	4.5	2.2	19.6	8.2	15	1.6	51.1	0.6	135.8	46.9	13.1	69.2	6	9.8	3	155.7	8.5	1.4
W1	Anhée Nord	123.3	26.9	1.6	1.0	0.3	13.2	1.6	5	0.3	11.8	0.2	12.9	9.8	2.8	58.7	6	2.0	2	126.4	1.8	0.3
W2	Anhée Nord	94.2	14.9	1.5	1.0	0.2	20.5	1.2	7	0.3	7.0	0.2	14.1	6.0	1.7	141.7	6	1.3	1	48.3	2.0	0.2
W3	Anhée Nord	353.6	13.6	1.2	0.8	0.2	14.4	1.1	7	0.2	5.5	0.1	20.1	5.6	1.4	79.5	6	1.3	2	137.6	2.7	0.2
W4	Anhée Nord	142.5	7.9	1.6	0.8	0.3	12.8	1.5	9	0.3	2.8	0.1	18.0	3.9	0.9	71.3	4	1.5	1	25.6	3.6	0.2
W5	Anhée Nord	84.5	18.8	2.6	1.4	0.3	13.4	2.2	7	0.5	7.5	0.2	21.6	9.4	2.2	72.0	10	2.4	2	68.1	2.1	0.4
W6	Anhée Nord	93.3	37.8	3.6	2.6	0.6	17.1	2.9	10	0.8	16.4	0.5	21.0	13.7	3.8	50.8	14	3.3	3	47.9	2.8	0.6

Appendix 2 Table 1 continued

Sample ID[1]	Sampling locality	Trace elements (ppm)[3]								Eu/Eu*[5]	ΣREE
		Th	Tm	U	V	W	Y	Yb	Zr		
M Lives-sur-Meuse	Lives-sur-Meuse	22.2	0.5	32.4	113.6	3.5	23.8	3.3	611	0.53	118.0
M Malonne	Malonne	6.4	0.2	8.4	84.1	2.5	14.9	1.5	142	0.50	96.1
L1 Lives-sur-Meuse	Lives-sur-Meuse	34.0	0.4	32.4	167.3	1.8	24.4	3.1	524	0.50	118.8
L1 Royseux	Royseux	33.9	0.5	18.0	204.0	3.6	34.6	3.5	414	0.47	116.4
L1a Sosoye	Sosoye	33.6	0.3	8.2	55.9	3.4	19.9	2.2	429	0.48	124.6
L1b Sosoye	Sosoye	10.7	0.3	7.0	45.5	3.7	17.5	2.1	220	0.51	67.8
L2 Lives-sur-Meuse	Lives-sur-Meuse	50.1	0.3	16.3	165.3	22.3	23.5	2.1	401	0.34	117.0
L2 Royseux	Royseux	19.3	0.2	12.5	69.7	2.5	6.8	1.2	216	0.53	65.7
L2 Sosoye	Sosoye	54.6	0.1	4.3	64.9	1.1	10.2	1.0	244	0.27	66.8
L3 Anhée Nord	Anhée Nord	36.6	0.2	7.4	28.6	0.8	10.2	1.1	189	0.19	104.0
L3 Awirs	Awirs West Quarry	67.5	0.2	8.4	25.9	0.5	12.9	1.2	315	0.19	122.2
L3 Engihoul	Engihoul Quarry	34.0	0.2	9.1	20.8	0.7	12.1	1.1	190	0.22	154.9
L3 Lives-sur-Meuse	Lives-sur-Meuse	65.4	0.3	10.1	33.3	1.7	16.5	1.8	375	0.20	244.6
L4 Awirs (base)	Awirs West Quarry	31.0	0.4	11.2	19.7	2.3	14.8	3.0	248	0.22	41.9
L4 Awirs (top)	Awirs West Quarry	50.2	0.4	18.2	65.3	17.9	14.7	2.9	243	0.19	78.8
L4 Engihoul	Engihoul Quarry	44.7	0.3	7.7	18.0	0.8	11.7	1.8	177	0.62	60.8
MAP 13-66	Awirs West Quarry	38.9	0.2	5.4	26.2	0.7	8.2	1.2	372	0.30	26.4
L5 Awirs (base)	Awirs West Quarry	39.9	0.4	6.9	42.0	2.5	19.2	2.8	369	0.20	48.9
L5 Awirs (top)	Awirs West Quarry	54.7	0.4	7.4	41.4	0.7	17.4	2.5	299	0.23	40.1
L5 Engihoul	Engihoul Quarry	15.3	0.7	14.5	51.6	1.4	42.9	4.4	631	0.73	270.8
W1	Anhée Nord	21.9	0.2	18.4	68.6	1.3	8.7	1.1	168	0.53	59.9
W2	Anhée Nord	26.7	0.2	22.4	79.0	22.8	8.4	1.2	225	0.50	36.8
W3	Anhée Nord	37.5	0.1	6.7	49.4	0.9	7.9	0.8	189	0.49	32.3
W4	Anhée Nord	50.3	0.1	11.7	66.7	1.8	9.1	0.8	247	0.51	22.8
W5	Anhée Nord	25.3	0.2	26.8	113.8	1.5	14.5	1.2	215	0.41	49.4
W6	Anhée Nord	29.4	0.4	28.0	126.6	1.4	26.9	2.8	333	0.56	89.7

Appendix 2 Table 1 continued

Sampling locality				Major elements (%)[3]											
Sample ID[1]	**Country**	**Locality Name**	**Geographical coordinates[2]**	SiO_2	Al_2O_3	CaO	Cr_2O_3	Fe_2O_3	K_2O	MgO	MnO	Na_2O	P_2O_5	TiO_2	LOI[4]
W7	Belgium	Anhée Nord	50.3170°N, 4.8760°E	49.19	23.54	1.21	0.00	5.58	0.31	9.02	0.10	0.10	0.15	0.33	12.29
W8 (base)	Belgium	Anhée Nord	50.3170°N, 4.8760°E	54.36	22.08	0.41	0.0005	2.19	0.16	8.63	0.023	0.03	0.16	0.33	9.76
W8 (top)	Belgium	Anhée Nord	50.3170°N, 4.8760°E	57.60	21.66	0.55	0.0005	1.56	0.13	8.63	0.018	0.01	0.14	0.32	9.63
W9	Belgium	Monceau	50.3949°N, 4.3749°E	46.72	26.67	3.06	0.018	4.13	3.70	2.13	0.060	0.17	0.84	0.68	12.42
W12	Belgium	Anhée Sud	50.2940°N, 4.8936°E	41.64	31.41	1.11	0.003	3.13	1.38	2.94	0.008	0.22	0.35	0.77	16.76
W13	Belgium	Anhée Sud	50.2940°N, 4.8936°E	42.77	31.67	0.70	0.003	4.02	1.78	2.79	0.020	0.51	0.31	0.84	14.48
MAP 11/07/01	Republic of Ireland	Ballyadams Quarry	S6216 9157	46.92	21.55	0.94	0.026	8.80	5.53	1.79	0.008	0.18	0.11	1.07	10.65
MAP 11/07/03	Republic of Ireland	Ballyadams Quarry	S6216 9157	37.00	18.17	11.40	0.021	6.49	5.03	1.81	0.014	0.17	0.10	0.79	16.52
MAP 11/07/06	Republic of Ireland	Ballyadams Quarry	S6216 9157	19.19	6.25	36.54	0.028	2.36	1.64	0.76	0.004	0.08	0.02	0.32	32.30
MAP 11/07/10	Republic of Ireland	Ballyadams Quarry	S6216 9157	50.99	22.67	0.42	0.021	10.18	5.76	1.88	0.003	0.19	0.03	0.83	8.13
MAP 09/07/01	Northern Ireland	Altscraghy	H1290 2893	39.10	19.18	0.16	0.002	15.59	1.51	0.77	0.020	1.86	0.07	0.55	21.59
MAP 09/07/05	Northern Ireland	Altscraghy	H1290 2893	40.45	18.01	2.95	0.00	14.70	1.28	1.68	0.10	2.46	0.17	0.39	18.01
B1	England	Vale of Edale	SK 1037 8512	40.71	25.87	1.22	0.008	12.32	1.63	1.65	0.185	0.37	0.26	0.47	15.85
B7	England	Vale of Edale	SK 1235 8595	48.13	27.51	0.90	0.002	5.99	2.41	1.28	0.727	0.86	0.14	0.97	12.73
B8	England	Oakenclough Brook	SK 0501 6369	19.49	12.70	2.69	0.0005	32.59	1.14	1.58	0.529	0.51	0.13	0.51	25.98
B9	England	Oakenclough Brook	SK 0501 6369	19.74	14.54	1.31	0.002	27.70	0.97	0.57	7.912	0.27	0.06	0.45	24.10
T75	Belgium	Zwartberg colliery	51.0136°N, 5.5038°E	53.31	29.25	0.03	0.008	1.32	2.51	0.68	0.005	0.43	0.06	0.55	11.27
Wilhelm	Germany	Unser Fritz colliery	51.5408°N, 7.1343°E	37.22	31.72	0.03	0.001	0.36	0.19	0.09	0.0005	0.11	0.16	0.21	27.27
Z1	Germany	Furst Leopold colliery	51.6713°N, 6.9777°E	22.85	15.92	1.47	0.0005	2.13	0.73	0.27	0.014	0.44	0.07	0.20	55.89
Hagen 1	Germany	Furst Leopold colliery	51.6713°N, 6.9777°E	51.66	31.05	0.09	0.0005	1.18	2.04	0.50	0.0005	0.57	0.07	0.21	13.37
Hagen 4	Germany	Altendorf colliery	51.6394°N, 7.0187°E	48.20	30.65	0.09	0.001	1.03	1.60	0.68	0.0005	0.46	0.08	0.25	17.43
T13	Belgium	Eisden colliery	51.0016°N, 5.7044°E	44.66	35.53	0.03	0.003	0.52	0.64	0.21	0.001	0.20	0.07	0.29	17.55
T10	Belgium	Eisden colliery	51.0016°N, 5.7044°E	43.77	36.08	0.06	0.0005	0.24	0.10	0.07	0.0005	0.22	0.18	0.18	17.48
T09	Belgium	Eisden colliery	51.0016°N, 5.7044°E	39.70	30.23	0.15	0.0005	0.27	0.13	0.06	0.0005	0.15	0.07	0.19	26.85
T1Gb	Belgium	KS20 (791.00-.08m)	51.1018°N, 5.1853°E	45.15	34.52	0.09	0.0005	0.84	0.13	0.20	0.003	0.25	0.07	0.29	19.46
T1P	Belgium	KS21 (464.02-.03m)	51.0902°N, 5.3025°E	43.15	35.10	0.005	0.009	0.45	0.13	0.05	0.0005	0.08	0.05	0.89	17.42
MAP 07-41 (limestone)	Belgium	Anhée Sud	50.2940°N, 4.8936°E	1.21	0.46	53.21	0.0005	0.07	0.05	0.70	0.009	0.03	0.02	0.01	42.68
MAP 03-02 (limestone)	Belgium	Lives-sur-Meuse	50.5905°N, 5.4089°E	3.17	0.45	51.31	0.0005	0.14	0.09	0.57	0.009	0.02	0.01	0.02	41.44
MAP 02-28 (limestone)	Belgium	Lives-sur-Meuse	50.5905°N, 5.4089°E	0.92	0.20	55.67	0.001	0.08	0.04	0.47	0.003	0.02	0.005	0.01	42.60
MAP 12/07/09 (shale)	England	Vale of Edale	SK 1235 8595	44.02	15.01	4.07	0.012	5.78	1.88	1.60	6.372	0.41	0.50	0.60	16.95
MAP 03/08/02 (shale)	England	Vale of Edale	SK 1037 8512	51.10	22.81	0.84	0.018	4.39	2.14	1.46	0.089	0.32	0.33	0.79	13.46

Appendix 2 Table 1 continued

Sample ID[1]	Sampling locality	Trace elements (ppm)[3]																				
		Ba	Ce	Dy	Er	Eu	Ga	Gd	Hf	Ho	La	Lu	Nb	Nd	Pr	Rb	Sc	Sm	Sn	Sr	Ta	Tb
W7	Anhée Nord	67.5	100.5	3.8	1.9	0.6	15.7	4.5	11	0.7	30.7	0.3	27.9	31.1	9.6	10.8	11	5.9	2	14.9	3.1	0.7
W8 (base)	Anhée Nord	32.9	66.3	3.0	1.5	0.5	15.6	3.5	5	0.6	26.7	0.2	18.3	22.6	6.7	3.5	9	4.3	1	15.7	1.8	0.5
W8 (top)	Anhée Nord	33.9	46.5	2.8	1.4	0.4	13.5	3.0	6	0.5	18.4	0.2	19.5	17.8	5.0	2.1	9	3.7	1	6.9	2.3	0.5
W9	Monceau	273.4	74.2	4.2	2.1	0.7	19.9	6.9	13	0.7	25.3	0.2	22.4	44.4	10.1	105.8	10	10.5	5	176.6	3.3	0.9
W12	Anhée Sud	162.9	25.7	1.1	0.7	0.2	24.1	1.3	11	0.2	11.3	0.1	10.1	9.2	2.5	36.2	5	1.6	2	128.5	2.0	0.2
W13	Anhée Sud	153.2	18.9	0.7	0.5	0.2	18.2	0.7	10	0.2	8.4	0.05	11.7	6.6	1.9	45.9	8	1.1	1	594.0	2.1	0.1
MAP 11/07/01	Ballyadams Quarry	283.1	41.7	2.5	2.0	0.5	26.4	2.2	6	0.5	22.5	0.4	22.0	16.9	5.0	274.0	19	2.6	4	68.6	3.0	0.4
MAP 11/07/03	Ballyadams Quarry	250.7	36.5	1.5	1.1	0.3	20.7	1.3	6	0.3	19.1	0.2	15.6	10.6	3.4	205.0	12	1.9	3	134.1	1.6	0.2
MAP 11/07/06	Ballyadams Quarry	78.4	19.3	1.5	1.1	0.4	7.5	1.5	2	0.3	12.1	0.2	7.0	8.6	2.3	65.3	7	1.8	1	375.6	0.8	0.3
MAP 11/07/10	Ballyadams Quarry	235.3	53.4	2.5	2.0	0.4	26.3	2.4	4	0.6	29.2	0.4	15.1	21.0	6.5	219.3	20	2.9	3	71.7	1.2	0.3
MAP 09/07/01	Altscraghy	192.0	43.0	8.0	4.3	1.8	17.5	6.8	9	1.6	13.8	0.5	31.7	23.5	5.3	36.4	6	6.2	3	133.3	5.7	1.2
MAP 09/07/05	Altscraghy	357.6	261.1	16.8	8.0	5.4	15.3	21.4	12	3.1	82.0	0.9	37.6	114.7	28.1	34.6	11	24.9	3	277.1	6.4	3.1
B1	Vale of Edale	88.0	60.7	4.0	2.3	0.6	20.5	5.1	5	0.8	24.2	0.3	7.6	27.5	6.9	47.0	16	5.9	11	32.9	1.5	0.7
B7	Vale of Edale	327.3	116.6	8.5	6.2	1.6	23.5	6.8	24	1.9	48.6	0.8	51.3	44.6	12.2	57.4	13	7.7	5	71.6	12.5	1.2
B8	Oakenclough Brook	159.7	101.0	17.9	8.4	4.4	9.0	19.4	10	3.2	35.3	0.9	18.6	58.7	13.1	27.5	12	17.1	2	66.0	6.5	3.1
B9	Oakenclough Brook	3016.0	85.6	35.0	17.9	6.5	12.7	33.6	9	7.1	26.4	1.6	13.2	66.0	12.6	26.8	14	21.9	3	33.0	6.8	5.7
T75	Zwartberg colliery	356.5	123.1	6.0	3.1	1.6	23.9	8.2	8	1.1	52.4	0.5	16.6	45.9	12.7	114.5	14	9.6	9	110.2	2.8	1.1
Wilhelm	Unser Fritz colliery	85.4	58.6	5.3	2.2	1.6	31.4	7.6	3	0.9	21.8	0.2	2.0	31.9	7.4	9.7	14	9.0	8	120.4	0.8	1.1
Z1	Furst Leopold colliery	149.3	124.7	7.5	4.5	1.3	15.3	8.7	8	1.5	48.1	0.8	31.2	51.0	13.6	23.5	8	11.0	5	54.8	2.1	1.3
Hagen 1	Furst Leopold colliery	23.0	180.5	23.0	13.0	1.2	42.6	20.3	14	4.4	63.2	1.8	28.1	74.9	20.4	92.7	8	19.9	56	41.6	7.0	3.7
Hagen 4	Altendorf colliery	121.6	114.3	11.0	6.2	1.0	44.0	10.2	8	2.0	48.3	0.9	16.9	42.8	12.0	73.7	13	10.2	35	110.9	4.5	1.8
T13	Eisden colliery	98.0	102.6	16.6	9.6	0.6	72.0	14.4	6	3.3	39.2	1.1	32.5	45.7	12.0	49.0	20	13.9	53	56.6	4.4	2.7
T10	Eisden colliery	106.0	146.7	6.4	2.8	1.0	37.3	11.2	5	1.0	53.8	0.3	10.2	72.6	18.1	3.9	4	15.8	22	418.3	2.6	1.4
T09	Eisden colliery	37.4	153.3	16.8	9.1	0.9	42.3	12.9	5	3.2	64.6	1.1	13.6	52.9	15.7	7.3	7	12.5	43	96.1	4.1	2.6
T1Gb	KS20 (791.00-.08m)	46.8	45.8	2.0	1.1	0.3	43.9	2.7	3	0.3	20.5	0.1	14.1	16.5	4.8	5.9	5	3.6	50	33.6	4.9	0.4
T1P	KS21 (464.02-.03m)	22.6	199.4	3.4	1.5	0.6	19.6	8.4	12	0.5	86.3	0.2	14.1	79.3	21.0	5.1	10	13.3	6	22.2	1.4	0.8
MAP 07-41 (limestone)	Anhée Sud	6.2	3.3	0.3	0.1	0.05	0.25	0.2	0.5	0.05	1.7	0.05	1.2	1.6	0.4	1.6	0.5	0.3	0.5	572.4	1.1	0.05
MAP 03-02 (limestone)	Lives-sur-Meuse	10.4	2.2	0.2	0.1	0.05	0.6	0.2	0.5	0.05	1.0	0.05	0.6	0.9	0.3	4.4	0.5	0.2	0.5	314.3	0.2	0.05
MAP 02-28 (limestone)	Lives-sur-Meuse	7.8	2.3	0.3	0.2	0.05	0.25	0.1	0.5	0.05	1.1	0.05	0.25	1.0	0.3	1.5	0.5	0.2	0.5	413.6	0.1	0.05
MAP 12/07/09 (shale)	Vale of Edale	351.6	89.7	8.1	4.1	2.5	24.6	10.2	3	1.6	39.9	0.5	19.4	41.5	10.4	102.7	13	9.9	3	150.0	0.8	1.5
MAP 03/08/02 (shale)	Vale of Edale	198.6	106.8	6.9	3.7	2.0	29.7	7.9	3	1.3	48.8	0.5	13.0	45.0	11.8	116.2	20	9.1	5	124.5	1.1	1.2

Appendix 2 Table 1 continued

Sample ID[1]	Sampling locality	Trace elements (ppm)[3]								Eu/Eu* [5]	ΣREE
		Th	Tm	U	V	W	Y	Yb	Zr		
W7	Anhée Nord	39.1	0.3	14.5	57.5	11.1	17.2	2.0	356	0.38	192.6
W8 (base)	Anhée Nord	26.1	0.2	8.2	18.0	1.5	13.0	1.3	143	0.41	137.9
W8 (top)	Anhée Nord	27.1	0.2	6.4	16.8	1.0	12.1	1.3	159	0.38	101.5
W9	Monceau	84.9	0.3	13.8	77.9	4.0	21.7	1.6	427	0.24	182.0
W12	Anhée Sud	58.9	0.1	9.4	83.0	9.1	5.9	0.6	338	0.48	54.9
W13	Anhée Sud	55.6	0.1	16.8	81.2	1.7	3.8	0.6	283	0.61	39.9
MAP 11/07/01	Ballyadams Quarry	17.1	0.3	21.1	210.2	3.3	17.2	2.4	228	0.60	100.0
MAP 11/07/03	Ballyadams Quarry	16.8	0.2	21.6	147.8	2.0	8.9	1.4	219	0.60	78.1
MAP 11/07/06	Ballyadams Quarry	4.7	0.2	6.2	203.8	1.2	11.0	1.3	72	0.65	50.7
MAP 11/07/10	Ballyadams Quarry	12.1	0.4	6.4	117.7	2.0	15.7	2.2	127	0.48	124.3
MAP 09/07/01	Altscraghy	13.2	0.6	9.3	77.6	18.7	50.9	3.3	265	0.83	119.8
MAP 09/07/05	Altscraghy	16.4	1.0	21.0	74.4	69.9	90.0	5.8	326	0.71	576.4
B1	Vale of Edale	41.5	0.3	10.0	116.5	9.3	21.2	2.2	100	0.34	141.5
B7	Vale of Edale	43.3	1.0	8.4	87.2	12.8	60.3	6.0	469	0.68	263.9
B8	Oakenclough Brook	19.1	1.1	23.7	134.4	147.2	95.6	6.0	154	0.73	289.5
B9	Oakenclough Brook	21.1	2.2	4.6	40.9	6.9	271.0	11.0	118	0.73	333.1
T75	Zwartberg colliery	39.8	0.5	12.4	79.0	3.0	30.4	3.1	265	0.55	268.9
Wilhelm	Unser Fritz colliery	26.1	0.3	3.4	11.3	0.25	20.2	1.8	75	0.58	149.6
Z1	Furst Leopold colliery	38.3	0.7	12.9	22.0	10.6	41.8	4.7	228	0.42	279.3
Hagen 1	Furst Leopold colliery	125.1	2.1	46.3	2.5	0.8	121.5	12.9	261	0.18	441.1
Hagen 4	Altendorf colliery	37.6	1.0	19.1	26.2	1.3	60.4	6.2	186	0.31	267.9
T13	Eisden colliery	26.7	1.4	26.7	26.3	6.0	90.9	8.2	102	0.12	271.2
T10	Eisden colliery	46.5	0.4	4.5	2.5	3.7	27.0	2.3	147	0.23	333.8
T09	Eisden colliery	101.1	1.4	40.1	2.5	2.8	86.3	8.4	97	0.21	355.5
T1Gb	KS20 (791.00-.08m)	10.3	0.2	11.4	10.8	3.3	10.3	1.0	98	0.30	99.3
T1P	KS21 (464.02-.03m)	39.2	0.2	7.7	60.7	2.4	14.8	1.5	401	0.19	416.5
MAP 07-41 (limestone)	Anhée Sud	0.3	0.05	7.3	17.2	1.4	2.2	0.1	9	Eu <LOD	8.2
MAP 03-02 (limestone)	Lives-sur-Meuse	0.2	0.05	1.4	17.0	5.9	1.3	0.1	4	Eu <LOD	5.6
MAP 02-28 (limestone)	Lives-sur-Meuse	0.1	0.05	1.7	22.3	1.0	2.3	0.2	4	Eu <LOD	5.9
MAP 12/07/09 (shale)	Vale of Edale	7.2	0.5	4.4	98.2	3.0	55.7	3.2	92	0.74	223.7
MAP 03/08/02 (shale)	Vale of Edale	9.8	0.5	9.1	172.7	2.6	39.4	3.4	76	0.71	248.9

Appendix 2 Table 1 continued

		Sampling locality		Major elements (%)[3]											
Sample ID[1]	**Country**	**Locality Name**	**Geographical coordinates[2]**	SiO_2	Al_2O_3	CaO	Cr_2O_3	Fe_2O_3	K_2O	MgO	MnO	Na_2O	P_2O_5	TiO_2	LOI[4]
Replicates															
L2 Royseux	Belgium	Royseux	50.4690°N, 5.2679°E	48.15	26.22	2.42	0.008	3.25	3.07	1.76	0.004	0.44	0.05	0.73	12.66
L2 Royseux	Belgium	Royseux	50.4690°N, 5.2679°E	49.16	27.40	2.55	0.008	3.31	3.13	1.79	0.004	0.45	0.04	0.72	12.63
L3 Awirs	Belgium	Awirs West Quarry	50.5905°N, 5.4089°E	47.44	27.03	2.61	0.002	2.34	4.08	2.94	0.002	0.05	0.16	0.40	12.65
L3 Awirs	Belgium	Awirs West Quarry	50.5905°N, 5.4089°E	47.97	27.11	2.76	0.002	2.45	4.29	3.01	0.002	0.06	0.17	0.40	12.60
L3 Engihoul	Belgium	Engihoul Quarry	50.5764°N, 5.4241°E	45.35	15.90	11.25	0.002	2.22	3.58	3.73	0.017	0.17	0.10	0.26	16.28
L3 Engihoul	Belgium	Engihoul Quarry	50.5764°N, 5.4241°E	46.46	15.87	11.45	0.002	2.09	3.68	3.65	0.017	0.17	0.10	0.25	16.09
W7	Belgium	Anhée Nord	50.3170°N, 4.8760°E	48.96	23.86	1.24	0.004	5.52	0.35	8.82	0.096	0.10	0.15	0.32	12.28
W7	Belgium	Anhée Nord	50.3170°N, 4.8760°E	49.42	23.21	1.18	0.005	5.64	0.27	9.22	0.100	0.10	0.15	0.33	12.29
MAP 09/07/05	Northern Ireland	Altscraghy	H1290 2893	40.36	17.91	2.95	0.004	14.54	1.27	1.67	0.098	2.43	0.17	0.38	17.95
MAP 09/07/05	Northern Ireland	Altscraghy	H1290 2893	40.53	18.11	2.95	0.003	14.87	1.29	1.69	0.095	2.48	0.17	0.39	18.06

Appendix 2 Table 1 continued

		Trace elements (ppm)[3]																				
Sample ID[1]	**Sampling locality**	Ba	Ce	Dy	Er	Eu	Ga	Gd	Hf	Ho	La	Lu	Nb	Nd	Pr	Rb	Sc	Sm	Sn	Sr	Ta	Tb
Replicates																						
L2 Royseux	Royseux	222.8	30.9	1.2	0.9	0.2	23.8	1.0	6	0.3	16.4	0.2	20.6	7.6	2.6	125.8	12	1.2	4	105.9	1.3	0.2
L2 Royseux	Royseux	228.0	32.3	1.2	0.9	0.2	25.2	1.0	7	0.3	17.7	0.2	22.4	8.0	2.7	128.7	13	1.3	4	114.1	1.7	0.2
L3 Awirs	Awirs West Quarry	103.2	57.8	3.0	1.5	0.2	26.7	3.6	10	0.6	19.7	0.2	23.8	23.2	6.5	118.2	7	4.7	8	40.3	3.6	0.6
L3 Awirs	Awirs West Quarry	103.5	56.4	3.2	1.5	0.3	26.8	3.7	11	0.5	19.2	0.2	24.2	23.2	6.5	118.9	8	4.8	7	39.9	3.7	0.6
L3 Engihoul	Engihoul Quarry	226.4	72.4	3.3	1.4	0.4	18.3	4.5	6	0.6	27.8	0.1	15.5	28.2	7.9	116.9	6	6.0	5	97.7	2.2	0.7
L3 Engihoul	Engihoul Quarry	214.4	72.9	3.3	1.4	0.4	18.3	4.4	6	0.6	28.2	0.2	15.1	28.2	7.9	115.4	6	6.0	4	95.1	2.0	0.6
W7	Anhée Nord	64.3	98.4	3.7	1.9	0.6	15.4	4.3	11	0.7	30.1	0.3	27.2	30.6	9.4	10.5	11	5.7	2	14.7	3.0	0.7
W7	Anhée Nord	70.8	102.6	3.9	1.9	0.6	16.0	4.6	11	0.7	31.2	0.3	28.5	31.5	9.8	11.0	11	6.0	2	15.1	3.1	0.7
MAP 09/07/05	Altscraghy	354.5	257.6	16.5	7.7	5.4	15.3	21.3	12	3.0	80.8	0.8	36.7	114.0	27.7	34.0	11	24.5	3	275.1	6.0	3.1
MAP 09/07/05	Altscraghy	360.7	264.7	17.2	8.3	5.4	15.3	21.6	12	3.1	83.2	0.9	38.5	115.4	28.5	35.2	11	25.3	3	279.1	6.8	3.1

		Trace elements (ppm)[3]							
Sample ID[1]	**Sampling locality**	Th	Tm	U	V	W	Y	Yb	Zr
Replicates									
L2 Royseux	Royseux	16.5	0.2	12.3	68.7	2.4	6.7	1.2	192
L2 Royseux	Royseux	22.0	0.2	12.7	70.6	2.5	6.9	1.3	241
L3 Awirs	Awirs West Quarry	68.1	0.2	8.4	25.4	0.8	13.0	1.2	311
L3 Awirs	Awirs West Quarry	66.9	0.2	8.3	26.4	0.25	12.9	1.2	320
L3 Engihoul	Engihoul Quarry	34.7	0.2	9.1	21.9	0.7	12.1	1.1	194
L3 Engihoul	Engihoul Quarry	33.3	0.2	9.1	19.7	0.8	12.0	1.1	186
W7	Anhée Nord	38.8	0.3	14.3	58.7	2.0	17.0	1.9	352
W7	Anhée Nord	39.3	0.3	14.7	56.4	20.2	17.4	2.2	359
MAP 09/07/05	Altscraghy	16.3	1.0	20.9	78.9	69.0	89.2	5.7	329
MAP 09/07/05	Altscraghy	16.5	1.0	21.0	69.8	70.8	90.8	6.0	322

Appendix 2 Table 2: Summary of X-ray diffraction (XRD) data

Key					
?	uncertain determination	x	mineral present	Qtz = Quartz	
trace	trace amounts of mineral	xx	mineral abundant	Kaol = Kaolinite	
(base / top)	sample taken from near to the base or top of a bed				

Sample	Illite-Mica	Main illite-mica peak (degrees 2θ)	Qtz	Chlorite	Kaol.	Calcite	Pyrite	Goethite	Feldspar	Gypsum
Bentonite 300	x	8.2					x		x	
M (Lives)	x	8.6								
M (Malonne)	trace		x			xx				
L1 (Royseux)	x	8.7						x		
L1 (Lives)	x	8.8								
L1a (Sosoye)	x	8.2, 8.8	x							
L1b (Sosoye)	x	8.8				xx				
L2 (Lives)	x	8.8						x		
L2 (Royseux)	x	7.7	x	x	x					
L2 (Sosoye)	x	8.1	x	x						
L3 (Anhée N)	x	7.8	x	x		x				x
L3 (Awirs)	x	7.6	x	trace	?					
L3 (Engihoul)	x	7.7	x			x				
L3 (Lives)	x	7.8	x	x	x	x				
L4 (Awirs; base)	x	8.0			x			x		
L4 (Awirs; top)	x	8.0			x					
L4 (Engihoul)	x	7.9, 8.7	x			x	x			
MAP 13-66	x	7.9			x			x		x
L5 (Engihoul)	trace	*c*. 7.6	x			xx	x			
L5 (Awirs; base)	x	7.7			x					
L5 (Awirs; top)	x	7.5			x					
W1	x	7.7	x	x	?	x				
W2	x	7.8	x	trace						
W3	x	7.8	xx	x	?	x				
W4	trace		xx	x		x				
W5	trace		xx	x		x				
W6	trace		xx	x		x				
W7	trace		xx	x		x				
W8 (base)			xx	x						
W8 (top)			xx	x						
W9 (Monceau)	x	7.7	x		x					
W12	x	8.0		x	x					
W13	x	7.9		x	x					
Bentonite B1	x	7.5	trace		x		x			
Bentonite B2	trace		x		x					
Bentonite B7	x	7.3	?	?	x		x		?	
Bentonite B8	x	7.5	?		x		x			
Bentonite B9	x	*c*. 7.8			x		x			
MAP 12/07/09	x	7.0 - 9.0	xx	x	x				?	?
MAP 03/08/02	x	7.0 - 9.0	xx	x	x				?	
MAP 11/07/01	x	8.7	x							
MAP 11/07/03	x	8.8	x			x				
MAP 11/07/06	x	8.8	x			xx				
MAP 11/07/10	x	8.5	x							
MAP 09/07/01	x	7.8	x				x		x	
MAP 09/07/05	x	7.5	x		trace		x		x	
T75	trace	*c*. 8.9	xx	trace	x				?	
Wilhelm			?		x					
Z1	trace	*c*. 8.2	?		x				x	
T13	trace	*c*. 8.7	?		x					
T10					x				trace	
T09					x					
T1Gb			?		x					
T1P			?		x					
Hagen 1	x	8.2	x		x					
Hagen 4	x	8.3	x		x					

Appendix 3

Magnetic susceptibility (MS) and stable isotope ($\delta^{13}C$ and $\delta^{18}O$) data from Belgian Livian and Warnantian strata

Appendix 3 Table 1: Magnetic susceptibility data from Lives-sur-Meuse, Section 1

Sample ID	Sampling height (m)	Mass (g)	MS (m^3/kg)
06-01	0.44	10.119	2.05E-08
06-02A	0.59	9.955	9.95E-09
06-02B	0.70	10.543	6.99E-09
06-03	0.98	10.228	7.03E-09
06-04A	1.17	10.117	3.70E-09
06-04B	1.23	10.323	1.69E-09
06-05A	1.39	10.968	3.41E-09
06-05B	1.46	10.844	3.45E-09
06-06A	1.71	10.462	1.15E-09
06-06B	1.76	10.223	4.19E-09
06-07A	1.91	10.194	1.11E-08
06-07B	1.98	10.386	4.30E-09
06-08A	2.55	10.757	6.51E-09
06-08B	2.65	10.692	7.91E-09
06-09	2.71	10.463	1.66E-08
06-10	2.90	10.067	2.08E-08
06-11	2.97	10.328	2.50E-08
06-12A	3.14	10.406	1.70E-08
06-12B	3.21	10.333	1.52E-08
06-13A	3.38	10.694	8.75E-09
06-13B	3.46	9.986	1.83E-08
06-14A	3.48	10.296	2.53E-08
06-14B	3.56	10.693	7.40E-09
06-14C	3.62	10.426	5.15E-09
06-15A	3.78	10.258	3.29E-09
06-15B	3.84	10.207	2.42E-09
06-16	3.91	10.828	2.03E-08
06-17A	4.05	10.478	2.21E-08
06-17B	4.11	10.622	2.74E-08
06-18A	4.20	10.544	3.20E-09
06-18B	4.26	10.609	3.87E-09
06-18C	4.31	10.184	3.85E-09
06-18D	4.39	10.085	2.45E-09
06-19A	4.47	10.578	2.16E-09
06-19B	4.55	10.265	9.92E-10
06-19C	4.60	10.779	2.12E-09
06-19D	4.67	10.506	2.87E-09
06-20A	5.01	10.433	3.41E-09
06-20B	5.09	10.679	1.97E-09
06-20BA	5.11	10.547	2.00E-09
06-20BB	5.16	10.870	2.44E-09
06-20BC	5.24	10.062	1.19E-09
06-21A	5.26	10.577	4.22E-09
06-21B	5.31	10.588	3.53E-09
06-23A	5.44	10.302	4.69E-09
06-23B	5.49	10.387	3.08E-09
06-23C	5.54	10.543	6.13E-09
06-24	5.66	10.645	5.05E-09
06-22A	5.68	10.843	1.61E-09
06-22B	5.74	10.468	1.67E-09
L2 (lower)	5.80	10.487	2.64E-08
L2 (m. carb)	5.86	10.447	2.71E-09
L2 (upper)	5.92	10.193	5.49E-08
06-25A	6.06	10.480	6.17E-09
06-25B	6.13	10.764	3.48E-09
06-26A	6.25	10.275	7.17E-09
06-26B	6.32	10.592	9.35E-09
06-26C	6.39	10.313	6.79E-09
06-27	6.49	10.161	1.12E-08
06-28A	6.61	10.654	2.49E-09
06-28B	6.70	10.183	2.78E-09
06-29A	6.79	10.245	7.02E-09
06-34	6.92	10.654	5.55E-09
06-32	7.42	10.106	3.70E-09
06-31	7.74	10.318	9.87E-10
06-30A	8.05	10.821	1.44E-09
06-30B	8.11	10.651	1.98E-09
06-33	8.77	9.797	3.63E-09

Appendix 3 Table 2: Magnetic susceptibility data from Lives-sur-Meuse, Section 2

Sample ID	Height (m)	Mass (g)	MS (m^3/kg)	MS spline (m^3/kg)
04-33	0.56	10.619	6.18E-10	8.96E-10
04-34	0.71	10.298	6.37E-10	1.30E-09
04-35A	0.83	10.566	3.37E-09	1.56E-09
04-35B	0.88	10.605	9.61E-10	1.62E-09
04-35C	0.94	10.784	1.79E-09	1.67E-09
04-37A	1.42	10.269	4.62E-10	1.52E-09
04-37B	1.49	10.277	1.70E-09	1.52E-09
04-36	1.61	10.168	2.25E-09	1.51E-09
04-38A	1.80	10.386	1.51E-09	1.41E-09
04-38B	1.88	10.598	1.13E-09	1.34E-09
04-39	2.54	10.110	1.19E-09	1.17E-09
04-40A	2.84	10.436	2.19E-09	1.68E-09
04-40B	2.94	10.316	2.40E-09	1.99E-09
04-40C	2.98	10.196	1.18E-09	2.14E-09
04-40D	3.06	10.518	1.66E-09	2.53E-09
04-41A	3.08	10.675	1.46E-09	2.64E-09
04-41B	3.14	10.344	1.51E-09	3.00E-09
04-42	3.17	10.478	2.70E-09	3.19E-09
04-43	3.32	10.324	1.06E-08	3.93E-09
04-44A	3.67	10.624	2.33E-09	3.18E-09
04-44B	3.73	10.583	7.91E-10	3.11E-09
04-45	3.95	10.330	3.80E-09	3.79E-09
04-46A	3.98	10.594	5.24E-09	3.99E-09
04-46B	4.03	9.956	3.76E-09	4.38E-09
04-46C	4.09	10.403	3.94E-09	4.93E-09
04-47	4.11	10.496	3.39E-09	5.14E-09
04-48	4.18	10.419	5.85E-09	5.94E-09
E2A	4.36	10.707	8.07E-09	8.13E-09
E2B	4.44	10.160	1.21E-08	8.93E-09
16-01	4.64	10.642	9.99E-09	9.83E-09
16-02	4.76	10.126	1.14E-08	9.70E-09
16-03	4.86	10.082	9.83E-09	9.29E-09
16-04	4.97	10.036	3.91E-09	8.74E-09
16-05	5.12	10.584	8.33E-09	8.12E-09
16-06	5.18	10.087	6.41E-09	7.85E-09
16-07	5.22	10.496	1.29E-08	7.63E-09
16-08	5.24	10.716	5.69E-09	7.50E-09
16-09	5.29	10.873	7.44E-09	7.15E-09
16-10	5.39	10.315	7.85E-09	6.28E-09
16-11	5.49	10.368	7.98E-09	5.24E-09
16-12	5.56	10.495	1.49E-09	4.50E-09
16-13	5.62	10.386	2.38E-09	3.95E-09
16-14	5.74	10.677	1.80E-09	3.20E-09
16-15	5.84	10.687	2.14E-09	2.96E-09
16-16	5.98	10.586	3.19E-09	3.02E-09
16-17	6.08	10.894	5.27E-09	3.16E-09
16-18	6.15	10.537	4.58E-09	3.23E-09
16-19	6.27	10.734	3.32E-09	3.29E-09
16-20	6.39	10.365	2.56E-09	3.50E-09
16-21	6.53	10.668	3.68E-09	4.19E-09
16-22	6.65	10.556	9.65E-10	5.29E-09
16-23	6.78	10.435	1.67E-09	6.97E-09
16-24	6.81	10.803	1.24E-08	7.37E-09
16-25	6.92	10.396	1.11E-08	8.55E-09
16-26	7.00	10.706	1.42E-08	8.96E-09
16-27	7.08	10.175	1.21E-08	8.92E-09
16-28	7.13	10.503	9.60E-09	8.71E-09
16-29	7.18	9.964	2.12E-09	8.43E-09
16-30	7.27	10.356	6.24E-09	7.93E-09
16-31	7.42	10.313	7.32E-09	7.26E-09
16-32	7.54	9.958	6.31E-09	6.81E-09
16-33	7.66	10.577	7.99E-09	6.38E-09
16-34	7.79	10.362	6.06E-09	5.84E-09
16-35	7.91	10.416	3.24E-09	5.35E-09
16-36	8.01	10.255	4.36E-09	5.00E-09
16-37	8.14	10.314	5.39E-09	4.52E-09
16-38	8.21	10.405	7.95E-09	4.15E-09
16-40	8.31	10.735	1.79E-09	3.45E-09
16-39	8.48	10.812	1.61E-09	2.25E-09
16-41	8.62	10.638	6.16E-10	1.52E-09
16-42	8.78	10.611	1.64E-09	1.14E-09
16-43	8.86	10.483	2.79E-10	1.11E-09
16-44	8.98	10.375	1.33E-09	1.25E-09
16-45	9.15	10.618	2.33E-09	1.69E-09
16-46	9.29	10.259	9.93E-10	2.13E-09
16-47	9.45	10.278	3.46E-09	2.64E-09
16-48	9.57	10.438	3.06E-09	2.88E-09
16-49	9.70	10.454	3.75E-09	2.90E-09
16-50	9.82	11.771	3.33E-09	2.72E-09
16-51	9.92	10.480	1.66E-09	2.49E-09
16-52	10.08	10.677	1.46E-09	2.18E-09
16-53	10.19	10.560	1.31E-09	2.08E-09
16-54	10.27	10.747	1.96E-09	2.07E-09
16-55	10.34	9.613	2.95E-09	2.07E-09
16-56	10.46	10.617	2.67E-09	2.03E-09
16-57	10.55	10.699	2.31E-09	1.94E-09
16-58	10.69	10.205	1.71E-09	1.79E-09
16-59	10.81	10.292	9.90E-10	1.75E-09
16-60	10.93	10.551	2.17E-09	1.89E-09
16-61	11.05	10.648	2.32E-09	2.21E-09
16-62	11.17	10.412	8.04E-10	2.75E-09
16-63	11.30	10.535	2.17E-09	3.59E-09
16-64	11.42	10.279	2.58E-09	4.37E-09
16-65	11.56	6.240	1.59E-08	4.70E-09
16-66	11.69	10.335	2.04E-09	3.95E-09
16-67	11.73	10.241	8.18E-10	3.62E-09
16-68	11.83	10.596	1.48E-09	2.81E-09
16-69	11.95	10.371	2.03E-09	1.99E-09
16-70	12.03	10.313	2.40E-09	1.58E-09
16-71	12.13	10.220	1.88E-09	1.26E-09
16-72	12.26	10.580	4.48E-10	1.31E-09
16-73	12.36	10.341	1.16E-09	1.87E-09
16-74	12.42	10.436	4.54E-10	2.46E-09
16-75	12.54	10.716	1.29E-09	4.23E-09
16-76	12.65	10.171	4.03E-09	6.31E-09
16-77	12.70	10.461	4.27E-09	7.27E-09
16-78	12.83	10.520	2.32E-08	9.20E-09
16-79	12.98	10.367	1.13E-08	9.17E-09
16-80	13.08	10.698	1.11E-08	8.07E-09
16-81	13.16	10.726	2.64E-09	6.94E-09
16-84g	13.25	10.289	3.81E-09	5.84E-09
16-82	13.31	10.212	2.42E-09	5.35E-09
16-83	13.40	10.350	3.44E-09	5.09E-09
16-84m	13.51	10.163	4.75E-09	5.55E-09
16-85	13.60	10.677	6.56E-09	6.44E-09
16-86	13.69	10.717	6.03E-09	7.66E-09
16-87	13.79	10.600	1.12E-08	9.20E-09
16-88	13.89	10.850	1.35E-08	1.07E-08
16-89	14.00	10.173	9.38E-09	1.20E-08
16-90	14.10	10.376	1.46E-08	1.31E-08

Appendix 3 Table 2 continued

Sample ID	Height (m)	Mass (g)	MS (m^3/kg)	MS spline (m^3/kg)
16-91	14.21	10.682	1.18E-08	1.38E-08
16-92	14.33	11.060	1.24E-08	1.41E-08
16-93	14.40	10.143	1.99E-08	1.39E-08
16-94	14.49	10.409	1.75E-08	1.31E-08
16-95	14.60	10.397	1.01E-08	1.15E-08
16-96	14.70	10.589	8.16E-09	9.83E-09
16-97	14.78	10.650	5.05E-09	8.66E-09
16-98	14.89	10.192	9.19E-09	7.50E-09
16-100	14.97	10.586	9.36E-09	6.99E-09
16-99	15.03	10.365	6.23E-09	6.83E-09
16-101	15.07	10.931	3.42E-09	6.85E-09
16-102	15.18	10.948	3.09E-09	7.54E-09
16-103	15.31	10.672	5.72E-09	9.38E-09
16-104	15.46	10.606	1.75E-08	1.18E-08
16-105	15.56	10.772	1.96E-08	1.27E-08
16-106	15.63	10.139	1.30E-08	1.27E-08
16-107	15.78	10.827	6.97E-09	1.17E-08
16-108	15.88	10.568	1.30E-08	1.07E-08
16-109	16.11	10.267	9.83E-09	7.52E-09
16-110	16.23	10.194	9.99E-10	6.02E-09
16-111	16.36	10.735	4.84E-09	5.10E-09
16-112	16.48	10.875	2.94E-09	4.90E-09
16-113	16.63	10.289	3.99E-09	5.25E-09
16-114	16.73	10.464	1.26E-08	5.50E-09
16-115	16.84	10.722	4.67E-09	5.50E-09
16-116	16.93	10.217	4.73E-09	5.39E-09
16-117	17.03	10.265	2.41E-09	5.34E-09
16-118	17.19	10.333	4.50E-09	5.50E-09
16-119	17.34	10.094	7.66E-09	5.58E-09
16-120	17.44	10.276	9.64E-09	5.31E-09
16-121	17.54	10.639	2.66E-09	4.74E-09
16-122	17.67	10.711	2.82E-09	3.93E-09
16-124	17.77	10.077	1.55E-09	3.44E-09
16-123	17.87	10.546	3.55E-09	3.13E-09
16-125	18.02	10.720	2.14E-09	2.86E-09
16-126	18.12	10.459	4.44E-09	2.70E-09
16-127	18.22	10.118	3.52E-09	2.45E-09
16-128	18.37	10.662	7.85E-10	1.98E-09
16-129	18.53	10.554	1.31E-09	1.59E-09
16-130	18.63	10.542	2.00E-09	1.46E-09
16-131	18.74	10.560	2.00E-09	1.41E-09
16-132	18.84	10.481	1.15E-09	1.49E-09
16-133	18.94	10.733	-4.04E-10	1.75E-09
16-134	19.02	10.120	1.37E-09	2.11E-09
16-135	19.14	10.484	3.40E-09	2.78E-09
16-136	19.22	10.442	3.76E-09	3.18E-09
16-137	19.33	10.286	3.81E-09	3.55E-09
16-138	19.45	10.391	5.52E-09	3.56E-09
16-139	19.54	10.791	4.98E-09	3.26E-09
16-140	19.64	10.473	1.32E-09	2.69E-09
16-141	19.77	10.400	9.80E-10	1.87E-09
16-142	19.87	10.658	7.86E-10	1.35E-09
16-143	19.98	9.962	-7.07E-11	9.51E-10
16-144	20.04	10.183	1.18E-09	8.14E-10
16-145	20.15	10.214	1.18E-09	6.68E-10
16-146	20.31	10.666	1.13E-09	6.05E-10
16-147	20.47	10.580	-2.38E-10	7.06E-10
16-148	20.58	10.171	6.45E-10	9.09E-10
16-149	20.68	10.408	2.20E-09	1.16E-09
16-150	20.76	10.170	2.88E-10	1.37E-09
16-151	20.83	10.381	1.33E-09	1.55E-09
16-152	20.91	10.349	2.21E-09	1.75E-09

Sample ID	Height (m)	Mass (g)	MS (m^3/kg)	MS spline (m^3/kg)
16-153	21.03	10.186	3.14E-09	1.92E-09
16-154	21.13	10.161	2.25E-09	1.92E-09
16-155	21.26	10.194	1.18E-09	1.80E-09
16-156	21.38	10.581	1.65E-09	1.67E-09
16-157	21.42	10.147	1.00E-09	1.64E-09
16-158	21.58	10.665	1.98E-09	1.57E-09
16-159	21.70	10.081	1.37E-09	1.56E-09
16-160	21.88	10.623	1.13E-09	1.59E-09
16-161	21.99	10.659	2.32E-09	1.62E-09
16-162	22.09	10.366	3.08E-09	1.62E-09
16-163	22.16	11.527	4.11E-10	1.61E-09
16-164	22.27	10.387	1.51E-09	1.67E-09
16-165	22.36	10.579	7.91E-10	1.81E-09
16-166	22.53	9.947	2.67E-09	2.30E-09
16-167	22.63	10.358	1.86E-09	2.65E-09
16-168	22.78	10.615	3.35E-09	3.13E-09
16-169	22.88	10.663	4.53E-09	3.29E-09
16-170	22.94	10.584	3.71E-09	3.30E-09
16-171	22.99	10.611	3.35E-09	3.24E-09
16-172	23.17	10.584	3.53E-09	2.76E-09
16-173	23.27	10.605	1.47E-09	2.39E-09
16-174	23.42	10.576	1.31E-09	1.98E-09
16-175	23.55	10.375	1.68E-09	1.88E-09
16-176	23.68	10.395	4.56E-10	2.02E-09
16-177	23.88	10.550	4.58E-09	2.49E-09
09-01A	25.34	10.461	9.74E-10	2.75E-09
09-01B	25.44	10.818	2.79E-09	3.64E-09
09-01C	25.57	10.119	4.77E-09	4.94E-09
09-01D	25.70	10.304	3.10E-09	6.03E-09
09-02A	25.78	10.210	1.98E-08	6.39E-09
09-02B	25.82	10.078	1.73E-09	6.42E-09
16-178	25.95	10.117	4.95E-09	6.09E-09
16-179	26.05	10.604	2.84E-09	5.65E-09
16-180	26.20	10.632	1.81E-09	5.03E-09
16-181	26.28	10.415	1.23E-08	4.66E-09
16-182	26.36	10.352	1.86E-09	4.18E-09
16-183	26.55	10.411	2.90E-09	3.04E-09
16-185	26.64	10.803	7.75E-10	2.69E-09
16-184	26.77	10.451	1.15E-09	2.58E-09
16-186	26.79	10.194	3.14E-09	2.60E-09
16-187	26.91	10.234	1.88E-09	2.85E-09
16-188	27.05	10.114	4.95E-09	3.20E-09
16-190	27.14	10.203	3.84E-09	3.26E-09
16-189	27.23	10.532	5.96E-09	3.11E-09
16-191	27.30	10.763	2.97E-09	2.85E-09
16-192	27.40	10.425	2.54E-09	2.40E-09
16-195	27.46	10.118	-7.88E-10	2.18E-09
16-194	27.54	10.142	1.10E-10	2.00E-09
16-193	27.64	10.513	1.83E-09	1.99E-09
16-196	27.79	10.771	1.45E-09	2.11E-09
16-197	27.85	10.728	7.54E-09	2.11E-09
16-198	27.88	10.646	3.17E-09	2.07E-09
16-199	27.96	9.960	-2.53E-10	1.92E-09
16-200	28.10	10.585	2.76E-10	1.75E-09
16-201	28.20	10.507	2.78E-10	1.88E-09
16-203	28.28	10.011	4.10E-09	2.15E-09
16-202	28.32	10.228	2.24E-09	2.33E-09
16-204	28.35	10.416	1.15E-09	2.48E-09
16-205L	28.40	10.418	1.07E-10	2.78E-09
16-205P	28.42	10.372	4.31E-09	2.91E-09
16-206	28.44	10.191	2.25E-09	3.04E-09
16-207	28.55	10.758	2.97E-09	3.78E-09

Appendix 3 Table 2 continued

Sample ID	Height (m)	Mass (g)	MS (m^3/kg)	MS spline (m^3/kg)
16-208	28.63	10.735	8.38E-09	4.19E-09
16-209	28.68	10.165	5.29E-09	4.32E-09
16-210	28.77	10.448	2.71E-09	4.32E-09
16-211	28.87	10.337	7.83E-09	4.02E-09
16-212	28.97	10.231	1.35E-09	3.45E-09
16-213	29.07	10.572	1.48E-09	2.83E-09
16-214	29.20	10.822	1.44E-09	2.15E-09
16-215	29.31	10.165	2.25E-09	1.72E-09
16-216	29.41	10.464	2.01E-09	1.41E-09
16-217A	29.47	10.420	4.55E-10	1.27E-09
16-217B	29.54	10.173	8.23E-10	1.14E-09
16-218	29.72	10.055	6.52E-10	9.63E-10
16-219	29.82	10.719	1.97E-09	8.99E-10
16-220	29.95	10.756	1.96E-09	7.59E-10
16-221	29.98	10.074	-4.30E-10	7.19E-10
16-222	30.12	10.284	4.61E-10	5.48E-10
16-223	30.20	10.657	-2.36E-10	4.80E-10
16-224	30.30	10.457	8.01E-10	4.32E-10
16-226	30.42	10.180	1.00E-09	3.95E-10
16-225	30.52	10.354	1.07E-10	3.70E-10
16-227	30.60	10.615	-6.64E-11	3.70E-10
16-229	30.70	10.507	6.24E-10	4.08E-10
16-228b	30.81	10.287	8.14E-10	4.84E-10
16-228t	30.85	10.593	1.05E-10	5.19E-10
16-230	31.03	10.610	4.47E-10	7.40E-10
16-231	31.13	10.427	9.77E-10	8.89E-10
16-232	31.24	10.822	1.28E-09	1.04E-09
16-233	31.45	10.065	1.91E-09	1.20E-09
16-235	31.71	10.342	4.59E-10	1.24E-09
16-234	31.79	10.821	2.12E-09	1.32E-09
16-236	31.89	9.996	1.02E-09	1.49E-09
16-237	31.99	9.748	1.79E-09	1.78E-09
16-238	32.07	10.202	2.42E-09	2.11E-09
16-239	32.12	10.716	1.46E-09	2.36E-09
16-240	32.22	10.204	2.87E-10	2.99E-09
16-241	32.30	10.423	8.03E-10	3.58E-09
16-241	32.40	10.092	8.30E-10	4.21E-09
16-242	32.43	10.241	2.08E-08	4.32E-09
16-243	32.52	10.816	1.61E-09	4.32E-09
16-244	32.57	10.430	2.81E-10	4.20E-09
16-245	32.69	10.678	2.31E-09	3.89E-09
16-246	32.77	10.033	3.91E-09	3.67E-09
16-247	32.85	10.904	4.76E-09	3.42E-09
16-248	32.93	10.601	3.53E-09	3.12E-09
16-249	32.99	10.347	2.74E-09	2.87E-09
16-250	33.12	10.111	1.01E-09	2.34E-09
16-251	33.22	10.530	3.55E-09	2.00E-09
16-252	33.30	10.225	4.64E-10	1.79E-09
16-253	33.38	10.330	1.86E-09	1.64E-09
16-254	33.48	10.773	1.45E-09	1.56E-09
16-255	33.53	10.756	1.28E-09	1.56E-09
16-256	33.59	10.581	1.31E-09	1.60E-09
16-257	33.70	10.498	2.70E-09	1.74E-09
16-258	33.80	10.025	8.35E-10	1.93E-09
16-259	33.95	10.756	2.47E-09	2.27E-09
16-260	34.04	10.686	2.48E-09	2.46E-09
16-261	34.19	10.205	3.31E-09	2.62E-09
16-262	34.26	9.639	4.63E-09	2.60E-09
16-263	34.36	10.594	1.30E-09	2.47E-09
16-264	34.44	10.102	8.29E-10	2.39E-09
16-265	34.58	10.489	2.87E-09	2.35E-09
16-266	34.73	10.380	2.73E-09	2.41E-09

Sample ID	Height (m)	Mass (g)	MS (m^3/kg)	MS spline (m^3/kg)
16-267	34.78	10.655	3.34E-09	2.44E-09
16-269	34.82	10.317	2.04E-09	2.48E-09
16-268	34.90	10.661	1.47E-09	2.59E-09
16-270	34.94	10.351	2.56E-09	2.67E-09
16-271	35.04	10.792	3.47E-09	2.95E-09
16-272	35.06	10.126	1.54E-09	3.02E-09
16-276	35.10	10.592	3.70E-09	3.16E-09
16-273	35.14	10.170	2.79E-09	3.30E-09
16-274	35.19	10.743	4.50E-09	3.48E-09
16-275	35.29	10.372	4.48E-09	3.78E-09
16-277	35.49	10.684	3.84E-09	4.16E-09
16-278	35.66	10.403	4.12E-09	4.31E-09
16-279	35.80	10.638	5.22E-09	4.32E-09
16-280	35.92	10.380	2.56E-09	4.23E-09
16-281	36.04	10.005	5.19E-09	4.09E-09
16-282	36.17	10.381	5.35E-09	3.80E-09
16-283	36.33	10.445	2.54E-09	3.31E-09
16-284	36.43	10.036	1.38E-09	3.12E-09
16-285	36.53	10.107	3.52E-09	3.09E-09
16-286	36.68	10.377	5.53E-09	3.26E-09
16-287	36.91	10.282	2.85E-10	4.16E-09
16-288	37.11	9.983	6.47E-09	6.21E-09
16-289	37.18	10.639	7.27E-09	7.07E-09
16-290	37.28	10.224	7.21E-09	8.28E-09
16-291	37.38	10.204	9.35E-09	9.33E-09
16-292	37.47	10.327	1.38E-08	9.97E-09
16-293	37.54	10.292	1.56E-08	1.02E-08
16-294	37.59	10.143	9.41E-09	1.02E-08
16-295	37.64	10.736	7.88E-09	1.02E-08
16-296	37.67	10.586	4.90E-09	1.02E-08
16-297	37.74	10.300	1.23E-08	1.01E-08
16-298	37.87	10.629	9.83E-09	1.01E-08
16-299	37.97	10.682	9.95E-09	1.01E-08
16-300	38.06	10.533	1.18E-08	1.02E-08
16-301	38.16	10.005	1.10E-08	1.03E-08
16-302	38.24	10.474	8.77E-09	1.06E-08
16-303	38.34	10.447	8.79E-09	1.11E-08
16-304	38.41	10.176	1.38E-08	1.17E-08
16-305	38.52	10.036	1.13E-08	1.29E-08
16-306	38.60	10.484	1.03E-08	1.39E-08
16-307	38.69	10.664	1.06E-08	1.51E-08
16-308	38.71	10.705	2.38E-08	1.54E-08
16-309	38.73	10.451	1.66E-08	1.56E-08
16-310	38.78	10.647	1.71E-08	1.62E-08
16-311	38.86	10.151	1.90E-08	1.69E-08
16-312	38.91	10.574	1.62E-08	1.73E-08
16-313	38.99	10.506	1.63E-08	1.77E-08
16-314	39.09	10.515	1.72E-08	1.82E-08
16-315	39.17	10.126	1.68E-08	1.86E-08
L3	39.22	10.256	1.71E-08	1.88E-08
03-14A	39.32	10.077	2.46E-08	1.91E-08
03-14B	39.40	9.717	2.14E-08	1.90E-08
03-15A	39.48	10.460	1.95E-08	1.86E-08
03-15B	39.56	10.535	1.16E-08	1.81E-08
03-16A	39.61	10.434	1.89E-08	1.79E-08
03-16B	39.67	10.196	1.81E-08	1.76E-08
03-16C	39.74	10.352	2.04E-08	1.73E-08
03-18	39.94	10.543	8.19E-09	1.67E-08
03-17	40.07	10.599	2.18E-08	1.70E-08
03-19A	40.18	10.194	1.65E-08	1.73E-08
03-19B	40.24	10.619	1.68E-08	1.73E-08
03-20	40.33	9.874	1.88E-08	1.72E-08

Appendix 3 Table 2 continued

Sample ID	Height (m)	Mass (g)	MS (m^3/kg)	MS spline (m^3/kg)
03-21A	40.41	10.049	1.92E-08	1.69E-08
03-21B	40.46	10.335	2.01E-08	1.65E-08
03-22	40.54	9.976	1.27E-08	1.57E-08
03-23	40.75	10.232	1.16E-08	1.37E-08
03-24	41.06	10.454	8.96E-09	1.31E-08
03-25A	41.22	10.331	1.85E-08	1.38E-08
03-25B	41.30	10.466	1.47E-08	1.42E-08
03-26	41.40	10.369	1.88E-08	1.46E-08
03-27A	41.43	10.435	1.16E-08	1.47E-08
03-27B	41.48	10.969	8.21E-09	1.49E-08
03-28A	41.68	10.215	1.96E-08	1.58E-08
03-28B	41.79	10.188	1.68E-08	1.58E-08
03-29	41.93	10.623	1.48E-08	1.49E-08
03-30A	41.95	10.224	1.61E-08	1.48E-08
03-30B	42.03	10.677	1.30E-08	1.38E-08
03-31A	42.11	10.209	1.61E-08	1.27E-08
03-31B	42.19	10.489	1.60E-08	1.14E-08
03-32A	42.21	10.621	7.28E-09	1.11E-08
03-32B	42.30	10.771	3.30E-09	9.76E-09
03-33	42.60	9.849	7.67E-09	7.79E-09
03-34	43.12	10.851	9.80E-09	7.06E-09
03-35	43.14	10.407	8.82E-09	6.93E-09
03-36A	43.38	10.244	2.94E-09	4.77E-09
03-36B	43.47	10.321	2.39E-09	4.12E-09
03-37	43.63	10.460	3.58E-09	3.57E-09
03-38	45.13	10.449	1.83E-08	1.72E-08
03-40A	45.23	10.222	1.48E-08	1.80E-08
03-40B	45.29	10.271	1.65E-08	1.83E-08
03-39	45.53	10.336	2.22E-08	1.81E-08
03-41A	45.57	10.507	1.82E-08	1.76E-08
03-41B	45.64	10.418	2.01E-08	1.64E-08
03-43A	45.73	10.323	1.64E-08	1.40E-08
03-43B	45.77	10.835	1.72E-08	1.28E-08
03-44A	45.91	10.793	1.78E-09	8.10E-09
03-44B	45.98	10.769	1.28E-09	6.09E-09
03-44C	46.05	10.342	1.86E-09	4.50E-09
03-42A	46.42	10.266	4.00E-09	1.67E-09
03-42B	46.53	10.160	2.07E-09	1.57E-09
03-45	47.67	10.222	1.88E-09	1.47E-09
03-47	48.24	10.485	1.32E-09	1.95E-09
03-46A	48.55	10.489	3.74E-09	3.68E-09
03-46B	48.62	10.725	3.83E-09	4.21E-09
03-49A	48.96	10.321	5.73E-09	7.02E-09
03-49B	49.06	10.577	6.62E-09	7.74E-09
03-48	49.13	10.082	1.20E-08	8.11E-09
03-50	49.16	10.589	6.96E-09	8.22E-09
03-51	49.42	10.677	1.05E-08	7.63E-09
03-52A	49.56	10.473	6.69E-09	6.20E-09
03-52B	49.64	10.698	3.50E-09	5.20E-09
D3A	49.70	10.470	3.92E-09	4.45E-09
D3B	49.75	10.453	3.75E-09	3.85E-09
D3C	49.80	10.095	4.60E-09	3.27E-09
D4A	49.93	10.809	6.07E-10	2.00E-09
D4B	50.04	10.530	-7.57E-10	1.35E-09
D4C	50.13	10.474	1.49E-09	1.16E-09
03-53A	50.62	10.723	3.15E-09	2.65E-09
03-53B	50.67	10.570	4.05E-09	2.78E-09
03-53C	50.74	10.304	2.93E-09	2.89E-09
03-54	50.86	10.633	3.18E-09	2.92E-09
03-55A	51.00	10.559	3.54E-09	2.82E-09
03-55B	51.09	10.562	2.51E-09	2.78E-09
03-56A	51.26	10.721	2.14E-09	3.05E-09

Sample ID	Height (m)	Mass (g)	MS (m^3/kg)	MS spline (m^3/kg)
03-56B	51.34	10.288	1.34E-09	3.47E-09
03-56D	51.41	10.317	1.52E-09	4.01E-09
03-56C	51.45	10.667	2.83E-09	4.37E-09
03-57A	51.50	10.386	9.01E-09	4.86E-09
03-57B	51.53	10.590	6.44E-09	5.14E-09
03-58	51.62	10.272	4.53E-09	5.91E-09
03-60	51.98	10.204	1.38E-08	6.76E-09
03-59	52.24	9.871	2.69E-09	4.36E-09
03-62A	52.26	10.176	2.07E-09	4.22E-09
03-62B	52.35	11.066	1.58E-09	3.88E-09
03-61A	52.40	10.579	2.68E-09	3.92E-09
03-61B	52.49	10.328	1.87E-09	4.37E-09
D5A	52.62	10.143	7.80E-09	5.65E-09
D5B	52.67	10.527	6.83E-09	6.20E-09
D5C	52.72	10.622	8.30E-09	6.75E-09
03-63	52.86	10.295	8.57E-09	8.13E-09
03-64A	52.99	10.753	7.86E-09	9.20E-09
03-64B	53.03	10.659	9.63E-09	9.50E-09
03-65A	53.08	10.668	9.97E-09	9.84E-09
03-65B	53.16	10.669	9.45E-09	1.03E-08
03-65C	53.25	10.423	1.32E-08	1.06E-08
03-66A	53.27	10.438	1.14E-08	1.07E-08
03-66B	53.36	10.415	8.99E-09	1.07E-08
03-67	53.44	10.535	8.89E-09	1.06E-08
03-68A	53.49	10.734	1.31E-08	1.05E-08
03-68B	53.57	10.564	1.04E-08	1.02E-08
03-69A	53.71	10.573	1.04E-08	9.29E-09
03-69B	53.81	10.223	7.92E-09	8.58E-09
03-69C	53.91	10.709	6.03E-09	7.95E-09
03-77A	54.22	10.724	7.38E-09	7.22E-09
03-77B	54.32	10.317	7.49E-09	7.31E-09
03-77C	54.41	10.344	8.00E-09	7.49E-09
03-70	54.75	10.457	8.43E-09	9.33E-09
03-71	54.91	10.501	5.12E-09	1.11E-08
03-72	54.94	10.653	1.39E-08	1.15E-08
03-73A	55.09	10.496	1.44E-08	1.33E-08
03-73B	55.13	10.726	1.48E-08	1.37E-08
03-74A	55.19	10.307	1.61E-08	1.41E-08
03-74B	55.27	10.280	1.46E-08	1.43E-08
03-75A	55.39	10.227	1.48E-08	1.40E-08
03-75B	55.47	10.484	1.46E-08	1.34E-08
03-76A	55.86	10.506	5.46E-09	8.84E-09
03-76B	55.95	10.437	6.54E-09	8.27E-09
04-08A	56.31	10.653	6.07E-09	7.76E-09
04-08B	56.40	10.717	1.62E-08	7.40E-09
04-09	56.42	10.174	5.46E-09	7.26E-09
04-10A	56.74	10.301	1.52E-09	3.67E-09
04-10B	56.84	10.046	1.19E-09	2.67E-09
04-10C	56.92	10.003	1.38E-09	2.09E-09
04-11	57.02	10.370	2.91E-09	1.58E-09
04-12	57.41	10.541	7.94E-10	1.06E-09
04-13A	57.57	9.951	1.57E-09	1.40E-09
04-13B	57.62	10.356	1.16E-09	1.55E-09
04-15A	57.71	10.273	1.88E-09	1.87E-09
04-15B	57.80	10.412	2.20E-09	2.21E-09
04-14A	58.21	10.692	3.50E-09	3.14E-09
04-14B	58.27	10.708	4.34E-09	3.08E-09
04-17	58.96	10.446	8.02E-10	1.47E-09
04-16A	59.07	10.510	1.14E-09	2.09E-09
04-16B	59.16	10.465	2.36E-09	2.95E-09
04-16C	59.26	10.448	2.02E-09	4.23E-09
04-18A	59.39	10.554	6.81E-09	6.22E-09

Appendix 3 Table 2 continued

Sample ID	Height (m)	Mass (g)	MS (m^3/kg)	MS spline (m^3/kg)
04-18B	59.44	10.677	8.09E-09	6.98E-09
04-18C	59.50	10.323	7.31E-09	7.82E-09
04-20	59.57	10.457	1.21E-08	8.68E-09
04-21	59.77	10.402	9.00E-09	1.02E-08
04-22A	59.79	10.570	8.69E-09	1.03E-08
04-22B	59.85	10.703	1.09E-08	1.05E-08
04-23A	59.95	10.541	1.01E-08	1.07E-08
04-23B	60.02	10.272	9.64E-09	1.06E-08
04-25A	60.05	10.775	1.79E-08	1.05E-08
04-25B	60.13	10.827	7.64E-09	9.97E-09
04-24A	60.20	10.582	7.82E-09	9.39E-09
04-24B	60.27	10.162	7.96E-09	8.75E-09
04-27A	60.31	10.509	8.22E-09	8.37E-09
04-27B	60.39	10.442	7.58E-09	7.59E-09
04-26A	60.45	10.165	8.50E-09	6.97E-09
04-26B	60.53	10.599	7.12E-09	6.13E-09
04-28	60.63	10.732	3.49E-09	5.11E-09
04-29A	60.71	10.535	2.52E-09	4.42E-09
04-29B	60.76	10.652	3.34E-09	4.08E-09
04-29C	60.81	10.416	4.29E-09	3.78E-09
04-30	61.02	10.521	4.59E-09	2.77E-09
04-32A	61.41	10.397	2.81E-10	5.61E-10
04-32B	61.47	10.739	-7.42E-10	2.43E-10
04-32C	61.53	10.147	2.88E-10	-5.33E-11
04-31B	61.57	10.655	-6.61E-11	-2.44E-10
04-31C	61.63	10.343	-2.44E-10	-5.27E-10

Appendix 3 Table 3: Magnetic susceptibility data from Awirs West Quarry

Sample ID	Height (m)	Mass (g)	MS (m^3/kg)	MS spline (m^3/kg)
L3	0.00	10.085	8.21E-09	8.50E-09
14-01	0.03	10.285	8.93E-09	8.32E-09
14-02	0.07	10.376	8.85E-09	8.09E-09
14-03	0.17	10.349	6.42E-09	7.51E-09
14-04	0.27	10.291	7.34E-09	7.00E-09
14-05	0.37	10.169	6.89E-09	6.58E-09
14-06	0.49	10.446	4.97E-09	6.24E-09
14-07	0.63	10.270	6.12E-09	6.11E-09
14-08	0.74	10.506	6.15E-09	6.15E-09
14-09	0.88	9.989	7.38E-09	6.27E-09
14-10	0.92	10.297	7.33E-09	6.30E-09
14-11	1.04	10.500	5.12E-09	6.42E-09
14-12	1.12	10.360	5.19E-09	6.58E-09
14-13	1.28	10.327	6.26E-09	7.10E-09
14-14	1.35	10.210	7.75E-09	7.35E-09
14-15	1.52	10.210	1.11E-08	7.61E-09
14-16	1.60	10.630	1.03E-08	7.45E-09
14-17	1.65	10.398	4.99E-09	7.28E-09
14-18	1.81	7.948	3.57E-09	6.79E-09
14-19	1.93	10.369	6.06E-09	6.78E-09
14-20	2.01	10.509	7.70E-09	6.95E-09
14-21	2.16	10.423	8.11E-09	7.44E-09
14-22	2.26	10.282	6.99E-09	7.83E-09
14-23	2.39	10.376	8.32E-09	8.34E-09
14-24	2.50	10.486	9.45E-09	8.69E-09
14-25	2.63	10.651	8.11E-09	8.90E-09
14-26	2.83	9.993	1.15E-08	8.58E-09
14-27	2.94	10.635	6.59E-09	7.97E-09
14-28	3.13	10.626	7.96E-09	6.54E-09
14-29	3.27	10.043	4.81E-09	5.43E-09
14-30	3.37	10.569	4.05E-09	4.84E-09
14-31	3.42	10.464	3.40E-09	4.65E-09
14-32	3.47	10.283	5.05E-09	4.54E-09
14-33	3.52	10.542	3.89E-09	4.51E-09
14-34	3.62	10.391	3.95E-09	4.67E-09
14-35	3.64	10.539	4.93E-09	4.74E-09
14-36	3.78	10.579	6.28E-09	5.40E-09
14-37	3.93	10.350	6.59E-09	6.35E-09
14-38	4.13	10.336	7.13E-09	7.80E-09
14-39	4.23	10.294	9.10E-09	8.56E-09
14-40	4.36	10.063	9.66E-09	9.52E-09
14-41	4.52	10.633	4.37E-09	1.06E-08
14-42	4.65	10.449	1.36E-08	1.11E-08
14-43	4.77	10.258	1.97E-08	1.06E-08
14-44	4.79	10.266	1.39E-08	1.04E-08
14-45	4.91	10.580	3.71E-09	8.47E-09
14-46	5.03	10.686	2.99E-09	6.17E-09
14-47	5.21	10.340	2.74E-09	3.22E-09
14-48	5.37	10.501	1.06E-10	1.45E-09
14-49	5.51	10.121	1.19E-09	6.36E-10
14-50	5.70	10.159	-6.06E-10	3.42E-10
14-51	5.88	10.467	1.15E-09	6.14E-10
14-52	6.06	10.202	2.42E-09	8.71E-10
14-53	6.18	10.262	1.17E-09	8.45E-10
14-54	6.30	10.386	6.31E-10	7.11E-10
14-55	6.45	10.248	-7.78E-10	5.84E-10
14-56	6.62	10.320	-6.84E-11	7.00E-10
14-57	6.77	10.398	1.68E-09	9.22E-10
14-58	6.89	10.510	2.52E-09	9.98E-10
14-59	7.01	10.164	2.88E-10	9.25E-10
14-60	7.19	10.301	2.84E-10	7.41E-10
14-61	7.36	10.266	6.39E-10	6.38E-10

Sample ID	Height (m)	Mass (g)	MS (m^3/kg)	MS spline (m^3/kg)
14-62	7.52	10.264	1.17E-09	6.21E-10
14-63	7.64	10.233	8.18E-10	6.66E-10
14-64	7.86	9.922	6.61E-10	1.11E-09
14-65	8.03	10.478	1.06E-10	2.03E-09
14-66	8.26	10.260	2.59E-09	4.01E-09
14-67	8.46	10.362	9.04E-09	5.27E-09
14-68	8.58	10.571	7.83E-09	5.12E-09
14-69	8.71	10.164	3.15E-09	4.19E-09
14-70	8.85	9.981	2.29E-09	2.84E-09
14-71	8.94	10.427	4.55E-10	2.02E-09
14-72	8.99	10.140	1.54E-09	1.63E-09
14-75	9.14	10.793	-5.70E-10	8.01E-10
14-73	9.23	10.249	9.94E-10	5.43E-10
14-76	9.38	10.081	1.01E-09	3.61E-10
14-77	9.48	10.089	4.70E-10	3.28E-10
15-01	10.22	10.165	8.24E-10	1.34E-09
15-02	10.42	10.054	2.28E-09	1.93E-09
15-03	10.64	10.039	2.64E-09	2.42E-09
14-101	10.67	10.256	1.70E-09	2.46E-09
14-102	10.78	10.016	4.82E-09	2.54E-09
14-104	10.92	10.438	2.37E-09	2.49E-09
14-103	11.01	10.378	1.51E-09	2.47E-09
14-105	11.10	9.962	2.30E-09	2.55E-09
14-106	11.20	10.073	1.37E-09	2.81E-09
14-107	11.31	10.089	2.81E-09	3.29E-09
14-108	11.39	9.983	4.47E-09	3.72E-09
14-109	11.47	10.059	5.52E-09	4.14E-09
14-110	11.55	9.935	2.49E-09	4.52E-09
14-111	11.64	10.009	5.37E-09	4.89E-09
14-112	11.67	10.021	5.91E-09	4.98E-09
14-113	11.76	10.071	6.78E-09	5.18E-09
14-114	11.83	10.072	5.16E-09	5.22E-09
14-115	11.88	10.323	4.50E-09	5.21E-09
14-78	11.98	10.064	4.80E-09	5.15E-09
14-79	12.08	10.019	6.81E-09	5.07E-09
14-80	12.17	10.014	4.10E-09	5.02E-09
14-82	12.23	9.904	4.51E-09	5.04E-09
14-81	12.28	9.883	1.77E-09	5.12E-09
14-82	12.38	9.948	7.95E-09	5.40E-09
14-83	12.47	9.987	5.20E-09	5.70E-09
14-84	12.59	10.165	3.50E-09	6.07E-09
14-85	12.69	10.006	7.91E-09	6.28E-09
14-86	12.73	9.928	9.07E-09	6.28E-09
14-87	12.78	9.970	8.30E-09	6.21E-09
14-88	12.88	10.034	3.01E-09	5.83E-09
14-89	12.96	10.108	6.03E-09	5.44E-09
14-90	13.07	10.139	4.23E-09	4.86E-09
14-91	13.19	10.170	3.32E-09	4.26E-09
14-92	13.29	10.043	3.36E-09	3.80E-09
14-93	13.39	10.028	3.37E-09	3.36E-09
14-94	13.49	10.052	5.35E-09	2.85E-09
14-95	13.57	9.922	3.40E-09	2.36E-09
14-96	13.66	10.027	8.35E-10	1.78E-09
14-97	13.68	9.934	2.95E-10	1.66E-09
14-98	13.85	10.121	2.89E-10	9.02E-10
14-99	14.00	10.141	6.47E-10	6.40E-10
14-100	14.14	10.191	1.09E-10	6.70E-10
12-01	14.17	10.041	8.34E-10	7.02E-10
12-02	14.26	10.200	9.99E-10	8.27E-10
12-03	14.35	10.332	1.34E-09	9.61E-10
12-05	14.38	10.188	8.22E-10	1.00E-09
12-06	14.44	10.151	2.08E-09	1.07E-09

Appendix 3 Table 3 continued

Sample ID	Height (m)	Mass (g)	MS (m^3/kg)	MS spline (m^3/kg)
12-07	14.55	10.151	6.46E-10	1.14E-09
12-08	14.64	9.987	1.75E-09	1.17E-09
12-09	14.73	10.159	1.18E-09	1.20E-09
12-10	14.82	10.237	8.18E-10	1.25E-09
12-11	14.91	10.362	6.33E-10	1.37E-09
12-12	15.04	10.125	1.01E-09	1.64E-09
12-13	15.20	10.227	1.71E-09	2.02E-09
12-14	15.32	10.159	5.47E-09	2.12E-09
12-16	15.42	10.093	1.91E-09	1.98E-09
12-17	15.49	10.111	2.89E-10	1.81E-09
12-18	15.70	10.049	1.19E-09	1.26E-09
12-19	15.78	9.987	1.20E-09	1.07E-09
12-20	15.84	10.202	2.87E-10	9.58E-10
12-21	15.92	10.149	1.54E-09	8.33E-10
12-22	15.94	10.085	8.30E-10	8.06E-10
12-23	16.05	10.336	1.07E-10	6.99E-10
12-24	16.15	10.207	1.09E-10	6.76E-10
12-26	16.34	10.388	1.51E-09	7.44E-10
12-25	16.46	10.254	1.70E-09	7.33E-10
12-27	16.56	10.220	2.86E-10	6.78E-10
12-28	16.71	10.202	1.09E-10	6.47E-10
12-29	16.78	10.180	1.71E-09	6.91E-10
12-30	16.93	10.389	1.07E-10	9.85E-10
12-31	17.00	10.208	4.65E-10	1.27E-09
12-32	17.07	10.299	-5.97E-10	1.66E-09
12-33	17.17	9.887	2.68E-09	2.36E-09
12-34	17.34	10.290	5.93E-09	3.35E-09
12-35	17.41	9.960	3.76E-09	3.51E-09
12-36	17.48	10.305	5.04E-09	3.48E-09
12-37	17.55	10.184	4.92E-09	3.27E-09
12-38	17.62	10.182	3.14E-09	2.95E-09
12-39	17.71	10.279	1.08E-10	2.49E-09
12-40	17.77	9.987	4.75E-10	2.24E-09
12-41	17.88	10.196	1.18E-09	2.02E-09
12-42	17.99	10.010	2.47E-09	2.03E-09
12-43	18.10	10.122	1.72E-09	2.15E-09
12-44	18.26	10.000	3.56E-09	2.31E-09
12-45	18.35	10.191	4.21E-09	2.26E-09
12-46	18.44	10.171	2.96E-09	2.10E-09
12-47	18.56	10.320	-6.83E-11	1.89E-09
12-48	18.63	9.946	8.42E-10	1.89E-09
12-49	18.74	10.076	2.27E-09	2.15E-09
12-50	18.87	9.959	3.03E-09	2.84E-09
12-51	18.96	10.062	1.10E-10	3.56E-09
12-52	19.13	10.002	4.74E-10	5.20E-09
12-53	19.22	10.034	2.10E-09	5.84E-09
L4 (base)	19.24	10.149	1.23E-08	5.91E-09
L4 (top)	19.26	9.985	1.95E-08	5.94E-09
12-54	19.34	10.266	2.41E-09	5.69E-09
12-55	19.54	10.016	2.92E-10	3.79E-09
12-56	19.66	10.164	1.36E-09	2.72E-09
12-57	19.76	10.392	1.16E-09	2.14E-09
12-58	19.93	9.020	7.27E-10	1.76E-09
12-59	20.03	10.171	2.96E-09	1.75E-09
12-60	20.13	10.229	2.59E-09	1.73E-09
12-61	20.23	10.360	2.38E-09	1.63E-09
12-62	20.38	10.267	1.17E-09	1.32E-09
12-63	20.58	10.096	1.01E-09	8.92E-10
12-64	20.72	10.151	-2.48E-10	7.61E-10
12-65	20.82	10.209	4.64E-10	8.30E-10
12-66	21.37	10.302	3.46E-09	2.00E-09
12-67	21.42	10.173	2.61E-09	1.98E-09

Sample ID	Height (m)	Mass (g)	MS (m^3/kg)	MS spline (m^3/kg)
12-68	21.47	10.060	1.91E-09	1.93E-09
12-69	21.56	10.079	1.19E-09	1.80E-09
12-70	21.67	10.055	6.52E-10	1.63E-09
12-71	21.81	10.199	2.60E-09	1.53E-09
12-72	21.89	10.211	9.98E-10	1.53E-09
12-73	21.95	10.428	1.50E-09	1.57E-09
12-75	22.04	10.150	8.25E-10	1.71E-09
12-74	22.10	9.996	-7.05E-11	1.86E-09
12-76	22.19	10.268	4.70E-09	2.14E-09
12-77	22.41	10.128	2.62E-09	2.62E-09
12-78	22.59	10.020	3.37E-09	2.76E-09
12-79	22.79	10.055	1.92E-09	2.70E-09
12-80	23.08	10.169	1.18E-09	2.66E-09
12-81	23.14	10.476	5.48E-09	2.64E-09
12-82	23.33	10.050	6.52E-10	2.49E-09
13-01	23.47	10.586	7.91E-10	2.48E-09
13-02	23.58	10.167	5.46E-09	2.46E-09
13-03	23.68	10.175	2.79E-09	2.30E-09
13-04	23.80	10.338	1.69E-09	1.94E-09
13-05	23.87	10.127	1.54E-09	1.70E-09
13-06	23.97	10.520	1.31E-09	1.39E-09
13-07	24.08	10.505	7.97E-10	1.14E-09
13-08	24.16	10.420	2.81E-10	1.06E-09
13-10	24.22	10.289	1.17E-09	1.06E-09
13-09	24.40	10.123	1.10E-10	1.36E-09
13-11	24.59	10.402	5.34E-09	1.87E-09
13-14	24.68	10.417	1.33E-09	2.01E-09
13-15	24.79	10.349	1.51E-09	2.16E-09
13-16	24.93	10.094	8.29E-10	2.50E-09
13-17	25.04	10.082	1.91E-09	2.94E-09
13-19	25.16	10.247	5.24E-09	3.47E-09
13-18	25.34	10.148	4.40E-09	3.90E-09
13-20	25.51	10.352	5.37E-09	3.73E-09
13-21	25.61	10.507	2.87E-09	3.39E-09
13-22	25.74	10.398	2.20E-09	2.88E-09
13-23	25.87	10.067	1.91E-09	2.48E-09
13-24	26.02	10.260	1.52E-09	2.29E-09
13-25	26.16	10.520	2.18E-09	2.38E-09
13-26	26.27	10.326	3.80E-09	2.52E-09
13-27	26.42	10.471	1.84E-09	2.70E-09
13-28	26.54	10.244	3.83E-09	2.83E-09
13-29	26.70	10.500	1.14E-09	2.94E-09
13-30	26.90	10.407	3.07E-09	2.96E-09
13-31	26.95	10.508	9.70E-10	2.87E-09
13-32	26.98	10.028	9.34E-09	2.79E-09
13-33	27.03	10.645	1.30E-09	2.59E-09
13-34	27.18	10.110	8.28E-10	1.81E-09
13-35	27.27	10.461	6.27E-10	1.36E-09
13-36	27.35	10.399	6.31E-10	1.05E-09
13-37	27.43	10.108	-6.97E-11	8.46E-10
13-38	27.51	10.313	6.36E-10	7.48E-10
13-39	27.61	10.674	1.12E-09	7.22E-10
13-40	27.71	10.360	1.33E-09	7.31E-10
13-41	27.84	10.467	1.15E-09	7.25E-10
13-42	27.90	10.168	4.66E-10	7.10E-10
13-43	27.96	10.238	4.63E-10	6.94E-10
13-44	28.02	10.255	1.08E-10	6.78E-10
13-45	28.16	9.607	2.19E-09	6.17E-10
13-46	28.38	10.445	-2.41E-10	4.02E-10
13-47	28.55	10.433	-6.76E-11	4.51E-10
13-48	28.69	10.517	2.78E-10	7.46E-10
13-49	28.80	9.857	6.65E-10	1.11E-09

Appendix 3 Table 3 continued

Sample ID	Height (m)	Mass (g)	MS (m^3/kg)	MS spline (m^3/kg)
13-50	29.04	10.505	2.70E-09	1.90E-09
13-51	29.14	9.996	3.20E-09	2.01E-09
13-52	29.56	10.188	2.87E-10	1.04E-09
13-53	29.73	10.552	2.77E-10	6.78E-10
13-54	29.90	10.747	6.10E-10	5.18E-10
13-55	30.02	9.774	1.79E-09	4.78E-10
13-56	30.12	10.223	-6.02E-10	4.78E-10
13-57	30.23	10.211	8.20E-10	5.77E-10
13-58	30.37	10.132	2.89E-10	8.83E-10
13-59	30.52	10.103	1.10E-10	1.46E-09
13-60	30.62	10.087	4.25E-09	1.93E-09
13-61	30.80	10.307	2.84E-10	2.73E-09
13-62	30.95	10.661	6.91E-09	3.36E-09
13-63	31.15	10.200	6.43E-10	3.85E-09
13-64	31.29	10.027	1.02E-09	4.21E-09
13-65	31.43	10.065	1.55E-09	4.29E-09
13-66	31.45	10.074	1.97E-08	4.23E-09
12-83	31.50	10.310	-6.84E-11	3.97E-09
12-84	31.58	10.225	2.06E-09	3.35E-09
12-85	31.69	10.312	8.12E-10	2.36E-09
12-86	31.81	10.172	-4.26E-10	1.38E-09
12-87	31.93	10.398	6.31E-10	6.72E-10
12-88	32.04	10.162	8.24E-10	2.10E-10
12-89	32.07	10.369	2.82E-10	1.07E-10
12-90	32.19	10.259	-6.87E-11	-2.21E-10
12-91	32.28	9.878	-1.17E-09	-3.68E-10
12-92	32.40	10.093	-2.50E-10	-4.25E-10
12-93	32.52	10.206	-6.91E-11	-3.72E-10
12-94	32.67	10.090	-9.70E-10	-2.17E-10
12-95	32.77	9.904	4.79E-10	-8.14E-11
12-96	32.80	9.995	1.11E-10	-4.33E-11
12-97	32.92	10.341	6.34E-10	7.52E-11
12-98	33.07	10.188	-6.04E-10	1.58E-10
12-99	33.22	10.256	2.85E-10	2.34E-10
13-68	33.42	9.178	1.31E-09	2.51E-10
13-67	33.52	10.153	2.88E-10	1.92E-10
13-69	33.58	10.276	-5.99E-10	1.56E-10
13-70	33.72	9.298	-2.71E-10	1.38E-10
13-71	33.87	9.773	2.99E-10	2.47E-10
13-72	34.01	10.370	2.82E-10	4.26E-10
13-73	34.17	10.399	-2.42E-10	6.55E-10
13-74	34.27	10.233	2.77E-09	7.56E-10
13-75	34.42	10.390	2.82E-10	7.28E-10
13-76	34.62	10.164	1.09E-10	5.56E-10
13-77	34.80	10.527	7.95E-10	4.19E-10
13-78	35.00	10.435	-2.42E-10	3.04E-10
13-79	35.24	9.365	1.09E-09	2.94E-10
13-80	35.40	10.834	-4.00E-10	3.03E-10
13-81	35.57	10.349	2.83E-10	4.09E-10
13-82	35.67	10.583	-6.66E-11	5.06E-10
12-100	35.73	9.856	1.40E-09	5.62E-10
12-101	35.87	9.891	1.03E-09	6.34E-10
12-102	36.02	10.302	4.60E-10	6.14E-10
12-103	36.22	10.410	2.81E-10	5.44E-10
12-104	36.35	10.771	7.77E-10	5.22E-10
12-105	36.46	9.849	2.97E-10	5.20E-10
12-106	36.61	10.412	8.04E-10	5.60E-10
12-107	36.71	10.115	-6.97E-11	6.15E-10
12-108	36.91	10.828	7.73E-10	7.74E-10
12-109	37.03	10.243	1.88E-09	8.08E-10
12-111	37.15	10.389	9.81E-10	7.38E-10
12-110	37.23	10.273	1.08E-10	6.62E-10

Sample ID	Height (m)	Mass (g)	MS (m^3/kg)	MS spline (m^3/kg)
12-113	37.46	10.726	-2.35E-10	5.41E-10
12-112	37.79	10.059	1.19E-09	7.12E-10
12-114	37.99	10.580	1.48E-09	6.32E-10
12-115	38.24	10.553	-7.55E-10	3.42E-10
12-116	38.44	10.529	2.78E-10	3.93E-10
12-117	38.74	10.015	1.56E-09	8.02E-10
12-118	38.87	10.632	4.46E-10	9.51E-10
12-119	39.07	9.875	1.03E-09	1.16E-09
12-120	39.23	10.565	1.65E-09	1.27E-09
12-121	39.53	10.052	1.56E-09	1.20E-09
12-122	39.60	9.930	4.77E-10	1.15E-09
12-123	39.69	10.437	1.50E-09	1.08E-09
12-124	39.88	10.640	2.75E-10	9.19E-10
12-125	40.03	10.494	9.71E-10	8.10E-10
12-126	40.14	10.238	1.17E-09	6.93E-10
12-127	40.33	10.443	4.54E-10	3.62E-10
12-128	40.42	10.155	4.67E-10	1.69E-10
12-129	40.59	10.492	-7.59E-10	-1.67E-10
12-130	40.78	10.367	-7.69E-10	-3.17E-10
12-132	40.90	10.600	-6.65E-11	-2.75E-10
12-131	40.96	10.658	-6.62E-11	-2.30E-10
12-133	41.08	10.117	1.10E-10	-1.14E-10
12-134	41.21	10.656	-9.18E-10	4.75E-11
12-135	41.33	10.321	9.87E-10	2.24E-10
12-136	41.43	10.429	4.55E-10	3.37E-10
12-137	41.55	10.209	9.98E-10	4.10E-10
12-138	41.70	10.251	-6.87E-11	4.43E-10
12-139	41.84	10.392	-6.78E-11	5.23E-10
12-140	41.97	10.016	4.73E-10	6.70E-10
12-141	42.07	10.167	4.66E-10	7.89E-10
12-142	42.11	10.409	1.68E-09	8.27E-10
12-143	42.19	10.246	1.53E-09	8.65E-10
12-144	42.35	10.571	1.05E-10	8.10E-10
12-145	42.43	10.769	6.09E-10	7.51E-10
12-146	42.54	10.380	1.33E-09	6.39E-10
12-147	42.64	10.259	4.62E-10	4.91E-10
12-148	42.89	9.943	1.12E-10	8.39E-11
12-149	42.99	10.688	-4.06E-10	-1.84E-11
12-150	43.10	10.285	-4.22E-10	-4.49E-11
12-151	43.20	10.213	2.87E-10	9.04E-12
12-152	43.38	10.319	-2.44E-10	2.31E-10
12-153	43.58	10.244	9.95E-10	5.55E-10
12-154	43.68	10.517	9.69E-10	6.60E-10
12-155	43.80	10.114	1.37E-09	7.02E-10
12-156	44.00	10.141	4.68E-10	6.88E-10
12-157	44.05	10.216	1.09E-10	7.14E-10
12-158	44.17	10.193	1.00E-09	8.82E-10
12-159	44.32	10.460	1.15E-09	1.31E-09
12-160	44.42	10.162	1.09E-10	1.75E-09
12-161	44.62	10.035	6.53E-10	2.80E-09
12-162	44.74	10.647	6.16E-10	3.17E-09
L5 (base)	44.76	10.726	9.57E-09	3.17E-09
L5 (top)	44.78	9.541	9.05E-09	3.15E-09
12-163	44.80	10.593	7.90E-10	3.11E-09
12-164	44.94	10.447	8.01E-10	2.34E-09
12-165	45.04	10.417	2.81E-10	1.58E-09
12-166	45.17	10.310	1.08E-10	6.51E-10
12-167	45.34	9.749	-6.31E-10	-2.49E-10
12-168	45.48	10.611	-1.09E-09	-6.59E-10
12-169	45.63	10.642	-2.37E-10	-8.06E-10
12-170	45.74	10.184	-7.82E-10	-7.87E-10
12-171	45.92	10.763	-1.08E-09	-5.63E-10

Appendix 3 Table 3 continued

Sample ID	Height (m)	Mass (g)	MS (m^3/kg)	MS spline (m^3/kg)
12-172	46.04	10.476	-2.41E-10	-2.93E-10
12-173	46.17	10.080	1.10E-10	3.62E-11
12-174	46.37	10.310	9.88E-10	4.39E-10
12-175	46.50	10.620	7.88E-10	5.43E-10
12-176	46.58	10.723	4.42E-10	5.46E-10
12-177	46.69	10.106	2.90E-10	5.04E-10
12-178	46.79	10.374	9.82E-10	4.39E-10
12-179	46.83	10.459	1.06E-10	4.10E-10
12-180	46.89	10.647	2.75E-10	3.67E-10
12-181	46.99	10.275	1.08E-10	3.14E-10
12-182	47.13	9.970	2.94E-10	3.03E-10
12-183	47.27	10.160	-2.48E-10	3.73E-10
12-184	47.38	10.324	1.16E-09	4.76E-10
12-185	47.45	10.577	1.05E-10	5.43E-10
12-186	47.52	10.070	1.73E-09	6.05E-10
12-187	47.58	10.370	2.82E-10	6.53E-10
12-188	47.68	10.529	7.95E-10	7.42E-10
12-189	47.74	10.078	6.51E-10	8.14E-10
12-190	47.84	10.393	2.82E-10	9.89E-10
12-191	47.93	10.126	-4.28E-10	1.21E-09
12-192	47.99	10.753	2.30E-09	1.39E-09
12-193	48.05	10.548	7.94E-10	1.55E-09
12-194	48.13	9.924	4.50E-09	1.70E-09
12-195	48.19	10.774	1.45E-09	1.73E-09
12-196	48.31	10.713	1.97E-09	1.63E-09
12-197	48.41	10.561	6.21E-10	1.41E-09
12-198	48.50	9.734	1.05E-09	1.18E-09
12-199	48.59	10.528	4.50E-10	9.23E-10
12-200	48.65	10.552	2.17E-09	7.42E-10
12-201	48.78	9.986	-7.06E-11	3.27E-10
12-202	48.90	10.928	1.02E-10	2.18E-11
12-203	49.03	9.495	-1.03E-09	-1.13E-10
12-204	49.10	10.315	-7.72E-10	-6.67E-11
12-205	49.16	11.016	4.30E-10	3.95E-11
12-207	49.22	9.966	-4.35E-10	1.93E-10
12-206	49.26	10.318	1.08E-10	3.16E-10
12-208	49.38	10.396	9.80E-10	7.18E-10
12-209	49.42	10.630	1.47E-09	8.40E-10
12-210	49.45	10.238	1.53E-09	9.21E-10
12-211	49.62	10.435	1.50E-09	1.19E-09
12-212	49.72	10.656	1.04E-10	1.21E-09
12-213	49.83	6.577	2.65E-09	1.14E-09
12-214	49.96	9.975	4.75E-10	8.91E-10
12-215	50.09	10.427	6.29E-10	5.56E-10
12-216	50.24	10.303	-2.45E-10	1.71E-10
12-217	50.38	10.124	-2.49E-10	-9.61E-11
12-218	50.50	10.390	-6.78E-11	-2.33E-10
12-219	50.67	9.896	-2.55E-10	-2.89E-10
12-220	50.73	10.655	-6.61E-11	-2.67E-10
12-221	50.86	10.055	-9.73E-10	-1.28E-10
12-222	50.99	10.433	6.29E-10	1.56E-10
12-223	51.12	9.996	8.38E-10	5.29E-10
12-224	51.25	10.529	1.05E-10	9.74E-10
12-225	51.38	10.294	2.84E-10	1.50E-09
12-226	51.48	10.090	1.91E-09	1.90E-09
12-227	51.51	10.139	4.05E-09	1.99E-09
12-228	51.61	9.915	1.94E-09	2.19E-09
12-229	51.69	10.192	3.31E-09	2.23E-09
12-230	51.94	12.550	3.78E-10	1.83E-09
12-231	51.97	11.088	1.90E-09	1.78E-09
12-232	52.00	10.069	8.32E-10	1.72E-09
12-233	52.12	9.796	4.00E-09	1.50E-09

Sample ID	Height (m)	Mass (g)	MS (m^3/kg)	MS spline (m^3/kg)
12-235	52.30	10.684	2.74E-10	1.07E-09
12-234	52.38	10.777	-7.39E-10	9.50E-10
12-236	52.55	10.293	2.05E-09	9.11E-10
12-237	52.69	9.504	1.07E-09	9.16E-10
12-238	52.91	10.731	1.29E-09	9.00E-10
12-239	52.94	12.033	9.23E-11	9.01E-10
12-240	53.04	10.515	2.78E-10	9.20E-10
12-241	53.14	10.201	1.71E-09	9.39E-10
12-242	53.28	10.386	1.68E-09	8.70E-10
12-243	53.38	10.069	1.19E-09	7.40E-10
12-244	53.51	9.831	-6.26E-10	5.55E-10
12-245	53.66	10.889	6.02E-10	4.95E-10
12-246	53.78	10.676	4.44E-10	5.89E-10
12-247	53.87	10.493	4.52E-10	7.45E-10
12-248	54.02	10.625	6.17E-10	1.14E-09
12-249	54.16	10.161	2.25E-09	1.57E-09
12-250	54.51	9.558	1.45E-09	2.08E-09
12-251	54.54	10.534	3.72E-09	2.06E-09
12-252	54.74	10.730	1.80E-09	1.70E-09
12-253	54.87	10.399	8.05E-10	1.39E-09
12-254	54.90	10.270	4.62E-10	1.33E-09
12-255	54.99	10.004	4.74E-10	1.20E-09
12-256	55.15	10.877	3.44E-09	9.86E-10
12-257	55.31	9.747	-4.45E-10	5.97E-10
12-258	55.47	10.638	7.87E-10	2.25E-10
12-259	55.59	10.677	-1.43E-09	3.09E-11
12-260	55.69	10.516	4.51E-10	-3.21E-11
12-261	55.84	9.895	-7.13E-11	-3.12E-11
12-262	55.98	9.325	5.09E-10	1.30E-12
12-263	56.14	10.390	-2.43E-10	1.23E-11
12-264	56.32	10.782	2.71E-10	1.58E-11
12-265	56.48	10.287	-4.22E-10	1.27E-11
12-266	56.60	9.878	1.12E-10	2.33E-11
12-270	56.70	9.685	3.02E-10	2.55E-11
12-267	56.74	10.114	-4.29E-10	2.14E-11
12-268	56.84	10.059	8.32E-10	-5.84E-12
12-269	57.04	10.533	-7.57E-10	-1.31E-10
12-271	57.15	10.466	2.80E-10	-1.70E-10
12-272	57.26	10.580	-9.25E-10	-1.72E-10
12-273	57.37	10.167	4.66E-10	-1.21E-10
12-274	57.47	10.377	-7.68E-10	-4.87E-11
12-275	57.63	9.586	8.73E-10	9.40E-11
12-276	57.89	10.057	-7.01E-11	1.99E-10
12-277	58.02	9.731	3.01E-10	2.34E-10
12-278	58.14	10.491	-6.72E-11	2.67E-10
12-279	58.28	10.108	8.28E-10	2.96E-10
12-280	58.49	10.675	1.04E-10	2.58E-10
12-281	58.66	10.100	-2.50E-10	2.17E-10
12-282	58.79	10.106	8.29E-10	1.92E-10
12-283	58.92	10.187	6.44E-10	1.33E-10
12-284	59.00	10.689	-7.45E-10	9.21E-11
12-285	59.11	9.871	-7.14E-11	6.89E-11
12-287	59.46	10.410	8.04E-10	1.24E-10
12-288	59.60	10.539	-2.39E-10	9.99E-11
12-289	59.80	10.450	1.06E-10	1.08E-10
12-290	59.91	10.269	-6.86E-11	1.64E-10
12-291	60.04	10.435	-6.76E-11	2.90E-10
12-292	60.17	10.301	4.60E-10	4.54E-10
12-293	60.29	10.435	1.32E-09	5.75E-10
12-294	60.49	10.066	2.91E-10	6.05E-10
12-295	60.60	10.183	1.00E-09	5.63E-10
12-296	60.73	10.113	-6.97E-11	4.80E-10

Appendix 3 Table 3 continued

Sample ID	Height (m)	Mass (g)	MS (m^3/kg)	MS spline (m^3/kg)
12-297	60.86	10.529	7.95E-10	4.01E-10
12-298	61.00	10.208	-2.47E-10	3.20E-10
12-299	61.14	10.185	8.22E-10	2.62E-10
12-301	61.30	10.568	2.77E-10	1.84E-10
12-300	61.44	9.928	-6.20E-10	1.48E-10
12-302	61.48	9.813	4.83E-10	1.51E-10
12-303	61.66	10.819	-6.52E-11	2.32E-10
12-304	61.80	10.256	8.16E-10	3.31E-10
12-305	61.94	10.666	2.74E-10	3.97E-10
12-306	62.14	10.417	2.81E-10	4.23E-10
12-308	62.24	10.602	7.90E-10	3.97E-10
12-307	62.39	10.637	4.46E-10	2.96E-10
12-309	62.49	10.341	4.59E-10	2.08E-10
12-310	62.69	10.318	-7.72E-10	1.20E-10
12-311	62.87	9.962	1.12E-10	3.31E-10
12-312	62.97	10.271	1.08E-10	5.46E-10
12-313	63.12	10.164	2.07E-09	8.86E-10
12-314	63.27	10.078	8.31E-10	1.08E-09
12-315	63.47	10.277	1.52E-09	1.12E-09
12-316	63.73	9.984	6.57E-10	9.12E-10
12-317	64.00	10.129	-2.49E-10	7.78E-10
12-318	64.17	9.886	1.77E-09	7.96E-10
12-319	64.29	10.123	1.19E-09	7.25E-10
12-321	64.52	10.485	-6.72E-11	4.11E-10
12-320	64.69	9.652	-7.31E-11	2.30E-10
12-322	64.87	10.814	1.03E-10	1.44E-10
12-323	65.01	10.704	6.13E-10	9.18E-11
12-324	65.16	10.359	2.83E-10	-6.86E-13
12-325	65.29	10.906	-5.64E-10	-7.32E-11
12-326	65.49	10.675	-5.76E-10	-2.59E-11
12-327	65.66	9.757	4.86E-10	1.61E-10
12-328	65.80	10.228	4.64E-10	3.09E-10
12-329	65.93	9.821	8.53E-10	3.90E-10
12-330	66.13	10.386	-2.43E-10	4.30E-10
12-332	66.26	10.231	-6.89E-11	4.77E-10
12-331	66.29	9.992	1.38E-09	4.89E-10
12-333	66.43	10.238	-6.89E-11	5.29E-10
12-334	66.57	9.814	1.78E-09	5.30E-10
12-335	66.69	10.916	-6.46E-11	4.61E-10
12-336	66.83	9.589	-2.63E-10	3.80E-10
12-337	67.01	9.981	1.02E-09	3.19E-10
12-338	67.17	10.530	1.05E-10	2.24E-10
12-339	67.33	10.419	2.81E-10	1.32E-10
12-340	67.51	9.958	-4.35E-10	1.17E-10
12-341	67.71	9.858	4.81E-10	3.06E-10
12-343	67.93	10.074	6.51E-10	6.65E-10
12-342	67.97	10.323	2.83E-10	7.40E-10
12-344	68.11	9.792	1.78E-09	1.00E-09
12-345	68.28	10.547	9.66E-10	1.23E-09
12-346	68.42	9.848	8.50E-10	1.38E-09
12-347	68.59	10.062	2.28E-09	1.47E-09
12-348	68.82	9.843	1.40E-09	1.26E-09
12-349	68.95	10.231	8.18E-10	1.01E-09
12-350	69.15	10.727	7.81E-10	6.19E-10
12-351	69.35	10.048	-2.51E-10	3.46E-10
12-352	69.51	10.325	2.83E-10	3.25E-10
12-353	69.70	9.669	6.78E-10	4.70E-10
12-355	69.95	10.160	8.24E-10	7.51E-10
12-354	70.00	10.426	8.03E-10	8.10E-10

Appendix 3 Table 4: Magnetic susceptibility data from Anhée Nord

Sample ID	Height (m)	Mass (g)	MS (m^3/kg)	MS spline (m^3/kg)
W1	0.05	10.368	1.64E-08	1.58E-08
17-01	0.20	10.181	1.03E-08	1.40E-08
17-02	0.28	9.927	1.33E-08	1.33E-08
17-03	0.36	10.093	1.50E-08	1.21E-08
W2	0.41	10.312	1.73E-08	1.07E-08
17-04	0.48	10.433	4.80E-09	8.02E-09
17-05	0.57	10.125	1.19E-09	4.60E-09
17-06	0.72	10.163	1.18E-09	1.24E-09
17-07	0.83	10.166	6.45E-10	6.91E-10
17-08	0.94	9.989	6.56E-10	1.56E-09
17-09	1.01	10.665	6.15E-10	2.71E-09
17-10	1.08	10.220	3.66E-09	4.08E-09
17-11	1.18	10.718	1.26E-08	5.32E-09
17-12	1.34	9.955	4.76E-10	3.80E-09
17-13	1.57	10.582	9.63E-10	1.66E-09
17-14	1.80	10.060	1.01E-09	2.02E-09
17-15	1.91	9.948	5.04E-09	2.39E-09
17-16	2.18	10.176	8.23E-10	1.81E-09
17-17	2.31	10.393	4.56E-10	2.86E-09
17-18	2.44	10.534	5.79E-09	5.12E-09
17-19	2.55	10.073	9.29E-09	6.58E-09
17-20	2.67	10.193	5.63E-09	6.70E-09
17-21	2.79	10.286	6.99E-09	5.77E-09
17-22	2.90	10.125	4.05E-09	4.35E-09
17-23	2.99	10.153	2.25E-09	3.27E-09
17-24	3.33	10.528	3.38E-09	3.59E-09
17-25	3.45	10.433	6.37E-09	5.42E-09
17-26	3.55	10.439	5.32E-09	7.58E-09
17-27	3.61	10.662	6.06E-09	9.24E-09
17-28	3.65	10.588	1.18E-08	1.04E-08
17-29	3.76	10.344	1.12E-08	1.29E-08
17-30	3.80	10.053	1.51E-08	1.32E-08
17-31b	3.84	10.545	1.90E-08	1.30E-08
17-31t	3.89	10.659	2.12E-08	1.18E-08
17-32	3.95	9.944	8.42E-10	9.51E-09
17-33	4.04	10.539	2.52E-09	6.04E-09
17-34	4.20	10.515	2.52E-09	2.96E-09
17-35	4.35	10.357	4.58E-10	3.77E-09
17-36	4.48	9.639	1.25E-09	6.10E-09
W3	4.53	10.926	2.26E-08	6.58E-09
17-37	4.60	10.835	6.05E-10	6.12E-09
17-38	4.80	10.522	7.96E-10	2.81E-09
17-39	4.94	10.193	1.00E-09	1.65E-09
17-40	5.03	9.879	1.95E-09	1.62E-09
17-41	5.11	9.601	2.57E-09	1.84E-09
17-42	5.16	9.778	8.56E-10	2.04E-09
17-43	5.24	10.585	2.85E-09	2.40E-09
17-44	5.36	10.810	4.13E-09	2.67E-09
17-45	5.47	10.365	1.68E-09	2.41E-09
17-46	5.59	10.440	3.58E-09	2.01E-09
17-47	5.67	10.799	1.03E-10	1.88E-09
08-28	5.72	10.079	1.73E-09	2.02E-09
08-29	5.74	10.546	6.22E-10	2.14E-09
08-30A	5.76	10.705	4.51E-09	2.28E-09
08-30B	5.81	10.464	1.67E-09	2.76E-09
17-48	6.04	10.083	2.27E-09	6.57E-09
17-49	6.13	9.853	1.47E-08	7.97E-09
08-32	6.26	10.196	8.65E-09	7.46E-09
08-31	6.32	9.669	4.24E-09	6.47E-09
17-50	6.43	10.803	5.65E-09	4.37E-09
08-33A	6.51	9.890	6.63E-10	2.94E-09
17-51	6.59	10.085	-6.99E-11	1.97E-09

Sample ID	Height (m)	Mass (g)	MS (m^3/kg)	MS spline (m^3/kg)
08-33B	6.63	10.816	4.63E-09	1.66E-09
17-52	6.75	10.689	-5.76E-10	1.12E-09
08-35	6.98	10.371	4.13E-09	1.47E-09
08-36	7.06	10.186	2.87E-10	1.31E-09
08-38	7.14	10.714	-6.58E-11	1.15E-09
08-37	7.24	10.766	1.79E-09	1.12E-09
08-39	7.41	9.481	1.84E-09	1.08E-09
08-40A	7.43	10.204	8.21E-10	1.07E-09
08-40B	7.46	10.263	6.39E-10	1.06E-09
08-41	7.51	10.419	9.78E-10	1.07E-09
08-42	7.60	9.477	3.09E-10	1.18E-09
08-43	7.63	10.454	2.19E-09	1.24E-09
08-44	7.76	10.301	1.34E-09	1.57E-09
08-47A	7.79	10.780	2.29E-09	1.65E-09
08-47B	7.81	10.189	2.07E-09	1.72E-09
08-47C	7.87	10.028	1.74E-09	1.94E-09
08-45	7.96	10.426	1.85E-09	2.54E-09
08-46	8.12	10.643	1.13E-09	4.80E-09
W4	8.30	10.366	1.83E-08	7.40E-09
08-48	8.34	10.343	1.07E-10	7.21E-09
08-49	8.45	10.110	1.37E-08	5.49E-09
08-50A	8.47	10.242	1.35E-09	5.02E-09
08-50B	8.53	10.077	1.01E-09	3.56E-09
08-51	8.56	9.545	1.07E-09	2.93E-09
08-52	8.58	10.490	1.84E-09	2.56E-09
08-53	8.68	10.573	1.31E-09	1.49E-09
08-55A	8.85	10.374	4.48E-09	1.88E-09
08-55B	8.89	10.179	1.36E-09	2.25E-09
08-56	8.91	10.042	1.20E-09	2.49E-09
08-57A	9.06	10.413	6.30E-10	5.43E-09
08-57B	9.11	10.312	1.87E-09	6.78E-09
W5	9.15	10.184	2.15E-08	7.76E-09
08-58	9.24	10.695	6.55E-09	8.88E-09
08-59A	9.41	10.470	7.38E-09	9.37E-09
08-60	9.55	10.761	1.21E-08	1.01E-08
08-61	9.64	9.717	7.96E-09	1.07E-08
08-62	9.79	10.491	9.27E-09	1.23E-08
08-63	9.86	10.172	1.90E-08	1.29E-08
08-64	10.18	10.841	6.30E-09	9.35E-09
08-65A	10.20	10.552	1.06E-08	9.17E-09
08-65B	10.25	10.422	9.85E-09	8.86E-09
08-66B	10.35	10.745	5.51E-09	9.00E-09
08-67A	10.37	9.387	5.92E-09	9.19E-09
08-67B	10.41	10.654	7.94E-09	9.68E-09
W6	10.54	10.472	3.00E-08	1.01E-08
08-68	10.58	10.659	3.51E-09	9.14E-09
08-69	10.66	10.304	9.89E-10	6.28E-09
08-70	10.78	10.259	1.70E-09	2.44E-09
08-71A	10.80	10.673	1.12E-09	1.98E-09
08-71B	10.82	10.541	4.50E-10	1.58E-09
08-73A	11.14	10.311	4.60E-10	7.87E-10
08-73B	11.17	9.138	2.90E-09	8.86E-10
08-72	11.28	10.804	1.62E-09	9.88E-10
08-74	11.38	9.456	1.65E-09	9.85E-10
08-75	11.48	10.513	-2.40E-10	1.50E-09
08-76	11.52	10.530	-6.70E-11	2.04E-09
08-77	11.62	10.874	2.27E-09	4.19E-09
08-78A	11.64	10.229	3.66E-09	4.71E-09
08-78B	11.67	10.843	4.12E-09	5.47E-09
08-80	11.72	10.504	4.25E-09	6.55E-09
W7	11.76	10.572	2.46E-08	7.00E-09
08-81	11.79	10.537	2.86E-09	6.97E-09

Appendix 3 Table 4 continued

Sample ID	Height (m)	Mass (g)	MS (m^3/kg)	MS spline (m^3/kg)
08-82	11.90	10.188	3.49E-09	5.27E-09
08-86	11.96	10.263	1.88E-09	4.10E-09
08-87A	11.97	10.487	3.22E-09	3.93E-09
08-87B	12.00	10.085	1.91E-09	3.49E-09
08-84	12.04	9.914	4.51E-09	3.02E-09
08-85A	12.07	10.365	2.38E-09	2.76E-09
08-85B	12.13	10.340	1.86E-09	2.43E-09
08-83	12.15	10.091	2.99E-09	2.37E-09
08-88	12.32	10.225	1.88E-09	2.75E-09
08-91	12.41	10.478	2.01E-09	3.37E-09
08-90A	12.51	10.310	8.55E-09	3.80E-09
08-90B	12.55	10.446	2.89E-09	3.69E-09
08-89A	12.61	9.774	3.83E-09	3.25E-09
08-89B	12.66	10.579	1.31E-09	2.75E-09
08-89C	12.69	10.744	2.30E-09	2.45E-09
08-92A	12.82	11.073	7.56E-10	1.37E-09
08-92B	12.88	10.835	1.11E-09	1.09E-09
08-93	12.90	10.808	1.28E-09	1.02E-09
08-94A	12.92	10.459	4.53E-10	9.78E-10
08-94B	12.97	10.739	1.12E-09	9.27E-10
08-94Y	13.04	10.881	6.03E-10	9.81E-10
08-94X	13.10	10.367	1.86E-09	1.11E-09
09-95A	13.21	10.453	1.84E-09	1.43E-09
08-95B	13.28	10.313	9.88E-10	1.72E-09
08-96	13.35	10.800	9.43E-10	2.16E-09
08-97	13.39	10.217	3.13E-09	2.47E-09
08-98	13.52	10.507	4.60E-09	3.37E-09
08-99B	14.06	9.553	4.30E-09	6.13E-09
08-99A	14.08	10.516	6.14E-09	6.51E-09
08-99D	14.14	10.002	5.74E-09	7.80E-09
08-99C	14.16	10.150	8.87E-09	8.27E-09
08-100A	14.23	10.798	1.19E-08	9.78E-09
08-100B	14.26	10.578	1.09E-08	1.03E-08
08-101	14.36	10.002	1.17E-08	1.11E-08
08-102	14.53	10.090	8.56E-09	9.00E-09
08-103	14.59	10.872	1.48E-08	7.25E-09
08-104A	14.65	10.807	1.45E-09	5.09E-09
08-104B	14.69	10.688	4.44E-10	3.71E-09
08-104C	14.73	10.246	1.53E-09	2.54E-09
08-105A	15.24	10.110	1.73E-09	5.41E-10
08-105B	15.30	10.787	6.08E-10	7.24E-10
08-106	15.46	10.532	4.50E-10	1.09E-09
08-107	15.56	10.569	1.31E-09	1.46E-09
08-108	15.76	10.881	3.27E-09	2.14E-09
08-109	15.85	10.215	2.42E-09	2.15E-09
08-110	15.87	10.468	1.84E-09	2.14E-09
08-111A	15.92	10.269	1.70E-09	2.13E-09
08-111B	15.96	10.559	2.51E-09	2.17E-09
08-112	15.98	9.862	1.59E-09	2.20E-09
08-125A	16.17	10.357	2.21E-09	3.26E-09
08113Z	16.33	10.641	6.75E-09	4.79E-09
08-113A	16.45	10.200	5.09E-09	5.51E-09
08-113B	16.50	10.511	4.59E-09	5.78E-09
08-113Y	16.65	10.582	7.99E-09	6.63E-09
08-113X	16.71	9.840	5.46E-09	6.83E-09
08-114	16.79	10.234	7.91E-09	6.97E-09
08-115A	17.17	10.242	4.72E-09	5.03E-09
08-115B	17.23	10.358	5.19E-09	4.58E-09
08-116A	17.49	10.609	3.36E-09	3.37E-09
08-116B	17.59	10.531	3.04E-09	3.90E-09
08-117	17.75	9.928	4.13E-09	6.54E-09
W8 (base)	17.99	10.227	1.54E-08	1.07E-08
W8 (mid.)	18.05	10.167	1.21E-08	1.02E-08
W8 (top)	18.10	10.243	1.29E-08	9.25E-09
08-118	18.15	10.185	8.22E-10	8.03E-09
08-119	18.41	10.034	2.82E-09	4.20E-09
08-122A	18.47	10.478	4.26E-09	4.04E-09
08-122B	18.52	10.382	3.95E-09	4.05E-09
08-122Z	18.67	10.354	6.07E-09	4.02E-09
08-120	18.77	10.405	3.77E-09	3.43E-09
08-121A	18.79	10.564	3.88E-09	3.27E-09
08-121B	18.84	10.584	1.13E-09	2.87E-09
08-121C	18.87	10.451	6.27E-10	2.66E-09
08-123A	18.89	10.589	4.22E-09	2.53E-09
08-123B	18.98	10.735	1.96E-09	2.05E-09
08-124A	19.04	10.335	2.57E-09	1.77E-09
08-124B	19.08	10.801	1.11E-09	1.58E-09
08-126	19.41	10.757	6.10E-10	3.99E-10
08-128	19.88	10.525	1.83E-09	2.07E-09
08-130	20.11	10.135	6.38E-09	6.73E-09
08-131	20.15	10.746	4.16E-09	7.86E-09
08-129	20.27	10.405	1.50E-09	1.11E-08
08-132A	20.30	10.136	1.89E-08	1.16E-08
08-132C	20.31	10.311	1.72E-08	1.17E-08
08-132B	20.32	10.632	1.82E-08	1.18E-08
08-133A	20.53	10.037	1.92E-09	6.90E-09
08-133B	20.60	10.210	2.95E-09	5.22E-09
08-134	20.62	10.617	5.74E-09	4.87E-09
08-135A	20.87	10.106	3.16E-09	3.89E-09
08-135B	20.90	9.171	5.07E-09	4.00E-09
08-136A	20.92	10.325	5.73E-09	4.07E-09
08-136B	20.96	10.663	2.66E-09	4.19E-09
08-137	21.01	9.999	4.47E-09	4.36E-09
08-138	21.17	9.368	4.57E-09	4.77E-09
08-139A	21.25	10.706	6.04E-09	4.73E-09
08-139B	21.29	10.326	4.85E-09	4.60E-09
08-140A	21.39	10.492	4.26E-09	4.10E-09
08-140B	21.44	10.599	3.02E-09	3.87E-09
08-140C	21.49	10.584	2.33E-09	3.75E-09
08-142	21.54	10.106	4.24E-09	3.74E-09
08-141A	21.78	10.075	4.25E-09	3.91E-09
08-141B	21.82	10.818	5.30E-09	3.78E-09
08-143	21.91	9.673	2.18E-09	3.25E-09
08-144A	22.02	10.455	2.36E-09	2.56E-09
08-144B	22.08	10.618	2.33E-09	2.25E-09
08-145	22.47	10.766	1.28E-09	1.64E-09
08-146	22.77	10.289	3.46E-09	2.97E-09
08-147A	23.00	10.721	2.98E-09	3.65E-09
08-147B	23.03	10.921	3.92E-09	3.74E-09
08-148A	23.25	10.654	4.02E-09	4.13E-09
08-148B	23.31	10.106	6.21E-09	4.03E-09
08-149A	23.35	10.778	2.97E-09	3.89E-09
08-149B	23.39	10.064	2.82E-09	3.74E-09
08-150	23.55	10.130	3.16E-09	3.23E-09
08-151A	23.73	10.174	3.14E-09	2.77E-09
08-151B	23.78	10.216	2.42E-09	2.62E-09
08-151C	23.83	10.180	2.43E-09	2.47E-09

Appendix 3 Table 5: Magnetic susceptibility data from Anhée Sud

Sample ID	Height (m)	Mass (g)	MS (m^3/kg)	MS spline (m^3/kg)
18-01	0.02	10.713	1.43E-08	8.91E-09
18-02	0.09	10.154	1.72E-09	5.14E-09
18-03	0.17	10.381	-1.29E-09	1.88E-09
18-04	0.19	10.365	-6.80E-11	1.32E-09
18-05	0.28	9.961	2.94E-10	-1.02E-10
18-06	0.37	10.026	8.35E-10	-3.41E-10
18-07	0.46	10.169	6.45E-10	-1.49E-10
18-08	0.61	10.070	6.51E-10	2.09E-10
18-09	0.65	10.856	1.02E-10	2.61E-10
18-10	0.76	10.502	4.52E-10	3.22E-10
18-11	0.92	10.639	2.75E-10	3.39E-10
18-12	1.12	10.461	4.53E-10	7.64E-10
18-13	1.28	10.781	1.11E-09	1.72E-09
18-14	1.48	10.207	3.13E-09	2.93E-09
18-15	1.56	10.318	5.91E-09	2.88E-09
18-16	1.64	10.721	4.42E-10	2.41E-09
18-17	1.72	10.224	1.17E-09	1.94E-09
18-18	1.82	10.364	1.86E-09	1.60E-09
18-19	1.92	10.553	1.31E-09	1.46E-09
18-20	1.96	8.590	1.40E-09	1.46E-09
18-21	2.01	10.823	2.12E-09	1.48E-09
18-22	2.08	10.632	6.17E-10	1.58E-09
18-23	2.24	9.887	1.76E-09	2.02E-09
18-24	2.31	10.560	3.54E-09	2.11E-09
18-25	2.44	10.692	1.29E-09	1.80E-09
18-26	2.60	10.325	1.16E-09	1.12E-09
18-28	2.78	10.089	2.78E-10	4.30E-10
18-27	2.98	10.533	-6.99E-11	1.79E-10
18-29	3.23	10.334	1.16E-09	4.75E-10
18-30	3.35	10.684	-6.60E-11	5.31E-10
18-31	3.46	10.187	1.00E-09	6.74E-10
18-32	3.55	10.494	1.06E-10	8.60E-10
18-33	3.62	10.190	1.18E-09	1.05E-09
18-34	3.72	10.873	1.44E-09	1.25E-09
18-35	3.76	10.786	1.95E-09	1.26E-09
18-36	3.97	10.819	6.06E-10	7.09E-10
18-37	4.29	10.211	2.87E-10	1.09E-09
18-38	4.47	10.654	3.00E-09	3.37E-09
18-41	4.51	10.254	3.65E-09	4.01E-09
18-42	4.61	10.504	4.94E-09	5.53E-09
18-40	4.76	10.464	1.02E-08	6.36E-09
18-43	4.86	10.605	6.78E-09	5.00E-09
18-44	4.95	10.467	4.53E-10	3.08E-09
18-45	5.08	10.763	2.72E-10	1.32E-09
18-46	5.18	10.029	1.38E-09	1.60E-09
18-47	5.25	10.463	6.27E-10	2.75E-09
18-48	5.35	10.208	6.51E-09	5.55E-09
18-49	5.41	10.278	7.35E-09	7.53E-09
18-50	5.50	10.403	6.91E-09	1.05E-08
18-51	5.56	10.704	1.69E-08	1.22E-08
18-52	5.64	10.443	1.56E-08	1.33E-08
18-53	5.71	10.518	1.61E-08	1.32E-08
18-54	5.78	10.675	1.01E-08	1.24E-08
18-55	5.89	10.682	7.07E-09	1.13E-08
18-56	5.91	10.143	1.44E-08	1.12E-08
18-57	6.07	10.232	8.97E-09	1.29E-08
18-58	6.21	10.228	1.50E-08	1.83E-08
18-59	6.24	10.555	2.10E-08	1.97E-08
18-60	6.33	10.566	2.46E-08	2.33E-08
18-61	6.44	10.500	3.97E-08	2.51E-08
18-62	6.48	10.686	1.86E-08	2.47E-08
18-63	6.58	10.777	1.86E-08	2.25E-08
18-64	6.69	10.391	1.69E-08	2.05E-08
18-65	6.81	9.953	2.14E-08	1.98E-08
18-67	6.91	10.797	2.09E-08	1.93E-08
18-66	6.97	10.134	2.21E-08	1.89E-08
18-68	7.07	10.126	9.96E-09	1.85E-08
18-69	7.27	10.567	2.09E-08	1.96E-08
18-70	7.38	10.503	3.13E-08	1.71E-08
18-71	7.50	10.149	8.25E-10	1.02E-08
18-72	7.62	10.105	8.29E-10	5.00E-09
18-73	7.87	10.359	6.41E-09	4.23E-09
18-74	7.95	10.573	8.34E-09	4.65E-09
18-75	7.99	10.075	1.91E-09	4.77E-09
18-76	8.17	10.344	4.32E-09	5.63E-09
18-77	8.51	10.359	9.91E-09	7.71E-09
18-78	8.80	10.743	2.64E-09	3.88E-09
18-79	8.84	10.897	3.60E-09	3.41E-09
18-80	8.90	10.709	1.80E-09	2.91E-09
18-81	8.99	10.705	3.16E-09	2.55E-09
18-82	9.10	10.601	2.84E-09	2.46E-09
18-83	9.21	10.434	2.72E-09	2.53E-09
18-84	9.30	10.555	2.00E-09	2.72E-09
18-85	9.48	10.430	3.93E-09	3.47E-09
18-86	9.57	10.159	3.68E-09	3.77E-09
18-87	9.69	10.533	3.21E-09	3.96E-09
18-88	9.79	10.615	5.40E-09	3.85E-09
18-89	10.11	10.656	2.75E-10	1.59E-09
18-90	10.20	10.616	1.47E-09	1.39E-09
18-91	10.35	10.304	1.52E-09	1.52E-09
18-92	10.45	10.451	2.89E-09	1.56E-09
18-93	10.59	10.592	6.19E-10	1.29E-09
18-94	10.72	10.418	1.33E-09	1.29E-09
18-95	10.88	10.844	7.72E-10	2.08E-09
18-97	11.00	10.610	4.89E-09	3.26E-09
18-96	11.20	9.939	2.67E-09	5.18E-09
18-98	11.33	10.830	7.47E-09	6.51E-09
18-99	11.45	10.789	1.02E-08	6.44E-09
18-101	11.61	10.398	2.03E-09	3.84E-09
18-100	11.71	10.514	1.31E-09	2.45E-09
18-102	11.83	10.786	1.11E-09	1.99E-09
18-103	12.03	10.659	4.19E-09	3.34E-09
18-104	12.24	10.800	4.64E-09	4.29E-09
18-105	12.34	7.326	5.35E-09	4.04E-09
18-106	12.48	9.307	2.26E-09	3.21E-09
18-107	12.58	10.545	1.31E-09	3.04E-09
18-108	12.68	10.743	2.98E-09	3.48E-09
18-109	12.82	10.836	7.80E-09	4.01E-09
18-110	12.96	10.188	1.36E-09	3.17E-09
18-111	13.08	10.493	1.84E-09	2.53E-09
18-112	13.28	10.333	2.92E-09	2.41E-09
18-113	13.44	10.041	2.64E-09	2.34E-09
18-114	13.57	10.504	1.49E-09	2.22E-09
18-115	13.73	10.007	2.65E-09	2.20E-09
18-116	13.91	10.133	2.08E-09	1.83E-09
18-117	14.17	10.235	2.86E-10	9.68E-10
18-119	14.19	10.440	1.15E-09	9.41E-10
18-118	14.27	10.741	1.62E-09	9.17E-10
18-120	14.35	9.738	6.73E-10	1.02E-09
18-121	14.51	10.737	1.63E-09	1.96E-09
18-122	14.61	10.223	2.59E-09	3.17E-09
18-123	14.71	10.301	4.16E-09	4.77E-09
18-124	14.81	10.415	5.33E-09	6.41E-09
18-125	14.91	10.182	1.19E-08	7.37E-09

Appendix 3 Table 5 continued

Sample ID	Height (m)	Mass (g)	MS (m^3/kg)	MS spline (m^3/kg)
18-126	14.99	10.479	7.90E-09	7.10E-09
18-127	15.05	10.396	4.30E-09	6.48E-09
18-128	15.17	10.626	4.03E-09	5.12E-09
18-129	15.27	10.177	4.57E-09	4.24E-09
18-130	15.42	9.912	3.77E-09	3.17E-09
18-131	15.54	10.494	2.01E-09	2.54E-09
18-132	15.69	10.851	2.11E-09	2.46E-09
18-133	15.76	10.871	1.44E-09	2.72E-09
18-134	15.85	10.293	5.22E-09	3.19E-09
18-135	15.97	10.544	3.20E-09	3.44E-09
18-136	16.02	10.334	3.80E-09	3.44E-09
18-137	16.20	10.433	3.41E-09	3.38E-09
18-138	16.33	10.863	2.78E-09	3.90E-09
18-139	16.47	10.450	5.49E-09	5.52E-09
18-140	16.59	10.356	5.36E-09	7.37E-09
18-141	16.67	10.469	1.33E-08	8.50E-09
18-142	16.73	10.212	6.68E-09	8.99E-09
18-143	16.83	9.972	9.03E-09	9.35E-09
18-144	16.93	10.470	1.02E-08	9.13E-09
18-145	17.43	10.249	1.53E-09	2.41E-09
18-146	17.54	9.998	1.38E-09	1.68E-09
18-147	17.60	7.501	2.33E-09	1.52E-09
18-148	17.65	10.366	9.83E-10	1.46E-09
18-149	18.11	5.460	2.20E-09	1.99E-09
18-150	18.18	8.100	3.27E-09	1.71E-09
18-151	18.25	10.219	1.09E-10	1.27E-09
18-152	18.39	9.903	-7.12E-11	5.02E-10
18-153	18.53	10.373	6.32E-10	2.20E-10
18-154	18.69	10.739	-4.04E-10	3.33E-10
18-155	18.77	10.355	8.09E-10	5.82E-10
18-156	18.86	10.272	1.35E-09	8.83E-10
18-157	18.97	10.165	1.54E-09	1.13E-09
18-158	19.07	10.601	1.30E-09	1.31E-09
18-159	19.15	10.667	1.30E-09	1.56E-09
18-160	19.26	10.814	2.12E-09	2.29E-09
18-161	19.35	10.219	2.95E-09	3.33E-09
18-162	19.48	10.761	3.81E-09	5.54E-09
18-163	19.59	9.938	3.58E-09	7.66E-09
18-164	19.68	9.896	2.63E-08	8.50E-09
18-165	19.70	10.231	1.17E-09	8.39E-09
18-167	19.84	9.152	2.10E-09	5.88E-09
18-166	19.93	10.601	3.70E-09	4.43E-09
18-168	20.09	9.453	3.00E-09	3.86E-09
18-169	20.27	10.399	3.95E-09	5.90E-09
18-170	20.39	10.510	9.94E-09	7.49E-09
18-171	20.44	10.269	1.07E-08	7.68E-09
18-172	20.56	10.048	4.45E-09	6.84E-09
18-173	20.79	10.543	3.55E-09	4.50E-09
18-174	20.82	10.594	5.59E-09	4.25E-09
18-175	20.94	10.514	3.04E-09	3.40E-09
18-176	20.98	10.569	2.17E-09	3.23E-09
18-177	21.06	10.161	3.15E-09	3.12E-09
18-178	21.16	10.047	4.45E-09	3.11E-09
18-179	21.29	10.300	2.93E-09	2.98E-09
18-180	21.40	11.389	2.81E-09	3.03E-09
18-181	21.48	10.235	1.88E-09	3.37E-09
18-182	21.58	10.570	5.77E-09	4.16E-09
18-183	21.66	10.529	4.93E-09	4.84E-09
18-184	21.80	10.317	4.68E-09	6.27E-09
18-185	22.00	10.346	8.87E-09	8.92E-09
18-186	22.11	10.427	1.00E-08	9.54E-09
18-187	22.21	10.901	1.31E-08	8.80E-09

Sample ID	Height (m)	Mass (g)	MS (m^3/kg)	MS spline (m^3/kg)
18-188	22.31	10.586	4.05E-09	6.80E-09
18-189	22.41	10.292	5.57E-09	4.77E-09
18-190	22.51	10.734	1.96E-09	3.42E-09
18-191	22.59	10.646	2.49E-09	3.30E-09
18-192	22.75	10.312	2.57E-09	5.80E-09
18-193	22.89	10.721	3.32E-09	9.52E-09
W12	22.93	10.397	2.48E-08	1.02E-08
18-194	23.12	10.467	4.44E-09	8.34E-09
18-195	23.32	10.633	2.32E-09	7.04E-09
W13	23.44	10.675	1.11E-08	8.25E-09
18-196	23.47	10.544	1.18E-08	8.66E-09
18-197	23.55	10.148	4.04E-09	8.01E-09
18-198	23.60	9.958	1.10E-08	7.54E-09
18-199	23.66	10.468	5.31E-09	6.95E-09
18-200	23.84	10.371	5.53E-09	4.27E-09
18-201	23.94	10.348	2.21E-09	2.50E-09
18-202	24.01	10.602	6.19E-10	1.41E-09
18-203	24.09	10.424	-6.76E-11	5.31E-10
18-204	24.18	10.629	1.04E-10	3.15E-11
18-205	24.28	10.465	6.27E-10	-7.59E-11
18-206	24.40	10.441	9.76E-10	2.32E-10
18-207	24.49	10.070	6.51E-10	9.16E-10
18-208	24.59	10.159	1.90E-09	2.54E-09
18-209	24.71	10.428	3.41E-09	6.15E-09
18-211	24.82	10.323	9.95E-09	1.09E-08
18-212	24.90	10.697	1.86E-08	1.44E-08
18-213	25.07	10.530	1.96E-08	1.92E-08
18-214	25.25	10.723	2.05E-08	2.16E-08

Appendix 3 Table 6: Stable isotope data from Lives-sur-Meuse, Section 2

Sample ID	Height (m)	$\delta^{13}C$ (‰ V-PDB)	$\delta^{18}O$ (‰ V-PDB)
16-02	4.76	1.37	-6.52
16-07	5.22	1.71	-4.93
16-12	5.56	2.09	-12.45
16-20	6.39	1.84	-7.17
16-26	7.00	1.98	-3.77
16-32	7.54	2.06	-6.64
16-35	7.91	2.10	-6.94
16-42	8.78	2.20	-7.17
16-48	9.57	1.99	-8.05
16-53	10.19	1.81	-7.90
16-56	10.46	2.00	-8.07
16-59	10.81	1.98	-7.35
16-64	11.42	2.94	-14.10
16-66	11.69	1.68	-7.71
16-68	11.83	2.42	-6.37
16-70	12.03	2.09	-7.33
16-74	12.42	1.97	-7.21
16-75	12.54	1.95	-7.61
16-77	12.70	2.24	-6.26
16-78	12.83	2.89	-2.59
16-80	13.08	2.57	-3.30
16-83	13.40	2.24	-6.56
16-85	13.60	1.95	-6.71
16-87	13.79	2.10	-5.99
16-92	14.33	2.19	-6.70
16-94	14.49	1.99	-6.39
16-99	15.03	1.89	-7.21
16-101	15.07	1.84	-6.41
16-104	15.46	2.12	-2.99
16-107	15.78	1.78	-6.29
16-109	16.11	2.00	-6.27
16-112	16.48	1.95	-5.09
16-116	16.93	2.01	-6.75
16-122	17.67	1.73	-6.07
16-127	18.22	2.01	-5.86
16-131	18.74	1.76	-7.09
16-135	19.14	1.81	-6.95
16-137	19.33	1.98	-6.63
16-140	19.64	2.24	-7.17
16-145	20.15	2.21	-6.75
16-152	20.91	1.89	-7.34
16-159	21.70	2.33	-6.31
16-162	22.09	1.78	-7.24
16-163	22.16	1.86	-7.29
16-168	22.78	1.74	-6.82
16-171	22.99	1.97	-7.15
16-177	23.88	1.84	-6.78
09-01A	25.34	2.12	-7.50
16-178	25.95	2.42	-7.07
16-182	26.36	2.13	-7.58
16-189	27.23	2.03	-7.18
16-193	27.64	2.15	-7.70
16-204	28.35	2.31	-7.82
16-207	28.55	2.63	-7.79
16-215	29.31	2.25	-7.86
16-222	30.12	2.15	-8.24
16-230	31.03	2.83	-7.69
16-232	31.24	3.07	-7.16
16-237	31.99	2.47	-7.75
16-240	32.22	2.42	-8.01

Sample ID	Height (m)	$\delta^{13}C$ (‰ V-PDB)	$\delta^{18}O$ (‰ V-PDB)
16-243	32.52	2.76	-7.62
16-246	32.77	2.45	-7.73
16-247	32.85	2.35	-7.73
16-249	32.99	2.50	-7.56
16-262	34.26	1.92	-7.89
16-266	34.73	2.07	-7.48
16-270	34.94	2.47	-7.16
16-281	36.04	2.02	-7.09
16-285	36.53	2.16	-6.68
16-291	37.38	2.32	-5.96
16-293	37.54	1.83	-6.77
16-300	38.06	2.39	-6.91
16-312	38.91	2.49	-6.98
13-315	39.17	2.26	-6.86
03-18	39.94	2.32	-6.70
03-22	40.54	2.65	-6.76
03-25B	41.30	2.52	-6.89
03-33	42.60	2.89	-6.39
03-37	43.63	2.65	-6.93
03-38	45.13	2.40	-6.93
03-43A	45.73	2.11	-7.93
03-44B	45.98	2.77	-7.09
03-42B	46.53	2.82	-7.22
03-45	47.67	2.94	-7.08
03-46B	48.62	2.73	-7.13
03-49B	49.06	2.43	-7.11
03-51	49.42	2.49	-7.10
D3C	49.80	2.94	-6.79
D4B	50.04	2.89	-7.02
03-53C	50.74	2.61	-6.92
03-55B	51.09	2.47	-7.09
03-57B	51.53	2.24	-7.30
03-59	52.24	2.57	-6.88
D5A	52.62	1.85	-6.74
03-64B	52.99	2.58	-6.76
03-68A	53.49	2.49	-6.89
03-77A	54.22	2.34	-7.09
03-74B	55.27	1.98	-7.29
03-75B	55.47	2.39	-7.09
04-08A	56.31	2.70	-7.37
04-11	57.02	2.59	-7.99
04-14A	58.21	2.39	-7.64
04-16B	59.16	2.44	-7.55
04-22B	59.85	1.85	-7.63
04-27A	60.31	1.83	-7.49
04-28	60.63	2.47	-7.59
04-31C	61.63	2.16	-7.61

Appendix 3 Table 7: Stable isotope data from Awirs West Quarry

Sample ID	Height (m)	$\delta^{13}C$ (‰ V-PDB)	$\delta^{18}O$ (‰ V-PDB)
14-40	4.36	2.41	-8.22
14-43	4.77	2.52	-7.32
14-44	4.79	2.49	-7.88
14-54	6.30	3.28	-9.17
14-64	7.86	2.02	-8.67
14-67	8.46	2.63	-7.71
14-70	8.85	2.24	-10.14
15-01	10.22	2.81	-9.38
14-102	10.78	1.99	-8.38
14-108	11.39	2.57	-8.46
14-78	11.98	2.38	-8.40
14-83	12.47	1.73	-8.21
14-90	13.07	2.25	-8.46
14-95	13.57	1.56	-7.64
14-97	13.68	2.07	-10.41
14-100	14.14	2.23	-8.92
12-12	15.04	2.11	-9.96
12-19	15.78	2.91	-10.30
12-26	16.34	1.27	-8.62
12-25	16.46	1.83	-7.74
12-27	16.56	2.82	-9.63
12-33	17.17	2.71	-9.60
12-39	17.71	2.79	-9.32
12-40	17.77	2.95	-9.06
12-42	17.99	2.52	-9.02
12-44	18.26	2.13	-8.34
12-46	18.44	2.10	-9.20
12-48	18.63	2.62	-10.17
12-53	19.22	0.93	-7.24
12-56	19.66	2.46	-9.18
12-65	20.82	2.33	-9.26
12-67	21.42	2.97	-9.14
12-76	22.19	2.39	-8.41
12-82	23.33	3.30	-9.15
13-07	24.08	2.89	-9.20
13-15	24.79	2.66	-9.13
13-20	25.51	2.85	-8.60
13-24	26.02	1.20	-8.42
13-28	26.54	2.66	-8.04
13-32	26.98	1.44	-8.65
13-34	27.18	2.25	-9.91
13-44	28.02	2.24	-7.41
13-46	28.38	1.02	-11.98
13-51	29.14	2.55	-8.32
13-52	29.56	2.37	-8.74
13-61	30.80	2.21	-10.53
13-69	33.58	2.62	-9.60
13-82	35.67	2.54	-10.21
12-113	37.46	2.32	-9.95
12-120	39.23	0.74	-9.20
12-133	41.08	0.78	-9.96
12-143	42.19	1.56	-9.98
12-144	42.35	1.35	-7.03
12-148	42.89	0.24	-7.69
12-153	43.58	0.53	-7.23
12-156	44.00	0.64	-9.30

Appendix 3 Table 8: Stable isotope data from Anhée Nord

Sample ID	Height (m)	$\delta^{13}C$ (‰ V-PDB)	$\delta^{18}O$ (‰ V-PDB)
17-02	0.28	-1.34	-10.97
17-04	0.48	0.29	-10.94
17-06	0.72	-0.93	-5.67
17-08	0.94	-1.53	-10.73
17-12	1.34	0.71	-9.36
17-14	1.80	-0.70	-10.28
17-17	2.31	0.02	-10.54
17-19	2.55	0.96	-10.00
17-21	2.79	0.77	-9.33
17-24	3.33	0.42	-8.56
17-29	3.76	0.21	-9.27
17-32	3.95	-0.23	-9.58
17-35	4.35	-0.11	-10.70
17-43	5.24	-2.87	-9.39
17-46	5.59	-1.94	-10.16
17-49	6.13	-3.32	-9.53
17-52	6.75	-2.11	-10.51
08-38	7.14	-1.20	-10.57
08-39	7.41	-0.98	-11.37
08-46	8.12	-0.09	-9.03
08-53	8.68	-0.32	-10.69
08-57A	9.06	0.08	-9.43
08-60	9.55	-0.04	-10.21
08-63	9.86	-0.21	-9.86
08-67A	10.37	0.31	-10.50
08-70	10.78	0.02	-7.37
08-72	11.28	-0.40	-11.31
08-77	11.62	-0.65	-10.82
08-85A	12.07	-0.73	-9.98
08-90A	12.51	-0.20	-11.12
08-94A	12.92	0.23	-10.61
08-96	13.35	-0.04	-11.13
08-97	13.39	0.08	-10.78
08-98	13.52	-0.22	-10.08
08-99B	14.06	0.31	-9.14
08-102	14.53	-0.19	-8.67
08-104A	14.65	-0.33	-9.23
08-105A	15.24	-0.81	-10.41
08-108	15.76	-0.35	-9.94
08-125A	16.17	-0.56	-10.89
08-113Z	16.33	-0.10	-9.96
08-113X	16.71	-0.07	-9.84
08-115A	17.17	0.01	-9.87
08-116A	17.49	-0.24	-10.89
08-117	17.75	-0.34	-10.72
08-122A	18.47	0.48	-9.33
08-123A	18.89	-0.31	-10.56
08-126	19.41	-0.26	-9.33
08-128	19.88	-0.48	-10.00
08-132B	20.32	-0.44	-11.01
08-137	21.01	-0.51	-10.21
08-142	21.54	-0.12	-9.92
08-143	21.91	-0.64	-11.06
08-145	22.47	-3.08	-10.75
08-147A	23.00	-0.12	-10.28
08-149A	23.35	-0.08	-10.73